université PARIS-SACLAY

NNT : 2017SACLS208

Thèse de doctorat

Study of the production cross section of the Higgs boson decaying into four leptons and study of muon isolation in the ATLAS experiment at the LHC

Thèse de doctorat de l'Université Paris-Saclay préparée au Commissariat à l'Énergie Atomique et aux Énergies Alternatives (CEA), au sein du Département de Physique des Particules (DPhP) de l'Institut de Recherche sur les lois Fondamentales de l'Univers (IRFU)

École doctorale n°517 Sciences physiques : particules, hadrons, énergie, noyau, instrumentation, imagerie, cosmos et simulation (PHENIICS)
Spécialité de doctorat : physique des particules

Thèse présentée et soutenue à Saint-Aubin, le 22 septembre 2017

M. Arthur Lesage

Composition du Jury :

M. Patrick Puzo Professeur, Université Paris Sud XI	Président
Mme Chiara Mariotti Professeure, INFN (Torino)	Rapporteuse
Mme Chara Petridou Professeure, Université Aristote (Thessaloniki)	Rapporteuse
Mme Chiara Roda Professeure assistante, Université des Études de Pise	Examinatrice
Mme Stefania Spagnolo Professeure associée, Université del Salento	Examinatrice
M. Reisaburo Tanaka Chargé de recherche, Laboratoire de l'Accélérateur Linéaire (LAL)	Examinateur
Mme Rodanthi Nikolaidou Ingénieure chercheuse, CEA Saclay IRFU/DPhP	Directrice de thèse

Acknowledgements

Conducting a PhD in physics was my objective as a student and I want to thank everyone who helped me in this adventure, as well as introducing me to the universe of particle physics.

My warmest thanks go to Rosy. You gave me the opportunity to do my PhD thesis within the ATLAS group of the DPhP at CEA under your valuable supervision. You constantly believed in my capability to perform challenging studies, giving me the chance to collaborate in an extraordinary international environment, which is CERN. On top of having a great visibility in the ATLAS collaboration, you made sure our work would be promoted among the analysis groups. We tackled the problems together with a great efficiency and achieved so much in three years. I thank you for your devolution every day: at the beginning when you assisted me with patience in my discovery of particle physics, and in the end to ensure I would defend our work in a great international conference (LHCP2017) and through the writing of my thesis. You gave me the opportunity to work on a well-structured project which combines performance and analysis works: from the muon isolation to studies in the Higgs-to-four-lepton final state. Although not always on the same boat, I enjoyed the scientifically rich conversations I had with you, which helped me to find the correct answers to my questions. I wish you all the best for your next challenges within the collaboration, but I already know you will face them brilliantly.

I also want to thank you Vanina for your support throughout the thesis. A bit like a second mother with Rosy, you took care my project was coherent and was progressing regularly. Your help in our battles against administration was immensely appreciated (and not only by me!). It is important for every PhD student to have a godmother/father and you played your role with great dedication.

I would also like to thank all the members of the jury of my thesis. Thank you Pr. Chiara Mariotti and Pr. Chara Petridou for being my *rapporteuses* and making very valuable comments to my manuscript. Thank you also Pr. Patrick Puzo, Dr. Chiara Roda, Dr. Stefania Spagnolo and Dr. Reisaburo Tanaka for your interesting remarks and the discussions we had. Thanks to all of you for helping me to graduate.

I thank the DPhP group (especially Claude), for accepting me within your team and funding my work as a PhD student. This adventure (including participation to lectures, seminars and conferences) would not have been possible without your support.

The preparation of the PhD is a demanding but exciting experience. I thank all my friends from CERN, CEA and other locations in the world for their support, help and understanding! Thank you Carlo and Andrea for the amazing time we had together. Thank you Joaquín, Florencia and Roberta for the moments we shared and for welcoming me at your lovely places. Between empanadas and matés, you helped me to improve my Espanish so much! Baptiste, I remember our enjoyable moments at the summer school in Norway and the seminars in France. Laura and Éloi, your company at CEA and CERN counted at lot and I learnt a lot meeting you. Thank you Maria for introducing me to CERN and for our conversations. I hope you will keep nice memories of France and French in general. I also spent nice time with you Denys, Inna, Martha and Martina. I want to thank you Philippe and Samira for your help, although I could not participate to the NSW project as much as I wanted.

My PhD thesis would not have been completed without the essential help of my colleagues at CERN. I want to thank you Bijan, Andrea and Sarah for your help in the analysis. Publishing the first $H4\ell$ paper at your side was very motivating. Thank you Dongliang and Miha for the dedication you brought to the muon isolation task force. We achieved to set up a robust framework useful to the entire collaboration.

Thank you Simona, Davide, Kostas, José and Luigi for the nice atmosphere in Saint-Genis. Having housemates and landlords like you is a rich experience which I enjoyed everyday.

My last thanks go to my family. Merci Huguette et Jean pour m'avoir accueilli très souvent sur Paris. Vous m'avez toujours soutenu dans mes études et je vous dois beaucoup. Merci à mes parents qui ont

toujours cru en moi et dont le soutien a été déterminant lors de ma thèse. Merci à tous les autres qui me sont proches et qui comptent beaucoup : avoir un premier docteur dans la famille, ça se fête !

Contents

List of Figures

List of Tables

Chapter 1

Introduction

Particle physics aims at studying the smallest constituents of matter in the universe by describing their fundamental properties and interactions. The underlying theory is the so-called Standard Model which was developed in the last century and proved to be really successful in predicting the elementary interactions between particles, as well as foreseeing the existence of new particles which were discovered afterwards. In order to perform particle physics research, state-of-the-art facilities were built at CERN (European Organization for Nuclear Research) close to Geneva, the latest being the LHC (Large Hadron Collider) which collides beams of protons at world-record centre-of-mass energies $\sqrt{s}$. The machine entered operation in 2009 and thanks to the data collected and analysed by the ATLAS and CMS experiments at $\sqrt{s} = 8\,\text{TeV}$, the discovery of the Higgs boson was announced in July 2012. This particle was the missing piece of the Standard Model and its discovery comforted the theory in its predictions, as the boson turned out to satisfy all the requirements from the model. After a long shut-down, the LHC restarted in 2015 and delivers proton-proton collisions at $\sqrt{s} = 13\,\text{TeV}$, doubling its previous records. In 2015 and 2016, $36.1\,\text{fb}^{-1}$ of data was recorded by the ATLAS experiment alone, superseding the statistics obtained from the previous periods of data taking. The higher centre-of-mass energy enables to probe a wider phase space to test the validity of the Standard Model and possibly discover new physics beyond the model. The increased statistics available also allow precise measurements of the properties of the particles to confirm or infirm the most recent predictions and theories.

The main topic of this thesis is the study of the recently discovered Higgs boson in its decay to two Z bosons, in turn decaying to four leptons. Thanks to very good detector resolution and lepton reconstruction, the mass of the two decaying Z bosons enables very fine measurement of the mass of the Higgs, as well as suppressing background contamination resulting in very low yields. The overall sensitivity is therefore high, and together with the Higgs boson decaying to two photons, the Higgs boson was discovered in 2012 in this channel. With the new data taking conditions in 2015 and 2016, the sensitivity is further improved by a factor of two with respect to 2012, with the increased $\sqrt{s}$. Precise measurements can hence be performed to better understand the properties of the Higgs boson, including the measurement of its mass and its couplings to other bosons, and probe the validity of the Standard Model and the possible existence of new physics. Using $36.1\,\text{fb}^{-1}$ of data, the total, differential and double-differential cross sections in the Higgs-to-four-lepton decay channel are calculated and compared to the most recent Standard-Model predictions.

In addition to the analysis of the Higgs boson decaying to four leptons, dedicated studies on the isolation of muons are performed. These studies consist in assessing whether a particle is produced together with ambient activity surrounding its trajectory in the detectors and in which proportions this activity relates to the energy of the particle. This is a powerful tool in discriminating signal events (composed of

well-isolated muons) from background processes. Isolation variables are defined and selection criteria are applied to them in order to reduce background contamination. The work described in this thesis consists in improving the definition of the variables to cope up with the challenging data taking conditions as well as to increase background rejection. Working points are defined as sets of cuts on the variables to fulfil the needs of the various analysis groups. One of these working points is specifically designed for the Higgs-to-four-lepton analyses. The related signal efficiencies are finally calculated using Z boson decays to two muons. The correspondence between data and simulation is estimated by deriving scale factors defined as ratios of efficiencies, and used by the analysis groups to correct their predictions.

The thesis is organised as follows. A brief description of the LHC machine is given in Chap. 2, which explains how the protons are accelerated in beams before colliding at the centres of the experiments. The programme of the physics runs, which correspond to period of data taking, is outlined with an overview of the future prospects of the machine. The physics conditions in Run 2 (2015 - 2016) are specifically compared to those of Run 1 (2011 - 2012). Chapter 3 focuses on the detailed description of the detector. The design and technologies used for each sub-detector to meet the requirements in terms of particle identification and reconstruction are outlined. For each system, a comparison is given between the expected performance, and the results obtained in Run 1 and Run 2. Changes in detector design during the long shut down 1 of the LHC (2013 - 2015) to face the increased radiation rates are detailed. Chapter 5 gives a definition of the isolation variables grouped into two categories: the track-based isolation using information from the Inner Detector, and the calorimeter-based isolation relying on energy deposits in the calorimeters. The changes with respect to Run 1 are highlighted, especially the use of a clustering algorithm to retrieve the energy of the calorimeter cells, as well as using a variable cone size for the track isolation. Cuts are applied to these variables to define isolation working points, described in Chap. 6. These working points are characterised in terms of expected signal efficiencies and background rejection. The performance studies of muon isolation are summarised in Chap. 7, corresponding to $36.1\,\text{fb}^{-1}$ of data recorded by the ATLAS detector. The distributions of the isolation variables are compared between data and simulation and deviations are further analysed. Specific care is brought to ensure the variables are robust against the challenging physics conditions. The signal efficiencies of the isolation working points are then calculated using the Tag-And-Probe method on Z boson decays to two muons. Agreement between data and simulation is translated into scale factors, which are measured along with systematic uncertainties. Chapter 8 finally presents the tool enabling the correction of the isolation variables in case of events where several signal objects are close to each other. After a brief summary of the Standard Model and its limitations in Chap. 10, insisting on how the Higgs boson is produced and decays at the LHC, the analysis strategy of the Higgs-to-four-lepton decay channel is described in Chap. 11. The theory predictions used for the studies are detailed together with the criteria applied on the leptons and jets to select the events. The methodology used to estimate the background yields and shapes is described, and results with $36.1\,\text{fb}^{-1}$ of data are presented in terms of the number of observed events and the expected signal and background yields for the various possible final states. Finally, Chap. 12 outlines the measurements of the Higgs-to-four-lepton production cross section. Using the signal and background yields and shapes, an extended Poissonian likelihood is defined and the cross sections are extracted using a fit on the four-lepton invariant mass. The results are given in the phase space corresponding to the analysis (fiducial cross section) and are also extrapolated to the total phase space (total cross section) using factors which are calculated for each production mode and each final state. Measurements are also performed in bins of differential variables (kinematics of the four-lepton final state and variables related to the jets of the event). The inclusive and differential measurements offer the opportunity to probe the validity of the Standard Model: observations are compared to predictions and constraints are set on the anomalous contact-interaction decays of the Higgs boson to left and right-handed leptons, and the anomalous coupling of the Higgs boson to the Z bosons.

Part I

The ATLAS experiment at the LHC

Chapter 2

The Large Hadron Collider

The LHC [1] is the world's most recent and most powerful accelerator designed to study particle physics. It is the biggest machine of the European Organisation for Nuclear Research (CERN) close to Geneva (Switzerland and France), which can deliver proton-proton collisions with a centre-of-mass energy up to $\sqrt{s} = 14\,\text{TeV}$ and can accelerate lead ions (Pb) up to $\sqrt{s} = 2.8\,\text{TeV}$ per nucleon.

The LHC is a 26.7 km superconducting double-ring collider, which was built using the tunnel hosting the Large Electron-Positron Collider (LEP). This tunnel is divided into eight straight sectors and eight arcs, and is located between 45 m and 170 m below the surface. While the LEP was in operation from 1989 to 2000, with electron-positron collisions from 90 GeV up to 209 GeV, the LHC entered in operation in 2008 after a major upgrade of the machine.

The LHC targets centre-of-mass energies which are about seven times higher than the records set by the particle accelerator Tevatron (now inactive, since 2011) in the United States, at the Fermi National Accelerator Laboratory [2]. For the LHC to reach its designed energies, several steps are needed. Figure 2.1 illustrates the various machines involved in accelerating and preparing the two beams of protons for the collisions. First, hydrogen atoms (composed of an electron and a proton) undergo a strong electric field which separates the orbiting electrons. The remaining protons are injected into the LINAC2 accelerator, which increases their energy up to 50 MeV. Afterwards, the Proton Synchrotron Booster (PSB) accelerates these protons from 50 MeV to 1.4 GeV. The beam is then injected into the Proton Synchrotron (PS) where it is accelerated to an energy of 25 GeV before being sent to the Super Proton Synchrotron (SPS) where the beam energy reaches 450 GeV. Finally, the beam enters the LHC (two beams are sent at the same time, one clockwise, the other anticlockwise, the filling time is 4 min 20 s per LHC ring). The two injected beams are accelerated for 20 min to a total $\sqrt{s} = 13\,\text{TeV}$ (reached so far).

Under optimal conditions, the beams can circulate in the LHC for approximately ten hours, travelling more than 10^{12} m, at a speed close to 0.999999991 times the speed of light. The beams are prepared in bunches in the smaller subsystems, because of the radio frequency (RF) technique used for the acceleration. Protons are accelerated when the electric field has the correct orientation while passing through an accelerating cavity and these conditions are fulfilled at special times of the RF cycle of the field. Under nominal operation, a proton beam is composed of 2808 bunches, each bunch containing about 10^{11} protons. While travelling around the LHC, the bunches get squeezed (they get a length of 16 µm close to the interaction points to maximise the probability of collisions) and expanded (they acquire lengths of a few centimetres far from the collision points).

The LHC consists of eight arcs and eight *insertions*. 154 bending magnets are installed in each arc, whereas an insertion is composed of a long straight section surrounded with two transition sections, referred to as the *dispersion suppressors*, which absorb the dispersed particles of the beams, avoiding

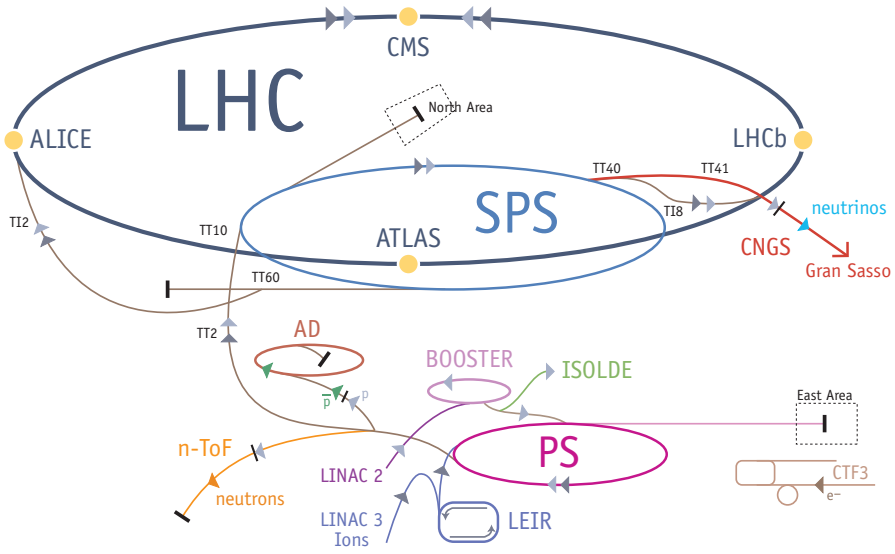

Figure 2.1 – The various experiments and accelerators at CERN. The collisions of the beams in the LHC happen at four points where the major experiments are located: ALICE, ATLAS, CMS and LHCb [3].

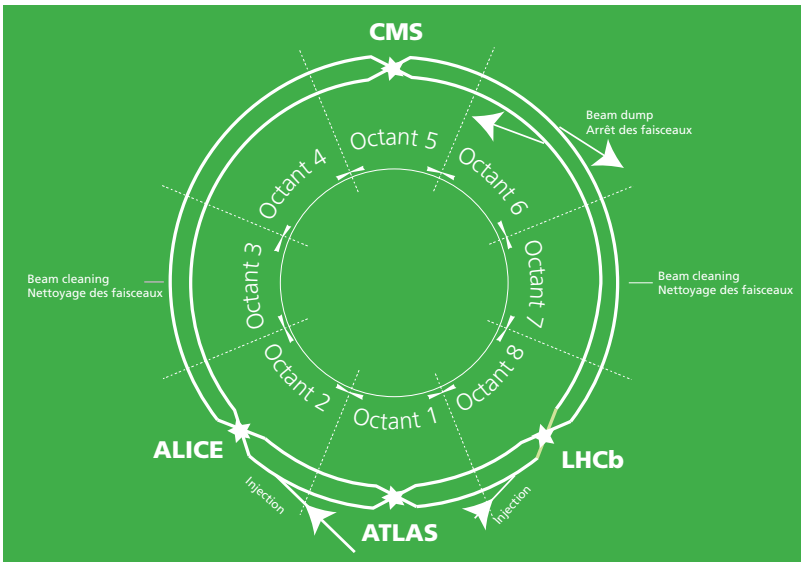

Figure 2.2 – The LHC is divided into eight octants, which start and end at the middle of an arc. Therefore, an octant includes a complete insertion [4].

reflections along the pipes. The straight sections have different layouts depending on the use of the insertion. Four types of insertions are used: for physics (beam collisions at the interaction points of the experiments), for the injection of the beams, for the dumping of the beams and for the beam cleaning (to increase the focusing and the purity of the beams). As shown in Fig. 2.2 [4], an octant starts and ends at the middle of an arc, therefore including a complete insertion.

The LHC has various vacuum systems ensuring the beam vacuum, which is essential for the purity and the stability of the collisions, and taking care of the insulation of the cryomagnets used to cool down

the magnets. Pressures as low as 10^{-8} Pa are achieved. Various types of magnets are used along the accelerator to bend the particles, for a total of about 9600 magnets. The limiting factor of the LHC is not the acceleration of the particles, but the bending power of the dipole magnets.

The LHC programme is composed of Runs, periods of time during which collisions happen (proton-proton or heavy ions) and long shut-downs, during which the equipments of the LHC and the experiments are upgraded to achieve the new targeted luminosity and $\sqrt{s}$. During the shut-downs, the caverns (where the experiments are located) and the LHC tunnel are accessible for maintenance and some parts of the detectors can be replaced or improved. On the contrary, during runs, the LHC provides collisions which are recorded by the various experiments, and both the tunnels and the caverns cannot be accessed.

2.1 Luminosity

One of the essential parameters of a collider is the instantaneous luminosity $\mathcal{L}$, which is a measurement of the probability of an interaction per unit of time. For a given process p, the number of events per second generated by the interactions is related to its integration over time:

$$N_{\mathrm{p}} = \sigma_{\mathrm{p}} \int \mathcal{L} \mathrm{d}t, \tag{2.1}$$

where σ_{p} is the cross section of the process p. The instantaneous luminosity depends on the parameters of the collider:

$$\mathcal{L} = \frac{{N_{\mathrm{b}}}^2 n_{\mathrm{b}} f_{\mathrm{r}} \gamma}{4\pi \varepsilon_{\mathrm{n}} \beta^*} F, \tag{2.2}$$

where N_{b} is the number of particles per bunch (10^{11} at the LHC), n_{b} is the number of bunches per beam, f_{r} is the revolution frequency, γ is the relativistic gamma factor, ε_{n} is the transverse beam emittance normalised to the beam size, β^* is the beta function at the collision point related to the beam focusing and F is the geometric luminosity reduction factor accounting for the angle between the two beams when they collide [5, 6, 7].

Increasing the number of bunches per beam is one of the ways to reach higher instantaneous luminosities. At full luminosity the LHC uses a bunch spacing of 25 ns (about 7 m of spacing), which corresponds to a frequency of 40 MHz. Each beam consists of about 3000 bunches of particles. Taking into account the frequency of the bunch injection, the LHC supports instantaneous luminosities of the order of $10^{34}\,\mathrm{cm}^{-2}\mathrm{s}^{-1}$. A second parameter which can be optimised to reach higher luminosities is the beta function at the collision points. This quantity is high far from the interaction points, but reduced as much as possible in the vicinity of the experiments.

To account for the total number of events for a specific process, the luminosity integrated over time is the relevant parameter (referred to as integrated luminosity $\int \mathcal{L} \mathrm{d}t$). During Run 1 (2012), the total integrated luminosity was of $23.3\,\mathrm{fb}^{-1}$ with an instantaneous luminosity of less than $10^{34}\,\mathrm{cm}^{-2}\mathrm{s}^{-1}$. After the long shut down, the LHC restarted in mid 2015 for the Run 2. Instantaneous luminosities of 1.5 to $2.0 \times 10^{34}\,\mathrm{cm}^{-2}\mathrm{s}^{-1}$ were reached in 2016, leading to an integrated luminosity of $36.1\,\mathrm{fb}^{-1}$ for the combined 2015 and 2016 datasets. By the end of 2018, the total integrated luminosity should reach $100\,\mathrm{fb}^{-1}$.

As an example, for the $H \to ZZ^* \to 4\ell$ decay channel, subject of the last part of this thesis, the integrated luminosity of the year 2012 corresponds to 20 expected Higgs candidates at $\sqrt{s} = 8\,\mathrm{TeV}$. During Run 2, about 200 candidates are expected with the increase of integrated luminosity (five times

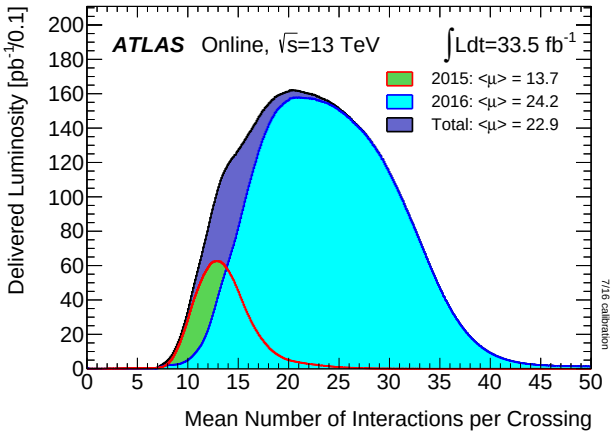

Figure 2.3 – Pile-up conditions in Run 2, represented using the number of interaction per bunch crossing μ for the data 2015, data 2016 and combined datasets [9].

greater) and the increase of cross section at $\sqrt{s} = 13\,\text{TeV}$ (two times greater). Note that for the data 2015 and 2016 combined, 106 events are expected in this channel.

A drawback from an increased instantaneous luminosity is the increased number of interactions per bunch crossing (referred to as *pile-up*). For each proton-proton interaction, a vertex is formed from which the decay products interesting to the studies emerge. This is the primary vertex. Additional vertices are also created from decay products or other interactions, referred to as secondary vertices. These vertices are recorded by the detectors at the same time as the primary vertex and mask the useful information coming from the latter. This makes the selection of good events for the analyses harder.

Two kinds of pile-up have to be taken into account. *In-time pile-up* corresponds to more than one interaction in the same bunch of crossings: the primary vertex is mixed with secondary vertices arising from the same interaction. The second type, referred to as *out-of-time pile-up*, concerns interactions between several consecutive bunch crossings. Because of the LHC bunch spacing of 25 ns, signal modulation from multiple interactions in surrounding bunch crossings is possible to which the sub-detectors are sensitive [8].

The notion of pile-up will be further detailed in the chapter 5.2. A general relationship between the instantaneous luminosity and in-time pile-up is given by:

$$\langle \mu \rangle = \frac{\mathcal{L}\sigma_{pp}}{n_{\text{b}} f_{\text{LHC}}}, \tag{2.3}$$

where $\langle \mu \rangle$ is the mean number of inelastic pp interactions per bunch crossing, σ_{pp} is the total inelastic pp cross section and f_{LHC} is the frequency of injection of the bunches (40 MHz for a bunch spacing of 25 ns). In 2012 (at the end of Run 1), the instantaneous luminosity reached $\mathcal{L} = 7.7 \times 10^{33}\,\text{cm}^{-2}\text{s}^{-1}$ with $\langle \mu \rangle \approx 22.7$. In 2015 (2016), the instantaneous luminosity reached $5.0 \times 10^{34}\,\text{cm}^{-2}\text{s}^{-1}$ ($14 \times 10^{34}\,\text{cm}^{-2}\text{s}^{-1}$), and $\langle \mu \rangle \approx 14$ ($\langle \mu \rangle \approx 25$) with a maximum value of 40 (50), as shown in Fig. 2.3 [9].

2.2 The experiments at the LHC and the physics reach

The current knowledge of the forces governing the physics of the particles and the properties of the universe is summarised by the Standard Model (SM). Whereas this model was experimentally tested and

provided very precise predictions of the physical constants as well as anticipating the existence of particles before their discoveries, some essential questions remain unanswered. The LHC was specifically designed to address these issues. This section briefly summarises the physics scopes of the experiments at LHC. A more detailed description of the SM and the Higgs mechanism is provided in part III.

With these challenging goals, the LHC was approved for construction in December 1994 and could be built within a single stage after the LEP closure in 2000. In the mean time, four experiments – ALICE (A Large Iron Collider Experiment), ATLAS (A Toroidal LHC ApparatuS), CMS (Compact Muon Solenoid) and LHCb – were installed at the four sites where the proton beams collide. The goals of these experiments are briefly described in the following. Later, smaller experiments joined the programme: MoEDAL [10], TOTEM [11] installed close to CMS and LHCf [12] located in the vicinity of ATLAS.

ALICE [13] was designed to analyse heavy ion collisions. It focuses on studying the quark-gluon plasma in conditions which are close to those at the very early stages of the universe, according to models. Although the other collaborations also benefit from the heavy ion collisions, ALICE is specifically devoted to studying them.

ATLAS [14], together with CMS [15], are general-purpose detectors which aim at covering the widest range of physics possible at the LHC. To name but a few, these experiments focus on the Higgs mechanism, precise measurements of the parameters of the SM, and the study of beyond-SM models such as SUSY or extra dimensions. The ATLAS experiment will be further described in Chap. 3.

The CMS detector is built around a huge superconducting solenoid which can generate a very high and homogeneous magnetic field up to 3.8 T. This compact structure enables the reconstruction of leptons and photons with high accuracy and efficiencies to probe the widest phase space.

LHCb [16] specialises in studying the violation of symmetry (CP violation) between matter and antimatter in interactions of particles containing the b-quark. Understanding this asymmetry would add valuable ground to the matter-antimatter issue. This experiment uses a detector which, instead of surrounding the beam line, is composed of a series of various sub-detectors, which aim at detecting the very forward particles.

2.3 Physics runs and upgrades

Since its original design, the LHC underwent several upgrades in order to increase its luminosity and $\sqrt{s}$. Increasing the luminosity and $\sqrt{s}$ pushes further the requirements on the various parts of the detectors, because of higher radiation levels necessitating more resilient equipment. Furthermore, the flow of data is also increased and more sophisticated trigger algorithms have to be developed to cope up with the data taking rates, and the new pile-up conditions.

The successful operation of the LHC in Run 1 allowed the various experiments to record data, which improved the common understanding of the Standard Model with the discovery of the Higgs boson [17, 18, 19] in 2012 [20, 21], as well as providing very precise measurements of the parameters of the model (mass of the bosons as well as cross sections and estimation of the fundamental constants). Overall more than 2000 papers were published by the various experiments at CERN (more than 400 for ATLAS alone).

For the Run 2, the trigger algorithms of the experiments were improved to abide by the reduced bunch spacing (reduced from 50 ns to 25 ns), which is the major change to reach higher instantaneous luminosities. A more detailed schedule of the Run 2 is given in Tab. 2.2.

Subsequently, the Runs 3 and 4 will allow the accelerator to provide even higher luminosities at the same centre-of-mass energy. Table 2.1 gives an overview of the various expected physics runs at the

Table 2.1 – The various physics Runs and upgrades of the LHC programme [22].

Phys. Run	Period	Max. $\mathcal{L}$ [$\mathrm{cm^{-2}s^{-1}}$]	$\sqrt{s}$ [TeV]	Bunch spacing	$\int \mathcal{L}dt$
Run 1	2010 - 2013 (passed)	$3 - 7 \times 10^{33}$	7 - 8	50 ns	25 $\mathrm{fb^{-1}}$ achieved
Long shut-down 1 (phase 0 upgrade)					
Run 2	2014 - 2018 (current Run)	1×10^{34}	13	25 ns	100 $\mathrm{fb^{-1}}$ expected
Long shut-down 2 (phase 1 upgrade)					
Run 3	2019 - 2022 (expected)	$2 - 3 \times 10^{33}$	14	25 ns	300 $\mathrm{fb^{-1}}$ expected
Long shut-down 3 (phase 2 upgrade)					
Run 4	2022 - 2030 (expected)	5×10^{34}	14	25 ns	3000 $\mathrm{fb^{-1}}$ expected

Table 2.2 – Run 2 expectations [22].

Year	Max. $\mathcal{L}$ [$\mathrm{cm^{-2}s^{-1}}$]	$\int \mathcal{L}dt$ [$\mathrm{fb^{-1}}$]
2015 (passed)	5.0×10^{33}	3.36
2016 (passed)	1.37×10^{34}	36
2017 and 2018 (expected)	1.7×10^{34}	≥ 75

LHC [22]. The targeted instantaneous luminosities are about five times bigger as compared to the original design. Parts of the detectors of the experiments will have to be replaced using technologies which are more resilient to extreme radiation conditions. In particular, ATLAS plans to replace the very forward regions of its detector. The discovery of new physics within these Runs may trigger the construction of an even bigger accelerator, in which the LHC would be a part of the injector [23].

Chapter 3

The ATLAS experiment

The ATLAS (A Toroidal LHC ApparatuS) experiment is one of the four biggest experiments at the LHC, located at point 1. To observe physical processes on a broad range, the detector has to meet the following requirements [14]:

- Full azimuthal coverage and optimised geometrical acceptance.
- Accurate measurement of the coordinates of the particles (tracking) and precise assessment of the momentum over a wide range (from a few MeV to the TeV scale).

3.1 Geometry of the detector

The ATLAS collaboration uses a set of coordinates which are related to the geometry of the detector, as presented in Fig. 3.1. The z axis of the right-handed Cartesian system used by the collaboration is the beam axis. Perpendicular to this axis is the (x, y) plane. The x and y axes point towards the centre of the LHC ring and upwards, respectively [14].

At $z = 0$, the detector is symmetric across the (x, y) plane (transverse plane), dividing the detector into two sides A ($z > 0$) and C ($z < 0$). The related cylindrical coordinates are defined as follows: R is the distance to the z axis, ϕ and θ are the azimuthal and polar angles, respectively.

The rapidity y is defined as

$$y = \frac{1}{2} \ln \left(\frac{E + p_z}{E - p_z} \right), \tag{3.1}$$

where E and p_z are the energy and the z component of the momentum of the particle, respectively. The rapidity transforms additively under boosts in the z direction: differences in rapidity Δy and the particle density per unit of rapidity $\mathrm{d}N/\mathrm{d}y$ are Lorentz invariants. In the ultra-relativistic limit, where E is much greater than the mass of the particle M, the pseudo-rapidity defined as

$$\eta = -\ln \left(\tan \frac{\theta}{2} \right) \tag{3.2}$$

approximates the rapidity. The pseudo-rapidity is a function of θ and is mass-independent. It is therefore widely used in particle physics [24]. Since particles are expected to be produced uniformly in η, the ATLAS detectors are segmented according to this variable.

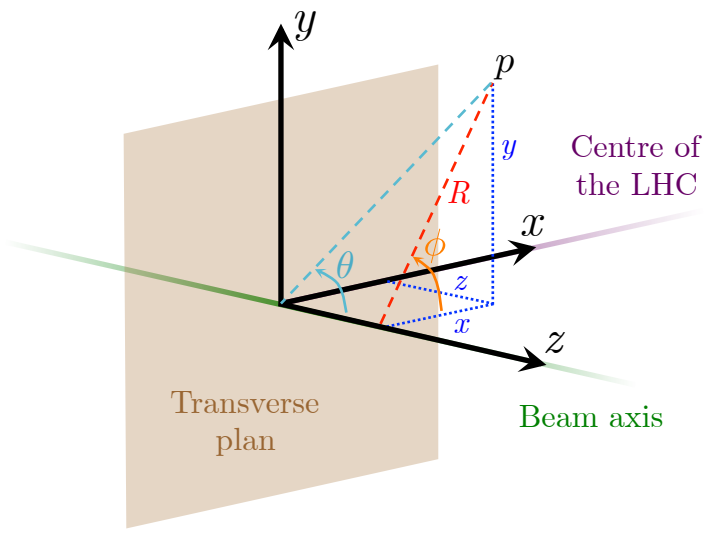

Figure 3.1 – The system of coordinates used in the ATLAS collaboration.

The azimuthal angle ϕ is not affected by boosts in the z direction. As a consequence, distances in the azimuthal pseudo-rapidity plane can easily be measured using $\Delta R = \sqrt{(\Delta\phi)^2 + (\Delta\eta)^2}$.

In the ATLAS frame, only components in the (x, y) plane are invariant under boosts in the z direction. Therefore, the transverse momentum of a particle is preferred and defined as $p_{\mathrm{T}} = p \sin\theta = \sqrt{p_x^2 + p_y^2}$, where p is the norm of the momentum of the particle. The momentum of the particle can then be calculated using $p = \sqrt{p_{\mathrm{T}}^2 + p_z^2}$.

In order for the ATLAS detector (shown in Fig. 3.2) to identify various physics processes, a good reconstruction of the final-state particles with their properties (the type of the particle, its charge, mass, energy, momentum and position) is needed. For all kinds of particles to be identified, the detector is divided into several sub-detectors with specific targets. The Inner Detector (ID) surrounds the beam pipe and charged particles produced at the interaction point (IP) are bent by the solenoidal magnetic field to assess their charge and measure their transverse momentum. Then, these particles reach the Calorimeters (Cal) where electrons, photons and hadrons shower, having their transverse energy estimated. Only muons traverse the calorimeters to enter the Muon Spectrometer (MS), where their momentum is precisely measured thanks to the toroid magnets surrounding the MS chambers. Only neutrinos remain transparent to the detectors and need to be identified using the missing energy in the transverse plane.

A brief description of the sub-detectors is given in the following subsections. A more detailed review can be found in Ref. [14].

3.2 The Inner Detector

Precise measurements of the coordinates of the track particles rely on a high bending power of the magnets and a fine granularity of the detectors in assessing the positions of the hits of the charged particles. Combining these two features, the Inner Detector (ID) provides a state-of-the-art pattern recognition, measurements of the momenta and vertices, and allows a good electron identification.

These functionalities are achieved using four sub-systems. Starting from the most inner part to the outer layers, the ID is composed of precision silicon detectors (the insertable B-layer IBL, the pixel

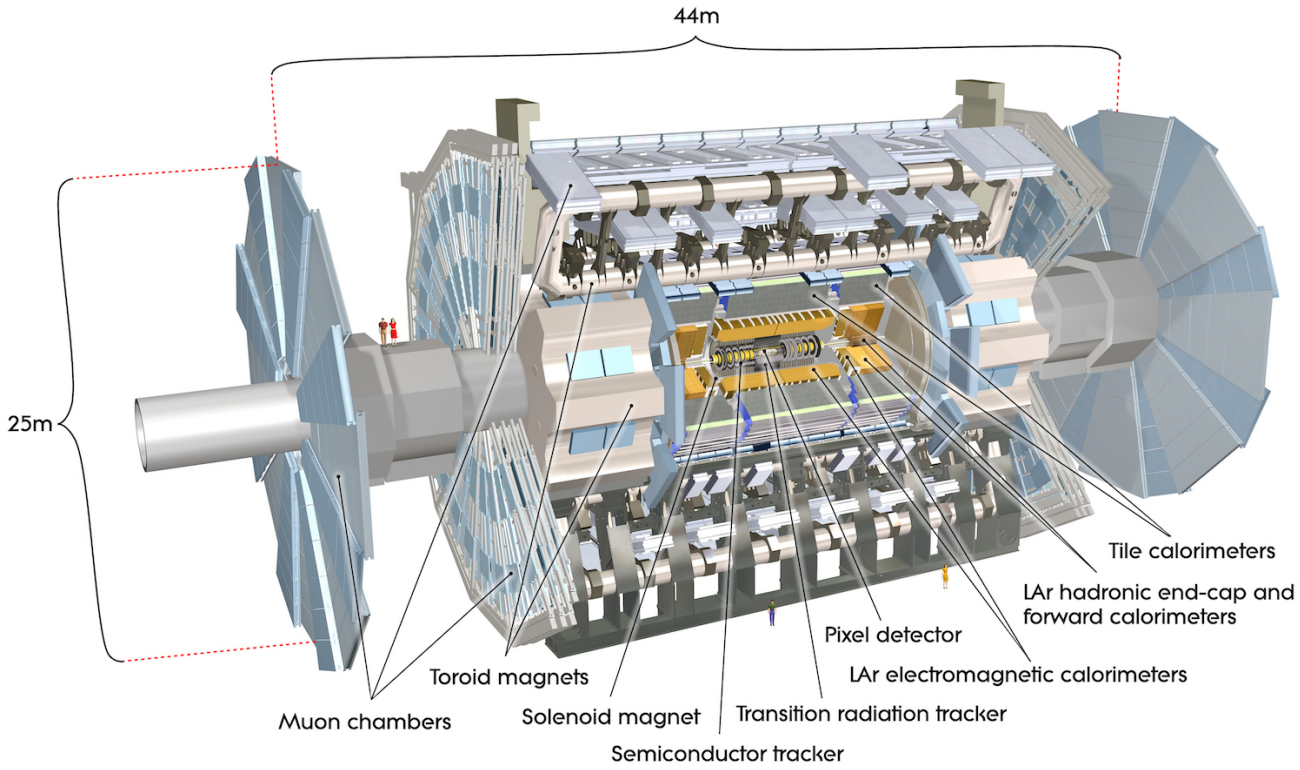

Figure 3.2 – Overview of the ATLAS detector. The interaction point (IP) is located at the centre of the detector, surrounded with the Inner Detector (ID), the Calorimeters (Cal) and the Muon Spectrometer (MS) [25].

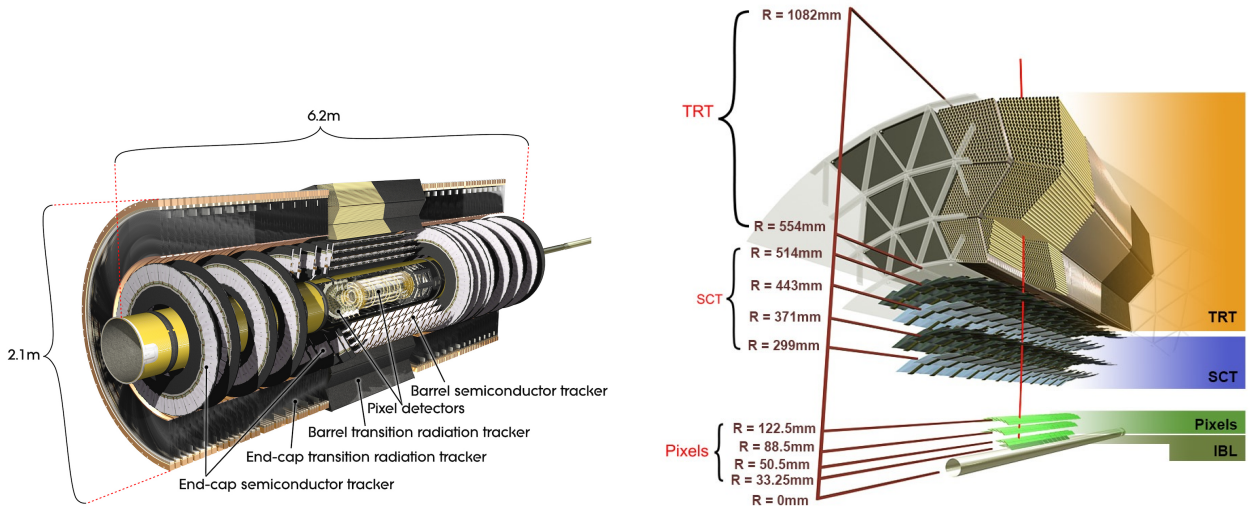

(a) General view

(b) Radial view

Figure 3.3 – Layout of the ATLAS Inner Detector (ID), with (a) the general and (b) the radial views [26].

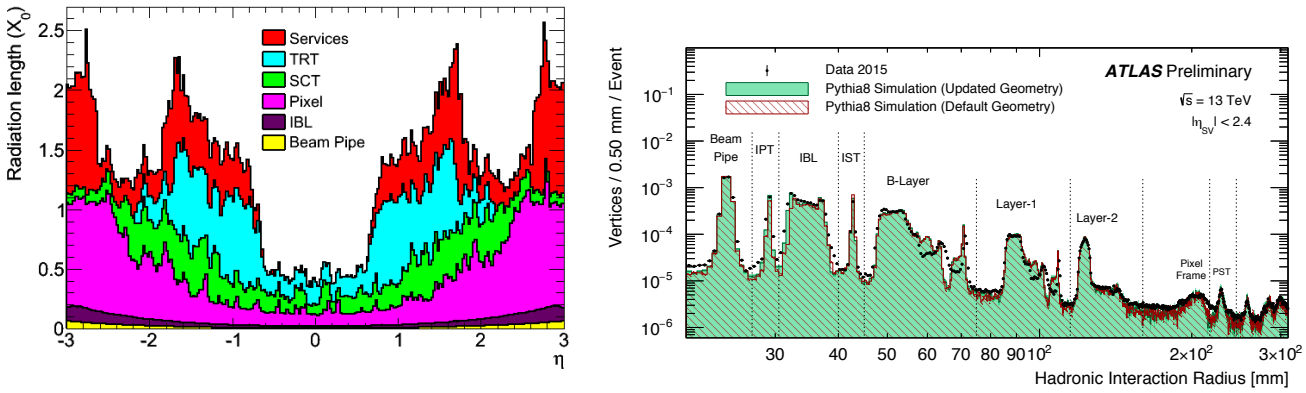

(a) Expected material depth

(b) Observed material depth

Figure 3.4 – Distribution of the material in the ID. (a) The expected material budget is given in X_0 units as a function of η [27]. (b) The material width is measured using 2015 data, and is expressed in hadronic interaction radius units [28].

detectors and the silicon micro-strip trackers), and straw-tube trackers generating and detecting transition radiations. A general view of the ID is presented in Fig. 3.3 (a).

The environment in which the ID operates requires a special care for the design of the detector. The high-radiation levels have a significant impact on the selection of the electronics and the technologies used. The silicon detectors therefore operate at controlled temperatures (in the range −10 °C to −5 °C) to keep low noise ratios after radiation damage (these requirements do not apply for the straw-tubes, which operate at room temperature). Despite these precautions, the innermost parts of the ID have to be replaced after three full years of operation at the luminosities delivered by the LHC. To increase the longevity of the innermost layers and to cope up with the increased instantaneous luminosity, the design used during Run 1 was completed by the IBL installed for the Run 2.

The amount of material of the detector is also limited because it affects the resolution of both tracking and calorimetry. Nonetheless, the distance a particle traverses in the material varies from $0.5X_0$ to $2.5X_0$, where X_0 denotes the radiation length. The distance traversed by the particles depends on η, as highlighted in Fig. 3.4. As a result, about 40% of the photons produced at the interaction point decay to electron pairs and electrons can loose a great amount of their initial energy due to Bremsstrahlung radiations, before they reach the calorimeters.

To ensure a high bending power, which is essential for the correct reconstruction, identification and transverse momentum p_{T} measurement of the particles, the ID is surrounded with a solenoid which generates a magnetic field in the z direction. This field can be assumed to be uniform in a first approximation thanks to insulation provided by the material. Its strength is close to 2 T near the z axis. The solenoid is 5.3 m long with a diameter of 2.5 m and is composed of magnets which operate at 4.5 K. In order to reach this low temperature, the magnets are located inside a cryostat which is also shared by the barrel electromagnetic calorimeter presented in the next section.

3.2.1 The Insertable B-Layer (IBL)

For the Run 2, a fourth layer has been added to the Pixel detector, between a new beam pipe and the previously innermost Pixel layer also referred to as the *B-layer* [27, 29]. The complementary layer ensures tracking robustness, as the number of failures of the modules in the B-layer increases over time.

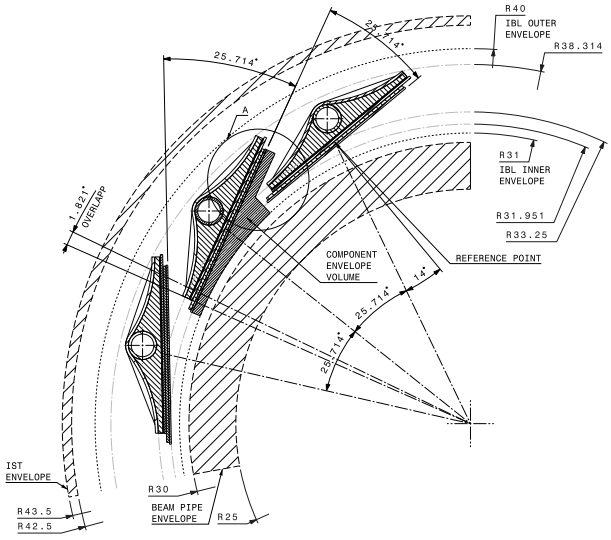

Figure 3.5 – Insertable B-layer layout [27].

This strongly affects the resolution on the impact parameter measurements. Furthermore, the increase of instantaneous luminosity for Run 2 and onwards requires the addition of the layer, as the fake rate can be controlled thanks to redundancy in the pixel layers, and more resilient electronics can resist higher radiation rates. This new layer minimises the amount of material and ensures a full ϕ symmetry.

After removing the old beam pipe, the layer could be inserted successfully and the layout is shown in Fig. 3.5. A full hermetic coverage in ϕ for high p_{T} tracks was made possible using 14 staves instrumented with planar and three-dimensional-silicon pixel sensors along 332 mm on each side from the centre of the ATLAS detector. The staves are arranged in a turbine-like fashion, with an overlap in ϕ, and are mounted at an average radius of 35.7 mm. A full geometrical coverage in z similar to the Pixel detector is not achievable. Indeed modules are tilted in z and partially overlapped, because there is not enough space. Overall, the added material does not exceed half of the material of the Pixel B-layer.

3.2.2 The Pixel detectors and the Silicon micro-Strip Trackers (SCT)

The second innermost part of the ID is instrumented with precision tracking detectors, composed of the pixel layers and the silicon micro-strip trackers (SCT), which cover the full $|\eta| < 2.5$ range. These two detectors are organised in concentric layers around the beam axis in the central region (barrel), and in concentric disks perpendicular to the z axis in the end-caps. A track crosses three pixel layers and four SCT strips on average, as shown in Fig. 3.3 (b).

The pixel layers are located at the radial distances of R = 50.5 mm, 88.5 mm and 122.5 mm in the barrel, and R = 49.5 mm, 58.0 mm and 65.0 m in the end-caps. The pixel detectors are all identically designed and are segmented in z and ϕ in the R plane (the precision of the segmentation is at the 10 µm level in R, ϕ, and 115 µm in z and R in the barrel and end-cap, respectively).

For the pixel layers to correctly perform the reconstruction and identification of short-lived particles and the associated vertices of production (especially for identification of b- or c-quark jets), about 80.4 million readout channels are installed to achieve the necessary high-granularity of the measurements.

Following the pixel detectors, eight layers of silicon strips are placed in two-by-two structures, providing four space point measurements for each track. The intrinsic accuracy per module is 17 µm in R — ϕ and

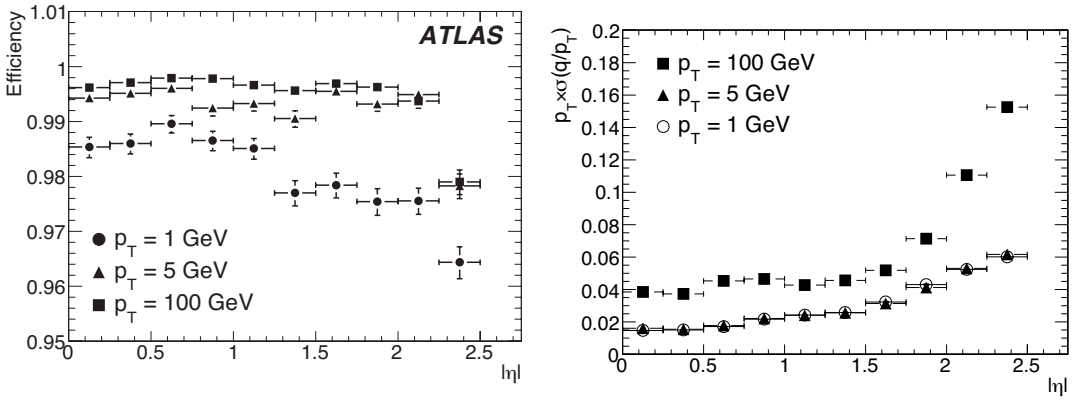

(a) Reconstruction efficiency

(b) Relative transverse momentum resolution

Figure 3.6 – Expected tracking performance of the Inner Detector against $|\eta|$ measured from simulated pions and electrons, prior to Run 1 [14]. (a) shows the expected reconstruction efficiency and (b) presents the expected relative transverse momentum resolution.

580 µm in z (R) in the barrel (end-cap), with a total of 6.3 million readout channels.

3.2.3 The Transition Radiation Tracker

The pixel layer and the SCTs are surrounded by the transition radiation tracker (TRT) [30, 31]. It is composed of layers of gaseous straw tubes inserted in transition radiation material. When a track associated to a charged particle passes through the TRT, it deposits on average 30 hits, providing a continuous tracking and enabling an identification of the electrons which is complementary to the calorimeters. This sub-detector also offers a precise pattern recognition and contributes to the measurement of p_{T}, improving the associated resolution. It is located between R = 56 cm and R = 107 cm and covers the full $|\eta| < 2.0$ range.

The TRT gives information on the R, z coordinates in the barrel and on the z, ϕ coordinates in the end-cap, with a precision of 130 µm per straw. In the central region, the straws have a diameter of 4 mm and are 144 cm long. They are parallel to the z axis with their wires divided around $\eta = 0$. In the end-caps, the straws are 37 cm long and are positioned radially in the disks. In total, the TRT has about 350 000 readout channels.

During the Run 1, the gas contained in the tubes was a non-flammable xenon-based mixture composed of 70% Xe, 20% CO_2 and 10% CF_4. However, due to the high cost of the xenon and the significant leakage losses, it was decided to replace the xenon by argon for the Run 2 in most of the chambers [32]. Both gas compositions ensure a high efficiency for detecting the ionisation signals and transition radiation photons, produced in the polypropylene fibres surrounding the straws and collected by the wires. In nominal conditions, seven to ten high-threshold hits from transition radiation are expected for electrons having energies above 2 GeV.

3.2.4 Inner Detector tracking performance

The expected performance presented in this subsection is obtained from simulated single particles (electrons and pions), prior to Run 1. The results obtained can be considered stable in the presence of addi-

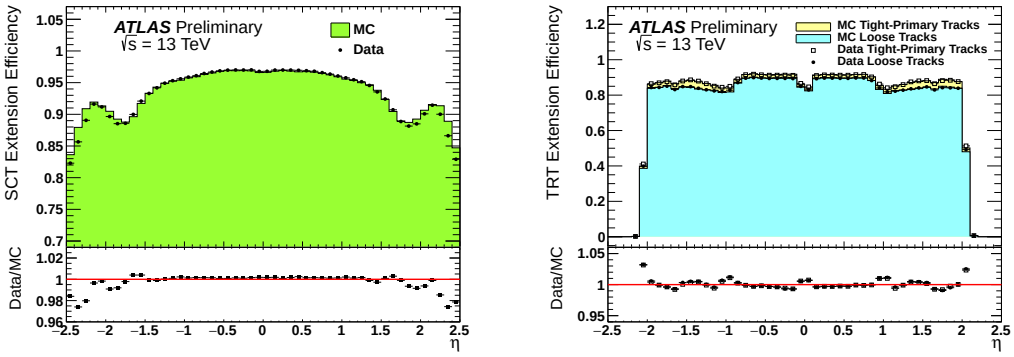

(a) Extension to SCT

(b) Extension to TRT

Figure 3.7 – Efficiency to extend a track reconstructed in the pixel detector measured using Run 2 data, and compared to simulation, with (a) extension to SCT and (b) extension to TRT [33].

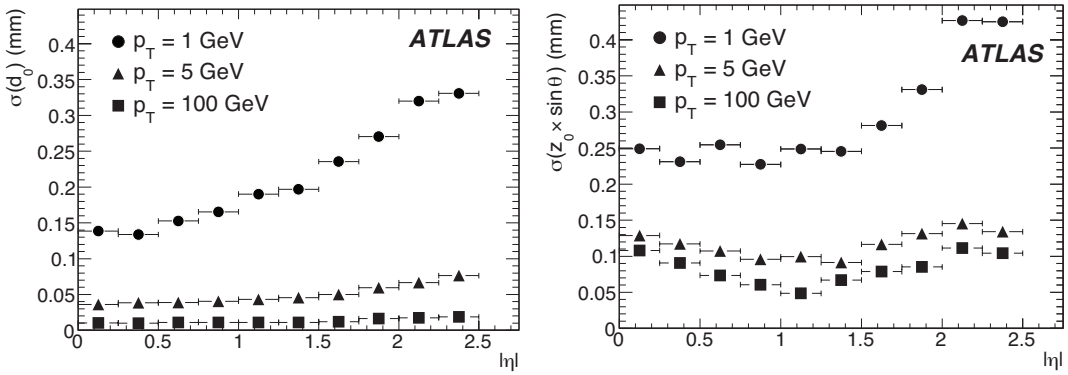

(a) Resolution of d_0.

(b) Resolution of $z_0 \sin\theta$.

Figure 3.8 – Expected (a) d_0 and (b) $z_0 \sin\theta$ resolutions of the ID against $|\eta|$ for simulated pions, prior to Run 1 [14].

tional tracks [34] thanks to the very fine granularity of the silicon detectors resulting in low occupancy rates (below 4%) for up to 100 interactions occurring per bunch crossing at the LHC (the corresponding instantaneous luminosity is $4 \times 10^{34}\,\mathrm{cm}^{-2}\mathrm{s}^{-1}$). This was proven to be the case with the data taken in Run 2 [33]. A drop in the resolution nevertheless occurs in the transverse momentum resolution because of the high occupancy rates of the TRT (up to 60%), causing a degradation up to a factor of two.

Combining the previously presented technologies, the ID can provide efficient particle identification and tracking. At high pseudo-rapidities, the silicon trackers are complemented by straw tubes to increase the number of measurements in these high radiation areas. As a consequence, the ID is expected to offer a reconstruction efficiency above 99% for muons ($p_\mathrm{T} > 5\,\mathrm{GeV}$) over a wide range of η, as shown in Fig. 3.6 (a). For pions and electrons whose transverse momenta are close to 5 GeV, the reconstruction efficiencies are expected to drop to approximately 80% in the very forward regions, but these efficiencies increase and gain in stability as a function of η at higher p_T. The inefficiencies can be accounted for multiple scattering, Bremsstrahlung effect losses in the case of electrons and hadronic interactions for what concerns the pions. The first results obtained in the Run 2 (presented in Fig. 3.7 [33]) show a good

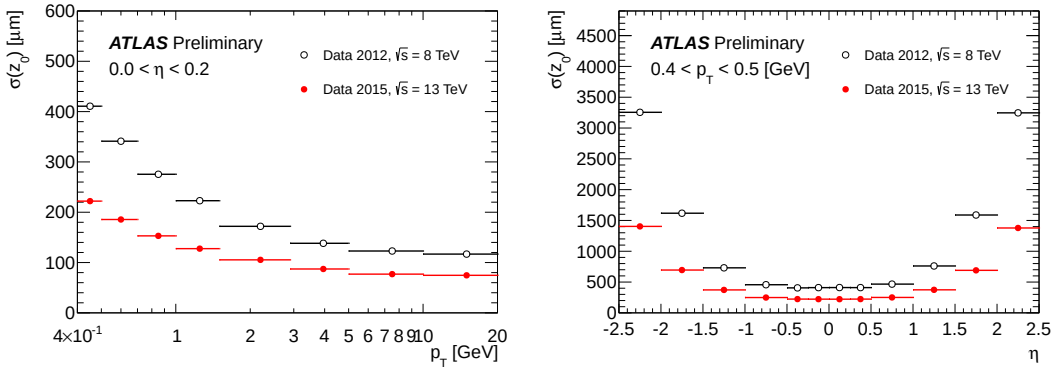

(a) Against p_{T} (b) Against η

Figure 3.9 – Measured longitudinal impact parameter resolution in data as a function of (a) p_{T} and (b) η, compared between Run 1 and Run 2 [33].

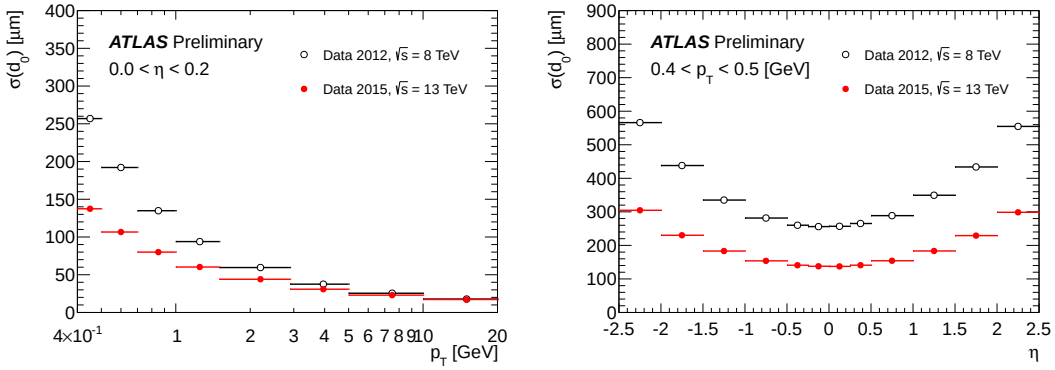

(a) Against p_{T} (b) Against η

Figure 3.10 – Measured transverse impact parameter resolution in data as a function of (a) p_{T} and (b) η, compared between Run 1 and Run 2 [33].

agreement with the expected track reconstruction efficiency. The observed efficiencies are presented for the SCT and TRT extensions, as a function of η, and are lower as compared to the expectation because all the p_{T} range is considered.

A first approximation of the transverse momentum resolution $\sigma_{p_{\mathrm{T}}}$ is given by

$$\frac{\sigma_{p_{\mathrm{T}}}}{p_{\mathrm{T}}} = a \times p_{\mathrm{T}} \oplus b = 5 \times 10^{-4} p_{\mathrm{T}}\,(\mathrm{GeV}) \oplus 0.01.$$

The various components of this expression can be explained by the low-p_{T} tracking which is degraded by the amount of material in the detectors, whereas the tracking in the forward regions is limited by the reduced coverage of the TRT. Using Run 1 data [35], the parameters of the previous equation were determined to vary from $a = 4 \times 10^{-4}\,\mathrm{GeV}^{-1}$ ($b = 1.55 \times 10^{-2}$) at low $|\eta|$ to $a = 7 \times 10^{-5}\,\mathrm{GeV}^{-1}$ ($b = 4.86 \times 10^{-3}$) at high $|\eta|$.

The ID provides precise information for reconstruction and coordinate measurements. It also offers accurate estimates of the impact parameter at the perigee, which corresponds to the point of closest approach of the reconstructed track with respect to the z axis. With the technologies used in the ID,

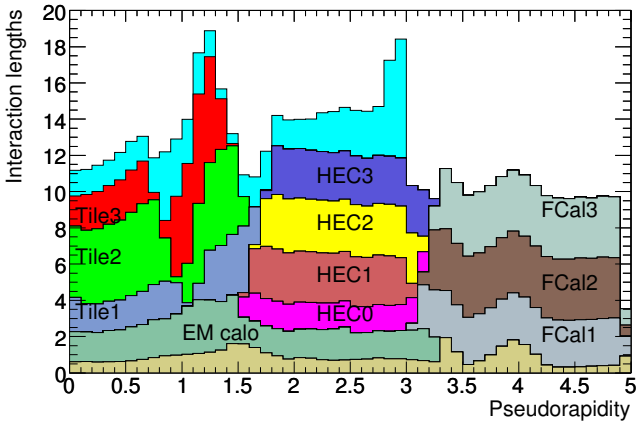

Figure 3.11 – Expected distribution of the material in the calorimeters as a function of $|\eta|$ [14].

the resolution of the modified longitudinal impact parameter ($z_0 \sin\theta$) is expected to be of less than few hundred microns, and even lower (10 µm) in the transverse plane (d_0). These results hold for high momentum tracks. Indeed, low-p_{T} tracks suffer more from multiple scattering which strongly affects the resolution. Results for simulated pions are presented in Fig. 3.8. Results based on early Run 2 data are shown in Fig. 3.9 and 3.10 for z_0 and d_0, respectively. Despite the increased pile-up conditions in Run 2, expectations are met taking into account the p_{T} range considered [33], thanks to the addition of the IBL.

3.3 The calorimeters

The various calorimeters are located between the ID and the Muon Spectrometer (MS) and cover the full range $|\eta| < 5$. To take into consideration the variations of radiation levels, the technologies used in the barrel and the end-caps differ. The main purpose of the calorimeters is to provide precise measurements of the energy deposited by the electrons, the photons and the jets, as well as the missing transverse energy. The calorimeters have to ensure a good insulation of the particles to the MS [36].

The showers produced by electrons and photons which escape the ID are measured by the liquid argon (LAr) electromagnetic calorimeters (EM), which offer a high resolution in energy and position measurements. The same technology is used for the Hadronic End-cap Calorimeter (HEC) and the Forward Calorimeter (FCal) for the detection of the activity of hadrons in the forward regions. Argon was selected for its linear response, which is stable over time, and its robustness against radiation. The detectors however need to operate at temperatures close to 88 K. To gain space, the EM calorimeter and the central solenoid have same cryostat. Due to their location, the end-cap calorimeters have their own cryostats, shared among the EM, HEC and FCal calorimeters. The hadronic calorimeters are assembled with a scintillating tile detector, whose technology is of lower cost. It covers the $|\eta| < 1.7$ region.

The size of the calorimeters was designed to limit the number of particles escaping these sub-detectors to provide good insulation to the MS. The total depth of the calorimeters is above $22X_0$ in the barrel and $24X_0$ in the end-caps. The hadronic calorimeters occupy a distance of $9.7X_0$ in the barrel and $10X_0$ in the end-caps. This enables a good resolution of the measurements combined with good insulation, even for highly energetic jets, so that only muons can enter the MS. For illustration, the distribution of the material of the calorimeters against η is given in Fig. 3.11.

Figure 3.12 presents the organisation of the calorimeters in the ATLAS detector. These are described

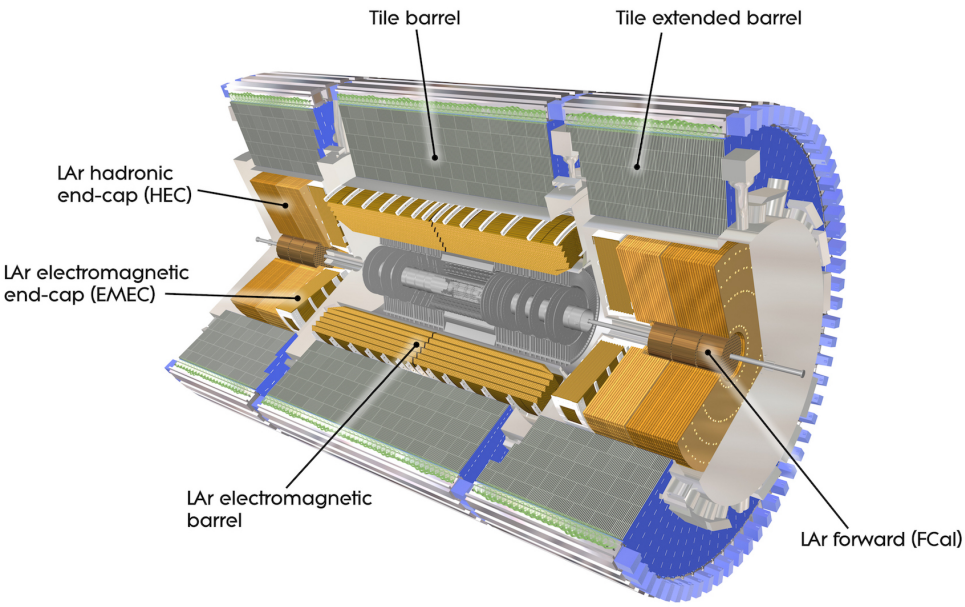

Figure 3.12 – The various calorimeters of the ATLAS detector [37].

in the following subsections. A segmentation of each sub-detector is summarised in Tab. 3.1.

3.3.1 The electromagnetic calorimeter

The EM calorimeters of ATLAS use the LAr technology with accordion shape absorbers and electrodes, as shown in Fig. 3.13. The choice of this geometry and these materials allows a full ϕ coverage without any gaps with a fast signal measurement and a fine division of the layers in the radial direction. The depth of the calorimeter is overall homogeneous over η, but three layers are instrumented in the central region $0 < |\eta| < 2.5$ covered by the ID, whereas there are only two layers in the higher-η regions ($2.5 < |\eta| < 3.2$), and in the overlap region between the barrel ($|\eta| < 1.475$) and the end-caps ($|\eta| > 1.375$).

In the central region ($|\eta| \leq 2.5$), the first layer is equipped with narrow strips of 4 mm pitch in order to provide accurate measurements of the position. The cell segmentation is $\Delta\eta \times \Delta\phi = 0.003 \times 0.1$ and depends on η in the end-caps. The middle layer is composed of cells having an identical size of $\Delta\eta \times \Delta\phi = 0.025 \times 0.025$ and is the thickest of the three compartments, where most of the energy and the position measurements of the clusters is expected to be recorded. Finally, a last layer with cells of dimensions $\Delta\eta \times \Delta\phi = 0.05 \times 0.025$ collects the remaining clusters of the shower in the EM calorimeter. At higher η ($2.5 < |\eta| < 3.2$), the cells have bigger sizes of $\Delta\eta \times \Delta\phi = 0.1 \times 0.1$ for the two last layers.

To account for the energy losses in the material in front of the calorimeters, the EM calorimeter is complemented by pre-samplers, composed of thin layers of LAr, for $|\eta| < 1.8$.

3.3.2 The hadronic calorimeters

Two different technologies are used for the hadronic calorimeters: the scintillating tiles in the barrel and the LAr in the end-caps.

Table 3.1 – Segmentation of the calorimeters. The granularity of the calorimeters is given for the various η regions [14].

Calorimeter	**Coverage**		**Granularity**
EM	**Barrel**	**End-cap**	$\Delta\eta \times \Delta\phi$
Pre-sampler	$\lvert\eta\rvert < 1.54$	$1.5 < \lvert\eta\rvert < 1.8$	0.025×0.1
Sampling 1	$\lvert\eta\rvert < 1.475$	$1.375 < \lvert\eta\rvert < 3.2$	0.003×0.1[a] 0.025×0.025[b] 0.003 — 0.025×0.1[c] 0.1×0.1[d]
Sampling 2	$\lvert\eta\rvert < 1.475$	$1.375 < \lvert\eta\rvert < 3.2$	0.025×0.025 0.075×0.025[b] 0.1×0.1[d]
Sampling 3	$\lvert\eta\rvert < 1.35$	$1.5 < \lvert\eta\rvert < 2.5$	0.05×0.025
TileCal	**Barrel**	**End-cap**	$\Delta\eta \times \Delta\phi$
Samplings 1 — 2	$\lvert\eta\rvert < 1.0$	$0.8 < \lvert\eta\rvert < 1.7$	0.1×0.1
Sampling 3	$\lvert\eta\rvert < 1.0$	$0.8 < \lvert\eta\rvert < 1.7$	0.2×0.1
HEC			$\Delta\eta \times \Delta\phi$
Samplings 1 — 4	$1.5 < \lvert\eta\rvert < 3.2$		0.1×0.1[e] 0.2×0.2[d]
FCal			$\Delta\eta \times \Delta\phi$
Samplings 1 — 3	$3.1 < \lvert\eta\rvert < 4.9$		0.2×0.2

[a] $\lvert\eta\rvert < 1.4$ [b] $1.4 < \lvert\eta\rvert < 1.475$ [c] $1.375 < \lvert\eta\rvert < 2.5$ [d] $2.5 < \lvert\eta\rvert < 3.2$
[e] $1.5 < \lvert\eta\rvert < 2.5$

The HEC is a sampling calorimeter composed of parallel copper plates and liquid argon, and was chosen for its robustness against radiation and its low cost. It covers the range $1.5 < \lvert\eta\rvert < 3.2$ and is located just around the EM end-cap calorimeters. The two wheels forming the HEC are divided into two segments in depth. Each wheel contains 32 identical modules following a projective geometry full in ϕ but only partial in η. The dimensions of the cells in the central region $\lvert\eta\rvert < 2.5$ are $\Delta\eta \times \Delta\phi = 0.1 \times 0.1$ and double in the forward regions. The inner (outer) radius of the calorimeter is 2.28 m (4.25 m), which ensures an optimal radial depth.

In the central region, the tile calorimeter (TileCal) [38] is located just around the envelope of the EM calorimeter. A succession of steel absorbers and scintillating tiles composes the calorimeter. The sides of the tiles are connected to the wavelength shifting fibres, and to the read-out electronics by photomultiplier tubes. The calorimeter is divided into three parts: a 5.8 m long barrel ($\lvert\eta\rvert < 1.0$) and two 2.6 m long extended barrels covering $0.8 < \lvert\eta\rvert < 1.7$. Each part regroups three layers in the radial direction, having a depth of about $1.5X_0$, $4.1X_0$ and $1.8X_0$ for the barrel, and $1.5X_0$, $2.6X_0$ and $3.3X_0$ for the extended barrel.

A 60 cm gap lies between the barrel and the extended barrel for cables and service equipment of the detectors placed before the TileCal. To overcome this gap, a so-called intermediate tile calorimeter complements the structure, composed of assembled scintillating tiles. The overall geometry of the TileCal

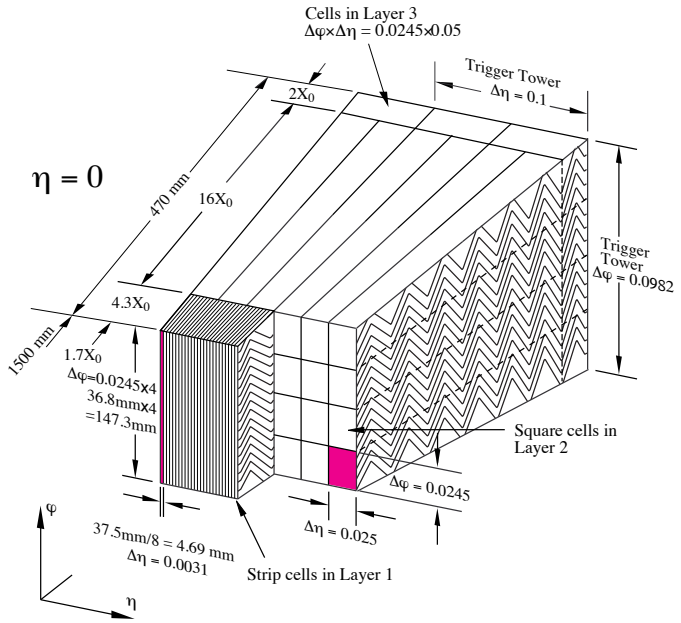

Figure 3.13 – Geometry of the electromagnetic calorimeters [14].

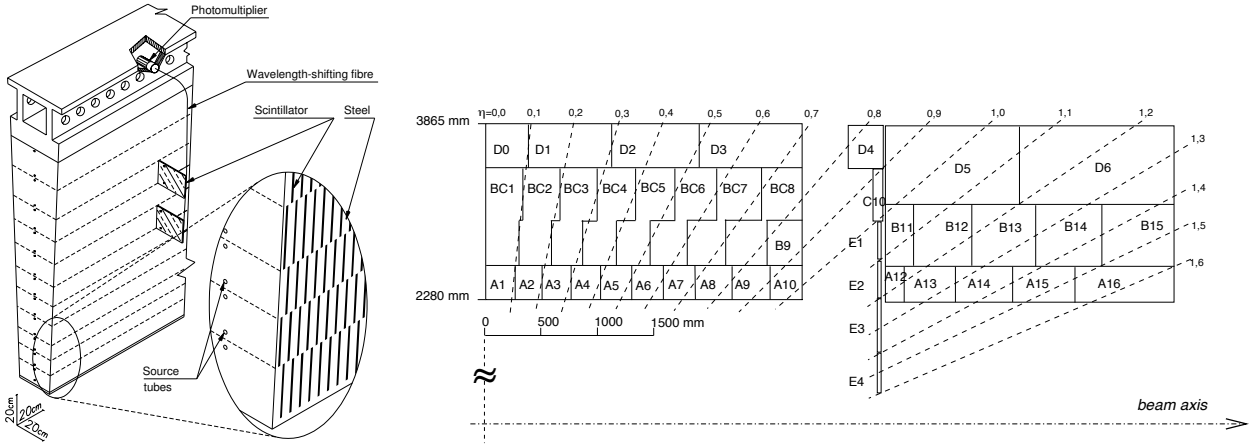

(a) Components in a module.

(b) R — z view of the tile calorimeters.

Figure 3.14 – Geometry of the tile calorimeters (TileCal), with (a) a module of the calorimeters and (b) the R — z view of the calorimeters [14].

is represented in Fig. 3.14. The layout of the tiles in the radial and normal directions allows a full projection in ϕ, which is only partial in η because of the place left for the readout fibres. The sizes of the cells are of $\Delta\eta \times \Delta\phi = 0.1 \times 0.1$ in the first two layers and 0.2×0.1 in the third.

3.3.3 The forward calorimeter

Finally, the forward calorimeter (FCal) closes the structure and offers both electromagnetic and hadronic energy measurements in the very forward regions from $|\eta| = 3.1$ to $|\eta| = 4.9$. Because of the high radiation rates in the region, small LAr gaps were selected for the design, spaced with copper absorbers in the first

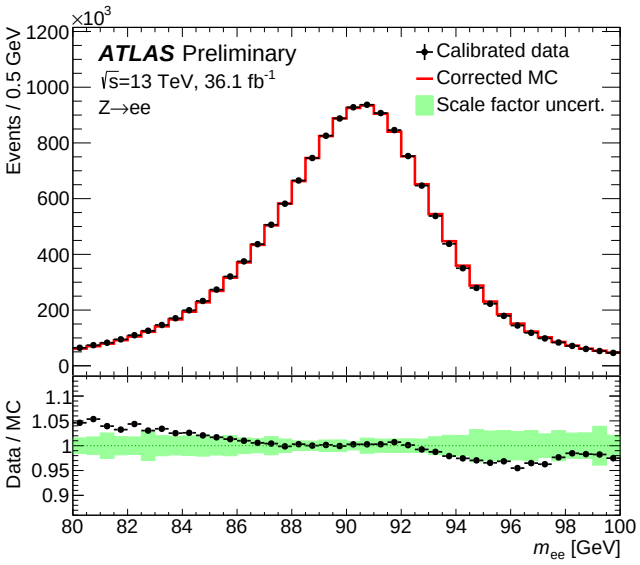

Figure 3.15 – Electron pair invariant mass distribution from $Z \to ee$ decays in data compared to simulation after the application of the full calibration, for 2015 and 2016 data combined [39].

layer and tungsten absorbers in the last two for an overall thickness of $10X_0$. This detector offers essential information about missing transverse energy and reconstruction of forward objects.

3.3.4 Performance of the calorimeters

The energy measured by the calorimeters has to be calibrated to take into account the detector response effects. The procedure consists in applying calibration to data and MC, which has been trained on dedicated simulated samples. Optimised corrections are then applied to data to mitigate the remaining detector effects. Finally, energy scale factors are calculated to have a good agreement between data and MC. Residual deviations are fitted and corrected in MC. The invariant dielectron mass spectra are presented in Fig. 3.15 [39], where the Tag-and-Probe method [40] is used to select the pairs. This method relies on the selection of a pair composed of a high quality object, the tag. The other object, the probe, is used for the measurements (see Sec. 7.1 for more details). The distributions for the data are shown without applying any background subtraction, and the simulation is normalised to data. The bottom panels show the residuals for the data-over-MC ratios together with the total uncertainty (shaded green band). Good performance of energy calibration is demonstrated as the agreement between corrected MC and data is at the percent level.

For Run 2, the noise in the calorimeters is determined using minimum bias events recorded in 2015. These events correspond to randomly filled bunch crossings triggered proportionally to the expected luminosity, with a number of interaction per bunch crossing $\mu \approx 14$. The calorimeter-cell noise is then estimated as the standard deviation of the total noise distribution measured in each cell. The procedure is also performed on simulated events, for which μ is chosen to match the data (generated events are overlaid to reach the correct pile-up conditions). Results are presented in Fig. 3.16 [41] for the LAr calorimeters. As expected, the noise increases with $|\eta|$, due to increased radiation and cell size.

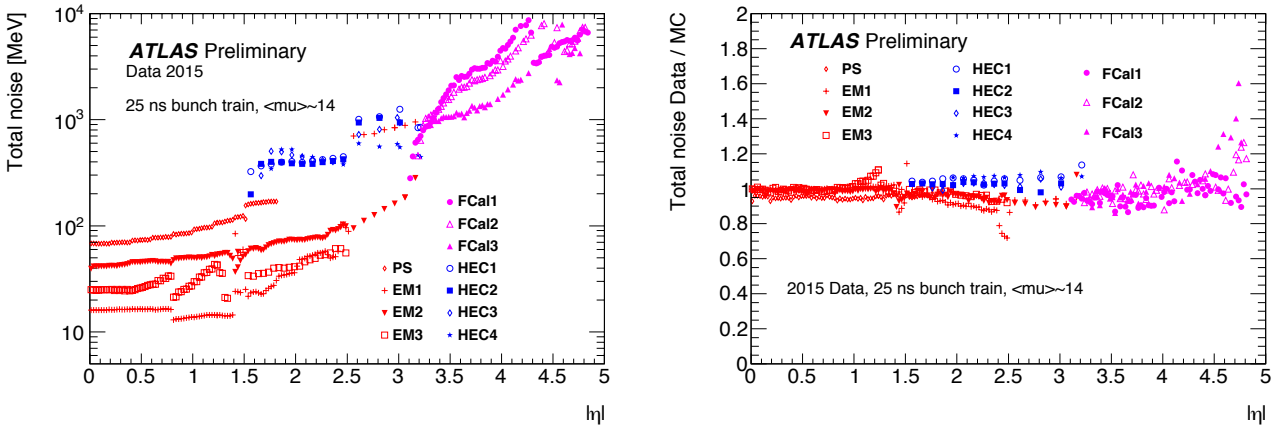

(a) Noise measured in data 2015

(b) Noise ratio of data over simulation

Figure 3.16 – Comparison of the noise in the LAr calorimeters between data 2015 and simulation [41].

3.3.5 Electron reconstruction and associated performance

The design of the EM calorimeter was optimised to offer an efficient electron and photon identification over a wide range of $p_{\mathrm{T}} > 5\,\mathrm{GeV}$. Between 20 and 50 GeV, the majority of events contain jets produced by QCD decays and only a small fraction of events have isolated electrons. The rejection of background has therefore to be very high to provide a good reconstruction efficiency.

In order to reconstruct electrons, information from both the ID and the calorimeters is used. The search starts with groups of cells in the EM calorimeter (referred to as clusters). Clusters are formed using a sliding window algorithm with fixed size (0.1×0.1 in $\Delta\eta\times\Delta\phi$) [42], looking for regions of the calorimeters in which the maximised deposited energy is above 2.5 GeV to define the cluster centre. In parallel, tracks are reconstructed in the ID using the hits in the chambers. If a cluster matches a reconstructed track in the ID (within $\Delta\eta \times \Delta\phi = 0.05 \times 0.10$), the object is reconstructed as an electron. Combining the information from the track and the clusters, the parameters of the electron are precisely measured.

A second search looks for tracks in the ID which correspond to clean deposits in the calorimeters to improve the reconstruction of electrons having a low p_{T}. The general procedure for electron reconstruction is outlined in Fig. 3.17 [43]. In Run 2, electron reconstruction takes advantage of the recently installed IBL, and photon conversion to two electrons can be identified thanks to the good granularity of the layer close to the interaction point. Indeed, two tracks close to each other in the ID, consistent with a particle with $m = 0$, are tagged as coming from photon conversion. These tracks are vetoed for electron reconstruction.

The quality of the reconstruction is assessed using the criteria outlined afterwards. These criteria are regrouped in so-called working points which aim at various signal efficiencies and background rejections depending on the analysis needs. In Run 2, a likelihood method based on the TRT high-threshold hits was introduced to compensate the lower transition radiation absorption probability of the argon gas mixture as compared to Run 1. Efficiencies are calculated using the Tag-and-Probe method on $Z \to ee$ events. The expected signal efficiencies and background rejections are calculated using dedicated simulated samples [14].

- ***Loose* working point.** The reconstruction is based on a limited amount of information from

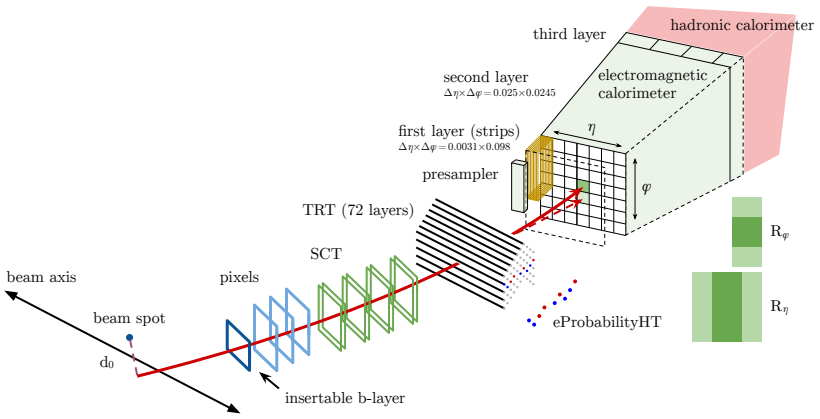

Figure 3.17 – Electron reconstruction procedure [43].

the calorimeters. Hadronic leakage (energy of the electron found in the hadronic calorimeters) and shower-shape parameters are taken from the middle layer of the EM calorimeters only. The corresponding reconstruction efficiency is close to 90%, but the background rejection is at a low value of 600.

- ***Medium* working point.** The rejection is increased by three to four times thanks to cuts on the first layer of the EM calorimeter (strips) to better separate electrons from pions, and on the quality of the associated track (the tracks must have enough hits in the silicon layers and a good d_0). The efficiency is decreased by about 10%, but background rejection increases by a factor of 3 to 4, with respect to the *Loose* working point.

- ***Tight* working point.** All information available from the ID and the calorimeters is used, combining the cuts of the *Medium* working point. The track is required to hit the first silicon layer to reject converted electrons. It should also have hit the TRTs to suppress hadronic background. The track has to strictly match a cluster in the calorimeters. The signal efficiencies decrease by about 10 to 15% and background rejections increase accordingly by a subsequent factor of 3 with respect to the *Medium* working point.

The efficiencies of these identification working points are presented in Fig. 3.18 for 2015 data.

3.4 The Muon Spectrometer

The outermost part of the ATLAS detector is composed of the Muon Spectrometer (MS), which was designed to cover a wide spectrum of the muon space. The MS has a volume of around $16\,000\,\mathrm{m}^3$, a surface of $5500\,\mathrm{m}^2$ [44, 45], and toroid magnets surround the muon chambers to bend particles for very precise momentum measurements. The performance of the MS was specifically optimised for the study of major processes such as $H \to ZZ^* \to 4\ell$ and Z' or W' decays. The MS must be able to precisely identify and reconstruct the trajectories of the muons and their momenta, to efficiently trigger the events with muon topologies, and to successfully combine its measurements with information from the ID.

Figure 3.19 presents the MS in the y — z plane. The MS is divided into two regions covering $|\eta| < 1.05$ (barrel) and $1.05 < |\eta| < 2.7$ (end-caps). In the first region, instrumentation is organised cylindrically around the z axis, whereas in the end-caps, chambers and electronics are gathered in disks perpendicular

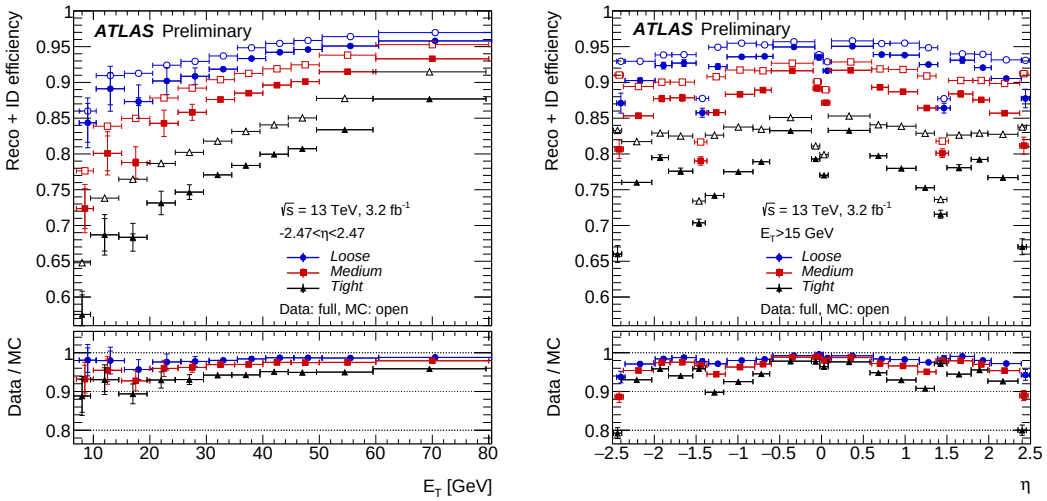

(a) Against p_{T} (b) Against η

Figure 3.18 – Electron reconstruction and identification efficiencies in $Z \to ee$ events using 2015 data [43].

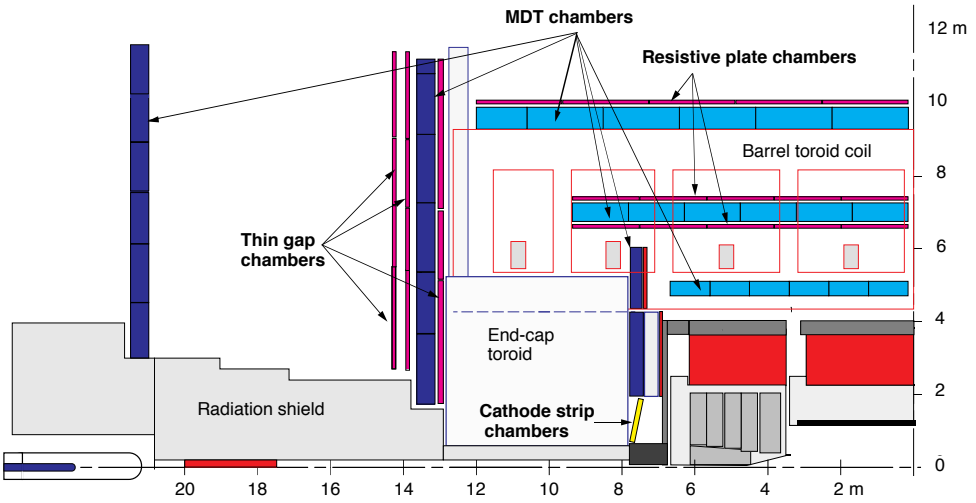

Figure 3.19 – The Muon Spectrometer in the y — z plane. The MS is divided into two regions covering $|\eta| < 1.05$ (barrel) and $1.05 < |\eta| < 2.7$ (end-caps) [14].

to this axis. In the two regions, the MS is composed of three layers often referred to as *stations*. The layers are positioned at R = 5, 7.5 and 10.5 m, respectively. Similarly, the end-cap disks are placed at z = 7.4, 14 and 21.5 m [14]. The MS is symmetrically distributed in the ϕ direction, with 16 ϕ regions to cover the full space.

During the shut down preparing the Run 2, the MS was completed with respect to its initial design: the missing chambers in the transition region between the barrel and the end-caps ($1.0 < |\eta| < 1.4$) were added. Four RPC-equipped MDT chambers were furthermore installed at the bottom of the detector to improve the efficiency. Some of the new MDT chambers are made of tubes with a smaller radius compared to the ones used in the rest of the detector, allowing them to cope with higher rates. Finally,

Table 3.2 – Number of muon chambers for each η region. For each technology, the designed z/R, ϕ and time resolutions are reported, as well as the total number of read-out channels [14].

	Chamber resolution			Measurements per track		Characteristics (number of)	
Technology	z/R	ϕ [mm]	Time [ns]	Barrel	End-caps	Chambers	Channels
MDT	35 µm	–	–	20	20	1154	≈ 350 k
CSC	40 µm (R)	5	7	–	4	32	≈ 70 k
RPC	10 mm (z)	10	1.5	6	–	606	≈ 370 k
TGC	2 – 6 mm (R)	3 – 7	4	–	20	4256	≈ 320 k

RPCs located in the foot region of the detector, and part of the outer chamber layer, were cabled during preparations for Run 2. These chambers were present in Run 1, but not read out. Their main purpose is to improve the trigger for muons with high transverse momentum [46]. The impact on the acceptance of the Muon Spectrometer can be estimated in terms of number of chambers traversed by muons in the (η, ϕ) plane: in the newly instrumented regions, twice more hits (from 2 to 4 on average) are expected for the precision and trigger chambers.

The number of muon chambers in each η region, for each technology is presented in Tab. 3.2 [14]. The numbers are given with the associated z/R, ϕ and time resolutions. The various technologies used are further detailed in the next paragraphs.

3.4.1 Momentum measurement

One of the key aspects of the MS is its ability to provide very precise measurements of the momentum of the muons. These measurements are performed thanks to the magnets of the detector, which are described in the next section. By measuring the curvature of the muon tracks under the magnetic field, the momentum of the particle can be determined. Figure 3.20 introduces the elements needed for the calculation. From the Sagitta, the bending radius R can be deduced and the transverse momentum calculated [47]:

$$p = 0.2998 B_{\perp} R, \tag{3.3}$$

where $B_{\perp}$ is the magnetic field undergone by the muon perpendicular to its trajectory (the deflection happens in the η plane). Whereas the ID bends charged particles in the transverse plane allowing the p_{T} to be measured, the MS directly measures the momentum of the particle. The lever arm of the MS is longer and therefore the precision of the measurements is improved.

The integral of the magnetic field is of 2.5 T m on average in the barrel and rises up to 6 T m in the end-caps. From Eq. 3.3, it appears that high-momentum muons will be less bent than muons having a smaller p. The precision of the measurements hence relies on the ability to determine the Sagitta with high accuracy, which in turn depends on the spatial resolution of the MS. For instance, for a muon having $p = 1$ TeV, the MS has to be able to estimate a Sagitta with a value close to 500 µm. The MS resolution on the Sagitta must therefore be of tens of micrometers.

Taking into account Eq. 3.3, the relative resolution can be written as:

$$\frac{\sigma_{p_{\mathrm{T}}}}{p_{\mathrm{T}}} = \frac{p_0}{p_{\mathrm{T}}} \oplus p_1^{\mathrm{MS}} \oplus \frac{p_{\mathrm{T}}}{p_2}, \tag{3.4}$$

where p_0 accounts for the energy loss fluctuations in the calorimeters, p_1^{MS} is related to the multiple scattering and p_2 describes the hit resolution which depends on the alignment and the calibration of the

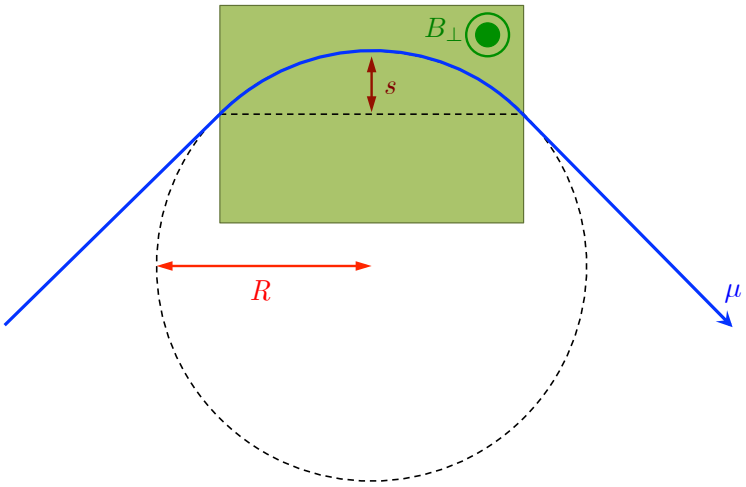

Figure 3.20 – The Sagitta (s) of the track of a muon (blue) in the Muon Spectrometer is used to assess the transverse momentum of the muon. The radius R of deflection under the magnetic field (green area) can be obtained from the measurement of s.

chambers [48]. For low p_{T} ($5 < p_{\mathrm{T}} < 50\,\mathrm{GeV}$), the MS offers a resolution of less than 3%, which increases up to about 11 to 12% at $p_{\mathrm{T}} = 1\,\mathrm{TeV}$ [14, 44, 45].

3.4.2 The toroid magnets

The MS is surrounded with toroidal magnets. This configuration allows to have a magnetic field orthogonal to the muon trajectories in the η planes and to minimise the amount of material in the areas of measurement, preventing the resolution from being degraded by multiple scattering. For $|\eta| < 1.4$, the bending of the muons is provided by the large barrel toroids, which are composed of eights coils distributed symmetrically over ϕ. For higher pseudo-rapidities ($1.6 < |\eta| < 2.7$), bending is ensured by two small end-cap magnets located at the very ends of the barrel system. End-cap toroids are rotated with respect to the barrel by an angle of 22.5°, so that the radial overlap of the fields creates a better bending power in the transition regions ($1.4 < |\eta| < 1.6$). Nonetheless, the resolution of the MS suffers from the limited number of coils and the field integral decreases in these transition regions.

Magnets are cooled down to 4.5 K using liquid helium and operate with a nominal current of 20.5 kA. However, the MS chambers can operate at room temperature.

3.4.3 Precision chambers

Technologies had to be chosen, which could enable the MS to provide accurate measurements of the coordinates of the muon tracks in the η direction to successfully estimate the momentum of the particle. These technologies are described in this section, focusing on the working principle and the performance achieved. More details can be found in Ref. [44].

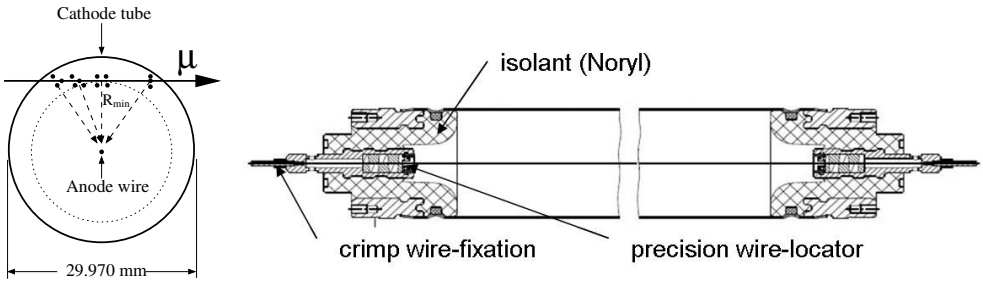

Figure 3.21 – Working principle (left) and design (right) of the MDT chambers [14].

Monitored Drift Tubes (MDT)

Monitored Drift Tubes (MDT) are responsible for precision tracking of the MS. Most of the space measurement can be covered at a limited cost and a good resolution in the η direction can be achieved. As indicated in Fig. 3.21 [45, 49], a tube is composed of a cylinder in aluminium (29.970 mm of diameter), a central anode wire of 50 µm and plugs which maintain the wires at their position in the ends. The gas inserted in the tube is composed of a mixture of Ar/CO_2 (93%/7%) at a pressure of 3 bar which reduces diffusion and ionisation fluctuations. Tubes only measure the bending coordinate. The missing coordinate has to be provided by the trigger chambers. The drift time of the particles produced in the tube is about 700 ns [50].

The resolution of a single tube depends on the drift distance (the average resolution is about 80 µm). The cylindrical layout of the tube suppresses any dependency on the angle of the incoming particle. A chamber is composed of three to eight layers of tubes and the overall resolution decreases to 35 µm [14]. The architecture of the chambers allows the operation of a tube to be independent from the others, which is of major interest in case a tube stops functioning properly. Because of the large dimensions of the tubes and high pressure, the tubes have to operate at limited rates, otherwise precision of the measurements is severely degraded. A counting rate of 200 MHz per tube is safe for operation [14, 49]. There are a total of 1150 MDT chambers.

Cathode Strip Chambers (CSC)

Because of radiation limitations on the MDTs, inner end-cap stations are using the Cathode Strip Chamber (CSC) technology in the range $2.0 < |\eta| < 2.7$. Precise spatial and time resolutions can be achieved, which exceed those of the CSCs even in more extreme operating conditions [14, 51]. Wires of the MDTs are oriented in the η direction and the distance between the anode and the cathode has been fixed to 2.54 mm to meet the required performances, as pictured in Fig. 3.22. The cathodes, which are located on both sides, are lithographically etched, one side with the strips perpendicular to the wires and the other side in the direction of the wires, so that measurements can be provided in both the η and ϕ directions simultaneously. The mixture composing the chambers is made of 80% Ar and 20% of CO_2. The anode potential is kept at 11 kV [51].

In nominal operating conditions, the resolution of the chambers is 60 µm per plane in the η direction and 5 mm for the second coordinate. Particles traverse four consecutive planes while being measured. Since the measurements performed do not rely on the drift time, the resolution is not dependent upon temperature and pressure. However, the quality of the measurements depends on the angle of the incoming

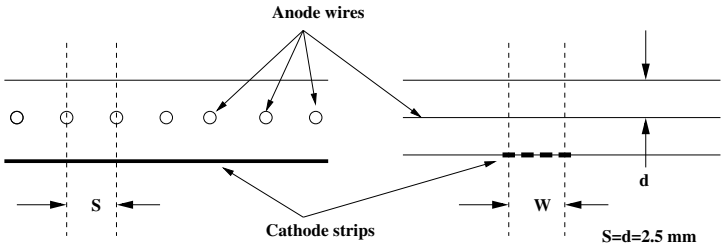

Figure 3.22 – Details of the design of a CSC chamber [51].

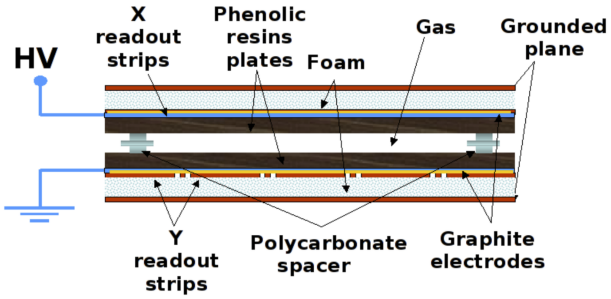

Figure 3.23 – Details of the design of a RPC chamber [52].

particle. The CSCs are therefore rotated by an angle of 11.59° to ensure the majority of the particles coming from the interaction point hit the chamber perpendicularly. There are 32 CSC chambers in total.

3.4.4 Trigger chambers

While precision chambers offer highly accurate measurements of muon coordinates, trigger chambers deliver fast information to allow a quick decision to be made by the L1 trigger (the trigger system is described in more details in a subsequent section of this chapter). Information must contain the missing second coordinate measurement for the MDTs.

Resistive Plate Chambers (RPC)

As illustrated in Fig. 3.23, Resistive Plate Chambers (RPCs) are composed of detectors organised in parallel plates, which are made of highly resistive components for the electrodes [52]. These electrodes are separated by insulators by a gap of 2 mm, in which the gas is filled. The signal is obtained by an AC coupling to the metallic strips which are grown on the outer sides of the electrodes. The strips are laid out in a grid structure to provide measurements in the η and ϕ coordinates. Each RPC is composed of two independent gas spaces, each of these being instrumented with its own read-out strips, whose granularity directly affects the resolution of the system.

The gas in the RPCs is a mixture of $C_2H_2F_4$/Iso-CH_{10}/SF_6 in the ratio 94.7%/5%/0.3% (nominal voltage of 9.8 kV). This configuration allows a fast signal to be delivered (5 ns), with a short time of relaxation and a low transition probability. The RPCs are used for triggering in the barrel region and are assembled together with the MDTs of equal dimensions. They also share the same mechanical structure. Three stations (two in between the MDTs and one mounted apart) compose the triggering system. The layout of the inner and outer RPCs allows to trigger high-momentum tracks from 9 to 35 GeV, while

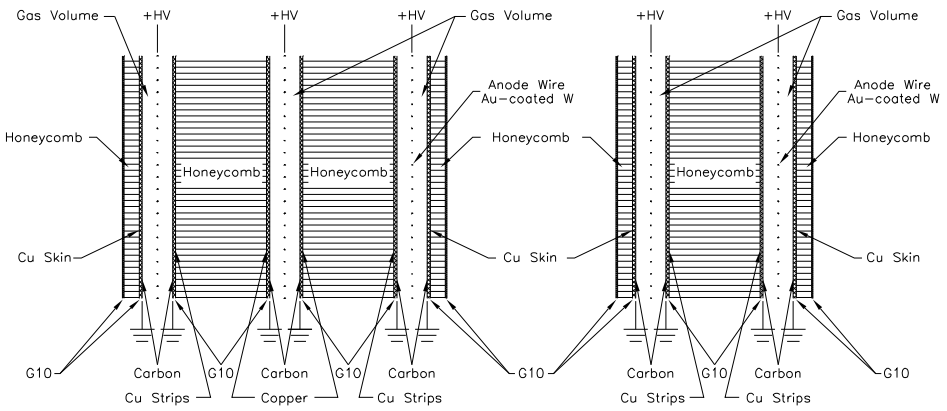

Figure 3.24 – Layout of the TGC chambers in a module [52].

the inner chambers provide triggering for lower-momentum tracks (6 to 9 GeV) [52]. There are 606 RPC chambers in total.

Thin Gap Chambers (TGC)

Thin Gap Chambers (TGCs) use a similar technology as RPCs, but the distance between the wire and the cathode (1.4 mm) is smaller than the distance between the wires (1.8 mm), as shown in Fig. 3.24 [14, 52]. The cathode planes are composed of 1.6 mm-thick plates coated with graphite on the side facing the wires and copper on the other. One of the copper layers is divided into strips to measure the ϕ coordinate, while the bending coordinate is measured by the wires. The gas is a mixture of CO_2 and C_5H_{12} operated in a quasi saturated mode (gain close to 3×10^5), with a nominal voltage of 2.9 kV to ensure a good time resolution for the vast majority of the tracks.

TGCs are placed in the end-caps, where they complement the MDTs in seven layers (three in front of the MDTs and four in the back) to provide trigger and second coordinate measurements. The precision of the slope of the muon tracks is of 2 to 3 mrad and only trajectories pointing to the primary vertex are selected for the L1 trigger. In the very forward regions, only two layers of TGCs are used which do not provide triggering but a measurement of the second coordinate. Triggering will be taken care of by the new stations installed during the long shut down after Run 2 (New Small Wheel) [53]. There are 3588 TGC chambers in total.

3.4.5 The alignment system

The precision of the measurements relies on the good positioning of the chambers. The design enables an accuracy of the alignment down to 5 mm, but this can be altered by thermal conditions and deformations of the materials. Since a precision of 50 µm is required for the Sagitta measurements, an optical system was incorporated to the detectors. This system monitors the relative position of each chamber with respect to its neighbours [14]. The system uses optoelectronic image sensors to point illuminated targets, as described in Fig. 3.25.

The overall position of the MS chambers with respect to each other and the chambers of the ID is complemented with alignment algorithms, which take advantage of the reconstructed tracks to assess the miss-positioning of the chambers. Indeed, at high p_T, the muon tracks are almost straight and can be

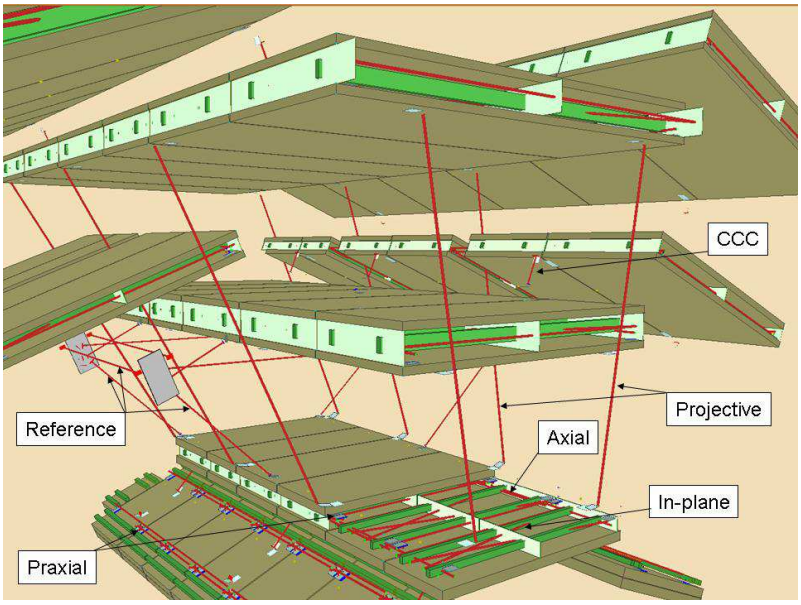

Figure 3.25 – The Muon Spectrometer alignment system [14].

used as calibration for the detectors. Combining these various technologies, the desired precision of 50 µm can be achieved, as shown in Fig. 3.26 [54] (taking into account the relatively large error bars).

3.4.6 Muon reconstruction

In ATLAS, muon reconstruction is done independently in the ID and the MS. Then, information from the two sub-detectors is combined to form the muon tracks used in physics analyses. The ID performs the reconstruction of muons like any other particles as described in Ref. [55, 56]. This section focuses on the MS side and more details can be found in Ref. [40]. The software performing the muon reconstruction was rewritten for Run 2 with respect to Run 1 in order to cope with the increased data acquisition rate and worse pile-up conditions.

In each MDT and its associated trigger chamber, a Hough transform [57] helps to find candidate hits in the bending plane. Afterwards, tracks are formed by fitting segments from the various layers thanks to an algorithm performing a segment-seeded combinatorial search (the seeds are first created in the middle layers and propagated to the other layers). Segments are selected according to the fit of the track and the number of hits (missing hits) they contain. A track should be at least composed of two segments, except in the transition region, where only one segment is required. If a segment is used to form several tracks, only the best assignment is kept (in certain cases, such as close-by muons, the segment can still be shared among two tracks). A χ^2 fit of the hits with the track candidates is used, and candidates are selected if the fit passes some criteria (the hits which penalise the fit can be removed and the fit repeated).

Combined muon reconstruction between the ID and the MS is based on information from the two detectors and the calorimeters. Various muon types are then defined.

The track of a *Combined* (CB) muon is obtained after the refit of two independently reconstructed tracks (one in the MS and one in the ID). The fit quality may require the inclusion of additional hits from the MS. The refit starts from the MS and is propagated to the reconstructed track in the ID.

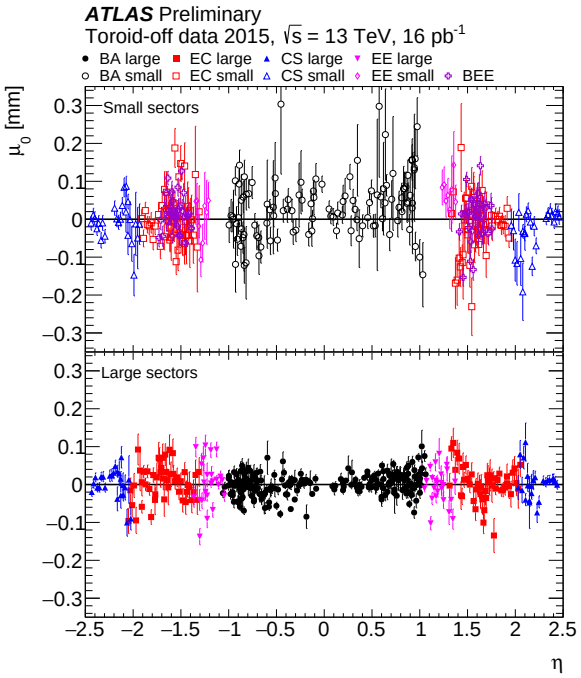

Figure 3.26 – Muon Spectrometer alignment performance in Run 2. For each tower of the muon spectrometer, the alignment bias on the sagitta is modelled as $\mu_0 + \frac{\theta-\langle\theta\rangle}{\mathrm{RMS}(\theta)}\mu_\theta + \frac{\phi-\langle\phi\rangle}{\mathrm{RMS}(\phi)}\mu_\phi$, where μ_0, μ_θ and μ_ϕ are parameters of the fit assessing the misalignment in the radial, polar (θ) and ϕ azimuthal directions. The means ($\langle\rangle$) and RMS are taken over the tower track sample. The estimated value of μ_0 is presented here, using the August 2015 toroid-off run, which reflects the misalignment of the chambers [54].

Segment-tagged (ST) muons result from the extrapolation of an ID track to the MS, which matches at least one local segment in the precision chambers. These muons are used to recover reconstruction efficiency in regions of low acceptance of the MS.

Calorimeter-tagged (CT) muons are formed from an ID track which can be matched with an energy deposit in the calorimeter. This deposit must be compatible with a muon (particle with minimal ionisation). Although this type has the highest fake rate, it is used to recover acceptance in the regions where the MS is only partially instrumented (because of cabling and space for the calorimeters).

Finally, the *Extrapolated* (ME) muons result from a MS track which can be extrapolated to the interaction point, where its parameters are defined, taking into account the estimated energy deposit in the calorimeters. Selection criteria are applied on the MS track and this muon type complements the regions outside the ID acceptance ($|\eta| > 2.5$).

In cases a track satisfies several muon types, the first type in the previous list is chosen to reduce the fake rate. Overlaps of ME muons is done by keeping the track having the best fit.

3.4.7 Muon identification

On top of a type, the muons are attached a quality, which allows users to choose various levels of selection to either improve background rejection (mostly pion and kaon decays), increase the efficiency of the

analyse or ensure good momentum measurements. Hadron decays produce tracks with low quality fits and muon whose momentum measurements do not agree between ID and MS. The study of $t\bar{t}$ simulated samples allows to define variables capable of good discrimination.

For the combined tracks, the following variables are included. The first variable is the q/p significance defined as the difference of ratios of charge over momentum in MS and ID normalised by the uncertainties summed in quadrature. The relative difference of momenta measured in the ID and the MS, as well as the normalised χ^2 of the combined track fit are also included. Requirements on the number of hits in the ID and the MS are enforced to ensure precise momentum measurements. The number of SCT hits and missing hits on the trajectory of the track, referred to as holes, must be greater (less) than thresholds, which are lower (increased) in the regions of anticipated inefficiencies of the detectors.

Using these selection criteria, four identification working points (quality of muons) are defined. The *Loose*, *Medium*, and *Tight* working points are defined such that a looser working point contains the muons passing the tighter working points:

- ***Tight* working point.** Muons have to pass the tightest selection criteria to maximise the purity of the reconstruction. The expected reconstruction efficiency is of 90%.
- ***Medium* working point.** Muons fulfil the standard requirements for an expected reconstruction efficiency of 96%.
- ***Loose* working point.** Muons satisfy looser cuts in order to provide higher reconstruction efficiencies while ensuring a good quality of the track. This last working point was specifically designed for the Higgs studies in the four-lepton final state. Reconstruction efficiencies of 97% are expected.
- ***High-pT* working point.** Muons have to pass specific selection criteria to maximise the resolution of the measurement of p for tracks having $p_{\mathrm{T}} > 100\,\mathrm{GeV}$. This working point is adequate for high-mass Z' and W' searches. The expected reconstruction efficiencies are of 78% on average.

The higher inefficiency observed for *Medium* as compared to *Loose* muons is mainly attributed to CT muons in the central region ($|\eta| < 0.1$), which are vetoed for the *Medium* and *Tight* working points.

3.4.8 Measurement of the reconstruction and identification efficiencies

Reconstruction and identification efficiencies are measured using the Tag-and-Probe method on a selection of $Z \to \mu\mu$ (for high and medium p_{T} muons) and J/ψ (for muons with $p_{\mathrm{T}} < 20\,\mathrm{GeV}$) events in data. The use of the two decay channels is highlighted by the measurement of the efficiencies of the *Medium* working point against p_{T} shown in Fig. 3.27 (a) [40].

Results for the *Loose*, *Medium* and *Tight* working points are presented against muon η in Fig. 3.27 (b) [40]. The *Loose* and *Medium* working points have similar efficiencies, except in the $|\eta| < 0.1$ region where the MS acceptance is recovered with the inclusion of CT and ST muons for the *Loose* working point. The efficiencies of these two working points are above 98%, whereas for the *Tight* selection, the efficiency varies between 90% and 98%. Inefficiencies are accounted for misaligned muon chambers or temporary failures in the SCT readout system. The efficiency of the *High-pT* working point is reduced due to tighter requirements.

In order to correct the simulation, the ratios of the efficiencies in data and simulation are calculated, referred to as scale factors. These are shown in the lower part of the plots. Overall, the scale factors are close to 1 indicating a good agreement between data and MC. The fake rates of the working points are

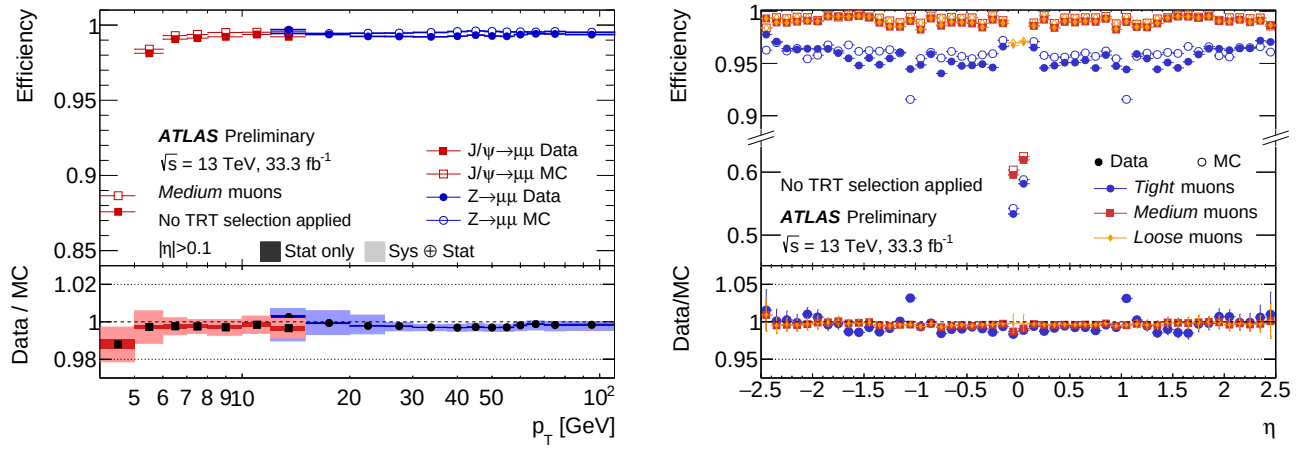

(a) *Medium* reconstruction efficiencies against p_{T}

(b) Reconstruction efficiencies against η

Figure 3.27 – Muon reconstruction efficiencies measured in $Z \to \mu\mu$ and $J/\psi \to \mu\mu$ events using Run 2 data. (a) Depending on p_{T} the J/ψ (red) or the Z (blue) decays are used for the measurements of the *Medium* working point. (b) Efficiencies are shown for the *Loose*, *Medium* and *Tight* working points as a function of η [40].

Table 3.3 – Muon reconstruction efficiencies and fake rates [40]. Muon efficiencies are measured using the Tag-And-Probe method on $Z \to \mu\mu$ decays, whereas fake rates are assessed using $t\bar{t}$ events in simulation, validated in data with $K_s^0 \to \pi^+\pi^-$ decays.

Working point	Efficiency (%)	Fake rate (%)
Loose	> 98	0.5 – 0.8
Medium	> 95	0.2 – 0.4
Tight	> 89	0.1 – 0.2
High-pT	> 78	0.1 – 0.2

estimated against p_{T} of the muon, from $K_s^0 \to \pi^+\pi^-$ decays in data or from $t\bar{t}$ events in simulation. In data, events are selected using triggers based on information from the calorimeter cells. These triggers are chosen to be as loose a possible and do not include any requirements on the muons of the event. This selection enables to have a dataset composed of fake muons. In MC ($t\bar{t}$ events), the information at generator level is used to ensure the muon is fake. From the study on simulation and after validation in the data, the fake rates are measured to be maximum at low and high p_{T} and minimum close to $p_{\mathrm{T}} = 25\,\mathrm{GeV}$. They are of 0.1% up to 0.2%, 0.2% up to 0.4%, 0.5% up to 0.8%, and 0.1% up to 0.3%, for the *Tight*, *Medium*, *Loose* and *High-pT* working points, respectively. The reconstruction efficiencies and fake rates are summarised in Tab. 3.3

3.5 The trigger, data acquisition and detector control systems

The LHC delivers collisions at a rate of 1 GHz at the designed luminosity. However, the recording of the data has to be restricted to 1000 Hz for resource reasons. In order to reduce the flow of events recorded,

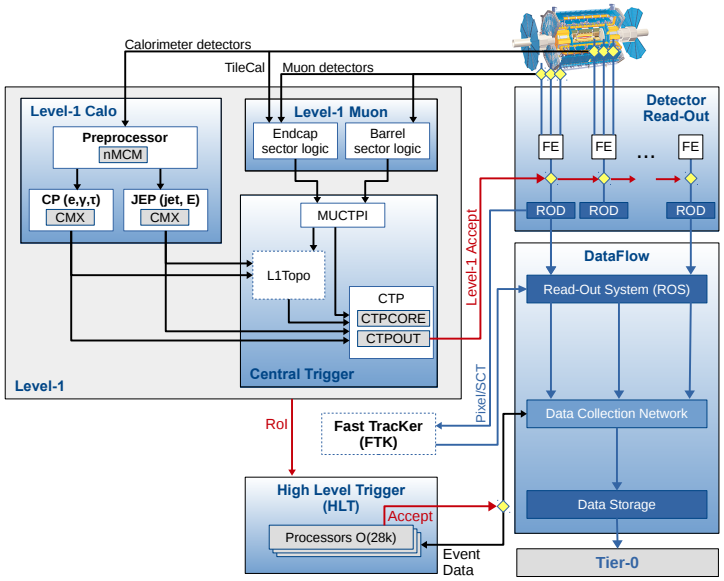

Figure 3.28 – The triggering scheme in ATLAS. The input flow is about 1 GHz and is reduced to 1000 Hz thanks to the two-level trigger [58].

only those presenting interesting features for the analysis have to be selected and decisions have to be made in extremely short times.

To perform these selections, ATLAS uses a two-level trigger pictured in Fig. 3.28 [58]. The level 1 (L1) trigger is hardware based and collects data from the MS (RPCs and TGCs) and the calorimeters at a frequency of 40 MHz and reduces the flow rate to 100 kHz. The decision has to be made in less than 10 µs and relies on the presence of high-p_{T} muons, electromagnetic clusters, jets, hadronic decays of τ, and large total or missing transverse energy. The data of the regions highlighted by the L1 trigger is transmitted to the level 2 trigger, referred to as *High Luminosity Trigger* (HLT). This trigger performs a selection based on input data from the L1 trigger, but also retrieves information from the detector readouts (MS, ID and calorimeters), if the event presents interesting features. A finer selection is then applied based on all the available information. Reconstruction algorithms are used to get a final event rate of about 1000 Hz. The events selected in this last step are recorded and sent to off-line analysis.

Two systems work at the same time as the triggers: the data acquisition system (DAQ) controlling the good taking of data, and the Detector Control System (DCS) which ensures the detectors are operating in optimal conditions (correct temperatures and pressures, correct power-supply voltages). The DAQ facilitates the monitoring of errors and allows recoveries in case of failure to take correct data. Some sub-detectors can be disabled and re-enabled if needed. An interface to the user was developed to provide an overview of the state of the sub-detectors and the functionalities of both the DAQ and the DCS.

3.6 The software framework

The software framework of ATLAS has to deal with the processing of large datasets and the interactions of users all around the world. Therefore, it is based on a robust basis on which users can develop their packages for the various needs of the physics analyses. Software interact with the grid to process the jobs with a better efficiency, a secure saving of resources and an optimised storage space.

The standard framework of ATLAS is called *ATHENA* [59] and is used for the simulation, the reconstruction and the various analyses. It implements the *Gaudi* architecture, originally developed by the LHCb collaboration. C++ packages using the ROOT libraries [60] are added to the frame and users can launch their jobs using Python scripts referred to as *jobOptions* to set the parameters. A subversion of *ATHENA* is the *RootCore* environment [61], in which parameters can directly be passed as arguments to functions and can be run interactively with the Python scripts. The founding principles of the implementation are the use of abstract interfaces, no interactions by the clients to the algorithms which produce the inputs, and storage of the data depending on its expected lifetime. Recorded data should always be saved permanently, whereas results of jobs should be temporarily kept on special disks before their possible deletion.

Algorithms are part of applications and can be configured in the framework. They perform well-defined tasks for each event and read or produce the data. An algorithm is composed of services responsible for subtasks and is called several times per event. It can be accessed for monitoring and data access. Information is written in files using data objects which represent the reconstructed particles along with their properties and the output of the detectors (calorimeter cells with their energy for example).

3.6.1 Data management and data formats

ATLAS produces about 10 PB data a year to be processed and analysed. This huge amount of data is spread all around the world in various sites and resources are shared through the Grid network. Distribution is based on a three level tier structure with one Tier 0 (CERN) responsible for event processing and storage of the raw data. The Tier 0 dispatches the raw data to a dozen of Tier-1 servers which keep a copy and ensure the needed capacity for reprocessing and access to the various versions. Finally the Tier 2 centres store the data for post-processing and offer resources for analysis, simulation and calibration.

ATLAS data are stored using several formats, each format corresponding to a step of the processing. First, the raw data directly contains the output of the ATLAS detector in the *byte-stream* format, as it is delivered by the sub-detectors. These files may have been produced using real data (physics runs) or simulation. The size of an event is close to 1.6 MB. The results after reconstruction are stored in an object-oriented format, the Analysis Object Data (AOD) [62, 63, 64], in which information from the sub-detectors is gathered to create objects like muons, electrons, clusters. Only objects used in the analysis are kept along with some information from the detectors themselves to allow refitting and various studies, in which an event occupies about 100 kB. A Derived Analysis Object Data (DAOD) format is created for each physics analysis groups, which contains all the necessary information from the AODs relevant to the specific studies. Finally, the meta-data format TAG contains the minimum information necessary for an event to be quickly selected. These files can be studied on-line and the event has a size of about 1 kB. In order to avoid any loss, the datasets are replicated over the various sites.

3.6.2 The simulation chain

The same chain and corresponding formats are used for simulated samples. In this case, the chain does not start with signal collected in the detectors, but from a set of four vectors describing the particles in the final states, which are created event by event thanks to a Monte Carlo generator [65, 66]. The behaviour of the entire ATLAS detector is simulated using GEANT4 [67], with a very realistic modelling of the sub-detectors, their geometries and the physics of the interactions. The generated particles are propagated through the simulated detectors and the responses are recorded the same way as for data (including trigger selection), producing AOD files. The rest of the chain remains unchanged.

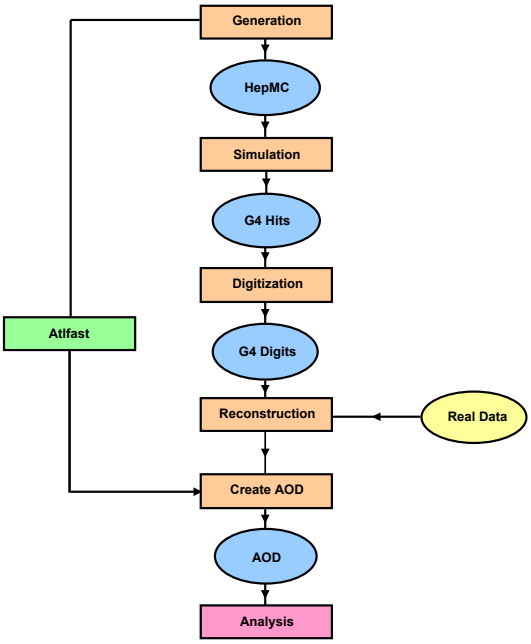

Figure 3.29 – The simulation chain of ATLAS [59].

In order to reduce the CPU time, which can explode when huge amounts of events have to be generated, fast simulation is used. For this purpose, the *Atlfast* software tools reproduce the geometry of the detector, based on simplified but still realistic models. The various chains (real data, simulation and *Atlfast*) are presented in Fig. 3.29 [59].

Part II

Muon isolation

Chapter 4

Introduction

Measuring the activity surrounding the trajectory of a particle in the sub-detectors, or the absence of activity (isolation), enables to efficiently discriminate signal decay products from background in many analyses. Indeed, signal objects studied by analysis groups often leave clean deposits and hits in the sub-detectors, and are therefore well isolated. On the other hand background objects are generally produced together with strong activity around their trajectories. In the case of the W and Z decays to muons, isolation constitutes a powerful tool to distinguish the decay products from semi-leptonic decays of heavy flavour mesons (containing b and c quarks). In the case of electrons, background contributions arising from electron conversion to photons, from misidentification of photons or muons in electrons, and from highly energetic jets (π^0 hadronisation or early energetic showers in the calorimeters) are strongly suppressed by isolation requirements.

Isolation variables measure the surrounding activity of a particle and are calculated using information from the ID (track-based isolation), which provides less pile-up-dependent variables, and the calorimeters (calorimeter-based isolation) which can also detect electrically-neutral hadrons. It is therefore possible to define working points corresponding to a set of cuts applied to these variables, tuned to suit the various needs of the analysis groups depending on the signal efficiency and background rejection targeted. Both discriminating variables can be used to suppress background with most of the analyses using both to increase background rejection. For highly-boosted regimes the calorimeter-based isolation is not optimal as calorimeter cells have small sizes, and the track-based isolation may be used alone.

During Run 1, each analysis group was defining its own isolation working points, directly applying the cuts on the isolation variables. In an effort of harmonisation, the procedure was centralised for Run 2 and a dedicated group now defines and characterises a limited number of isolation working points. These working points cover the needs of the analysis groups and harmonisation enables to centrally manage and control all the necessary work on this field.

The author took part in this common effort by developing the framework for the muon isolation. He defined and validated the cut maps (introduced afterwards) of the working points, and implemented the tool which retrieves and applies isolation cuts. He then calculated muon efficiencies and associated scale factors for each working point, using data recorded in 2015 and 2016. On top of this main task, the author studied possible improvements in the muon isolation variable definitions, by optimising the core energy of the calorimeter-based isolation, and by understanding the data-to-MC discrepancy of the track-based isolation. He finally developed a tool enabling isolation correction for close-by objects.

After an introduction to the isolation variables used for Run 2 in Chap. 5, the isolation working points are defined in Chap. 6. The muon isolation performance is summarised in Chap. 7, where results using data 2015 and 2016 are presented. Finally, Chap. 8 outlines the features and performance of the tool

developed for the isolation correction for close-by objects. In this part of the thesis, definitions concern muons and electrons only, otherwise stated. Results on the 2015 and 2016 datasets only include muons.

Chapter 5

Isolation variable definitions

This chapter is dedicated to the definition of the two sets of isolation variables used for Run 2. In each case, the energy (transverse momentum of the tracks in the ID, or energy of the cells in the calorimeters) which falls into a cone surrounding the particle is added to calculate the relevant variables. The contribution to the total energy of the particle itself is subtracted. Particles leaving clean traces in the detectors have isolation variables with low values and are said to be isolated. They have more chances to be signal objects (prompt). On the other hand, non-isolated particles are accompanied with important energy activity in the detectors, and are more likely to be background objects.

5.1 Track-based isolation

5.1.1 Inner Detector tracks

For the calculation of the track(-based) isolation, reconstructed tracks in the ID are selected, which are close to the trajectory of the object λ, and their transverse momentum is added. The transverse momentum of the track associated to the object (referred to as the core energy) is subtracted to the total to get the isolation variable.

The tracks (t) selected for the calculation of the isolation variables have to satisfy the following criteria:

- $\left|\eta^t\right| < 2.5$.
- Number of hits in the silicon layers $N^t_{\text{Si}} \geq 7$.
- Number of modules (subcomponent of the layers of the ID sub-detectors) shared with other tracks $N^t_{\text{shared mod}} \leq 1$.
- Number of missing hits in the silicon layers $N^t_{\text{Si holes}} \leq 2$.
- Number of missing hits in the Pixel detector $N^t_{\text{Pix holes}} \leq 1$.
- $p^t_{\text{T}} \geq 1\,\text{GeV}$.
- $\left|z^t_0 \sin\left(\theta^t\right)\right| < 3\,\text{mm}$.

The set of tracks selected is denoted $\mathcal{T}$ afterwards.

The first criterion is directly related to the ID acceptance. The four following criteria are optimised to ensure selection of tracks of good quality [68]. The set of these four criteria is referred to as the Loose track working point. These criteria should reduce the number of miss-reconstructed tracks: a good track has to hit a minimum number of layers of the ID and limit the number of missing hits, occurring when the reconstructed track should have passed in a region of the ID but no hits were recorded by the detector. Finally, the last two cuts are specific to isolation. The first requirement aims at maximising the tracks coming from fake leptons (from $t\bar{t}$ events for instance), whereas the criterion on z_0 reduces the dependence of the selection upon pile-up conditions, since only tracks coming from particles produced close to the interaction point are selected, therefore suppressing the contributions from secondary vertices.

Only tracks close enough to the trajectory of the particle λ are considered. For the leptons, the coordinates $\left(\eta^{\lambda}, \phi^{\lambda}\right)$ are those at the interaction point. For the photons, which do not leave any tracks in the ID, the coordinates are those obtained in the calorimeters extrapolated to the interaction point (using linear extrapolation, as photons are not bent in the ID).

Vertex choice. For the track selection, it is required that all selected objects arise from the primary vertex (defined as the vertex with the highest arithmetic sum of the transverse momenta of the participating tracks). Although this requirement is already partially ensured using the cut on $\left|z_0^t \sin\left(\theta^t\right)\right|$, the origin of the track is specifically checked. For some analyses ($H \to \gamma\gamma$ for instance), it can be useful to specify which vertex to use for the track selection if this does not correspond to the default one. The user would then have to recompute the track isolation variable with the vertex corresponding to the hard process [69].

5.1.2 Calculation of isolation variables

In order to calculate the track isolation variables of the particle λ, the momenta of the tracks t reconstructed in the ID are added if the distance between t and the track of the particle t^{λ} is small enough. The distance between the two tracks is calculated in the plane (η, ϕ), using the opening angle $\Delta R_{\lambda,t} = \sqrt{{\Delta\eta_{\lambda,t}}^2 + {\Delta\phi_{\lambda,t}}^2}$, where $\Delta\eta_{\lambda,t} = |\eta(\lambda) - \eta(t)|$ and $\Delta\phi_{\lambda,t} = (\phi(\lambda) - \phi(t))\,[2\pi]$. A cone of size ΔR_{raw} and centre t^{λ} is thus defined, and only tracks falling into it are selected ($\Delta R_{\lambda,t} < \Delta R_{\text{raw}}$).

Two kinds of variables (named ptcone and ptvarcone) are defined depending on the choice of the cone size ΔR_{raw}. The first variables (ptcone) have a fixed cone size $\Delta R_{\text{raw}} \in \{0.2, 0.3, 0.4\}$ and were used during Run 1. For Run 2, ptvarcone variables were introduced for which $\Delta R_{\text{raw}X}(\lambda) = \min\left(\frac{k_{\text{T}}}{p_{\text{T}}^{\lambda}}, \frac{X}{100}\right)$, with $X \in \{20, 30, 40\}$ and $k_{\text{T}} = 10\,\text{GeV}$. This p_{T}-dependent cone size enables to increase the efficiency for boosted searches, for which particles have a high momentum. For these searches, the cone size is reduced and the isolation variables keep lower values.

The following formula summarises the calculation [69] of the ptvarcone variable:

$$p_{\text{T}}^{\text{varcone, raw}X}(\lambda) = \sum_{t \in \mathcal{T}} p_{\text{T}}^{t}\left(1 - \Theta\left(\Delta R_{\lambda,t} - \Delta R_{\text{raw}X}(\lambda)\right)\right),$$

where $\mathcal{T}$ is the set of tracks satisfying the quality criteria introduced before, and Θ is the Heavyside function (equals to 1 for positive real numbers and nil elsewhere).

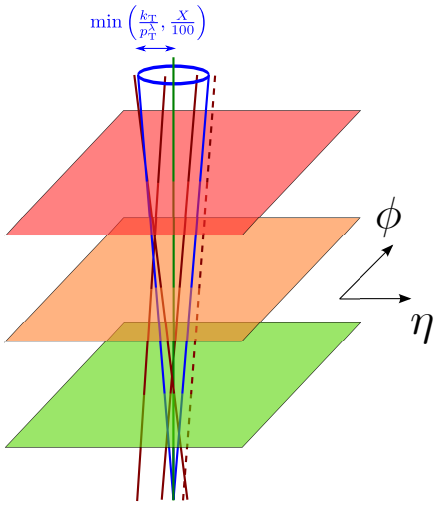

Figure 5.1 – In order to calculate the ptvarcone variables, only the tracks (represented by brown lines) of the set $\mathcal{T}$ are selected. Only the tracks (in full lines) inside the cone (blue) of radius $\Delta R_{\text{raw}X}(\lambda) = \min\left(\frac{k_T}{p_T^\lambda}, \frac{X}{100}\right)$ centred on the track of the particle λ (green line) are used for the calculation. Their transverse momenta are added. Finally, the contribution of the particle itself is subtracted.

5.1.3 Core energy

For the track isolation, the contribution of the object must also be subtracted. This contribution is referred to as the core energy. For muons, this energy corresponds to the transverse momentum of the track associated to the muon (assuming the track belongs to $\mathcal{T}$, if not the muon has no core energy).

For the electron, associating tracks to the object is more complicated as electrons can undergo a Bremsstrahlung radiation and the lost energy should still be counted as core energy. In order to do so the tracks are extrapolated until the middle layer of the calorimeters. All the extrapolated tracks which lay within a rectangle of dimensions $\Delta\eta \times \Delta\phi = 0.05 \times 0.1$ around the position $\left(\eta_{\text{ext}}^\lambda, \phi_{\text{ext}}^\lambda\right)$ of the electron are selected for the core energy of λ [69].

5.1.4 Variable calculation

Taking into account the core energy of the object $p_T^{\text{core}}(\lambda)$, the variables can be calculated as

$$p_T^{\text{varcone}X}(\lambda) = p_T^{\text{varcone, raw}X}(\lambda) - p_T^{\text{core}}(\lambda).$$

Figure 5.1 summarises the various steps of the calculation for the muons. For muons, $X = 30$, as this corresponds to the cone size used for the isolation criteria of the triggers. For electrons, there is no such requirement and $X = 20$ is chosen as it provides the best background rejection for a given signal efficiency.

5.2 Calorimeter-based isolation

The calorimeter-based isolation measures the surrounding activity of a particle by summing up the energy in the calorimeter cells close to the trajectory of the particle. As for the track-based isolation, a cone

centred around the particle in the (η, ϕ) plane is defined and cells inside it are selected. The contribution of the particle itself (referred to as the core energy) is estimated and subtracted to only account for the contributions of the other objects.

All the energy deposited in the various calorimeters described in Sec. 3.3 is considered. As a reminder, the LAr calorimeters are segmented into three layers in the azimuthal direction, and the middle layer retrieves almost 80% of the energy contained in an electromagnetic shower, where the cell granularity is of $\Delta\eta \times \Delta\phi = 0.025 \times 0.025$, which increases with $|\eta|$. A pre-sampler covers the regions $|\eta| < 1.8$ to account for particles hadronising before the LAr calorimeters. Concerning the hadronic calorimeter, the central region covers $|\eta| < 1.0$, two extensions (extended-barrel) cover the regions $|\eta| > 0.8$, with a cell granularity ranging from $\Delta\eta \times \Delta\phi = 0.1 \times 0.1$ to 0.2×0.2 at higher $|\eta|$. Composing the hadronic calorimeters, the Tile Calorimeter is divided into three layers depending on the longitudinal direction, whereas the HEC has four layers, and the FCal has three modules in depth. Combining all the calorimeters, the energy of the cells comes from the following subsets:

- Electromagnetic calorimeter (barrel): EMB1, EMB2 and EMB3 corresponding to the strip, middle and back layers.
- Electromagnetic pre-sampler (barrel).
- Electromagnetic pre-sampler (extremities).
- Electromagnetic calorimeter (extremities): EME1, EME2, EME3.
- Hadronic calorimeter: HEC0, HEC1, HEC2, HEC3, corresponding to the four layers.
- Tile calorimeter (hadronic energy): TileBar0 (TileGap1), TileBar1 (TileGap2), TileBar2 (TileGap3), corresponding to the three layers in the central region (extremities).
- FCal calorimeter (forward energies): FCAL0 (MINIFCAL0), FCAL1 (MINIFCAL1), FCAL2 (MINIFCAL2 et MINIFCAL3), corresponding to the three modules (extended).

In Run 1, the energy of the calorimeter cells was directly collected if the cells were falling into a cone around the particle in the calorimeters. The strategy changed for Run 2: the calorimeter cells are first gathered into clusters of cells (referred to as topoclusters) and the energy of these topoclusters (defined as the sum of the energy of the constituting cells) is added to calculate the isolation variables. Only topoclusters falling into a cone around the particle are selected.

The use of topoclusters enables to capture the shape of the energy deposits in the calorimeters. Leptons leave highly energetic and focused deposits, which correspond to a limited number of sizeable topoclusters. On the other hand, noise in the calorimeters (especially pile-up noise, introduced in Sec. 2.1) results in homogeneous noise in the cells and topoclusters of small size with low energy. Applying selection criteria on the size of the topoclusters, the noise contamination can be reduced and motivated the use of clustering algorithms for Run 2, as the pile-up conditions are more challenging.

5.2.1 Topocluster definition

The noise contained in the measurements by the calorimeters has two sources: the electronic noise and the pile-up noise. The first contribution arises from the detector itself, whereas the second comes from the secondary interactions which can happen at the same time as the main event (in-time pile-up) or coming from previous and next events (out-of-time pile-up).

In order to reduce the effects of these sources, it was decided to use a clustering algorithm to regroup the calorimeter cells depending on their transverse energy. The clustering algorithm [42] introduced for Run 2 collects and regroups calorimeter cells which present interesting features for the study of the energy deposits. These groups of cells, referred to as *topoclusters*, have an increased size and their manipulation is easier for the calculation of the isolation variables. The topoclusters created have various dimensions depending on the number of cells they contain, and should reproduce the shape of the energy deposits from the objects in the event as good as possible.

The first step consists in finding starting points (seeds). All the cells with energy deposits (in green in Fig. 5.2 a) having a signal over background ratio S/B greater than t_{seed} are added to a list l_{seeds}. The corresponding cells are in orange in Fig. 5.2 b. The S/B is defined as the value of the measured energy divided by the standard deviation of the expected electronic noise in this cell under the operating conditions (which depends on the gain and the current recorded). The elements of l_{seeds} are then ordered by decreasing order of S/B. Each element constitutes a topocluster on its own which will be enlarged with other cells.

For each cell of the list, the neighbouring cells are tested (the four cells surrounding a cell inside the same layer and the two cells in the nearby layers are labelled *neighbouring cells*). The cells are added to the topocluster if their S/B is greater than a second threshold $t_{\text{neighbour}}$ ($t_{\text{neighbour}} < t_{\text{seed}}$) and if they do not belong to l_{seeds}, as indicated by the arrows in Fig. 5.2 b. The selected cells are also added to an auxiliary list $l_{\text{neighbour}}$. If a neighbouring cell is close to several topoclusters and its S/B is quite low, this cell is only added to the topocluster with which it shares the most neighbouring cells. In case of high S/B, the close-by topoclusters are grouped to form only one cluster.

Once all the elements of l_{seeds} were processed, the list is replaced by $l_{\text{neighbour}}$ and the procedure is repeated until there are no more neighbouring cell candidates. In the end, topoclusters containing too few cells, or having a total energy lower than a threshold are removed.

The electronic and pile-up noises can be estimated knowing the luminosity. The number of topoclusters resulting from saturated cells only is linked to the threshold used for the definition of the topoclusters using the following expression:

$$N \propto N_{\text{cells}} \sqrt{\frac{2}{\pi}} \int_{t_{\text{seed}}}^{+\infty} e^{-t^2/2} \mathrm{d}t,$$

where N_{cells} is the total number of cells of all the calorimeters combined.

Tuning the parameters (t_{seed}, $t_{\text{neighbour}}$, as well as energy and kinematic cuts on the created clusters) enables to reduce the noise contamination. Indeed, pile-up and electronic noises are evenly distributed among the cells: the thresholds can therefore remove the cells which only contain noise energy. Requiring the created topoclusters to have a minimum size prevents isolated energetic cells to be included, as these cells more often result from noise fluctuations.

The splitting of the created clusters can be cumbersome if the event is rich in activity. For this reason, a second algorithm was designed, which improves the definition of the topoclusters. Starting from the list of topoclusters created previously, local maxima are searched for, represented by blue crosses in the Fig. 5.2 c: these correspond to cells in which the energy is higher as compared to the energy of the neighbours, and greater than a threshold. Topoclusters containing several maxima are divided (one local maximum per group), the other topoclusters remain unchanged as shown in Fig. 5.2 d. In case a splitting has to be undertaken, the new topoclusters will be built starting from the local maxima, following the same procedure as described previously except that this time, only the cells contained in the group will be used. No thresholds are required and no gatherings of topoclusters are performed. In case a cell would have to be shared among several topoclusters, it is added to the two most energetic topoclusters. Then each of these topoclusters gets a fraction of the cell energy depending on the energy of the topocluster

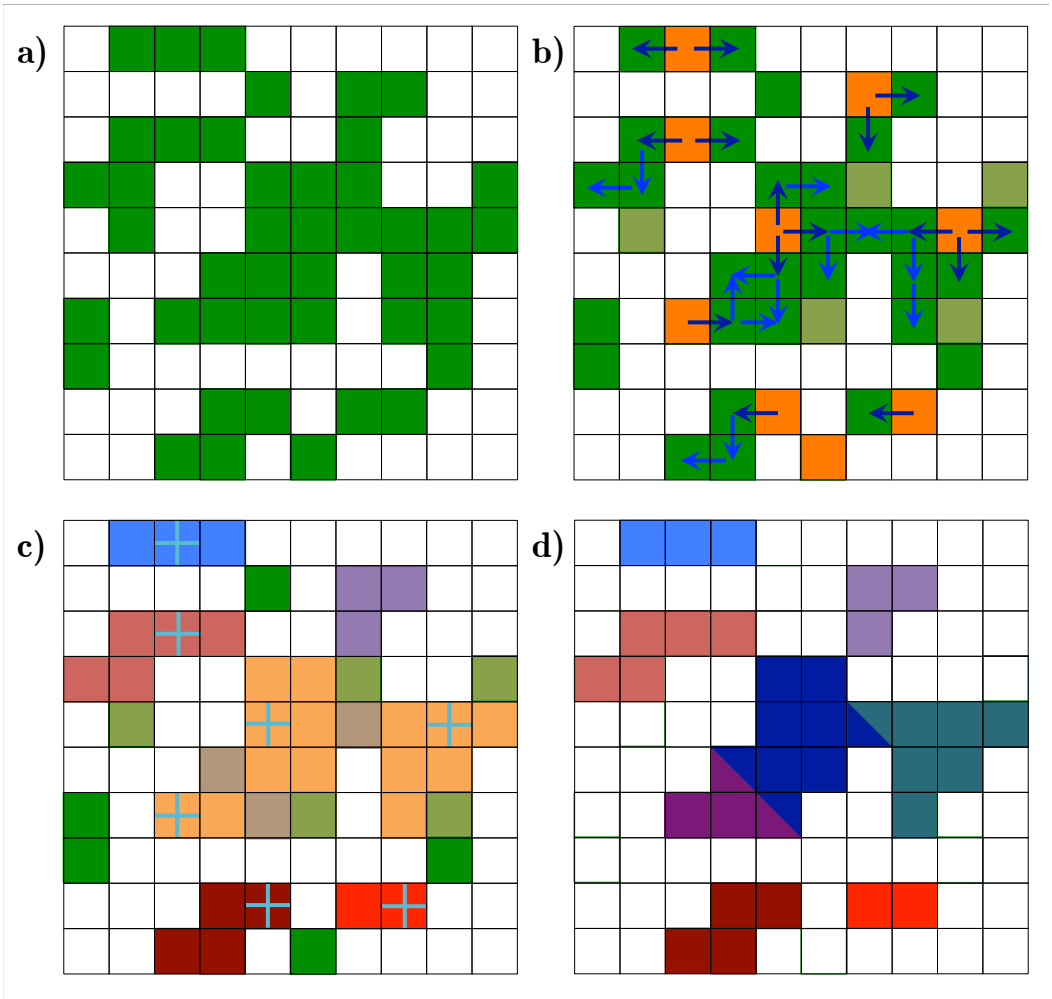

Figure 5.2 – The three following steps are needed to form the topoclusters: from the cells (in green in Fig. a), topoclusters are formed gathering the seed cells (in orange in Fig. b) with their neighbours (the arrows indicate the propagation of the clusters). In order to better split the topoclusters (for instance the orange topocluster in Fig. c), local maxima (blue crosses) are searched for and the groups are divided into new topoclusters so that they do not contain more than one local maxima. Finally, the bordering cells (triangles in Fig. d) are shared among the topoclusters.

and the distance of the cell to the clusters (in the η — ϕ plane). This division ensures all the energy of the cells was used to construct the topoclusters (no double-counting). The shared cells are represented by triangles in the Fig. 5.2 d.

5.2.2 Calculation of the calorimeter-based isolation

For Run 2, the variables calculated are referred to as the topoetcone variables (and written as $E_{\mathrm{T}}^{\mathrm{topocone}}$) [69, 70]. From the selected topoclusters, two quantities are calculated corresponding to the total energy surrounding the trajectory of the particle in the calorimeters (raw variables), as well as the energetic contribution of the particle itself (core energy). The latter is subtracted to the former to get the isolation

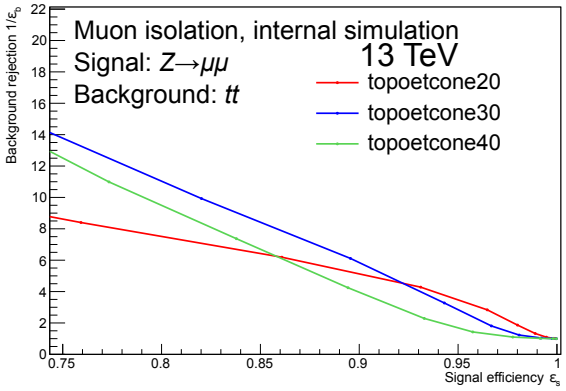

Figure 5.3 – Background rejection ($t\bar{t}$) as a function of the signal efficiency ($Z \to \mu\mu$) for the topoetcone20, topoetcone30 and topoetcone40 variables. For the range of efficiencies $\varepsilon > 90\%$ topoetcone20 is the optimal variable [71].

variables. To these variables, corrections are applied, which are the topic of the next subsection.

Topocluster selection and calculation of the raw variables

Only topoclusters having a total transverse energy $E_{\mathrm{T}} > 0$ (due to noise fluctuations, the energy of some calorimeter cells can be negative) and $|\eta| < 7.0$ are selected. Furthermore, these topoclusters must be close enough to the trajectory of the particle in the calorimeters.

Considering the coordinates of the hits $\overrightarrow{OA_i}(\eta_i, \phi_i)$ of the particle in the layers $i \in [1, N]$ of the calorimeters, the extrapolated coordinates are defined as the averaged coordinates: $\overrightarrow{OA}(\eta_{\mathrm{ext}}, \phi_{\mathrm{ext}}) = \frac{1}{N}\sum_{i=1}^{N}\overrightarrow{OA_i}$.

The topocluster centres $\{T_j\}_j$ are defined as barycentres of cells (of coordinates $\left\{\overrightarrow{OC_c}\right\}_{c\in[1,N_j]}$), weighted by the cell energies. Hence, the topocluster coordinates can be calculated as $\overrightarrow{OT_j}(\eta_j, \phi_j) = \frac{\sum_{c=1}^{N_j} E_c \times \overrightarrow{OC_c}}{\sum_{c=1}^{N_j} E_c}$, where E_c is the energy of the cell c.

Only topoclusters j close enough to the trajectory of the particle λ are selected for the raw variable denoted $E_{\mathrm{T}}^{\text{topocone, raw}X}$. The topolcusters have to lay in a cone of radius $\Delta R_{\mathrm{raw}X} = X/100$ in the (η, ϕ) plane. Their transverse energy E_{T}^{j} is added:

$$E_{\mathrm{T}}^{\text{topocone, raw}X}(\lambda) = \sum_{j=1}^{N} E_{\mathrm{T}}^{j}\left(1 - \Theta\left(\Delta R_{\lambda,j} - \frac{X}{100}\right)\right),$$

where Θ is the Heavyside function, and the distance between the topocluster j and the trajectory of the particle λ is denoted $\Delta R_{\lambda,j} = \sqrt{\left(\Delta\eta_{\lambda,j}\right)^2 + \left(\Delta\phi_{\lambda,j}\right)^2}$. For the calculation of ΔR, the extrapolated coordinates are used: $\Delta\eta_{\lambda,j} = |\eta_{\mathrm{ext}}(\lambda) - \eta_j|$ and $\Delta\phi_{\lambda,j} = (\phi_{\mathrm{ext}}(\lambda) - \phi_j)\,[2\pi]$.

Core energy

The calculation of the core energy (referred to as the topocore variable, denoted $E_{\mathrm{T}}^{\text{topocore}}$) depends on the lepton considered.

In the case of electrons, the core energy is composed of the sum of the energy of cells contained into a rectangle of dimensions 5×7 [69] in η and ϕ, centred on the extrapolated coordinates of the particle. The core energy is always composed of the same number of cells.

In the case of muons, the core energy is defined as the sum of the transverse energy of the topoclusters which fall into a small cone of radius $\Delta R_{\text{core}} < \Delta R_{\text{raw}X}$, centred on the extrapolated coordinates of the particle. The related variable (named topocore and written $E_{\text{T}}^{\text{topocore}}$) is calculated as follows:

$$E_{\text{T}}^{\text{topocore}}(\lambda) = \sum_{j=1}^{N} E_{\text{T}}^{j}\left(1 - \Theta\left(\Delta R_{\lambda,j} - \Delta R_{\text{core}}\right)\right).$$

The detail of the calculation is sketched in Fig. 5.4.

Fig. 5.5 (a) presents the distribution of the number of topoclusters selected for the calculation of $E_{\text{T}}^{\text{topocore}}$ of muons coming from $Z \to \mu\mu$ signal events (taken from MC simulation). On average, two topoclusters are selected. Fig. 5.5 (b) shows various definitions of the muon core energy in $Z \to \mu\mu$ MC events. $E_{\text{T}}^{\text{topocore}}$ is in blue (used to calculate the topoetcone variables). Other distributions are plotted for information, with the sum of E_{T} of the calorimeter cells falling in a cone $\Delta R \leq \Delta R_{\text{core}}$ in green, the estimate of the muon energy loss in the core cone in purple, and the electron-like core energy (corresponding to the sum of E_{T} of calorimeter cells in a rectangle of dimensions 5×7 around the muon) in red. The peak close to 0 in the $E_{\text{T}}^{\text{topocore}}$ distribution corresponds to muons in the forward regions for which the cells fail to pass the signal over background ratios, preventing the formation of topoclusters. The two peaks in the red and purple distributions correspond to the electromagnetic and hadronic fractions of the muon energy in the calorimeter cells. The values found here correspond to expectations presented in Fig. 5.6 [72] and based on the study of muons interacting with detector material. Muons deposit about 1 GeV of energy the ID and the MS, and 2 GeV of energy in the calorimeters.

Core radius optimisation for the muons

Prior to Run 1, the optimal value of $\Delta R_{\text{core}} = 0.1$ was found and has been used for the isolation performance in 2015 and 2016 (to which the results presented in this thesis correspond). However a recent study using the Run 2 pile-up conditions, outlined in the next paragraphs, shows that $\Delta R_{\text{core}} = 0.05$ is providing better results in terms of background rejection. This new value will therefore be used in the next years of operation.

The study for the optimisation of the cone sizes is based on Monte Carlo (MC) samples for which the pile-up conditions were specifically calibrated to those of the data 2015. The following decay processes are selected: $Z \to \mu\mu$[1] and $t\bar{t}$[2]. The first channel only offers signal muons, whereas the second offers both signal and background muons. The selection of signal and background is done on the truth type of the muon which is saved in the MC samples. Signal events are therefore only composed of well-isolated muons in the calorimeters, while background muons are not isolated and come from b, c hadron decays.

Efficiencies are then calculated by counting the number of muons (N_{pass}) passing a given cut on the isolation variable, divided by the total number of muons (N_{sample}) generated in the sample (for both signal and background). The following cuts are applied (given in GeV): $1 \times 10^6, 250, 200, 150, 100, 75, 50, 40, 30, 20, 15, 10, 7.5, 6, 5, 4, 3, 2, 1, 0.9, 0.8, 0.7, 0.6, 0.5, 0.4, 0.3, 0.2, 0.1, 0.05, 0.0$. The cut values are chosen to ensure smooth curves of r against ε. For each of these values, efficiencies and rejections are

[1] $Z \to \mu\mu$ MC sample POWHEG-BOX [73] is used, interfaced to PYTHIA 8 [74] for hadron showering, using the AZNLO parameter set [75], and interfaced to EvtGen [76] for the simulation of b-hadron decays

[2] $t\bar{t}$ MC sample POWHEG-BOX [77] is used, interfaced to PYTHIA [78] for hadron showering, and interfaced to EvtGen [76]

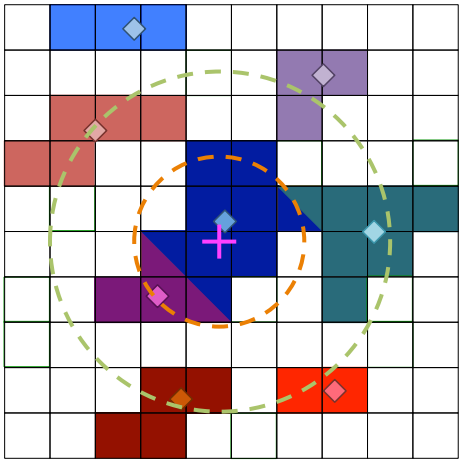

Figure 5.4 – On the figure the object λ, whose isolation is being determined, is represented by the pink cross and the various topoclusters appear in coloured groups of cells, whose barycentres are indicated by coloured diamonds. The topoclusters selected for the calculation of the isolation variables have to verify $\Delta R_{\lambda,j} < \frac{X}{100}$ (the limit corresponds to the green circle). Their transverse energy is added to obtain $E_{\mathrm{T}}^{\text{topocone, raw}X}$. The core energy is removed from this sum, defined as the sum of the transverse energies of topoclusters satisfying $\Delta R_{\lambda,j} < \Delta R_{\text{core}}$ (the corresponding limit is materialised by the orange circle). Hence, in the example in the Fig., the dark blue, dark purple, turquoise, salmon pink and brown topoclusters take part in the calculation of $E_{\mathrm{T}}^{\text{topocone, raw}X}$. Only the first two topoclusters participate to the calculation of $E_{\mathrm{T}}^{\text{topocore}}$ and are therefore removed.

calculated: $\varepsilon = N_{\text{pass}}/N_{\text{sample}}$ and $r = 1/\varepsilon$, respectively. The highest cut value provides the point $\varepsilon = r = 1$, since all the muons are selected, whereas the lowest cut value returns very low values for ε and extremely high values for r, as only a few muons are selected.

To validate the choice of $\Delta R_{\text{raw}} = 0.2$ ($X = 20$), the topoetcone20, topoetcone30 and topoetcone40 variables (for which $\Delta R_{\text{core}} = 0.1$) were tested and the results are shown in Fig. 5.3. In this plot, the background rejection in the $t\bar{t}$ samples as a function of the efficiency ε measured from the $Z \to \mu\mu$ decays is presented. The most optimal variable is the one which provides the best rejection at a given efficiency, confirming the good choice of topoetcone20.

Using the same technique, Fig. 5.7 presents the study carried out with the topoetcone20 variable, for which $\Delta R_{\text{core}} \in \{0.2, 0.4, 0.5, 0.6, 0.8, 0.1\}$ were tested. The optimal value found here is $\Delta R_{\text{core}} = 0.05$. Note that since this last study was carried out after the beginning of data taking, the results presented in this thesis are based on topoetcone20 having $\Delta R_{\text{core}} = 0.1$ (the original value, optimised using MC samples configured with the Run 1 conditions).

5.2.3 Isolation corrections

In order to improve the calculation of the calorimeter-based isolation, corrections are added to take into account the pile-up conditions in the event, as well as the leakage of the core energy for electrons.

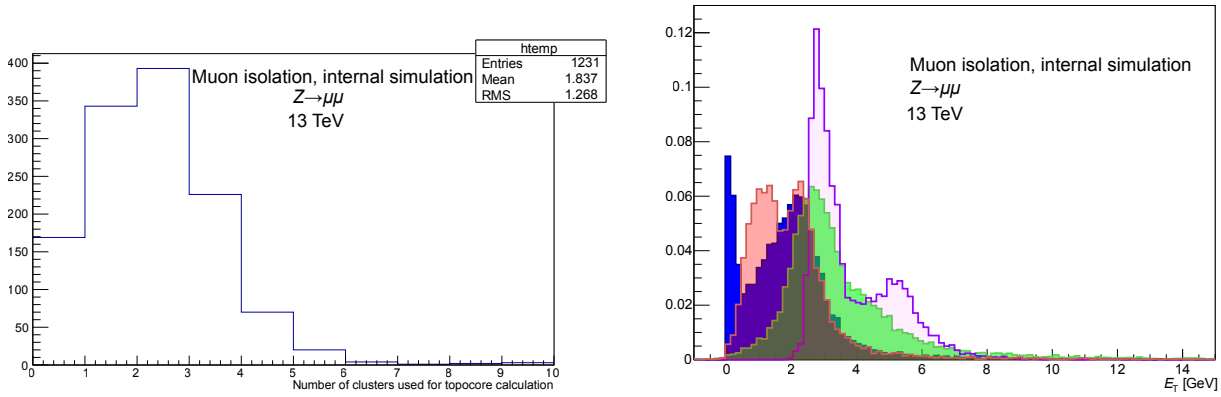

(a) Number of topoclusters selected for the topocore variable (b) Comparison of various methods for the calculation of the muon core energy

Figure 5.5 – Fig. (a) shows the number of topoclusters selected for the calculation of $E_{\mathrm{T}}^{\mathrm{topocore}}$. Fig. (b) presents the comparison of various definitions of the core energy for muons coming from $Z \to \mu\mu$ decays in simulation. $E_{\mathrm{T}}^{\mathrm{topocore}}$ is in blue (definition retained for the calculation of the topoetcone variables). The sum of E_{T} of the calorimeter cells falling in a cone $\Delta R \leq \Delta R_{\mathrm{core}}$ is plotted in green. The estimate of the muon energy loss in the core cone is represented in purple. Finally, the electron-like core energy (corresponding to the sum of E_{T} of calorimeter cells in a rectangle of dimensions 5×7 around the muon) is shown in red.

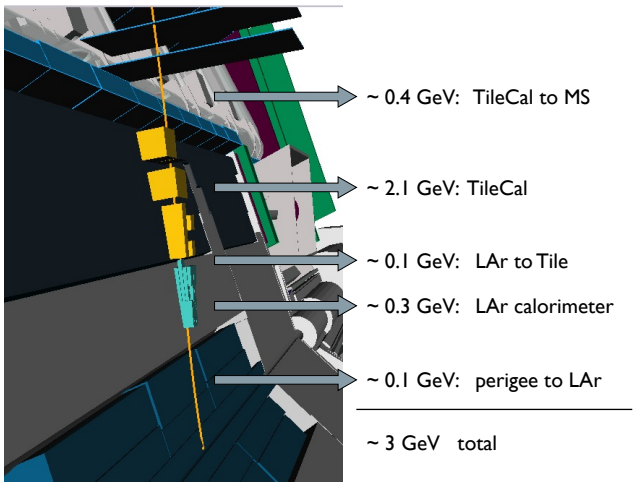

Figure 5.6 – Average energy loss of muons in the various layers of the calorimeters and in the ID and MS [72].

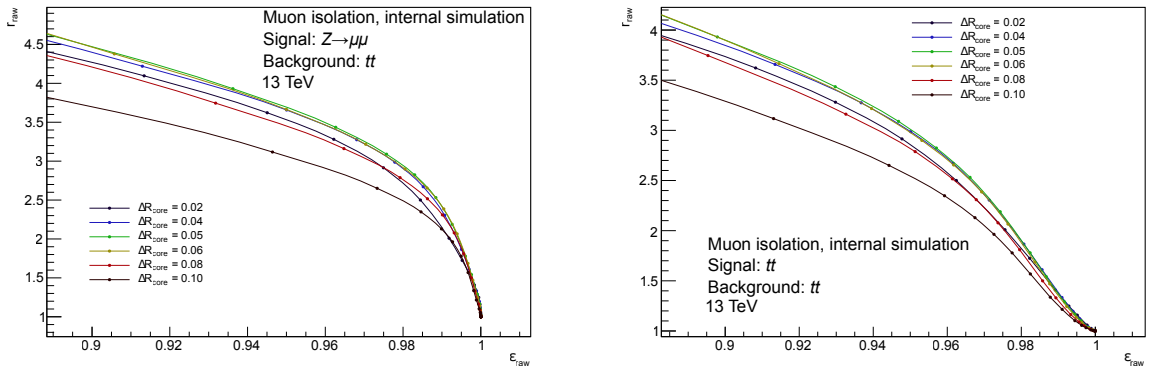

(a) $Z \to \mu\mu$ as signal

(b) $t\bar{t}$ as signal

Figure 5.7 – Background ($t\bar{t}$) rejection as a function of the signal efficiency for the topoetcone20 variable with $\Delta R_{\text{core}} \in \{0, 0.02, 0.04, 0.05, 0.06, 0.08, 0.1\}$. The signal comes from the two decays: (a) $Z \to \mu\mu$ and (b) $t\bar{t}$. For the range of efficiencies interesting to analysis groups ($\varepsilon > 90\%$), $\Delta R_{\text{core}} = 0.05$ offers the best performance [71].

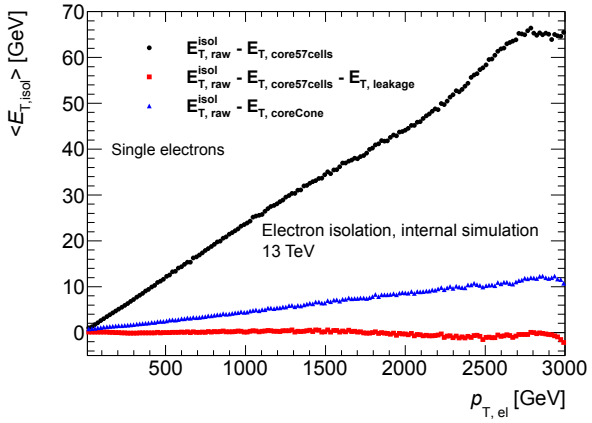

Figure 5.8 – Evolution against p_{T}^{e} of $E_{\text{T}}^{\text{topocone20}}$ for electrons with and without leakage correction [69]. The electrons are taken from single electron MC. The uncorrected and corrected variables are plotted in black and red. As a comparison, the muon-like core energy subtraction (coreCone, or $E_{\text{T}}^{\text{topocore}}$) is represented in blue.

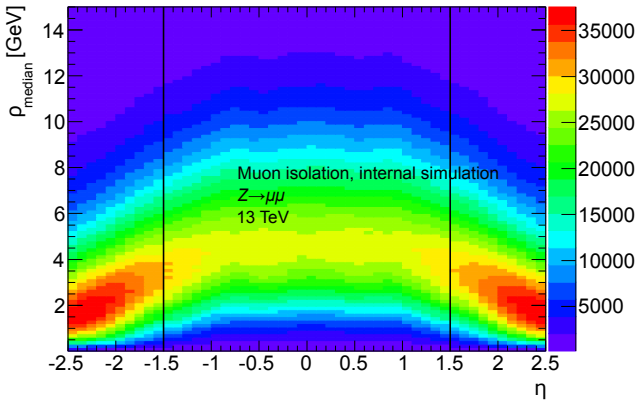

Figure 5.9 – Distribution of the pile-up density as a function of η^{μ}. Due to the dependence, ρ_{med} is calculated in two bins of $|\eta^{\mu}|$, highlighted by the black lines [79].

Leakage correction for electrons

Since the core energy of electrons is calculated in a rectangle of well-defined dimensions, it is important to correct this energy to take into account the energy deposits which may fall outside this rectangle. These deposits are called core energy leakage [69].

This leakage is assessed using MC samples (single electrons without pile-up[3]), with the p_{T} distribution in the range 4 GeV – 3 TeV. The corrections to apply are calculated for ten bins in η and the isolation energy is parametrised with a Crystal-Ball function, whose parameters are fit following a maximum-likelihood method. These parameters depend on the transverse momentum of the particle. The most probable value μ_{CB} and the width σ_{CB} of the Crystal-Ball depend on p_{T}^2. The threshold parameter α_{CB} follows the law $a - b/p_{\text{T}}$ and the power of the function is fixed to $n = 10$. The average leakage for a given p_{T} is assessed using the most probable value:

$$E_{\text{T, leakage}}\left(p_{\text{T}}\right) = \mu_{\text{CB}}\left(p_{\text{T}}\right) \times \frac{E_{\text{cal}}}{\cosh\left(\eta_{\text{ext}}\right)},$$

where E_{cal} is the calibrated energy of the electron.

The leakage correction as a function of the transverse momentum of the electron is presented in Fig. 5.8. It increases linearly with p_{T}^{e} and allows the mean of $E_{\text{T}}^{\text{topocone20}}$ to reach values close to 0. There is an overcorrection at very high momenta.

Pile-up correction

The pile-up contribution has also to be corrected. Two types of pile-up exist in an event: the in-time and out-of-time pile-ups, as introduced in Sec. 2.1. Pile-up has a general effect on the calorimeters, as it overall increases energies measured in sub-detectors. Calorimeter-based variables may therefore be biased.

In order to assess the pile-up contribution, the method of the ambient energy density is used, which is detailed thereafter [79]. First of all, jets (indexed by i) are reconstructed from energy clusters in the calorimeters using an anti-k_{t} algorithm (of radius size 0.5), without any threshold on the transverse momentum. Then, the area $\mathcal{A}_i$ of each jet of the event is calculated thanks to an algorithm of type

[3]Single electron MC sample generated using ParticleGun [67]

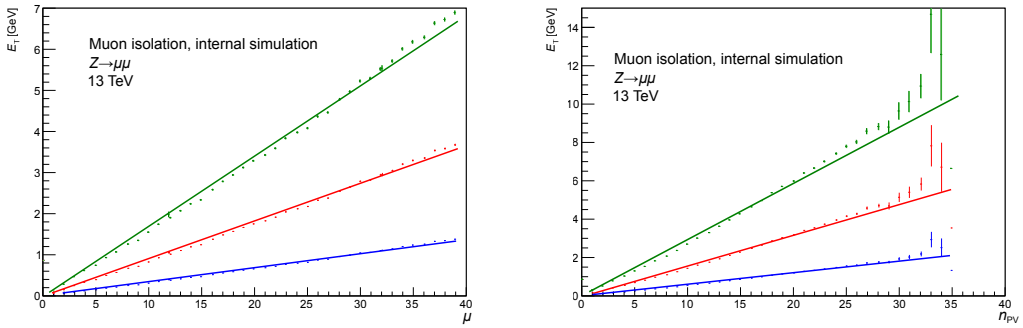

(a) Against μ (b) Against n_{PV}

Figure 5.10 – Evolution of the pile-up correction against (a) μ the average number of interactions per bunch crossing, and (b) n_{PV} the number of primary vertices. The distributions are plotted for various cone sizes $\Delta R_{\mathrm{raw}} \in \{20, 30, 40\}$ in blue, red and green, respectively, using $Z \to \mu\mu$ simulation.

tessellation Voronoi. The energy density is finally estimated for each jet by $\rho_i = p_{\mathrm{T}}^i / \mathcal{A}_i$. The median value of the given distribution is used as estimator of the density of the event ρ_{med}.

As shown in a study [79], ρ_{med} is quite homogeneous in the central regions of the calorimeters (as shown in Fig. 5.9). Hence, the density is only calculated in the two bins $|\eta| < 1.5$ and $1.5 < |\eta| < 3$. Finally, the correction to add to the isolation variables is defined as:

$$E_{\mathrm{T}}^{\text{pile-up corr}X}\left(\eta^{\lambda}\right) = \rho_{\mathrm{med}}\left(\eta^{\lambda}\right) \times \left(\mathcal{A}_{\mathrm{raw}X} - \mathcal{A}_{\mathrm{core}}\right),$$

where $\mathcal{A}_{\mathrm{raw}X}$ and $\mathcal{A}_{\mathrm{core}}$ are the areas of the big isolation cone and of the core cone, respectively equal to $\pi\Delta R^2_{\mathrm{raw}X}$ and $\pi\Delta R^2_{\mathrm{core}}$ ($5{\times}7{\times}0.025\pi/128$) for the muons (electrons), according to the previous definitions.

Since this correction is highly dependent on the pile-up conditions which it corrects for, it is important to have the Monte Carlo correctly reweighted such that the pile-up distributions (assessed using μ, the average number of interaction per bunch crossing) are really close between measured data and simulation. The reweighting procedure is described in Sec. 7.1. The resulting correction is presented in Fig. 5.10 for muons in a $Z \to \mu\mu$ MC sample. As expected, due to the linear dependence upon ρ_{med}, the pile-up correction increases linearly with μ and n_{PV}, the number of primary vertices.

5.2.4 Final formula for the calorimeter-based isolation

Combining the raw variables, the core energy and the corrections, the topoetcone20 variable for muons can be expressed as:

$$E_{\mathrm{T}}^{\text{topocone20}}(\mu) = E_{\mathrm{T}}^{\text{topocone, raw20}}(\mu) - E_{\mathrm{T}}^{\text{topocore}}(\mu) - E_{\mathrm{T}}^{\text{pile-up corr20}}(\eta^{\mu}). \tag{5.1}$$

In the case of muons, on average the isolation corrections in the previous equation are of about 2 GeV for the core energy, and 0.1 GeV for the pile-up correction.

Chapter 6

Muon isolation working points

In order to reduce background contamination, cuts can be applied to isolation variables to only select well-isolated objects. These cuts are gathered into so-called isolation working points: each analysis group shall chose the set of cuts which suppresses background events maintaining high signal efficiencies, within the limited list of available working points. The role of the isolation team is to develop the tool which takes care of applying the isolation cuts corresponding to the chosen working point. Users can then reject or accept events depending on the decision of the tool. In the next chapters of this part of the thesis, only the case of muons is described, otherwise stated.

6.1 Working point definition

While during Run 1 each analysis group was using its own isolation cuts for their analyses, it was decided in Run 2 that the whole procedure would be centralised. A survey was therefore filled by the various analysis groups of the collaboration [80], and according to the results, several working points were defined and are supported by the dedicated teams. Thanks to this approach, only a limited number of isolation working points is selected.

For instance the Higgs-to-four-lepton channel uses a working point which ensures a higher background rejection at low p_{T} (at a cost of a drop in signal efficiency), and high signal efficiencies at high p_{T} (at a cost of lower background rejection). In the context of isolation studies, the signal efficiencies are defined as the number of signal events passing the isolation cuts over the total number of signal events. The choice of the working point is motivated by the high background contamination in the low-p_{T} region (the lower signal efficiencies are accompanied with higher background rejections, which correspond to the total number of background events divided by the subset passing the isolation cuts).

Two kinds of working points are defined. A first category aims at signal efficiencies which depend on the transverse momentum of the object λ. A second category consists of fixed cuts on the isolation variables. As many background contributions from the Standard Model decrease in intensity with p_{T}^{λ}, and since many searches look for phenomena at high momentum requiring high signal efficiencies, the cuts on the isolation variables have to be loosened at high p_{T}^{λ}. This is particularly true for topoetcone20, because the leakage correction for the electrons dominates at high p_{T}^{λ}. In order to avoid any loss of efficiency, the cuts are hence defined on the isolation variables divided by p_{T}^{λ} (referred to as *relative isolation variables*).

For the first category of working points, the cuts on the isolation variables depend on the kinematics of the object to reach the targeted signal efficiency ε. The cut values are therefore calculated in bins of $\left(p_{\mathrm{T}}^{\lambda}, \eta^{\lambda}, \varepsilon\right)$ and results are stored in three-dimensional histograms, named *cut maps*. For the second

Table 6.1 – Muon and electron isolation working points are presented in two categories: for the first five working points, an efficiency is targeted as a function of p_{T}^{μ} [80, 69]. For the remaining working points, fixed cuts on isolation variables are used.

(a) Muon working points

Working point	Calorimeter isolation	Track isolation
LooseTrackOnly	-	$\varepsilon = 99\%$
Loose	$\varepsilon = 99\%$	$\varepsilon = 99\%$
Tight	$\varepsilon = 96\%$	$\varepsilon = 99\%$
Gradient	$\varepsilon(25\,\mathrm{GeV}) = 90\%$, $\varepsilon(60\,\mathrm{GeV}) = 99\%$	$\varepsilon(25\,\mathrm{GeV}) = 90\%$, $\varepsilon(60\,\mathrm{GeV}) = 99\%$
GradientLoose	$\varepsilon(25\,\mathrm{GeV}) = 95\%$, $\varepsilon(60\,\mathrm{GeV}) = 99\%$	$\varepsilon(25\,\mathrm{GeV}) = 95\%$, $\varepsilon(60\,\mathrm{GeV}) = 99\%$
FixedCutTightTrackOnly	-	$p_{\mathrm{T}}^{\mathrm{varcone30}}/p_{\mathrm{T}} < 0.06$
FixedCutLoose	$E_{\mathrm{T}}^{\mathrm{topocone20}}/p_{\mathrm{T}} < 0.3$	$p_{\mathrm{T}}^{\mathrm{varcone30}}/p_{\mathrm{T}} < 0.15$

(b) Electron working points

Working point	Calorimeter isolation	Track isolation
LooseTrackOnly	-	$\varepsilon = 99\%$
Loose	$\varepsilon = 99\%$	$\varepsilon = 99\%$
Tight	$\varepsilon = 96\%$	$\varepsilon = 99\%$
Gradient	$\varepsilon(25\,\mathrm{GeV}) = 90\%$, $\varepsilon(60\,\mathrm{GeV}) = 99\%$	$\varepsilon(25\,\mathrm{GeV}) = 90\%$, $\varepsilon(60\,\mathrm{GeV}) = 99\%$
GradientLoose	$\varepsilon(25\,\mathrm{GeV}) = 95\%$, $\varepsilon(60\,\mathrm{GeV}) = 99\%$	$\varepsilon(25\,\mathrm{GeV}) = 95\%$, $\varepsilon(60\,\mathrm{GeV}) = 99\%$
FixedCutTightTrackOnly	-	$p_{\mathrm{T}}^{\mathrm{varcone20}}/p_{\mathrm{T}} < 0.06$
FixedCutTight	$E_{\mathrm{T}}^{\mathrm{topocone20}}/p_{\mathrm{T}} < 0.06$	$p_{\mathrm{T}}^{\mathrm{varcone20}}/p_{\mathrm{T}} < 0.06$
FixedCutLoose	$E_{\mathrm{T}}^{\mathrm{topocone20}}/p_{\mathrm{T}} < 0.2$	$p_{\mathrm{T}}^{\mathrm{varcone20}}/p_{\mathrm{T}} < 0.15$

category, the cut value is already known, as it is part of the working-point definition. A tool was developed which takes care of retrieving the cuts values on the topoetcone and ptvarcone variables, looking at the bin in the cut map corresponding to the object's kinematics or taking the defined cut value directly, depending on the working point. Then, the object is tested: if its isolation variables are below (above) the isolation cuts, the object passes (fails) the isolation working point.

6.1.1 Muon working points

The various supported muon working points are listed in Tab. 6.1 (a) [80, 69]. The five first working points (*LooseTrackOnly*, *Loose*, *Tight*, *GradientLoose* and *Gradient*) aim at a specific efficiency as a function of p_{T}^{μ}. The last two working points (*FixedCutTightTrackOnly* and *FixedCutLoose*), on the other hand, apply fixed cuts to the relative isolation variables and do not target any efficiencies. The *LooseTrackOnly* and *FixedCutTightTrackOnly* working points only use the track isolation whereas the others use both variables. While for the *Loose*, *LooseTrackOnly* and *Tight* working points the targeted efficiencies are fixed over p_{T}^{μ}, for the *GradientLoose* and *Gradient* working points, efficiencies are fixed for $p_{\mathrm{T}}^{\mu} < 25\,\mathrm{GeV}$ and $p_{\mathrm{T}}^{\mu} > 60\,\mathrm{GeV}$, but vary linearly in between. For the working points using the two isolation variables, the cuts are applied separately. The final efficiency may therefore be lower than the expected value for each of the cuts.

6.1.2 Electron working points

Similarly to muons, electron working points are defined and summarised in Tab. 6.1 (b) [80, 69]. The working points are built the same way as for muons, with the addition of *FixedCutTight*, similar to *FixedCutTightTrackOnly* but including the calorimetric isolation. Also the cut value for the calorimeter-based isolation of the *FixedCutLoose* working point changes ($E_{\mathrm{T}}^{\mathrm{topocone20}}/p_{\mathrm{T}}^{e} < 0.2$ instead of 0.3 for muons). Finally, the electron working points use the ptvarcone20 variable, as the trigger studies do not require the use of ptvarcone30, which offers less background rejection as compared to ptvarcone20.

6.2 Cut values associated to isolation working points

In this section, the example of muons is outlined, but the procedure is similar for electrons. The various steps are only needed for the first category of working points for which the cut maps are calculated. The cut values are stored for each $\left(p_{\mathrm{T}}^{\mu}, \eta^{\mu}, \varepsilon\right)$ bins. This allows all the muon kinematics to be covered, for any targeted efficiency. A cut map is created per isolation variable and is passed to the tool (`IsolationSelectionTool` [81]) responsible for testing whether the object passes the requirements of the working point. The tool calculates the targeted efficiency depending on p_{T}^{μ} and the working point considered. Then, the cut value is retrieved by looking at the corresponding bin in the cut map, knowing the kinematics of the object. The cut maps are not segmented in ϕ since the cut values are independent upon this coordinate, thanks to the symmetry of the detector.

6.2.1 Creation of the cut maps for muons

In order to create the cut maps, the distributions of the isolation variables are plotted in histograms $\mathfrak{D}$ using $Z \to \mu\mu$ MC samples, in which no selections were applied. The distributions are generated for various cuts on $\left(p_{\mathrm{T}}^{\mu}, \eta^{\mu}\right)$, which correspond to the bins of the cut maps.

For each histogram $\mathfrak{D}$ obtained, the total integral $N_0^{\mathfrak{D}} = \sum_{i=0}^{B_{\mathfrak{D}}} b_i^{\mathfrak{D}}$ is calculated, where $B_{\mathfrak{D}}$ is the total number of bins of $\mathfrak{D}$ and $b_i^{\mathfrak{D}}$ is the number of muons in each bin of this histogram. $N_0^{\mathfrak{D}}$ is thus the number of muons in the $\left(p_{\mathrm{T}}^{\mu}, \eta^{\mu}\right)$ bin corresponding to $\mathfrak{D}$.

Then, the integrals $N_j^{\mathfrak{D}} = \sum_{i=j}^{B_{\mathfrak{D}}} b_i^{\mathfrak{D}}$ are successively calculated until $N_j^{\mathfrak{D}}/N_0^{\mathfrak{D}} < \varepsilon$, where ε is the targeted efficiency. The cut value associated to the bin $\left(p_{\mathrm{T}}^{\mu}, \eta^{\mu}, \varepsilon\right)$ is therefore the lower edge of the bin $j-1$ of the histogram $\mathfrak{D}$. This method guarantees to obtain at least the desired efficiency. The limits and binning of the distributions have to be carefully defined and were chosen depending on the MC statistics available. Note that the same histogram is used for all the efficiencies, and the cut values are calculated for efficiencies in increasing order to speed up the process.

6.2.2 Cut map binning for muons

After a study on the statistics available in the $Z \to \mu\mu$ MC samples used to create the maps, the following binning was chosen [46, 40]:

- p_{T}^{μ}(GeV) : 4, 7, 10, 15, 20, 25, 27, 28.5, 30, 31.5, 33, 35, 37, 38, 39, 40, 41, 42, 43, 44, 45, 46, 47.5, 50, 55, 60.
- η^{μ} : −3.0, −2.7, −2.47, −1.52, −1.37, −1.15, −0.8, 0, 0.8, 1.15, 1.37, 1.52, 2.47, 2.7, 3.0.

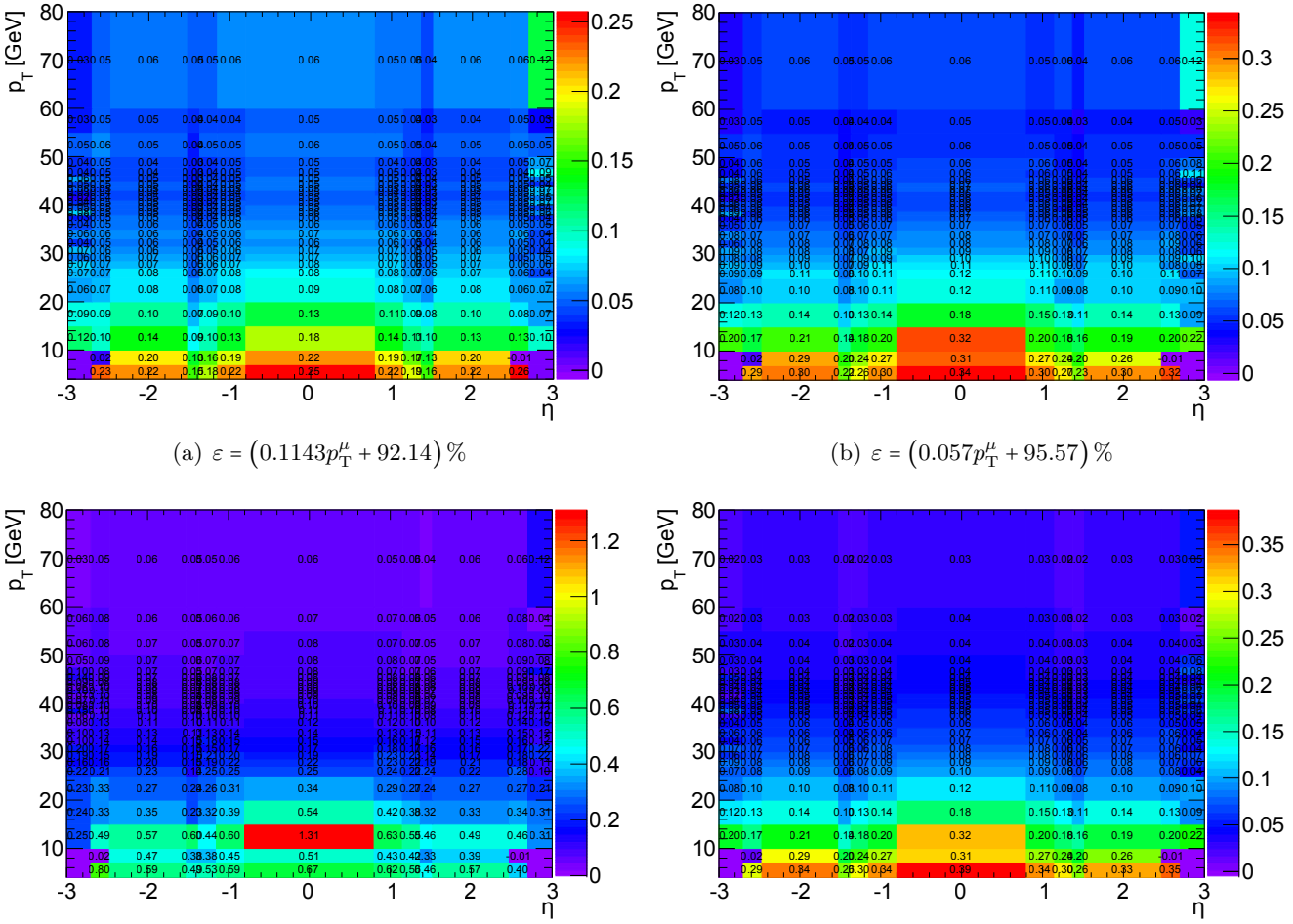

(a) $\varepsilon = \left(0.1143 p_{\mathrm{T}}^{\mu} + 92.14\right)\%$

(b) $\varepsilon = \left(0.057 p_{\mathrm{T}}^{\mu} + 95.57\right)\%$

(c) $\varepsilon = 99\%$

(d) $\varepsilon = 96\%$

Figure 6.1 – Cut values on topoetcone20 as a function of p_{T}^{μ} and η^{μ} [46], for the (a) *Gradient*, (b) *GradientLoose*, (c) *Loose* and (d) *Tight* working points, respectively.

The p_{T}^{μ} binning takes into account the topology of the $Z \to \mu\mu$ channel. The η^{μ} binning follows the geometry of the detector, because isolation variables are highly dependent on the segmentation of the calorimeters and the ID acceptances.

6.2.3 Cuts applied to the muon isolation variables

Having defined and used these tools, it is possible to retrieve the cut values for the two isolation variables, for a given efficiency. Figures 6.1 and 6.2 present the cut values for the efficiencies required by the isolation working points. The formulae $\varepsilon = 0.1143 p_{\mathrm{T}}^{\mu} + 92.14\%$ and $\varepsilon = 0.057 p_{\mathrm{T}}^{\mu} + 95.57\%$ correspond to the *Gradient* and *GradientLoose* working points, respectively. For *FixedCutLoose* and *FixedCutTightTrackOnly*, the cut values are not shown as they are fixed.

For both variables, cut values are higher at low p_{T}^{μ} and decrease progressively. This is due to the fact that relative variables are used to define the working points: at low p_{T}^{μ} the relative distribution has higher average value as compared to higher p_{T}^{μ}.

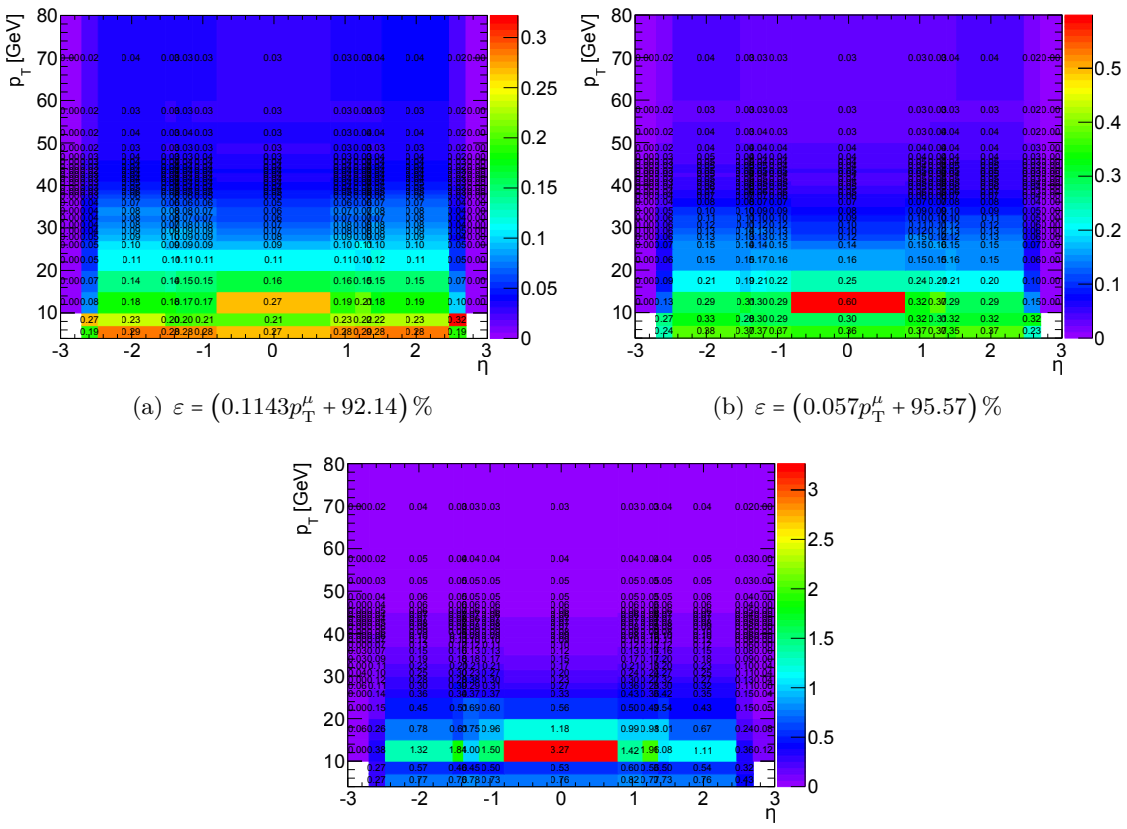

(a) $\varepsilon = \left(0.1143 p_{\mathrm{T}}^{\mu} + 92.14\right)\%$

(b) $\varepsilon = \left(0.057 p_{\mathrm{T}}^{\mu} + 95.57\right)\%$

(c) $\varepsilon = 99\%$

Figure 6.2 – Cut values on ptvarcone30 as a function of p_{T}^{μ} and η^{μ} [46], for the (a) *Gradient*, (b) *GradientLoose*, (c) *Loose*, *LooseTrackOnly* and *Tight* working points, respectively.

Table 6.2 – Signal efficiencies in the $Z \to \mu\mu$ channel are presented for the various working points in a preliminary study [71], for each muon type.

Signal efficiencies [%]	*Combined*	*Extrapolated*	*Segment-Tagged*	*Calo-Tagged*	All muons
Tight	86.8	87.0	86.2	87.4	86.8
Loose	96.8	90.2	96.6	97.7	96.5
LooseTrackOnly	97.7	98.7	97.5	98.4	97.8
Gradient	92.0	89.1	91.8	93.1	91.9
GradientLoose	94.0	89.6	93.8	95.0	93.9

6.2.4 Validation of the muon cut maps

A first quick study was carried out in order to assess the expected efficiency and rejection of the working points, while the working points were already defined [71]. This study aimed at validating the cut maps and provides a first estimation of the rejection, which is analysis-dependent.

MC samples were used to model signal ($Z \to \mu\mu$ and $t\bar{t}$ processes) and background ($t\bar{t}$ process only). Muons originating from W decays were treated as signal whereas non-isolated muons originating from b

Table 6.3 – Preliminary assessment of the signal efficiencies and background rejections of the isolation working points from $t\bar{t}$ decays [71].

(a) Signal efficiencies

Signal efficiencies [%]	*Combined*	*Extrapolated*	*Segment-Tagged*	*Calo-Tagged*	All muons
Tight	81.9	85.6	80.8	83.1	82.0
Loose	92.1	88.7	91.2	93.6	92.0
LooseTrackOnly	93.4	98.0	92.7	94.6	93.4
Gradient	87.3	87.6	86.4	89.3	87.3
GradientLoose	89.2	88.2	88.4	91.1	89.2

(b) Background rejections

Background rejections	*Combined*	*Extrapolated*	*Segment-Tagged*	*Calo-Tagged*	All muons
Tight	44.9	2.9	43.4	94.1	40.8
Loose	23.1	2.5	27.3	35.5	21.9
LooseTrackOnly	16.0	1.2	17.2	22.7	14.7
Gradient	42.8	2.7	45.0	78.4	38.8
GradientLoose	34.2	2.7	38.6	63.8	31.6

and c hadrons as well as light mesons were treated as background. In addition, *Extrapolated* muons had to satisfy $p_{\mathrm{T}}^{\mu} > 6\,\mathrm{GeV}$ and $|\eta^{\mu}| > 2.5$. *Calo-Tagged* muons should satisfy $|\eta^{\mu}| < 0.1$ with $p_{\mathrm{T}}^{\mu} > 15\,\mathrm{GeV}$.

Tables 6.2, and 6.3 present signal efficiencies (and background rejections) for the various muon isolation working points and the various reconstruction types of the muons (see Sec. 3.4.6). Signal efficiencies of the $t\bar{t}$ process are lower because of the increased surrounding activity in the events as compared to the $Z \to \mu\mu$ process. This activity arises from the boosted jets resulting from the top pair annihilation. *Extrapolated* and *Combined* muons have lower signal efficiencies due to the additional cuts applied in the analysis.

Chapter 7

Muon isolation performance

Muon isolation performance studies include data-to-MC comparisons of the isolation variable distributions (topoetcone20 and ptvarcone30), as well as the calculation of the working point efficiencies and scale factors.

7.1 The Tag-And-Probe method

Isolation efficiencies are defined as the ratio of the number of signal muons passing the cuts of a working point over the total number of signal muons. In order to select prompt, well-reconstructed signal muons, measurements are performed on $Z \to \mu\mu$ events with the so-called Tag-And-Probe method [40].

The choice of the Z resonance is motivated by good detector resolution. Signal muons can be selected from events containing oppositely-charged muon pairs, whose invariant mass is close enough to the Z boson pole mass.

The Tag-and-Probe method relies on the stringent selection of one of the two muons of the pair (named the *tag*) to ensure it was correctly reconstructed and belongs to the Z decay. Since the tag serves for the selection of the pair, it cannot be used for the measurements, for which the second muon (referred to as the *probe*) is used. In order not to bias the definition of the pairs and the efficiency calculation, correlations between the tag and the probe should be reduced as much as possible. For this reason, the Tag-And-Probe method is only valid if the tag and the probe are reconstructed using two different sub-detectors: if the track of the tag was reconstructed in the ID, the track of the probe should be reconstructed in the MS and vice-versa.

Having found a subset of reconstructed muons (the tag and probe muons) which can be studied, the efficiencies can be measured as: $\varepsilon = \frac{N_{\text{pass}}^{\text{signal}}}{N_{\text{tot}}^{\text{signal}}} = \frac{N_{\text{pass}}^{\text{probe, signal}}}{N_{\text{tot}}^{\text{probe, signal}}}$, where $N_{\text{pass}}^{\text{signal}}$ and $N_{\text{tot}}^{\text{signal}}$ ($N_{\text{pass}}^{\text{probe, signal}}$ and $N_{\text{tot}}^{\text{probe, signal}}$) are the number of reconstructed muons (probes) passing the isolation working point criteria and the total number of reconstructed muons (probes), respectively.

Selected muons of the pairs have to fulfil the criteria detailed in Tab. 7.1.

The signal is composed of pairs of oppositely charged muon and efficiencies are corrected to remove the background contributions, as described in the next section. MC samples are normalised to data. The distribution of the average number of interactions per bunch crossing μ and the number of primary vertices n_{PV} in data and MC are presented in Fig. 7.1. The μ variable is shifted by 1.0/1.09 in data. As shown, the disagreement between data and MC is important (ratios up to 10 for $\mu \approx 30$), which affects

Table 7.1 – Selection criteria on tag and probe muons for isolation efficiency measurements [40].

Criterion	Tag selection	Probe selection
Kinematic cuts	$p_{\mathrm{T}} > 24\,\mathrm{GeV}$ and $\lvert\eta\rvert < 2.5$	$p_{\mathrm{T}} > 4\,\mathrm{GeV}$
Type	*Combined*	
Quality	*Medium* and pass the *passIDCuts* requirements [82]	
Trigger matching	Triggered event recording	
Impact parameter significance	$\lvert d_0\rvert/\sigma_{d_0} < 3$, $\lvert z_0 \sin\theta\rvert < 0.5\,\mathrm{mm}$ and $\lvert z_0\rvert < 10\,\mathrm{mm}$	
Invariant mass	Close to the Z pole mass: $81\,\mathrm{GeV} < m_{\mu\mu} < 101\,\mathrm{GeV}$	
Pair opening angle	$\Delta R_{\mu\mu} > 0.3$	
Isolation selection	*Loose*	
Muon opening angle with closest jet		$\Delta R_{\mu j} > 0.4$

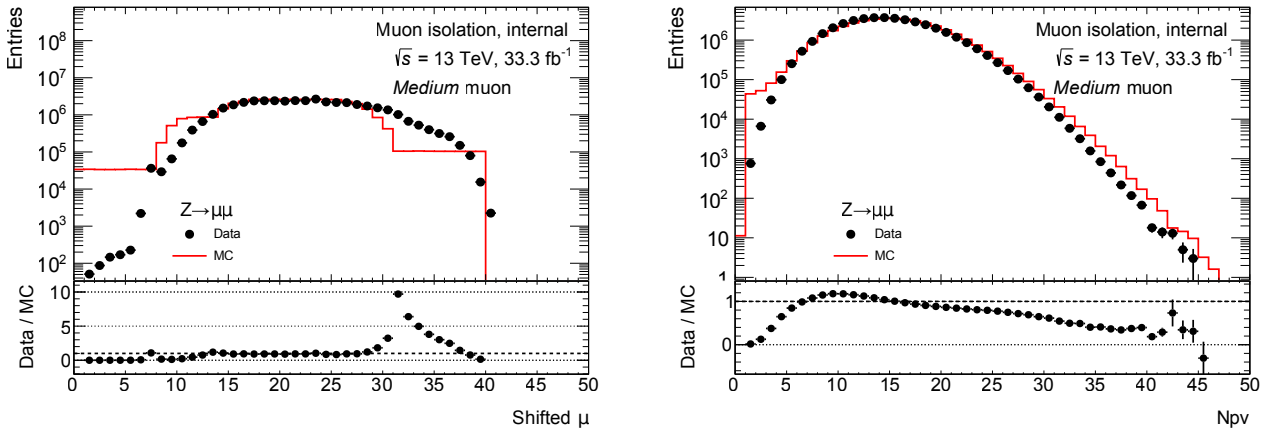

(a) Shifted μ

(b) n_{PV}

Figure 7.1 – Data-simulation comparison of shifted μ and n_{PV} before MC reweighting.

the isolation variable distributions. For the μ profiles to be the same, MC is reweighted to match the distribution in data. The results of the reweighting process are presented in Fig. 7.2. The agreement is good for the shifted μ (the reweighting is done with a shifted distribution to improve the agreement in n_{PV}). The agreement is fine for n_{PV} but not as good as for μ, as the reweighting is not directly done on this variable. One of the issues of the pile-up reweighting is the loss of MC statistics. Indeed, before reweighting the average μ in MC is close to 20, whereas after reweighting, it increases to more than 25. This shift is at a cost of increased weights of MC events for which the statistical uncertainties are bigger.

The cuts on the transverse momenta ensure the non-contamination of the signal with QCD background which dominates at very low p_{T}^{μ}. The cut on the tag pseudo-rapidity ensures the muons are within the ID acceptance. The quality of the reconstruction of the tag is further enforced by the criteria on the type and quality of the muon, as well as the quality of track left in the ID (`passIDCuts`) [82].

The fact that the tag muon has to trigger the event ensures the pair comes from a boson decay, as triggers were optimised in the recognition of such events. This is furthermore complemented with the requirement on the invariant mass, which must be close to the Z pole mass. The triggers used for the isolation

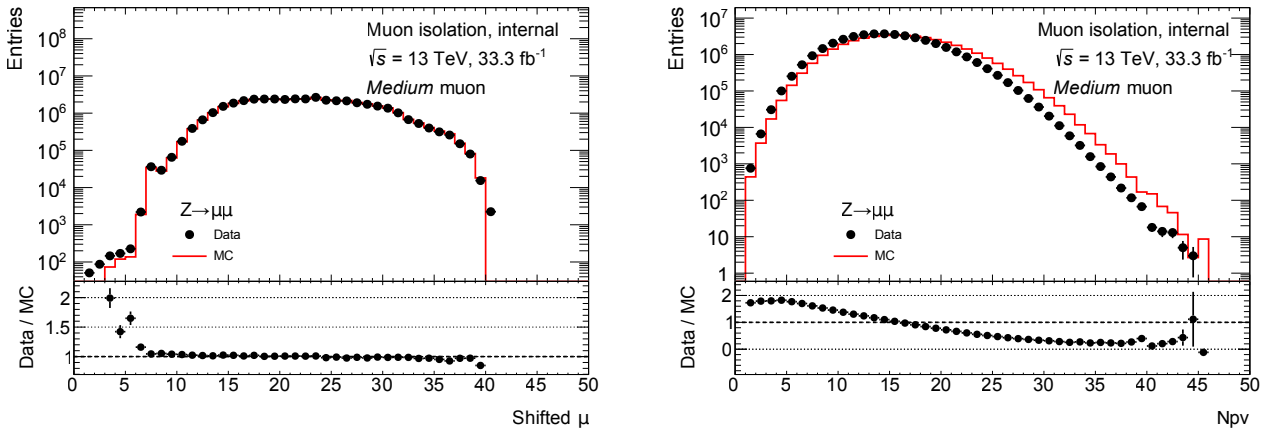

(a) Shifted μ

(b) n_{PV}

Figure 7.2 – Data-MC comparison of shifted μ and n_{PV} after MC reweighting [69].

studies are `HLT_mu20_iloose_L1MU15` (data 2015), `HLT_mu24_ivarmedium` and `HLT_mu26_ivarmedium` (data 2016). More information concerning the naming conventions of the triggers in ATLAS are given in Sec. 11.3.5.

Cuts on the impact parameter and z_0 suppress contaminations due to pile-up and make sure the muons come from the primary vertex (and not from b or c decays).

The isolation cut on the tag allows to have a muon free of any surrounding activity, which facilitates the discriminating power of the isolation on the probe. The opening angle between the two muons of the pair ($\Delta R_{\mu\mu}$) must be above a threshold to avoid any interferences in the isolation between the two objects. This ensures no close-by corrections have to be applied on the probe isolation variables for the measurements. This correction is the subject of Chap. 8.

The jets used for the study are reconstructed using the anti-k_{t} algorithm with a radius of $R = 0.4$, where the topological clusters are at the electromagnetic scale [83, 84]. The jets are required to be far enough from the probe because the efficiencies are highly affected by the presence of a close-by jet. Events for which the probe is close to a jet are treated separately, as described thereafter.

7.2 Isolation variable distributions

Before calculating isolation efficiencies, it is important to first check the good modelling of the isolation variables by MC. The study of the variable distributions focuses on ptvarcone30 and topoetcone20, as these are the variables used for muons. In order to make the following plots, the Tag-And-Probe selection is performed the same way as described in Sec. 7.1 and the probe variables are considered. In this study, background contributions from electroweak processes ($W^- \to \mu\nu$, $W^+ \to \mu\nu$, $Z \to \tau\tau$, $WW \to \ell\nu\ell\nu$, $WZ \to \ell\nu\ell\ell$, $ZZ \to \nu\nu\ell\ell$, $ZZ \to 4\ell$, $WZ \to qq\ell\ell$ and $ZZ \to qq\ell\ell$, where $\ell \in \{e, \mu\}$) and $t\bar{t}$ decays are assumed to be negligible and are not accounted for. Contributions from QCD events are considered using a transfer factor as explained below.

The number of selected pairs of same-sign muons $N^{\text{SC probe, signal}}$ is first estimated. It is then assumed that the background contamination in the signal region can be estimated using $N^{\text{SC probe, signal}}$, scaled by a transfer factor T. The corrected signal yields (and efficiencies) can then be determined using

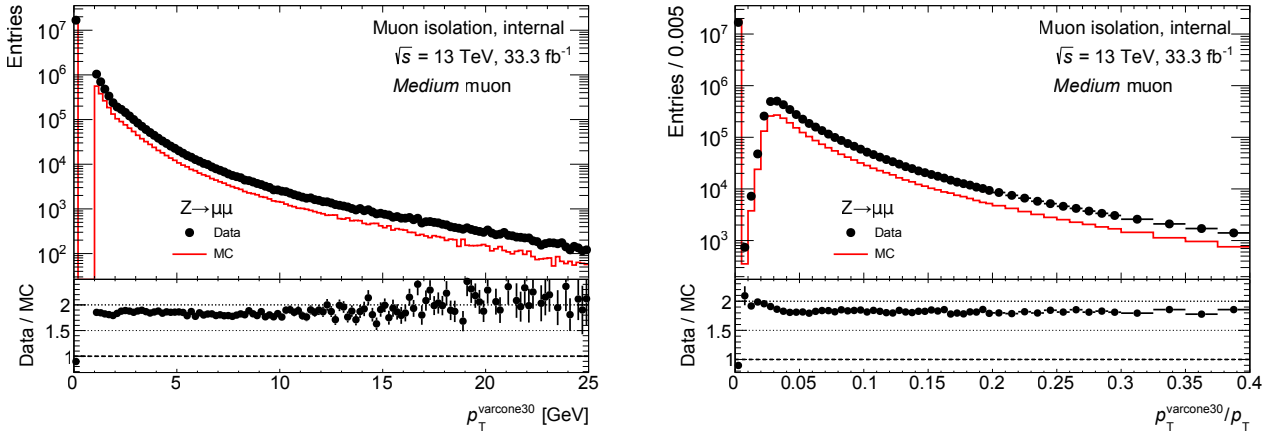

(a) $p_{\mathrm{T}}^{\mathrm{varcone30}}(\mu)$ (b) $p_{\mathrm{T}}^{\mathrm{varcone30}}(\mu)/p_{\mathrm{T}}^{\mu}$

Figure 7.3 – Data / simulation comparison of ptvarcone30 (a) before and (b) after division by p_{T}^{μ} [46, 40, 69].

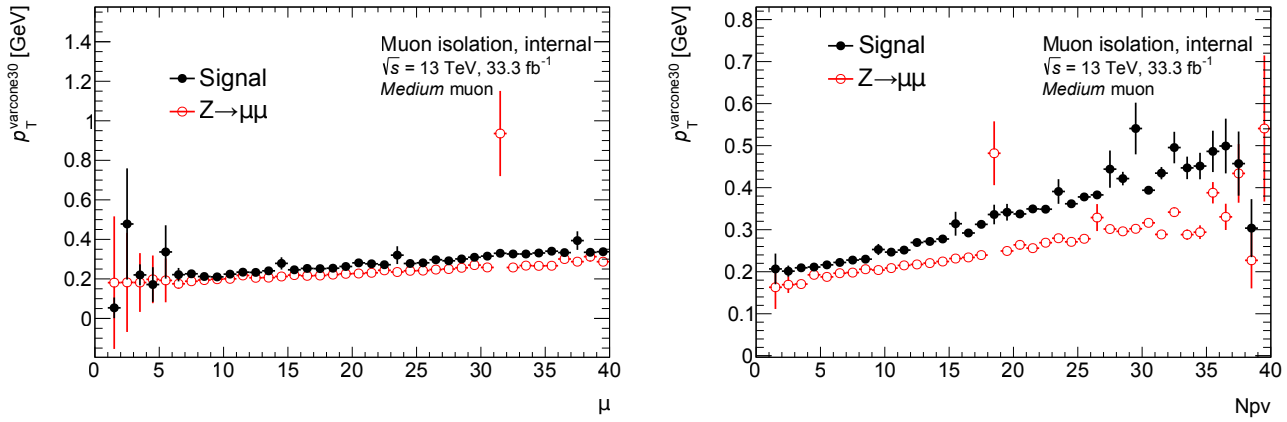

(a) Evolution against μ (b) Evolution against n_{PV}

Figure 7.4 – Evolution of ptvarcone30 with pile-up: as a function of (a) μ and (b) n_{PV} [69].

$N_{\mathrm{total}}^{\text{OC probe}} - TN_{\mathrm{total}}$ and $\varepsilon = \frac{N_{\mathrm{pass}}^{\text{OC probe}} - TN_{\mathrm{pass}}^{\text{SC probe}}}{N_{\mathrm{total}}^{\text{OC probe}} - TN_{\mathrm{total}}^{\text{SC probe}}}$, respectively. After studies in side-band regions of the dimuon invariant mass spectrum, the value of $T = 1$ was chosen.

In each of the following plots, simulation is in red and data in black. Errors are statistical only. The various ratios are presented in the bottom of each plot to assess the degree of agreement between data and MC. The MC is reweighted so that the pile-up conditions are same as compared to the data.

7.2.1 Track-based isolation

Figure 7.3 shows the relative ptvarcone30 variable. There is a strong discrepancy between data and MC. Normalisation of the MC to the data yields forces the tail of the data to be more populated as for the MC, which has more events in the bin 0. The discrepancy was first observed in data 2015 but has worsened in

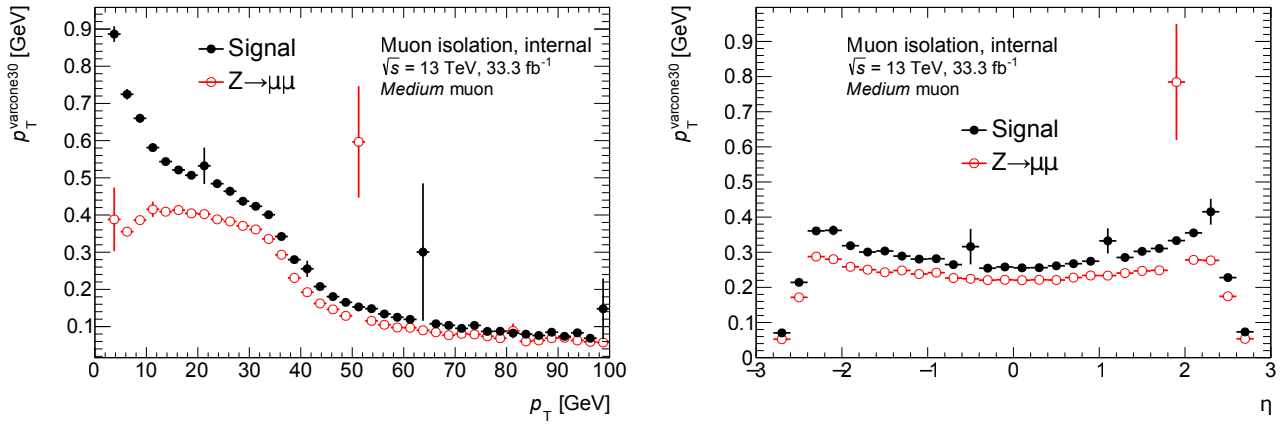

(a) Evolution against p_{T}

(b) Evolution against η

Figure 7.5 – Evolution of ptvarcone30 with the probe kinematics: as a function of (a) p_{T} and (b) η.

data 2016. In Fig. 7.4, the ptvarcone30 variable is plotted against the average number of interactions per bunch crossing μ and the number of primary vertices n_{PV}. Although the discrepancy can be reproduced (data points have higher mean values than MC for all the bins), the shift between the two distributions seems stable over the bins for the two variables.

In order to further investigate the discrepancy, comparison plots are shown in Fig. 7.5, in which the ptvarcone30 variable is plotted against p_{T} and $|\eta|$, to study the dependence of the variable upon the kinematics of the muon. No strong correlations are found against η. The disagreement seems worse at low-p_{T} indicating a possible background contamination of the data, but the discrepancy remains at higher values. Although the two curves tend to get closer at high p_{T}, the relative discrepancy remains similar.

Study of the discrepancy between data and simulation

Since the discrepancy does not seem to depend too strongly on the probe kinematics and the pile-up reweighting, and since it has worsened with data 2016 as compared to data 2015, it was proposed to change the cuts applied to the selection of the tracks for the calculation. A second study was carried out to see how a miss-modelling of the vertex density, defined thereafter, could affect the distributions of the $p_{\mathrm{T}}^{\mathrm{varcone}}$ variables.

Effects of the track selection. In this study, the 2015 and 2016 datasets are compared to the same $Z \to \mu\mu$ MC sample, pile-up reweighted to match the μ profile of 2015 and 2016 combined. A similar selection as for the isolation distributions presented previously is applied, also based on the Tag-And-Probe method. Since pile-up reweighting is applied on the two datasets combined, results presented here differ slightly from the results shown in Fig. 7.2, but the study remains valid as the discrepancy is not strongly correlated with pile-up reweighting. In the following plots, MC 2015 and MC 2016 labels actually refer to the same dataset (since pile-up reweighting is done the same way for both).

The effects of the track selection are studied by applying the following changes to the standard selection (described in Sec. 5.1.1): tighter p_{T} cut (1 GeV → 1.5 GeV), a tighter cut on the impact parameter $\max|z_0 \sin\theta|$ (3 mm → 1 mm) and using a different track working point (Loose → TightPrimary, where

Table 7.2 – Cuts on the ID tracks which define the Loose and TightPrimary working points [68].

Loose working point	TightPrimary working point (additional cuts w.r.t. Loose)
$p_{\mathrm{T}}^{t} > 400\,\mathrm{MeV}$ (default track reconstruction cut)	
$\lvert\eta^{t}\rvert < 2.7$	
$N_{\mathrm{Si}} \geq 7$	$N_{\mathrm{Si}} \geq 9$ if $\lvert\eta^{t}\rvert \leq 1.65$, $N_{\mathrm{Si}} \geq 11$ else
$N_{\mathrm{mod}}^{\mathrm{sh}} \leq 1$	
$N_{\mathrm{Si}}^{\mathrm{hole}} \leq 2$	
$N_{\mathrm{Pix}}^{\mathrm{hole}} \leq 1$	$N_{\mathrm{Pix}}^{\mathrm{hole}} = 0$
	$N_{\mathrm{IBL}} + N_{\text{B-layer}} > 0$ if both IBL hit and B-layer hit are expected
	$N_{\mathrm{IBL}} + N_{\text{B-layer}} \geq 0$ if either IBL hit or B-layer hit is not expected

Loose is the working point used as default). The differences between the two working points are presented in Tab. 7.2.

To first assess how the track selection affects the ptvarcone30 variable, plots of the track isolation are made in the standard case, and with the three variations, as shown in Fig. 7.6. Data 2015 and 2016 are compared to MC. The ratio plots indicate that the discrepancy can be reproduced in the standard case, and worsens as expected with data 2016. A tighter cut on $\max|z_0 \sin\theta|$, or the use of a tighter working point improves the agreement.

Study of the vertex density. Despite changes in the track selection, the discrepancy between data and simulation remains. A second study therefore assesses the dependence of the track-based isolation upon the vertex density. This quantity measures the density of tracks in the event (mm^{-1}) and is defined as [69]

$$\rho_{\mathrm{vtx}} = \mu \times \frac{1}{\sqrt{2\pi\sigma_{z_{\mathrm{beam}}}^{2}}} \times \exp\left(-\frac{1}{2}\left(\frac{z_{\text{p-vtx}} - z_{\mathrm{beam}}}{\sigma_{z_{\mathrm{beam}}}}\right)^{2}\right),$$

where z_{beam} and $\sigma_{z_{\mathrm{beam}}}$ are the z coordinate of the beam and its associated variance, and $z_{\text{p-vtx}}$ is the z position of the primary vertex (to which the tracks used for the calculation of the isolation variable belong). The density directly relates to the number of tracks in the event and is most likely to be correlated with the track isolation.

Figure 7.7 presents ρ_{vtx} before and after reweighting of the variable in data and MC 2015, 2016. The same cuts as in the previous study are applied for the selection of the tag-and-probe pairs. The conclusion of this comparison of ρ_{vtx} is that the variable is not modelled by simulation very well, and high values in data 2016 cannot be reached. The reweighting of the variable is done on top of a cut $\rho_{\mathrm{vtx}} < 0.29$ applied to both data and MC. Note that in the following, the MC samples labelled 2015 and 2016 only differ in the case of ρ_{vtx} reweighting, since it is different for data 2015 and data 2016.

In order to understand the origins of the miss-modelling, the z_{beam}, $\sigma_{z_{\mathrm{beam}}}$ and $z_{\text{p-vtx}}$ distributions are presented in Fig. 7.8. The main discrepancies arise from z_{beam} and $\sigma_{z_{\mathrm{beam}}}$. However, reweighting the MC to achieve a better agreement would be at a cost of statistics physics analyses cannot afford.

In order to study the dependence upon ρ_{vtx}, the distributions of the track-based isolation are plotted against the density in Fig. 7.9, for various track selection criteria introduced in the previous study.

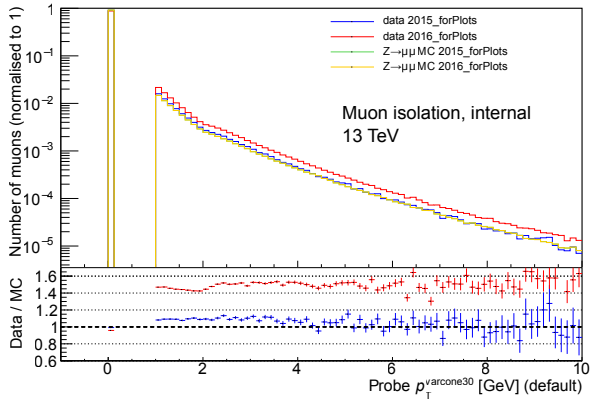

(a) Standard track selection

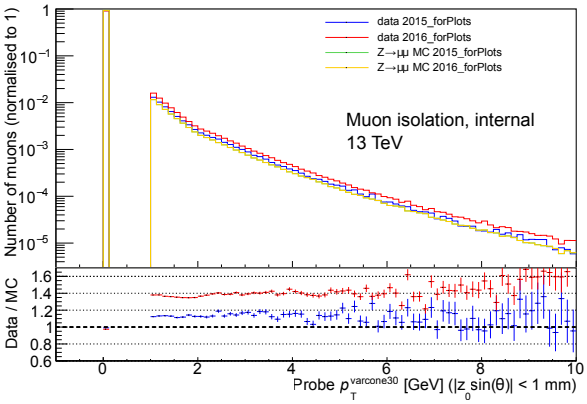

(b) Tighter $\max|z_0 \sin\theta|$ cut

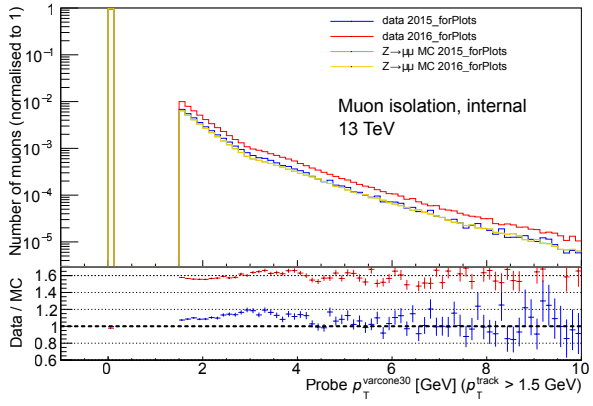

(c) Tighter p_{T} cut

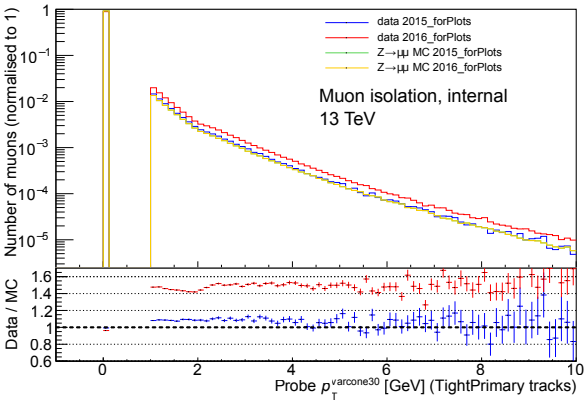

(d) TightPrimary working point

Figure 7.6 – Distributions of $p_{\mathrm{T}}^{\mathrm{varcone30}}$ with various track selection criteria. MC 2015 and MC 2016 are the same as no ρ_{vtx} are applied and μ reweighting is applied on the combination of the 2015 and 2016 datasets [69].

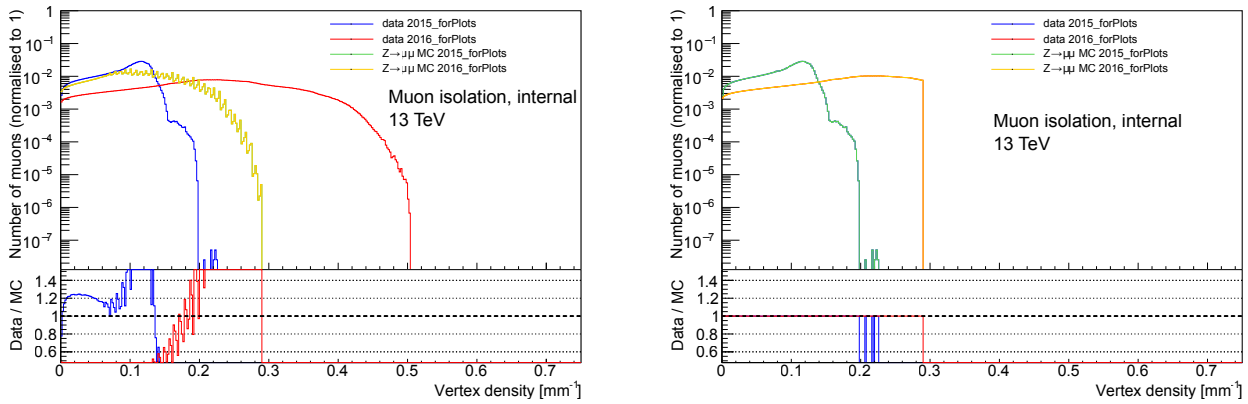

Figure 7.7 – Distributions of the vertex density in data (2015 in blue, 2016 in red) and $Z \to \mu\mu$ MC (2015 in green, 2016 in yellow). In the left figure, MC 2015 and 2016 are the same as the pile-up reweighting is done on the years 2015 and 2016 combined for both samples. In the right figure, a reweighting of ρ_{vtx} is applied on top of the pile-up reweighting so that the MC distribution matches the data, and the cut $\rho_{\text{vtx}} < 0.29$ is also applied on both data and MC, as the simulation cannot reproduce the high values in data 2016. The additional ρ_{vtx} reweighting is separately performed for 2015 and 2016, explaining why the MC distributions 2015 and 2016 differ [69].

Whereas against μ or n_{PV} these distributions showed a stable shift between MC and data 2016, here the curves collapse one onto each other, whichever year is used. It can therefore be concluded that the missing high ρ_{vtx} values in MC are correlated with the discrepancy. A tighter cut on $\max|z_0 \sin\theta|$ or the use of a tighter working point flattens the distributions against ρ_{vtx}, explaining why the discrepancies are reduced in Fig. 7.6.

The same plots were generated, having reweighted ρ_{vtx} (and applying the cut $\rho_{\text{vtx}} < 0.29$) so that data 2015, 2016 and MC look similar. Note that this time, MC 2015 and MC 2016 differ as the reweighting depends on the year considered. The results are shown in Fig. 7.10 and 7.11. Agreement between data and simulation is improved and the changes of track selection do not further affect the comparisons. In the plots against the density, it can be seen that the reweighting does not affect the distributions, but removes the high values in data.

Conclusions on the discrepancy. From these studies it became evident that the miss-modelling of the vertex density in simulation is the main origin of the observed discrepancy between data and simulation. For the year 2016, high ρ_{vtx} values are not reached by the MC and the discrepancy is worse than for data 2015, where the full ρ_{vtx} range is covered by simulation. Ensuring the vertex density distributions are same between data and MC would result in reweighting the variables entering the calculation of ρ_{vtx}. This would considerably decrease the MC statistic available which would penalise measurements of the various analysis groups. This option was therefore not considered. The ptvarcone discrepancy could however be improved by changing the selection of the tracks used to calculate the variable: a tighter $\max|z_0 \sin\theta|$ cut or the use of the TightPrimary working point seem to offer promising results.

However, the discrepancy does not have a strong impact on the efficiency of isolation working points. The data efficiency decreases by only a few percent and isolation scale factors correct for this.

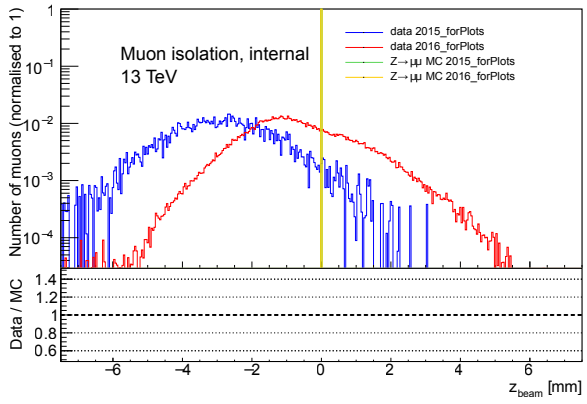

(a) z_{beam}

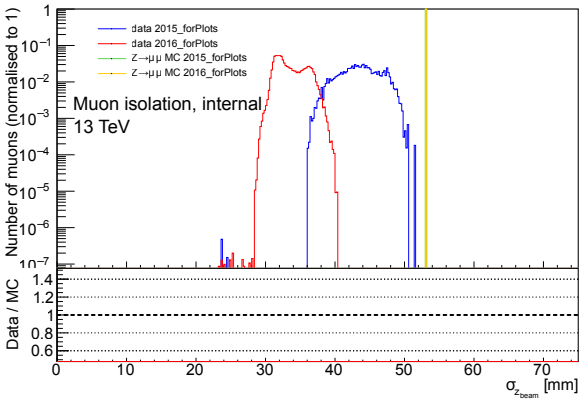

(b) $\sigma_{z_{\text{beam}}}$

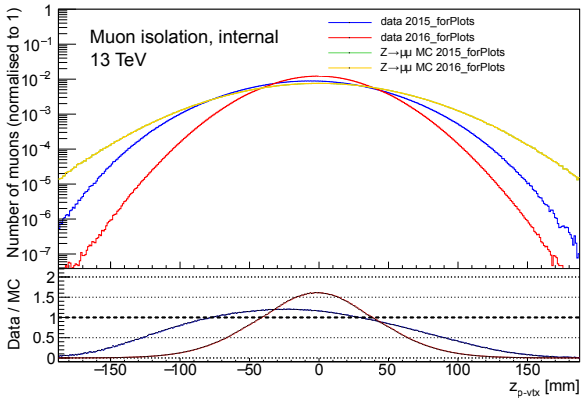

(c) $z_{\text{p-vtx}}$

Figure 7.8 – Distribution of the variables used to calculate ρ_{vtx} in data (2015 in blue, 2016 in red) and $Z \to \mu\mu$ MC (2015 in green, 2016 in yellow) [69]. MC 2015 and 2016 are the same as the pile-up reweighting is done on the years 2015 and 2016 combined for both samples.

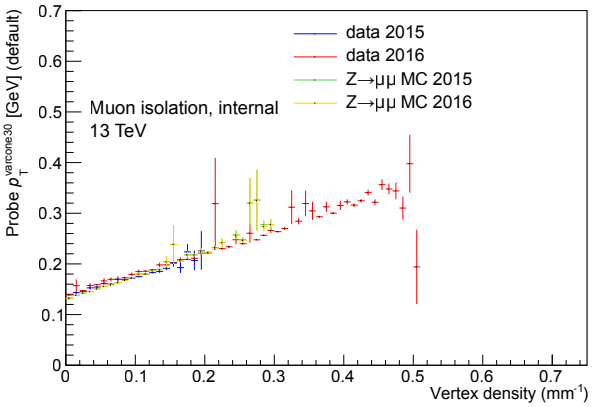

(a) Standard track selection

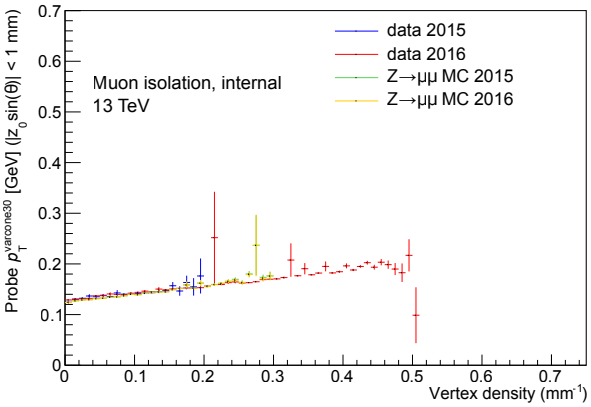

(b) Tighter $\max|z_0 \sin\theta|$ cut

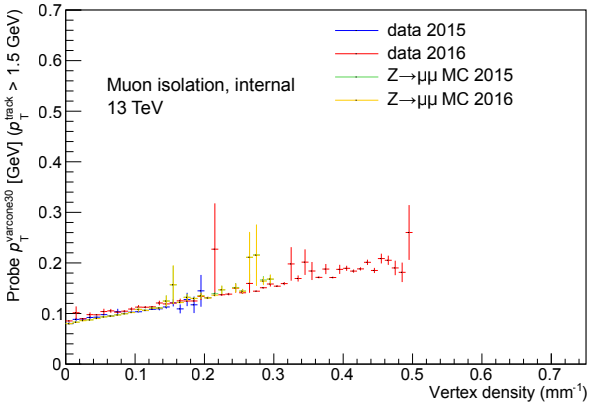

(c) Tighter p_{T} cut

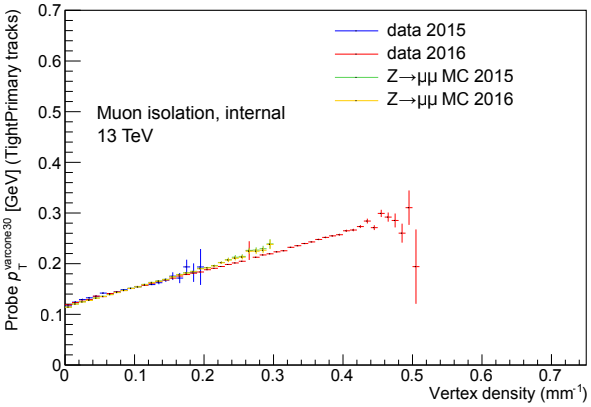

(d) TightPrimary working point

Figure 7.9 – Distributions of $p_{\mathrm{T}}^{\mathrm{varcone30}}$ against the vertex density ρ_{vtx}. MC 2015 and MC 2016 are the same as no ρ_{vtx} are applied and μ reweighting is applied on the combination of the 2015 and 2016 datasets [69].

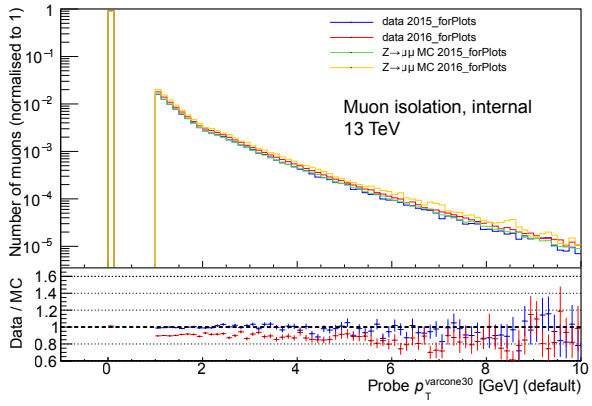

(a) Standard track selection

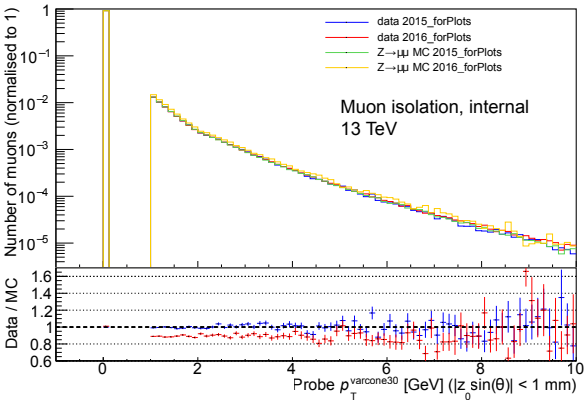

(b) Tighter $\max|z_0 \sin\theta|$ cut

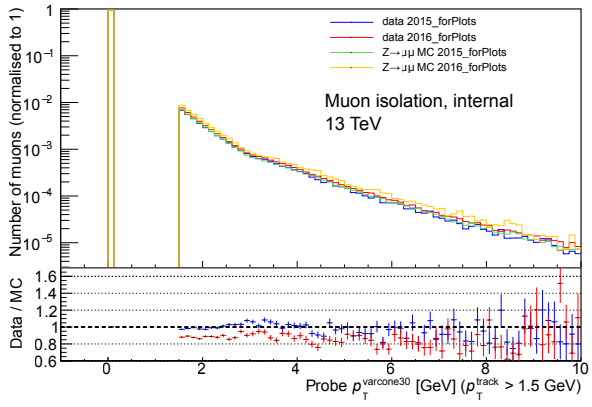

(c) Tighter p_T cut

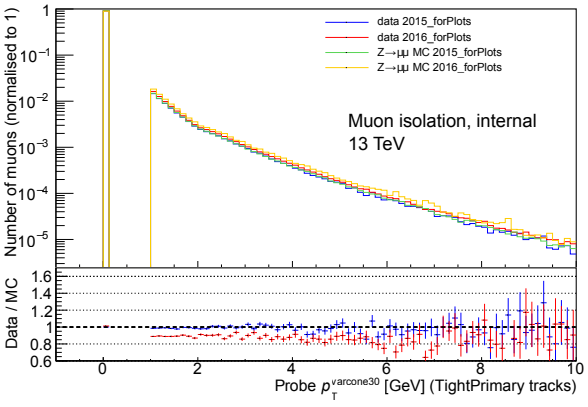

(d) TightPrimary working point

Figure 7.10 – Distributions of $p_T^{varcone30}$ with various track selection criteria, after ρ_{vtx} reweighting [69].

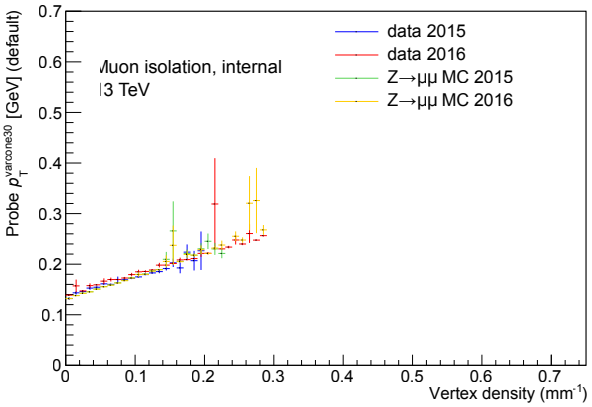

(a) Standard track selection

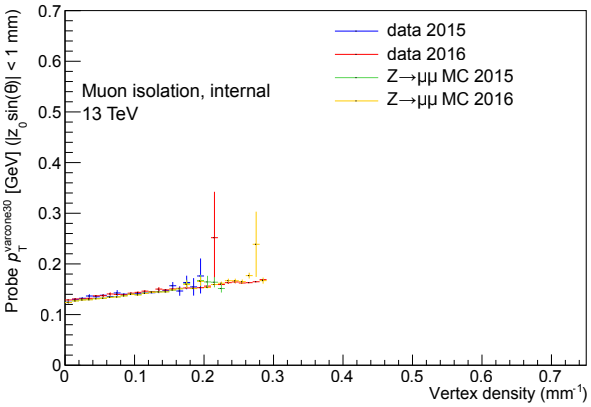

(b) Tighter $\max|z_0 \sin\theta|$ cut

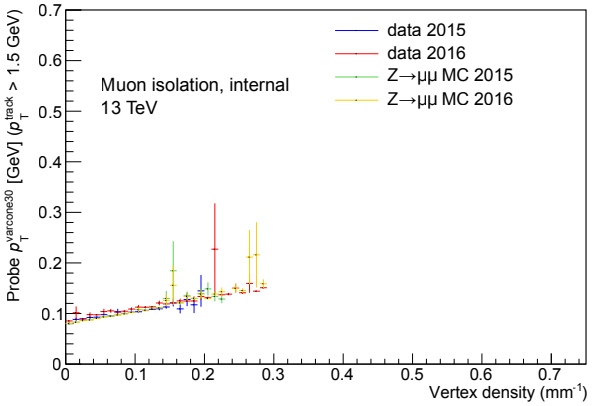

(c) Tighter p_{T} cut

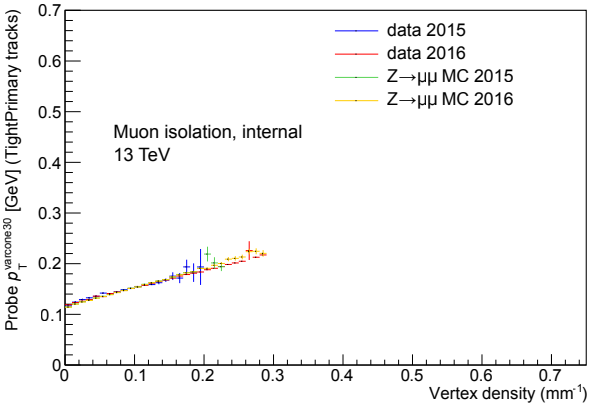

(d) TightPrimary working point

Figure 7.11 – Distributions of $p_{\mathrm{T}}^{\mathrm{varcone30}}$ against the reweighted vertex density ρ_{vtx} [69].

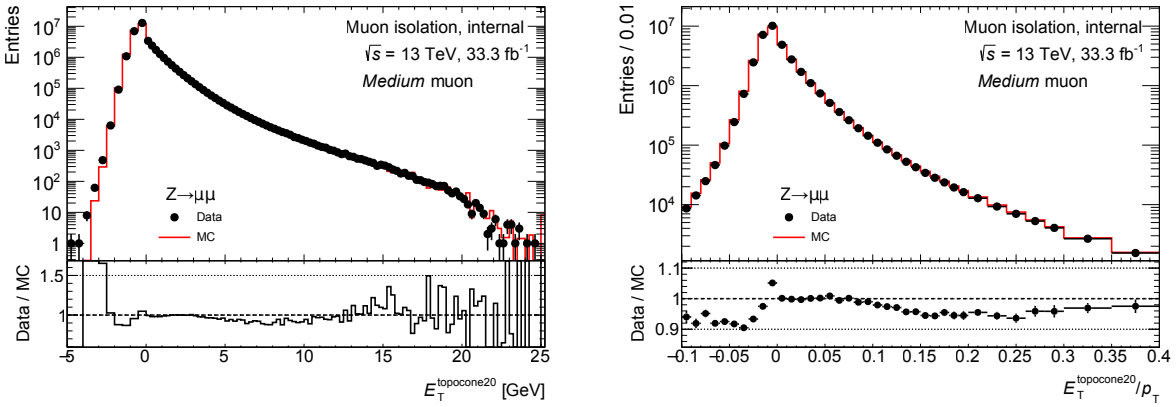

(a) $E_{\mathrm{T}}^{\mathrm{topocone20}}(\mu)$ (b) $E_{\mathrm{T}}^{\mathrm{topocone20}}(\mu)/p_{\mathrm{T}}^{\mu}$

Figure 7.12 – Data-simulation comparison of topoetcone20 (a) raw and (b) divided by p_{T}^{μ} [46, 40, 69].

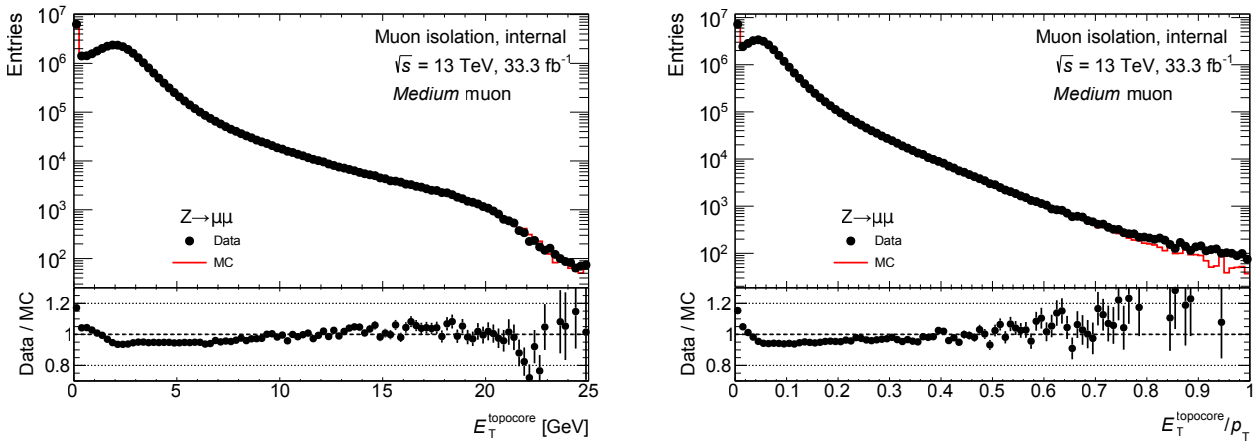

(a) $E_{\mathrm{T}}^{\mathrm{topocore}}(\mu)$ (b) $E_{\mathrm{T}}^{\mathrm{topocore}}(\mu)/p_{\mathrm{T}}^{\mu}$

Figure 7.13 – Data-simulation comparison of core (a) raw and (b) divided by p_{T}^{μ} [69].

7.2.2 Calorimeter-based isolation

The distribution of the topoetcone20 variable for data and MC (divided by p_{T}^{μ} or not) is shown in Fig. 7.12. The topocore variable (core energy subtracted from the topoetcone variable) is presented in Fig. 7.13. Simulation is pile-up reweighted, which improves the agreement. The bin $E_{\mathrm{T}}^{\mathrm{topocore}} = 0$ is more populated in data as compared to simulation due to more noise in the calorimeter cells. This abundant noise, not well modelled by MC, causes the cells not to be added to topoclusters, since their S/B ratios are below the thresholds. In such events, no topoclusters can be formed close to the probe muon leading to $E_{\mathrm{T}}^{\mathrm{topocore}} = 0$. Thanks to pile-up correction, this effect is however diluted in the negative part of the $E_{\mathrm{T}}^{\mathrm{topocone20}}$ distributions and disagreement between data and MC is minor. The working points are therefore not strongly affected by this miss-modelling.

It is important to check the robustness of the topoetcone20 variable against pile-up conditions, as this

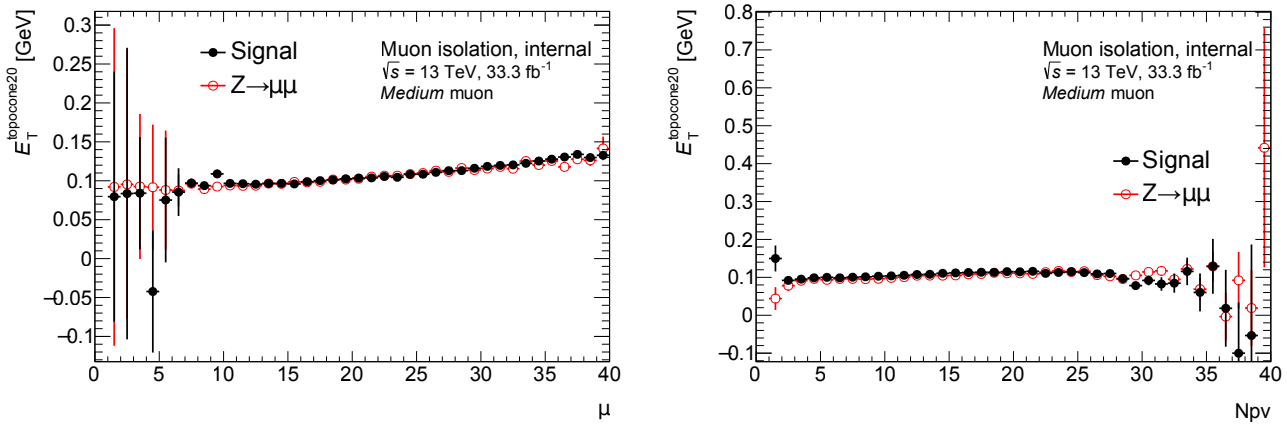

(a) Evolution against μ

(b) Evolution against n_{PV}

Figure 7.14 – Evolution of topoetcone20 with pile-up: as a function of (a) μ and (b) n_{PV} [69]. The distributions are flat, which proves the adequate correction for pile-up.

variable was specifically designed to cope up with higher μ values. Figure 7.14 presents the dependence of topoetcone20 with μ and n_{PV}. The distributions are flat, which proves the pile-up correction is correctly assessed and is efficient. Note that the higher values of $E_{\mathrm{T}}^{\mathrm{topocone20}}$ at high μ are due to the pile-up reweighting which is not fully optimal as the peak of the μ distribution is around 25 in data.

7.3 Efficiency calculation

Having applied the various selection criteria, efficiencies can be calculated as [46, 40]:

$$\varepsilon = \frac{N_{\mathrm{pass}}^{\mathrm{OC\ probe,\ signal}}}{N_{\mathrm{total}}^{\mathrm{OC\ probe,\ signal}}},$$

where OC refers to pairs of muons having opposite charge.

Since efficiencies of the working points depend on p_{T} and η by construction of the cut maps, it was decided to provide the measurements in bins of p_{T}. In case of a strong η dependence, two-dimensional measurements would be carried out.

In order to ensure only signal events are selected in the data, efficiencies have to be corrected to remove any contamination from background. Initially, the background contribution was subtracted from data and MC using a transfer factor $T = 1$, introduced in Sec. 7.2. However, as more data was available, the studies were extended to muons having $p_{\mathrm{T}} < 10\,\mathrm{GeV}$ and it appeared that this background correction was inefficient in the low-p_{T} region. Another method was hence developed to remove the background contamination, and turned out to give good results, decreasing the systematic uncertainties in the low-p_{T} region. This method is now used for the correction of the efficiencies and is further described in the next paragraphs.

This method takes into account the QCD and EW background sources, so that the measured efficiencies can be expressed as [69]:

$$\varepsilon_{\mathrm{measured}}^{\mathrm{data}} = f_{\mathrm{QCD}}\varepsilon_{\mathrm{QCD}}^{\mathrm{data}} + f_{\mathrm{EW}}\varepsilon_{\mathrm{EW}}^{\mathrm{data}} + \left(1 - f_{\mathrm{QCD}} - f_{\mathrm{EW}}\right)\varepsilon_{Z\to\mu\mu}^{\mathrm{data}},$$

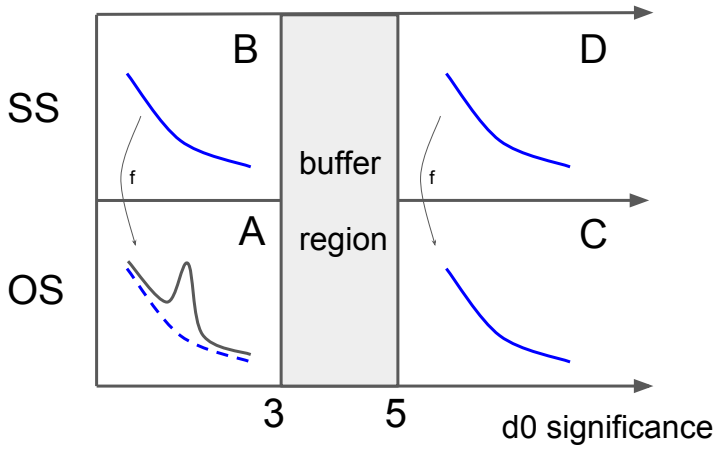

Figure 7.15 – Control regions for the background correction of the isolation efficiencies. The various regions are defined using cuts on the d_0 significance and same- opposite-charge pairs. A buffer region is defined to avoid contamination of the signal. The transfer factor f is calculated as the ratio of the yields in regions C over D and is assumed to be the same as between regions A and B. Region B is used as nominal and the three other regions are used for the systematic uncertainties [69].

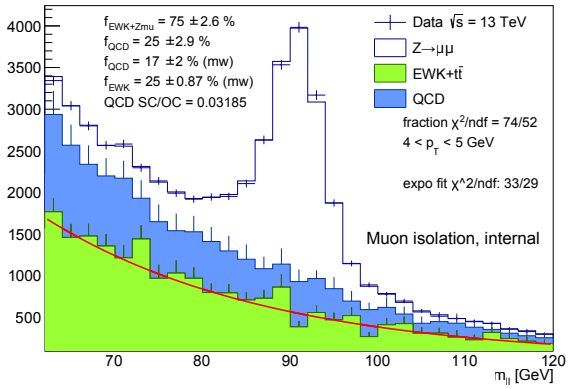

Figure 7.16 – Fit of the background fractions in the bin $4 < p_{\mathrm{T}} < 5\,\mathrm{GeV}$ for the background correction of the isolation efficiencies. The QCD template (blue) is taken from same-charge pairs in data, whereas the EW template (green) is retrieved from simulation. Since for $p_{\mathrm{T}} < 10\,\mathrm{GeV}$ the EW template suffers from statistical fluctuations, it is fitted using a decreasing exponential function, as highlighted in red [69].

where f_{QCD} and f_{EW} are the QCD and EW background fractions in data, and $\varepsilon_{\text{QCD}}^{\text{data}}$ and $\varepsilon_{\text{EW}}^{\text{data}}$ are the related efficiencies. $\varepsilon_{Z\to\mu\mu}^{\text{data}}$ is the efficiency of $Z \to \mu\mu$ events in data, which is the desired quantity. The previous equation can be rewritten to isolate $\varepsilon_{Z\to\mu\mu}^{\text{data}}$:

$$\varepsilon_{Z\to\mu\mu}^{\text{data}} = \frac{\varepsilon_{\text{measured}}^{\text{data}} - f_{\text{QCD}}\varepsilon_{\text{QCD}}^{\text{data}} - f_{\text{EW}}\varepsilon_{\text{EW}}^{\text{data}}}{1 - f_{\text{QCD}} - f_{\text{EW}}} = \frac{\varepsilon_{\text{measured}}^{\text{data}} + \mathcal{S}}{\mathcal{N}},$$

where $\mathcal{S} = -f_{\text{QCD}}\varepsilon_{\text{QCD}}^{\text{data}} - f_{\text{EW}}\varepsilon_{\text{EW}}^{\text{data}}$ and $\mathcal{N} = 1 - f_{\text{QCD}} - f_{\text{EW}}$ are the subtraction and scaling terms. The objective is to estimate the value of these two terms for each working point in bins of p_{T}^{μ}.

The EW efficiencies can be computed using MC for each working point as a function of p_{T}^{μ}, assuming $\varepsilon_{\text{EW}}^{\text{data}} \approx \varepsilon_{\text{EW}}^{\text{MC}}$. The following samples were generated using the POWHEG [85, 86] generator interfaced to PYTHIA 8 [74]: $W^- \to \mu\nu$, $W^+ \to \mu\nu$, $Z \to \tau\tau$, $WW \to \ell\nu\ell\nu$, $WZ \to \ell\nu\ell\ell$, $ZZ \to \nu\nu\ell\ell$, $ZZ \to 4\ell$, $WZ \to qq\ell\ell$, $ZZ \to qq\ell\ell$ and $t\bar{t}$, where $\ell \in \{e, \mu\}$. The QCD efficiencies are estimated using the same-sign pairs in data, as $\varepsilon_{\text{QCD}}^{\text{data}} = \frac{N_{\text{pass}}^{\text{SC probe}}}{N_{\text{total}}^{\text{SC probe}}}$.

In order to assess the QCD and EW fractions, a template fit to the dimuon invariant mass spectrum is performed on the opposite-charge pairs in the data, in bins of p_{T}^{μ}. Up to $p_{\text{T}} = 25\,\text{GeV}$, the fractions rapidly decrease to become negligible above this threshold. Therefore, for transverse momenta greater than 25 GeV, the old method using the transfer factor $T = 1$ is used to correct the efficiencies, as the effects of background subtraction do not affect the results and the fits of the fractions do not converge in this region due to the lack of background statistics.

The fitted values of the fractions do not depend on the chosen working point but on the shape of the templates. Two templates are used. The first one models the QCD background shape taken as same-charge pairs in the data: it is assumed that the shape of opposite-charge pairs is the same as for same-charge pairs, and a systematic uncertainty is associated to this assumption, as described later. The second template models the EW backgrounds combined with the $Z \to \mu\mu$ signal. This is taken from simulation. A third template is defined, which is not used for the fit, but is useful to compute the fractions under the Z peak.

Although the mass range used for the analysis is restricted to 81 – 101 GeV, the fit is performed on a wider range 61 – 121 GeV to be able to discriminate between the shapes of the two templates (the EW part is close to the Z peak, whereas QCD is smoother). Additional QCD background-enriched regions are introduced, as shown in Fig. 7.15. The four control regions are defined using cuts on the d_0 significance and using same- or opposite-charge muon pairs. A buffer region, defined as a gap in the d_0 significance cuts is introduced to avoid contamination from the signal into the control regions. The QCD templates are taken from the regions B, C and D (see Fig. 7.15). The region A cannot be used, as it corresponds to the signal region and the template is hidden under the Z peak. The corresponding template is therefore estimated using region B multiplied by a transfer factor f converting from same-charge pairs to opposite-charge pairs. This factor is estimated using the ratio of the shapes in the regions C over D (it is assumed the cuts on d_0 have only minor impact on f). Since the regions C and D suffer from low statistics and the estimation of f is very sensitive to fluctuations, region B is used for the nominal case, and region A serves for the estimation of the systematics, as described thereafter. To get the number of QCD events under the Z peak, the QCD template is integrated over the dimuon-mass range 81 – 101 GeV. This number is then divided by the number of opposite-charge pairs in the same range to calculate f_{QCD}.

A more complicated procedure is carried out for the EW fraction. The EW background combined with the $Z \to \mu\mu$ template is fitted and then used to scale the EW-background-only template. Afterwards, this template is integrated over the analysis range to obtain the number of EW background events. Unfortunately, due to a lack of statistics in the MC, the integral is sensitive to fluctuations for $p_{\text{T}}^{\mu} < 10\,\text{GeV}$.

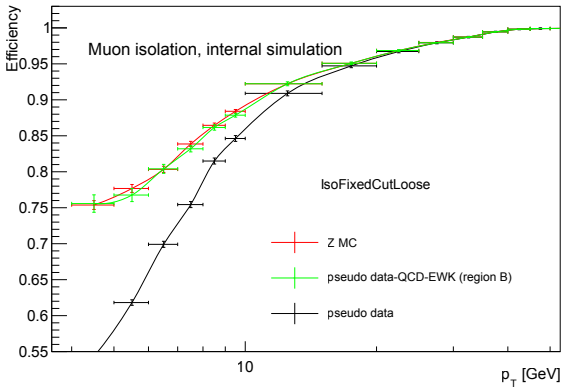

Figure 7.17 – Validation checks using pseudo data for the background corrections of the isolation efficiencies (*FixedCutLoose* working point). The fit of the fractions and the efficiency correction give expected results, as the corrected pseudo-data efficiencies are very close to the simulated efficiencies [69].

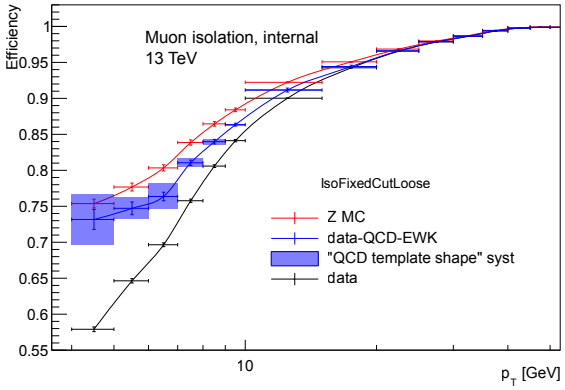

Figure 7.18 – Results of the isolation efficiency correction for the *FixedCutLoose* working point. The corrected data efficiencies (blue) are closer to the simulation (red), as compared to the uncorrected results (black). The blue bands indicate the background systematic uncertainties [69].

To overcome this issue, the EW-background only template is fitted using a decreasing exponential for $p_{\mathrm{T}}^{\mu} < 10\,\mathrm{GeV}$. In the same way as for the QCD background, the number of EW background events is divided by the number of opposite-charge pairs in the data, from the dimuon-mass range 81 – 101 GeV to calculate the EW fraction f_{EW}. Figure 7.16 shows an example of the fit of the fractions in the $4 < p_{\mathrm{T}} < 5\,\mathrm{GeV}$ bin.

The whole procedure is validated using pseudo data whose efficiencies are known. Thanks to this, the results of the fit can be compared to the input efficiencies. Data composed of opposite-charge pairs of muons is built combining all the EW MC samples, including the signal $Z \to \mu\mu$ and QCD template. The background corrected efficiency should match the signal efficiency. This is indeed the case in Fig. 7.17. The final results of the corrected efficiencies are plotted in Fig. 7.18.

7.4 Scale factors

Efficiency variations between data and simulation have to be corrected so that the MC describes the data as accurately as possible. The corrections to apply are translated into scale factors. These factors are used by the analysis groups, each analysis applying the corrections corresponding to the working point used.

Scale factors are defined as the ratio of efficiencies measured in data over MC [46, 40]:

$$\mathcal{F}\left(p_{\mathrm{T}}^{\mu}\right) = \frac{\varepsilon_{\mathrm{data}}\left(p_{\mathrm{T}}^{\mu}\right)}{\varepsilon_{\mathrm{MC}}\left(p_{\mathrm{T}}^{\mu}\right)},$$

where $\varepsilon_{\mathrm{data}}$ and $\varepsilon_{\mathrm{MC}}$ are the efficiencies measured in data and MC, respectively. Note that for Moriond 2017 recommendations, the *FixedCutTightTrackOnly* working point has its scale factors calculated in two-dimensions: $\left(p_{\mathrm{T}}^{\mu}, \eta^{\mu}\right)$.

In order for the results to be consistent, it is important to check the dependence of the factors with respect to the muon kinematics and other variables. After correction of the simulation (which is performed using a dedicated tool), the various efficiencies of the MC have to correspond to the efficiencies in data, taking into account the statistical and systematic uncertainties.

7.5 13 TeV results

The last part of this chapter is dedicated to the results of the muon isolation efficiencies and scale factors using Run 2 data [46, 40].

7.5.1 Efficiencies and scale factors

The comparison between data and MC is presented in Fig. 7.19, in the top part of the plots. Data points are in black, and simulation in red. The bottom part of the plots shows the corresponding scale factors, with the statistical uncertainties in blue and the combined (statistical and systematic) uncertainties in yellow. The chosen p_{T}^{μ} bins are: $4, 5, 6, 7, 8, 9, 10, 15, 20, 25, 30, 35, 40, 45, 50, 60, 80, 120, 150, 200, 300, 500$ GeV. The results for the *FixedCutTightTrackOnly* are presented separately in Fig. 7.20. The underflow and overflow bins are not presented. For these bins, the central values and uncertainties of the efficiencies and scale factors are assumed to be equal to the values of the closest bin shown in the figures. For the scale factors, an extra 5% systematic uncertainty is added to the underflow bin as a conservative approach. Similarly, 2% are added to the systematic uncertainties of the overflow bins, except for the *LooseTrackOnly* and *FixedCutTightTrackOnly* working points, where the addition is reduced to 1%. These additional uncertainties were calculated extrapolating the statistical and systematic errors from the measurements in the range $4 < p_{\mathrm{T}}^{\mu} < 500\,\mathrm{GeV}$.

As compared to the preliminary study, the efficiencies are closer to the expected results, for the five working points targeting a specific efficiency. It has to be noticed that efficiencies are a bit too high for muons having p_{T}^{μ} close to 10 GeV for the *Loose* and *LooseTrackOnly*. This is observed in both the data and simulation, indicating this issue comes from a poor definition of the cut maps in this region. At high p_{T}^{μ}, efficiencies are close to 1, which is the objective of most of the analyses, the SM background contributions being more dominant at low transverse momentum. Efficiencies drop from $p_{\mathrm{T}}^{\mu} < 10\,\mathrm{GeV}$, as the quality of the probes worsens and the ptvarcone30 cone is bigger. Overall, for medium transverse momenta, the observed efficiencies follow the expectations.

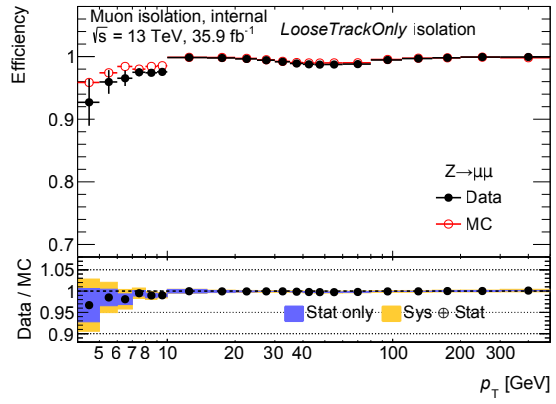

(a) *LooseTrackOnly*

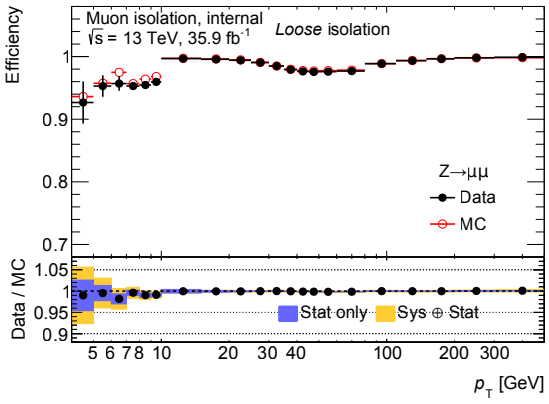

(b) *Loose*

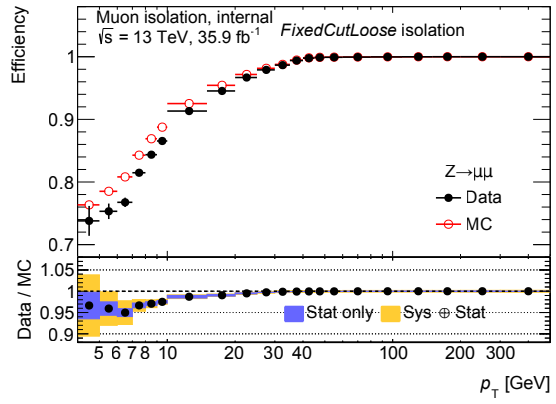

(c) *FixedCutLoose*

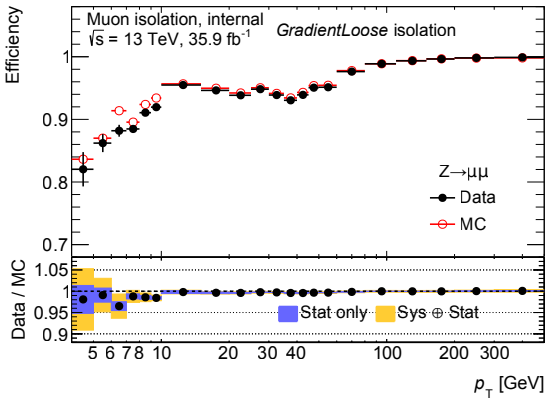

(d) *GradientLoose*

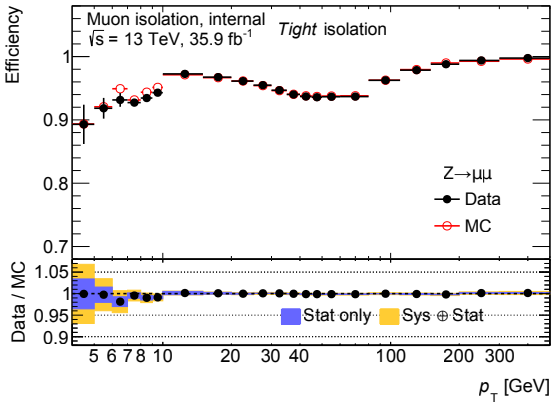

(e) *Tight*

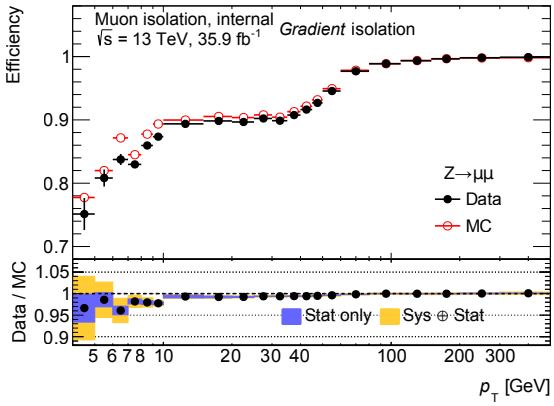

(f) *Gradient*

Figure 7.19 – Efficiencies and scale factors of the *LooseTrackOnly*, *Loose*, *FixedCutLoose*, *GradientLoose*, *Tight* and *Gradient* working points [46, 40]. Top panels present the comparison of the efficiencies in data (black) and MC (red). Bottom panels show the associated scale factors with the statistical uncertainties in blue and the combined (statistical and systematic) uncertainties in yellow. Underflow and overflow bins are not included.

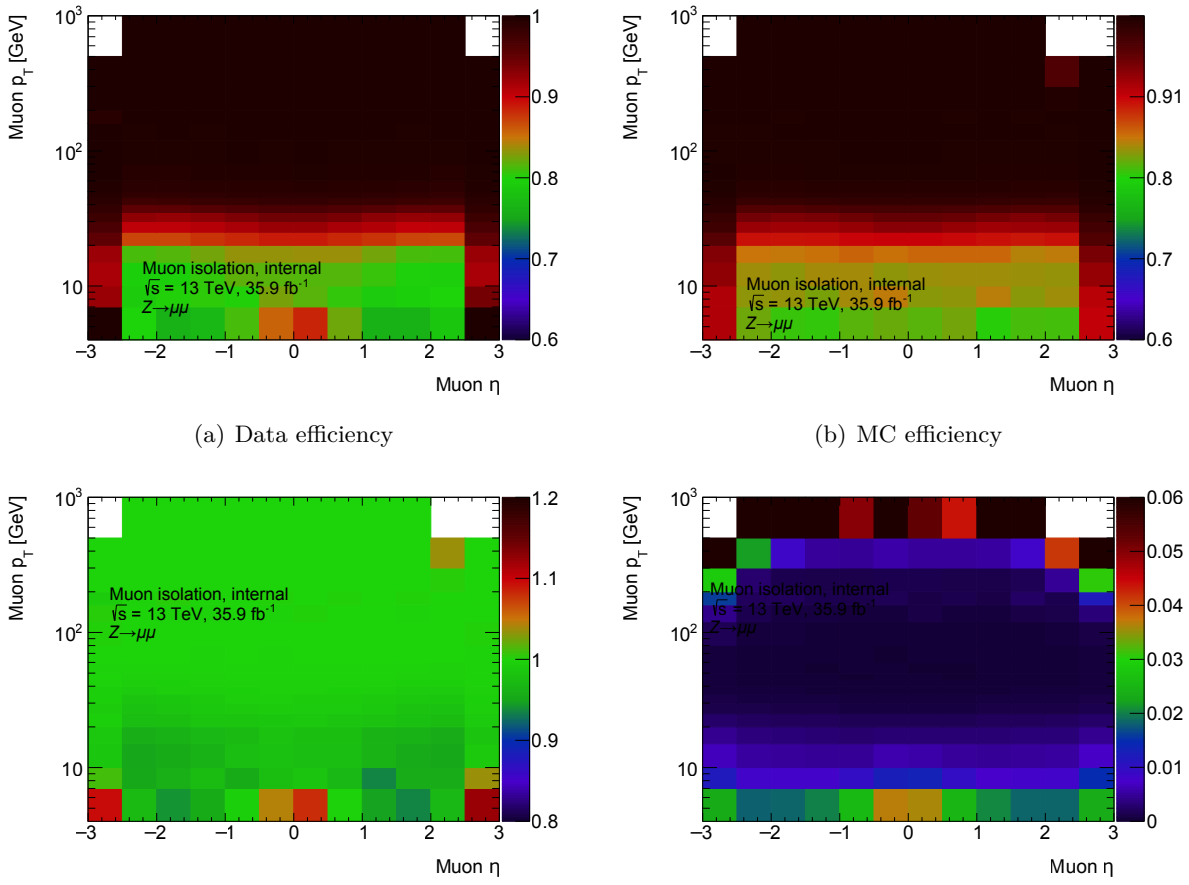

(a) Data efficiency

(b) MC efficiency

(c) Scale factors

(d) Scale factor, data statistical uncertainties

Figure 7.20 – Muon isolation efficiencies and scale factors for the *FixedCutTightTrackOnly* working point [69]. The underflow and overflow bins are not included.

Simulation describes the data well, which results in scale factors really close to 1, also showing the discrepancy on ptvarcone30 does not affect the results so much. Deviations mainly arise at low p_{T}^{μ} where despite a good background correction, disagreement persists. However, systematics remain below the 10% level indicating a good stability of the results.

Statistical errors on the efficiencies are calculated as $\delta\varepsilon = \sqrt{\frac{\varepsilon(1-\varepsilon)}{N^2}}$ using a binomial law, where N is the denominator of the fraction used to calculate the efficiency. These errors are centred and are propagated to the scale factors. From the previous graphs (Fig. 7.19 and 7.20), it is possible to observe an expected increase of the statistical uncertainties at low and high p_{T}^{μ} (in purple in the ratio plots). This is due to the topology of the Z decays with a majority of muons having a transverse momentum close to 50 GeV.

7.5.2 Systematic uncertainties

Several systematic contributions are considered in the calculation of the scale factors, corresponding to the various cuts applied to the tag and probe pairs, as summarised in Tab. 7.3. For each contribution, the relevant cuts are varied and the efficiencies are calculated accordingly. From these new efficiencies, new scale factors are derived and compared to the nominal values. For each bin of p_{T}^{μ} (and η^{μ} for two-

dimensional scale factors), the maximum absolute variation is taken as a systematic uncertainty and symmetrised around the central value. This procedure is repeated for each systematic contribution. In the end, the total uncertainty per bin is calculated as the sum in quadrature of the various contributions in the bin, assuming the errors are uncorrelated (conservative approach).

The overall uncertainty (including statistical and systematic errors) is plotted in yellow in the ratio plots of Fig. 7.19 and 7.20. The various contributions to the systematic uncertainties are decomposed in Fig. 7.21 and 7.22. The cut variations related to the systematic contributions are further detailed in the next paragraphs.

First of all, systematic uncertainties related to the background correction are taken into account [69]. The uncertainty arises from the choice of the QCD template for the fit of f_{QCD}, which is estimated from same-charge muon pairs in data. In order to assess the systematic uncertainties, $\mathcal{S}$ and $\mathcal{N}$ are computed for each of the four QCD templates, corresponding to the regions A, B, C and D of Fig. 7.15. The template from region B is the nominal one, and the three others are used for the uncertainties. The errors are computed on the corrected efficiencies directly ($\varepsilon^{\text{data}}_{Z\to\mu\mu}$). If ε_X is the corrected efficiency using the template from region $X \in \{\text{A},\text{B},\text{C},\text{D}\}$, the uncertainties are defined as (for each p^{μ}_{T} bin): $\delta\varepsilon^{\text{data}}_{Z\to\mu\mu} = \max_{X\in\{\text{A,C,D}\}} |\varepsilon_{\text{B}} - \varepsilon_X|$. The systematic uncertainties are plotted in Fig. 7.18 as an example for the *FixedCutLoose* working point.

Then, the selection cuts on the invariant mass are modified (up and down variations): $86\,\text{GeV} < m_{\mu\mu} < 96\,\text{GeV}$ or $71\,\text{GeV} < m_{\mu\mu} < 111\,\text{GeV}$. The probe quality is also changed to *Loose* and *Tight* (up and down variations).

The three first contributions have more effects for $p^{\mu}_{\text{T}} < 10\,\text{GeV}$, as the background contamination increases (the p^{μ}_{T} spectrum of QCD events follows a decreasing exponential shape). Since both the background corrections, the mass requirement and the probe quality are strong tools to discriminate against background, the choice of the cut values has a huge impact on the efficiencies. Thanks to accurate background correction, the systematics however remain under the 10% level.

The isolation criterion on the tag is varied using all the supported working points. The corresponding systematic contribution is taken as the envelope of all the variations and symmetrised. Apart from the low p^{μ}_{T} region, the effects of the tag isolation are negligible (less than 0.0001, up to 0.05 at low p^{μ}_{T}). This demonstrates that the calculation of the efficiencies is not biased by the Tag-And-Probe method as no correlations are found between the criteria on the isolation of the tag and the probe.

The requirement on the opening angle between the two muons of the pair is modified as follows: $\Delta R_{\mu\mu} > 0.2$ or $\Delta R_{\mu\mu} > 0.5$ (up and down variations). This contribution becomes more significant at high transverse momenta, as the Z bosons are more boosted and the muons of the pairs are produced quite close to each other. Nevertheless, the effects remain below 1 per-mill.

The same variations apply to the minimum opening angle between the probe and the closest jet: $\Delta R_{\mu j} > 0.3$ or $\Delta R_{\mu j} > 0.5$. Apart from the low p^{μ}_{T} region, where the chances to find a jet reconstructed as a muon increase, the effects are below 0.1 per-mill.

An additional uncertainty on the η dependence of the scale factors is added. It is fixed to 0.2% over the entire p^{μ}_{T} range. This value was obtained after a first comparison of the corrected efficiencies in simulation with the data. In some η^{μ} regions, the systematic uncertainties were not covering the data variation and it was decided to add a flat uncertainty to overcome this. Even with the addition of this systematic, the scale factors of the *FixedCutTightTrackOnly* working point were still showing some η^{μ} dependence. Therefore, these scale factors are provided in bins of $\left(p^{\mu}_{\text{T}}, \eta^{\mu}\right)$, at a cost of an increased statical uncertainty. With more accumulated statistics, the scale factors could be provided in two dimensions for all working points, keeping in mind each time that the increased statistical uncertainties should remain lower than the flat η

Table 7.3 – The various systematic contributions for the muon isolation scale factors are added in quadrature, assuming no correlations between the various components [46, 40].

Name of the systematic variation	Range of variation	Maximum contribution
Z mass	(86 – 96) GeV or (71 – 111) GeV	2%
Tag isolation	Maximum variation among all isolation working points	1%
Probe muon quality	*Loose* or *Tight*	6%
$\Delta R_{\mu\mu}$	$\Delta R_{\mu\mu} > 0.2$ or $\Delta R_{\mu\mu} > 0.5$	< 0.1%
$\Delta R_{\mu j}$	$\Delta R_{\mu j} > 0.3$ or $\Delta R_{\mu j} > 0.5$	0.5%
Background correction	Correction using other control regions	3.5%

uncertainty currently added. This additional uncertainty clearly dominates at medium p_{T}^{μ}, but is of equal magnitude with respect to the MC and data statistical uncertainties at high transverse momenta. In the low p_{T}^{μ} region, this η systematic is negligible.

In the plots, data statistical uncertainties also include the statistical uncertainties coming from the efficiency fit for the background correction. It is therefore expected that these uncertainties increase (and dominate the scale factor uncertainties) at low p_{T}, as less Z events are available for the fit.

The effect of pile-up reweighting was also checked using various shifts for the correction of μ (the pile-up reweighting is not directly done on μ, but on a shifted value of μ). However, it was found that this systematic had only little impact on the scale factors and it was agreed that since all users of the collaboration would follow the reweighting conventions, there was no need to include this contribution to the systematic uncertainties.

The scale factors were initially calculated without any cut on $\Delta R_{\mu j}$, and were found to be highly dependent upon this variable in the region $\Delta R_{\mu j} < 0.4$. The origin of this dependence could be due to a bad description of the isolation variables by the simulation, in case of high activity close to the muon. Studies within the muon isolation team are currently being undertaken to understand the origin of the jets and their effects on the efficiencies. Indeed, the close-by jet could affect differently the results whether it comes from final state radiation or whether it is a miss-reconstructed object.

It was not possible to introduce a higher systematic to cover the differences at low $\Delta R_{\mu j}$ by changing the down variation to $\Delta R_{\mu j} > 0$, as the resulting systematics were too large and would penalise all the analysis groups using muon isolation. It was therefore decided to bin this uncertainty as a function of $\Delta R_{\mu j}$ (on top of the usual p_{T}^{μ} or η^{μ} bins). By doing so, only analyses using events which contain close-by jets would be affected by increased systematics.

Analyses using muons far from a jet can use the standard systematics (variations $\Delta R_{\mu j} > 0.3$ or $\Delta R_{\mu j} > 0.5$). For the analyses having close-by jets, the extra systematic is calculated as follows. The efficiencies in simulation are corrected using the standard scale factors and usual systematics (taken from the case $\Delta R_{\mu j} > 0.4$). These efficiencies are compared to data in bins of p_{T}^{μ} (and η^{μ} if applicable) for various cuts on $\Delta R_{\mu j}$ $(0, 0.1, 0.2, 0.3, 0.4)$. For each of these four bins, the remaining difference between efficiencies in MC as compared to data is taken: this is assumed to be the additional systematic. Having done so, the additional systematics are added to the standard ones. This is a conservative approach, but this ensures that the corrected efficiencies will always cover the data whichever the $\Delta R_{\mu j}$ configuration is.

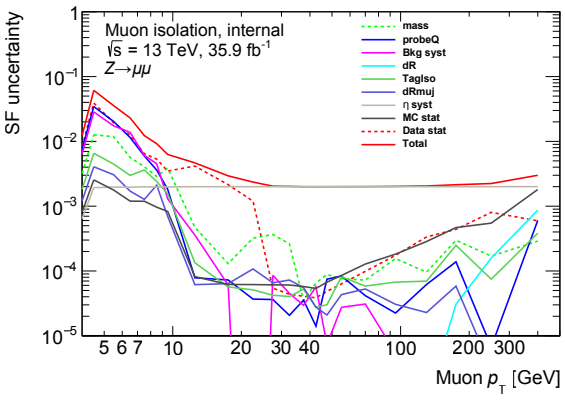

(a) *LooseTrackOnly*

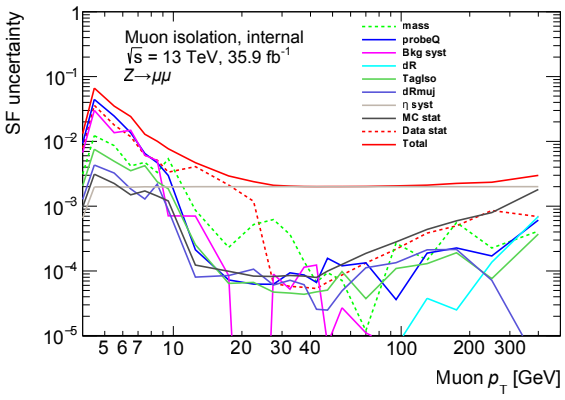

(b) *Loose*

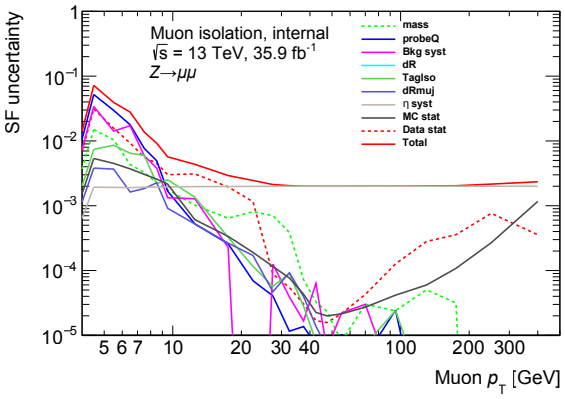

(c) *FixedCutLoose*

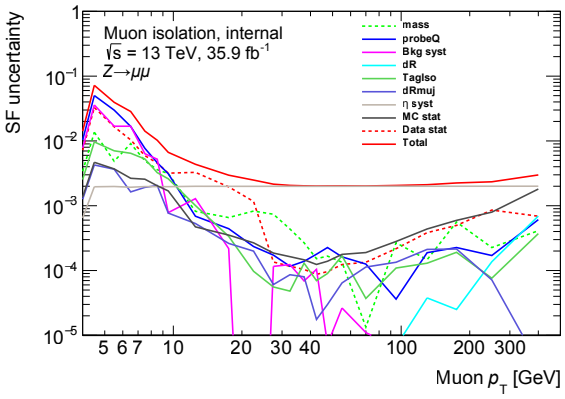

(d) *GradientLoose*

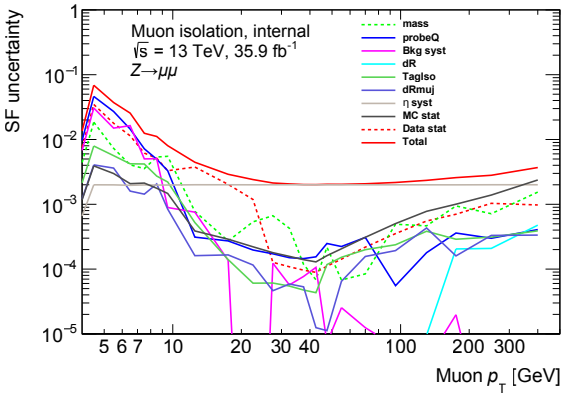

(e) *Tight*

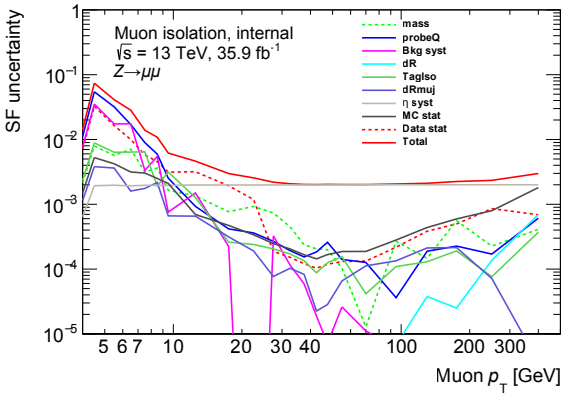

(f) *Gradient*

Figure 7.21 – Systematic uncertainty contributions for the *LooseTrackOnly*, *Loose*, *FixedCutLoose*, *GradientLoose*, *Tight* and *Gradient* isolation working points [46].

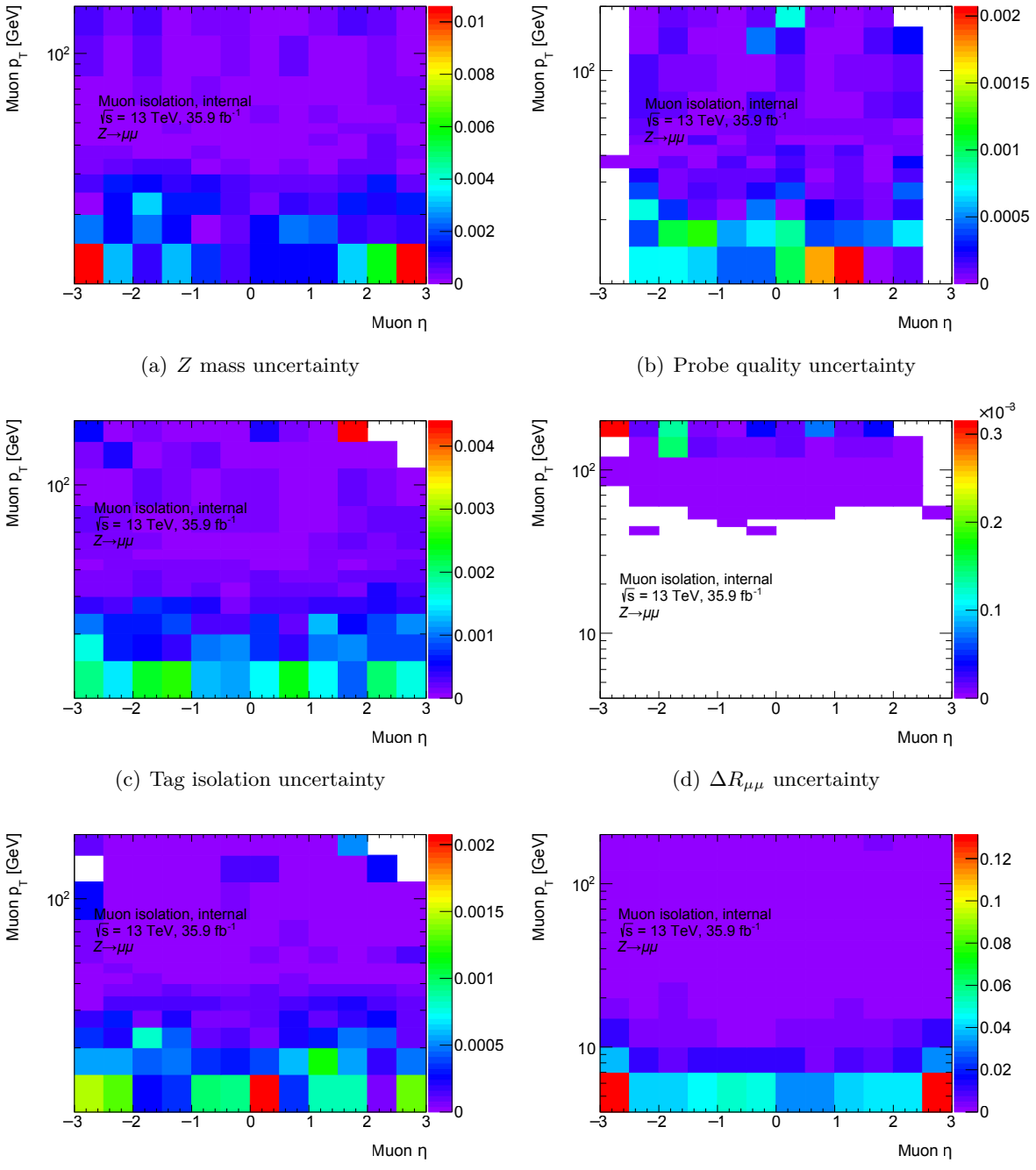

(a) Z mass uncertainty

(b) Probe quality uncertainty

(c) Tag isolation uncertainty

(d) $\Delta R_{\mu\mu}$ uncertainty

(e) $\Delta R_{\mu j}$ uncertainty

(f) Total uncertainty

Figure 7.22 – Systematic uncertainty contributions on the muon isolation scale factors for the *FixedCutTightTrackOnly* working point. The various contributions are presented in bins of $\left(p_{\mathrm{T}}^{\mu}, \eta^{\mu}\right)$, including (a) the Z mass, (b) probe quality, (c) tag isolation, (d) the opening angle between the tag and the probe and (e) the opening angle between the probe and the closest jet. Figure (f) presents the total systematic uncertainty where all the contributions are summed in quadrature.

7.5.3 Scale factor validation (closure test)

Validation of the scale factors (also referred to as *closure test*) is performed in order to check whether after correcting MC efficiencies using the scale factors, these match the data efficiencies (having taken into account the statistical and systematic uncertainties). This validation is performed using the dedicated tool which returns the scale factors depending on the kinematics of the muon. The corrected efficiencies are then calculated having reweighted the MC using the scale factors. Validation checks are only presented for the *FixedCutLoose* working point. Similar plots can be found in App. A for the other working points.

Figures 7.23, 7.24 and 7.25 show the comparison between the efficiencies in the data and the corrected simulation as a function of p_{T}^{μ}. The results are presented integrated over η, to check the perfect matching in p_{T} bins (except for the *FixedCutTightTrackOnly* working point, since the p_{T} bins used differ from those used for the validation), and in various η regions to check there are no strong discrepancies. A further check of the additional $\Delta R_{\mu j}$ systematics is summarised in Fig. 7.26 (no additional $\Delta R_{\mu j}$ systematic added) and Fig. 7.27 (additional $\Delta R_{\mu j}$ systematic added).

In all these plots, data points are in black, whereas the non corrected simulation is in red. The corrected efficiencies are shown by the green areas (statistical uncertainties) and orange (statistical and systematic uncertainties combined). These areas are centred on the central value after correction. The bottom panels present the same efficiencies, but divided by the central value of the corrected simulation. The black points should all be covered by the orange areas to validate the scale factors. For the graphs in bins of $\Delta R_{\mu j}$, it is clearly seen that the extra systematic is only applied in the case $\Delta R_{\mu j} < 0.4$.

For all the working points, the validation against p_{T} (integrated over η) shows good agreement: the data points lay within the orange bands. Some discrepancies are observed in the regions $-1.0 < \eta < 1.0$, and for $|\eta| > 2.5$, for low-p_{T} muons only. The latter is explained by the limitations of the acceptance of the ID. For the central region, the discrepancies are minor and it was decided not to provide two-dimensional scale factors. Note that these discrepancies disappear for the *FixedCutTightTrackOnly* working points, thanks to the (p_{T}, η) binning of the scale factors.

For the validation against $\Delta R_{\mu j}$, there is good agreement for regions which do not have extra systematics. In the regions needing these special systematics, the orange bands reach the black dots, as expected (by definition of the systematic). Note that some efficiencies are negative due to an overestimated background correction (the corresponding muons are probably not well reconstructed). For these cases, an uncertainty of 100% was assigned.

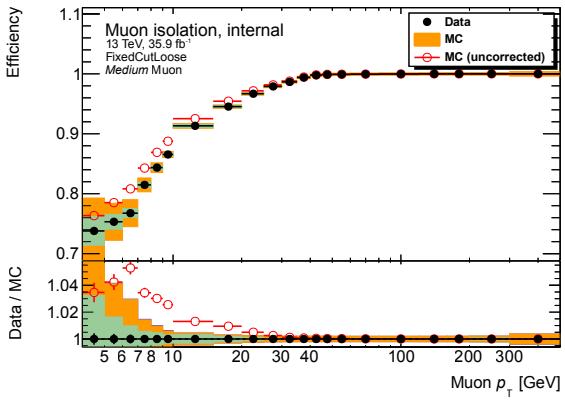

Figure 7.23 – Validation of the *FixedCutLoose* scale factors integrated over η.

7.6 Conclusion and potential improvements

Results on muon isolation with the pp-collision data recorded in 2015 and 2016 by the ATLAS detector were presented in this chapter. Two variables were defined to assess muon isolation: a track-based isolation variable and a calorimeter-based isolation variable. Despite more challenging pile-up conditions with respect to Run 1, the definition of these two new variables enabled to maintain good and robust performance results.

The calorimeter-based isolation now relies on a clustering algorithm to retrieve the energy of the calorimeter cells and includes a pile-up correction. After pile-up reweighting the distributions in data and simulation showed good agreement. The study performed on the core energy led to a new definition of the variable offering higher background rejection for a given signal efficiency.

The track-based isolation has a p_{T}-dependent cone size not to penalise the selection of boosted decay products. The comparison of the distributions between data and simulation showed a discrepancy: more tracks are selected for the calculation of the variable in data than in simulation. This is attributed to an inadequate modelling of the vertex density which measures the average number of vertices in unit of length along the z axis. The option to reweight the simulated samples to improve the agreement was not considered, as this would have penalised analyses with an increase of MC statistical uncertainties. However, the signal efficiencies of the isolation working points are not too strongly affected by the discrepancy and scale factors correct the deviations.

Isolation working points are centrally supported in Run 2. They were defined to suit the needs of various analysis groups in terms of background rejections and signal efficiencies. These were calculated using the Tag-And-Probe method on Z boson decays to two muons. In order to correct the simulation, scale factors were derived for each working point, depending on the kinematics of the muon. Thanks to good agreement between data and MC, they are close to unity.

To further improve on the performance of isolation, the following points could be considered:

- **Treatment of the η dependence of the scale factors.** Although the code was implemented to provide two-dimensional scale factors, it was decided to only do so for the *FixedCutTightTrackOnly* (for which the extra η uncertainty is not added), since the cost in statistics is too high. However, combining these results with the data 2017, checks should be undertaken again. Statistical uncertainties will decrease, but it may also be possible to decrease the flat η uncertainty (or to limit its addition to specific regions of the phase space).

- **Improvement of the cut maps.** This could be achieved using the latest MC samples, in order to be as close as possible to the pile-up conditions in the data. The new core cone dimensions will be used for the topoetcone20 variables, improving the background rejection and hopefully obtaining efficiencies closer to the expected values.

- **Curing the discrepancy between data and MC in the track isolation variable.** Although a reweighing density may not be possible due to MC-limited statistics, a change in the selection criteria of the tracks to compute this variable could result in a better data-MC agreement, if the conditions of data taking in 2017 remain the same as the ones of 2016.

- **Reduction of the $\Delta R_{\mu j}$ systematic uncertainty.** This could be achieved by a dedicated study of the jets close to muon probes that could lead to a finer selection of the jets used for the analysis.

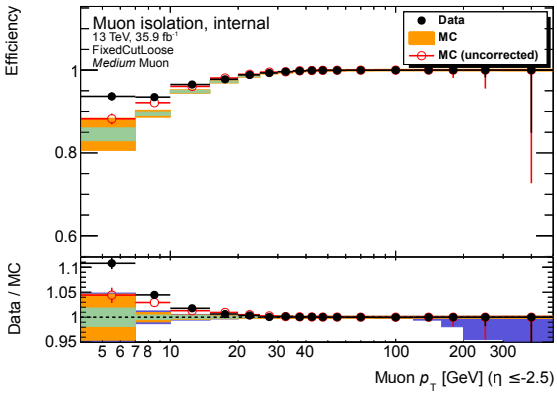

(a) $\eta < -2.5$

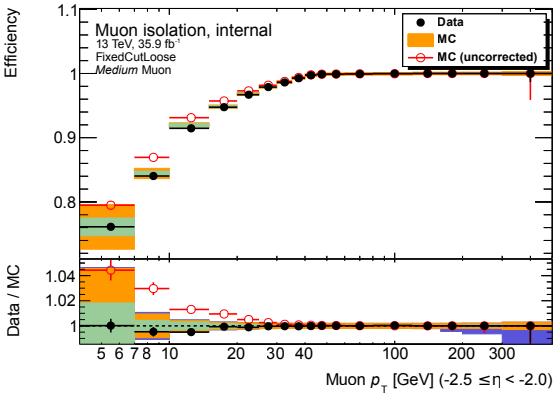

(b) $-2.5 < \eta < -2.0$

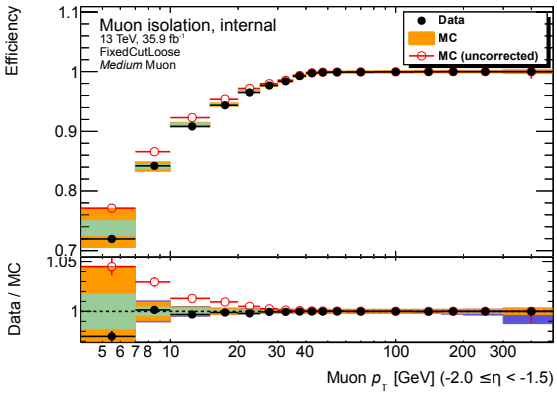

(c) $-2.0 < \eta < -1.5$

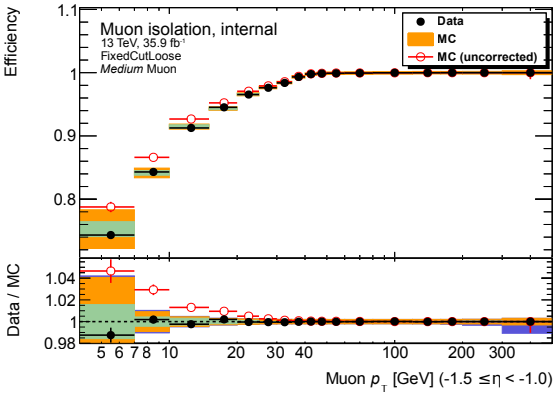

(d) $-1.5 < \eta < -1.0$

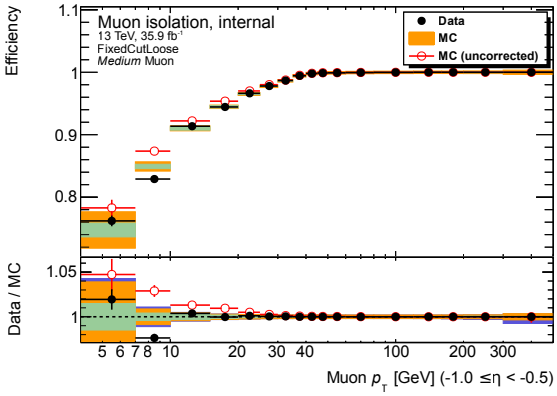

(e) $-1.0 < \eta < -0.5$

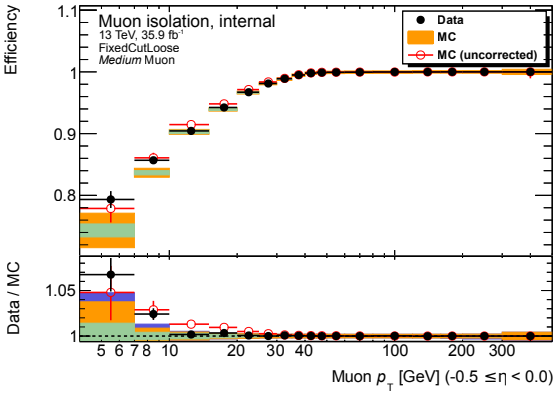

(f) $-0.5 < \eta < 0.0$

Figure 7.24 – Validation plots of the *FixedCutLoose* scale factors in various η regions ($\eta < 0$).

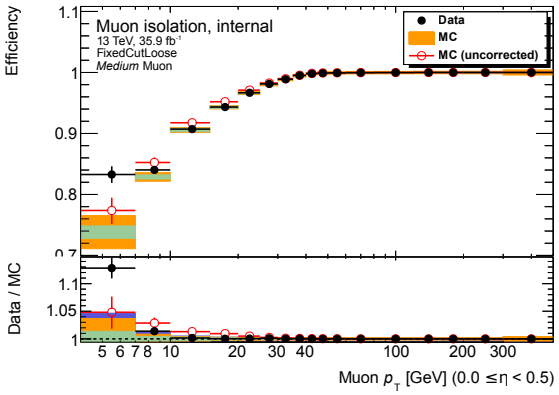

(a) $0.0 < \eta < 0.5$

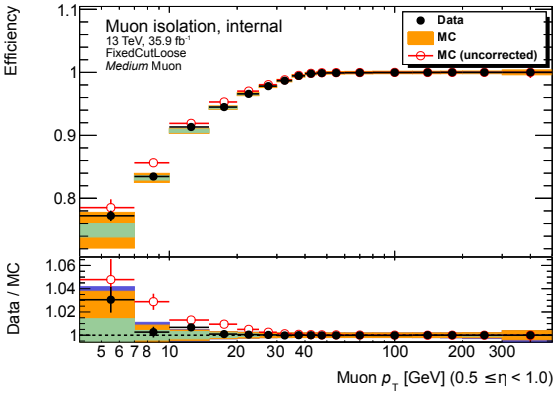

(b) $0.5 < \eta < 1.0$

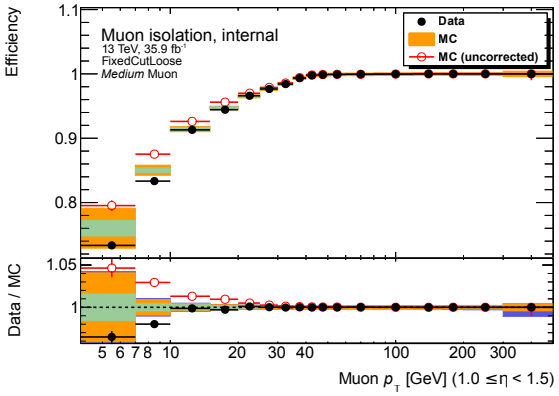

(c) $1.0 < \eta < 1.5$

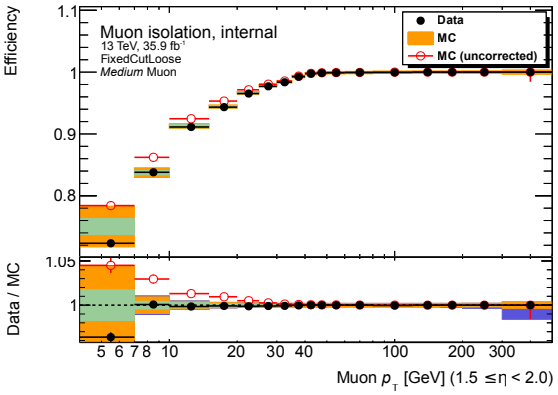

(d) $1.5 < \eta < 2.0$

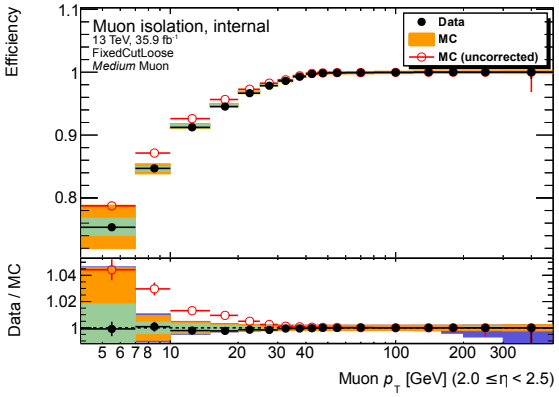

(e) $2.0 < \eta < 2.5$

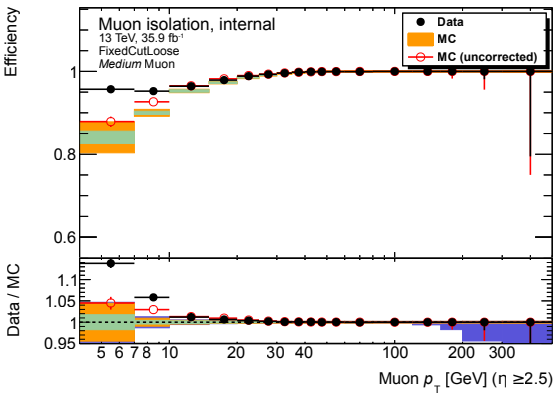

(f) $\eta > 2.5$

Figure 7.25 – Validation plots of the *FixedCutLoose* scale factors, integrated over η and in various η regions ($\eta > 0$).

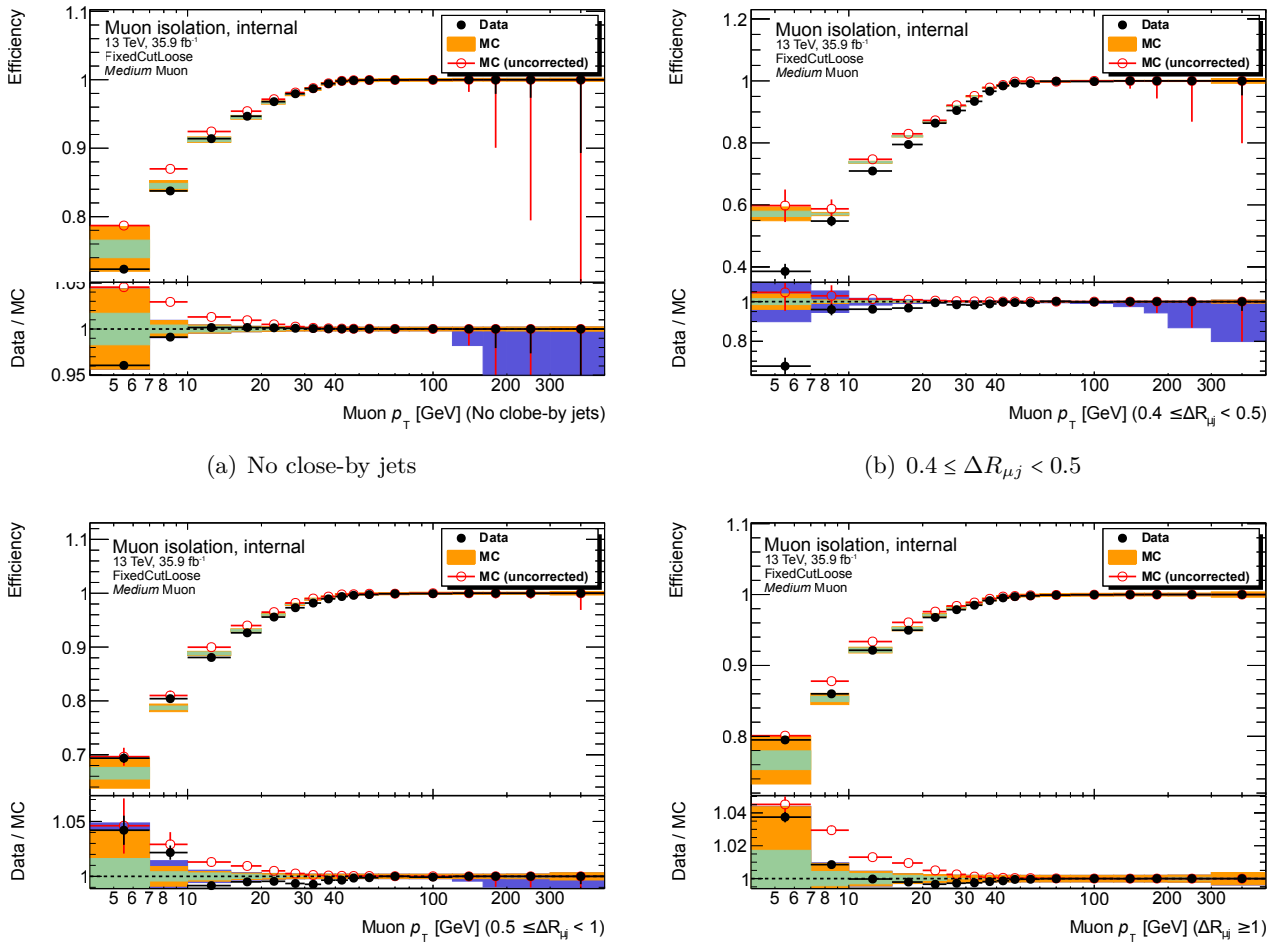

(a) No close-by jets

(b) $0.4 \leq \Delta R_{\mu j} < 0.5$

(c) $0.5 \leq \Delta R_{\mu j} < 1.0$

(d) $\Delta R_{\mu j} \geq 1.0$

Figure 7.26 – Validation plots of the *FixedCutLoose* scale factors, in various $\Delta R_{\mu j}$ regions, where no additional $\Delta R_{\mu j}$ systematics were added.

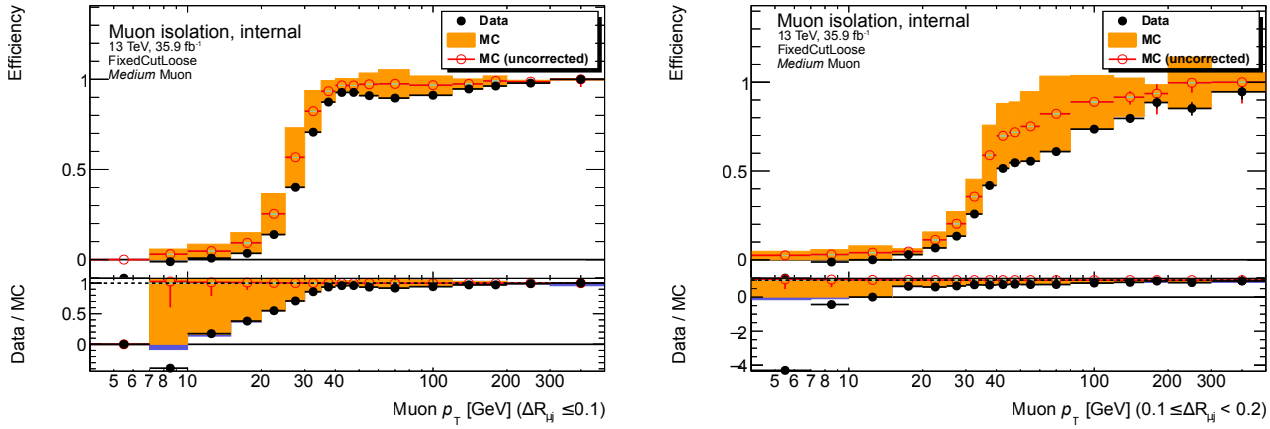

(a) $\Delta R_{\mu j} \leq 0.1$

(b) $0.1 \leq \Delta R_{\mu j} < 0.2$

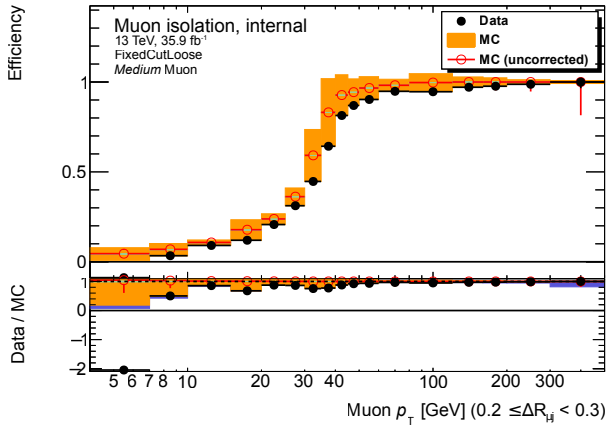

(c) $0.2 \leq \Delta R_{\mu j} < 0.3$

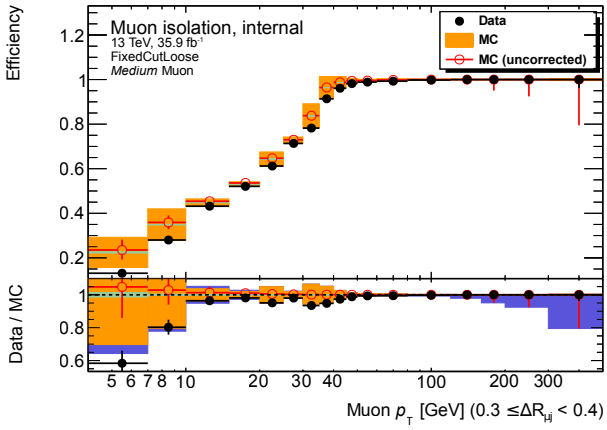

(d) $0.3 \leq \Delta R_{\mu j} < 0.4$

Figure 7.27 – Validation plots of the *FixedCutLoose* scale factors, in various $\Delta R_{\mu j}$ regions, where additional $\Delta R_{\mu j}$ systematics were added.

Chapter 8

Correction for close-by objects

Isolation variables are calculated to distinguish signal objects (which are well isolated) from background objects (not isolated). As described in the previous chapters, isolation regroups the contribution of the objects (leptons or jets) close to the particle, summing up their energies or transverse momenta.

However, specific physics analyses study processes with close-by signal objects. An example is the $Z \to \mu\mu$ decay. At high p_{T}, the signal muons tend to be closer (due to the boosted production of the Z): although close-by, the two muons should still be selected for the analysis. In these situations, a signal object may be marked as non-isolated because of the contribution of another signal object close-by.

A tool was therefore developed to correct for these extra contributions, improving the isolation of the signal objects and increasing the signal significance (background objects are corrected at a lesser extent and should not pass the isolation criteria after correction).

This chapter describes how the correction is technically performed by the tool with a brief presentation of the performance results. The author was responsible for developing and validating the tool.

8.1 Correcting for the contributions of close-by objects

Contributions of signal close-by objects have to be removed from isolation variables. These correspond to the core energies of the objects, as defined in the previous chapters.

8.1.1 Calorimetric isolation

As a reminder, the topoetcone variables are calculated as follows [69]:

$$E_{\mathrm{T}}^{\mathrm{topocone}X}(\lambda) = E_{\mathrm{T}}^{\mathrm{topocone,\ raw}X}(\lambda) - E_{\mathrm{T}}^{\mathrm{topocore}}(\lambda) - E_{\mathrm{T}}^{\mathrm{corrections}X}\left(\eta^{\lambda}\right). \tag{8.1}$$

The two first components in the equation are calculated by summing up over the topoclusters close enough to the object λ. Since these two components are the dominating contributions to isolation, the influence of the last term (including the pile-up and leakage corrections) is not considered for the close-by correction. The core energy represents the contribution of an object in the calculation of the variables. Therefore, the energy of a close-by object λ' to be removed is set to the sum of the transverse energy E_{T}^{c} of the topoclusters c which are used for the calculation of both $E_{\mathrm{T}}^{\mathrm{topocone,\ raw}X}(\lambda)$ and $E_{\mathrm{T}}^{\mathrm{topocore}}(\lambda')$. The E_{T}^{c} of these topoclusters should be removed only once even if the topoclusters contribute to the core

energy of several close-by objects. Topolcusters have to be selected the same way as for the calculation of $E_{\mathrm{T}}^{\mathrm{topocone}X}$.

The correction to be applied can be summarised through this equation:

$$E_{\mathrm{T}}^{\text{close-by corr}}(\lambda) = \sum_{\substack{c, \\ \Delta R_{c,\lambda'} \leq \Delta R_{\mathrm{core}}, \\ \Delta R_{\mathrm{core}} \leq \Delta R_{c,\lambda} \leq \frac{X}{100}}} E_{\mathrm{T}}^{c}. \tag{8.2}$$

In order to properly perform the correction, information about topoclusters must be available.

8.1.2 Track-based isolation

The procedure is similar to that of the calorimetric isolation: the core energy $p_{\mathrm{T}}^{\mathrm{core}}$, which is subtracted in the calculation of the variables ptvarcone, is taken for the contribution of close-by objects. The track-based isolation of an object λ is calculated using [69]

$$p_{\mathrm{T}}^{\mathrm{varcone}X}(\lambda) = \sum_{\substack{t,\, t \neq \lambda \\ \Delta R_{t,\lambda} \leq \Delta R_{\mathrm{track}X}}} p_{\mathrm{T}}^{\mathrm{core}}(t), \tag{8.3}$$

where t is part of the set of tracks which pass the selection requirements (as described in the previous chapter) and $\Delta R_{\mathrm{track}X} = \min\left(\frac{k_T}{p_{\mathrm{T}}^{\lambda}}, \frac{X}{100}\right)$.

Using Eq. 8.3, the correction to be applied can easily be inferred:

$$p_{\mathrm{T}}^{\text{close-by corr}}(\lambda) = \sum_{\substack{\lambda', \\ \Delta R_{\lambda,t_{\lambda'}} \leq \Delta R_{\mathrm{track}X}}} p_{\mathrm{T}}^{\mathrm{core}}(t_{\lambda'}), \tag{8.4}$$

where λ' are the close-by objects, whose contributions have to be removed. Note that the track associated to these objects should also pass the quality requirements.

8.2 Software implementation

The algorithm performing the correction was developed as part of the `IsolationCloseByCorrectionTool` (member of the `IsolationSelection` package) and allows the user to calculate the correction to apply to the isolation variables, given a particular set of close-by objects. It is important to highlight that the user is responsible for choosing which objects should have their contributions removed, as this is very analysis-dependent. The tool will then take care of checking whether the selected objects pass the extra criteria (which are part of the definition of the isolation variables only and are therefore analysis-independent). Finally, the contributions will be subtracted where applicable and the isolation variables corrected. In the last step, the tests to determine whether the object passes the isolation cuts associated to the working point are checked a second time, taking the corrected isolation values as input.

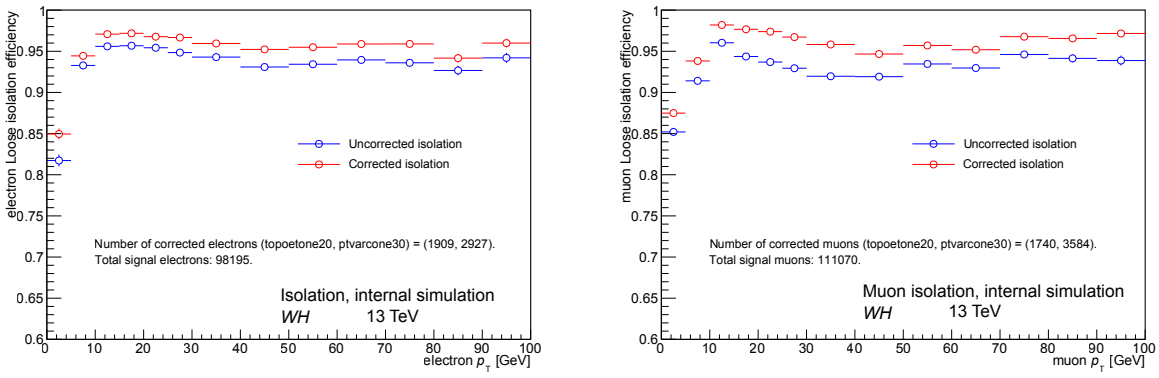

Figure 8.1 – Efficiencies of the *Loose* isolation working point [69] for (left) electrons and (right) muons, before and after correction for close-by objects, as a function of the transverse momentum [69].

8.3 Case of missing information from the topoclusters

For the calorimeter-based isolation, topocluster information is needed. If missing, models assuming a uniform density of the transverse energy of the topoclusters can be used, which do not require any additional information. Calculating the corrections using the topocluster information is precise, whereas models calculate estimates of the correction to apply [69, 87]. They are briefly described in App. B. So far, all users using the tool for close-by object correction decided to add topocluster information to their data files, avoiding the use of the models.

8.4 Performance

The validation is performed [69, 87] for muons and electrons using WH samples[1], where the Higgs boson is produced in association to a W boson, and decays to four leptons. 80000 events are processed. The choice of this set of samples is motivated by the abundance of muons and electrons close to each other.

Muons (electrons) having a truth type of 6 (2) are selected, which correspond to well-isolated objects. These objects both serve for the studied particles, as well as for the particles whose contributions have to be subtracted (close-by objects).

The following figures validate the functionalities of the tool performing the correction for close-by objects. For each particle (muon and electron), the efficiency of the *Loose* isolation working point [69] (using cuts on both calorimeter- and track-based isolations) is presented before and after applying the correction. Then, for the muons only, the distributions of the isolation variables before and after correction are compared (both in the case where the muon has a non-zero correction and for all muons without any distinction). An additional plot presents the comparison of the uncorrected isolation for muons which should not require any corrections (ΔR with the closest object greater than the isolation cone or muon alone in the event), with the corrected isolation for muons which should require correction. Ideally these two distributions should be quite close to each other.

[1] WH MC samples with ID 341964 (Pythia8EvtGen_A14NNPDF23LO)

8.4.1 The *Loose* isolation working point

To briefly validate the functionality of the tool which tells whether an object passes the cuts of an isolation working point after correction, the efficiencies of the *Loose* isolation working point are calculated before and after correction for electrons and muons. The results are shown in Fig. 8.1.

The corrected efficiency is higher, especially for muons. The correction affects more muons than electrons because they are intrinsically more isolated and the low efficiencies are due to the contribution of close-by objects. For electrons on the other hand the contribution of close-by objects does not play a major role in the activity around the electron.

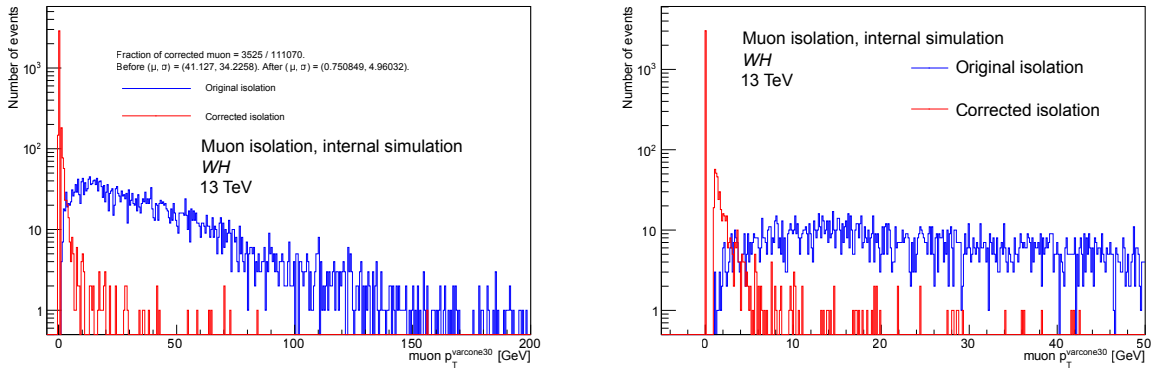

Figure 8.2 – Muon distribution of $p_{\mathrm{T}}^{\mathrm{varcone30}}$ before (blue) and after (red) correction for close-by objects [69]. Only muons for which the correction was not nil are selected. The right plot shows a view close to zero of the distribution presented in the left plot.

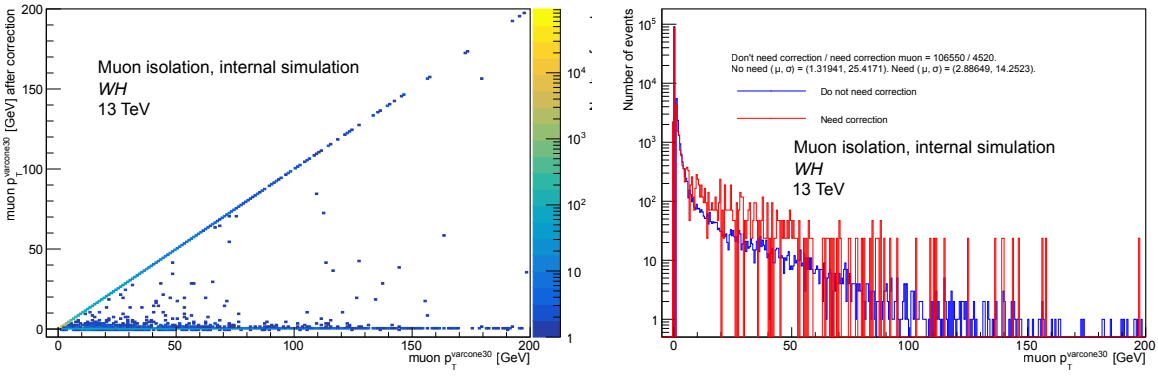

Figure 8.3 – The left plot shows the distribution of the $p_{\mathrm{T}}^{\mathrm{varcone30}}$ variable before (x axis) and after correction (y axis). The right plot shows the distributions of the uncorrected $p_{\mathrm{T}}^{\mathrm{varcone30}}$ of the muons for which no corrections are expected (blue) and the distribution of the corrected variable for muons whose correction may not be nil (red) [69].

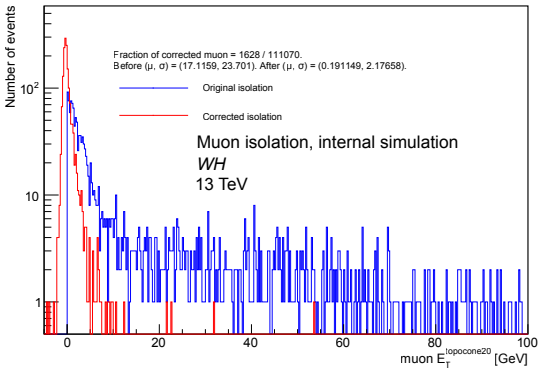

Figure 8.4 – Muon distribution of $E_{\mathrm{T}}^{\mathrm{topocone20}}$ before (blue) and after (red) correction for close-by objects [69]. Only muons for which the correction was not nil are selected.

8.4.2 Muon variables

In order to further validate the correction in the case of muons, the following variables were chosen for the study, representative to the ones used for the isolation working points: ptvarcone30 and topoetcone20.

Figures 8.2 (ptvarcone30) and 8.4 (topoetcone20) present the distribution before and after applying the correction, for muons for which the correction applied is not nil. A zoom is proposed close to zero to check the behaviour of the corrected variable: the absence of negative values for ptvarcone30 indicates that the correction may not be overestimated. For topoetcone20, the conclusion is less significative (because of the pile-up correction the presence of negative values is possible), but the peak of the corrected isolation is close to zero, which is the behaviour expected.

Figures 8.3 (ptvarcone30) and 8.5 (topoetcone20) give more information on the correction. In the left figures, the comparison of the variable after correction (y axis) and before (x axis) is presented in a two-dimensional graph, in which all muons are included. The diagonal indicates muons for which the correction is nil, whereas the low tail provides an idea of the impact of the correction. This tail should not go to negative values for ptvarcone30. On the right figures, the uncorrected isolation variable is plotted in blue for muons whose correction should be nil ($\Delta R_{\lambda,\lambda'}$ greater than the isolation cone size, or muon alone in the event), whereas the corrected isolation variable is plotted in red for muons whose correction may not be nil ($\Delta R_{\lambda,\lambda'}$ less than the isolation cone size). Ideally the red distribution should look really similar to the blue one, indicating that the correction is able to remove the unwanted close-by contributions.

8.4.3 Conclusions

The behaviour of the corrected variables is as expected both for electrons and muons (similar checks as for the muon variables were performed for electrons, but are not presented in this chapter). Corrected distributions look very close to the uncorrected distributions in the case no correction should be needed.

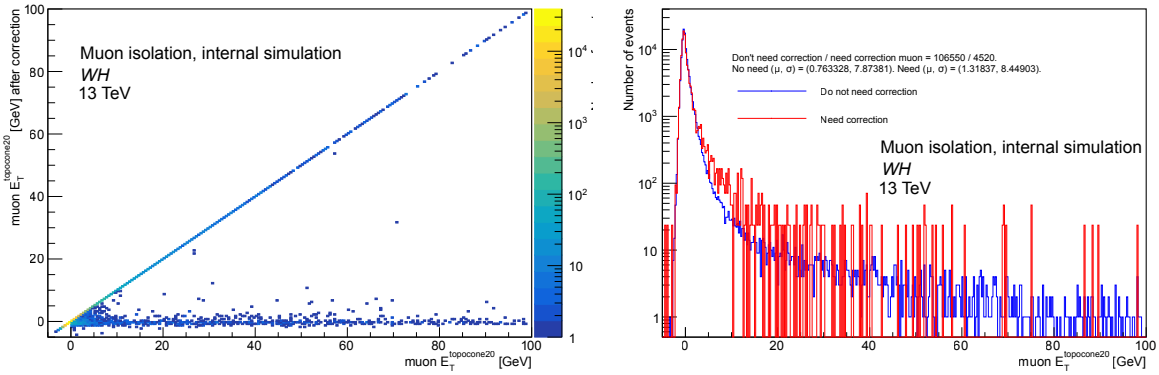

Figure 8.5 – The left plot shows the distribution of the $E_{\mathrm{T}}^{\mathrm{topocone20}}$ before (x axis) and after correction (y axis). The right plot shows the distributions of the uncorrected $E_{\mathrm{T}}^{\mathrm{topocone20}}$ of the muons for which no corrections are expected (blue) and the distribution of the corrected variable for muons whose correction may not be nil (red) [69].

Part III

Production cross-section of the Higgs boson decaying into four leptons

Chapter 9

Introduction

The Standard Model (SM) has been extremely successful in describing particle interactions. The missing piece, the Higgs boson as a manifestation of the Higgs field giving mass to other particles, was discovered by CMS [20] and ATLAS [21] in Run 1, mainly through the $H \to \gamma\gamma$ and $H \to ZZ^* \to 4\ell, \ell \in \{e, \mu\}$ decay channels. Studies on the properties of this new particle (mass [88, 89], spin-parity [90, 91, 92, 93], Higgs couplings to fermions, production cross section and decay branching ratios [94, 95, 96, 97, 98, 99, 100, 101]) were assessed using Run 1 data recorded by the two experiments. This huge effort by the two collaborations enabled the Higgs boson to be characterised as the missing particle predicted by the Standard Model.

With collisions delivered by the LHC at higher instantaneous luminosities and centre-of-mass energies, Run 2 offers a unique chance to further improve the general knowledge of the Higgs boson. In this context, precision measurements of the parameters of the Standard Model are performed benefiting from the increased statistics of the data collected by the two experiments. These measurements can refine the current knowledge and highlight possible deviation from prediction indicating new physics, providing state-of-the-art results at higher centre-of-mass energy of $\sqrt{s} = 13\,\text{TeV}$.

In this scope, this thesis reports the studies of the Higgs-boson-to-four-lepton production cross section using data collected by the ATLAS collaboration during early Run 2 (years 2015 and 2016 corresponding to $36.1\,\text{fb}^{-1}$). The $H \to ZZ^* \to 4\ell$ decay channel offers a high sensitivity thanks to low background yields and good detector resolution. Measurements performed in Run 1 are already superseded and Run 2 results include (double-)differential cross sections.

After a summary of the Standard Model and an introduction to the Higgs mechanism described in Chap. 10, the general analysis strategy of the Higgs-boson-to-four-lepton channel is outlined in Chap. 11, presenting the event and background yields observed in Run 2. Finally, Chap. 12 focuses on the methodology of the measurements of the production cross section, including the results using $36.1\,\text{fb}^{-1}$ collected in Run 2.

The author took part in improving the selection criteria of the Higgs-to-four-lepton channel, as well as measuring its production cross section, with the implementation of the fiducial space and the calculation of the acceptance and correction factors.

Chapter 10

The Higgs boson in the Standard Model

The phenomena governing particle interactions are described in a commonly accepted frame, the so-called Standard Model (SM). This model combines the electroweak (EW) theory of Glashow [102], Weinberg [103] and Salam [104], with quantum chromodynamics (QCD) and quantum electrodynamics (QED). The overall framework includes four forces (the strong interactions described by QCD, the electromagnetic interactions described by QED, the weak charged and weak neutral interactions), which correspond to interactions between particles through the mediation of bosons. All the elementary particles composing the universe are classified in this model.

The SM was developed in various steps during the last fifty years and its current formulation was finalised in the mid-seventies after the experimental confirmation of the existence of the quarks. Following this, other particles predicted by the model were experimentally discovered, such as the top quark and the τ neutrino. The Higgs boson completed the frame in 2012, establishing the successfulness of the model. The SM is perturbative at sufficiently high energies and can be renormalised thanks to its gauge invariance [105], which enables calculations to be developed at any orders. These calculations could be verified by experiments with a great precision, notably the properties of the weak neutral current and the W and Z bosons.

However, the model suffers from limitations. Indeed, it fails to clearly explain the mechanism responsible for the baryon asymmetry and the abundance of matter over antimatter (CP violation), it does not include gravity, nor does it give an origin to dark matter (four times more abundant than matter). The number of free parameters of the model can also be unsatisfactory, due to the large variations in the values measured (from the mass of the electron of about 0.5 MeV to the mass of the heaviest quark close to 173 GeV), which can fundamentally change the description of particle processes.

10.1 The electromagnetic, strong and weak interactions

10.1.1 From the Dirac equation to the photon

According to the SM, the elementary constituents composing matter are point like spin-half particles named fermions. Their wave function, using the four component spinor $\psi(x)$ and the Dirac notations, is governed by the Dirac equation, which describes the free motion of a particle

$$(i\gamma^{\mu}\partial_{\mu} - m)\,\psi(x) = 0, \tag{10.1}$$

where x denotes the space-time coordinates of the particle, γ^μ are the Dirac matrices and m is the mass of the fermion. A corresponding Lagrangian can be expressed as

$$L_{\text{QED, free}} = i\bar{\psi}(x)\gamma^\mu\partial_\mu\psi(x) - m\bar{\psi}(x)\psi(x), \tag{10.2}$$

where $\bar{\psi}$ is the conjugate of ψ. Reading this equation, the fermionic field creates and annihilates fermions ($\psi(x)$) and anti-fermions ($\bar{\psi}(x)$).

To introduce interactions between fermions, the gauge principle is invoked. According to this principle, the underlying physics remains unchanged under local phase transformations of the fields. In other words, different configurations of the same observable field $\psi(x)$ have to lead to the same observable quantities. Therefore, redefining $\psi(x)$ with $\psi(x) \mapsto \psi'(x) = e^{i\theta(x)}\psi(x)$, where $\theta(x)$ describes the transformation ($U(1)$ symmetry), should not affect the Lagrangian by more than a total derivative of a function of x. The current expression of $L_{\text{QED, free}}$ in Eq. 10.2 does not satisfy this requirement.

Adding a spin-one field $A_\mu(x)$, which transforms as $A_\mu(x) \mapsto A'_\mu(x) = A_\mu(x) - \frac{1}{Q}\partial_\mu\theta(x)$ under the same $U(1)$ symmetry, can overcome this problem. Redefining the derivative ∂_μ by the covariant derivative $D_\mu(x) : \psi(x) \mapsto [\partial_\mu + iQA_\mu(x)]\,\psi(x)$, the new version of the Lagrangian can be written as

$$L_{\text{QED}} = i\bar{\psi}(x)\gamma^\mu D_\mu\psi(x) - m\bar{\psi}(x)\psi(x) = L_{\text{QED, free}} - QA_\mu\bar{\psi}(x)\gamma^\mu\psi(x), \tag{10.3}$$

which is invariant under $U(1)$ transformations.

In this new expression, the fermionic field is coupled to the vector field A_μ. In order to comply with the formalism of Maxwell, a kinetic term $-\frac{1}{4}F^{\mu\nu}F_{\mu\nu}$ can be added to the Lagrangian, where $F^{\mu\nu} = \partial^\mu A^\nu - \partial^\nu A^\mu$. The strength of this new interaction is proportional to Q, which can be interpreted as a charge. The two fields are therefore identified to the electron and a gauge boson, the photon. The later is massless, as no mass terms appear in the Lagrangian.

The Lagrangian L_{QED} is the ground of the theory of Quantum Electrodynamics (QED), which has been comforted with experimental data. An example of this achievement is the prediction of the value of the gyromagnetic ratio g, which appears in the calculation of the magnetic momentum of the electron [106]. Whereas a classical calculation leads to a value of 1, the Dirac formalism was capable of predicting a value close to 2, in very good agreement with the measurements carried out at the time. The inclusion of higher order calculations provide a value of g (which slightly differs from 2) with an agreement to the experiments up to the twelfth digit.

10.1.2 The strong interactions

By analogy to QED, the quantum chromodynamics (QCD) theorise the existence of the mesons (bosons) and baryons (fermions) composed of elementary components, the quarks (q). These are charged and are attributed a quantum number, the colour (red, green, blue). In this system, baryons and mesons are colour-singlet combinations of $qq'q''$ or $q\bar{q'}$, respectively, where q, q' and q'' are quarks (of various flavours).

In order to describe the interactions between quarks, the gauge principle is once more used, but for $SU(3)$. The Lagrangian of a free quark is derived as

$$L_{\text{QCD, free}} = \sum_f \bar{q}_f \left(i\gamma^\mu\partial_\mu - m_f\right) q_f, \tag{10.4}$$

where the sum is over the six flavours $f \in \{rgb, rbg, gbr, grb, brg, bgr\}$ of the quarks $q_f = \left(r_f\, g_f\, b_f\right)$ (r, g, b are the red, green and blue components, respectively). m_f is the mass of the quark. In order to abide

Table 10.1 – Properties of the quarks [107].

Generation	Flavour	Charge (e)	Mass (MeV)
I	u	2/3	2.3
	d	−1/3	4.8
II	c	2/3	1275
	s	−1/3	95
III	t	2/3	123.21×10^3
	b	−1/3	4.18×10^3

by the gauge invariance, gauge bosons referred to as gluons (g), are introduced and the Lagrangian takes the final form of

$$L_{\text{QCD}} = L_{\text{QCD, free}} - g_{\text{s}} G_a^{\mu} \sum_f \bar{q}_f^{\alpha} \gamma_{\mu} \left(\frac{\lambda^a}{2} \right)_{\alpha\beta} q_f^{\beta} - \frac{1}{4} G_a^{\mu\nu} G_{\mu\nu}^a, \tag{10.5}$$

where g_{s} is the strength of the interaction (equivalent to Q for QED, it is universal for all the quark flavours), λ_a are the matrices of $SU(3)$ which account for the interactions between the quarks and the gluon field G_a^{μ}. Finally, the last component is the kinetic term for the gluon field, with $G_a^{\mu\nu} = \partial^{\mu} G_a^{\nu} - \partial^{\nu} G_a^{\mu} - g_{\text{s}} f^{abc} G_b^{\mu} G_c^{\nu}$, where f^{abc} are the structure constants of $SU(3)$.

There are eight generators of $SU(3)$, each one corresponding to a gluon. These also carry colour charge, since the group is non Abelian. They can therefore interact with each other and give rise to bound-states instead of free quarks (also referred to as quark confinement).

10.1.3 The electroweak sector

Having introduced electromagnetic and weak interactions, this last paragraph presents the weak sector, which will be completed with the Higgs mechanism in the next section. The theory behind the weak interactions was motivated by various experimental observations, such as the decays of charged pions, muons and neutrons. The strength of these decays was found to be universal. The decays involved the chirality of the fermions (left-handed for fermions, and right-handed for anti-fermions), which describes the way the particle transforms in the Poincaré group, as well as charged current interactions (transitions down-up quarks, and leptons and their corresponding neutrinos, as summarised in Tab. 10.1 and Tab. 10.3). Neutrinos can also interact with neutral current with fermions, preserving flavour.

Following up these experimental facts, both these weak interactions were combined into the $SU(2)_L$ (L refers here to the left-handed fields), following the same reasoning developed for the strong sector.

The partition between electroweak and strong sectors drives the organisation of elementary particles. Leptons only interact electroweakly: e, μ, τ (charged particles, ordered by increasing masses) and their corresponding down partners ν_e, ν_{μ}, ν_{τ} (neutrinos, massless in the original formulation, and neutral). Quarks strongly interact: u, c, t (charged $\frac{2}{3}$, ordered by increasing masses), and their down partners d, s, b (charged $\frac{-1}{3}$, also ordered by increasing masses). Each particle has an anti-particle with the same properties, but opposite charge. This organisation allows the left-handed fermions to be doublets, while the right-handed partners transform as singlets under $SU(2)_L$ (right-handed neutrinos are not included in the SM).

The doublets and singlets are noted

$$\mathfrak{L}^i = \begin{pmatrix} \psi_L^i \\ \psi'^i_L \end{pmatrix} \quad \psi_R^i \;\; \psi'^i_R, \tag{10.6}$$

where i indexes the generation in the triplets and ψ (ψ') refers to the up (down) partners. This notation is valid for both the leptons (l) and the quarks (q). The Lagrangian can be written as (based on the Dirac's Lagrangian)

$$L_{\text{EW, free}} = \sum_{q,l} \sum_{i=1}^{3} \left(\bar{\mathfrak{L}^i} i\gamma^\mu \partial_\mu \mathfrak{L}^i + \bar{\psi_R^i} i\gamma^\mu \partial_\mu \psi_R^i + \bar{\psi'^i_R} i\gamma^\mu \partial_\mu \psi'^i_R \right). \tag{10.7}$$

This Lagrangian assumes the fermions have no mass (if the masses would have been included, they should have been equal, which contradicts experimental measurements). It is invariant under a global $SU(2)_L$ transformation. To have an invariance under local transformations (x dependent), the formalism developed for the $SU(3)$ group of the QCD can be transposed, and gauge bosons are generated introducing the covariant derivative

$$D_\mu = \partial_\mu + i g_{\text{w}} \frac{\sigma_a}{2} W_\mu^a, \tag{10.8}$$

where σ_a are the three Pauli matrices, which relate to the generators T_a of the $SU(2)_L$ group through $T_a = \frac{1}{2}\sigma_a$, and g_{w} is the weak coupling constant. There are therefore three gauge bosons denoted W_a. The resulting charged bosons are a combination of the gauge bosons ($a \in \{1, 2\}$) $W_\mu^\pm = \frac{1}{\sqrt{2}} \left(W_\mu^1 \mp i W_\mu^2 \right)$ and mediate the charged currents. The neutral current cannot be directly related to W_3, as it would have to possess the same structure as the charged currents. This is forbidden by experimental measurements of the cross-section of the process $\bar{\nu}_\mu N \to \bar{\nu}_\mu X$, which turned out to be about a third of that of $\bar{\nu}_\mu N \to \mu^+ X$, where μ denotes the muon, N and X represent a nucleus and its remaining after the decay, respectively.

To overcome this difficulty, Glashow, Salam and Ward (1964) enlarged the gauge group from $SU(2)_L$ to $SU(2)_L \otimes U(1)_Y$, where Y denotes the new introduced quantum number, the weak hypercharge. The unification of the electromagnetism and the weak interaction (the former is independent upon the chirality, but the latter is) was possible with the following relationship, which unifies the currents $Q = T_3 + \frac{Y}{2}$, where T_3 are the eigenvalues of the third generator of the $SU(2)_L$ group. Two Lagrangians can then be derived (for doublets and singlets), adding the interaction terms coming from the covariant derivatives:

$$\begin{aligned} \mathfrak{L}: \quad & D_\mu = \partial_\mu + i g_{\text{w}} T_i W_\mu^i + i g \tfrac{Y}{2} B_\mu, \\ \psi_R, \psi'_R: \quad & D_\mu = \partial_\mu + i g \tfrac{Y}{2} B_\mu, \end{aligned} \tag{10.9}$$

where B_μ is the gauge boson of $U(1)_Y$ and g is the corresponding coupling constant.

The resulting Lagrangian is written as the sum of the free Lagrangian and the interaction term

$$L_{\text{EW}} = L_{\text{EW, free}} + L_{\text{int}}, \tag{10.10}$$

where

$$\begin{aligned} L_{\text{int}} = -\sum_{f \in \{q,l\} \times [\![1,3]\!]} \quad & \tfrac{g_{\text{w}}}{\sqrt{2}} \bar{\mathfrak{L}} \gamma^\mu T_+ \mathfrak{L} W_\mu^+ + \tfrac{g_{\text{w}}}{\sqrt{2}} \bar{\mathfrak{L}} \gamma^\mu T_- \mathfrak{L} W_\mu^- + \\ & g_{\text{w}} \bar{\mathfrak{L}} \gamma^\mu T_3 \mathfrak{L} W_\mu^3 + g \bar{\mathfrak{L}} \gamma^\mu \tfrac{Y}{2} \mathfrak{L} B_\mu + \\ & g \bar{\psi_R} \gamma^\mu \tfrac{Y}{2} \psi_R B_\mu + g \bar{\psi'_R} \gamma^\mu \tfrac{Y}{2} \psi'_R B_\mu, \end{aligned} \tag{10.11}$$

where the notation $T_\pm$ follows the same logics as for $W^\pm$.

From this expression, it is possible to couple the bosons using the Weinberg angle θ_w

$$\begin{pmatrix} A_\mu \\ Z_\mu \end{pmatrix} = \begin{pmatrix} \cos\theta_w & \sin\theta_w \\ -\sin\theta_w & \cos\theta_w \end{pmatrix} \begin{pmatrix} B_\mu \\ W_\mu^3 \end{pmatrix}. \tag{10.12}$$

From this angle, the coupling constant of the electromagnetism and the neutral current can be derived: $e = \frac{g_w g}{\sqrt{{g_w}^2+g^2}}$, $g_{nc} = \frac{g_w}{\cos\theta_w}$. The angle can be calculated through $\cos\theta_w = \frac{g_w}{\sqrt{{g_w}^2+g^2}}$ and $\sin\theta = \frac{g}{\sqrt{{g_w}^2+g^2}}$.

Due to the fact the group is not Abelian, the theory predicts interactions between the gauge bosons. Although this Lagrangian incorporates charged and neutral interactions (weak sector) and electromagnetism (QED introduced formerly), it fails to predict the mass of the fermions and the bosons. Indeed, any mass terms added to the Lagrangian would violate the gauge symmetry.

10.2 The Higgs mechanism

After the work carried out in the late fifties on symmetry breaking in superconductivity and a paper of Yoichiro Nambu discussing its application to particle physics, Philipp Warren Anderson [108] proposed a mechanism introducing symmetry breaking to particle interactions. Following this proposal, a theory explaining mass generation without breaking the gauge principle within the SM was published almost simultaneously by three independent groups in 1964: Robert Brout and François Englert [17]; Peter Higgs [18]; and Gerald Guralnik, C. R. Hagen, and Tom Kibble [19]. This corresponds to the so-called Higgs mechanism.

10.2.1 The Higgs potential

A doublet of complex scalar fields $\Phi(x)$ and the associated potential $V(\Phi)$

$$\Phi(x) = \begin{pmatrix} \phi^+(x) \\ \phi^0(x) \end{pmatrix} = \begin{pmatrix} \frac{1}{\sqrt{2}}(\phi_1 + i\phi_2) \\ \frac{1}{\sqrt{2}}(\phi_3 + i\phi_4) \end{pmatrix}, V(\Phi) = \mu^2\Phi^\dagger\Phi + \lambda\left(\Phi^\dagger\Phi\right)^2, \tag{10.13}$$

were considered, where $\{\phi_i\}_i$ are real scalar fields. The form of the potential is appropriate to generate the spontaneous symmetry breaking and has to respect gauge invariance and has to allow renormalisation. In order to enable minima, λ has to be positive. Due to the positively defined derivative terms of the Hamiltonian introduced by V, the minimal solution has to consist in fixed fields ϕ^0 and ϕ^+.

10.2.2 The ground state

In the case of $\mu^2 \geq 0$, the minimum is reached for $\phi^0 = 0$ and $\phi^+ = 0$. The ground states do not allow spontaneous symmetry breaking. On the other hand, if $\mu^2 < 0$, the non zero minima verify

$$|\Phi|^2 = \sum_{i=1}^{4} {\phi_i}^2 = \frac{-\mu^2}{\lambda} \equiv v^2. \tag{10.14}$$

There is an infinity of ground states as presented in Fig. 10.1, but the component ϕ^+ carries an electrical charge, and since the vacuum in the universe is neutral, it is consistent to choose $\phi^+ = 0$. The choice of $\phi_4 = 0$ is motivated by the preservation of the $U(1)_Q$ gauge invariance, as well as ensuring the photon stays massless. The resulting Lagrangian remains invariant under $SU(2)_L \otimes U(1)_Y$ transformations, but

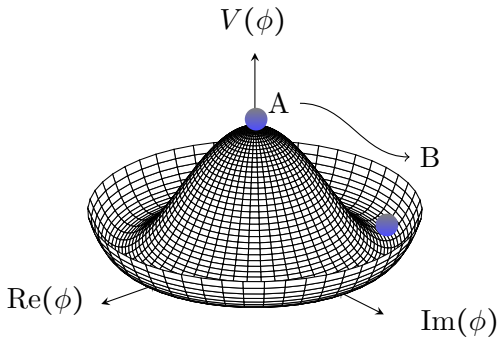

Figure 10.1 – Plot of the Higgs potential in the case $\mu^2 < 0$. There is an infinity of ground states. In A, the global symmetry remains unbroken. But once a local minimum was chosen (B), the spontaneous symmetry breaking occurs and both fermions and bosons can acquire masses [109].

the choice of a particular value for the ground state breaks the symmetry and violates both $SU(2)_L$ and $U(1)_Y$ symmetries, because $\sigma_i \phi_{\text{ground state}} \neq 0$ for $i \in [\![1,3]\!]$, as well as $Y\phi_{\text{ground state}} \neq 0$. However, the choice of this ground state satisfies $Q\phi_{\text{ground state}} = (\sigma_3 + Y)\,\phi_{\text{ground state}} = 0$. This last property ensures that the vacuum remains neutral.

The theory can be developed in the vicinity of this ground state

$$\Phi(x) = e^{i\theta^a(x)\sigma_a} \begin{pmatrix} 0 \\ \frac{1}{2}(v + h(x)) \end{pmatrix}, \tag{10.15}$$

where a loops over the three generators, and $\{\theta_a\}_a$ and h are scalar fields. Due to the invariance of $SU(2)$, it is possible to choose $\theta_a = 0$. The Goldstone theorem states that there should be as many Goldstone bosons as the number of broken generators (three in this case, as Q remains unbroken). Therefore, a mechanism was proposed to eliminate the three non-physical massless Goldstone bosons (which had not been observed in experimental data).

10.2.3 The vacuum expectation value

Imposing the local invariance requires the introduction of the covariant derivative $D_\mu = \partial_\mu + ig_{\text{w}} T_i W_\mu^i + ig\frac{Y}{2} B_\mu$. All the other fields of the theory (W_μ and ψ), which are sensitive to rotations because of their spin, have to vanish in the vacuum (in average) to avoid space rotation to be broken. Note that the new scalar field Φ has non zero average in the vacuum, since $\langle 0 | \Psi | 0 \rangle = \frac{v^2}{2}$. Therefore, the field is fixed and present in the vacuum and its quanta are represented by the excitation of the vacuum with $h(x)$, associated to the particle, referred to as the Higgs boson. v is called the vacuum expectation value.

10.2.4 Generation of the boson masses

Injecting the field Φ into the equation of the Lagrangian (and omitting the trilinear and quadrilinear terms), the following expression is obtained:

$$\begin{aligned} L^{\Phi}_{\text{EW, no tri, no quad}} = \; & \tfrac{1}{2}\left(\partial_\omega h \partial^\omega h + 2\mu^2\right) \\ & -\tfrac{1}{4}({W^-}_{\omega\iota})^\dagger W^{-\omega\iota} + \tfrac{1}{2}\left(\tfrac{g_\text{w} v}{2}\right)^2 ({W^-}_{\omega})^\dagger W^{-\omega} \\ & -\tfrac{1}{4}({W^+}_{\omega\iota})^\dagger W^{+\omega\iota} + \tfrac{1}{2}\left(\tfrac{g_\text{w} v}{2}\right)^2 ({W^+}_{\omega})^\dagger W^{+\omega} \\ & -\tfrac{1}{4} Z_{\omega\iota} Z^{\omega\iota} + \tfrac{1}{2}\left(\tfrac{g_\text{w} v}{2\cos\theta_\text{w}}\right)^2 Z_\omega Z^\omega \\ & -\tfrac{1}{4} A_{\omega\iota} A^{\omega\iota} \\ & +\tfrac{{g_\text{w}}^2 v}{2} h {W^-}_\omega W^{+\omega} + \tfrac{{g_\text{w}}^2}{4} h^2 {W^-}_\omega W^{+\omega} + \tfrac{{g_\text{w}}^2 v}{4\cos^2\theta_\text{w}} h Z_\omega Z^\omega + \tfrac{{g_\text{w}}^2}{8\cos^2\theta_\text{w}} h^2 Z_\omega Z^\omega \\ & +\tfrac{\mu^2}{v} h^3 + \tfrac{\mu^2}{4v^2} h^4. \end{aligned} \tag{10.16}$$

If the Euler-Lagrange formulae are applied to each line, the Klein-Gordon equations can be retrieved and the mass terms can be identified. It is therefore possible to infer $m_H = \sqrt{2\lambda} v$, $m_W = m_{W^-} = m_{W^+} = \frac{g_\text{w} v}{2}$, $m_Z = \frac{m_W}{\cos_\text{w}}$ and $m_\gamma = 0$. Taking into account the Fermi constant G_F, the value of v can be determined $v^2 = \frac{1}{\sqrt{2} G_F}$.

Thanks to the gauge principle, it is possible to absorb the three non-physical Goldstone bosons into the longitudinal components of the $W^\pm$ and the Z. The mass terms of the fermions do not violate the gauge symmetry, as they are allowed thanks to the scalar field Φ. These mass terms take a form $-\frac{1}{2}(v+h)\frac{\sqrt{2} m_f}{v}\bar{\psi}_f \psi_f$, where m_f are the masses of the fermions, which are free parameters of the theory, and ψ_f is the fermionic field.

10.3 Inclusion of the Higgs mechanism to the Standard Model

Summarising the different groups introduced in the previous paragraphs, the Standard Model takes into account the strong and electroweak interactions with $SU3_C \otimes SU2_L \otimes U(1)_Y$. The first subgroup is related to the colour charges of quarks and gluons, while the remaining groups relate to weak left-handed ispospin and hypercharge Y. With the introduction of the Higgs mechanism, the electroweak symmetry is spontaneously broken into the electromagnetic $U(1)_Q$ group.

Four vector bosons mediate the electroweak interactions, the photon, the $W^\pm$ and Z bosons. The Higgs mechanism allows the three bosons to acquire masses, whereas the photon remains massless. The masses of these bosons are input parameters of the model and have been determined by experimental measurements, as indicated in Tab. 10.2. To these four bosons, the Standard Model adds the Higgs particle, a scalar boson appearing as an interaction of the field Φ with itself or with the other particles, whose mass was recently determined experimentally. The strong sector is composed of eight gluons which rule the interactions between the quarks.

Similarly to the vector bosons, the quarks and the leptons acquire masses through the Higgs mechanism and their masses are also free parameters of the SM. The resulting factors $\frac{\sqrt{2} m_f}{v} = \lambda_f$ are referred to as the Yukawa couplings and have to be determined experimentally. The values of the masses are given in Tab. 10.3. An important aspect concerning the quarks is that the mass eigenstates do not correspond to the eigenstates of the group. Indeed whereas the weak eigenstates propagate through electroweak interactions, the mass eigenstates, taking part in the QCD, are a mixture of the former. Weak and mass

Table 10.2 – Properties of the bosons [107].

Boson	Charge (e)	Mass (GeV)	Interaction
g	0	0	strong
γ	0	0	electromagnetic
$W^{\pm}$	± 1	80.385	weak
Z	0	91.188	weak

Table 10.3 – Properties of the leptons [107].

Generation	Flavour	Charge (e)	Mass (MeV)
I	e	-1	0.511
	ν_e	0	$< 2 \times 10^{-3}$
II	μ	-1	105.66
	ν_μ	0	$< 2 \times 10^{-3}$
III	τ	-1	1776.82
	ν_τ	0	$< 2 \times 10^{-3}$

eigenstates are related to each other with the Cabbibo-Kobayashi-Maskawa (CKM) matrix:

$$\begin{pmatrix} d' \\ s' \\ b' \end{pmatrix} = \begin{pmatrix} V_{ud} & V_{us} & V_{ub} \\ V_{cd} & V_{cs} & V_{cb} \\ V_{td} & V_{ts} & V_{tb} \end{pmatrix} \begin{pmatrix} d \\ s \\ b \end{pmatrix}, \tag{10.17}$$

where d', s' and b' are the weak eigenstates, and d, s, b are the mass eigenstates. The CKM matrix is unitary (and can be defined using only four parameters). The matrix is almost diagonal according to experimental measurements. This distinction between mass states and eigenstates explain why the transitions $u \to s$ are possible, while $\mu \to e$ are forbidden. A similar matrix (PNMS, Pontecorvo–Maki–Nakagawa–Sakata matrix) is also introduced to give mass to neutrinos, which enables their oscillations between the various mass states.

In the end, the SM has eighteen free parameters decomposed as follows: nine fermion masses (Yukawa couplings), four CKM parameters, three couplings and two parameters for the scalar sector. The mass of the Z boson was determined at LEP and SLD, decays of $Z \to e^+e^-$ allowed α_s to be determined at m_Z (QCD coupling), the fine structure constant α was measured using the quantum Hall effect [107], the Fermi constant G_F was measured using muon decays [110], and the Higgs mass was measured at CERN [89].

All the observables can be predicted from these eighteen parameters and precision can be improved including more loop diagrams into the computation, thanks to the renormalisabielity of the SM (perturbation theory). Measurements of these observables can therefore test the validity of the model and extensive studies were carried out, as for example the mass and the width of the W boson, the widths

(total and partial) of the Z boson [111, 112, 113], and the recent discovery of the missing particle, the Higgs boson. So far the agreement between data and prediction is good for all the energies probed.

10.4 The Higgs discovery

In this section, the history of the Higgs discovery is outlined. After a brief summary of the various constraints which have been set on the mass m_H of the Higgs boson over the years, the conditions of the discovery are detailed.

10.4.1 Constraints on the mass of the Higgs boson

Before the discovery of the Higgs boson, constraints on the mass were set from theoretical and experimental arguments.

Theoretical constraints

Perturbative calculations, on which the SM is based, are valid at limited energy ranges. These limitations prevent the Higgs mass to have too large values, in which case new phenomena, which are not covered by the SM, would have to be introduced in order to restore the perturbative expressions of the Lagrangian.

A first constraint is obtained from the scattering of the W boson ($W^+W^- \to W^+W^-$), which obeys unitarity and involves exchanges of Z, γ and eventually H. If m_H were greater than 870 GeV, the Higgs boson could not act as a propagator of the W scattering and the associated cross-section would diverge at high orders and high centre-of-mass energies, unless a new mechanism (beyond the SM) were introduced.

According to the theory, the parameter λ in the definition of the Higgs potential in Eq. 10.13 increases with the energy of the process under study. Therefore, a cut-off scale Λ has to be introduced to keep the calculations convergent, above which the expression of the potential cannot be used for the physics processes. Above Λ, new physics are supposed to arise in order to retrieve finite values of the corresponding cross sections. Assuming the SM remains valid up to 10^{16} GeV, which corresponds to the order of the Fermi constant, masses above 200 GeV are not allowed. However, for the sole electroweak scale, this limit (referred to as the triviality limit) rises up to 1 TeV.

Lastly, a limit is set from the Higgs boson self-coupling, called the vacuum stability bound. This coupling depends on the fermion and gauge boson loop diagrams. The most important contribution arises from the top quark, and has a negative sign which directly influences the value of λ, parameter of the Higgs potential. If m_H were too low, this would lead to $\lambda < 0$ and the Higgs mechanism would not be able to explain the spontaneous symmetry breaking, as a local minimum. The minimal value of the mass which enables λ to remain positive depends on the cut-off scale Λ.

Taking into account the triviality limit and the vacuum stability limit, the possible values of m_H can be calculated, as presented in Fig. 10.2, where the two limits (triviality bound in red, and stability bound in green) are given as a function of Λ. Note that the limits converge for high cut-off due to more and more stringent conditions on the convergence of the terms. More information concerning these limits can be found in Ref. [114].

Experimental constraints

Observations from experiments at the Stanford Linear Collider (SLC) [115] at SLAC, at the Large Electron-Positron Collider (LEP) [116] at CERN and at the Tevatron [2] at Fermilab complemented

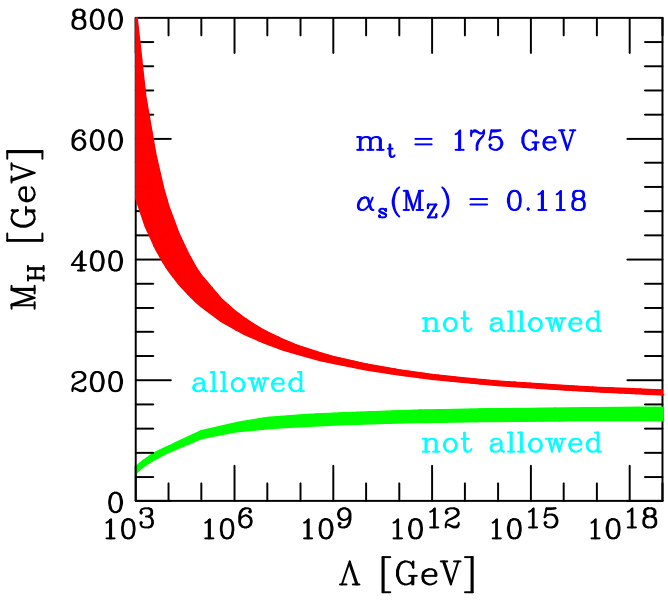

Figure 10.2 – Theoretical limits on m_H taking into account the triviality bound (red curve) and the vacuum stability bound (green curve). The bands indicate the uncertainties. The allowed values of m_H lie between the two curves [114].

the theoretical constraints on the mass of the Higgs boson. The constraints were obtained from measurements of other parameters of the SM (indirect constraints) or from direct searches of the Higgs boson (direct constraints).

Indirect constraints. Using the fact that the Higgs mechanism enters radiative corrections of the electroweak sector, precise measurements of the electroweak couplings and the masses of W and Z bosons, as well as their widths, can constrain the mass range of the Higgs boson. The combination in a global fit of the various electroweak precision measurements obtained at SLC, LEP ad Tevatron, as shown in Fig. 10.3(a), lead to the constraints presented in Fig. 10.3(b). This second figure also gives the $\Delta\chi^2$ distribution of the fit as a function of m_H. The most probable value (minimum of the parabola) stands at $m_H = 114^{+69}_{-45}$GeV. The lower values are excluded, as represented by the yellow area. The same combination allowed an upper limit to be set, with a 95% confidence level of $m_H < 260\,\text{GeV}$ [117].

Direct constraints. Direct searches of the Higgs boson were performed at LEP and Tevatron. The measurements at the LEP were capable to set that $m_H > 114.4\,\text{GeV}$ at 95% confidence level [118], as shown in Fig. 10.4(a). The Tevatron experiments alone were able to set limits of $90 < m_H < 109\,\text{GeV}$ and $149 < m_H < 182\,\text{GeV}$ at 95% confidence level [119] (Fig. 10.4(b)).

10.4.2 The discovery of the Higgs boson

Following the direct searches performed by LEP and Tevatron, the LHC was capable to deliver enough luminosity during Run 1 to the two dedicated experiments ATLAS and CMS, and a new particle was discovered in July 2012 [20, 21], compatible with the Higgs boson of the SM. The additional assessment of its properties confirmed its consistence as part of the Higgs mechanism, being a scalar boson [120, 121, 90, 122] with a mass of $m_H = 125.09 \pm 0.21(\text{stat.}) \pm 0.11(\text{syst.})\text{GeV}$ [89].

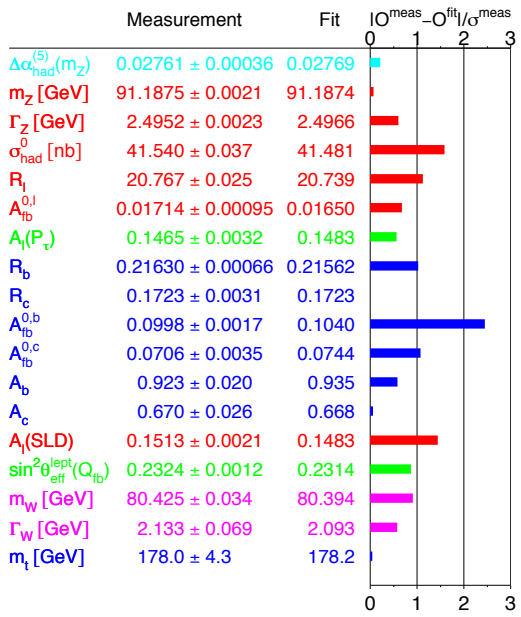

(a) Electroweak precision measurements from experiments at the LEP, SLC and Tevatron.

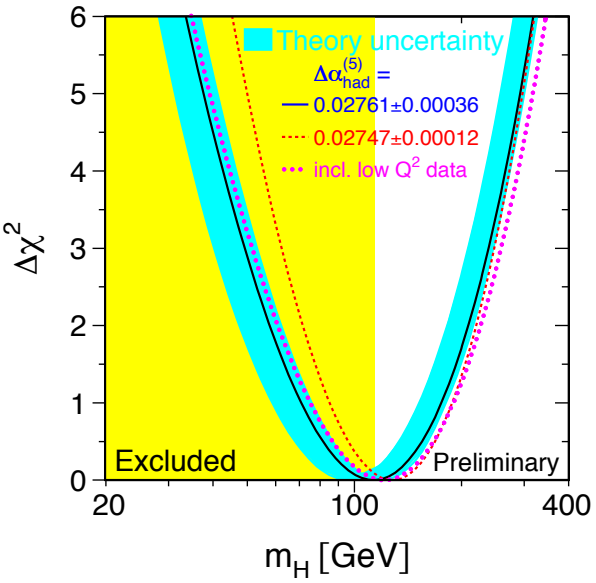

(b) The $\Delta\chi^2$ fit of the combined measurements.

Figure 10.3 – The results of precision measurements from the experiments at the LEP, SLC and Tevatron are shown in the left Fig. The $\Delta\chi^2$ fit of the combined results as a function of m_H is presented in the right Fig. The yellow region indicates the excluded values of the fit [117].

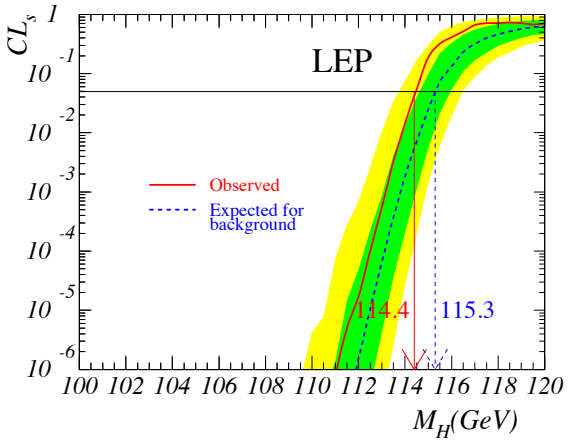

(a) Exclusion limits of m_H measured by the LEP experiments.

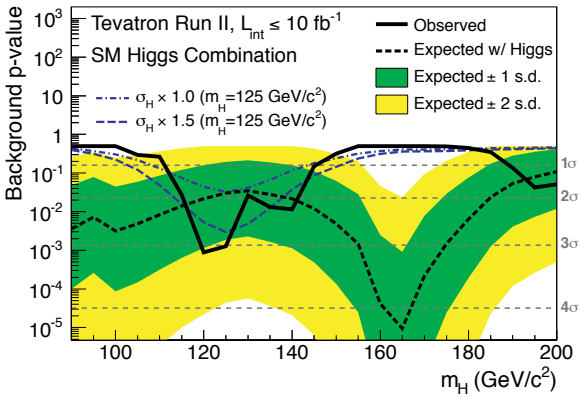

(b) Exclusion limits of m_H measured by the Tevatron experiments.

Figure 10.4 – Exclusion limits of m_H measured by the LEP (left) and Tevatron (right) experiments. The following limits were set at 95% CL: (LEP) $m_H >$ 114.4 GeV, (Tevatron) $90 < m_H < 109$ GeV and $149 < m_H < 182$ GeV [118, 119].

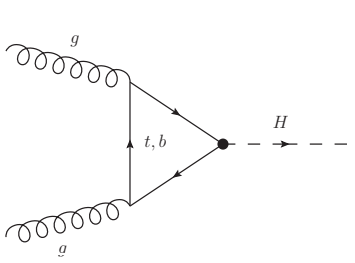

(a) The gluon-gluon fusion.

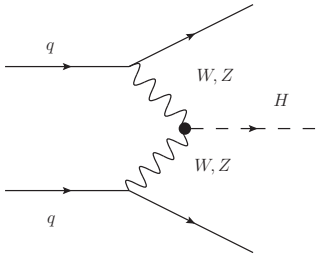

(b) The virtual boson fusion.

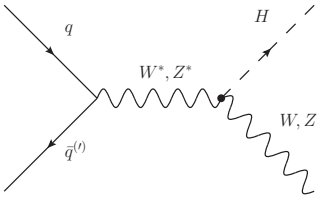

(c) The associated production with a vector boson.

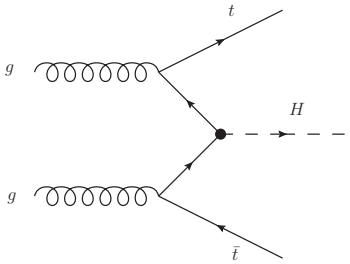

(d) The associated production with top quarks.

Figure 10.5 – Diagrams of the main Higgs boson production mechanisms at the LHC: (top left) gluon-gluon fusion, (top right) virtual boson fusion, (bottom left) associated production with a vector boson, and (bottom right) associated production with top quarks.

This event marked the start of a whole new way of considering particle physics. From a period of intensive searches for a new particle, experimentalists moved to taking more data in Run 2 of the LHC, to refine the knowledge about this new particle and to possibly find deviations from the SM, as well as new physics phenomena.

10.5 The Higgs boson production and decay channels at the LHC

10.5.1 Production mechanisms at the LHC

The LHC has collided protons at centre-of-mass energies ranging from $\sqrt{s} = 7\,\text{TeV}$ to $13\,\text{TeV}$. The main mechanisms entering the production of the Higgs boson are the gluon-gluon fusion ($gg\text{F}$), the virtual boson fusion (VBF), the associated production with a vector boson ($VH, V \in \{Z, W^{\pm}\}$), and the production with a top-quark or a bottom-quark pair ($t\bar{t}H$ or $b\bar{b}H$). The leading-order Feynman diagrams of these processes are given in Fig. 10.5. The absence or the presence of byproducts created with the Higgs boson can be exploited to distinguish between the various production mechanisms.

Gluon fusion is the dominant production mechanism, mediated by a top quark loop (or b-quark loop at a lesser extent). Gluon fusion is by far the dominant production process and occurs about 87% of the time at the LHC. The Higgs boson is produced without any other byproducts. The predicted production cross sections are of the order of $20\,\text{pb}$ at $\sqrt{s} = 7, 8\,\text{TeV}$ and increase up to $50\,\text{pb}$ at $\sqrt{s} = 13\,\text{TeV}$, as shown in Fig. 10.6 [123].

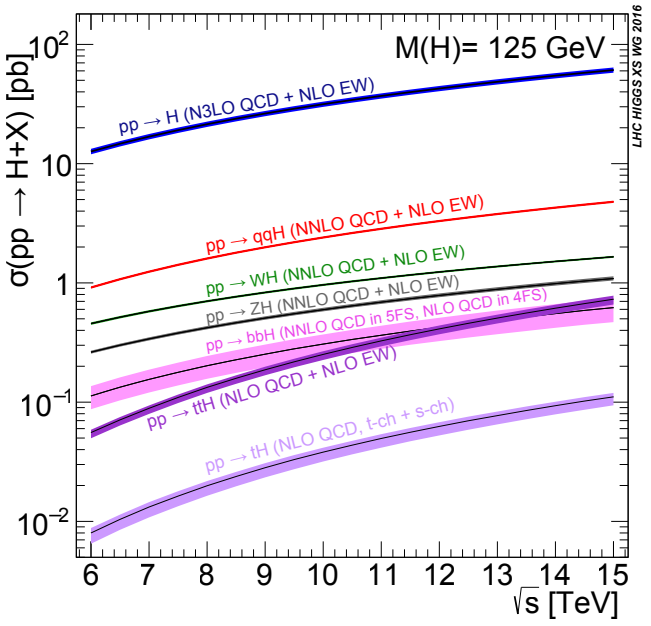

Figure 10.6 – Higgs boson production cross sections as a function of the centre-mass energy [123].

The next most important production mechanism of the Higgs boson at LHC is the vector boson fusion, in which the Higgs boson is produced in association with two quarks. This process is ten times less probable than gluon-gluon fusion and occurs 7% of the time. Due to the topology of the event, the two quarks are characterised with two strongly energetic reconstructed jets in the forward regions of the detector, highly separated in η, with transverse momenta above 20 GeV. This jet description can be used as a discriminant to reduce the QCD backgrounds and identify the production mode. The cross sections are close to 1 to 1.6 pb at $\sqrt{s} = 7, 8$ TeV and rise up to 3.8 pb at $\sqrt{s} = 13$ TeV.

The associated production with W or Z is the third dominant process, happening about 4% of the time. The off-shell vector bosons arise from the annihilation of a $q\bar{q}$ pair and a Higgs boson is mediated with its vector boson counterpart. The later decays into leptons, whose products can be used for triggering the event and for suppressing QCD background. These extra leptons (two for HZ and one for HW) can be used to identify the production mode. The corresponding cross sections are of 0.4 pb, 0.7 pb at $\sqrt{s} = 7, 8$ TeV up to 0.9 pb, 1.5 pb at $\sqrt{s} = 13$ TeV, for ZH and WH productions, respectively.

The last main process is the associated production with top or bottom quarks. A pair of gluons or quarks emits the top (bottom)-quark pair with the Higgs boson being radiated. At the LHC, the rates of these events are extremely low (about 2%, corresponding to cross sections of 0.2 pb, 0.13 pb at $\sqrt{s} = 7, 8$ TeV up to 0.5 pb at $\sqrt{s} = 13$ TeV, for bbH and ttH productions, respectively). These processes however offer good opportunities to test the validity of the Standard Model.

The various production cross sections are calculated by the LHC Higgs Cross Section Working Group and analyses of the LHC experiments can compare their results with the most up-to-date predictions. The total production cross section of the Higgs boson at LHC increases with centre-of-mass energies from 8 TeV to 13 TeV, corresponding to the Run 1 and Run 2 LHC operating conditions.

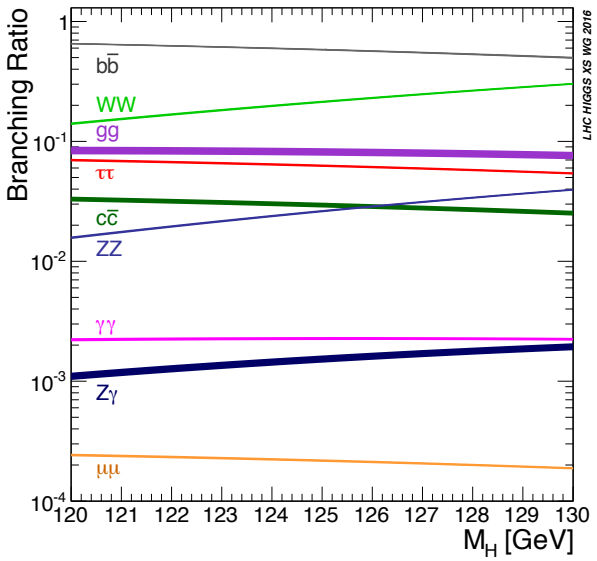

Figure 10.7 – Higgs boson branching ratios as a function of m_H [123].

10.5.2 Decay channels of the Higgs boson

As described in the previous section, the coupling strength of the Higgs boson is directly proportional to the mass of the particle it couples to if this is a fermion, and proportional to the square of the mass if this is a boson. The Higgs boson is therefore more likely to couple to the heaviest kinematically accessible final state.

Figure 10.7 [123] shows the branching ratios (BR) as a function of the Higgs mass m_H, close to 125 GeV. A SM-like Higgs boson decays mainly into $b\bar{b}$ pair (57% of the time), but this decay is dominated with QCD background and is not easily accessible. Then, the Higgs boson can decay into a WW pair (21% chances), where the final state is half-composed of missing transverse energy making the search difficult. Decays to gg (9%), $\tau\bar{\tau}$ (6%) and $c\bar{c}$ (3%) follow, but are either QCD background-dominated for gg and $c\bar{c}$, or needing high missing E_{T} searches for $\tau\bar{\tau}$.

The Higgs boson can also decay to two Z bosons 3% of the time. This channel offers great resolution in the four-lepton final state, which is the subject of this thesis and is further detailed in Chap. 11. Since $m_H \approx 125\,\mathrm{GeV}$, one of the two bosons at least has to be off-shell. Other final states are more difficult to reconstruct due to the missing E_{T}.

The Higgs boson decays to two photons or to $Z\gamma$ happen 0.2% of the time, respectively. These two last decays are easily identifiable thanks to the energetic photons which can be used to discriminate against background. The Higgs boson was discovered using the high sensitivity of this channel together with the Higgs-to-four-lepton decays. Finally, other decays are possible, including the $\mu\mu$ channel, but their low branching ratios make their search very challenging.

10.5.3 The total width of the Higgs boson

The width of the Higgs boson Γ_H is defined as the width of the m_H distribution at half-maximum. This quantity is equal to the sum of the partial widths $\Gamma_{H\to X}$ of the decay processes of the boson. The branching ratios r of each of the Higgs boson decays are therefore defined as the ratio between the corresponding partial width and the total width $r_{H\to X} = \frac{\Gamma_{H\to X}}{\Gamma_H}$. The total width is predicted to increase with m_H as

more decays are possible, and is of 4.07 MeV at 125 GeV. The measurement of this value is a good test of the validity of the SM.

10.6 Beyond the Standard Model

The Standard Model has proven to be really powerful in predicting experimental measurements in particle physics. This is however an effective field theory and is only valid at low energy scales accessible to current experiments. Furthermore, a series of deficiencies and unresolved issues highlight the fact the SM is not a complete theory in its current description and hence cannot be a final theory, implying new physics beyond the SM (BSM) must exist.

The eighteen parameters of the SM widely differ in order of magnitude, from the mass of the electron of about 0.5 MeV to the top-quark mass of nearly 173 GeV. Including the mass of the neutrinos (below the eV scale), this large range of values and the large number of parameters cannot be satisfactory from a theoretical point of view. The PNMS matrix has to be introduced to explain the oscillations of the neutrinos, with a specific Lagrangian, without any theoretical ground apart from the experimental observations. The coupling constants α of the two sectors appear to have very different values and no convergence is expected at higher energies.

An issue arises from the baryon asymmetry, which boils down to the question of explaining why the universe is mainly composed of matter, whereas the Standard Model predicts a production of matter and antimatter in equal proportions. Experiments are actively looking for the so-called CP violation, which would prove the unbalance of matter over antimatter. This mechanism, although still not understood and not included in the Standard Model, would give a huge insight on how the universe was formed.

The description given by the Standard Model is robust at energies close to the electroweak scale, but is not valid near the Planck energy scale of 10^{19} GeV where effects of gravity cannot be neglected. The model does not provide any theoretical inclusion of the gravitational sector and attempts to do so have been strongly disfavoured by experimental measurements.

Concerning the Higgs mechanism, a major drawback of the Standard Model is the so-called hierarchy problem. Most of the divergences of the theory are logarithmic when including higher order corrections. In case of the Higgs mass, contributions from fermions and bosons (single loops) represented in Fig. 10.8 lead to a quadratic divergence. Therefore, a cut-off scale Λ is introduced, above which the current description of the theory is not valid. The physical mass of the Higgs boson is then the difference between a bare mass and a quadratic term in Λ. At sufficiently high energies, the cancellation of the divergent contributions to keep $m_H < 1$ TeV have to happen with precisions of more than ten digits, making it very improbable. This fine-tuning is highly non-physical for many theorists. Many Beyond-Standard-Model theories predict the existence of a bosonic (fermionic) partner for each fermion (boson) of the Standard Model, enabling divergence terms to automatically cancel out with opposite signs. Such models, referred to as SUSY (Supersymmetry) would safely leave the mass of the Higgs boson at the 125 GeV electroweak scale.

No theoretical grounds in the Standard Model support the negative value of μ^2 in the expression of the Higgs potential, apart from the fact it allows spontaneous symmetry breaking. Although the model unifies the strong and the electroweak sectors, it fails to build a common frame to the group theory.

Astronomical experimental measurements suggest the Standard Model is only capable of describing about five percent of the total mass-energy content of the universe. The remaining is composed of about 27% of dark matter and 60% of dark energy, still not characterised by theory [124, 125]. SUSY models could offer a potential candidate for dark matter, which would be undetectable by current detectors. Also, in these models μ^2 entering the Higgs potential is positive at high energies and would only have a negative value at the electroweak scale.

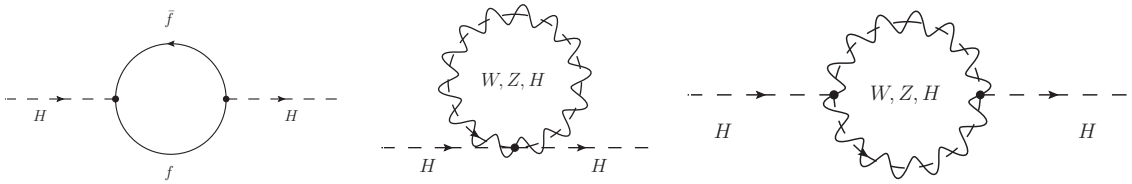

(a) Fermion loop. (b) Vector boson loop 1. (c) Vector boson loop 2.

Figure 10.8 – Feynman diagrams for the first corrective loops contributing to m_H.

Chapter 11

The Higgs boson decaying into four leptons

After a brief description of the Higgs mechanism in the Standard Model and the corresponding production modes at the LHC, this chapter focuses on a specific decay channel: the Higgs boson decaying into two Z bosons, which in turn decay into four leptons. This channel was one of the discovery channels together with $H \to \gamma\gamma$ using Run 1 data collected by the two experiments CMS [20] and ATLAS [21]. The consequent work on the discovery is followed in Run 2 by precise measurements of the properties of the Higgs boson by the two collaborations at higher centre-of-mass energies to probe any deviations from the SM. In this effort, the analysis presented in this thesis takes advantage of the increased statistics to perform state-of-the-art measurements in the Higgs-to-four-lepton decay channel.

The analysis steps of this *so-called golden channel*, are outlined in this chapter. The selection criteria are described, as well as the assessment of the background yields. Finally the event yields observed from the analysis of 2015 and 2016 pp-collision data and the expected sensitivity are presented at the end of this chapter.

In this analysis, the author contributed to the development of the code for the production of the samples used by the group, as well as performing the studies on the late quadruplet selection and the inversion of the isolation cuts (see 11.4.4).

11.1 The four-lepton final state

The Higgs boson decay into four leptons $H \to ZZ^* \to 4\ell$, with $\ell \in \{e, \mu\}$, provides good sensitivity for the measurement of the properties of the Higgs boson thanks to a high signal over background ratio, which is close to 2 for the various final states $4\mu = \mu^+\mu^-\mu^+\mu^-$, $4e = e^+e^-e^+e^-$, $2\mu 2e = \mu^+\mu^-e^+e^-$ and $2e2\mu = e^+e^-\mu^+\mu^-$, where the first lepton pair is chosen to be the closest to the Z boson pole mass.

Thanks to easily identifiable backgrounds and the particular topology of signal events, the sensitivity of the Higgs boson to four leptons is high. Z boson decays to leptons can be identified with really fine resolution by the ATLAS detector, since these decays are often used as reference for the calibration of particles. The analysis naturally benefits from this improved resolution and can be of very good interest for the measurements of the Higgs mass and width. The fact that one of the two Z bosons of the study is off-shell makes the mass of the second pair highly sensitive to the spin of the Higgs boson. Although this channel has lower event yields than Higgs boson to two photons decays, the couplings and decay rates can be assessed primarily through ratios of cross sections times branching ratios.

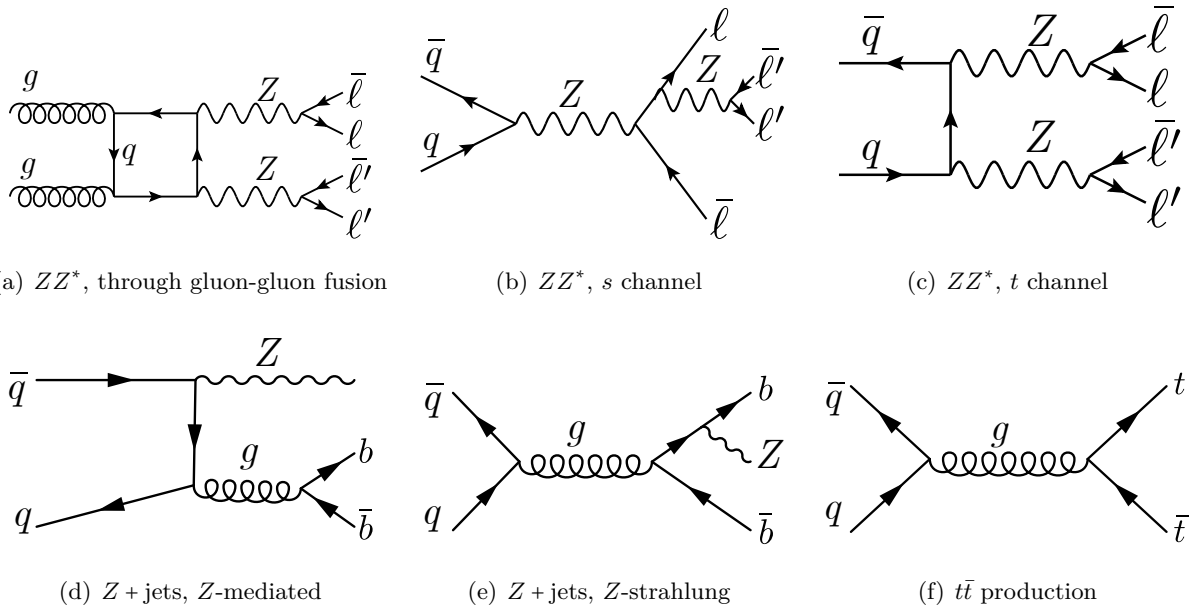

(a) ZZ^*, through gluon-gluon fusion (b) ZZ^*, s channel (c) ZZ^*, t channel

(d) Z + jets, Z-mediated (e) Z + jets, Z-strahlung (f) $t\bar{t}$ production

Figure 11.1 – Feynman diagrams of the main background processes of the Higgs-to-four-lepton decay channel. The diagrams are given at their lowest order.

The main background in this analysis is the Z continuum $(Z^{(*)}/\gamma^*)(Z^{(*)}/\gamma^*)$, which will be denoted ZZ^* thereafter. In the low mass range (corresponding to Standard-Model-like Higgs boson decays), important background arises from Z + jets and $t\bar{t}$ productions with two prompt leptons, where the additional leptons originate from b- or c-quark decays, photon conversions or jet misidentification. The selection criteria of this analysis aim at reducing the contamination of these processes and enhance the selection of signal events. The Feynman diagrams of these background decay channels are presented in Fig. 11.1. All these diagrams are at Leading order, except the ZZ^* continuum in the s channel and the $Z + b\bar{b}$ final state with the Z strahlung.

During Run 1, data collected at $\sqrt{s}$ = 7 and 8 TeV enabled the ATLAS collaboration to not only confirm the existence of the new boson, but also to refine the current knowledge about its properties. The group was involved in the measurement of the Higgs boson mass and couplings, the Higgs boson spin-parity, and the Higgs boson production cross sections (differential and total) [89, 94, 128, 91, 95, 97]. The group also conducted a search to probe the existence of a heavy Higgs boson [129].

At centre-of-mass energies of $\sqrt{s}$ = 13 TeV, the Higgs boson production cross section is expected to be enhanced by a factor of two as compared to Run 1 ($\sqrt{s}$ = 8 TeV). This increase is larger than for the dominant ZZ^* background, which means that the overall sensitivity of the channel should be improved in Run 2 with respect to the previous measurements. This thesis presents the first results obtained in Run 2 for the measurements of the Higgs-to-four-lepton production cross section. These state-of-the-art measurements add valuable knowledge to test the validity of the Standard Model at newly probed centre-of-mass energies.

11.2 Data and Monte Carlo samples

The various inputs for the analysis are outlined, which are composed of data recorded by the ATLAS detectors and simulated samples to which the data is compared.

11.2.1 Data samples

For the analysis presented in this thesis, the datasets of 2015 and 2016 were used, with a bunch spacing of 25 ns. The total recorded luminosity is of $\int \mathcal{L}dt = 32.2\,\text{fb}^{-1}$ ($\int \mathcal{L}dt = 3.9\,\text{fb}^{-1}$), with an average pile-up of $\langle\mu\rangle = 24.9$ ($\langle\mu\rangle = 13.6$) in 2016 (2015). The data taking efficiency was of 92.4% (92.0%) in 2016 (2015). Between 2015 and 2016, the pile-up profiles have changed (because of the increase of instantaneous luminosity), as well as the gas mixture in the TRT chambers. These changes are taken into account in the Monte Carlo samples, as described in Sec. 11.2.2.

Only events for which the entire detector was operational are selected. The LHC delivers pp collisions in so-called physics runs, corresponding to two stable colliding beams. A run starts at the injection of new beams. A run is divided into luminosity blocks, corresponding to events for which the instantaneous luminosity is the same. From each luminosity block, events recorded by ATLAS are analysed after reconstruction: all sub-detectors must have recorded data correctly and specific distributions (occupancy rates of chambers and elementary kinematic distributions) must have suitable shapes. A list is created for each run indicating which blocks were of good quality and can be used for analyses. Various runs and their associated lists are then gathered into data taking periods, often corresponding to few weeks of data taking, which regroup events with similar luminosity conditions. From these lists, the so-called *Good Run List* (GRL) aggregates the good quality runs for data 2015 and 2016, and the associated recorded luminosity. Only events falling into this list are used for this analysis, which corresponds to an overall data quality efficiency of 93 to 95% for Run 2.

11.2.2 Simulated samples

Events generated (Monte Carlo) are fully simulated using the ATLAS detector simulation within the GEANT4 framework, as described in Sec. 3.6.2. Pile-up, consisting of additional pp interactions per event, is done during the digitalisation step of the simulation. To this purpose, minimum bias events, which were previously generated, are superimposed to the main event making sure the distribution of μ, the average number of interactions per bunch crossing, reproduces the data. Since the Monte Carlo (MC) events are used for both data 2015 and 2016, events are reweighted to a luminosity weighted combination of the pile-up conditions for the two years. MC samples use the TRT gas mixture of 2015, therefore an extra systematic is used to account for the 2016 new conditions.

Signal samples

The Higgs boson production cross sections and branching ratios are taken from Ref. [130, 131, 123] and simulation samples are renormalised using these predictions. For ggF, predictions are calculated up to next-to-next-to-leading order (NNLO) in QCD [132, 133, 134], including QCD soft-gluon re-summations with NNNLO (next-to-NNLO) approximation [135, 136, 137], as well as NLO (next-to-leading-order) EW radiative corrections [138, 139]. A review of these results can be found in Ref. [140, 141, 142] (factorisation between QCD and EW corrections is assumed). Concerning the VBF process, full NLO QCD and EW corrections [143, 144, 145], and approximate NNLO QCD corrections [146] are used. For the VH processes, cross sections are calculated up to NNLO [147] in QCD and NLO in EW radiative corrections [148]. The

last two mechanisms $t\bar{t}H$ and $b\bar{b}H$, although contributing at a lesser extent to the analysis, are included. For the former, cross sections are estimated up to NLO QCD [149, 150, 151, 152]. For the latter, the cross sections are estimated by the Santader matching with five-flavour scheme (NNLO) and four-flavour scheme (NLO) [153].

The branching ratios [154] of the Higgs boson decaying to the four-lepton final states are calculated by PROPHECY4F [155, 156], including NLO corrections for QCD and EW. In these calculations, interference effects between identical final-state fermions are taken into account. The various cross sections used to normalise the MC for $m_H = 125.09\,\text{GeV}$ are presented in Tab. 11.1 [123]. Due to these effects, the expected branching ratios of the 4μ and $4e$ channels are 10% higher than for the $2\mu 2e$ and $2e2\mu$ final states.

The POWHEG-BOX MC event generator [85, 86] is used to simulate the ggF [157], VBF and VH [158] processes. The PDF4LHC_NLO Parton Distribution Function (PDF) set is used [159]. For the ggF process, predictions are accurate up to NNLO in QCD thanks to the merging of the NLO H + jets cross section with the parton shower, using the MiNLO method [160]. On top of this, a reweighting procedure is carried out using the HNNLO programme [161, 162] to achieve the NNLO precisions. The VBF and VH samples include NLO predictions in QCD. For VH, the MiNLO method is also used to merge the 0- and 1-jet events [163]. The showering, hadronisation and b-hadron decays are modelled interfacing POWHEG to PYTHIA 8 [74] (the AZNLO parameter set [75] is used). Concerning $t\bar{t}H$ ($b\bar{b}H$) events, NLO corrections are achieved using MADGRAPH5_AMC@NLO [164] with the CT10nlo [165] (NNPDF23) PDF set, interfaced to HERWIG++ [166] for showering and hadronisation, using the UEEE5 parameter set [167].

In order to further estimate the uncertainties due to theory predictions, data is also compared to two additional ggF samples. The first sample is generated using MADGRAPH5_AMC@NLO at the NLO level in QCD for the 0, 1 and 2 additional jet events, merged using the FxFx scheme [164, 168] (the NNPDF30_nlo_as_0118 PDF set is used). The same procedure as for POWHEG is used for interfacing the generator (Pythia 8 using the AZNLO parameter set). The second sample is generated using HRes v2.3 [169, 170] with the MSTW2008 NNLO PDF set [171]. In this sample, fixed-order cross sections for ggF are computed up to NNLO in QCD, and the $p_{\text{T}}^{4\ell}$ distribution is described at NLO. The re-summation of soft-gluon effects at small transverse momenta is included up to NNLL (next-to-next-to-leading logarithmic order) in QCD, using dynamic factorisation and re-summation scales whose central scale are chosen to be $m_H/2$. The generator takes into account top and bottom quark-mass dependence up to NNL and NLO in QCD. Only the top quark contribution is considered at NNL and NNLO. In this sample, no parton showering is performed and QED final-state radiations are therefore not included. Both the two samples used for theory uncertainties are normalised to the predictions given by the POWHEG MC. All the previously listed samples are generated assuming $m_H = 125\,\text{GeV}$.

For the studies described in Sec. 12.7, the pseudo observables [172, 173] used to constrain deviations from the SM are generated for $m_H = 125\,\text{GeV}$ with MADGRAPH5_AMC@LO using FeynRules 2 [174] and the NN23PDF set [172, 173]. This sample is interfaced to PYTHIA 8 using the A14 parameter set [175]. As for the other samples, normalisation is set to the most up-to-date cross section predictions.

Background samples

The main background, the ZZ^* continuum, is modelled using POWHEG for quark-antiquark ($q\bar{q}$) annihilation interfaced to PYTHIA 8 for parton shower and hadronisation. The CT10nlo PDF set is used for the hard process. For the quark-initiated ZZ^*, NNLO QCD and NLO EW corrections are applied [176, 177, 178], as a function of the diboson invariant mass. An additional sample was generated using SHERPA [179] for systematic studies (NLO QCD accuracy for the 0- and 1-jet events, and LO

Table 11.1 – Calculated SM Higgs boson production cross sections (σ) for gluon fusion, vector-boson fusion and associated production with a W or Z boson or with a $b\bar{b}$ or $t\bar{t}$ pair in pp collisions at $\sqrt{s} = 13\,\text{TeV}$. The first and second quoted uncertainties correspond to the theoretical systematic uncertainties calculated by adding in quadrature the QCD scale and PDF + α_s uncertainties, respectively. The decay branching ratio (B) for $H \to 4\ell$ with $\ell = e, \mu$, is reported in the last column [123].

m_H [GeV]	$\sigma(gg \to H)$ [pb]	$\sigma(qq' \to Hqq')$ [pb]	$\sigma(q\bar{q} \to WH)$ [pb]	$\sigma(pp \to ZH)$ [pb]
124.0	$49.27\ ^{+4.6\%\ +3.2\%}_{-6.8\%\ -3.2\%}$	$3.812\ ^{+0.4\%\ +2.1\%}_{-0.3\%\ -2.1\%}$	$1.408\ ^{+0.6\%\ +1.9\%}_{-0.6\%\ -1.9\%}$	$0.9051\ ^{+3.6\%\ +1.6\%}_{-3.1\%\ -1.6\%}$
124.5	$48.92\ ^{+4.6\%\ +3.2\%}_{-6.7\%\ -3.2\%}$	$3.798\ ^{+0.4\%\ +2.1\%}_{-0.3\%\ -2.1\%}$	$1.390\ ^{+0.6\%\ +1.9\%}_{-0.6\%\ -1.9\%}$	$0.8943\ ^{+3.8\%\ +1.6\%}_{-3.0\%\ -1.6\%}$
125.0	$48.58\ ^{+4.6\%\ +3.2\%}_{-6.7\%\ -3.2\%}$	$3.782\ ^{+0.4\%\ +2.1\%}_{-0.3\%\ -2.1\%}$	$1.373\ ^{+0.5\%\ +1.9\%}_{-0.7\%\ -1.9\%}$	$0.8839\ ^{+3.8\%\ +1.6\%}_{-3.1\%\ -1.6\%}$
125.09	$48.52\ ^{+4.6\%\ +3.2\%}_{-6.7\%\ -3.2\%}$	$3.779\ ^{+0.4\%\ +2.1\%}_{-0.3\%\ -2.1\%}$	$1.369\ ^{+0.5\%\ +1.9\%}_{-0.7\%\ -1.9\%}$	$0.8824\ ^{+3.8\%\ +1.6\%}_{-3.0\%\ -1.6\%}$
125.5	$48.23\ ^{+4.6\%\ +3.2\%}_{-6.7\%\ -3.2\%}$	$3.767\ ^{+0.4\%\ +2.1\%}_{-0.3\%\ -2.1\%}$	$1.355\ ^{+0.5\%\ +1.9\%}_{-0.7\%\ -1.9\%}$	$0.8744\ ^{+3.7\%\ +1.6\%}_{-3.1\%\ -1.6\%}$
126.0	$47.89\ ^{+4.5\%\ +3.2\%}_{-6.7\%\ -3.2\%}$	$3.752\ ^{+0.4\%\ +2.1\%}_{-0.3\%\ -2.1\%}$	$1.337\ ^{+0.6\%\ +1.9\%}_{-0.8\%\ -1.9\%}$	$0.8649\ ^{+3.8\%\ +1.6\%}_{-3.1\%\ -1.6\%}$

m_H [GeV]	$\sigma(gg \to ZH)$ [pb]	$\sigma\left(q\bar{q}/gg \to t\bar{t}H\right)$ [pb]	$\sigma\left(q\bar{q}/gg \to b\bar{b}H\right)$ [pb]	$B\left(H \to ZZ^{(*)} \to 4\ell\right)$ [10^{-3}]
124.0	$0.1242\ ^{+25.1\%\ +2.4\%}_{-18.9\%\ -2.4\%}$	$0.5193\ ^{+5.9\%\ +3.6\%}_{-9.2\%\ -3.6\%}$	$0.4999\ ^{+20.1\%}_{-24.0\%}$	$0.1131\ \pm 2.24\%$
124.5	$0.1235\ ^{+25.1\%\ +2.4\%}_{-18.9\%\ -2.4\%}$	$0.5132\ ^{+5.8\%\ +3.6\%}_{-9.2\%\ -3.6\%}$	$0.4930\ ^{+20.0\%}_{-23.9\%}$	$0.1185\ \pm 2.21\%$
125.0	$0.1227\ ^{+25.1\%\ +2.4\%}_{-18.9\%\ -2.4\%}$	$0.5071\ ^{+5.8\%\ +3.6\%}_{-9.2\%\ -3.6\%}$	$0.4880\ ^{+20.2\%}_{-23.9\%}$	$0.1240\ \pm 2.18\%$
125.09	$0.1227\ ^{+25.1\%\ +2.4\%}_{-18.9\%\ -2.4\%}$	$0.5065\ ^{+5.7\%\ +3.6\%}_{-9.3\%\ -3.6\%}$	$0.4863\ ^{+20.1\%}_{-23.9\%}$	$0.1251\ \pm 2.16\%$
125.5	$0.1221\ ^{+25.1\%\ +2.4\%}_{-18.9\%\ -2.4\%}$	$0.5023\ ^{+5.7\%\ +3.6\%}_{-9.3\%\ -3.6\%}$	$0.4809\ ^{+20.1\%}_{-23.8\%}$	$0.1297\ \pm 2.14\%$
126.0	$0.1218\ ^{+25.1\%\ +2.4\%}_{-18.9\%\ -2.4\%}$	$0.4964\ ^{+5.7\%\ +3.6\%}_{-9.3\%\ -3.6\%}$	$0.4760\ ^{+20.2\%}_{-24.0\%}$	$0.1355\ \pm 2.12\%$

precisions for higher multiplicities). The gluon induced ZZ^* is modelled using Sherpa. The k-factor including the higher order QCD effects for the $gg \to ZZ^*$ production mode is calculated for massless quark loops [180, 181] in the heavy-top-quark approximation [182], including the ggF processes [183]. The value of 1.7 was retained based on the studies, and a conservative uncertainty of 60% is applied to the normalisation of the invariant-mass distribution.

The second most important background, Z + jets, is modelled using Sherpa at NLO for 0-, 1- and 2-jet events, and at leading order (LO) for 3- and 4-jet events, including the decay and showering. These events are filtered into three categories, depending on the origin of the jets: $Z + b$-jets (b-hadron filter), $Z + c$-jets (c-hadron filter, and b-hadron veto), and Z + light jets (b-hadron and c-hadron vetoes). In the same way, 4ℓ- and 3ℓ-filtered Z + jets samples are prepared. For comparison, additional Z + jets samples are simulated using POWHEG and MadGraph [184]. These are interfaced to PYTHIA 8 for parton shower and hadronisation, and to EvtGen [76] for the simulation of b-hadron decays.

The $t\bar{t}$ background is modelled using POWHEG interfaced to PYTHIA 6 [78] for parton showering and hadronisation. These samples are interfaced to PHOTOS [185] for quantum electrodynamics (QED) radiative corrections, to Tauola [186, 187] for the simulation of τ decays, and to EvtGen for the simulation of b-hadron decays.

The vector boson backgrounds are the last simulated events. WZ background is modelled using POWHEG interfaced to PYTHIA 8. The triboson backgrounds ZZZ, WZZ and WWZ with four or more leptons, are modelled using Sherpa. Finally, for all-leptonic $t\bar{t} + Z$ backgrounds, the generator madGraph interfaced to PYTHIA 8 is used.

11.3 Lepton reconstruction and trigger

Since this study focuses on reconstructing the Higgs boson in the four-leptons final state, special care is taken for electrons and muons. Triggers are selected accordingly. Jets are also taken into account, as they are useful for the categorisation of the production mechanisms as well as the differential measurements.

11.3.1 Electron reconstruction and identification

Candidates are reconstructed from energy deposits in the EM calorimeters which match an ID track. The track associated to a cluster has to pass the loose shower shape requirement and is refitted using a Gaussian-Sum Filter [188]. In order to discriminate isolated electrons from background (hadronic jets for instance), specific variables are used, especially in the forward region where radiation is more intense. These variables are summarised in Tab. 11.2 [189].

In order to improve the background rejection, all the variables which are not related to the track hits are combined into a likelihood discriminant [188]. This discriminant is based on probability density functions for signal and background candidates from simulation (2015 and 2016 configurations [189]) which are combined into a score function on which the cuts are applied to define the working points. The cut values depend on $|\eta|$ and E_{T}, the pseudo-rapidity and the transverse energy of the electron candidate. To complement this selection, a cut is applied on the track hits to only select high quality tracks for high precision four-vector measurements. The score on the likelihood is chosen so that the signal efficiency is of 95% (*Loose* LH working point). The track associated to the electron candidate must have at least one IBL hit, or if no hits are expected, at least an innermost Pixel hit.

Table 11.2 – Definition of electron discriminating variables [189].

Type	Description	Name
Hadronic leakage	Ratio of E_{T} in the first layer of the hadronic calorimeter to E_{T} of the EM cluster (used over the range $\lvert\eta\rvert < 0.8$ or $\lvert\eta\rvert > 1.37$)	R_{Had1}
	Ratio of E_{T} in the hadronic calorimeter to E_{T} of the EM cluster (used over the range $0.8 < \lvert\eta\rvert < 1.37$)	R_{Had}
Back layer of EM calorimeter	Ratio of the energy in the back layer to the total energy in the EM accordion calorimeter	f_3
Middle layer of EM calorimeter	Lateral shower width, $\sqrt{(\Sigma E_i \eta_i^2)/(\Sigma E_i) - ((\Sigma E_i \eta_i)/(\Sigma E_i))^2}$, where E_i is the energy and η_i is the pseudo-rapidity of cell i and the sum is calculated within a window of 3×5 cells	W_{η^2}
	Ratio of the energy in 3×3 cells over the energy in 3×7 cells centred at the electron cluster position	R_ϕ
	Ratio of the energy in 3×7 cells over the energy in 7×7 cells centred at the electron cluster position	R_η
Strip layer of EM calorimeter	Ratio of the energy difference between the largest and second largest energy deposits in the cluster over the sum of these energies	E_{ratio}
	Ratio of the energy in the strip layer to the total energy in the EM accordion calorimeter	f_1
Track quality	Number of hits in the innermost pixel layer (the newly added B layer), discriminates against photon conversions	n_{Blayer}
	Number of hits in the pixel detector	n_{Pixel}
	Number of total hits in the pixel and SCT detectors	n_{Si}
	Transverse impact parameter with respect to the beam-spot	d_0
	Significance of transverse impact parameter defined as the ratio of d_0 and its uncertainty	σ_{d_0}
	Momentum loss of the track between the perigee and the last measurement point divided by the original momentum	$\Delta p/p$
TRT	Likelihood probability based on transition radiation in the TRT	TRTPID
Track-cluster matching	$\Delta\eta$ between the cluster position in the strip layer and the extrapolated track	$\Delta\eta_{\mathrm{L}}$
	$\Delta\phi$ between the cluster position in the middle layer and the extrapolated track, where the track momentum is rescaled to the cluster energy before extrapolating the track to the middle layer of the calorimeter	$\Delta\phi_{\mathrm{Res}}$

11.3.2 Muon reconstruction and identification

The various ways of reconstructing muons were outlined in Sec. 3.4.6. Concerning identification, described in Sec. 3.4.7, the *Loose* selection criteria are used for the analysis. These restrict the use of *Calorimeter tagged* (CT) and *Segment tagged* (ST) muons for the region $|\eta| < 0.1$. *Extrapolated* (ME) muons are only permitted in the region $2.5 < |\eta| < 2.7$.

On top of these restrictions, a series of quality requirements, included in the *Loose* identification working point, are applied. Where applicable (all muon working points expect ME muons), hit requirements are requested on the reconstructed ID tracks. At least 1 Pixel hit, 5 SCT hits are necessary, as well as less than 3 Pixel or SCT holes (missing hits where they are expected). If inefficiencies are expected for a specific part of the detectors, the requirements on the Pixel and SCT holes and hits are loosened.

Requirements on the hits in the MS are also applied. ME muons should have at least 3 hits in each of the three layers of the MDT or the CSC. CB muons must have at least 3 hits in at least two stations of MDT, except in the very central region ($|\eta| < 0.1$).

In order to reduce the background coming from hadrons misidentified as muons (in-flight decays), correspondence of the momentum measurements between ID and MS tracks is assessed using the charge over momentum significance [46]:

$$\sigma_{q/p} = \frac{|q/p_{\mathrm{ID}} - q/p_{\mathrm{MS}}|}{\sqrt{\sigma^2_{q/p,\ \mathrm{ID}} + \sigma^2_{q/p,\ \mathrm{MS}}}}, \tag{11.1}$$

where q is the charge of the muon, and p_{ID} (p_{MS}) are the momentum measured in the ID (MS). $\sigma_{q/p,\ \mathrm{ID}}$ and $\sigma_{q/p,\ \mathrm{MS}}$ are the uncertainties on the q/p ratios. For the *Loose* working point of the muon identification, $\sigma_{q/p} < 7$ is required.

11.3.3 Jet reconstruction and identification

The ATLAS collaboration uses the anti-k_{t} algorithm [83] to reconstruct the jets in the calorimeters. The radius parameter is chosen to be $R = 0.4$, and only positive-energy topological clusters (topoclusters) [84, 190] are used.

Jet calibration remains the same as for Run 1 [191]. Small updates take into account the IBL layer added to the ID, as well as the new beam conditions, the changes in the LAr sampling points and the improved track reconstruction [192].

The main jet backgrounds arise from interactions which are beam-induced when protons collide upstream of the IP, or from cosmic ray showers and highly coherent noise in the calorimeters. In order to disentangle pile-up effects, jets having $p_{\mathrm{T}} < 60\,\mathrm{GeV}$ and $|\eta| < 2.4$ are required to have a jet-vertex-tagger (JVT) score greater than 0.59 [193]. This score is obtained from a two-dimensional likelihood which relies on the corrected jet-vertex fraction (fraction of the total momentum of tracks in the jet which is associated to the primary vertex) and the ratio of the scalar sum of hard-vertex associated track p_{T} to the jet p_{T}. In order to further suppress the backgrounds, jets which pass the JVT selection (or to which the selection does not apply) are required to pass a set of criteria, which compose the *Loose* working point [194]. If any of the jets fail the quality requirements, the event is rejected.

11.3.4 b tagging

In order to identify b-quark jets, the ATLAS collaboration combines the results of three methods into a multivariate discriminant (MV2). The three methods consist in studying the impact parameter, consider-

ing the inclusive secondary vertex reconstruction and the decay chain of a multi-vertex. A brief summary of these techniques is outlined in the next paragraphs, but more information can be found in Ref. [195].

A first way of selecting b jets is to take advantage of the long lifetime of the particle, and hence the relatively large impact parameters (d_0 and $z_0 \sin\theta$). Probability density functions of the impact parameter significances (obtained from simulation) are used to calculate the probability of each track (which has to pass quality criteria) to come from a b, c or light-flavour particle. These probabilities are combined into a log-likelihood ratio for the jet (one function per jet flavour).

A second manner of discriminating b jets is to reconstruct the displaced secondary vertices inside a jet by testing all pairs of tracks passing quality criteria, against the assumption of a two-track vertex hypothesis. Pairs of tracks more likely to come from long-lived particles (Λ or K_s) or background (photon conversions, hadronic interactions with ID material) are rejected. Vertices having an invariant mass greater than 6 GeV are vetoed.

The last method relies on the JetFitter algorithm [196], which tries to reconstruct the full b-hadron decay channel, taking advantage of the specific structure of the decays inside the jet.

The MV2 algorithm combines outputs of the methods described above and a Boosted Decision Tree (BDT) [197] is trained on MC samples (5 millions of $t\bar{t}$ events). Jets are given a flavour by trying to find b or c hadrons close-by ($\Delta R < 0.3$ between the jet and the hadron candidate). If no candidates are found, the jet is tagged as light-flavoured. Working points are then defined aiming at specific efficiencies of b-jet tagging on the trained $t\bar{t}$ sample. In this analysis, an efficiency of 70% is expected, corresponding to rejections of light-flavour and c jets of 100 and 50, respectively.

11.3.5 Triggers

Selected events have to pass the single lepton, di-lepton and tri-lepton triggers. A summary of the various triggers used for the data 2015 (2016) is presented in Tab. 11.3 (11.4) [198]. For the two datasets, the lowest unprescaled HLT (high luminosity triggers introduced for the Run 2) are used. In the tables, the following naming convention applies [199]:

- `e` and `mu` indicate whether the trigger applies to electrons or muons, respectively.
- the following number corresponds to the E_{T} (p_{T}) threshold in GeV of the electrons (muons).
- if the name of the trigger contains the letter `v`, the previous cuts vary with η of the particle. This variation is intended to account for the amount of uninstrumented material in front of the calorimeters, which is highly η-dependent.
- `i` and `h` characters denote additional requirements on the isolation and on the energy deposits in the hadronic calorimeter, respectively.
- `T` corresponds to a higher E_{T} threshold on the level-1 trigger.
- `loose`, `medium` and `tight` finally refer to the requirements on the reconstruction quality of the objects.

Efficiencies of the various triggers and their combinations are presented in Tab. C.1, C.2 and C.3 [198] of App. C, corresponding to the 2015 and 2016 (early and late) datasets. Results are shown for Higgs boson samples produced via gluon-gluon fusion, at a mass of 125 GeV. For the four channels the combined efficiencies with the 2015 dataset are 0.994 ± 0.003 ($4e$), 0.992 ± 0.002 (4μ), 0.9996 ± 0.0003 ($2e2\mu$) and

Table 11.3 – Summary of the HLT triggers that are used during the 2015 data taking. When multiple chains are indicated, an OR among them is requested [198].

Channel	Single-lepton	Dilepton	Trilepton
$4e$	e24_lhmedium_L1EM18VH (Period D) e24_lhmedium_L1EM20VH (Period E-J) e60_lhmedium e120_lhloose	2e12_lhloose_L12EM10VH	e17_lhloose_2e9_lhloose
4μ	mu20_iloose_L1MU15 mu40 mu60_0eta105_msonly	2mu10 mu18_mu8noL1	3mu6 3mu6_msonly mu18_2mu4noL1
$2e2\mu$	$4e$ OR 4μ	$4e$ OR 4μ OR e17_lhloose_mu14 e24_medium_L1EM20VHI_mu8noL1 e7_medium_mu24	$4e$ OR 4μ OR 2e12_lhloose_mu10 e12_lhloose_2mu10

0.989 ± 0.004 ($2\mu2e$). The same efficiencies with the 2016 dataset are 0.9951 ± 0.0004 ($4e$), 0.9859 ± 0.0006 (4μ), 0.9952 ± 0.0004 ($2e2\mu$) and 0.968 ± 0.001 ($2\mu2e$) for data taking happening before autumn 2016, and 0.9933 ± 0.0006 ($4e$), 0.9808 ± 0.0007 (4μ), 0.9870 ± 0.0007 ($2e2\mu$) and 0.956 ± 0.001 ($2\mu2e$) for the data recorded afterwards.

In data 2015, an inefficiency of about 10% was observed for the muon trigger in the barrel region, as compared to the simulation. This inefficiency was found to arise from the L1 trigger. Scale factors are applied to the simulation to overcome these discrepancies, but currently only single-lepton triggers are supported by the CP groups and no scale factors are given for the di- and tri-lepton triggers. A study on the 4μ and $2e2\mu$ channels was carried out [200]. Calculating the corresponding scale factors and applying them to the simulation, the discrepancy observed in data could be reduced to 1.0% for the $2e2\mu$ channel, and to almost 0% for the 4μ channel.

Using events firing the triggers described previously, the various objects passing the requirements are selected. From these, it is possible to start the reconstruction of the Higgs boson, which has decayed into four leptons.

11.4 Event selection

11.4.1 Selection of events for the analysis

Only electrons and muons passing the quality requirements as described in the Sec. 11.3, are selected for the analysis. The electrons must have their transverse energy $E_{\mathrm{T}} > 7\,\mathrm{GeV}$ and their pseudo-rapidity $|\eta| < 2.47$. Concerning the muons, their transverse momentum p_{T} must be greater than 5 GeV, except for CT muons, for which the cut is tighter to 15 GeV. Finally, only jets passing the quality requirements and having $p_{\mathrm{T}} > 30\,\mathrm{GeV}$ and $|\eta| < 4.5$ are selected.

Following the recommendations of the harmonisation group [201], overlap removals of selected leptons and jets are performed. In an $e - \mu$ pair, the electron is removed if the associated tracks are too close to each other. In a lepton-jet pair, the jet is removed if $\Delta R_{\ell j} < 0.2$ (0.1) in case of an electron (muon). In order to maintain a high acceptance, overlaps with a jet where the lepton should be removed are not

Table 11.4 – Summary of the HLT triggers that are used during the 2016 data taking. When multiple chains are indicated, an OR among them is requested [198].

Channel	Single-lepton	Dilepton	Trilepton
$4e$	e24_lhmedium_ivarloose (Period A-D3)	2e15_lhvloose_nod0_L12EM13VH (Period A-D3)	e17_lhloose_nod0_2e9_lhloose_nod0 (Period A-D3)
	e26_lhtight_nod0_ivarloose (Period D4-F)	2e17_lhvloose_nod0 (Period D4-F)	replaced by
	e60_lhmedium_nod0		HLT_e17_lhloose_nod0_2e10 _lhloose_nod0_L1EM15VH_3EM8VH
	e60_lhmedium		when $\mathcal{L} > 1.2 \times 10^{34}\,\mathrm{cm}^{-2}\mathrm{s}^{-1}$
	e140_lhloose_nod0		
	e300_etcut (Period A-D3)		
4μ	mu24_ivarloose_L1MU15 (Period A)	2mu10 (Period A)	3mu4 (Period A, I4-)
	mu24_iloose_L1MU15 (Period A)	2mu10_nomucomb (Period A)	3mu6 (Period B-D3)
	mu24_ivarmedium (Period B-E)	2mu14 (Period B-)	3mu6_msonly (Period D4-F)
	mu24_imedium (Period B-E)	2mu14_nomucomb (B-D3)	mu11_nomucomb_2mu4noL1_nscan03 _L1MU11_2MU6 (Period A-D3)
	mu26_ivarmedium (Period D4-)	mu20_mu8noL1 (Period A-E)	mu20_2mu4noL1
	mu26_imedium (Period D4-E2)	mu20_nomucomb_mu6noL1_nscan03 (Period A-D3)	mu20_nomucomb_mu6noL1 _nscan03
	mu40 (Period A)	mu22_mu8noL1 (Period D4-F)	mu20_msonly_mu10noL1_msonly_ nscan05_noComb (Period A-D3)
	mu50		
$2e2\mu$	$4e$ OR 4μ	$4e$ OR 4μ OR	$4e$ OR 4μ OR
		e17_lhloose_nod0_mu14 (Period A-D3)	HLT_e17_lhloose_nod0_mu14
		e24_lhmedium_nod0_L1EM20VHI _mu8noL1 (Period A-D3)	HLT_e24_lhmedium_nod0 _L1EM20VHI_mu8noL1 (Period A-D3)
		e7_lhmedium_nod0_mu24 (Period A-D3)	HLT_e26_lhmedium_nod0 _L1EM22VHI_mu8noL1 (Period D4-)
		e17_lhloose_mu14 (Period D4-F)	HLT_e7_lhmedium_nod0_mu24
		e24_lhmedium_L1EM20VHI_mu8noL1 (Period D4-F)	HLT_e12_lhloose_nod0_2mu10
		e7_lhmedium_mu24 (Period D4-F)	HLT_2e12_lhloose_nod0_mu10

applied if the opening angle between the jet and the lepton verifies $0.2 < \Delta R_{\ell j} < 0.4$. Finally, CT muons are removed if they share the same ID track as an electron to avoid misidentification. In case of electrons sharing the same ID track or having clusters in common in the EM calorimeters, the electron having the greatest E_{T} is kept.

The primary vertex, from which the final-state leptons arise, is defined as the vertex having the greatest sum over the transverse momenta of its constituting particles. Therefore, only leptons having tracks satisfying $|z_0 \sin(\theta)| < 0.5\,\mathrm{mm}$ are selected. In order to limit the contamination from cosmic background, muon tracks are required to have a low transverse impact parameter $|d_0| < 1\,\mathrm{mm}$.

The various selection criteria for electrons, muons and jets are presented in Tab. 11.5. From the selected leptons, candidate quadruplets are formed gathering two pairs of leptons having same flavour (electron or muon) and opposite charges. These two pairs correspond to the Z candidates, whereas the four vector resulting from the four leptons corresponds to the Higgs boson candidate. In each quadruplet formed, the leading, sub-leading and sub-sub-leading transverse momenta of the leptons are required to be greater than 20 GeV, 15 GeV and 10 GeV, respectively. Quadruplets having more than one CT or one ME muons are removed. The invariant mass of the Z candidates is calculated. The pair having an invariant mass the closest to the pole mass of the Z (m_Z), is called the leading pair composed of the leptons $\ell_1\ell_2$. The second pair is referred to as the sub-leading pair with the leptons $\ell_3\ell_4$. The corresponding masses are denoted m_{12} and m_{34}. Note that the first lepton of each pair has a positive charge by convention.

Additional cuts are applied to the quadruplet. The leading mass should lay in the window $50\,\mathrm{GeV} < m_{12} < 106\,\mathrm{GeV}$. The sub-leading mass has to satisfy $12\,\mathrm{GeV} < m_{34} < 115\,\mathrm{GeV}$. In order to suppress contamination from J/ψ decays, a veto is applied. If any combination of the four remaining leptons is found, which would lead to a pair of opposite-charge same-flavour leptons with an invariant mass less than 5 GeV, the quadruplet is dropped. Finally leptons should be well separated. The opening angle between two leptons having same (different) flavour should be at least of 0.10 (0.20). If these criteria are not fulfilled, the quadruplet is not selected.

After these selection cuts, isolation selection is applied to leptons, using the *FixedCutLoose* working point for both electrons and muons. The description of the working points is given in Sec. 6. Only muons (electrons) satisfying $p_{\mathrm{T}}^{\mathrm{varcone30}}/p_{\mathrm{T}} < 0.15$ and $E_{\mathrm{T}}^{\mathrm{topocone20}}/p_{\mathrm{T}} < 0.30$ ($p_{\mathrm{T}}^{\mathrm{varcone20}}/p_{\mathrm{T}} < 0.15$ and $E_{\mathrm{T}}^{\mathrm{topocone20}}/p_{\mathrm{T}} < 0.20$) are selected. Before applying isolation cuts, isolation variables are corrected for close-by objects, corresponding here to the other leptons of the quadruplets. The calculation of this correction, which improves the efficiency of isolation selection, is described in Chap. 8.

The last cut on leptons is on the significance of the transverse impact parameter, calculated as d_0/σ_{d_0}, where σ_{d_0} is the error on the measurement of d_0. For muons (electrons), this value must be below 3 (5). A recent cut was added to complete the selection: the fit quality of the vertex formed by the four leptons. This new selection criterion is developed in the next paragraphs.

In the end, if several quadruplets remain, the one from the channel with the higher rate and $m_{4\ell}$ resolution is selected, using the following order: 4μ, then $2e2\mu$, then $2\mu2e$, then $4e$. If several quadruplets remain after this selection, only the one minimising $|m_Z - m_{12}|$ is kept. In case of equality, the quadruplet minimising both $|m_Z - m_{12}|$ and $|m_Z - m_{34}|$ is kept. An example cut flow using gluon-gluon fusion simulated events is presented in Tab. 11.6.

11.4.2 Vertexing of the four leptons in the final state

With respect to Run 1, the muon p_{T} cuts were loosened (from 7 GeV to 5 GeV) to increase acceptance. This however lead to an increase of the reducible background yields (Z + jets and $t\bar{t}$ in majority). In order to counterbalance this, a new cut was introduced in the analysis, which complements d_0 and isolation cuts.

Table 11.5 – Summary of the event selection requirements. The two lepton pairs are denoted as m_{12} and m_{34} [198].

Physics Objects	
Electrons	
Loose Likelihood quality electrons with hit in innermost layer, $E_T > 7\,\text{GeV}$ and $\lvert\eta\rvert < 2.47$	
Interaction point constraint: $\lvert z_0 \times \sin\theta\rvert < 0.5\,\text{mm}$ (if ID track available)	
Muons	
Loose identification with $p_T > 5\,\text{GeV}$ and $\lvert\eta\rvert < 2.7$	
Calo-tagged muons with $p_T > 15\,\text{GeV}$ and $\lvert\eta\rvert < 0.1$, *Segment-Tagged* muons with $\lvert\eta\rvert < 0.1$	
Extrapolated restricted to the $2.5 < \lvert\eta\rvert < 2.7$ region	
Combined, *Extrapolated* (with ID hits if available) and *Segment-Tagged* muons with $p_T > 5\,\text{GeV}$	
Interaction point constraint: $\lvert d_0\rvert < 1\,\text{mm}$ and $\lvert z_0 \times \sin\theta\rvert < 0.5\,\text{mm}$ (if ID track available)	
Jets	
anti-k_t jets with *bad-Loose* identification, $p_T > 30\,\text{GeV}$ and $\lvert\eta\rvert < 4.5$	
Jets with $p_T < 60\,\text{GeV}$ and $\lvert\eta\rvert < 2.4$ are required to pass the pile-up jet rejection	
at the 92% working point (JVT score > 0.59).	
b-tagging	
Previously selected jets with $\lvert\eta\rvert < 2.5$ passing the `MV2_c10` algorithm at its 70% working point	
overlap removal	
Jets within $\Delta R < 0.2$ of an electron or $\Delta R < 0.1$ of a muon are removed	
Event Selection	
Quadruplet Selection	Require at least one quadruplet of leptons consisting of two pairs of same-flavour opposite-charge leptons fulfilling the following requirements: - p_T thresholds for three leading leptons in the quadruplet: 20, 15 and 10 GeV - Maximum one *Calo-Tagged* or *Extrapolated* muon per quadruplet - Select best quadruplet (per channel) to be the one with the (sub)leading dilepton mass the (second) closest to the Z pole mass - Leading dilepton mass requirement: $50 < m_{12} < 106\,\text{GeV}$ - Sub-leading dilepton mass requirement: $12 < m_{34} < 115\,\text{GeV}$ - $\Delta R(\ell,\ell') > 0.10$ (0.20) for all same (different) flavour leptons in the quadruplet - Remove quadruplet if alternative same-flavour opposite-charge dilepton gives $m_{\ell\ell} < 5\,\text{GeV}$
Isolation	- Contribution from the other leptons of the quadruplet is subtracted - Muon track isolation: $p_T^{\text{varcone30}}/p_T < 0.15$ - Muon calorimeter isolation: $E_T^{\text{topocone20}}/p_T < 0.30$ - Electron track isolation: $p_T^{\text{varcone20}}/p_T < 0.15$ - Electron calorimeter isolation: $E_T^{\text{topocone20}}/p_T < 0.20$
Impact Parameter Significance	Apply impact parameter significance cut to all leptons of the quadruplet - For electrons: $d_0/\sigma_{d_0} < 5$ - For muons: $d_0/\sigma_{d_0} < 3$
Vertex Selection	Require a common vertex for the leptons: - $\chi^2/\text{ndof} < 6$ for 4μ and < 9 for others.

Table 11.6 – Example cut flow using gluon-gluon fusion simulated events for each of the four final states [198]. Event yields are given with their corresponding efficiencies. Yields are normalised to the total integrated luminosity of 36.1 fb^{-1}. Efficiencies are calculated with respect to the total number of generated events.

Final states	4μ		$2e2\mu$		$2\mu2e$		$4e$		Combined	
	N_{pass}	Efficiency [%]	N_{pass}	Efficiency [%]	N_{pass}	Efficiency [%]	N_{pass}	Efficiency [%]	N_{pass}	Efficiency [%]
Initial	51.08	100	51.08	100	51.08	100	51.08	100	204.32	100
After selection	18.25	35.7	13.00	25.5	9.81	19.2	9.73	19.0	50.79	24.9

This new cut relies on a vertexing algorithm [202] which performs the fit of the tracks of the four-lepton candidates of the quadruplet, assuming these tracks originate from a common vertex. Imposing a good fit quality, assessed using χ^2/N_{dof} (sum of the squared differences between data and fit, divided by the number of degrees of freedom), the reducible background contributions were reduced. For instance, the $Z + b\bar{b}$ background contains muons originating from b decays which are misplaced as compared to muons coming from the Z boson. There are several vertices, the fit quality is therefore poor, and the quadruplet is rejected.

The efficiency of the vertex cut as a function of the cut value for both signal and background events (generated using MC) is presented in Fig. 11.2 [198]. For a minor reduction of signal, Z + jets background can be suppressed by about 25%. The signal efficiency is rather flat against the cut value, but the best value is chosen to ensure the highest efficiency. Therefore the 4μ channel was given a cut of $\chi^2/N_{\text{dof}} < 6$, whereas the other three channels $2\mu2e$, $2e2\mu$ and $4e$ have a looser cut of $\chi^2/N_{\text{dof}} < 9$. No case of non convergent fits was found in MC studies [203].

In order to further validate the use of the vertex cut, a control region was designed to be rich in $t\bar{t}$ events in data. Quadruplets of the form $e\mu\mu\mu$ were taken, with isolation and d_0-significance cuts only applied to the $e\mu$ pair. The control region being defined, the rejection power of two cuts was studied. The first cut $d_0/\sigma_{d_0} < 3$ was applied to the muons of the sub-leading pair. The second corresponded to a requirement on the vertex fit quality $\chi^2/N_{\text{dof}} < 7$ (this threshold was chosen to be close to the 4μ case, as three muons compose the quadruplet, but looser as one electron is present). The conclusion of this study is that rejection powers of the two cuts were found to be very similar on simulated $t\bar{t}$ samples. The requirement on the fit quality even performs better than the d_0 cut. A combination of the two cuts provides best rejection, therefore it was decided to apply the quality requirement on top of d_0 cuts.

11.4.3 Final state radiation recovery and mass constraints

In order to improve the measurement of the Higgs mass, two techniques are used. First of all, the energy lost by photon radiation is added to the four vector of the Higgs boson (FSR recovery). Secondly, the invariant mass of the on-shell Z boson of the decay product of the Higgs boson (corresponding to m_{12} with the previous notations) is constrained to allow for a better resolution. A detailed review of the studies of the performance of these two techniques can be found in Ref. [204].

FSR recovery

The leptons resulting from the Z decays can radiate photons, according to QED. This is called Final-State Radiation (FSR). These radiations are well modelled by simulation and cause a loss of energy of

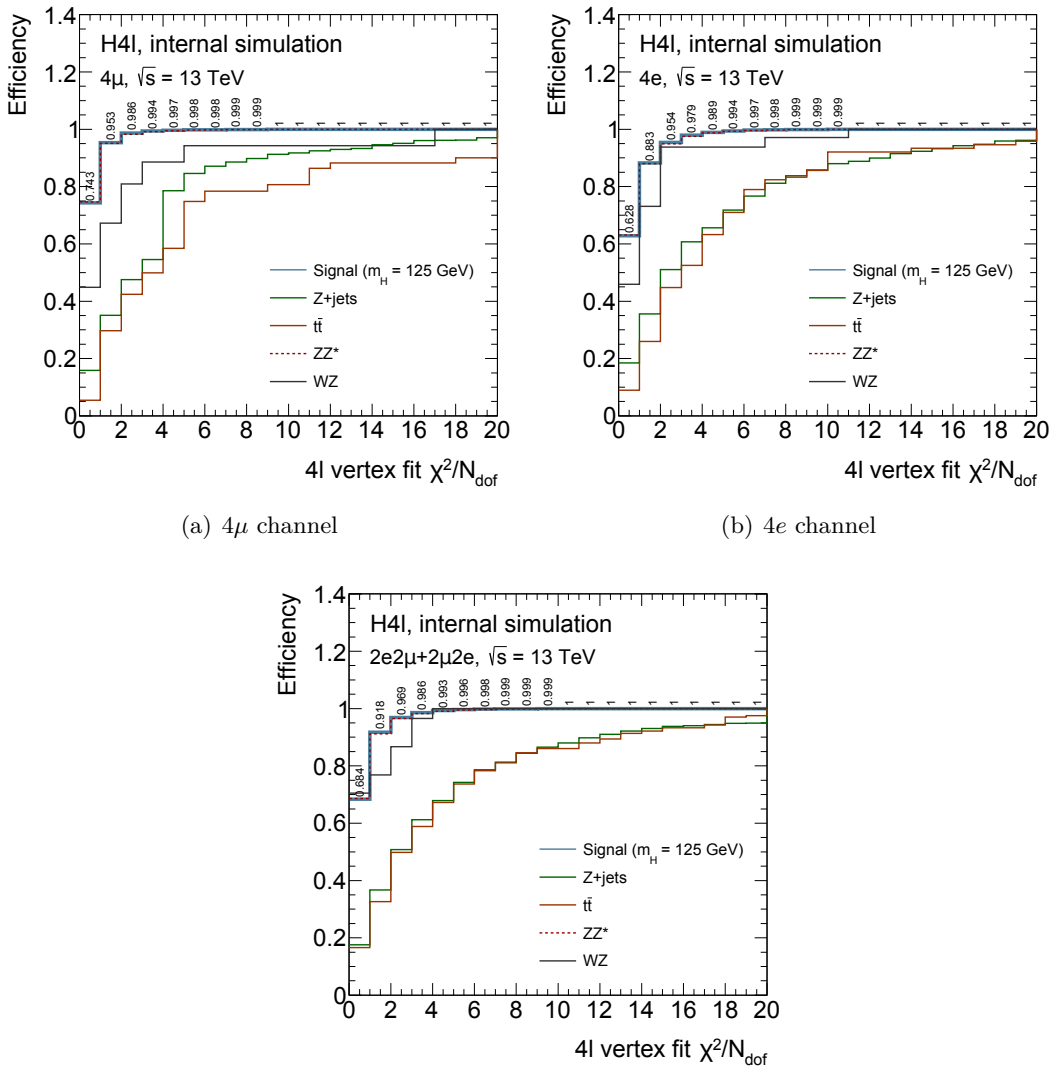

(a) 4μ channel

(b) $4e$ channel

(c) $2\mu 2e$ channel

Figure 11.2 – 4ℓ vertex cut efficiencies for the various decay channels. Efficiencies are presented for various cuts on the vertex χ^2/N_{dof}, for signal and background events generated using simulation [198]. The two major contributions from the reducible background ($t\bar{t}$ and Z+jets) are suppressed by the new cut, for a relative stable signal efficiency. The WZ and ZZ^* background contributions are not strongly impacted by the new cut, as the vertices have same signatures as for the signal.

the leptons. The radiated photons, which can be detected, have to be included in the four-vector of the leptons.

The search for radiated photons can be performed collinearly to the trajectory of the lepton in the detectors (small opening angle between the lepton and the photon $\Delta R_{\ell\gamma} < 0.15$). If this search fails, non-collinear search tries to recover photons radiated far from the trajectory. A specific tool for FSR recovery was developed, using results from dedicated studies [205]. For the $H \to ZZ^* \to 4\ell$ study, FSR recovery is only allowed for one photon per event, whose energy is added to the leading Z four-momentum.

For the collinear search, any photon close enough to a muon ($\Delta R_{\gamma\mu} < 0.05$) and satisfying one of the two following sets of criteria is added. The first type of photon should correspond to a 3×5 cluster rectangle seeded by topoclusters, having a cluster energy verifying $1.5\,\text{GeV} < E_\text{T} < 3.5\,\text{GeV}$, $\Delta R_{\text{cluster},\,\mu} < 0.08$ and at least 20% of the cluster energy deposited should be located into the front sampling of the calorimeter (strips). The second type of photon should be a standard `Egamma` photon or electron with $E_\text{T} > 3.5\,\text{GeV}$, $\Delta R_{\text{cluster},\,\mu} > 0.15$ and at least 10% of the cluster energy deposited should come from the front sampling of the calorimeter. If several clusters are found in the cone, the cluster having the highest E_T is selected. The requirement on the energy deposits in the strips is only applied if $E_\text{T} < 15\,\text{GeV}$, to reduce the background induced by the muon during its ionisation (at these low energies, the Landau tail of the muon energy loss distribution is still significant). 400 MeV are subtracted from the energy of the selected collinear photon to account for muon ionisation.

While the collinear search only concerns muons, the non-collinear search is performed for both electrons and muons. Selected photons should pass the tight identification criteria, be far enough from the lepton ($\Delta R_{\text{cluster},\,\ell} > 0.15$), have $E_\text{T} > 10\,\text{GeV}$ and should be isolated using the *FixedCutLoose* working point of the isolation selection ($E_\text{T}^{\text{topocone20}} < 0.065 E_\text{T}^{\gamma}$ and $p_\text{T}^{\text{cone20}}/E_\text{T}^{\gamma} < 0.05$). The cut on E_T reduces the hadronic background mainly due to pion decays.

The addition of FSR photons only happens for events which pass the selection requirements before the recovery. Since only one photon per event is added to the on-shell Z, priority is given to the collinear photons associated to the leading pair (only a muon-muon pair is considered). The recovery is applied only if $66 < m_{\mu_1\mu_2} < 89\,\text{GeV}$ and the resulting mass is $m_{\mu_1\mu_2\gamma} < 100\,\text{GeV}$. If the collinear correction fails, non collinear FSR photons are searched for. The photon having the highest E_T is added, if $m_{12} < 81\,\text{GeV}$ and the resulting mass is $m_{\ell_1\ell_2\gamma} < 100\,\text{GeV}$. The upper cuts on $m_{\ell_1\ell_2\gamma}$ suppress the initial-state radiations (ISR), the pion and muon ionisation backgrounds. These cuts only decrease the efficiency of few percent. Indeed, FSR photons mostly correspond to events with a Z invariant mass well below the Z pole mass, whereas ISR photons, pion and muon ionisation clusters do not.

The results of the FSR recovery are presented in Fig. 11.3. About 3% more signal events pass the selection cuts after FSR correction thanks to this technique. The collinear search succeeds about 70% of the time (with 85% genuine photons). The non-collinear search achieves recovery of the photon 60% of the time.

Constraint on the Z mass

The leading pair is most likely resulting from the decay of an on-shell Z and the corresponding resonance can benefit from high resolution of the detector, which is improved for the $Z \to \mu\mu$ and $Z \to ee$ decays. The probability of observing a Z boson with a true mass μ_{12} and decaying into two leptons (indexed $i \in \{1,2\}$) having true four-momenta of $\mathbf{p}_i^{\text{true}}$, and measuring the four-momenta $\mathbf{p}_i^{\text{rec}}$ can be expressed as [198]

$$\mathcal{P}\left(\mathbf{p}_1^{\text{true}}, \mathbf{p}_2^{\text{true}}, \mathbf{p}_1^{\text{rec}}, \mathbf{p}_2^{\text{rec}}\right) = B\left(\mathbf{p}_1^{\text{true}}, \mathbf{p}_2^{\text{true}}\right) \times R_1\left(\mathbf{p}_1^{\text{true}}, \mathbf{p}_1^{\text{rec}}\right) \times R_2\left(\mathbf{p}_2^{\text{true}}, \mathbf{p}_2^{\text{rec}}\right), \tag{11.2}$$

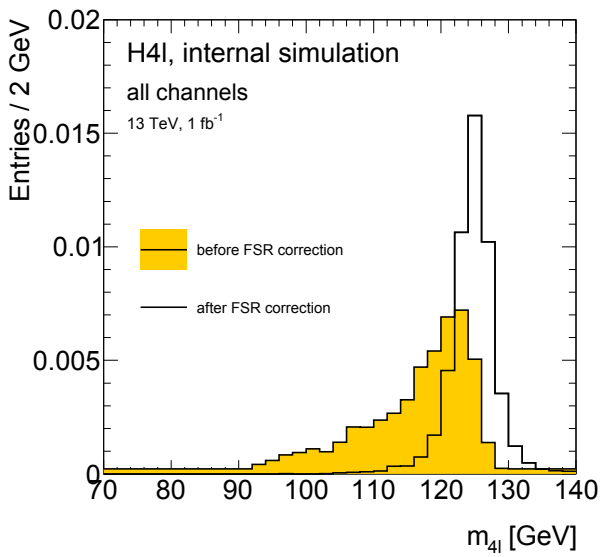

Figure 11.3 – Impact of the FSR recovery on the four-lepton invariant mass distribution. The distributions of the unconstrained four-lepton invariant mass are presented before (yellow histogram) and after (transparent histogram) FSR recovery, using MC (gluon-gluon fusion). Only events with an identified FSR are selected [198].

where B is the probability density function (pdf) of the Z line shape at generator level and R_i are the pdfs of the energy or momentum response functions for the two leading leptons. The function B only depends on μ_{12} and is written

$$\mu_{12}{}^2 = 2 \times \epsilon_1 \epsilon_2 \left(1 - \cos\theta\right), \tag{11.3}$$

where $\{\epsilon_i\}_{i\epsilon\{1,2\}}$ are the true lepton energies (or momenta) and θ is the opening angle (in radians) between these two leptons. This angle can be calculated using the true values of η_i^{true} and ϕ_i^{true}. The response functions R_i associate the true values of four-momenta to their measurements. Since η and ϕ of the leptons are measured with high precision, it is safe to assume $\eta_i^{\text{true}} = \eta_i^{\text{rec}}$ and $\phi_i^{\text{true}} = \phi_i^{\text{rec}}$. Taking this into account, the response functions are only dependent upon the true energies and the measured four-momentum:

$$R_i\left(\mathbf{p}_i^{\text{true}}, \mathbf{p}_i^{\text{rec}}\right) = R_i\left(\epsilon_i | \mathbf{p}_i^{\text{rec}}\right). \tag{11.4}$$

Combining all the previous equations, it appears that the only unknowns in Eq. 11.2 are the true lepton energies ϵ_i. Taking into consideration that the mass of the Z boson can be known using the truth information of the simulated samples, these energies can be constrained using Eq. 11.3 and 11.4. In order to do so, the likelihood $\mathcal{P}$ is maximised for each event with the knowledge of the measured four-momenta of the leptons. At the maximum value, the most likely four-momenta $\mathbf{p}_i^{\text{max}}$ are retrieved and used to reconstruct the Z boson and hence assess the invariant mass with greater precision. This whole procedure is referred to as the *Z-mass constraint*.

The function B is modelled using a Breit-Wigner function $\mathcal{F}_{\text{BW}}\left(\mu_{12} | m_Z, \Gamma_Z\right)$. The mean and the width of this distribution are set to the Z pole mass m_Z and the Z width Γ_Z, respectively. The single lepton response functions R_i are approximated by a Gaussian function $\mathcal{F}_{\text{G}}\left(\epsilon_i | E_i, \sigma_i\right)$. The mean and the variance of the Gaussian are set to the measured lepton energies E_i and the corresponding momentum resolution estimated using simulation, respectively. A dedicated tool was implemented which constrains the leading pair mass using the above procedure [198].

The response functions for the energy or the momentum of the leptons do not have a pure Gaussian shape. Because of reconstruction effects and photon radiation, the tails of the distributions are more enhanced. The more these effects are pronounced, the more the response functions deviate from a Gaussian. This is particularly true for electrons, where photon radiation occurs at a higher extent with respect to muons. To account for these deviations, response functions are parametrised with the sum of Gaussian distributions, as described in Ref. [206]. The parametrised functions are used to validate the Gaussian approximation introduced in the previous paragraph. Validation is carried out on $4e$ final states which only contain electrons, and should therefore be the most affected by the approximation. For this study, the R_i functions are extended to the sum of three Gaussians. Comparing the results obtained using the extended functions, or the basic approximation, it is possible to estimate the importance of the enhancement of the tails. According to the study, it turns out that the use of a single Gaussian approximation does only affect the Z-mass constraint by a minor amount, validating the use of the approximation for the analysis.

As well as the R_i are not true Gaussians, the true Z line shape does not exactly follow a Breit-Wigner distribution. In order to refine the distribution, the line shape of m_Z^{true} can be obtained from simulation and B is replaced by the smoothed m_Z^{true} distribution normalised to unity. The study indicated that the Z-mass constraint is not affected by the change of expression for B in the case of single-Gaussian approximations for the functions R_i [207]. Thanks to the constraints on the mass of the leading Z boson, the resolution on the four-lepton invariant mass is improved by about 15%.

11.4.4 Possible improvements of the general selection

Possible improvements of the general event selection (as described in Sec. 11.4.1) were studied by the author. The studies concern the possibility of a late selection of the quadruplets, as well as applying the isolation cuts at an earlier stage of the selection. These changes are only studied for the low mass $H \to ZZ^* \to 4\ell$ analysis.

While in the current cut-flow the best quadruplet is selected just before the dilepton-invariant-mass requirements, the first study proposes to delay this selection to the very last step of the process, after the isolation and d_0 significance cuts. The second study evaluates the opportunity of applying the isolation cuts at an earlier stage, just after the quadruplet formation (therefore several quadruplets may be tested). The two studies were performed using ggF, VBF, ZH, WH MC and ttH signal samples at $m_{4\ell} = 125\,\text{GeV}$. The reducible background was composed of the 3ℓ and 4ℓ $Z \to ee$ and $Z \to \mu\mu$ samples, while the irreducible background was formed using $qq/gg \to ZZ^*$ samples.

Overall the studies did not show significant improvement in terms of increased signal yield and sensitivity, and it was chosen to keep the current selection as a baseline for the analysis. More details concerning the studies are presented in App. D.

11.5 Background estimation and shape modelling

For the analysis presented in this thesis, various backgrounds have to be taken into consideration. The most important is the $pp \to ZZ^*$ production which has the same characteristics as the $H \to ZZ^* \to 4\ell$ signal channel, and is therefore historically referred to as the *irreducible background*. Thanks to the good MC description, the shapes of this background are taken from simulation, normalised to predictions including NNLO QCD and NLO EW corrections [208].

On top of this main contribution, several *reducible backgrounds* are considered, including the Z + jet (both heavy- and light-flavour jets), the $t\bar{t}$ and WZ productions. These backgrounds are not well modelled

by MC and data techniques are used to estimate the corresponding yields. A short description of the procedure is outlined in this section, but more information can be found in Ref. [198].

Finally, ZZZ, WZZ, WWZ and $t\bar{t} + Z$ background channels, which are not dominant in the scope of the analysis, are modelled using MC simulation and normalised to most up-to-date predictions.

Reducible backgrounds contain non-isolated leptons and data-driven techniques used to extract their yields consist in the following steps. First, background compositions and shapes are studied in regions of the phase space specially defined to enrich the samples with the desired background. These regions, referred to as *control regions* (CRs), are built inverting or loosening the selection criteria or the lepton identification quality. Improved statistics for the backgrounds in these regions enable several distributions to be compared between data and simulation. Then the background yields in the signal region (SR) are extrapolated from the CRs using transfer factors (also referred to as extrapolation or fake factors). These factors are derived after the estimation of the efficiencies in the CRs for the data and MC, but they can also be defined as the ratios of the expected yields between CRs and the SR.

Since the main reducible background contributions are highly dependent upon the flavour of the sub-leading pair, the analysis is separately performed for the two final states $Z + ee$ and $Z + \mu\mu$. While the electron background mostly originates from jets (which were misidentified as electrons) produced in association to a Z boson, the muon background results in most of the cases from heavy-flavour jets produced with the Z boson or in $t\bar{t}$ decays.

In the following paragraphs, systematic uncertainties are introduced, which account for the background yields and shape. These uncertainties are taken into account for the measurements performed in the Higgs-to-four-lepton decay channel, on top of the theoretical and experimental uncertainties. The latter two are described in Sec. 11.6.

11.5.1 $Z + \mu\mu$ background channel

The main contribution arises from the production of Z bosons with muons coming from semi-leptonic decays of heavy-flavour hadrons ($Z +$ HF jets). A smaller contribution from Z produced with muons from in-flight decays of π/K (light flavour jets) is also taken into account ($Z +$ LF jets). A third component regroups the WZ diboson productions when accompanied by a jet, and the $t\bar{t}$ production. The two first backgrounds are denoted $Z +$ jets.

In order to estimate the contribution of the various backgrounds, three orthogonal CRs enriched in each of the components are constructed (which in turn are orthogonal to the SR) as detailed afterwards. These CRs will be labelled A, B and C. The two regions A and B are enriched in $Z +$ HF jet and $t\bar{t}$ background events. A global fit is performed simultaneously in these two regions to extract the yields of these contributions. The results are used for the fit of a third CR (CR C) enriched in $Z +$ LF jets. The overall results of these two fits are finally applied to a fourth CR (labelled D), which contains all the background contributions. The yields in this CR can finally be extrapolated to the SR using transfer factors.

Global simultaneous fit

The first CR, denoted CR A, is enhanced in heavy-flavour jets ($Z +$ HF) and $t\bar{t}$. The standard selection is applied to the leading pair, but no vertex cuts are applied. Concerning the sub-leading pair, the d_0 significance cut is inverted for at least one lepton, and no isolation cuts are applied.

The second CR, referred to as CR B, is enhanced in $t\bar{t}$, for which the leading pair has to be composed of opposite-flavour and opposite-charge leptons. Standard analysis selection is applied, except the vertex

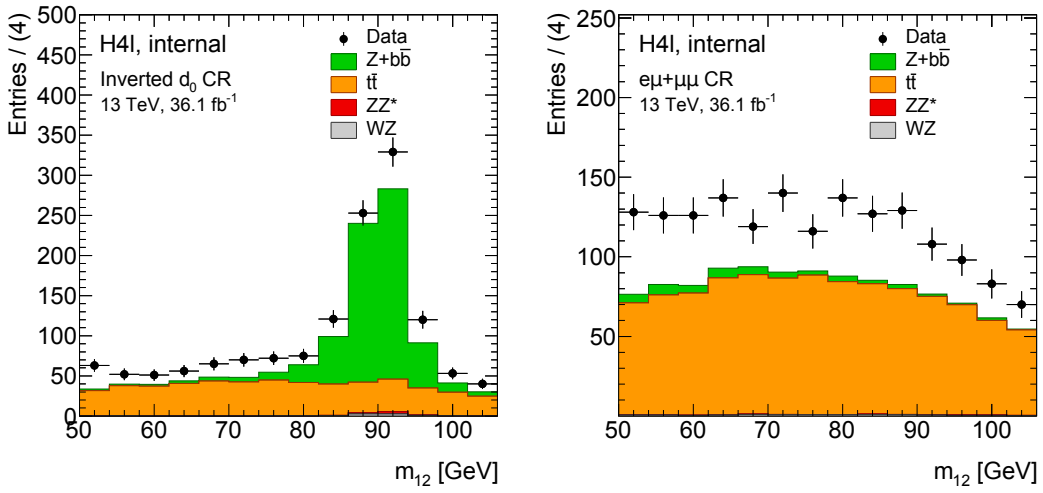

(a) Inverted d_0 significance CR (CR A)

(b) $e\mu + \mu\mu$ CR (CR B)

Figure 11.4 – The distributions of the leading mass m_{12} for data compared to simulation are presented in the (a) inverted d_0 significance and (b) $e\mu + \mu\mu$ CRs, before the fit [198].

cut which is again not applied. For the sub-leading pair, no selections are requested on the d_0 significance and isolation, and both pairs of same and opposite charges are accepted.

The global simultaneous fit used offers the opportunity to increase the statistics available, and relies on an unbinned maximum likelihood fit of m_{12} performed on the CRs A and B at the same time. The choice of m_{12} allows Z + jet events abundant in A to be well separated from the $t\bar{t}$ production channel dominant in region B, due to the non-resonant shape of the distribution in the latter. The CRs are defined to prevent any contamination from the ZZ^* continuum and the Higgs boson signal decays. Distributions of the leading pair in each CR are presented in Fig. 11.4, for which the various background components are detailed. These distributions are normalised to the theoretical cross-sections and the discrepancy between data and simulation highlights the need for data-driven techniques to estimate the background normalisation and shapes. The difference of shape between the two CRs justifies the use of m_{12} as discriminant to separate Z + jet from $t\bar{t}$ backgrounds, as Z + HF (CR A) has a resonant shape, which is not observed in the $t\bar{t}$ CR (CR B).

A third CR, named CR C, is defined to assess the Z + LF jet background where the standard selection is applied, including the vertex cut. One of the leptons of the sub-leading pair is required to fail isolation requirements. Since the d_0 significance criterion is still applied, Z + LF jet events are favoured in this region with respect to Z+HF jet events. Because of a lack of statistics from the Z+LF jet MC samples, the last CR is not fitted at the same time as the two others. The yields of the Z + HF jet and $t\bar{t}$ backgrounds are first fitted. The third Z + LF jet component is fitted separately in the inverted isolation CR, in which the contributions of the two previously fitted backgrounds are taken into account as fixed contaminations.

For the simultaneous fit, the $t\bar{t}$ shape is modelled using a second-order-Chebyshev polynomial for all the CRs. In the Z + jet enhanced CRs, a Breit-Wigner function convoluted with a Crystal Ball function is used. In the $e\mu + \mu\mu$ CR (B), the Z + jet component has a specific shape, due to the non-resonant type of the mass spectrum. A first-order polynomial is thus used which is also deduced from the fit of MC-simulated events. Since the WZ and ZZ^* contaminations of the CRs are minor, the shape of these processes is included in the Z + jets shape, and their yields are fixed to the expected values obtained from

MC-simulated samples. All the parameters of the fit can vary within the statistical uncertainties from the expected values based on the fits on simulated samples (each CR is then treated separately).

Validation of the fit is performed on pseudo data, to which all the procedure is applied. The various distributions of the leading-mass spectra are presented in Fig. 11.6, and the background yields are summarised in Tab. 11.7. Overall, results are consistent and validate the fit. Results of the fit on data are shown in Fig. 11.7 for the various CRs, with the background contributions. No correlations are found between the parameters of the fit.

Relaxed OS control region and extrapolation

A complementary CR, referred to as CR D, is defined using looser selection criteria than the other CRs, which contains all the background components altogether. This CR, referred to as *relaxed OS*, regroups the three previously defined CRs and is used to renormalise each background component, so that the fit results are expressed in terms of number of events. The standard analysis selection criteria are applied, but isolation and d_0 significance cuts are only applied to the leptons of the leading pair. Vertex cuts are not applied.

The probability density functions in each CR (A, B and C) for the simultaneous fit are composed of the sum of the density functions for each background components b_i ($i \in \{Z + \text{HF}, t\bar{t}, WZ, ZZ^*\}$), weighted by the ratios f_i of the contributions of the background in the CR over the same contributions in the relaxed OS CR: $b_{\text{CR}} = \sum_i f_i \times b_i$. The calculated ratios f_i can fluctuate in the global fit within their statistical uncertainties, having Gaussian constraints. These fluctuations broaden the uncertainties on the background components.

To extrapolate the results from CR D to the SR, transfer factors (calculated from simulation) are used, as shown in Fig. 11.5. These transfer factors are derived having calculated the efficiencies of the special isolation and d_0 significance cuts for MC and data in a sample called the $Z + \mu$ control sample. The definition of this sample is described afterwards.

Results in the signal region

The background yields and resulting transfer factors (estimated from simulation) are presented in Tab. 11.8. The fit is carried out again separately for the 4μ (55% of the total yields) and $2\mu 2e$ channels to obtain the corresponding yields. On top of the statistical uncertainty, systematics are added to the transfer factors to account for the variations in efficiencies between data and simulation observed in the $Z + \mu$ control samples. The final results extrapolated to the SR are presented in Tab. 11.9, as well as the variations between data and simulation from which the systematics are inferred. The statistical uncertainties are from the fit only.

Two additional methods were introduced to extrapolate the background yields into the SR. The first one also relies on a simultaneous fit, except that this time an additional CR is defined (same-sign pair CR). The fit is performed for all the categories of backgrounds at the same time in the four CRs, in a similar way as the method presented previously. A second additional method was introduced, which relies on the definition of a $3\ell + \mu$ CR. This method is very much like the electron background case, as described in the next section. These two additional techniques are used as cross-check of the main method and results are found to be in good agreement. More details concerning these validation methods can be found in Ref. [198].

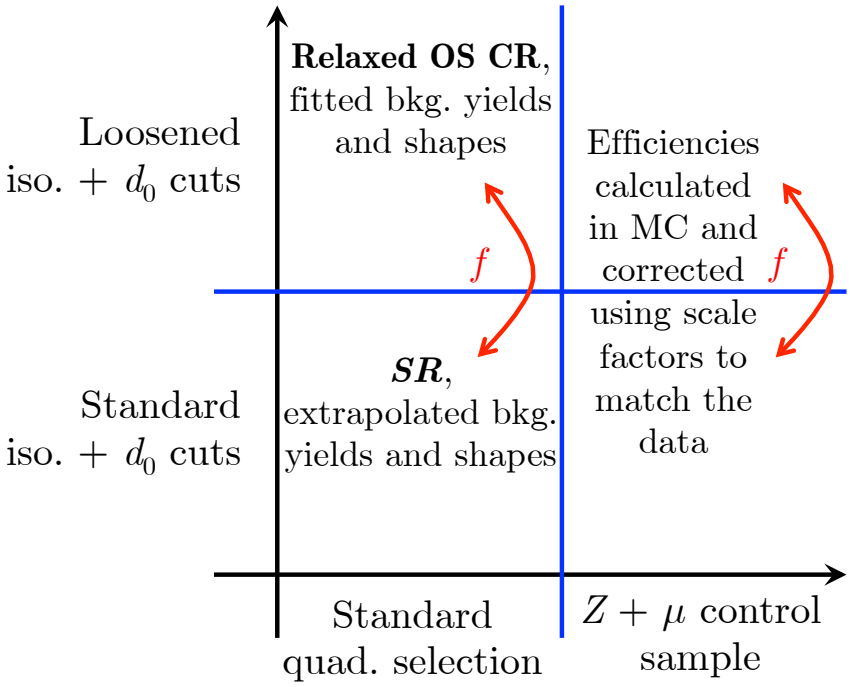

Figure 11.5 – Sketch presenting the method used to extrapolate the $Z + \mu\mu$ background yields to the signal region. Transfer factors calculated in the $Z + \mu$ control sample are used to extrapolate the yields in the signal region.

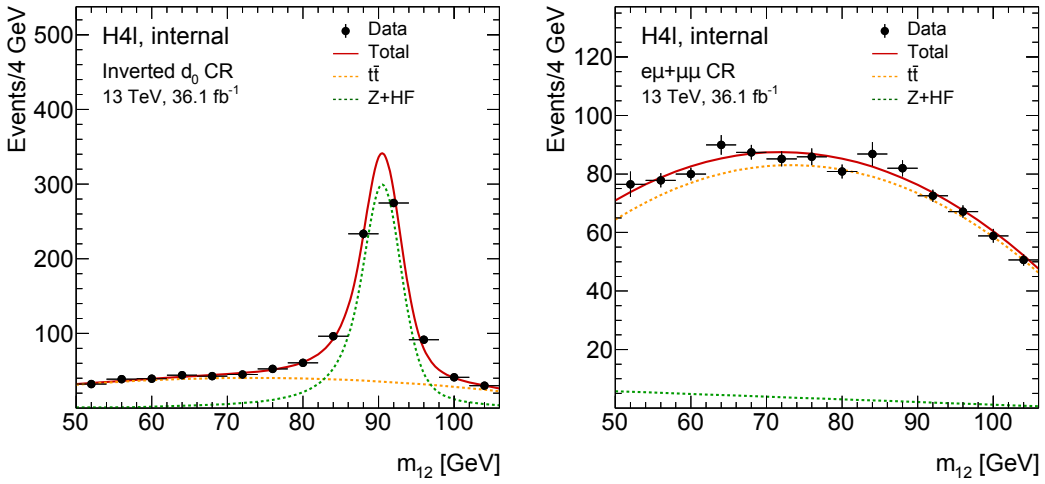

(a) Validation in the inverted d_0 significance CR (CR A)

(b) Validation in the $e\mu + \mu\mu$ CR (CR B)

Figure 11.6 – Distributions of the leading mass using pseudo data in the two simultaneously fitted CRs. These plots validate the good performance of the fit [198].

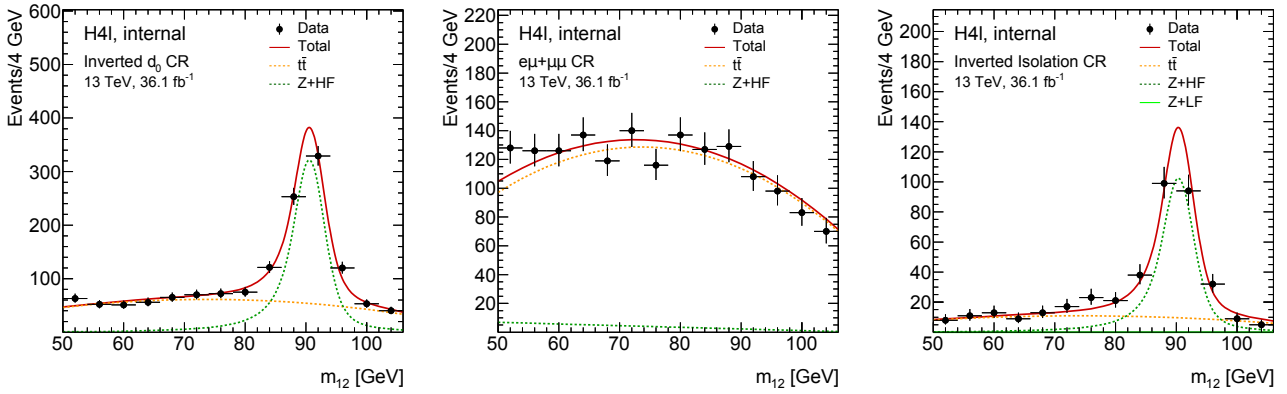

(a) The inverted d_0 significance CR (CR A)

(b) The $e\mu + \mu\mu$ CR (CR B)

(c) The inverted isolation CR (CR C)

Figure 11.7 – Results of the fit for the data in the three control regions.

Table 11.7 – Results of the closure test of the simultaneous fit to the inverted-d_0 and $e\mu$+$\mu\mu$ CRs using pseudo data. The sum of the yields of the Z + HF and $t\bar{t}$ components in the relaxed OS CR are quoted with their statistical uncertainties and compared to the fit results, quoted also with their statistical uncertainties from the fit [198].

Reducible background	MC yield	MC fit estimation
Z + jets (HF)	874 ± 27	877 ± 48
$t\bar{t}$	638 ± 5	638 ± 8
total	1463 ± 16	1465 ± 26

Table 11.8 – Data fit results for the Z + HF, $t\bar{t}$ and Z + LF yields in the relaxed control region, shown together with the per-event efficiencies from MC simulation. Errors on the fit results and transfer factors are statistical only. The final estimate in the signal region is also shown with its statistical and systematic uncertainties. The WZ contribution is also shown [198].

4μ+$2e2\mu$			
type	data fit	extrapolation factor [%]	SR yield
Z + jets (HF)	928 ± 50	0.75 ± 0.09	$6.96 \pm 0.37 \pm 1.19$
$t\bar{t}$	934 ± 23	0.25 ± 0.03	$2.33 \pm 0.06 \pm 0.44$
Z + jets (LF)	0 ± 16	3.0 ± 0.40	$0 \pm 0.49 \pm 0.25$
WZ	(MC-based estimation)		0.91 ± 0.50

Table 11.9 – Final estimates in the signal region for the $Z + \text{HF}$, $t\bar{t}$, $Z + \text{LF}$ and WZ background components in each channel with both statistical and systematic uncertainties [198].

type	4μ	$2e2\mu$
$Z + \text{HF}$	$4.44 \pm 0.30(\text{stat}) \pm 1.05(\text{syst})$	$2.64 \pm 0.22(\text{stat}) \pm 0.36(\text{syst})$
$t\bar{t}$	$0.65 \pm 0.02(\text{stat}) \pm 0.17(\text{syst})$	$1.70 \pm 0.05(\text{stat}) \pm 0.35(\text{syst})$
$Z + \text{LF}$	$0 \pm 0.44(\text{stat}) \pm 0.22(\text{syst})$	$0 \pm 0.33(\text{stat}) \pm 0.17(\text{syst})$
WZ	$0.53 \pm 0.30(\text{stat} + \text{syst})$	$0.38 \pm 0.24(\text{stat} + \text{syst})$

Table 11.10 – Efficiencies of isolation and impact parameter selections for background muons selected in $Z + \mu$ events [198]. Errors are statistical only.

Selection applied	Data [%]	MC [%]
d_0 significance	63.7 ± 0.2	65.9 ± 0.9
isolation	17.7 ± 0.1	16.3 ± 0.4
d_0 and isolation	11.6 ± 0.2	10.5 ± 0.3

Table 11.11 – Isolation and impact-parameter efficiencies for background muons in the light- and heavy-flavour enriched $Z + \mu$ samples [198]. These efficiencies are used to derive the transfer factors to extrapolate the results from the relaxed OS CR (CR D) to the SR. The d_0 efficiencies are in good agreement between data and simulation. On the other hand, MC isolation efficiencies need to be corrected by a scale factor. After corrections, good agreement enables the use of the transfer factors. Errors presented in this table are statistical only.

Selection efficiency	Data [%]	MC [%]	(Data - MC) / MC
d_0 significance (LF)	90.7 ± 0.5	94.6 ± 2.0	-4.1%
isolation before d_0 significance (LF)	13.9 ± 0.2	9.2 ± 0.6	51%
isolation after d_0 significance (LF)	14.1 ± 0.2	9.4 ± 0.7	50%
d_0+isolation (LF)	12.8 ± 0.2	8.9 ± 0.6	44%
isolation (HF)	18.3 ± 0.2	19.0 ± 0.4	-3.7%

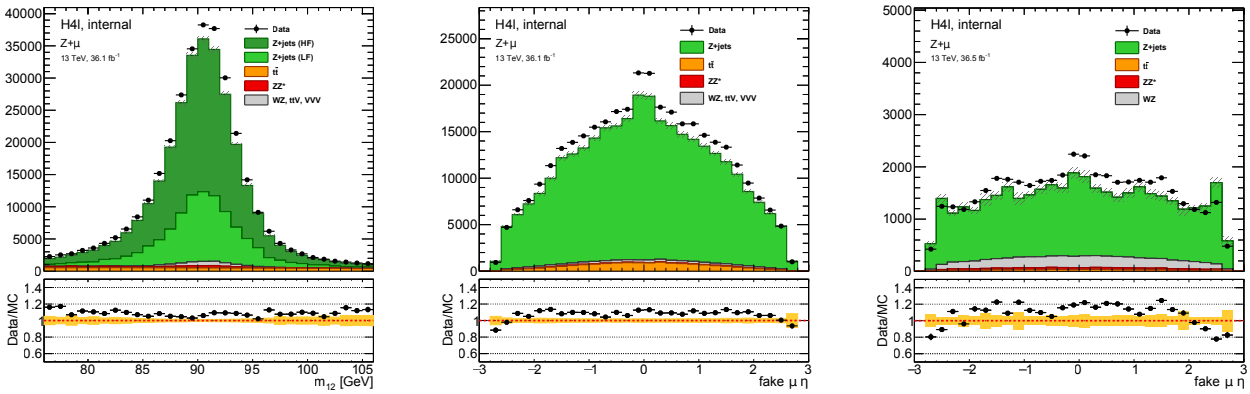

(a) Distribution of the invariant mass of the Z candidates

(b) η^{μ} distribution before applying the isolation and d_0 significance cuts

(c) η^{μ} distribution after applying the isolation and d_0 significance cuts

Figure 11.8 – Kinematic distributions in the $Z + \mu$ control sample, with (a) invariant mass of Z candidates and η distributions of the additional muons (b) before and (c) after d_0 and isolation selections. Data and MC are compared, and show that the sample is mainly composed of Z + jet events [198].

The $Z + \mu$ control sample

In order to study the efficiencies of the isolation and d_0 cuts used to define the CRs, a specific sample was created, referred to as the $Z + \mu$ control sample. Muons are produced along with a Z boson decaying into two leptons. Single and dilepton triggers are used, but the trileptons ones are not considered to prevent any bias in the quality of the muon studied. A Z candidate must be well reconstructed, which satisfies the following requirements. A pair of oppositely-charged muons or electrons has to pass the standard requirements and have $p_{\mathrm{T}} > 20\,\mathrm{GeV}$ (15 GeV) for the leading (sub-leading) lepton. Only the pair having the invariant mass the closest to the Z pole mass is retained, which has to lay within $76 < m_{12} < 106\,\mathrm{GeV}$. This pair has to pass isolation and d_0 cuts, as well as to have leptons well separated ($\Delta R_{\ell_1\ell_2} > 0.1$). Only events having an additional muon of $p_{\mathrm{T}} > 5\,\mathrm{GeV}$ are kept (the 4ℓ events are vetoed). This muon must satisfy $\Delta R_{\mu\ell_i} > 0.1(0.2)$ with the leptons of the leading pair having same (opposite) flavour. A J/ψ veto is also applied, and pairs of opposite charge and same flavour leading to $m_{\mu\ell_i} < 5\,\mathrm{GeV}$ are excluded.

The distribution of the Z mass of the leading pair is presented in Fig. 11.8 (a) and indicates that the sample is mainly composed of Z + jet background, where the extra muon (μ) comes from a heavy-flavour hadron two thirds of the time. Other contributions are minor, but diboson events become more important at high p_{T}^{μ}. The distributions of η^{μ} before and after applying the isolation and d_0 cuts show a sizeable increase of the WZ contribution, as shown in Fig. 11.8 (b) and (c). The shape of the distributions changes because the cuts reduce the fake rate, especially in the central region (region where muons of lower quality are used with the inclusion of CT and ST muons for $|\eta| < 0.1$).

Efficiencies of the isolation and d_0 cuts are assessed on the sample, and the expected contamination of real muons is subtracted considering the W and Z boson decays to only keep background muons. The resulting efficiencies are presented in Tab. 11.10. While efficiencies related to the d_0 significance cut are in good agreement between data and MC, isolation efficiencies have a 10% variation. This discrepancy explains the ratio plots in Fig. 11.8 (b) and (c), which are not close to unity. This disagreement is separately studied for light- and heavy-flavour jets in order to correct the efficiencies in simulation.

The study of the light-flavour contribution is carried out using a subset of the previous control sample.

Adding a cut on the momentum balance between the transverse momentum measurements of the muon in the ID and the MS $\frac{\Delta p_{\mathrm{T}}}{p_{\mathrm{T}}} = \frac{p_{\mathrm{T}}^{\mathrm{ID}} - p_{\mathrm{T}}^{\mathrm{MS}}}{p_{\mathrm{T}}^{\mathrm{ID}}} > 0.1$, it is possible to enrich the light-flavour component. Using the particle-level information of the MC, it is possible to determine that 67% of the sample created is composed of light-flavour background. The contributions of WZ and ZZ^* are minor and are subtracted for the efficiency calculations. In order to disentangle the $Z + \mathrm{HF}$ contributions, an iterative method is deployed (similar to what is described in paragraph 11.5.2). The results of efficiency measurements of isolation and d_0 cuts are presented in Tab. 11.11. There is a disagreement between data and MC of about 50% for the isolation efficiencies, but scale factors are calculated in bins of p_{T} to overcome this.

The same procedure is applied for the study of isolation efficiencies in the case of heavy flavour jets, and a subset enriched in $Z + \mathrm{HF}$ is created. The $Z + \mu$ control sample is taken and an additional inverted d_0 cut is applied on the additional muons. Using particle-level information of the MC, it is possible to determine that heavy-flavour jet backgrounds compose 93% of the created sample. In the same way, contributions of diboson backgrounds are subtracted for the calculation of efficiencies. Data and MC isolation efficiencies are calculated in the same way as for the light-flavour jet case, and were found to agree within 4%, as shown in Tab. 11.11.

Having corrected the efficiencies using the scale factors, the transfer factors to extrapolate the background yields from the relaxes OS CR (CR D) to the SR can be safely derived.

11.5.2 $Z + ee$ background channel

The main source of electron background arises from jets misidentified as electrons. Background yields are extracted using a CR denoted $3\ell + X$. The standard selection and identification criteria are applied to three leptons (two compose the leading pair and the last one has the highest p_{T} in the sub-leading pair), and loosened for the fourth lepton (X). The decomposition of the background contributions can be easily done by imposing discriminating cuts on X. A second CR, referred to as $Z + X$, is created to have more statistics than the $3\ell + X$ CR. It is used to estimate the efficiencies of the selection of X as compared to the standard selection in the SR region, enabling the extrapolation of the background yields from the $3\ell + X$ CR to the SR. The description of the two CRs is given at the end of this section.

Background components

Various processes are involved in the electron background. The major part comes from light jets leading to deposits in the calorimeter which fake an electron (f). Electrons can also come from photon conversion of FSR (γ). Finally, a third component is considered, consisting of electrons resulting from semi-leptonic decays of heavy quarks (q).

The three contributions are unfolded using a template fit in the $3\ell + X$ CR on the number of pixel hits (n_{InnerPix}) in the IBL, or in the closest layer of the ID if no hits are expected (because of a dead region of the detector). This variable provides good discrimination for γ over f and q, because photons populate the $n_{\mathrm{InnerPix}} = 0$ bin of the distribution. Two sub-regions enriched in f-q (γ) are therefore created, requiring $n_{\mathrm{InnerPix}} > 0$ ($n_{\mathrm{InnerPix}} = 0$). Purities of these two subsets in the $3\ell + X$ CR are respectively of 90% and 98%, according to particle-level information of MC. The yields obtained in these subsets are then extrapolated to the SR using transfer factors.

Template fit and extrapolation

Templates for n_{InnerPix} of the f and γ (q) components are retrieved from the $Z+X$ ($3\ell+X$) CR, respectively. In each case, templates are taken from simulation, where the particle-level information is used to determine

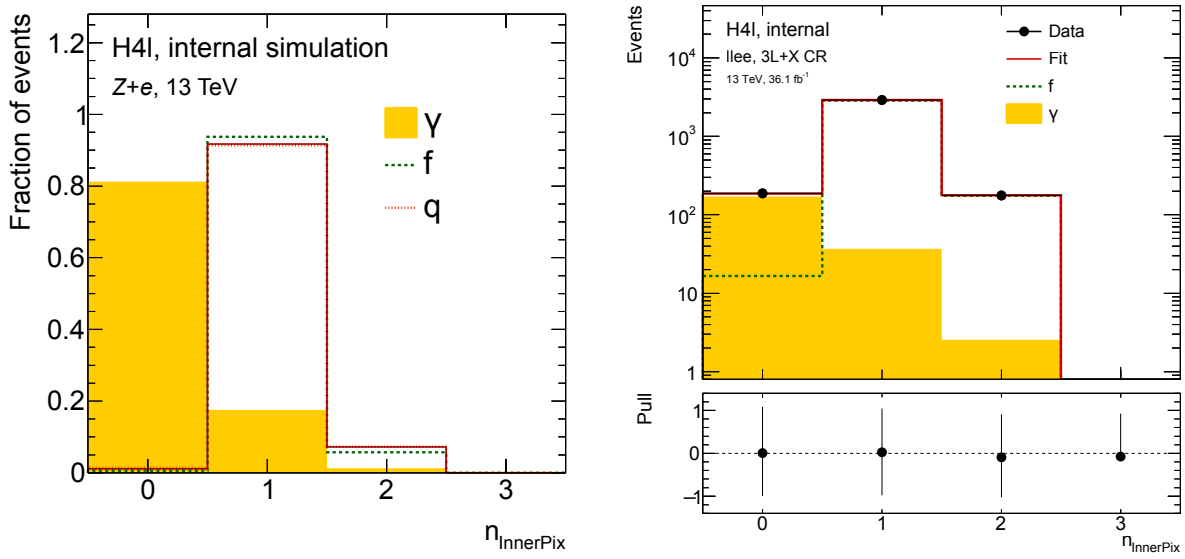

(a) Shapes used for the fit

(b) Distributions after fit

Figure 11.9 – (a) Shapes used for the fit and (b) distributions after the fit of n_{innerPix} in the $3\ell + X$ control region. Distributions are given for the various contributions and are extracted from simulation in the $Z + X$ CR (except for q, where it is in the $3\ell + X$ CR). Dashed lines distributions are obtained before applying the data-driven corrections. The fit combines the $2\mu 2e$ and $4e$ channels [198].

the origin (f, γ or q) of the extra electron X. The various shapes are presented in Fig. 11.9 (a). A correction to the f component in MC is applied to match the data. Systematic uncertainties are taken into account by applying the same corrections to the q channel. The corrected distribution of n_{InnerPix} is quite similar for f and q justifying the use of a common template for the two components. As a result, only f is fitted and the q contributions composed of $Z +$ jets and $t\bar{t}$ are subtracted. These yields are assessed using MC.

The fit of n_{InnerPix} in the $3\ell + X$ CR is performed on data, including the $2\mu 2e$ and $4e$ channels. Results are shown in Fig. 11.9 (b). In order to distinguish the contributions of the various backgrounds, the *sPlot* method [209] is applied to data in p_{T} bins. The dedicated tool returns a covariance-weighted quantity $sWeight$, for all the contributions, which is equal to the probability of X to be of kind f or γ. The distributions for each contributions are obtained by summing up the generated weights over all the events.

The extrapolation of the yields into the SR (N_{SR}) is then performed for the two components separately using $N^b_{\text{SR}} = \sum_{ij} \varepsilon^b_{ij} \times s^b_i \times {N_{sP}}^b_{ij}$, where i indexes the p_{T} bins and j indexes the n_{jets} bins. The sum of $sWeight$ is denoted by ${N_{sP}}^b_{ij}$, ε^b and s^b are the efficiencies and scale factors of the background components, respectively.

Estimation of ε^b and s^b

The estimation of the selection efficiencies ε^b of X in the $3\ell + X$ CR is performed separately for the various backgrounds $b \in \{f, \gamma\}$. In order to do so, the standard selection (corresponding to the SR) is applied to the X electron in simulated events and the efficiency is defined as the ratios of selected X over the entire

set of events in the SR. Scale factors s^b, defined as ratios of efficiencies in data over MC, are derived to correct simulation. Differences between data and MC are studied in the $Z + X$ enriched samples.

Since the Z + HF contribution is subtracted from the CR, it is not included in the extrapolation and the contribution in the SR is directly taken from MC (Z + jets and $t\bar{t}$). As a cross-check, the $Z + b\bar{b}$ cross-section was measured by ATLAS [210] and was found to be in good agreement with simulation used in this analysis. An overall systematic is assigned to this contribution to account for possible miss-modelling.

Observed variations in the scale factors s^b are not only attributed to bad description of the selection in MC, but also to contamination by impurities in the samples, which affect the efficiencies at a large extent, since their contribution in data is not similar as in MC. These impurities have larger effects in the f enriched sample, because the efficiency of this channel is low, as compared to γ. In order to cope with these impurities, an iterative method is developed to properly assess the scale factors.

Iterative method

The efficiency calculation and the corresponding corrections are performed starting with the γ contribution: $\varepsilon_\gamma = \mathcal{S}_\gamma \times \frac{N^\gamma_{\text{pass}}}{N^\gamma_{\text{tot}}} = \frac{s^\gamma_{\text{pass}} \times N^\gamma_{\text{pass}}}{s^\gamma_{\text{tot}} \times N^\gamma_{\text{tot}}}$, where pass (tot) denote the events passing the selection cuts (all the events in the sample). N and s refer to the number of events and the scale factors, respectively. The resulting scale factor for the efficiency is labelled $\mathcal{S}_\gamma$. A similar formula can be derived for f. In order to calculate $\mathcal{S}_\gamma$, the partial scale factors s are assessed after three iterations of the following procedure.

It is possible to express s^γ using

$$s^\gamma_c = \frac{N^{\text{data}}_c - N^e_c - N^f_c}{N^\gamma_c}, \tag{11.5}$$

where $c \in \{\text{passtot}\}$, N^{data} is the observed yield in data, and N^e, N^f and N^γ are the yields predicted by the MC simulation (e refers to true electrons). The same calculation is performed for f, but replacing N^γ by its corrected value:

$$s^f_c = \frac{N^{\text{data}}_c - N^e_c - s^\gamma_c \times N^\gamma_c}{N^f_c}. \tag{11.6}$$

Then, Eq. 11.5 is used with the corrected value of N^f to reassess s^γ, which is in turn injected into Eq. 11.6. Repeating these operations three times enables the scale factors to reach their stable values and ensures a correct measurement. From the values of s^γ_c and s^f_c, it is possible to deduce $\mathcal{S}_\gamma$ and $\mathcal{S}_f$. The results of these measurements are summarised in Tab. 11.13. The scale factors have systematics which include miss-modelling of MC, contributions of the heavy-flavour background (subtracted from the yields) as well as the statistical uncertainties of measurements. They dominate the uncertainties on the final estimate of the background yields.

Results

The summary of the results is presented in Tab 11.12. The yields of each components in the SR are given with the yields returned by the fit (averaged over p_{T}). Dominant uncertainties are systematics related to the measurements of the efficiencies for f and γ in the $Z + X$ CR, as well as the estimation of the heavy-flavour contributions from simulation.

Table 11.12 – Fit result of the yields in the $3\ell+X$ CR with statistical errors, shown together with the $ZZ^* + \text{HF}$ contamination and the efficiency used to extrapolate the yields to the SR. The SR yields for the f and γ components are quoted with statistical uncertainty as returned from the data fit, and systematic uncertainty of the calculated efficiency. For the q component that is not fitted in the data, the SR yield is taken directly from MC simulation and is quoted with its total uncertainty [198].

$4e + 2\mu 2e$				
type	data fit	$ZZ^* + \text{HF}$	efficiency [%]	SR yield
f	3075 ± 56	280 ± 6	0.20 ± 0.04	$5.68 \pm 0.36 \pm 1.19$
γ	208 ± 17	19.4 ± 0.5	0.71 ± 0.14	$1.34 \pm 0.35 \pm 0.27$
q	(MC-based estimation)			6.34 ± 1.93

Table 11.13 – Data/MC scale factors for MC simulated light-flavour jets (f) and photon conversions (γ) accompanying reconstructed Z events [198]. The factors are shown per bin of the transverse momentum of the electron X studied. The errors are statistical only.

p_{T} [GeV]	scale factor [%]
light-flavour jets (f)	
$[7, 10]$	1.42 ± 0.09
$[10, 15]$	2.57 ± 0.27
$[15, 70]$	4.38 ± 0.63
photon conversions (γ)	
$[7, 10]$	1.01 ± 0.04
$[10, 15]$	1.18 ± 0.07
$[15, 70]$	1.91 ± 0.12

Definition of the CRs

The selection of the electron having the lowest E_{T} of the quadruplet (X) in the $3\ell + X$ CR is done by relaxing the identification criteria. A modified *Loose* working point is used in which the likelihood identification and n_{InnerPix} criteria are removed. Only track quality requirements are needed. On top of this cut, the d_0 significance and 4ℓ vertex cuts are imposed. No isolation criteria are applied. In order to reduce the contamination from ZZ^*, only sub-leading pairs of same-charge electrons are selected. The remaining contribution of ZZ^* of about 5%, which is due to fake electron replacing the fourth true electron, is subtracted to the estimation of the yields. All quadruplets sharing the same m_{12} are retained. This CR was chosen thanks to reduced systematics, although it suffers from low statistics as compared to $Z + XX$ CRs.

The construction of the $Z + X$ CR is similar to the muon case ($Z + \mu$ control sample). Single- and dilepton triggers are used. The Z-boson candidates are also formed of a pair of opposite-charge same-flavour leptons having $p_{\text{T}} > 20\,\text{GeV}$ and $p_{\text{T}} > 15\,\text{GeV}$, which pass the standard selection criteria. The

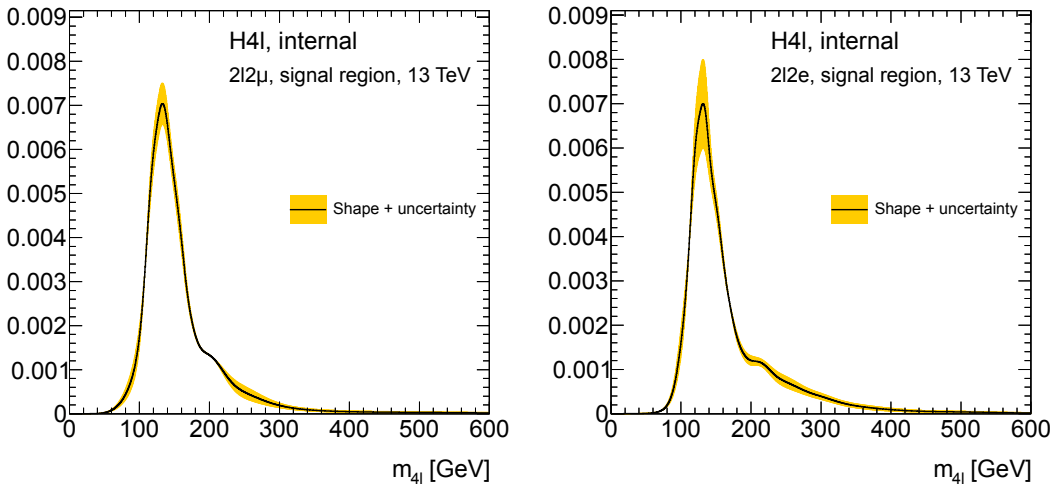

(a) $Z + \mu\mu$ backgrounds (b) $Z + ee$ backgrounds

Figure 11.10 – Shape of the 4ℓ invariant mass for reducible backgrounds ($t\bar{t}$ and Z+jets) after smoothing. The solid line represents the nominal shape, whereas the variations are shown by the yellow areas, obtained by varying the $t\bar{t}$ and Z + jets contributions by 20% [198].

candidate having an invariant mass the closest to the Z-boson pole mass is retained, and must satisfy $76 < m_{12} < 106\,\text{GeV}$. Isolation requirements are also applied on the leading pair, requiring a separation of $\Delta R > 0.1$ between the two leptons. The selection of the additional electron X is the same as described previously, where only basic track and impact-parameter cuts are applied. No 4ℓ vertexing cuts are applied. As for the muon case, the extra electron must be well-separated from the leptons of the Z boson, with $\Delta R > 0.2(0.1)$ in the case of muons (electrons). A J/ψ veto is also applied to the three leptons.

11.5.3 Results of the $Z + \mu\mu$ and $Z + ee$ background yields per category

Whereas the previous results for the $Z + \mu\mu$ and $Z + ee$ backgrounds were presented for the inclusive events, this section focuses on the yields per category $4\mu, 2\mu 2e$, $2e2\mu$ and $4e$. Background yields of each category are scaled [211, 212], taking the fraction of events per category from MC simulation (Z+jets and $t\bar{t}$ samples), which enters the various CRs. Data-driven estimations can then be scaled to reproduce the measured fractions. The shapes of the reducible backgrounds are also estimated using simulation, having loosened the isolation requirements in order to maintain high statistics, which is the leading uncertainty of the derived scaling terms.

11.5.4 Background shape modelling

For the $Z + \mu\mu$ reducible background, the Z + LF shape is not considered as too few simulated events pass the selection criteria in the SR. The shapes for the Z + HF and $t\bar{t}$ components are directly taken from simulation. In the three cases, the 4μ and $2e2\mu$ final states are combined to get more statistics (as the shapes in the two final states are very similar).

For the $Z + ee$ background, the shape of the Z + HF contribution is taken from simulation. The Z + LF and photon conversion components are treated simultaneously. Their shapes are estimated using the *sPlot*

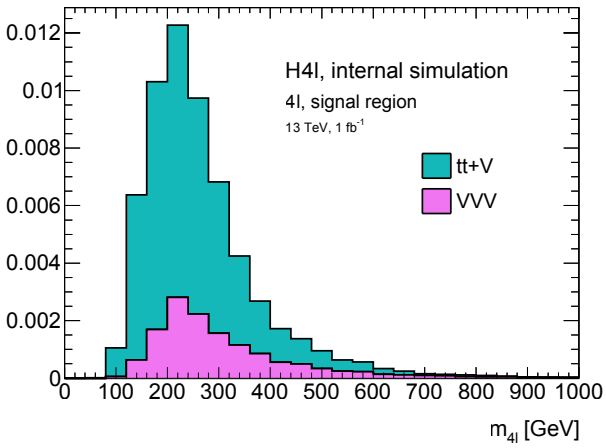

Figure 11.11 – Distributions of the 4ℓ invariant mass for the triboson and $t\bar{t}+V$ backgrounds [198].

technique in the $3\ell + X$ CR and the extrapolation to the SR using transfer factors is done the same way as for the yield determination (described in Sec. 11.5.2).

In both the two cases, the shapes are then smoothed using a Kernel estimation (`RooKeysPDF` [213]) for each components. The resulting distributions are normalised and added following the measured fractions in data, as described in the previous paragraphs. Applying the Z-mass constraint has only a minor effect on the shape. Validation is performed by checking the lepton kinematics and shows very good agreement between data and MC. Final results are presented in Fig. 11.10. The distributions are peaked around the mass of the Higgs boson because of the resonant shape of the leading pair of the $Z+$jets component. Systematics on the shapes are introduced by varying the fractions of each background contribution by ±20% (chosen to be conservative, considering the systematics on the background yields).

In order to model the ZZ^* continuum, the quadruplet-invariant-mass distribution ($m_{4\ell}$) is simulated by MC. For the triboson decays (ZZZ, WZZ and WWZ decompositions where the final states are composed of four true leptons or more) and $t\bar{t}+V$ backgrounds with leptonic decays (where $V \in \{W^{\pm}, Z\}$), the shapes are also modelled using MC simulation and the results are presented in Fig. 11.11.

11.6 Systematic uncertainties

In the calculation of the Higgs-to-four-lepton production cross sections, systematic uncertainties are taken into account through nuisance parameters. These parameters are not of immediate interest for the study, but have to be estimated to obtain the desired cross sections. They add more parameters to the fits performed, which results in broadening the errors on the parameters of interest.

There are two kinds of systematic uncertainties affecting the measurement of the production cross sections: the uncertainties linked to the determination of the signal and background yields, and the uncertainties associated to the unfolding method used for the measurements. This paragraph only presents the uncertainties of the first category, and the other uncertainties are described in the next chapter.

For the calculation of the signal and background yields, the systematic uncertainties are gathered into three categories: theory uncertainties on the modelling of the ZZ^* background, experimental uncertainties, and uncertainties induced by the background estimation using data-driven techniques. Unlike

the latter category which regroups uncertainties on background normalisation and shape described in the previous section, the theory and experimental uncertainties correspond to variations of event weights.

11.6.1 Background theoretical systematic uncertainties

The theoretical systematic uncertainties take into account the effects of the chosen PDF, the QCD scales and the hadron shower description. They are described in details in the note [214] for the ZZ^* background. The QCD scales arise from QCD perturbative calculations (with the inclusion of loops in the Feynman diagrams). These lead to divergent integrals which cannot be computed, due to infra-red collinear singularity and ultra-violet divergence. In order to overcome these, the renormalisation and factorisation are introduced, to cancel the ultra-violet and infra-red divergences, respectively. The choice of these scales is highly dependent on the energy scale of the experiment. They were therefore set to m_{ZZ} for the nominal case.

In order to estimate the variations caused by the change of the PDF sets, various sets of weights are added to the MC samples, with each set corresponding to a PDF variation. In order to assess the differences between two PDF sets, the study has to be carried out using two different sets of weights. Then, the comparison of the resulting yields leads to the systematic uncertainty. The CT10nlo PDF sets are composed of 26 parameters, which in turn correspond to $N = 52$ possible variations (one variation up and one variation down per parameter). The envelopes denoted δf^+ and δf^- are calculated summing up the various variations in quadrature:

$$\delta f^+ = \sqrt{\sum_{i=1}^{N} \left[\max\left(f_i^+ - f_0, f_i^- - f_0, 0\right)\right]^2}, \delta f^- = \sqrt{\sum_{i=1}^{N} \left[\max\left(f_0 - f_i^+, f_0 - f_i^-, 0\right)\right]^2}. \tag{11.7}$$

A second theoretical uncertainty concerns the QCD scale, which is composed of the QCD factorisation scale (μ_F) and the renormalisation scale (μ_R). As for the PDF variations, weights corresponding to the variations in both the two scales can be included in the simulated samples. The nominal scales are set to one unit of the continuum-invariant mass: $\mu_F = \mu_R = 1.0 \times m_{ZZ}$. In total, eight variations are considered for the systematic uncertainties. Expressing the tested scales in units of m_{ZZ}, the following list of doublets was generated: $(\mu_F, \mu_R) \in \{0.5, 1.0, 2.0\}^2$. Note that here, the doublet $(1.0, 1.0)$ corresponds to the nominal values. The technique employed is the same as for the PDF variations: each weight set corresponds to a doublet, and the various outcomes are compared to the nominal case. The maximum differences are then used as envelopes.

11.6.2 Experimental systematic uncertainties

Experimental uncertainties include uncertainties on lepton reconstruction, identification and trigger efficiencies, as well as energy and momentum scale and resolution. The first uncertainties are related to the scale factors, translated into event weights, applied to MC to match data efficiencies. These weights are varied from the nominal case to calculate the uncertainty, as described thereafter. The second uncertainties concern the adjustments of the simulation to mitigate second-order effects in the measurement of the lepton energy and transverse momentum. These uncertainties are obtained by varying the value of the corresponding quantity, keeping the weight of the event unchanged.

For each efficiency variations, a set of weights is applied, which corresponds to the resulting combination of the various scale factors, increased or decreased by the associated variation. MC efficiencies are therefore varied and can be compared to the nominal case. The nominal yield, denoted $I_{\text{nom.}}$, is defined

as the integral of the four-lepton invariant mass ($m_{4\ell}$) having applied all the nominal weights. For each variation, a modified yield $I_{\text{mod.}}$ is calculated in the same manner, but using the varied weights. The relative uncertainty $\left|\frac{I_{\text{nom.}}-I_{\text{mod.}}}{I_{\text{nom.}}}\right|$ is derived (in percent). Each variation is symmetrical and corresponds to $\pm 1\sigma$ deviation from the nominal case. A conservative approach is adopted, which consists in applying the weights associated to a certain quantity assuming their effect is correlated with respect to the relevant leptons of the event. If the nominal and the varied weights corresponding to the i-th lepton of the event are w_i and $w_i + \delta w_i$, the nominal weight will be $\prod_{i=1}^{4} w_i$ and its total variation $\prod_{i=1}^{4} (w_i + \delta w_i)$, in the case the uncertainty concerns all the leptons of the quadruplet.

Uncertainties on the energy (electrons) and momentum (muons) scale or resolution are derived by shifting the quantity by a scale factor (calculated comparing data and MC) before the event selection, and comparing the resulting yields after the full selection. The shift on the quantity α corresponds to $\pm 1\sigma_\alpha$, where σ_α is the standard deviation of α. This shifting procedure is often referred to as *smearing*.

Concerning the electron reconstruction and identification, four variations are taken into account. The first regroups the total contributions from reconstruction, whereas the three last ones gathers identification (total correlated uncertainty, sum of the components of the uncertainties, and simplified version of the uncorrelated uncertainties). Muons benefit from a finer description and four parameters are included, depending on p_{T}. Two components (statistical and systematic contributions) are introduced for the high (low) momentum regions, corresponding to $p_{\text{T}} > 15\,\text{GeV}$ ($< 15\,\text{GeV}$).

In the case of the electron E_{T}, a variation for the scale and another one for the resolution are considered. The same applies to muon momentum, except that the resolution systematics are split into three categories, depending on the ID and MS (general MS, and Sagitta bias) contributions.

Jet uncertainties are composed of two sets of nuisance parameters. The jet energy scale contains grouped nuisance parameters in three variables, as well as one additional variable describing the jet η inter-calibration. The second set corresponds to the jet energy resolution for which only one nuisance parameter is considered.

Isolation uncertainties are propagated using one nuisance parameter for electrons, and two for muons, where the statistical and systematic components are separated.

Two variations (statistical and systematic components) describe the effects of the uncertainties on the muon track-to-vertex association (corresponding to the $\left|d_0^{\text{BL}}\text{significance}\right| < 3$ and $\left|\Delta z_0^{\text{BL}} \sin\theta\right| < 0.5\,\text{mm}$ cuts).

A nuisance parameter is associated to the uncertainty on the integrated luminosity, which is of ±3.4% for Run 2. The uncertainty on the luminosity also affects the signal and ZZ^*-background modellings, since the luminosity is used to renormalise the MC samples.

Systematics are assigned to the flavour tagging of jets taking into consideration the flavour (b, c, light flavour) and the extrapolation of the vertex.

An uncertainty is attributed to the value used for the rescaling of the average number of interaction per bunch crossing μ. The nominal scaling is 1.0/1.09, but two variations are considered (up 1.0/1.0 and down 1.0/1.18). On top of these variations, the systematics associated with the pileup jet rejection tool (JVT score) are also considered (five nuisance parameters).

Modelling of the electroweak and QCD high orders is taken into account through three nuisance parameters (one for EW and two for QCD).

Finally, a systematic uncertainty of 0.5% is attributed to the μ trigger differences between data and simulation.

The contributions of each of the systematic uncertainties are presented in Tab. 11.14.

Table 11.14 – Contributions of the systematic uncertainties for the cross-section measurements in the $H4\ell$ channel. Among the three categories (background shapes and yields, theory and experimental), uncertainties are gathered into six groups, including the indicated uncertainties. The contribution of each group on the $m_{4\ell}$ spectrum is given in percentage per final state and for all the final states combined. Note that for the cross-section measurements, additional uncertainties on the detector acceptance and correction are not included in this table (see Chap. 12).

Category	**Group**	Included uncertainties	Contribution (%)				
			4μ	$4e$	$2\mu2e$	$2e2\mu$	Combined
Experimental	**Muon**	p_{T} scale and resolution Reconstruction and identification Isolation Trigger efficiency (0.5%) d_0 and z_0 cuts	4	0	2	2	3
Experimental	**Electron**	E_{T} scale and resolution Reconstruction and identification Isolation	0	6	5	1	5
Experimental	**Jet**	Jet experimental uncertainties Flavour tagging and vertex extrapolation JVT score	< 1	< 1	1	< 1	< 1
Theory	$qqZZ$ **theory**	PDF Factorisation and renormalisation scales Modelling of QCD higher orders	2	3	2	2	2
Theory	**Signal theory**	PDF Factorisation and renormalisation scales Modelling of QCD higher orders	< 1	< 1	< 1	< 1	< 1
All	**All**	Background yields and shapes Integrated luminosity (3.4%) Pile-up reweighting Theory Experimental	5	7	7	4	5

11.7 Event yields at 36.1 fb^{-1}

Selection criteria are applied to the 2015 and 2016 datasets, which correspond to a total integrated luminosity of 36.1 fb^{-1}. In the range 115 GeV < $m_{4\ell}$ < 130 GeV, 102 events were observed, corresponding to 33 4μ, 32 $2e2\mu$, 21 $2\mu2e$ and 16 $4e$ events. The total number of expected events for signal and background is presented in Tab. 11.15 [198]. In this table, symmetrised errors include both statistical and systematic uncertainties. MC signal yields are normalised to the most up-to-date predictions presented in Sec. 11.2. Background yields are either obtained from MC for the ZZ^* continuum, or using data driven techniques for the reducible contributions, as described in Sec. 11.5 and 11.5.3. Results are presented including all production modes, for each final state. These yields serve as input for the inclusive cross section measurements, which are the subject of Chap. 12.

Expected signal yields per final state are converted into rates in Tab. 11.16. As expected, the 4μ ($4e$) final state has the highest (lowest) efficiency since muon kinematic cuts are looser than for electrons. In between, the $2e2\mu$ final state is more efficient than $2\mu2e$, because in the latter two electrons compose the sub-leading pair, corresponding to Z^*. These leptons are often less boosted than those composing the leading pair and have more chances to fail the kinematic cuts.

Comparing data with expectation, an excess of 1.3σ is observed, especially for the $2e2\mu$ and $2\mu2e$ final states. Although the yields are still compatible with SM predictions, these excesses have been

Table 11.15 – Number of events expected and observed for a $m_H = 125\,\text{GeV}$ hypothesis for the four-lepton final states in a window of $115 < m_{4\ell} < 130\,\text{GeV}$, using the constrained $m_{4\ell}$, corresponding to 36.1 fb^{-1} at $\sqrt{s} = 13\,\text{TeV}$ [198].

Final state	Signal	ZZ^*	$Z+\text{jets}$, $t\bar{t}$, WZ, ttV, VVV	Expected	Observed
4μ	20.1 ± 1.6	9.8 ± 0.8	1.3 ± 0.3	31.2 ± 1.8	33
$4e$	10.6 ± 1.0	4.4 ± 0.4	1.3 ± 0.2	16.3 ± 1.1	16
$2e2\mu$	14.2 ± 1.1	7.1 ± 0.5	1.0 ± 0.2	22.3 ± 1.2	32
$2\mu2e$	10.8 ± 1.0	4.6 ± 0.5	1.4 ± 0.3	16.8 ± 1.1	21
Total	56 ± 4	25.9 ± 2.0	5.0 ± 0.7	87 ± 5	102

Table 11.16 – Expected signal yields and rates per final state. Rates correspond to the yield per final state over the total signal yield.

Signal	4μ	$4e$	$2e2\mu$	$2\mu2e$	Total
Yields	20.1	10.6	14.2	10.8	56
Rates [%]	36	19	25	19	100

intensively studied. Kinematic distributions for each of the four leptons were compared both for signal and background in the CRs and the SR. No suspicious behaviours were observed. A cross-check of the number of selected events in the range $118 < m_{4\ell} < 129\,\text{GeV}$ was performed over time, as shown in Fig. 11.12. The yields are presented per data period, as changes in the detector or the LHC operation could result in affecting the event selection. However, the curve is flat indicating no strong dependence upon run period.

In each of the following figures, the variables are presented, comparing data with simulation. The latter is divided into signal and the background events, namely the ZZ^* continuum, the $Z+\text{jets}$ and $t\bar{t}$ contributions, and the $t\bar{t}+V, V \in \{Z, W^{\pm}\}$ and triboson production. Event yields are estimated using the procedures described previously.

First of all, the invariant mass of the lepton quadruplet is presented in Fig. 11.13 and 11.14 [215] for the inclusive events, and per final state.

Figures 11.15, 11.16 and 11.17 [215] show the distributions of $p_{\text{T}}^{4\ell}$, $p_{\text{T}}^{4\ell}$ ($n_{\text{jets}} = 0$), $p_{\text{T}}^{4\ell}$ ($n_{\text{jets}} = 1$), $p_{\text{T}}^{4\ell}$ ($n_{\text{jets}} \geq 2$), m_{12}, m_{34}, $|y_{4\ell}|$, $|\cos(\theta^*)|$, n_{jets}, $p_{\text{T}}^{\text{leading jet}}$, m_{jj}, $|\Delta\eta_{jj}|$, $\Delta\varphi_{jj}$ and $n_{\text{b jets}}$, respectively, for the inclusive events. The distribution binning is chosen to match the one used for the differential cross section measurements presented in Chap. 12, where the variables are defined. This binning was chosen to facilitate the combination of the cross section analyses between the $H \to \gamma\gamma$ and $H \to ZZ^* \to 4\ell$ decay channels.

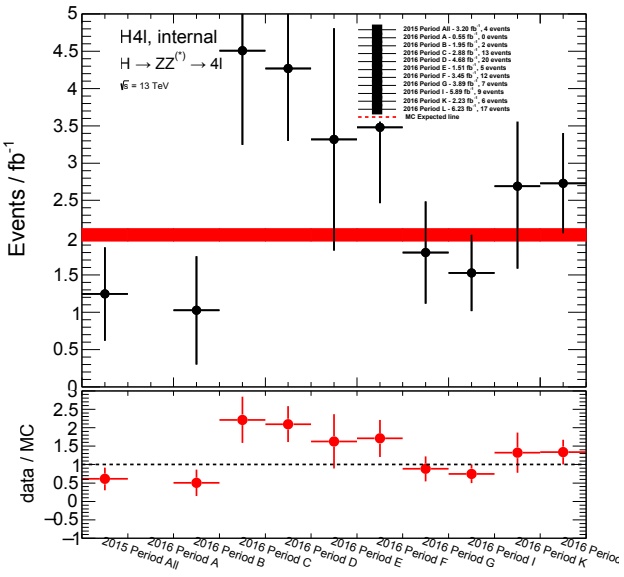

Figure 11.12 – Selected event yields against data period [198]. The yields are normalised by the amount of data recorded for each period. The yields observed in data (black dots) are compared to expectation from simulation (red curve). On average, two events are expected per fb^{-1}. Taking into account the statistical fluctuations, data and simulation are in good agreement.

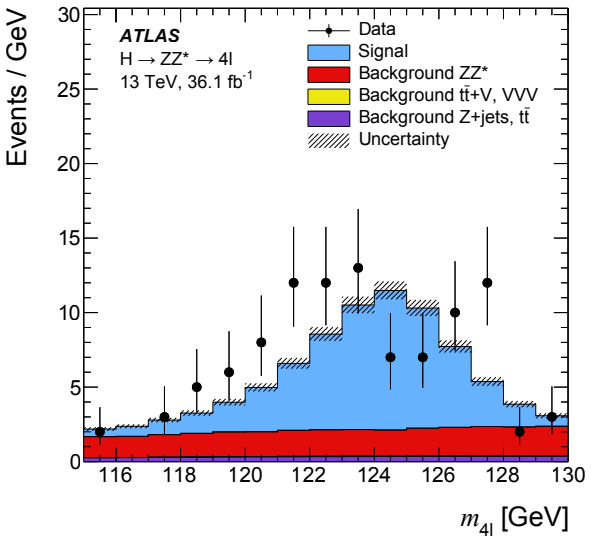

Figure 11.13 – Inclusive $m_{4\ell}$ distribution [215]. Events passing the event selection are presented in data (black dots), and in simulation (blue: signal, red: ZZ^* continuum, yellow: triboson production and $t\bar{t}+V$ contribution with $V \in \{W^{\pm}, Z\}$, and purple: $t\bar{t}$ and Z+jets contributions). The statistical uncertainties on the MC predictions are shown by the striped area. Taking into account the uncertainties, the agreement between data and simulation is good with a small excess in data.

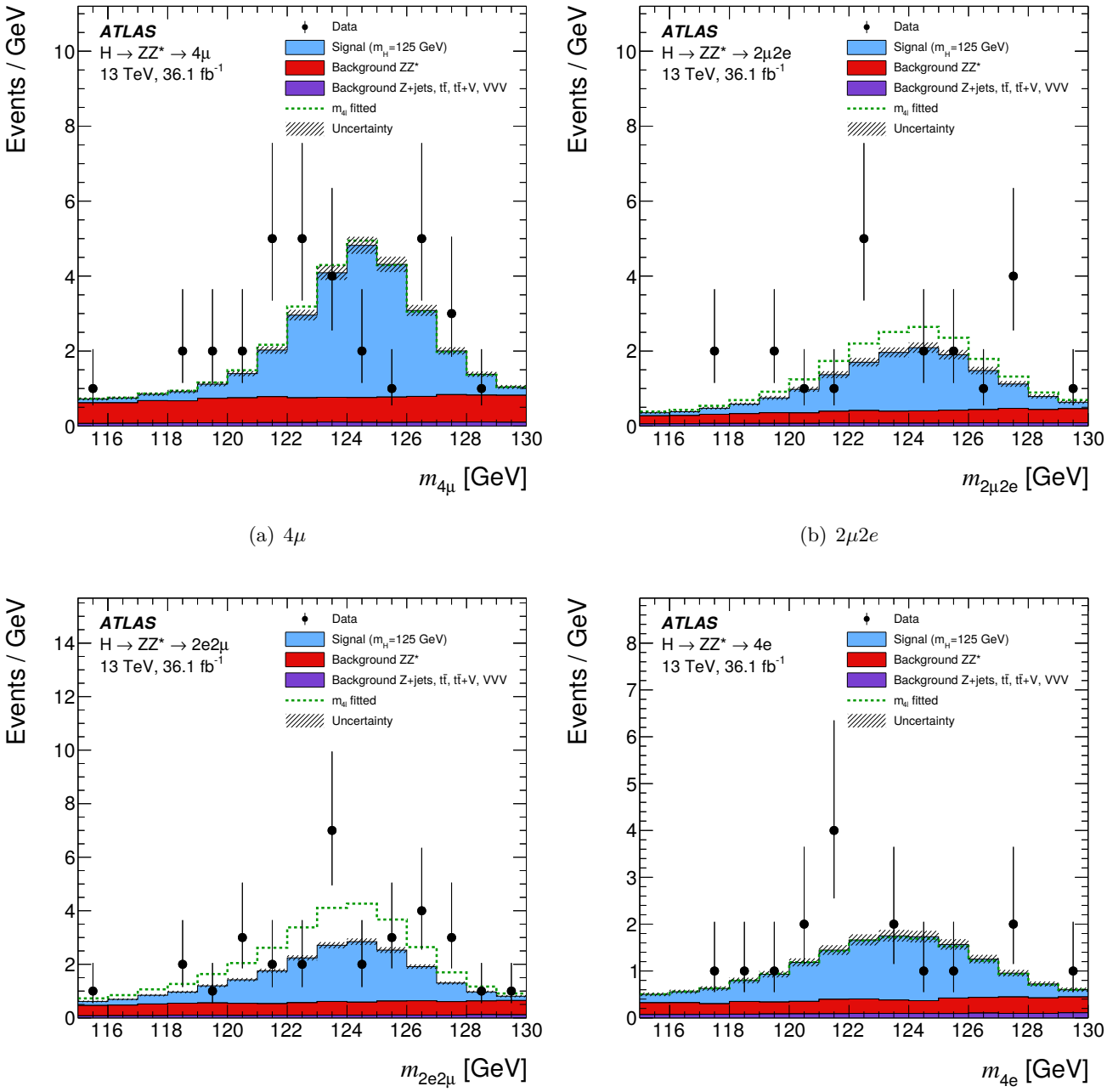

(a) 4μ

(b) $2\mu 2e$

(c) $2e2\mu$

(d) $4e$

Figure 11.14 – $m_{4\ell}$ distribution per decay channel [215]. Events passing the event selection are presented in data (black dots), and in simulation (blue: signal, red: ZZ^* continuum, yellow: triboson production and $t\bar{t}+V$ contribution with $V \in \{W^{\pm}, Z\}$, and purple: $t\bar{t}$ and $Z+$jets contributions). The statistical uncertainties on the MC predictions are shown by the striped area. There are small excesses in data for the $2\mu 2e$ and $2e2\mu$ final states.

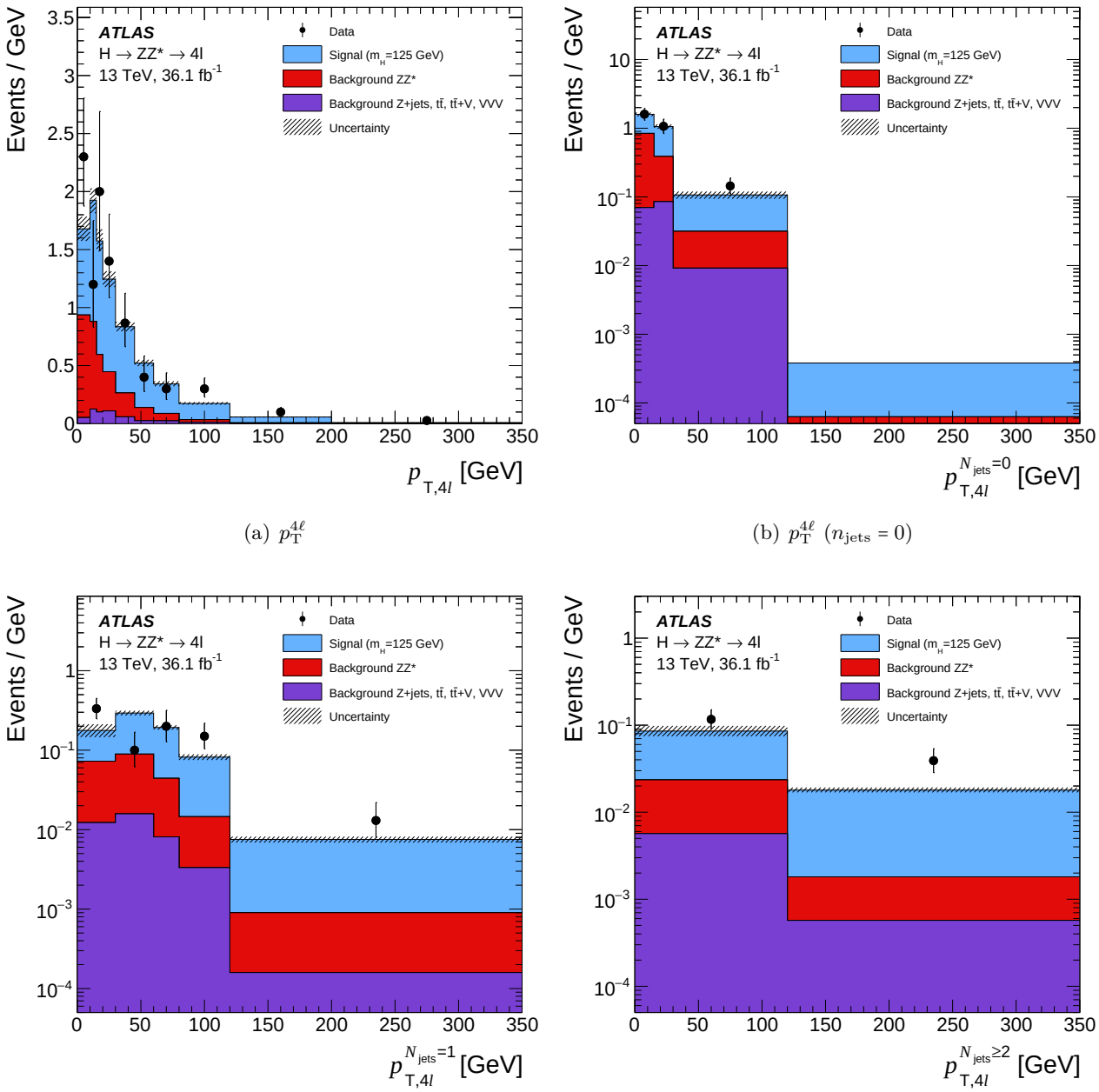

(a) $p_{\mathrm{T}}^{4\ell}$

(b) $p_{\mathrm{T}}^{4\ell}$ ($n_{\mathrm{jets}} = 0$)

(c) $p_{\mathrm{T}}^{4\ell}$ ($n_{\mathrm{jets}} = 1$)

(d) $p_{\mathrm{T}}^{4\ell}$ ($n_{\mathrm{jets}} \geq 2$)

Figure 11.15 – Inclusive four-lepton p_{T} distributions for (a) all events and (b, c, d) per jet multiplicity [215]. Events passing the event selection are presented in data (black dots), and in simulation (blue: signal, red: ZZ^* continuum, yellow: triboson production and $t\bar{t} + V$ contribution with $V \in \{W^{\pm}, Z\}$, and purple: $t\bar{t}$ and Z + jets contributions). Statistical uncertainties on the MC predictions are shown by the striped area. Taking into account the uncertainties, the agreement between data and simulation is good. The second bin of the $p_{\mathrm{T}}^{4\ell}$ distribution shows a downward statistical fluctuation.

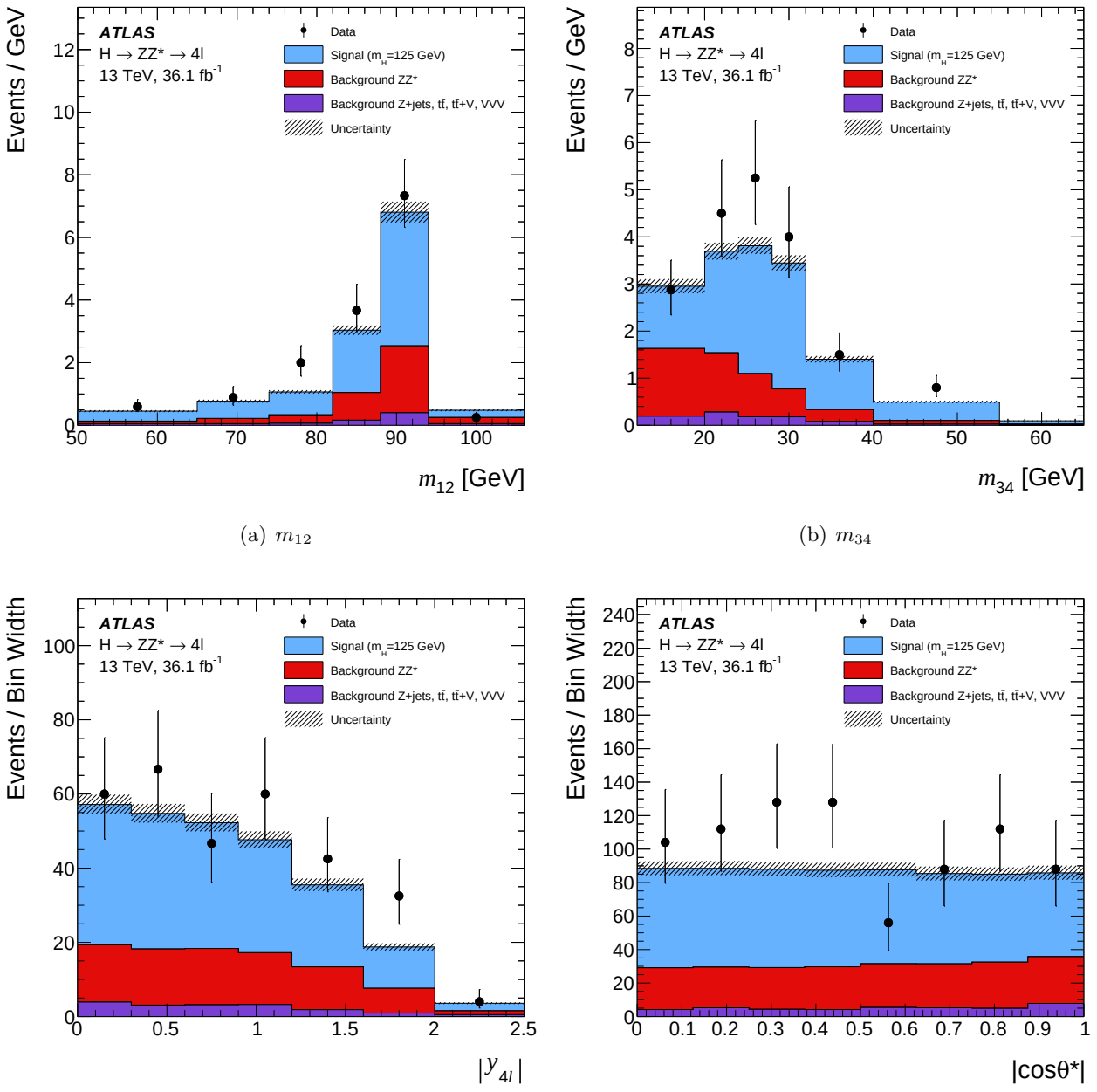

(a) m_{12}

(b) m_{34}

(c) $|y_{4\ell}|$

(d) $|\cos(\theta^*)|$

Figure 11.16 – Inclusive Higgs boson variable distributions, with the invariant mass of the (a) leading and (b) sub-leading pairs, (c) the rapidity of the Higgs candidate and (d) the cosine of the polar angle of the Higgs boson decay in the rest frame [215]. Events passing the event selection are presented in data (black dots), and in simulation (blue: signal, red: ZZ^* continuum, yellow: triboson production and $t\bar{t}+V$ contribution with $V \in \{W^{\pm}, Z\}$, and purple: $t\bar{t}$ and $Z+$jets contributions). The statistical uncertainties on the MC predictions are shown by the striped area. Taking into account the uncertainties, the agreement between data and simulation is good.

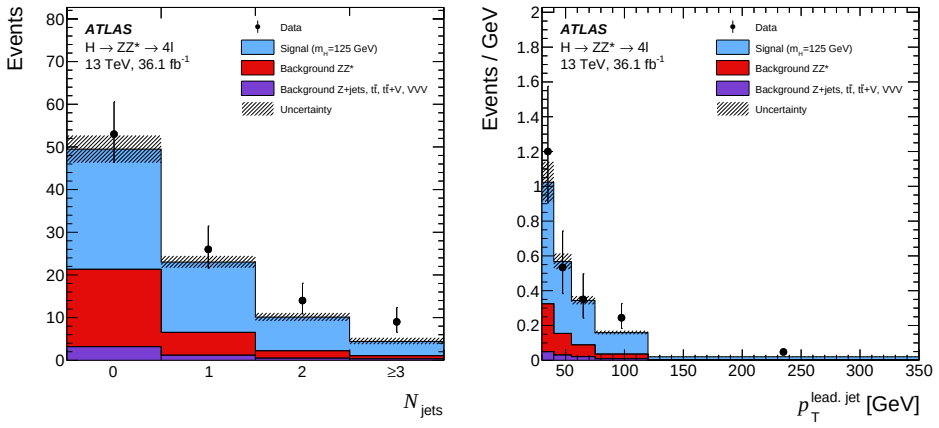

(a) n_{jets} (b) $p_{\text{T}}^{\text{leading jet}}$

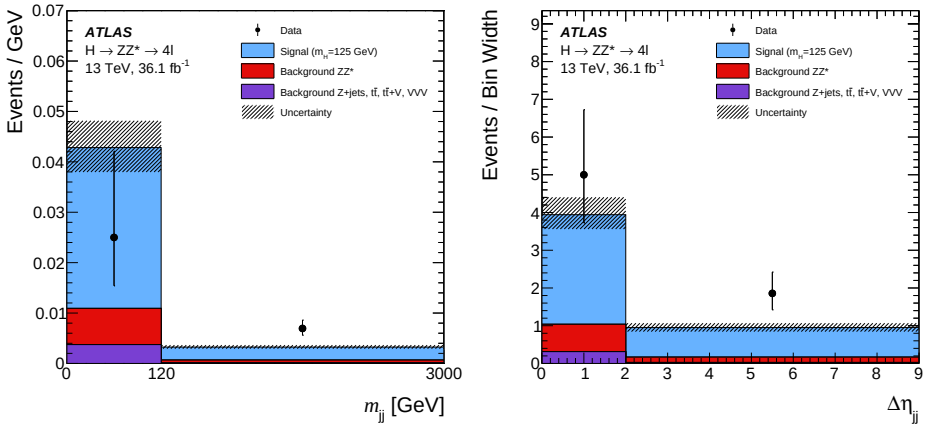

(c) Leading m_{jj} (d) Leading $|\Delta\eta_{jj}|$

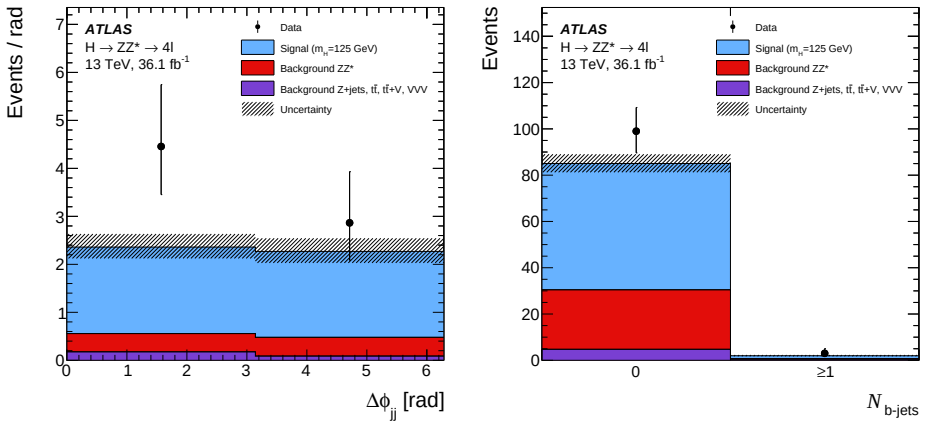

(e) Leading $|\Delta\phi_{jj}|$ (f) $n_{b\text{ jets}}$

Figure 11.17 – Inclusive jet distributions, with (a) the jet multiplicity, (b) p_{T} of the leading jet, (c) the leading dijet invariant mass, (d) the pseudo-rapidity and (e) azimuthal separations of the two leading jets and (e) the number of b-tagged jets [215]. Data and simulation are in good agreement.

Chapter 12

Measurements of the inclusive and differential cross sections

The CMS and ATLAS collaborations measured the inclusive and differential production cross sections of the Higgs boson, using Run 1 data from proton-proton pp collisions at centre-of-mass energy of $\sqrt{s} = 8\,\text{TeV}$, in the 4ℓ, $\gamma\gamma$, and $e\nu\mu\nu$ final states [95, 96, 97, 98, 100, 101]. The cross sections were defined as background-subtracted event yields corrected for the detector response, and were found to be in good agreement with the SM predictions.

This chapter presents these measurements in the Higgs-to-four-lepton decay channel using $36.1\,\text{fb}^{-1}$ of data recorded by the ATLAS detector during Run 2 (2015 and 2016 combined datasets). These newfangled measurements explore a new phase space at new record centre-of-mass energies of $\sqrt{s} = 13\,\text{TeV}$ and their very fine precision enables to probe possible deviations from the SM.

The total production cross section can be inferred knowing the signal and background yields. Using these yields as well as the signal and background shapes, an extended Poissonian likelihood representing the Poissonian probability to observe data events given an expectation is built, in which uncertainties are treated as nuisance parameters. The production cross section can be calculated having expressed the signal yields as a function of this variable and having fitted the $m_{4\ell}$ spectrum using a binned template fit. In order to extrapolate the results from the phase space accessible to the analysis (fiducial phase space) taking into account the selection criteria, factors are defined to unfold the various final states and production modes. In order to remove the model dependence of the unfolding method, the fiducial cross section is defined, which corresponds to the production of the Higgs boson within the fiducial phase space. Theorists can then easily compare their predictions to the measurements, having applied the same event selection as for the analysis.

In summer 2016, the Higgs-to-four-lepton production cross sections were presented [216] based on $14.8\,\text{fb}^{-1}$ of recorded data. The results in this thesis include 2015 and 2016 data, and present the measurements of the inclusive (per final state and combined), differential and double-differential production cross sections. The differential variables include the four-lepton kinematics as well as variables which are sensitive to the Higgs boson production mechanisms. The four-lepton spectrum is restricted to the range $115 < m_{4\ell}^{\text{FSR}} < 130\,\text{GeV}$, where the cross sections are measured performing a fit of the four-lepton invariant mass. The results are interpreted by constraining the anomalous contact-interaction decays of the Higgs boson to left and right-handed leptons, and the anomalous coupling of the Higgs boson to the Z bosons.

The cut-based selection described in Sec. 11.4.1 is applied to reconstructed events, including FSR recovery but without any constraints on the mass of the Z bosons. Similar cuts are applied on particle-

level events to define the fiducial phase space, which must be as close as possible to the phase space accessible to the detector.

In this study, the author took part in the fiducial selection of the events in MC (see 12.1), producing the samples used for the analysis, and derived the various factors (see 12.2), per production mode, per final state and in bins of the differential variables, with their associated uncertainties. The author also contributed to the study of the purities (see 12.4, 12.5 and 12.6). More information on the measurements can be found in the internal note [215].

12.1 Fiducial phase space definition

Only a limited fraction of the physics phase space is accessible to the ATLAS detector, referred to as the detector acceptance. This induces a reduction of the efficiency to record signal events, which is further decreased by the cuts applied to suppress background contamination. The total reduction of the efficiency is measured by the so-called acceptance factor, whose calculation is outlined in Sec. 12.2. The measurements are performed in the fiducial phase space and extrapolated to the full space using the acceptance factors to assess the total production cross section.

The good estimation of the acceptance factors, which are measured using simulation, relies on a robust definition of the acceptance phase space. In order to facilitate the extrapolation, the phase space is defined based on cuts applied to measurable quantities and mimics the standard selection of reconstructed events, described in Sec. 11.4.1.

12.1.1 Fiducial event selection

For the definition of the fiducial phase space, only particle-level objects generated by MC are used. Their type (electron, muon, jets) is assessed using the Particle Data Group Identification (PDGID) [107] numbering scheme stored in the High Energy MC (HepMC) record [217], which traces the evolution of the particle throughout the simulation and decays. The selection of these particles follows the recommendations of Ref. [218, 219]. The cuts applied are as close as possible to the selection criteria for the reconstructed events to minimise the model dependence, keeping the requirements the simplest to facilitate the comparison between various MC generators. The cut flow is summarised in Tab. 12.1. Any event having a quadruplet which includes a τ lepton is rejected.

12.1.2 Electrons

Electrons must have $p_{\mathrm{T}}^{e} > 7\,\mathrm{GeV}$ and $|\eta^{e}| < 2.47$. These cuts are the same as for the reconstructed events and correspond to the ID acceptance. Electrons should originate from W or Z boson decays.

12.1.3 Muons

The same selection as for the electrons is required, except that the detector acceptance is increased to $p_{\mathrm{T}}^{\mu} > 5\,\mathrm{GeV}$ and $|\eta^{\mu}| < 2.7$.

Table 12.1 – Fiducial phase space definition. Cuts applied to particle-level objects aim at reproducing the reconstruction selection and also making it easy for theorists to compare their results [215].

Lepton definition	
Muons: $p_{\mathrm{T}}^{\mu} > 5\,\mathrm{GeV}$, $\lvert\eta^{\mu}\rvert < 2.7$	Electrons: $p_{\mathrm{T}}^{e} > 7\,\mathrm{GeV}, \lvert\eta^{e}\rvert < 2.47$
Pairing	
Leading pair:	Same-flavour opposite-charge (SFOS) lepton pair with smallest $\lvert m_Z - m_{\ell\ell}\rvert$
Sub-leading pair:	Remaining SFOS lepton pair with smallest $\lvert m_Z - m_{\ell\ell}\rvert$
Event selection	
Lepton kinematics:	Lepton transverse momenta $p_{\mathrm{T}} > 20$, 15, 10 GeV
Mass requirements:	$50 < m_{12} < 106\,\mathrm{GeV}$; $12 < m_{34} < 115\,\mathrm{GeV}$
Lepton separation:	$\Delta R_{\ell_i\ell_j} > 0.1(0.2)$ for same (opposite) flavour leptons
J/ψ veto:	$m_{\ell_i\ell_j} > 5\,\mathrm{GeV}$ for all SFOS lepton pairs
Mass window:	$115 < m_{4\ell} < 130\,\mathrm{GeV}$

12.1.4 Jets

In the fiducial space, jets generated by the MC and coming from WZ decays are selected (the detection in the calorimeters is done using an anti-k_{t} algorithm, corresponding to the `Antikt4TruthWZJets` container). The jets j must have $\left|y^{j}\right| < 4.4$ and $p_{\mathrm{T}}^{j} > 30\,\mathrm{GeV}$ to mimic the reconstruction cuts. Overlap removal of jets is performed with electrons and muons passing the fiducial kinematic cuts, if the jet is too close to the lepton ($\Delta R_{\mu j} < 0.1$ or $\Delta R_{ej} < 0.2$). This overlap removal is only performed for the dressed variables, as all the jets should be selected for the total phase space.

b-tagging of jets at generator level is performed the following way: a particle-level jet is marked as b-jet if a particle-level b-hadron h with an energy above 5 GeV is found in its vicinity ($\Delta R_{jh} < 0.3$) [220]. b-tagged jets (J) obtained using this method should also have $p_{\mathrm{T}} > 30\,\mathrm{GeV}$, be close enough to a jet j from the `Antikt4TruthWZJets` container ($\Delta R_{Jj} < 0.3$) and have a matching transverse momentum $\left|\frac{p_{\mathrm{T}}^{J} - p_{\mathrm{T}}^{j}}{p_{\mathrm{T}}^{J}}\right| < 0.25$.

12.1.5 Higgs boson candidates

The Higgs boson candidates must be composed of two pairs of opposite-charge same-flavour (SFOS) leptons, following the reconstructed event selection. The leading pair $(1,2)$ is the pair having the invariant mass m_{12} the closest to the Z pole mass (m_Z). The sub-leading pair is the remaining pair $(3,4)$ having the invariant mass m_{34} the closest to m_Z. The leading lepton (lepton of the quadruplet having the greatest transverse momentum) is required to satisfy $p_{\mathrm{T}}^{\ell} > 20\,\mathrm{GeV}$ (15 GeV, 10 GeV for sub-leading and sub-sub-leading leptons). No such requirements are imposed on the fourth lepton. The invariant mass of the two pairs has to be in the following ranges: $50 < m_{12} < 106\,\mathrm{GeV}$ and $12 < m_{12} < 115\,\mathrm{GeV}$. Any of the SFOS pairs of leptons (ℓ_i, ℓ_j) must have $m_{\ell_i\ell_j} > 5\,\mathrm{GeV}$ to veto J/ψ events. Finally, the four-lepton invariant-mass has to lay within $115 < m_{4\ell} < 130\,\mathrm{GeV}$. The restriction of the signal range was optimised to provide the highest significance for a Higgs boson of mass $m_H = 125\,\mathrm{GeV}$ [95]. Miss-pairing is allowed for the pairing of leptons to imitate the reconstruction selection (selected lepton pairs may not come from the same Z, nor from the Higgs boson).

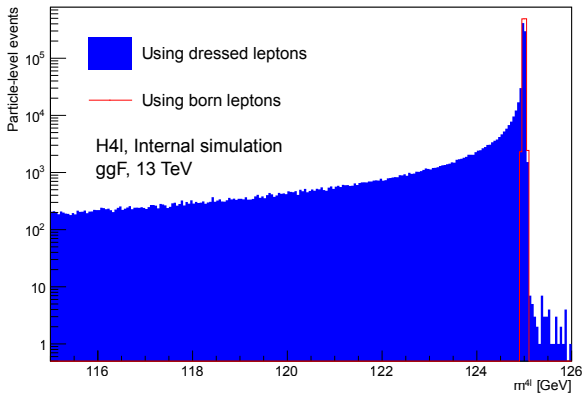

Figure 12.1 – Comparison of the four-lepton invariant mass using dressed and born lepton definitions. Imperfect FSR recovery used in the dressed lepton definition leads to a down-shift of the $m_{4\ell}$ distribution with respect to the born lepton case.

12.1.6 Dressed lepton definition

Following its generation by the MC after the decay of a Z or W boson, a lepton emits several photons due to QED FSR. From the initial state (*born*), the lepton further decays into a pair composed of a photon and another lepton having same charge and same flavour. After several radiations, the lepton achieves its final state (*bare*). To ensure a good selection of events, the born leptons should be used. It is however important to perform a FSR recovery similar to reconstructed events.

In order to do so, the bare leptons are selected using the `status` provided by the generator and the four-momenta of the photons are added to the lepton to retrieve the state before FSR (*dressed*). Dressed and born leptons may differ as the FSR recovery is not perfect. The photons selected have to be stable photons not coming from hadrons. The photons have to be close enough to the lepton with $\Delta R_{\ell\gamma} < 0.1$.

The imperfect FSR recovery leads to a down-shift in the $m_{4\ell}$ distribution as shown in Fig. 12.1, as not all the photons emitted by the lepton are recovered resulting in less energetic dressed leptons. Particularly, the dressed-lepton transverse momenta have lower values as for the born leptons. Overall, the acceptance of the detector decreases by about 5% whether dressed or born leptons are used for the selection, as shown in Tab. 12.2. The cut on $m_{4\ell}$ and the criteria on the lepton kinematics account to 2.5% and 1.5% in the efficiency drop, respectively. The remaining decrease is due to the criteria on the mass of the Z bosons. In order to better understand the origins of this variation, the effects of changing the $\Delta R_{\ell\gamma}$ cuts are presented in Tab. 12.3. From these results, imperfect FSR recovery is attributed to far FSR causing photons to fall out of the cone around the lepton for the selection. Cone sizes up to $\Delta R_{\ell\gamma} = 2$ were tried to recover far FSR, and the relative loss between the use of dressed and born leptons decreases to 1%. However, in order to mimic the reconstruction selection where $\Delta R_{\ell\gamma} < 0.01$ in most of the cases, $\Delta R_{\ell\gamma} < 0.1$ is retained in the definition of dressed leptons.

The definition of the fiducial phase space is performed using dressed leptons.

12.2 Acceptance and correction factors

From the previously defined phase space, and in order to extrapolate the fiducial measurements to the total phase space, acceptance factors $\mathcal{A}$ are calculated. A second factor, the correction factor $\mathcal{C}$, is introduced

Table 12.2 – Relative loss in event yields using born or dressed lepton definitions [215].

Relative loss [%]	
Fiducial Cuts	Born to Dressed
All fid. cuts	5.4
No $m_{4\ell}$ cut	2.5
Only lepton fid. cuts	1.5

Table 12.3 – Relative loss in event yields using born or dressed lepton definitions [215].

Relative loss [%]	
$\Delta R_{\ell\gamma}$ cut	Born to Dressed
0.1	5.4
0.2	4.0
0.3	3.4
0.5	2.6
0.7	2.3
1.0	1.5
2.0	0.9

to correct for detector resolution and misidentification effects.

12.2.1 Acceptance factor

The acceptance factor is used to extrapolate the signal yields of the fiducial volume N_{Fid} to the total phase space N_{Tot}. It is defined as:

$$\mathcal{A} = \frac{N_{\text{Fid}}}{N_{\text{Tot}}}. \tag{12.1}$$

This corresponds to the fraction of signal events passing the fiducial selection criteria, measured from simulation. The factor is calculated for each production mode (ggF, VBF, WH, ZH, $t\bar{t}H$, $b\bar{b}H$ and combined) per final state (4μ, $4e$, $2\mu2e$, $2e2\mu$, $4\ell = 4\mu + 4e$, $2\ell2\ell = 2\mu2e + 2e2\mu$ and combined) and per bin of the differential variables (for the differential and double-differential measurements only). τ leptons are vetoed for both N_{Fid} and N_{Tot}. The $\mathcal{A}$ factors are model-dependent as N_{Tot} is directly dependent on the MC chosen.

Since N_{Tot} has to represent the total phase space, born leptons are used. On the other hand, N_{Fid} represents the fiducial space, therefore dressed leptons are used. The effects of using dressed leptons instead of born for the numerator leads to a decrease of $\mathcal{A}$ of about 5%, as highlighted in Fig. 12.2. In this study, the ggF and $b\bar{b}H$ productions were treated using the ggF signal MC normalised to the sum of the predicted ggF and $b\bar{b}H$ cross sections.

In order to validate the good definition of the fiducial phase space, studies were carried out to assess from the number of reconstructed signal events N_{Reco} (following the criteria described in Sec. 11.3 and

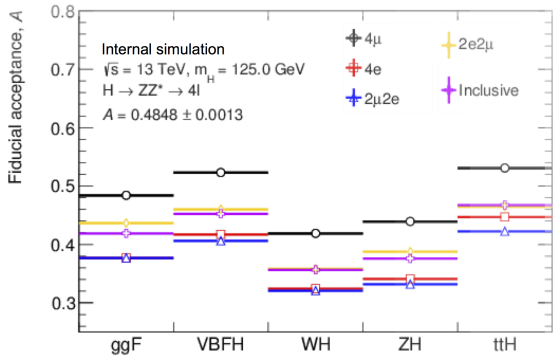

(a) $\mathcal{A}$ factors using dressed leptons.

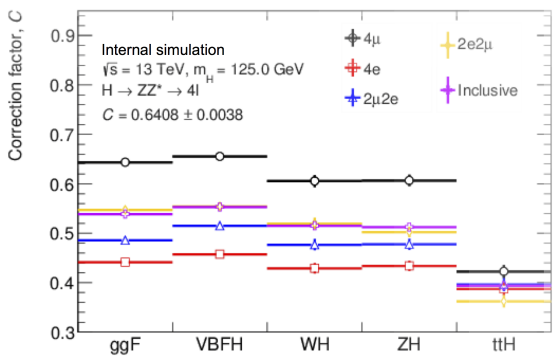

(b) $\mathcal{C}$ factors using dressed leptons.

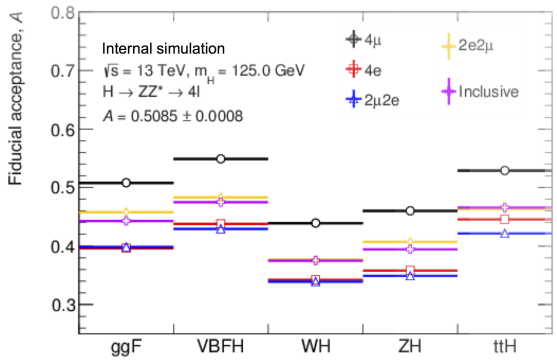

(c) $\mathcal{A}$ factors using born leptons.

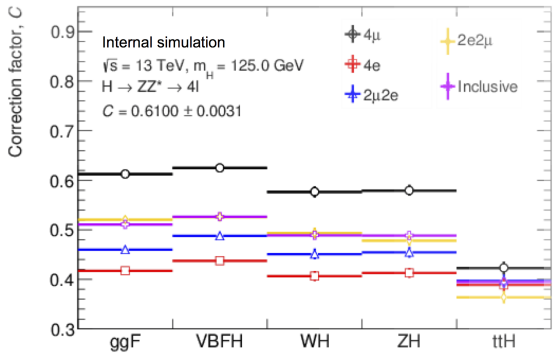

(d) $\mathcal{C}$ factors using born leptons.

Figure 12.2 – Comparison of the $\mathcal{A}$ and $\mathcal{C}$ factors at $m_H = 125\,\text{GeV}$ using the dressed and born particle-level lepton definitions. A 5% difference in the number of fiducial events is observed, leading to an increase of the correction factor and a decreasing of the acceptance factor [215]. In this study, the $gg\text{F}$ and $b\bar{b}H$ productions were treated using the $gg\text{F}$ signal MC normalised to the sum of the predicted $gg\text{F}$ and $b\bar{b}H$ cross sections.

Table 12.4 – Fiducial leakage estimation from the ggF production mode at m_H = 125 GeV for various lepton definitions [215].

Fiducial Leakage [%]			
Decay Channel	Born	Dressed	Bare
4μ	0.6	1.3	2.3
$4e$	2.5	3.2	10.1
4ℓ	1.4	2.1	5.7

11.4.1), the number of events falling out of the fiducial volume:

$$\mathcal{F}_{\text{leak}} = \frac{N_{\text{Reco}} - N_{\text{Reco \& Fid}}}{N_{\text{Reco}}}, \tag{12.2}$$

where $N_{\text{Reco \& Fid}}$ is the number of signal events passing both the reconstruction selection as well as the fiducial cuts. The *leakage* fractions are not nil due to detector resolution and reconstruction effects, which cause event migration in and out the analysis space. A good definition of the fiducial volume reduces the model dependence of the measurements. Important leakage would indicate that the fiducial space does not mimic the reconstruction space very well as reconstructed signal events fall out of the fiducial space. Results of the study for the ggF production mode are presented in Tab. 12.4. Leakage is more important for the $4e$ channel, but results overall indicate a good definition of the fiducial volume. The lack of FSR recovery for bare leptons causes important leakages (up to 10% and 2.5% for the $4e$ final state, if bare or born leptons are used).

12.2.2 Correction factor

The effects of detector acceptance, resolution and identification have to be considered to correct the measured cross sections. Acceptance effects are covered by the good definition of the fiducial space and the calculation of $\mathcal{A}$, assuming the leakage fractions are low. For the remaining two effects, correction factors $\mathcal{C}$ are defined:

$$\mathcal{C} = \frac{N_{\text{Reco}}}{N_{\text{Fid}}}. \tag{12.3}$$

These factors are calculated in parallel of acceptance factors (per production mode, per final state and per differential bin).

The choice of this unfolding method, which enables to translate particle-level information from the generator to reconstructed events, was motivated by the good matching between generated and reconstructed events. The correction factor method introduces a bias in the measurements because their calculation only relies on a MC sample, in which variable distributions may not reproduce the data perfectly. The bias introduced is proportional to the off-diagonal terms of the response matrix[1] [221]. These matrices were calculated for the differential variables and the event types, and were found to be almost diagonal. Thanks to this, the $\mathcal{C}$ factors can be considered model-independent and can be used for the measurements. As a complementary check, the unfolding was also carried out by inverting the response matrices instead of using the $\mathcal{C}$ factors, but the results remained consistent with respect to the standard analysis presented in this thesis.

[1] The response matrix R_{ij} is the matrix of probabilities $R_{ij} = P(\text{observed in bin } i \mid \text{generated in bin } j)$. It is therefore dependent upon the MC generator, the detector and the variable considered.

12.2.3 Fiducial and total cross sections

Using these factors to extrapolate to the full phase space and to correct for detector effects, the total cross section can be calculated:

$$\sigma_{\text{Tot}} = \frac{n_{\text{s}}}{\mathcal{A} \times \mathcal{C} \times \mathcal{B} \times \mathcal{L}_{\text{int}}}, \tag{12.4}$$

where n_{s} is the signal yield measured in data, $\mathcal{B} = (1.24 \pm 0.03) \times 10^{-4}$ [123] is the branching ratio of the $H \to ZZ^* \to 4\ell, \ell \in \{e, \mu\}$ final state and $\mathcal{L}_{\text{int}} = \int \mathcal{L} dt$ is the integrated luminosity recorded.

To remove the model dependence, the fiducial cross section is also defined:

$$\sigma_{\text{Fid}} = \sigma_{\text{Tot}} \times \mathcal{A} \times \mathcal{B} = \frac{n_{\text{s}}}{\mathcal{C} \times \mathcal{L}_{\text{int}}}. \tag{12.5}$$

This cross section corresponds to the fiducial volume and is model independent if the leakage fractions are low enough. This quantity can easily be compared to predictions. Equation 12.5 explicitly shows how the two cross sections are related one to each other, having factorised the model-dependent term.

12.3 Signal extraction

This section presents the statistical procedure to extract the signal yields for the calculation of the cross sections. Extraction is based on a binned template fit of the $m_{4\ell}$ spectrum, using a logarithmic likelihood minimisation. The methodology described here is employed for both the inclusive and differential measurements, details being given in the next sections.

The probability of observing n events with an expectation of $n_{\text{e}} = n_{\text{s}} + n_{\text{b}}$ (where n_{s} and n_{b} are the expected number of signal and background events) is modelled by an extended Poisson likelihood:

$$L\left(m_{4\ell} \middle| n_{\text{s}}, n_{\text{b}}, \vec{b}, \vec{\theta}\right) = P_{\text{Pois}}\left(n, n_{\text{e}}\right) \times F_{\text{sb}}\left(m_{4\ell} | n_{\text{s}}, n_{\text{b}}\right) \times \prod_{i=1}^{N} P_{\text{bkg}}\left(b^i \middle| {b_{\text{e}}}^i\right) \times \prod_{j=1}^{M} P_{\text{nuis}}\left(\theta^j \middle| {\theta_{\text{e}}}^j\right), \tag{12.6}$$

where $\vec{b} = \left(b^i\right)_{i \in [\![1,N]\!]}$ are the background yields (of associated expectation $\vec{b_{\text{e}}} = \left({b_{\text{e}}}^i\right)_{i \in [\![1,N]\!]}$), and $\vec{\theta} = \left(\theta^j\right)_{j \in [\![1,M]\!]}$ are the nuisance parameters (of associated expectation $\vec{\theta_{\text{e}}} = \left({\theta_{\text{e}}}^j\right)_{j \in [\![1,M]\!]}$), which include experimental and theory systematics, as well as background shape uncertainties, and factor uncertainties. The three first kinds of systematic uncertainties were described in the previous chapter. The uncertainties on the factors only concern cross-section measurements and are described in Sec. 12.4.3.

The Poisson pdf directly models the probability to observe n events given an expectation of n_{e}:

$$P_{\text{Pois}}\left(n, n_{\text{e}}\right) = \frac{{n_{\text{e}}}^n}{n!} \exp\left(-n_{\text{e}}\right). \tag{12.7}$$

The function F_{sb} modelling the signal and the various backgrounds is written as

$$F_{\text{sb}}\left(m_{4\ell} | n_{\text{s}}, n_{\text{b}}\right) = \frac{n_{\text{s}}}{n_{\text{e}}} F_{\text{s}}\left(m_{4\ell} | n_{\text{s}}\right) + \frac{n_{\text{b}}}{n_{\text{e}}} \sum_{i=1}^{N} F_{\text{b}}^i\left(m_{4\ell} \middle| n_{\text{b}}^i\right), \tag{12.8}$$

where F_{s} is the signal pdf introduced previously, F_{b}^i is the i-th background pdf, and n_{b}^i is the corresponding number of expected background events ($n_{\text{b}} = \sum_{i=1}^{N} n_{\text{b}}^i$). The background shapes F_{b}^i and their uncertainties are directly obtained using the techniques described in Sec. 11.5. The remaining probability densities P_{bkg} and P_{nuis} are Gaussian pdfs modelling the knowledge on the background yields and the

nuisance parameters, respectively. They include the experimental and theory uncertainties associated to the background shapes, the signal efficiencies ($\varepsilon = \mathcal{A} \times \mathcal{C}$) and the integrated luminosity $\mathcal{L}_{\text{int}}$. The last two parameters ε and $\mathcal{L}_{\text{int}}$ can have a fixed value in the fit (set to the expectation) or can be left floating within the associated uncertainties. For each of the densities, the mean (standard deviation) of the Gaussian is set to the expected value (associated uncertainty). The effect of these densities is to broaden the likelihood reflecting the degradation of the precision on the measurements.

From the likelihood function, a profile likelihood ratio $\Lambda\left(m_{4\ell}|\sigma_{\text{Tot}}\right)$ is built, in which the total cross section is the parameter of interest (the change of variable $n_{\text{s}} = \sigma_{\text{Fid}} \times \mathcal{C} \times \mathcal{L}_{\text{int}} \times \mathcal{A} \times \mathcal{B}$ is performed):

$$\Lambda\left(m_{4\ell}|\sigma_{\text{Tot}}\right) = \frac{L\left(m_{4\ell}\middle|\sigma_{\text{Tot}}, \hat{\hat{\vec{\Theta}}}\left(\sigma_{\text{Fid}}\right)\right)}{L\left(m_{4\ell}\middle|\hat{\sigma_{\text{Tot}}}, \hat{\hat{\vec{\Theta}}}\right)}, \tag{12.9}$$

where the vector $\vec{\Theta} = \left(n_{\text{b}}, \vec{b}, \vec{\theta}\right)$ regroups the various parameters of the fit. For a variable x, $\hat{x}$ denotes the value which maximises L. $\hat{\hat{\vec{\Theta}}}\left(\sigma_{\text{Tot}}\right)$ is the vector of parameters which maximises L for a given σ_{Tot}. The numerator of the ratio is the conditional likelihood (which depends on σ_{Tot}), whereas the denominator is the maximised unconditional likelihood estimator. The ratio is calculated using the RooFit and RooStats frameworks [222, 223].

12.3.1 Asymptotic approximation

The Wilk's theorem [224] states that for samples of sufficiently large number of events, the quantity $-2\ln\Lambda$ follows a χ^2 law with one degree of freedom. With enough statistics, it is therefore possible to estimate the confidence intervals at 68% and 95% of the fit of the cross sections. This corresponds to intervals in fitted cross-sections for which $-2\ln\Lambda < 1$ and 4, respectively. For the scope of this thesis, only 68% intervals are searched.

12.3.2 Pseudo data generation

The asymptotic approximation has to be verified, to ensure that with the statistics available, the ratio indeed follows a χ^2 distribution. Since MC generation is too resource-consuming, pseudo-data events are used, referred to as Asimov datasets [225]. Generation of pseudo data does not require as many resources as for the MC generation, as the shapes of the variables are already known. Pseudo-data events are generated such that the distributions of the interesting variables approximate the pdfs, assuming a SM Higgs boson having $m_H = 125\,\text{GeV}$. The ZZ^* background (including $q\bar{q}$ and gg initiated events), as well as the $Z+\text{jets}$, $t\bar{t}$, VVV backgrounds ($V \in \{Z, W^{\pm}\}$) are taken from the shapes determined as described in Sec. 11.5, setting the nuisance parameters to their nominal values.

In order to better understand the effects of statistical errors on the cross section measurements for each parameter of interest, the logarithmic likelihood ratio is minimised the same way as for the real data, with or without systematic uncertainties. While on real data, the measured 68% confidence interval can be assessed, pseudo-data experiments allow to determine the expected values. Checks on the Asimov datasets are also an opportunity to verify the validity of hypotheses, especially that the dataset is large enough for $-2\ln\Lambda$ to have the expected behaviour and that the fit does not introduce any biases in the results. A symmetric curve is therefore expected for the $-2\ln\Lambda$ distribution, centred in its minimal value, which should be close enough to the prediction.

12.4 Measurement of the inclusive cross sections

This section is dedicated to the measurements of the inclusive Higgs-boson-to-four-lepton production cross sections. Four categories c are defined corresponding to the final states (4μ, $4e$, $2\mu 2e$, $2e2\mu$). For each category, the number of signal events is calculated:

$$n_{\mathrm{s}}^{c}\left(m_{4\ell}\right) = F_{\mathrm{s}}^{c}\left(m_{4\ell}\right) \times \mathcal{L}_{\mathrm{int}} \times \sum_{p} \sigma_{\mathrm{Tot}} \times r_{p} \times \mathcal{B}^{c} \times \mathcal{A}_{p}{}^{c} \times \mathcal{C}_{p}{}^{c}, \tag{12.10}$$

where p indexes the production modes (ggF, VBF, WH, ZH, $t\bar{t}H$, $b\bar{b}H$) and F_{s}^{c} is the signal pdf for the category. The proportion factors $r_{p} = \sigma_{p}^{\mathrm{SM}}/\sigma_{\mathrm{Tot}}^{\mathrm{SM}}$ measure the contribution of each production mode, as predicted by theory for each final state. These factors are very close to 1 for the ggF production mode and have low values for the rest. The factors and branching ratios are calculated per production mode and category. The parameters of interest (POI) measured by the fit are composed of

- the fiducial cross section per category:

$$\mathrm{POI}_{1}^{c} = \left[\sigma_{\mathrm{Tot}} \times \mathcal{B}^{c}\right] \times \mathcal{A}^{c}, \tag{12.11}$$

  where $\mathcal{A}^{c}$ is the total acceptance factor for the category c, including all productions.

- the fiducial cross section for $4\mu + 4e$ and $2\mu 2e + 2e2\mu$ events:

$$\mathrm{POI}_{2}^{4\mu+4e} = \sigma_{\mathrm{Tot}} \times \left[\mathcal{B}^{4\mu} \times \mathcal{A}^{4\mu} + \mathcal{B}^{4e} \times \mathcal{A}^{4e}\right] \tag{12.12}$$

  and

$$\mathrm{POI}_{2}^{2\mu2e+2e2\mu} = \sigma_{\mathrm{Tot}} \times \left[\mathcal{B}^{2\mu2e} \times \mathcal{A}^{2\mu2e} + \mathcal{B}^{2e2\mu} \times \mathcal{A}^{2e2\mu}\right]. \tag{12.13}$$

- the fiducial cross section for all the decay channels:

$$\mathrm{POI}_{3} = \sum_{c} \sigma_{\mathrm{Tot}} \times \mathcal{B}^{c} \times \mathcal{A}^{c}. \tag{12.14}$$

- the total cross section:

$$\mathrm{POI}_{4} = \sigma_{\mathrm{Tot}}. \tag{12.15}$$

12.4.1 Inclusive acceptance and correction factors

Following the previous definitions, the $\mathcal{A}$ and $\mathcal{C}$ factors are calculated per final state and production mode. The values are presented in Tab. 12.5 and 12.6, corresponding to $m_{H} = 125\,\mathrm{GeV}$. Errors are statistical only.

The dominant production mode, ggF has an overall acceptance of 42%, with a maximum of 48% for the 4μ channel thanks to the looser cuts applied on muons. The stricter cuts on electrons explain the low values for $4e$ (38%). The difference between the $2\mu 2e$ and $2e2\mu$ channels comes from the fact that the sub-leading pair is composed of less boosted leptons (since the corresponding Z is off-shell). These are therefore more sensitive to the p_{T} cuts which are looser for the muons, explaining why the $2e2\mu$ channel dominates. The results are quite similar for the other production modes. The WH and ZH production modes have lowest acceptances due to internal miss-pairing of the leptons, which is allowed by the definition of the fiducial phase space. Therefore, some lepton pairs may not originate from the same Z boson decay and cause the event to fail requirements on m_{12} or m_{34}. This particularly impacts WH, as some leptons may even originate from W decays.

Table 12.5 – Inclusive acceptance factors per production mode and decay channel [215].

Acceptance factor [%]						
Channel	Production mode					
	ggF	VBF	WH	ZH	$t\bar{t}H$	$b\bar{b}H$
4μ	48.32 ± 0.14	52.16 ± 0.07	42.37 ± 0.22	45.22 ± 0.22	53.15 ± 0.59	52.66 ± 0.90
$4e$	37.86 ± 0.11	41.31 ± 0.07	33.39 ± 0.21	35.40 ± 0.21	44.62 ± 0.59	39.23 ± 0.93
$2\mu 2e$	37.94 ± 0.10	40.56 ± 0.07	32.70 ± 0.20	34.99 ± 0.21	42.26 ± 0.59	40.94 ± 0.90
$2e2\mu$	43.95 ± 0.13	46.02 ± 0.07	36.74 ± 0.21	39.55 ± 0.22	46.55 ± 0.58	43.25 ± 0.91
All	42.07 ± 0.06	45.38 ± 0.04	36.36 ± 0.10	38.87 ± 0.11	46.76 ± 0.30	44.22 ± 0.46

Table 12.6 – Inclusive correction factors per production mode and decay channel [215].

Correction factor [%]						
Channel	Production mode					
	ggF	VBF	WH	ZH	$t\bar{t}H$	$b\bar{b}H$
4μ	63.95 ± 0.32	67.32 ± 0.29	61.21 ± 0.71	60.50 ± 0.69	42.91 ± 1.36	62.77 ± 2.61
$4e$	42.35 ± 0.28	45.98 ± 0.26	43.57 ± 0.63	41.80 ± 0.61	38.96 ± 1.40	44.32 ± 2.47
$2\mu 2e$	47.82 ± 0.30	52.37 ± 0.28	48.13 ± 0.68	48.68 ± 0.68	39.29 ± 1.50	47.19 ± 2.54
$2e2\mu$	55.16 ± 0.31	58.72 ± 0.28	52.47 ± 0.68	53.65 ± 0.68	36.44 ± 1.33	52.31 ± 2.68
All	53.22 ± 0.15	56.92 ± 0.14	52.05 ± 0.34	51.87 ± 0.34	39.61 ± 0.70	52.73 ± 1.31

Concerning the correction factors, similar remarks can be made. The 4μ channel is further enhanced, as it benefits from high muon reconstruction efficiency as compared to electrons. The $\mathcal{C}$ factors appear to be quite model independent as their values do not strongly depend on the production mode considered. Exception has be noticed for the $t\bar{t}H$ mode, because of the lepton isolation requirements. Indeed, in this mode the Higgs boson is produced in association to two boosted jets coming from the $t\bar{t}$ pair. These jets leave tracks in the ID and energy deposits in the calorimeters which contribute to worsen the isolation of the decaying leptons. This effect is not reproduced in the fiducial volume, as no isolation cuts are applied.

12.4.2 Background checks

As stated in Sec. 11.5, ZZ^* normalisation is taken from MC, whereas reducible background yields are calculated using data driven techniques. In order to ensure these normalisations are done properly, the background yields are compared between data and simulation in specifically designed control regions. The background shapes, which are parametrised using simulated samples, are also compared in these regions to check the good agreement between data and MC.

The CRs are defined applying the standard selection criteria and removing the criterion on the 4ℓ vertex. The sub-leading pair, which is the object of the study, has to be composed of same-flavour leptons having same or opposite charge, therefore defining two orthogonal regions (opposite-sign and same-sign).

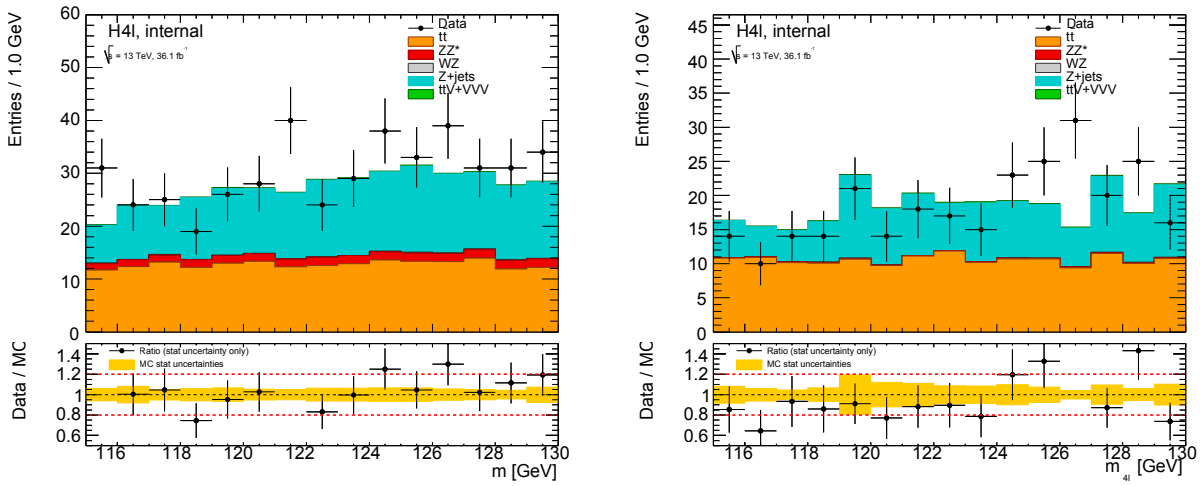

(a) $Z + \mu\mu$, opposite-sign

(b) $Z + \mu\mu$, same-sign

Figure 12.3 – Invariant mass distributions of the lepton pair in the $Z + \mu\mu$ control sample for the (a) opposite-sign and (b) same-sign control regions. Black dots represent the data corresponding to $36.1\,\text{fb}^{-1}$, whereas the various background components are shown by the coloured areas ($t\bar{t}$ in orange, ZZ^* continuum in red, WZ production in grey, $Z+$jets in blue and $t\bar{t}V$, VVV productions in green with $V \in \{Z, W^{\pm}\}$). The bottom plots show the ratios data over simulation. Taking into account the statistical uncertainties, the comparison shows a good agreement reflecting good MC normalisation. In these regions, background is dominated by $Z+$jets and $t\bar{t}$ events [215].

The isolation and d_0 requirements are not applied to the sub-leading pair. The final states of the sub-leading pair are divided into two groups: $Z + 2\ell$, $2\ell \in \{2\mu, 2e\}$.

Data and simulation are then compared in bins of $m_{2\ell}$ for the muon (Fig. 12.3) and electron (Fig. 12.4) cases, for the mass range useful to the analysis. Results indicate a good normalisation of the MC to the data. The main contribution of the ZZ^* background in this analysis is initiated by the annihilation of a quark / anti-quark pair, however a small fraction (2%) of gluon-gluon induced background is added to the MC yields, following theoretical predictions. Interferences between the gluon-gluon initiated background and the ggF signal are below the percent level and are neglected in this analysis.

12.4.3 Uncertainties

Uncertainties on the total and fiducial cross sections can be grouped in four categories. The three first categories (background normalisations and shapes, theory, experimental) were described in Sec. 11.5 and 11.6. They affect the events and signal yields and shapes used for the fit. In addition to these three categories, uncertainties are linked to the calculation of the factors $\mathcal{A}$ and $\mathcal{C}$ and affect the measurements. These last uncertainties are further described in the following paragraphs. All the uncertainties of the four categories are included into the Poissonian likelihood as nuisance parameters.

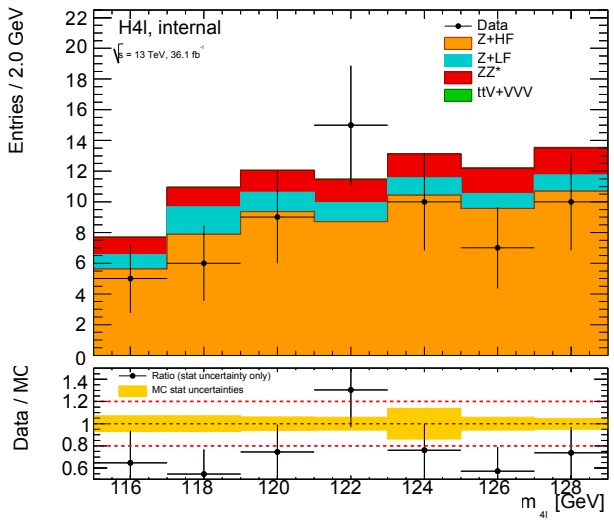

Figure 12.4 – Invariant mass distributions of the lepton pair in the $Z + ee$ control sample (opposite-sign control region). Black dots represent the data corresponding to 36.1 fb^{-1}, whereas the various background components are shown by the coloured areas (Z + HF in orange, Z + LF in blue, ZZ^* continuum in red, and $t\bar{t}V$, VVV productions in green with $V \in \{Z, W^{\pm}\}$). The bottom plots show the ratios data over simulation. Taking into account the statistical uncertainties, the comparison shows a good agreement reflecting good MC normalisation. In the control region, background is dominated by Z + HF events [215].

Scale and PDF uncertainties

The effect of the QCD renormalisation and factorisation scales, as well as the PDF set chosen for the generation of the simulated signal events is taken into account the same was as described in Sec. 11.6 [214]. The envelope of the variations is taken as the systematic uncertainty on the acceptance and correction factors.

Higgs mass

Experimental uncertainties [89] on the Higgs boson mass affect measurements of the $\mathcal{A}$ and $\mathcal{C}$ factors. The central value of the factors is estimated at m_H = 125 GeV. Mass uncertainties are obtained by linearly interpolating the values of the factors between the three available mass points 124, 125, and 126 GeV and retaining the interpolated values of $\mathcal{A}$ and $\mathcal{C}$ for m_H shifted by ±240 MeV. The systematic is then calculated as the difference between central and shifted values. The effect of this uncertainty is of 0.04% and 0.62% on the acceptance and correction factors, respectively.

Note that the effects of the mass uncertainty were also checked by shifting the $m_{4\ell}$ templates by ±240 MeV. The fit was carried out with the new templates and cross sections were extracted. However, the variations with respect to the nominal case were found to be below 0.5% and were neglected in the final results.

Experimental and detector uncertainties

Experimental uncertainties introduced in Sec. 11.6 also affect correction factors. The weights of the generated events for the calculation of N_{Reco} are varied and the correction factors are recalculated for each variation. The total systematic uncertainty on $\mathcal{C}$ is defined as the sum in quadrature of all the variations. In the end, the experimental uncertainties both affect the signal and background yields and shapes (as described in Sec. 11.6), but also the correction factors. They however do not enter the calculation of the acceptance factors.

Signal composition

The next uncertainty concerns the composition of the production modes, referred to as signal composition, and affects both the $\mathcal{A}$ and $\mathcal{C}$ factors. The latest cross-section measurements performed by CMS and ATLAS, assuming a SM-like Higgs boson, constrained the ratios $r_p = \sigma^p/\sigma^{gg\text{F}}$ of the various Higgs-boson-to-four-lepton production cross sections, where p indexes the production mode with $p \in \{\text{VBF}, WH, ZH, t\bar{t}H\}$. From these measurements, the covariance matrix C of the errors on the ratios was calculated and is presented in Ref. [94]. This matrix is diagonalised to remove the correlations among uncertainties, and variances are retrieved from the diagonal elements. Using both the eigenvectors and eigenvalues of C, it is possible to calculate the uncertainties on the ratios r_p with a 68% confidence interval.

The variations $\vec{v_p}$ on the eigenvectors $\vec{\lambda}_p$ (corresponding to eigenvalues λ_p) are estimated as follows:

$$\vec{v_p} = \left(\vec{\sigma} - \left(\sqrt{\lambda}_p, 0, 0, 0\right) \times {}^t\vec{\lambda}_p\right)/\sigma_{\vec{\text{SM}}}, \tag{12.16}$$

where ${}^t\vec{\lambda}_p$ is the transposed eigenvector, $\vec{\sigma}$ and $\sigma_{\vec{\text{SM}}}$ are the vectors of ratios $(r_{\text{VBF}}, r_{WH}, r_{ZH}, r_{t\bar{t}H})$ measured and predicted by the SM, respectively. In this equation, the division of two vectors $\vec{x} = \{x^p\}_p$ and $\vec{y} = \{y^p\}_p$ gives the following result $\vec{x}/\vec{y} = \{x^p/y^p\}_p$. $gg\text{F}$ and $b\bar{b}H$ variations are set to 0.

From the eigenvector variations, it is possible to calculate the uncertainties on the factors $\mathcal{F} \in \{\mathcal{A}, \mathcal{C}\}$:

$$\sigma_{\mathcal{F}} = \sqrt{\sum_p (\mathcal{F} - \mathcal{F}_p)^2}, \mathcal{F}_p = \frac{\mathcal{N}_{gg\text{F}} + \sum_i \mathcal{N}_i \times v_p^i}{\mathcal{D}_{gg\text{F}} + \sum_i \mathcal{D}_i v_p^i}, \tag{12.17}$$

where $\mathcal{N}$ and $\mathcal{D}$ are the numerator and denominator of the factor $\mathcal{F}$, respectively.

ggF uncertainty

In order to ensure a good description of the Higgs boson kinematics, studies were also performed using alternative ggF MC generators (see description in Sec. 11.2.2) to estimate the model dependence of $\mathcal{A}$ and $\mathcal{C}$ factors. These variations mostly affect the $p_{\text{T}}^{4\ell}$ distribution, as NNLOPS (standard sample) contains the most up-to-date predictions (NNLO in QCD, using the merging of the NLO H+jets cross section with the parton shower). This sample is compared to MadGraph5_aMC@NLO at the NLO level in QCD for the 0, 1 and 2 additional jet events, merged using the FxFx scheme, and to HRes v2.3 where fixed-order cross sections for ggF are computed up to NNLO in QCD, and the $p_{\text{T}}^{4\ell}$ distribution is described at NLO. In this sample, re-summation of soft-gluon effects at small transverse momenta are included up to NNLL.

Table 12.7 – Uncertainties on the inclusive correction and acceptance factors [215].

Systematic Uncertainties [%]		
	Up	Down
Detector correction factors		
Experimental, electrons	3.15	2.65
Experimental, muons	2.74	2.24
Signal composition	1.20	1.20
MC statistics	0.18	0.18
μR and μF Scale	0.13	0.14
Alternative PDFs	0.07	0.07
Higgs boson mass	0.04	0.04
Acceptance factors		
Alternative PDFs	0.66	0.66
Higgs boson mass	0.62	0.62
Signal composition	0.57	0.57
μR and μF Scale	0.32	0.47
MC statistics	0.06	0.06

Results

The various contributions of systematic uncertainties are presented in Tab. 12.7. For the correction factors, the main contribution arises from experimental uncertainties, which is expected since detector effects directly impact N_{reco}. Acceptance factor uncertainties are much lower, dominated by the Higgs mass variation.

12.4.4 Checks on pseudo data

In order to check the Asimov dataset produced for the closure test of the fitting method, the $m_{4\ell}$ distributions are compared using the Asimov data and the MC samples. Results are presented in Fig. 12.5 and show a very good agreement, confirming the good definition of the Asimov dataset. In these pots, errors are statistical only and assume an integrated luminosity of 36.1 fb^{-1}. The large error bars are attributed to the lack of statistics, since the distributions are split per final state.

Using the validated pseudo data, fits are performed for each of the POIs defined in Sec. 12.4, and Fig. 12.6 and 12.7 show the results for POI$_1^c$ ($c \in \{4\mu, 4e, 2\mu2e, 2e2\mu\}$) and other POIs, respectively. These plots are often referred to as *Log likelihood scans*, as they present $-2\ln\Lambda$ in the vicinity of the minimum. Results are calculated with $\mathcal{L}_{\text{int}} = 36.1\,\text{fb}^{-1}$, corresponding to the data recorded in the Run 2, and a significance above 4σ is expected for each of the POIs (corresponding to a minimum of $-2\ln\Lambda = 0$). The 68% and 95% confidence level intervals are highlighted by the dotted lines in the plots at 1 and 4, respectively.

The fitted values are found at the minimum of the curves, which are quite symmetrical showing $-2\ln\Lambda$ indeed follows a χ^2 distribution. A summary of the results obtained with Asimov data is presented in Tab. 12.8, with and without systematic uncertainties. Expected statistical uncertainties on the fiducial

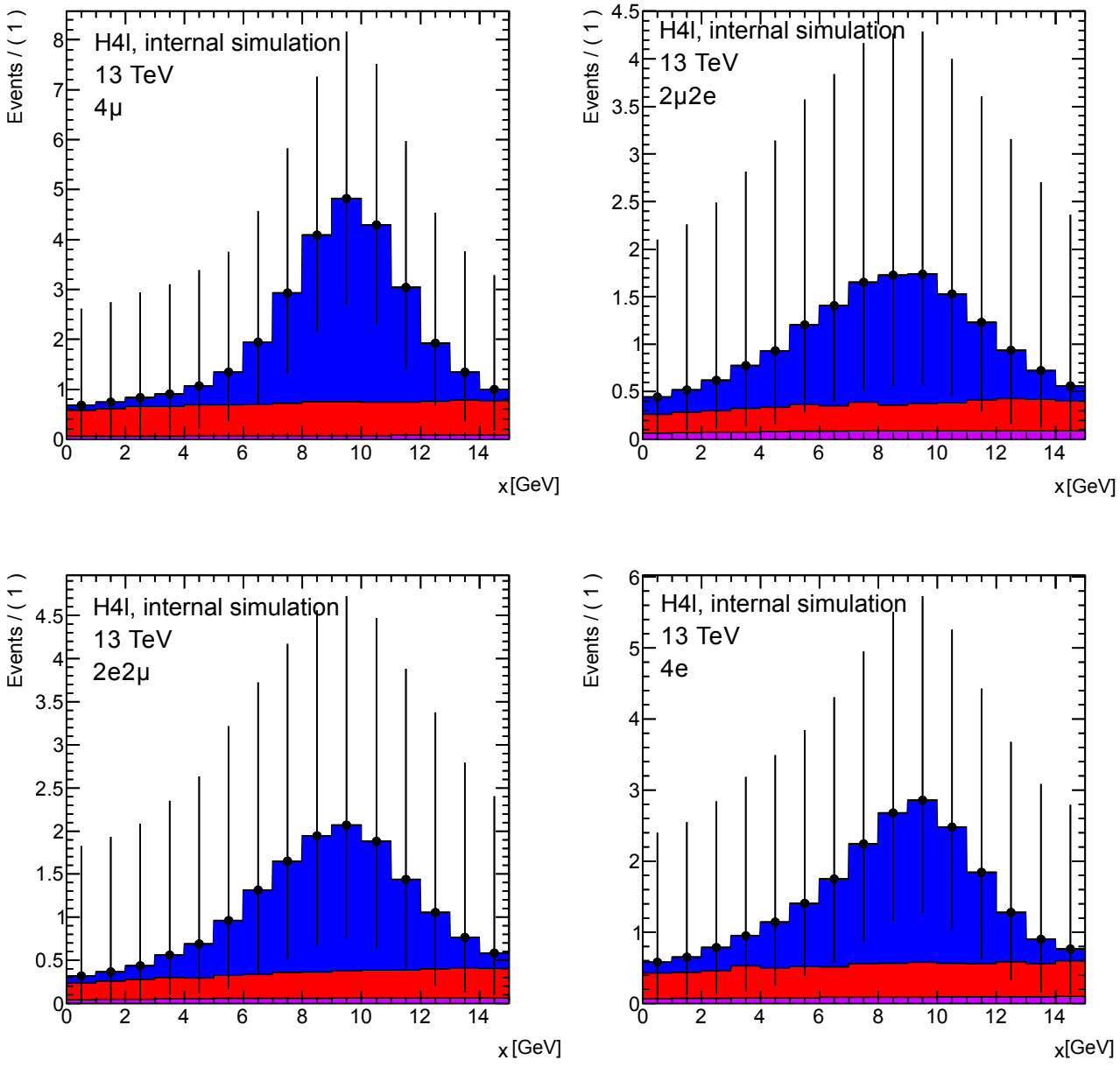

Figure 12.5 – Comparison of the $x = m_{4\ell} - 115\,\text{GeV}$ (bin number) distributions between Asimov data and MC for closure test. The various final states are shown with 4μ in the top left, $4e$ in the top right, $2\mu 2e$ in the bottom left and $2e2\mu$ in the bottom right. The range plotted is $115 < m_{4\ell} < 130\,\text{GeV}$. The black dots represent the Asimov dataset, while the blue, the red and violet areas represent the signal, the ZZ^* and the reducible background, respectively. An integrated luminosity of $36.1\,\text{fb}^{-1}$ at $\sqrt{s} = 13\,\text{TeV}$ was assumed, and errors are statistical only [215].

Table 12.8 – Expected and fitted inclusive cross section using Asimov dataset and assuming an integrated luminosity of 36.1 fb^{-1} at $\sqrt{s}$ = 13 TeV. (a) is without systematics and (b) with systematics [215].

(a) Without systematics

POI	σ_{inj} [fb]	σ_{fit} [fb]	Relative Error
$\sigma_{4\mu}$	0.886	$0.9^{+0.2}_{-0.2}$	$^{+28\%}_{-24\%}$
σ_{4e}	0.692	$0.7^{+0.3}_{-0.2}$	$^{+40\%}_{-34\%}$
$\sigma_{2\mu 2e}$	0.631	$0.6^{+0.2}_{-0.2}$	$^{+39\%}_{-33\%}$
$\sigma_{2e2\mu}$	0.726	$0.7^{+0.2}_{-0.2}$	$^{+34\%}_{-29\%}$
$\sigma_{4\mu+4e}$	1.58	$1.6^{+0.4}_{-0.3}$	$^{+23\%}_{-21\%}$
$\sigma_{2\mu 2e+2e2\mu}$	1.36	$1.4^{+0.3}_{-0.3}$	$^{+25\%}_{-22\%}$
σ_{Fid}	2.94	$2.9^{+0.5}_{-0.5}$	$^{+17\%}_{-15\%}$
σ_{Tot} [pb]	55.6	56^{+9}_{-8}	$^{+16\%}_{-15\%}$

(b) With systematics

POI	σ_{inj} [fb]	σ_{fit} [fb]	Relative Error
$\sigma_{4\mu}$	0.886	$0.9^{+0.3}_{-0.2}$	$^{+30\%}_{-26\%}$
σ_{4e}	0.692	$0.7^{+0.3}_{-0.2}$	$^{+42\%}_{-35\%}$
$\sigma_{2\mu 2e}$	0.631	$0.6^{+0.2}_{-0.2}$	$^{+39\%}_{-33\%}$
$\sigma_{2e2\mu}$	0.726	$0.7^{+0.2}_{-0.2}$	$^{+35\%}_{-30\%}$
$\sigma_{4\mu+4e}$	1.58	$1.6^{+0.4}_{-0.3}$	$^{+25\%}_{-22\%}$
$\sigma_{2\mu 2e+2e2\mu}$	1.36	$1.4^{+0.3}_{-0.3}$	$^{+26\%}_{-23\%}$
σ_{Fid}	2.94	$2.9^{+0.5}_{-0.5}$	$^{+18\%}_{-16\%}$
σ_{Tot} [pb]	55.6	56^{+10}_{-9}	$^{+18\%}_{-16\%}$

cross sections are of the order of 30% for the single final states and reduce to 16% for all the final states combined. Results of the fits (σ_{fit}) are consistent with σ_{inj} within the errors (left column of Tab. 12.8).

12.4.5 Results with 36.1 fb^{-1}

The $m_{4\ell}$ distributions for 36.1 fb^{-1}, comparing data and MC, are presented in Fig. 11.13 and 11.14 all final states combined and per final state, respectively. No strong deviations are observed.

From the $m_{4\ell}$ distributions per final state, and using the fit on $-2\ln\Lambda$ on real data, the various POIs can be measured. The log likelihood scans are shown in Fig. 12.8 and Fig. 12.9 for POI$_1^c$ and other POIs, respectively. As for pseudo data fits, the curves are quite symmetrical ($-2\ln\Lambda$ is well modelled by a χ^2 law) and the minimum value is 0, indicating a strong significance of the measurements for all the POIs. The 68% confidence level intervals are used as error measurements on the cross sections, and the scans are restricted to these intervals.

Results are presented in Tab. 12.9 and Fig. 12.10. Overall an excess of less than 1.3σ is observed with respect to the SM, particularly marked in the $2e2\mu$ channel (corresponding to the excess of observed signal and background yields shown in Tab. 11.15). As mentioned in Sec. 11.7, checks were carried out to understand this discrepancy, such as stability of the signal yields with time of data recording (plot of observed event yields par data period), and comparison of isolation and d_0 distributions (between data and simulation in the signal and control regions). No unexpected behaviour in the methodology was found. Despite this disagreement, results remain consistent with SM predictions taking into account the uncertainties.

The agreement with the SM prediction is estimated calculating the p-values. These correspond to the probability, when the SM is assumed to be describing the data well, for the measurement to take same or better values in favour of the SM prediction, with respect to the observed result [226]. Low p-values

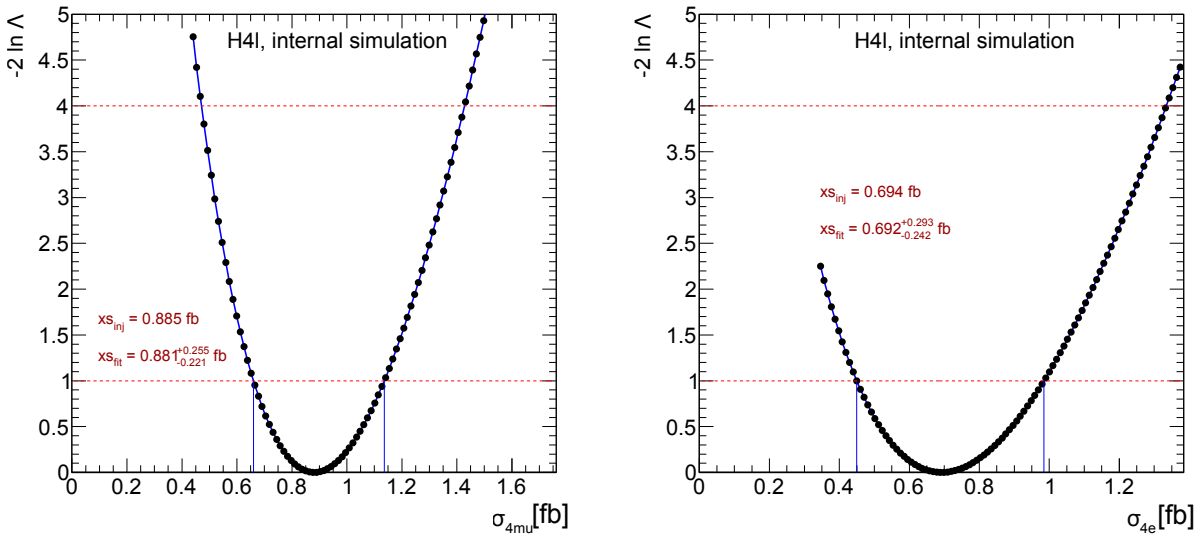

(a) $\mathrm{POI}_1^{4\mu}$ (b) POI_1^{4e}

(c) $\mathrm{POI}_1^{2\mu 2e}$ (d) $\mathrm{POI}_1^{2e2\mu}$

Figure 12.6 – Inclusive fiducial cross section fit on Asimov data, per single channel (POI_1), showing (a) $\sigma_{4\mu}$, (b) σ_{4e}, (c) $\sigma_{2\mu 2e}$ and (d) $\sigma_{2e2\mu}$. An integrated luminosity of 36.1 fb^{-1} at $\sqrt{s}$ = 13 TeV was considered. Systematic uncertainties are included [215]. Symmetric distributions centred on the minimum indicate $-2\ln\Lambda$ follows a χ^2 distribution, such that the confidence level intervals on the fitted cross sections can be obtained looking at the ranges of cross sections corresponding to $-2\ln\Lambda < 4$ and 1 for 95% and 68% confidence level, respectively. These limits are highlighted by the red dotted lines on the plots, and the scans are performed to determine the 68% confidence level interval used as error on the measurements.

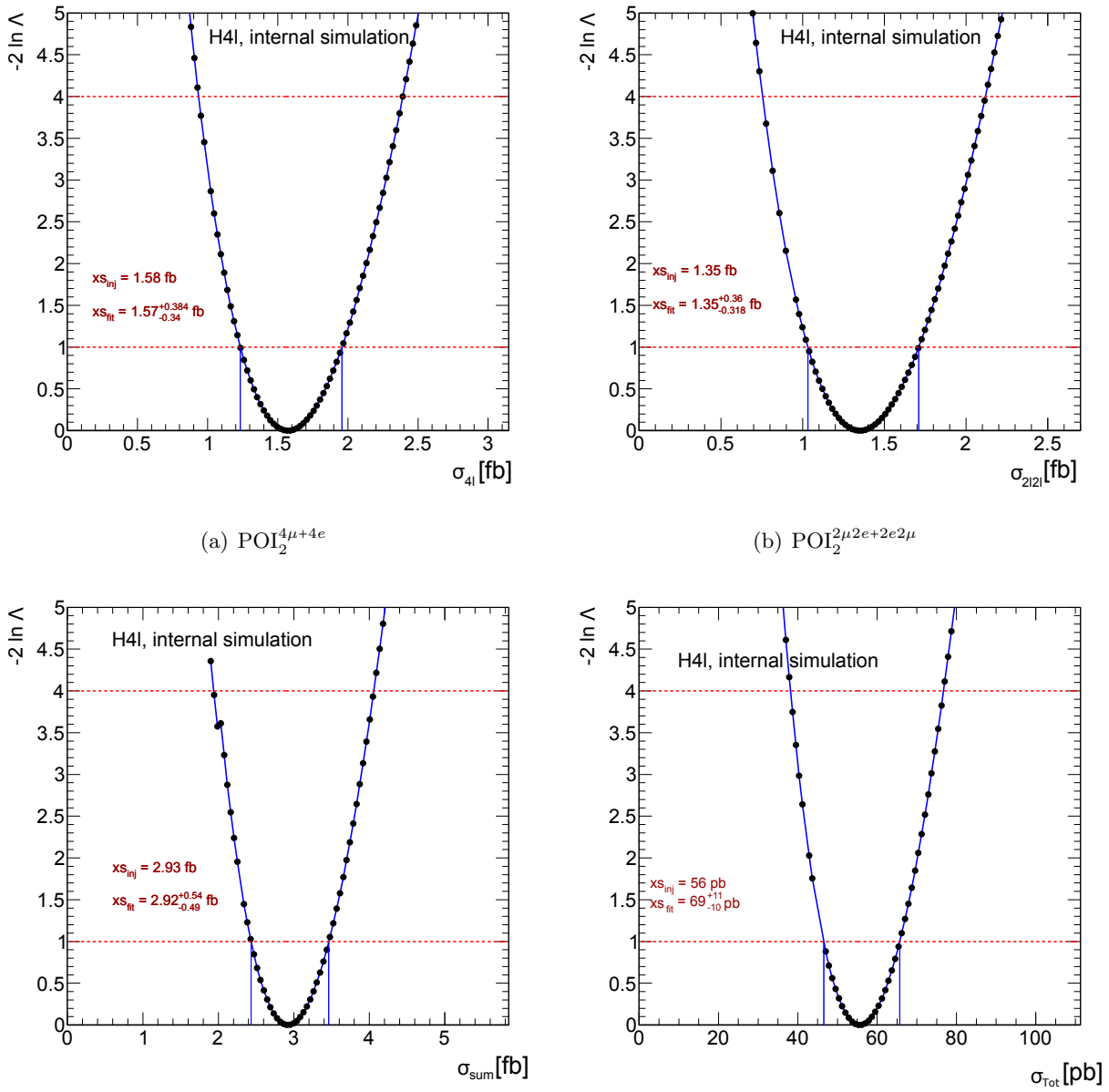

(a) $\mathrm{POI}_2^{4\mu+4e}$

(b) $\mathrm{POI}_2^{2\mu 2e+2e2\mu}$

(c) $\mathrm{POI}_3 = \sigma_{\mathrm{Fid}}$

(d) $\mathrm{POI}_4 = \sigma_{\mathrm{Tot}}$

Figure 12.7 – Inclusive fiducial cross section fit on Asimov data, for the various parameters of interest (a) $\mathrm{POI}_2^{4\mu+4e}$, (b) $\mathrm{POI}_2^{2\mu 2e+2e2\mu}$, (c) $\mathrm{POI}_3 = \sigma_{\mathrm{Fid}}$ and (d) $\mathrm{POI}_4 = \sigma_{\mathrm{Tot}}$. An integrated luminosity of 36.1 fb^{-1} at $\sqrt{s} = 13$ TeV was considered. Systematic uncertainties are included [215]. Symmetric distributions centred on the minimum indicate $-2\ln\Lambda$ follows a χ^2 distribution, such that the confidence level intervals on the fitted cross sections can be obtained looking at the ranges of cross sections corresponding to $-2\ln\Lambda < 4$ and 1 for 95% and 68% confidence level, respectively. These limits are highlighted by the red dotted lines on the plots, and the scans are performed to determine the 68% confidence level interval used as error on the measurements.

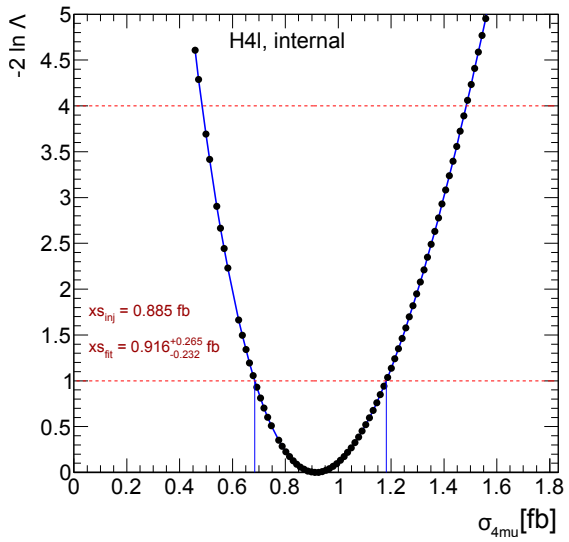

(a) $\mathrm{POI}_1^{4\mu}$

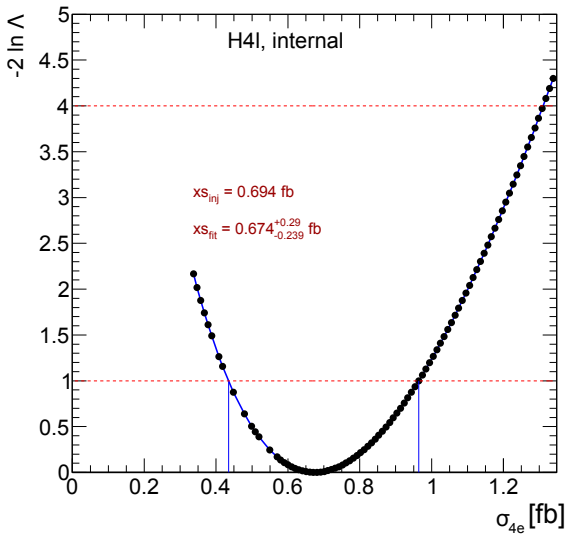

(b) POI_1^{4e}

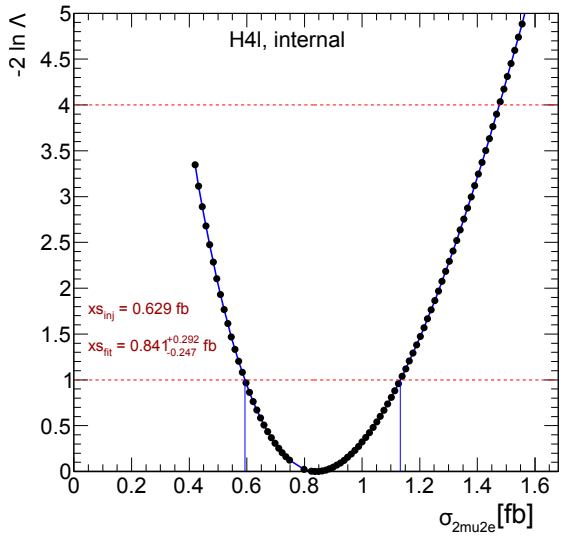

(c) $\mathrm{POI}_1^{2\mu 2e}$

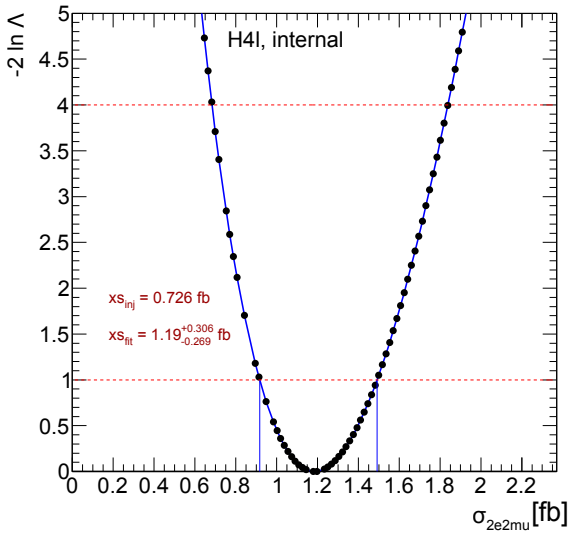

(d) $\mathrm{POI}_1^{2e2\mu}$

Figure 12.8 – Log-likelihood scans for the inclusive fiducial cross section per single channel (POI_1), showing (a) $\sigma_{4\mu}$, (b) σ_{4e}, (c) $\sigma_{2\mu 2e}$ and (d) $\sigma_{2e2\mu}$. The results correspond to 36.1 fb^{-1} at $\sqrt{s}$ = 13 TeV of data recorded. Systematic uncertainties are included [215]. The confidence intervals on the fitted cross sections can be obtained looking at the ranges of cross sections corresponding to $-2\ln\Lambda < 4$ and 1 for 95% and 68% confidence levels, respectively. These limits are highlighted by the red dotted lines on the plots, and the scans are performed to determine the 68% confidence level interval used as error on the measurements.

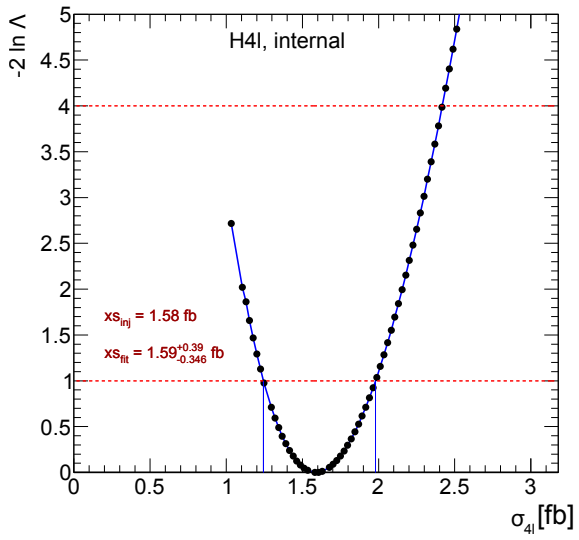

(a) $\mathrm{POI}_2^{4\mu+4e}$

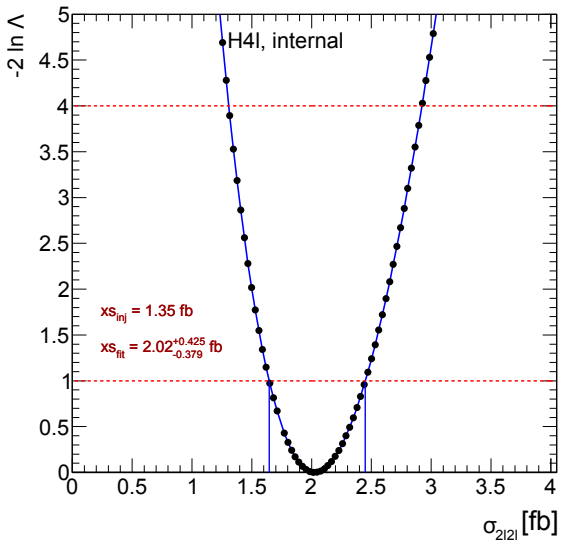

(b) $\mathrm{POI}_2^{2\mu 2e+2e2\mu}$

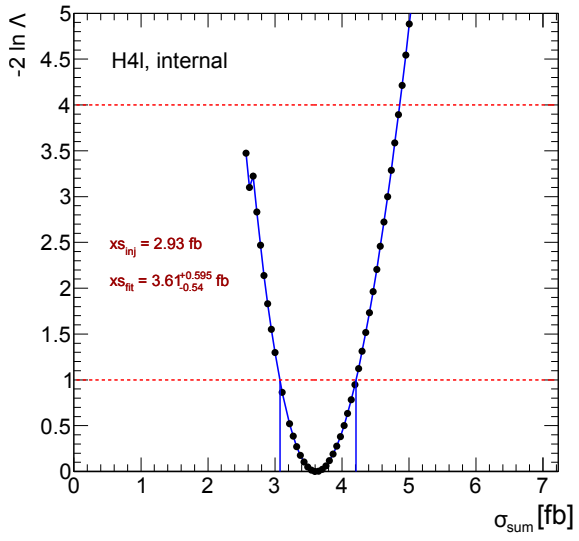

(c) $\mathrm{POI}_3 = \sigma_{\mathrm{Fid}}$

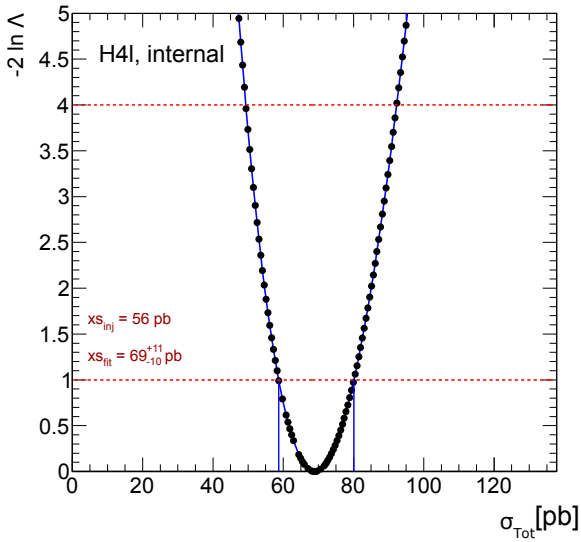

(d) $\mathrm{POI}_4 = \sigma_{\mathrm{Tot}}$

Figure 12.9 – Log-likelihood scans for the inclusive fiducial cross, for various parameters of interest (a) $\mathrm{POI}_2^{4\mu+4e}$, (b) $\mathrm{POI}_2^{2\mu 2e+2e2\mu}$, (c) $\mathrm{POI}_3 = \sigma_{\mathrm{Fid}}$ and (d) $\mathrm{POI}_4 = \sigma_{\mathrm{Tot}}$. The results correspond to 36.1 fb^{-1} at $\sqrt{s} = 13$ TeV of data recorded. Systematic uncertainties are included [215]. The confidence level on the fitted cross sections can be obtained looking at the ranges of cross sections corresponding to $-2\ln\Lambda < 4$ and 1 for 95% and 68% confidence levels, respectively. These limits are highlighted by the red dotted lines on the plots, and the scans are performed to determine the 68% confidence level interval used as error on the measurements.

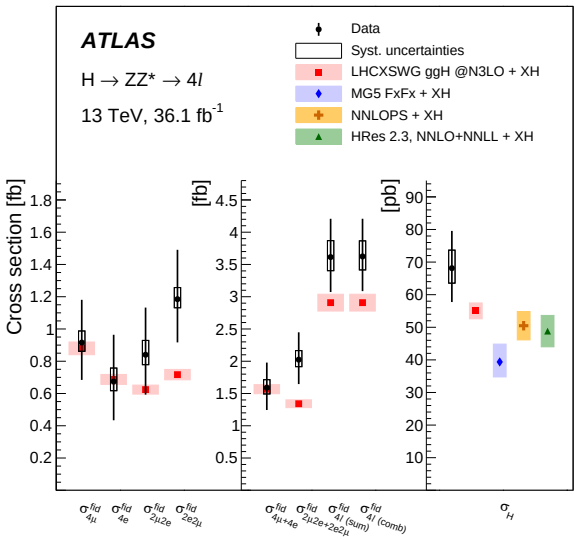

Figure 12.10 – Observed (black circles) and expected (rectangles) inclusive cross sections for each of the POIs [215]. The total uncertainties are represented by error bars for data. Systematic uncertainties are presented by the black (data) and coloured (prediction) rectangles. From the left to the right, fiducial cross sections are presented per final state and for the combined final states. σ_{sum} corresponds to the sum of the four final states, whereas σ_{comb} is the fitted fiducial cross section taking into account all observed events. These two values are expected to be very close, but might differ due to the fitting procedure. On the right, the total cross section is presented, deduced from the fiducial measurements.

therefore strongly reject the hypothesis of a good agreement with the SM, but high p-values do not allow to draw any conclusions. In particle physics, the claim of a discovery happens if the SM prediction is rejected with a p-values less than 5.7×10^{-7}. The results presented here hence do not exclude the good validity of the SM.

12.5 Differential measurements

With data recorded in late 2016, it is now possible to perform differential measurements of the total and fiducial production cross sections of the Higgs boson decaying to four leptons. The cross sections are measured in bins of differential variables, which were chosen to describe the Higgs boson kinematics or to be sensitive to the branching ratios. These measurements add further insight on the possible deviations of the data with respect to the SM predictions.

12.5.1 Methodology of the measurements

The methodology for the differential measurements is similar to the inclusive case, described in Sec. 12.4. A binned template fit is performed on the $m_{4\ell}$ distribution to extract the fiducial and total cross sections. Since differential measurements have to be performed in bins of the differential variables, the reduced

Table 12.9 – Observed and expected inclusive cross section using $36.1\,\text{fb}^{-1}$ at $\sqrt{s} = 13\,\text{TeV}$ of recorded data. The systematic uncertainties are included [215]. Overall an excess of less than 1.3σ is observed, coming essentially from the $2e2\mu$ channel.

Cross section	Observation ($\pm$(stat) $\pm$ (syst))	Prediction	p-value [%]
$\sigma_{4\mu}$ [fb]	$0.92\,^{+0.25}_{-0.23}\,^{+0.07}_{-0.05}$	0.880 ± 0.039	88
σ_{4e} [fb]	$0.67\,^{+0.28}_{-0.23}\,^{+0.08}_{-0.06}$	0.688 ± 0.031	96
$\sigma_{2\mu 2e}$ [fb]	$0.84\,^{+0.28}_{-0.24}\,^{+0.09}_{-0.06}$	0.625 ± 0.028	39
$\sigma_{2e2\mu}$ [fb]	$1.18\,^{+0.30}_{-0.26}\,^{+0.07}_{-0.05}$	0.717 ± 0.032	7
$\sigma_{4\mu+4e}$ [fb]	$1.59\,^{+0.37}_{-0.33}\,^{+0.12}_{-0.10}$	1.57 ± 0.07	65
$\sigma_{2\mu 2e+2e2\mu}$ [fb]	$2.02\,^{+0.40}_{-0.36}\,^{+0.14}_{-0.11}$	1.34 ± 0.06	6
σ_{sum} [fb]	$3.61 \pm 0.50^{+0.26}_{-0.21}$	2.91 ± 0.13	19
σ_{comb} [fb]	$3.62 \pm 0.50^{+0.25}_{-0.20}$	2.91 ± 0.13	18
σ_{Tot} [pb]	$69\,^{+10}_{-9}\,\pm 5$	55.6 ± 2.5	19

statistics do not enable to split the results per final states. The categories of the fits are therefore set to the bins of the differential variables and the four-lepton invariant-mass distribution of all the final states is combined. The parameters of interest are defined as

$$\text{POI}_v^i = [\sigma_{\text{Tot}} \times \mathcal{B}] \times \mathcal{A}_v^i, \tag{12.18}$$

where $i \in [\![1, N_v]\!]$ indexes the bins of the differential variable v. The acceptance factor $\mathcal{A}_v^i$ is calculated for all production modes and final states combined, in bins of the differential variables.

For each category i and variable v, the number of signal events is expressed as

$$n_{\text{s}v}^i\,(m_{4\ell}) = F_{\text{s}v}^i\,(m_{4\ell}) \times \mathcal{L}_{\text{int}} \times \sum_p \sigma_{\text{Tot}} \times r_{p_v}^{\ i} \times \mathcal{B} \times \mathcal{A}_{p_v}^{\ i} \times \mathcal{C}_{p_v}^{\ i}, \tag{12.19}$$

where $\mathcal{A}$, $\mathcal{C}$ and $r_{p_v}^{\ i} = \frac{\sigma_{p\ v}^{\text{SM}\,i}}{\sigma_{\text{Tot}\,v}^{\text{SM}\,i}}$ are the acceptance, correction and proportion factors calculated in bins of the differential variable, for each production mode. The proportion factor is defined similarly as for the inclusive case and gives, for each bin, the contribution of each production mode with respect to the total. Following the notations previously introduced, $F_{\text{s}v}^i\,(m_{4\ell})$ is the signal shape, $\mathcal{L}_{\text{int}}$ is the integrated luminosity and $\mathcal{B}$ is the $H \to ZZ^* \to 4\ell$ branching ratio.

As for the inclusive case, the dressed variables (variables calculated using dressed leptons) are used for N_{Fid} (numerator and denominator of $\mathcal{A}$ and $\mathcal{C}$, respectively). For N_{Tot} (denominator of $\mathcal{A}$), the born variables are used.

Table 12.10 – Binning chosen for the Higgs kinematic differential variables [215].

Variable	Bin Edges	N_{bins}
$p_{\text{T}}^{4\ell}$	0, 10, 15, 20, 30, 45, 60, 80, 120, 200, 400 GeV	10
$\lvert y_{4\ell}\rvert$	0, 0.3, 0.6, 0.9, 1.2, 1.6, 2, 2.5	7
$\lvert\cos(\theta^*)\rvert$	0, 0.125, 0.25, 0.375, 0.5, 0.625, 0.75, 0.875, 1.0	8
m_{12}	50, 65, 74, 82, 88, 94, 106 GeV	6
m_{34}	12, 20, 24, 28, 32, 40, 55, 65 GeV	7

12.5.2 Differential variables

For each differential variable, two definitions are provided. The first one corresponds to the detector phase space and reconstructed objects are used to calculate the variable (described in Sec. 11.3). In the second case, the variable is assessed in the fiducial volume and information at particle-level serves the calculation (see Sec. 12.1).

In order to define the binning of each variable, simulation is used and the significance is calculated in the fiducial volume for each tested bin, defined as

$$\sigma = \frac{S}{\sqrt{S+B}}, \tag{12.20}$$

where S and B are the signal and background yields predicted by MC (all the final states and production modes combined). In the low statistical regime, another expression is preferred [227]:

$$Z_0 = \sqrt{2\left[(S+B)\times\ln(1+S/B)-S\right]}. \tag{12.21}$$

The choice of the binning should maximise σ and Z_0, but also limit the event migration between bins. Migration of events is assessed by calculating the migration matrices, as described in Sec. 12.5.3, which should be as diagonal as possible. Two categories of variables are defined: the Higgs boson kinematics and jet variables.

Higgs boson kinematic variables

The variables related to the kinematics of the Higgs boson are of major interest for probing deviations to the SM, in case the Higgs boson were to be produced in association to other particles not predicted by the current theory. The Higgs-to-four-lepton channel offers the opportunity to precisely reconstruct these variables benefiting from an optimal lepton resolution. The Higgs boson kinematics include its transverse momentum $p_{\text{T}}^{4\ell}$, rapidity $y_{4\ell}$ and azimuthal direction $\phi_{4\ell}$. To fully describe the decay to four leptons, the masses of the two lepton pairs (m_{12} and m_{34}) and five decay angles ($\phi_{4\ell}, \phi_1, \theta_1, \theta_2, \theta^*$) are needed. These five angles are sketched in Fig. 12.11 and correspond to the Higgs azimuthal direction and the azimuthal direction of the leading lepton of the leading pair, the polar angles of the leptons with respect to the $H \to ZZ^*$ decay, and the polar angle of this decay in the rest frame (whose axis is set to the proton-proton beam).

For the calculation of the reconstructed variables, the four momentum of each of the four leptons composing the final state is added to get the total four momentum (of the Higgs boson or the Z bosons). From this, the variables can be accessed, having corrected the momentum for FSR. The procedure is

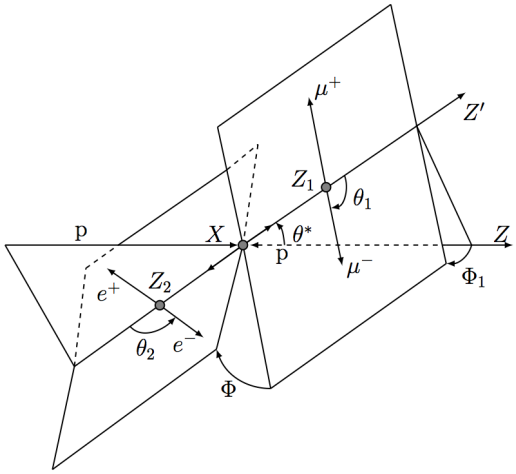

Figure 12.11 – Sketch showing the Higgs boson kinematic variables needed to fully describe the Higgs-to-four-lepton decay [215].

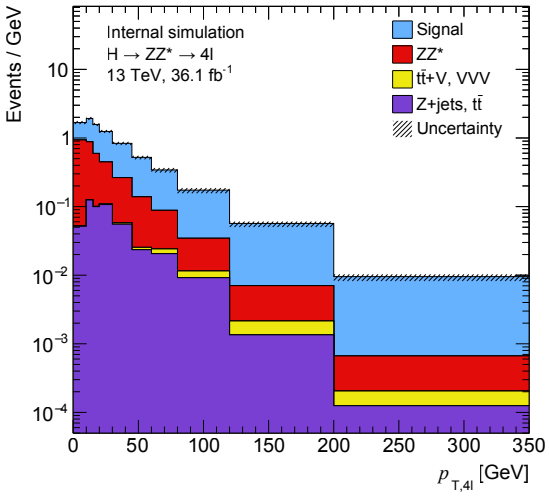

Bin	Signal	ZZ	$Z+\text{jets}\ /\ t\bar{t}$	$t\bar{t}V + VVV$	S/B	σ	Z_0
0	7.4	8.8	0.52	0.006	0.79	1.8	2.2
1	5.2	3.8	0.62	0.004	1.2	1.7	2.1
2	4.9	2.5	0.5	0.005	1.6	1.7	2.3
3	8	3.4	1.1	0.02	1.8	2.3	3.1
4	8.6	3.1	0.83	0.05	2.2	2.4	3.4
5	5.7	1.7	0.35	0.03	2.8	2.1	3
6	5.1	1.3	0.41	0.07	2.9	1.9	2.9
7	5.6	0.92	0.37	0.09	4	2.1	3.4
8	4	0.39	0.11	0.06	7.1	1.9	3.3
9	1.3	0.07	0.02	0.01	13	1.1	2.2

Figure 12.12 – Expected signal and background yields, and significances for the $p_{\mathrm{T}}^{4\ell}$ differential variable [215].

similar for the fiducial variables, except that the variables use dressed or born leptons for the calculation, depending whether they refer to the total phase space, or if they are restricted to the fiducial volume.

Among these variables, $p_{\mathrm{T}}^{4\ell}$, $|y_{4\ell}|$, m_{12}, m_{34} and $|\cos(\theta^*)|$ were selected for the fiducial measurements thanks to their easy measurement and their high resolution. Note that the Higgs boson transverse momentum is of major interest as differential cross sections against this variable have already been extensively studied [228, 169, 170, 229], and the results can then be compared to the available predictions or measurements.

The binning choices for these variables are presented in Tab. 12.10. For each variable, the MC distributions of signal and backgrouds are plotted. Expected signal and background yields (and the corresponding significances) are also calculated for each bin. The results are presented in Fig. 12.12, 12.13, 12.14, 12.15 and 12.16, for $p_{\mathrm{T}}^{4\ell}$, $|y_{4\ell}|$, $|\cos(\theta^*)|$, m_{12} and m_{34}, respectively. Overall, significances

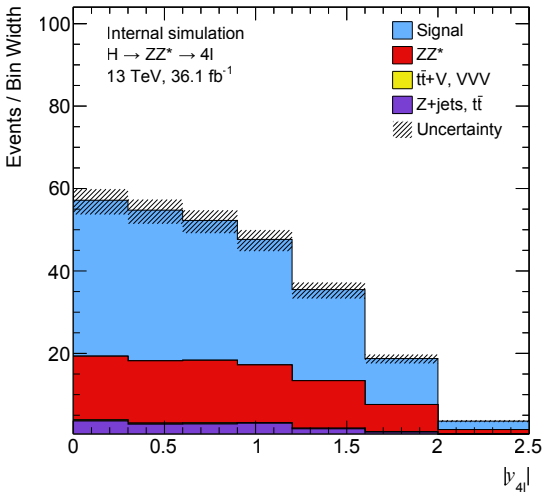

Bin	Signal	ZZ	$Z+\text{jets}\ /\ t\bar{t}$	$t\bar{t}V+VVV$	S/B	σ	Z_0
0	11	4.6	1.1	0.09	2	2.7	3.8
1	11	4.5	0.85	0.07	2	2.7	3.8
2	10	4.6	0.87	0.08	1.8	2.6	3.5
3	9.1	4.2	0.92	0.05	1.8	2.4	3.3
4	8.8	4.6	0.68	0.06	1.7	2.3	3.2
5	4.5	2.7	0.36	0.01	1.5	1.6	2.1
6	1	0.73	0.03	0.003	1.3	0.77	1

Figure 12.13 – Expected signal and background yields, and significances for the $|y_{4\ell}|$ differential variable [215].

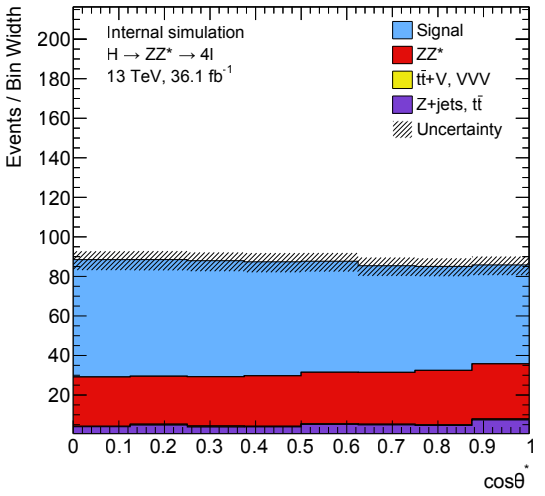

Bin	Signal	ZZ	$Z+\text{jets}\ /\ t\bar{t}$	$t\bar{t}V+VVV$	S/B	σ	Z_0
0	7.4	3.1	0.49	0.03	2	2.2	3.1
1	7.4	3	0.6	0.05	2	2.2	3.1
2	7.3	3.1	0.48	0.06	2	2.2	3.1
3	7.2	3.2	0.48	0.04	1.9	2.2	3
4	7	3.3	0.64	0.03	1.8	2.1	2.9
5	6.7	3.3	0.61	0.05	1.7	2.1	2.8
6	6.6	3.4	0.58	0.03	1.6	2	2.7
7	6.3	3.5	0.92	0.06	1.4	1.9	2.5

Figure 12.14 – Expected signal and background yields, and significances for the $|\cos(\theta^*)|$ differential variable [215].

$\sigma > 2$ or $Z_0 > 3$ were targeted, except for the first and last bins.

Jet variables

For the calculation of these variables, fiducial or reconstructed jets are used, described in Sec. 11.3.3 and 12.1.4, respectively. There are no jet overlap removals in the total phase space.

Using these definitions, the following jet variables are selected for the differential measurements of the cross sections: n_{jets}, the jet multiplicity in the event, $p_{\text{T}}^{\text{leading jet}}$, the transverse momentum of the leading jet, and $n_{b\text{ jets}}$, the number of b-tagged jets in the event. To these three variables, three dijet quantities are added, which involve the two leading jets: m_{jj}, the invariant mass, $|\Delta\eta_{jj}|$, the difference in

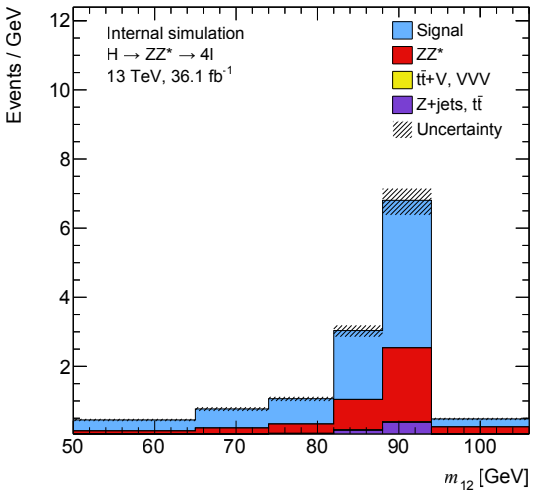

Bin	Signal	ZZ	$Z+\text{jets}$ / $t\bar{t}$	$t\bar{t}V + VVV$	S/B	σ	Z_0
0	4.8	1.6	0.37	0.07	2.4	1.8	2.6
1	5	1.5	0.39	0.04	2.5	1.9	2.7
2	5.9	2.2	0.46	0.04	2.2	2	2.8
3	12	5.3	0.9	0.07	1.9	2.8	3.9
4	26	13	2.3	0.11	1.7	4	5.4
5	2.8	2.6	0.39	0.04	0.93	1.2	1.4

Figure 12.15 – Expected signal and background yields, and significances for the m_{12} differential variable [215].

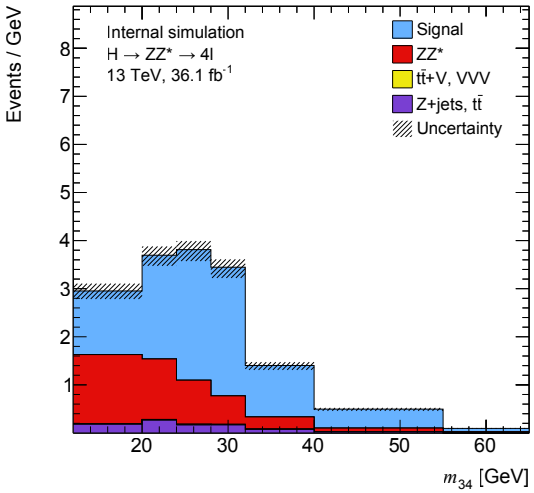

Bin	Signal	ZZ	$Z+\text{jets}$ / $t\bar{t}$	$t\bar{t}V + VVV$	S/B	σ	Z_0
0	11	11	1.4	0.10	0.81	2.2	2.6
1	8.6	5	1.1	0.06	1.4	2.2	2.9
2	11	3.7	0.66	0.06	2.5	2.8	4
3	11	2.4	0.67	0.05	3.5	2.9	4.5
4	8.6	2	0.59	0.05	3.2	2.6	3.9
5	5.9	1.2	0.32	0.04	3.9	2.2	3.4
6	0.7	0.2	0.05	0	2.8	0.72	1.1

Figure 12.16 – Expected signal and background yields, and significances for the m_{34} differential variable [215].

pseudo-rapidity, and $\Delta\phi_{jj}$, the difference in ϕ. For the last variable, the values are taken in the interval $[0, 2\pi]$ and for the difference, the jets are ordered in decreasing order of $|\eta^j|$, such that ϕ of the jet having the lowest $|\eta^j|$ is subtracted to those of the other jet. This definition enables to catch any asymmetries in the cross section measurements which would result in deviations with respect to the SM predictions.

The jet variables enable to probe QCD radiation effects [230] (especially the inclusion of soft gluons in the Feynman diagrams) and to better disentangle the contributions of the various production modes, as more events populate the bins $n_{\text{jets}} \geq 1$, which do not come from ggF production. The VH and VBF production modes leave on average one or two jets in the detector (due to the vector boson decays), whereas the $t\bar{t}$ mechanism populates the higher jet multiplicities, thanks to the $t\bar{t}$ pair in the final state. The gluon-gluon fusion process, on the other hand is expected to create softer jets. Effects of quark and

Table 12.11 – Binning chosen for the jet differential variables [215].

Variable	Bin Edges	N_{bins}
n_{jets}	0, 1, 2, ≥3	4
$p_T^{\text{leading jet}}$	30, 40, 55, 75, 115, 350 GeV	5
m_{jj}	0, 120, 3000 GeV	2
$\lvert\Delta\eta_{jj}\rvert$	0, 2, 10	2
$\Delta\phi_{jj}$	0, π, 2π	2
$n_{b\text{ jets}}$	0, ≥1	2

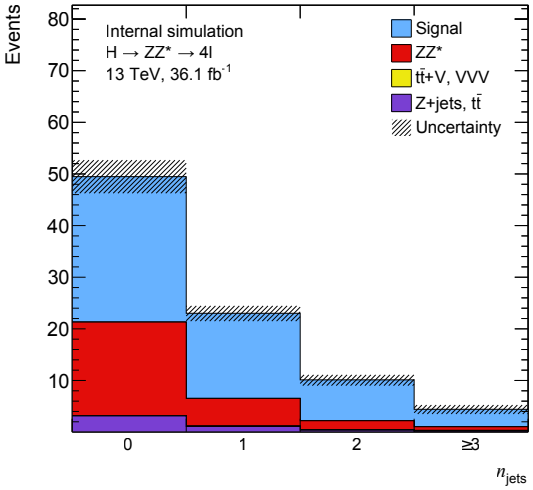

Bin	Signal	ZZ	$Z+\text{jets}$ / $t\bar{t}$	$t\bar{t}V + VVV$	S/B	σ	Z_0
0	28	18	3.1	0.03	1.3	4	5.2
1	16	5.4	1.1	0.08	2.5	3.4	5
2	7.9	1.7	0.38	0.11	3.6	2.5	3.9
3	3.4	0.71	0.19	0.14	3.2	1.6	2.5

Figure 12.17 – Expected signal and background yields, and significances for the n_{jets} differential variable [215].

gluon radiations can be assessed studying the transverse momentum of the leading jet (jet having the highest p_{T}).

The various bins of the jet variables are presented in Tab. 12.11. As for the Higgs boson kinematic variables, event yields in each bin and resulting significances are estimated to ensure the good binning choice. These are shown in Fig. 12.17, 12.18, 12.22, 12.19, 12.20 and 12.21, for n_{jets}, $p_{\text{T}}^{\text{leading jet}}$, m_{jj}, $|\Delta\eta_{jj}|$, $\Delta\phi_{jj}$ and $n_{b\text{ jets}}$, respectively. Again, significances $\sigma > 2$ or $Z_0 > 3$ were targeted, except for the first and last bins, where applicable.

12.5.3 Migration studies

In order to estimate the good definition of the variable binning, it is important to assess the migration of events within the bins, which should be as small as possible. A migration occurs when a reconstructed event falls into a different bin as the particle-level event (taken from MC generation directly in the fiducial space). Whereas leakage fractions measure the migrations in and out of the fiducial space, the migration matrices estimate the migration within the phase space, but between the variable bins.

Migration matrices are two-dimensional matrices whose columns correspond to the reconstructed

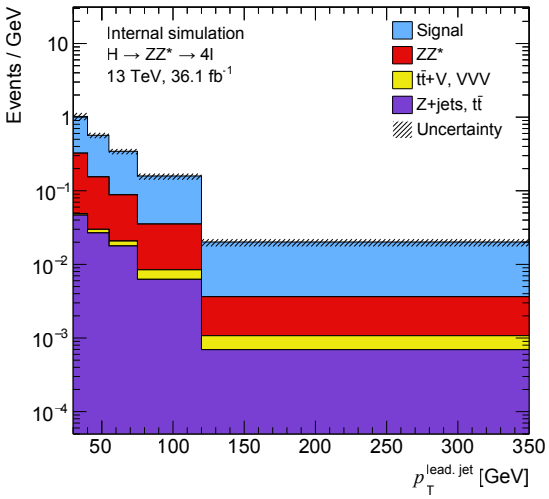

Bin	Signal	ZZ	$Z+\text{jets}\ /\ t\bar{t}$	$t\bar{t}V+VVV$	S/B	σ	Z_0
0	7	2.7	0.47	0.02	2.2	2.2	3.1
1	6.2	1.9	0.4	0.05	2.7	2.1	3.1
2	5.1	1.3	0.36	0.06	2.9	2	2.9
3	5.6	1.2	0.28	0.10	3.5	2.1	3.2
4	3.8	0.59	0.16	0.09	4.5	1.8	2.9

Figure 12.18 – Expected signal and background yields, and significances for the $p_{\text{T}}^{\text{leading jet}}$ differential variable [215].

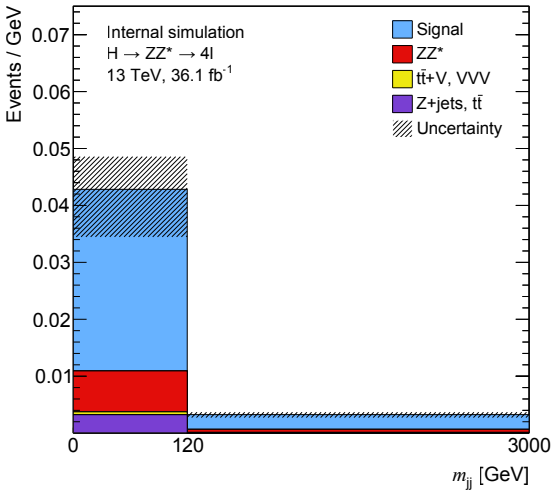

Bin	Signal	ZZ	$Z+\text{jets}\ /\ t\bar{t}$	$t\bar{t}V+VVV$	S/B	σ	Z_0
0	3.8	0.86	0.39	0.06	2.9	1.7	2.5
1	7.4	1.6	0.18	0.18	3.8	2.4	3.8

Figure 12.19 – Expected signal and background yields, and significances for the m_{jj} differential variable [215].

variables, whereas the rows correspond to the particle-level (MC generated) variables (dressed variables). Events which pass both the reconstruction and the fiducial selections are retained. They are filled with their relative weights in the matrix depending on the bins they belong to. Each row of the matrix is then normalised to unity. A good definition of the variable bins (and therefore low event migrations) will result in almost diagonal matrices. The event migration can hence be estimated judging the relative importance of the off-diagonal terms with respect to the diagonal elements.

The migration matrices are presented in Fig. 12.23, 12.24, 12.25, 12.26, 12.27 and 12.28, for $p_{\text{T}}^{4\ell}$ — m_{12}, m_{34} — $|y_{4\ell}|$, $|\cos(\theta^*)|$ — n_{jets}, $p_{\text{T}}^{\text{leading jet}}$ — m_{jj}, $|\Delta\eta_{jj}|$ — $\Delta\phi_{jj}$ and $n_{b\text{ jets}}$, respectively. The bin-to-bin migrations are less than 25% (up to 35% for m_{12} due to resolution effects) for the Higgs boson kinematic variables, but can rise up to 35% for the jet variables. These overall confirm the good definition of the

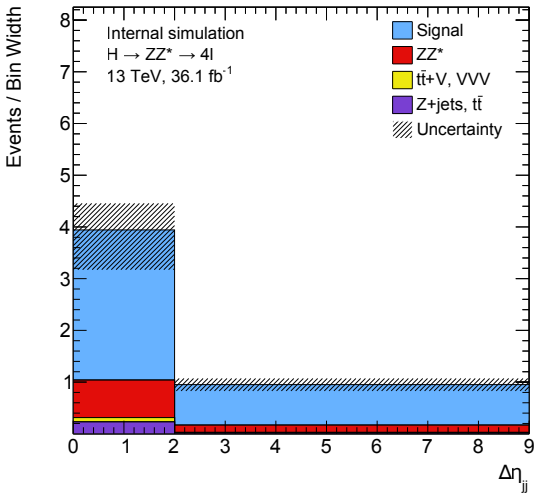

Bin	Signal	ZZ	$Z+\text{jets}$ / $t\bar{t}$	$t\bar{t}V + VVV$	S/B	σ	Z_0
0	5.8	1.4	0.46	0.17	2.8	2.1	3.1
1	5.5	0.98	0.11	0.08	4.7	2.1	3.5

Figure 12.20 – Expected signal and background yields, and significances for the $|\Delta\eta_{jj}|$ differential variable [215].

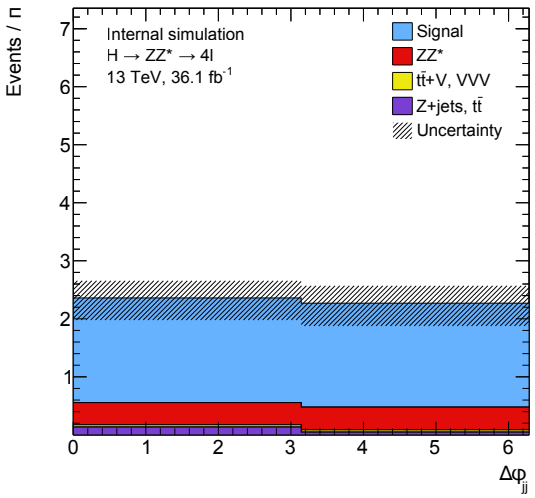

Bin	Signal	ZZ	$Z+\text{jets}$ / $t\bar{t}$	$t\bar{t}V + VVV$	S/B	σ	Z_0
0	5.7	1.2	0.42	0.12	3.2	2.1	3.2
1	5.6	1.2	0.15	0.12	3.8	2.1	3.3

Figure 12.21 – Expected signal and background yields, and significances for the $\Delta\phi_{jj}$ differential variable [215].

variable binning.

12.5.4 Purity studies

To assess the correctness of the unfolding method relying on bin-by-bin correction ($\mathcal{C}$ factors), the purity of the variable bins was studied. The purity is defined for each bin i of the differential variables v

$$\mathfrak{p}_v^i = \frac{N_{\text{Reco \& Fid}_v}^i}{N_{\text{Reco}_v}^i}, \tag{12.22}$$

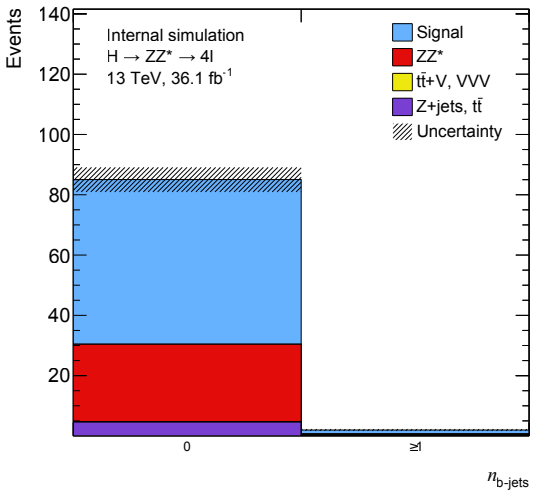

Bin	Signal	ZZ	$Z+\text{jets}$ / $t\bar{t}$	$t\bar{t}V + VVV$	S/B	σ	Z_0
0	55	26	4.6	0.12	1.8	5.9	8.1
1	1.3	0.24	0.2	0.23	1.9	0.92	1.3

Figure 12.22 – Expected signal and background yields, and significances for the $n_{b\text{ jets}}$ differential variable [215].

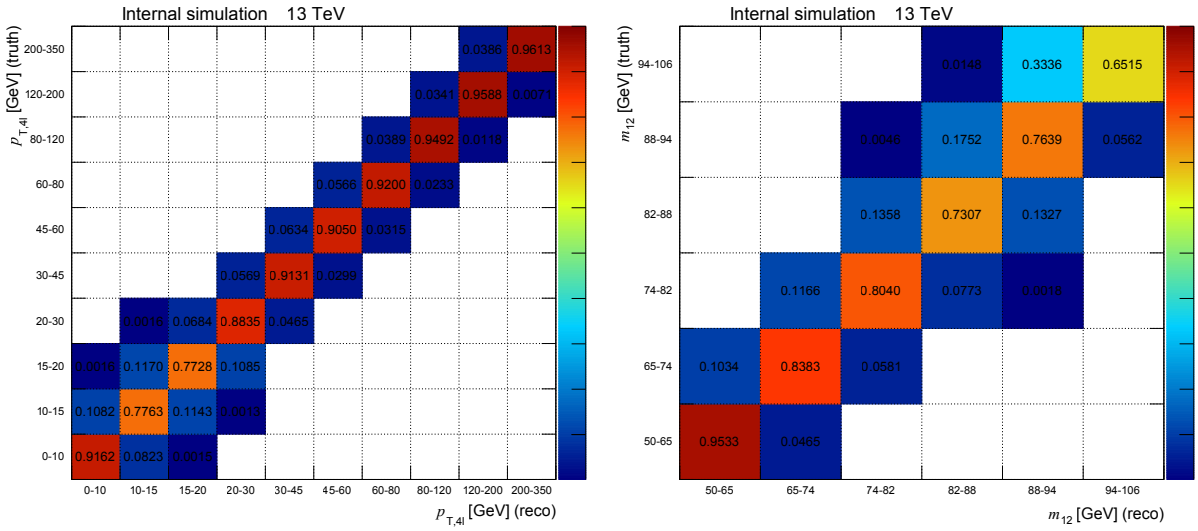

(a) $p_{\text{T}}^{4\ell}$ (b) m_{12}

Figure 12.23 – $p_{\text{T}}^{4\ell}$ and m_{12} migration matrices [215].

where ${N_{\text{Reco \& Fid}}}_v^i$ is the number of events passing both the reconstruction and fiducial selection (dressed variables), and falling in the same bin i of the differential variable v. ${N_{\text{Reco}}}_v^i$ is defined as previously. Only reconstructed signal events which did not migrate will be counted in the numerator. This quantity can hence measure the accuracy of the detector correction, since the $\mathcal{C}$ factors should only be applied to reconstructed events populating the numerator of $\mathfrak{p}$.

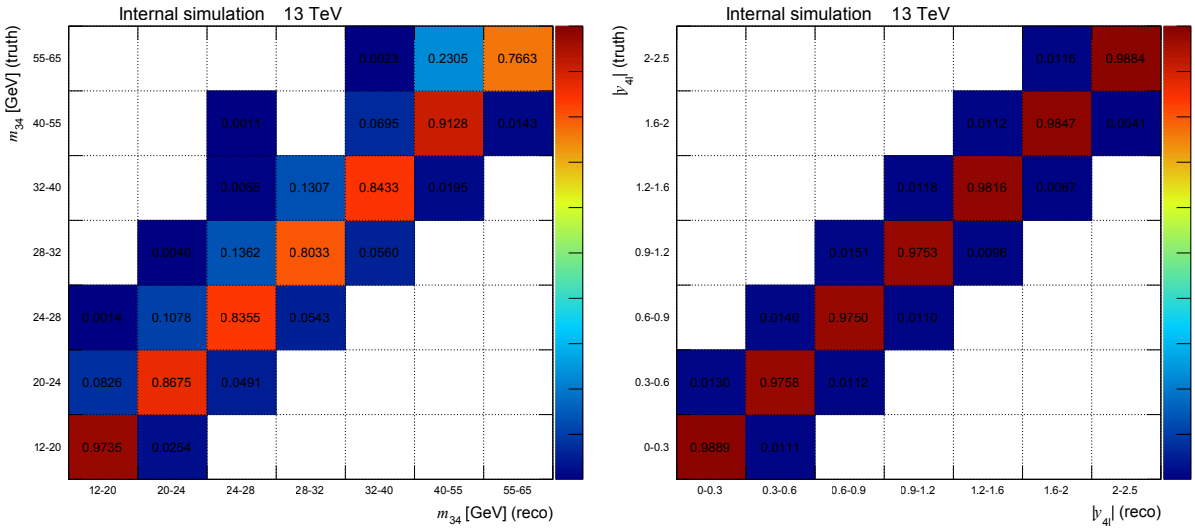

(a) m_{34} (b) $|y_{4\ell}|$

Figure 12.24 – m_{34} and $|y_{4\ell}|$ migration matrices [215].

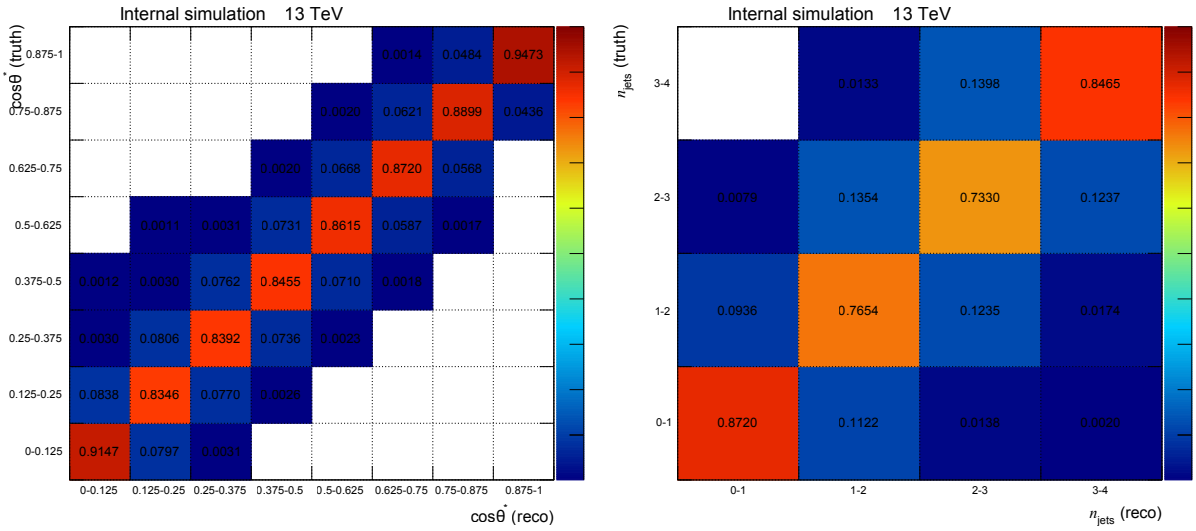

(a) $|\cos(\theta^*)|$ (b) n_{jets}

Figure 12.25 – $|\cos(\theta^*)|$ and n_{jets} migration matrices [215].

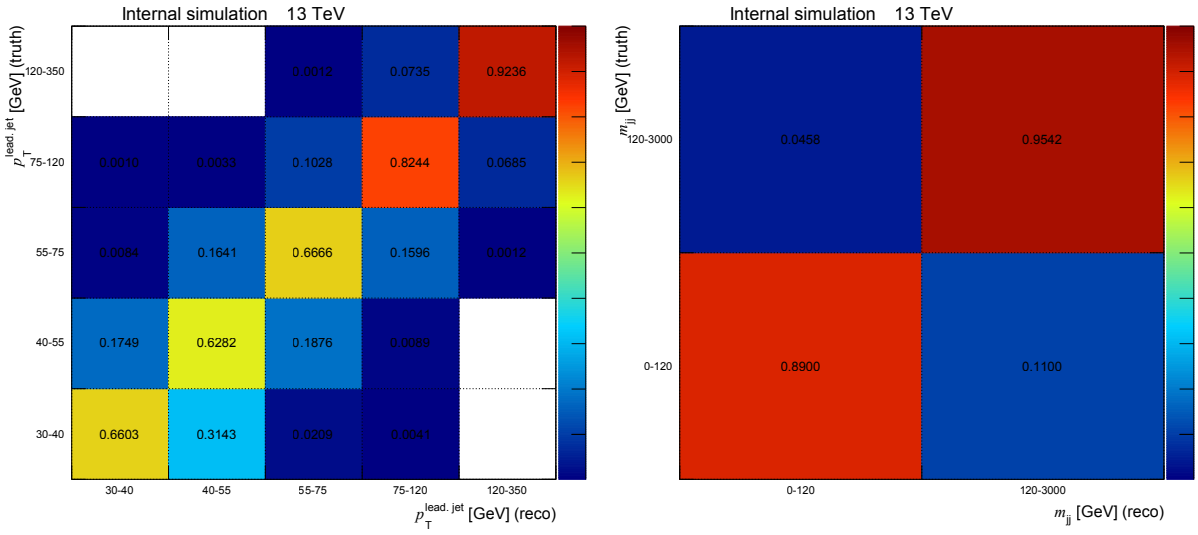

(a) $p_{\mathrm{T}}^{\text{leading jet}}$ (b) m_{jj}

Figure 12.26 – $p_{\mathrm{T}}^{\text{leading jet}}$ and m_{jj} migration matrices [215].

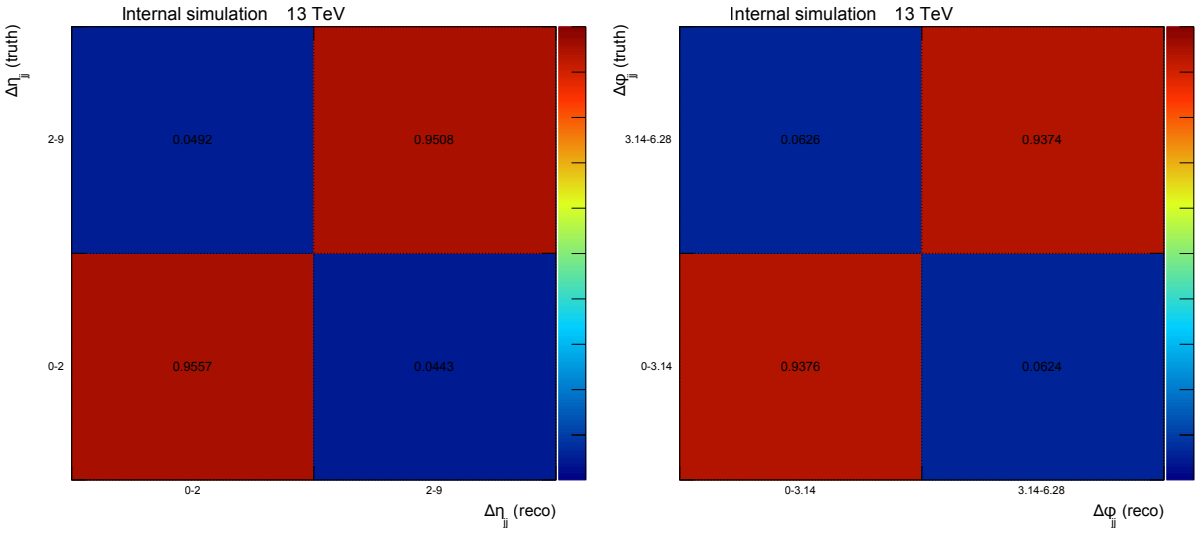

(a) $|\Delta\eta_{jj}|$ (b) $\Delta\phi_{jj}$

Figure 12.27 – $|\Delta\eta_{jj}|$ and $\Delta\phi_{jj}$ migration matrices [215].

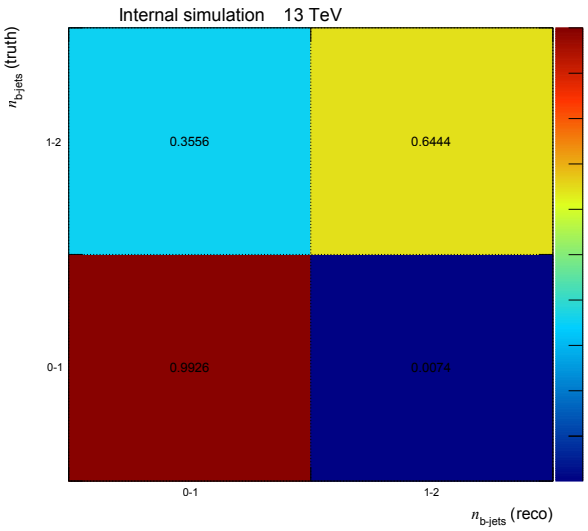

Figure 12.28 – $n_{b\text{ jets}}$ migration matrix [215].

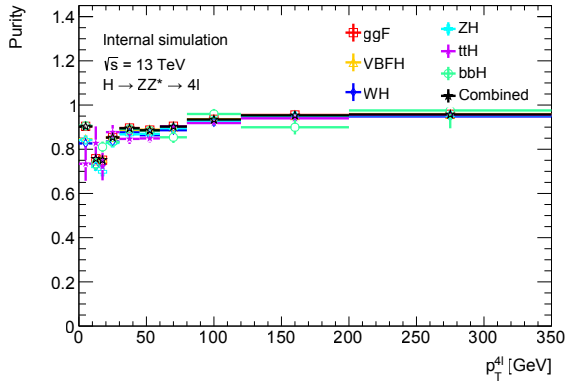

(a) $p_{\mathrm{T}}^{4\ell}$

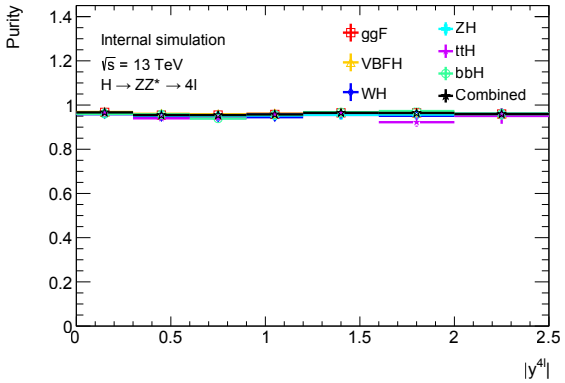

(b) $|y_{4\ell}|$

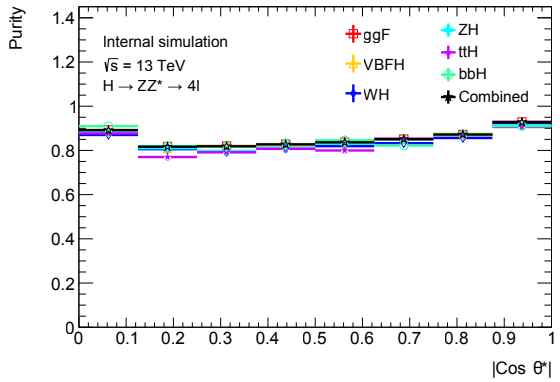

(c) $|\cos(\theta^*)|$

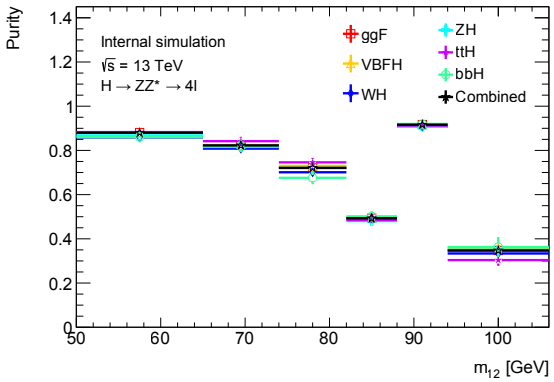

(d) m_{12}

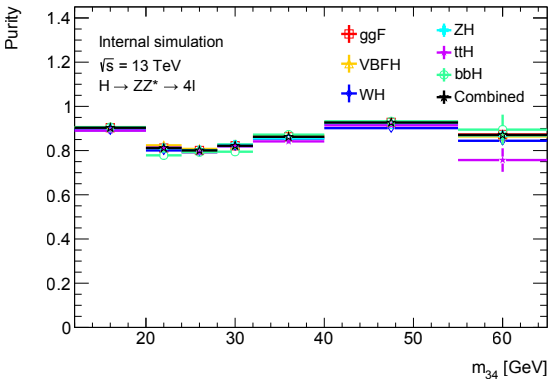

(e) m_{34}

Figure 12.29 – Purity of production modes for variables (a) $p_{\mathrm{T}}^{4\ell}$, (b) $|y_{4\ell}|$, (c) $|\cos(\theta^*)|$, (d) m_{12} and (e) m_{34} in each bin [215].

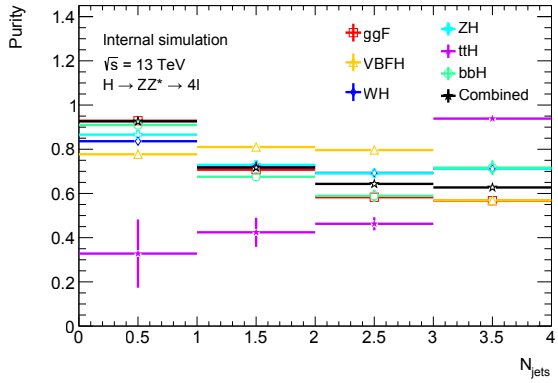

(a) n_{jets}

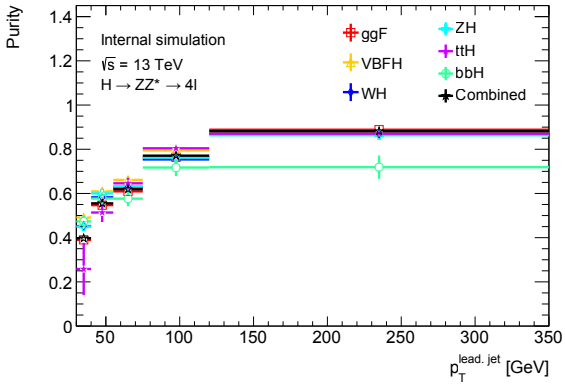

(b) $p_{\text{T}}^{\text{leading jet}}$

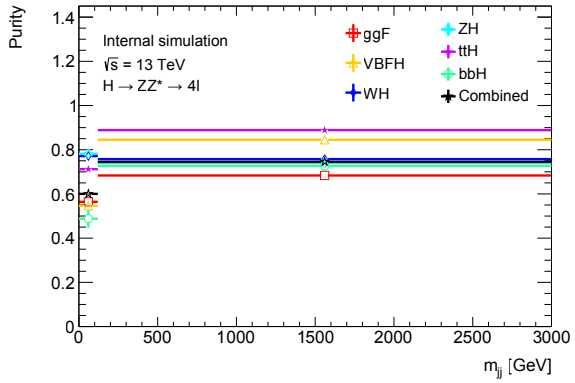

(c) m_{jj}

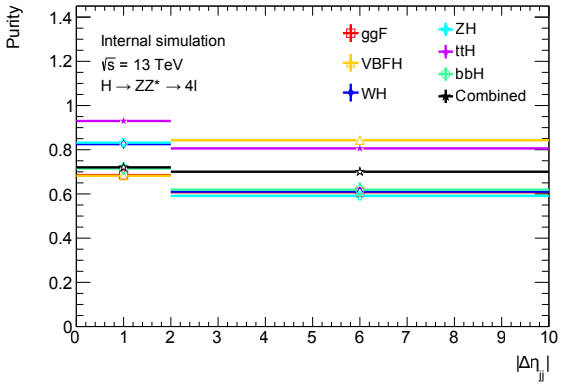

(d) $|\Delta\eta_{jj}|$

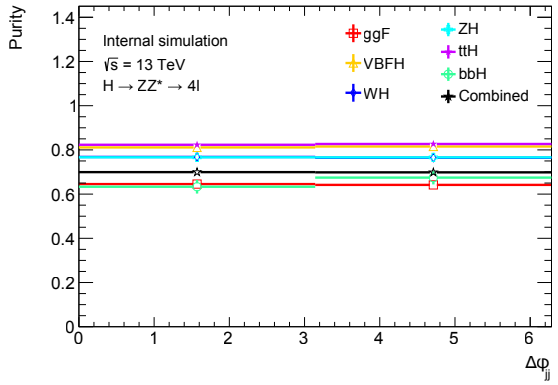

(e) $\Delta\phi_{jj}$

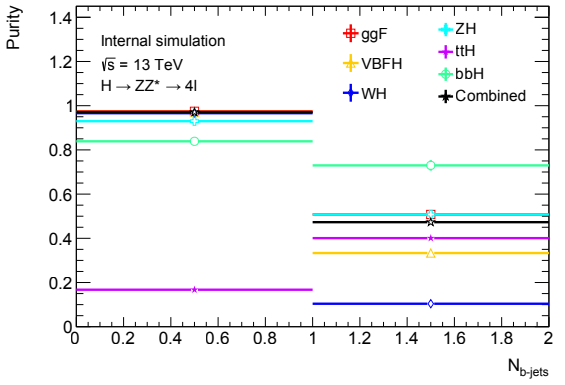

(f) $n_{b\text{ jets}}$

Figure 12.30 – Purity of production modes for variables (a) n_{jets}, (b) $p_{\text{T}}^{\text{leading jet}}$, (c) m_{jj}, (d) $|\Delta\eta_{jj}|$, (e) $\Delta\phi_{jj}$ and (f) $n_{b\text{ jets}}$ in each bin [215].

Since the Higgs boson variables benefit from good lepton reconstruction resolutions, the purities are high as shown in Fig. 12.29. They are overall greater than 70% for all the bins, except for m_{12} because of the narrow resonance peak of the on-shell Z. A closer look at the corresponding migration matrix indicates reconstructed events migrate between bins close to the peak (27%, 76% and 65% in the lower, middle and upper bins). The low bin contains more reconstructed events, but only a small fraction matches the associated fiducial bin. In the upper bin, a large fraction of reconstructed events results from migration from the peak and do not fall in the same fiducial bin. Finally, only a small fraction of reconstructed events falls in the middle bin, but these events quite often match the corresponding fiducial bin. These observations do not hold for the off-shell Z (m_{34}), as the width of the distribution broadens, reducing the bin migration.

For the jet variables presented in Fig. 12.30, the situation is a bit worse, with purities going down to 60%, and even lower for n_{jets} and $n_{b\text{ jets}}$. The former is due to low statistics for the $t\bar{t}H$ channel, and in all the channels (except in the 0 bin, excluding the $t\bar{t}H$ mechanism) for the latter. Taking into account all these results, the bin-by-bin correction is justified as in most of the cases the purities in each bins are above 50%.

12.5.5 Acceptance and correction factors

Calculation of acceptance and correction factors is performed the same way as described in Sec. 12.2, for each production mode (and all the productions combined), per bin of the differential variables. Numerators of $\mathcal{A}$ (also denominators of $\mathcal{C}$) are calculated using dressed variables, as they have to represent the fiducial space. Numerators of correction factors are calculated using reconstructed variables, whereas denominators of acceptance factors use born variables, as they correspond to the total phase space.

Results are presented in Fig. 12.31 (Tab. 12.12) for $p_{\text{T}}^{4\ell}$, Fig. 12.32 (Tab. 12.13) for $|y_{4\ell}|$, Fig. 12.34 (Tab. 12.15) for m_{12}, Fig. 12.33 (Tab. 12.14) for m_{34}, Fig. 12.35 (Tab. 12.16) for $|\cos(\theta^*)|$, Fig. 12.36 (Tab. 12.17) for n_{jets}, Fig. 12.37 (Tab. 12.18) for $p_{\text{T}}^{\text{leading jet}}$, Fig. 12.38 (Tab. 12.19) for m_{jj}, Fig. 12.39 (Tab. 12.20) for $|\Delta\eta_{jj}|$, Fig. 12.40 (Tab. 12.21) for $\Delta\phi_{jj}$ and Fig. 12.41 (Tab. 12.22) for $n_{b\text{ jets}}$.

Overall acceptance and correction factors are quite similar between production modes, showing results are quite model independent. Acceptance factors are lower for the VH production mechanisms because of increased lepton miss-pairing: a lepton originating from the additional vector boson and not the Higgs boson will cause the quadruplet to fail the $m_{4\ell}$ cut. Correction factors are lower for $t\bar{t}H$ because of increased activity around the leptons (due to the boosted t jets), which fail the isolation criteria more often.

$\mathcal{A}$ factors increase with $p_{\text{T}}^{4\ell}$ due to more boosted leptons which are more likely to pass fiducial cuts. The effect cancels out for the $\mathcal{C}$ factors in the reconstruction over fiducial space fraction. The opposite effect happens against $|y_{4\ell}|$ because of more forward leptons at high Higgs boson rapidities, causing the quadruplets to fail the kinematic cuts (once more this effect cancels out for $\mathcal{C}$). Concerning m_{12}, dressed leptons being less boosted than their born associates (due to imperfect FSR recovery), the Z masses are shifted towards lower values, explaining the decrease of $\mathcal{A}$. Another effect is that higher m_{12} values lead in general to lower m_{34} values, and therefore less boosted leptons forming the sub-leading pair which have less chances to pass the cuts. These effects cancel out for $\mathcal{C}$, but the narrow Z peak causes migration of reconstructed events to the benefit of the surrounding bins, explaining the lower values of the factors close to the Z pole mass. Against m_{34}, the effect is inverted: higher mass values are formed from pairs of more boosted leptons which are more likely to pass the fiducial cuts, resulting in higher acceptance. This effect cancels out for the correction factors, and since the Z is off-shell there is not the same bin migration as for m_{12}. The last variable, $|\cos(\theta^*)|$ is not affected by boosts and the factor distributions are flat.

Concerning the jet variables, results are less conclusive. Against n_{jets}, factors increase. For the acceptance, this is related to the fact that boosted Higgs bosons are more likely to be produced in association to highly energetic jets close-by (especially for the VH and $t\bar{t}H$ mechanisms), but overall the distributions are flat. For correction factors, this effect is enhanced, as the calorimeter deposits from boosted leptons have more chances to be reconstructed as jets. Note that the first bin $n_{\text{jets}} = 0$ for $t\bar{t}H$ should be interpreted as statistically insignificant. These conclusions can be drawn for $\mathcal{A}$ against $p_{\text{T}}^{\text{leading jet}}$ as well, as the more boosted the Higgs boson (and therefore the leptons), the more likely the leading jet will be boosted as well. This effect almost cancels out for $\mathcal{C}$, but the higher values for low transverse momenta can be attributed to jets reconstructed from highly energetic (and hence boosted) leptons in the calorimeters, which have more chances to pass the selection criteria. Although there are no strong correlations between m_{jj} and $\mathcal{A}$, where a slight increase would be expected, the same remark as for $\mathcal{C}$ against $p_{\text{T}}^{\text{leading jet}}$ can be made: low values of m_{jj} may come from boosted lepton deposits in the calorimeters. Concerning $|\Delta\eta_{jj}|$ and $\Delta\phi_{jj}$, the factor distributions are flat indicating no correlations. The same remark can be made for the $n_{b\text{ jets}}$ differential variable.

Table 12.12 – Acceptance and correction factors per production mode, in bins of $p_{\text{T}}^{4\ell}$ [215]. Errors are statistical only.

Acceptance factor [%]						
Bin	Production mode					
	ggF	VBF	WH	ZH	$t\bar{t}H$	$b\bar{b}H$
0	40.03 ± 0.17	39.74 ± 0.30	31.52 ± 0.79	34.93 ± 0.84	43.85 ± 3.10	40.02 ± 1.33
1	40.29 ± 0.19	39.37 ± 0.27	31.37 ± 0.72	35.34 ± 0.75	46.98 ± 3.09	40.01 ± 1.40
2	40.60 ± 0.27	39.92 ± 0.24	32.28 ± 0.63	34.27 ± 0.65	43.60 ± 2.38	47.19 ± 1.28
3	40.89 ± 0.14	39.90 ± 0.14	32.30 ± 0.39	34.51 ± 0.40	41.77 ± 1.49	43.17 ± 1.04
4	41.54 ± 0.14	40.68 ± 0.10	32.72 ± 0.28	34.98 ± 0.29	42.46 ± 1.01	44.24 ± 1.02
5	42.76 ± 0.17	41.85 ± 0.10	33.30 ± 0.28	35.62 ± 0.29	45.32 ± 0.99	45.81 ± 1.31
6	43.70 ± 0.17	43.24 ± 0.09	34.66 ± 0.26	36.93 ± 0.26	44.87 ± 0.79	48.68 ± 1.68
7	45.65 ± 0.17	46.02 ± 0.07	37.03 ± 0.23	39.49 ± 0.23	46.16 ± 0.61	49.13 ± 2.11
8	49.90 ± 0.22	50.75 ± 0.08	41.86 ± 0.27	44.62 ± 0.27	48.50 ± 0.60	54.43 ± 3.48
9	55.00 ± 0.41	55.55 ± 0.16	47.64 ± 0.47	50.65 ± 0.49	53.50 ± 0.88	61.28 ± 8.64
Correction factor [%]						
Bin	Production mode					
	ggF	VBF	WH	ZH	$t\bar{t}H$	$b\bar{b}H$
0	53.64 ± 0.43	52.43 ± 1.16	49.10 ± 2.71	46.20 ± 2.54	30.82 ± 7.36	56.44 ± 4.23
1	53.19 ± 0.50	53.60 ± 1.12	46.39 ± 2.40	46.34 ± 2.33	29.98 ± 5.67	57.75 ± 4.54
2	53.05 ± 0.51	53.49 ± 0.94	48.09 ± 2.05	47.63 ± 2.08	40.38 ± 6.08	48.73 ± 3.31
3	52.75 ± 0.40	54.40 ± 0.59	49.54 ± 1.35	48.85 ± 1.33	32.65 ± 3.45	55.10 ± 3.09
4	52.42 ± 0.38	54.12 ± 0.42	48.50 ± 0.93	48.78 ± 0.96	35.32 ± 2.40	51.34 ± 2.88
5	51.80 ± 0.45	55.16 ± 0.40	49.91 ± 0.94	49.74 ± 0.93	34.54 ± 2.13	52.90 ± 3.62
6	52.49 ± 0.49	55.05 ± 0.35	50.57 ± 0.85	50.48 ± 0.84	35.79 ± 1.81	46.60 ± 4.25
7	53.92 ± 0.49	56.84 ± 0.29	51.62 ± 0.73	51.57 ± 0.70	38.40 ± 1.44	51.77 ± 5.82
8	57.00 ± 0.61	60.02 ± 0.32	55.49 ± 0.83	55.58 ± 0.81	42.48 ± 1.45	46.51 ± 8.30
9	61.82 ± 1.21	63.65 ± 0.60	60.95 ± 1.49	60.14 ± 1.39	47.44 ± 2.10	43.80 ± 18.24

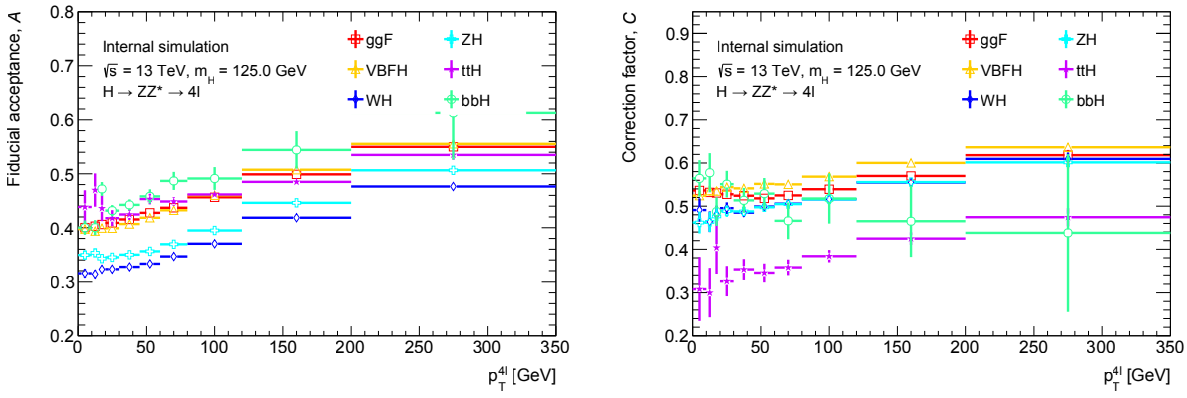

(a) Acceptance factor

(b) Correction factor

Figure 12.31 – Acceptance and correction factors per production mode, in bins of $p_{\mathrm{T}}^{4\ell}$ [215]. Errors are statistical only.

Table 12.13 – Acceptance and correction factors per production mode, in bins of $|y_{4\ell}|$ [215]. Errors are statistical only.

Acceptance factor [%]						
Bin	Production mode					
	ggF	VBF	WH	ZH	$t\bar{t}H$	$b\bar{b}H$
0	57.49 ± 0.13	58.82 ± 0.09	53.08 ± 0.31	56.28 ± 0.31	52.37 ± 0.66	57.84 ± 1.15
1	57.34 ± 0.13	58.62 ± 0.09	52.89 ± 0.31	55.34 ± 0.31	52.97 ± 0.67	57.11 ± 1.13
2	56.23 ± 0.14	57.80 ± 0.09	52.09 ± 0.32	54.62 ± 0.32	51.07 ± 0.71	55.78 ± 1.17
3	54.13 ± 0.14	55.39 ± 0.10	50.23 ± 0.32	52.84 ± 0.32	51.19 ± 0.81	53.62 ± 1.30
4	46.57 ± 0.13	49.30 ± 0.09	44.89 ± 0.28	46.32 ± 0.29	47.49 ± 0.79	45.17 ± 1.18
5	30.26 ± 0.14	34.26 ± 0.10	31.52 ± 0.28	32.73 ± 0.29	32.19 ± 0.93	28.36 ± 1.23
6	9.04 ± 0.09	11.01 ± 0.07	9.87 ± 0.18	10.23 ± 0.19	11.77 ± 0.85	8.32 ± 0.90
Correction factor [%]						
Bin	Production mode					
	ggF	VBF	WH	ZH	$t\bar{t}H$	$b\bar{b}H$
0	54.36 ± 0.34	58.52 ± 0.32	53.20 ± 0.82	53.69 ± 0.82	39.82 ± 1.52	55.10 ± 2.92
1	54.01 ± 0.35	58.40 ± 0.33	54.44 ± 0.85	53.90 ± 0.82	40.28 ± 1.47	51.32 ± 2.82
2	53.88 ± 0.36	58.17 ± 0.34	52.97 ± 0.83	52.96 ± 0.83	40.02 ± 1.58	54.13 ± 3.01
3	54.33 ± 0.39	57.22 ± 0.36	53.01 ± 0.87	52.95 ± 0.86	41.01 ± 1.86	51.79 ± 3.32
4	52.18 ± 0.38	55.68 ± 0.34	50.44 ± 0.80	50.25 ± 0.78	37.89 ± 1.80	49.08 ± 3.33
5	49.84 ± 0.51	52.77 ± 0.45	49.69 ± 1.01	48.05 ± 0.95	36.89 ± 2.83	56.22 ± 4.88
6	43.25 ± 0.89	44.95 ± 0.78	42.48 ± 1.65	42.44 ± 1.65	32.74 ± 5.17	50.85 ± 9.70

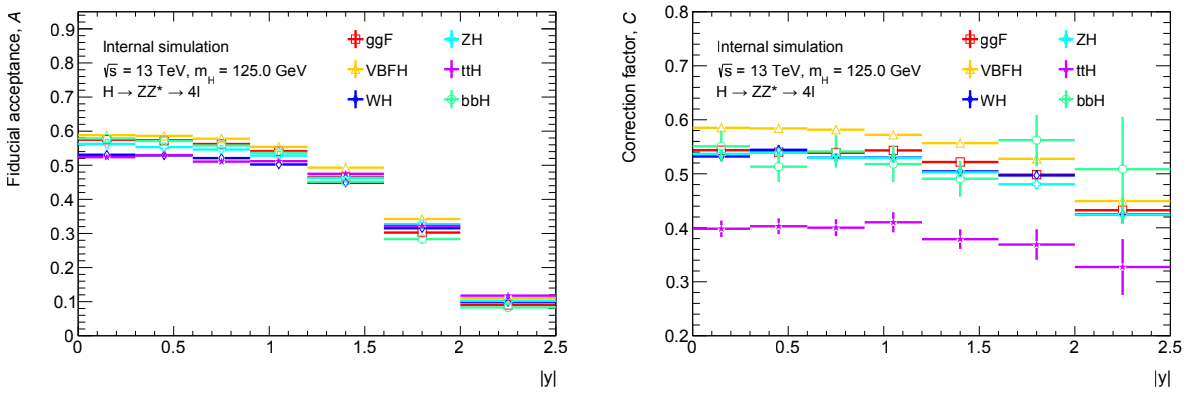

(a) Acceptance factor

(b) Correction factor

Figure 12.32 – Acceptance and correction factors per production mode, in bins of $|y_{4\ell}|$ [215]. Errors are statistical only.

Table 12.14 – Acceptance and correction factors per production mode, in bins of m_{34} [215]. Errors are statistical only.

Acceptance factor [%]						
Bin	Production mode					
	ggF	VBF	WH	ZH	$t\bar{t}H$	$b\bar{b}H$
0	38.82 ± 0.14	43.63 ± 0.08	35.58 ± 0.23	37.92 ± 0.24	44.07 ± 0.67	39.32 ± 1.00
1	43.38 ± 0.15	47.63 ± 0.09	38.04 ± 0.28	41.76 ± 0.28	48.05 ± 0.78	44.95 ± 1.16
2	47.27 ± 0.15	50.39 ± 0.09	41.02 ± 0.26	44.44 ± 0.27	52.49 ± 0.72	51.09 ± 1.14
3	50.53 ± 0.15	52.57 ± 0.09	43.00 ± 0.27	46.00 ± 0.27	55.65 ± 0.71	52.29 ± 1.13
4	52.41 ± 0.16	54.53 ± 0.10	44.97 ± 0.31	47.57 ± 0.31	56.55 ± 0.81	56.30 ± 1.29
5	55.39 ± 0.34	58.21 ± 0.13	48.33 ± 0.40	50.41 ± 0.41	60.70 ± 1.02	58.72 ± 1.58
6	54.86 ± 0.53	57.95 ± 0.36	49.29 ± 1.11	47.93 ± 1.12	65.24 ± 2.76	51.22 ± 4.50
Correction factor [%]						
Bin	Production mode					
	ggF	VBF	WH	ZH	$t\bar{t}H$	$b\bar{b}H$
0	53.40 ± 0.35	58.46 ± 0.33	52.33 ± 0.77	52.99 ± 0.76	37.57 ± 1.66	52.43 ± 3.13
1	53.60 ± 0.39	58.21 ± 0.36	53.05 ± 0.89	51.74 ± 0.85	38.24 ± 1.77	54.40 ± 3.36
2	53.56 ± 0.35	56.83 ± 0.32	52.96 ± 0.81	51.98 ± 0.78	41.50 ± 1.61	55.26 ± 3.01
3	51.04 ± 0.33	55.11 ± 0.31	49.98 ± 0.75	49.60 ± 0.74	36.98 ± 1.49	53.63 ± 2.95
4	52.98 ± 0.39	55.73 ± 0.36	51.50 ± 0.87	52.43 ± 0.88	41.63 ± 1.81	48.51 ± 3.15
5	56.49 ± 0.51	57.71 ± 0.45	53.86 ± 1.12	53.81 ± 1.10	43.87 ± 2.30	51.27 ± 3.97
6	52.34 ± 1.34	54.29 ± 1.25	49.26 ± 2.91	48.02 ± 2.84	42.86 ± 5.77	49.54 ± 12.65

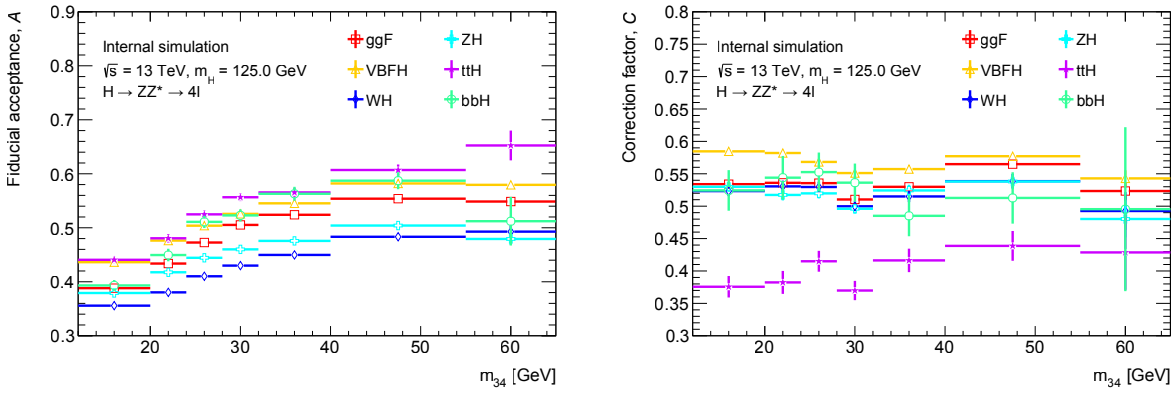

(a) Acceptance factor

(b) Correction factor

Figure 12.33 – Acceptance and correction factors per production mode, in bins of m_{34} [215]. Errors are statistical only.

Table 12.15 – Acceptance and correction factors per production mode, in bins of m_{12} [215]. Errors are statistical only.

Acceptance factor [%]						
Bin	Production mode					
	ggF	VBF	WH	ZH	$t\bar{t}H$	$b\bar{b}H$
0	56.56 ± 0.24	59.35 ± 0.15	48.41 ± 0.46	51.08 ± 0.47	62.32 ± 1.18	56.90 ± 1.84
1	53.89 ± 0.34	57.39 ± 0.14	47.33 ± 0.44	49.03 ± 0.44	57.72 ± 1.13	55.44 ± 1.73
2	52.40 ± 0.19	55.28 ± 0.13	44.89 ± 0.40	48.16 ± 0.41	54.53 ± 1.10	58.79 ± 1.68
3	50.40 ± 0.20	53.34 ± 0.10	43.71 ± 0.31	45.71 ± 0.31	50.57 ± 0.85	50.79 ± 1.27
4	38.32 ± 0.07	41.41 ± 0.04	33.16 ± 0.13	35.77 ± 0.13	44.25 ± 0.37	40.31 ± 0.58
5	30.54 ± 0.36	33.50 ± 0.17	26.07 ± 0.47	28.93 ± 0.49	35.82 ± 1.39	32.44 ± 2.04
Correction factor [%]						
Bin	Production mode					
	ggF	VBF	WH	ZH	$t\bar{t}H$	$b\bar{b}H$
0	59.77 ± 0.60	61.91 ± 0.54	56.88 ± 1.33	56.44 ± 1.28	43.89 ± 2.49	57.35 ± 5.20
1	57.81 ± 0.57	59.35 ± 0.50	56.90 ± 1.27	53.37 ± 1.19	45.22 ± 2.74	55.42 ± 4.70
2	60.12 ± 0.55	62.89 ± 0.49	57.48 ± 1.20	58.17 ± 1.18	41.75 ± 2.41	57.01 ± 4.30
3	76.37 ± 0.50	83.51 ± 0.47	74.43 ± 1.12	76.26 ± 1.14	58.64 ± 2.46	74.08 ± 4.39
4	42.61 ± 0.17	46.02 ± 0.16	41.73 ± 0.39	41.78 ± 0.39	31.47 ± 0.81	43.99 ± 1.53
5	90.71 ± 1.29	97.83 ± 1.12	95.74 ± 3.10	92.98 ± 2.90	82.74 ± 6.07	79.21 ± 9.60

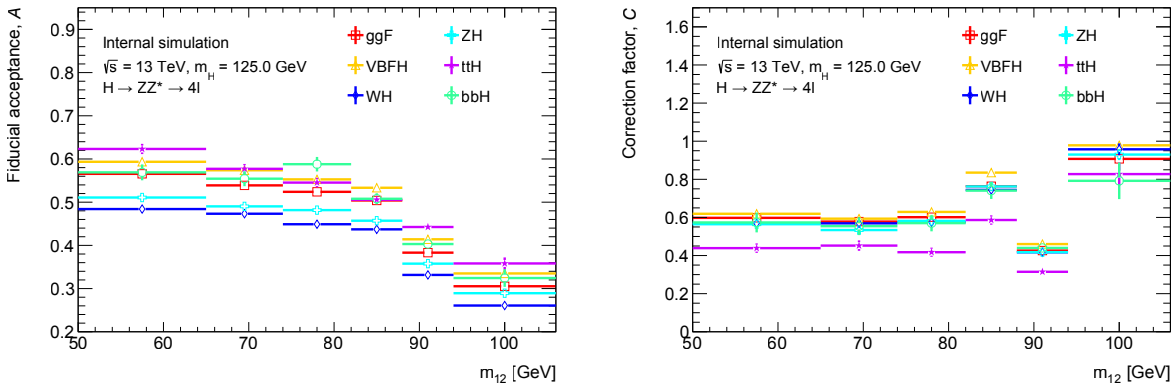

(a) Acceptance factor

(b) Correction factor

Figure 12.34 – Acceptance and correction factors per production mode, in bins of m_{12} [215]. Errors are statistical only.

Table 12.16 – Acceptance and correction factors per production mode, in bins of $|\cos(\theta^*)|$ [215]. Errors are statistical only.

Acceptance factor [%]						
Bin	Production mode					
	ggF	VBF	WH	ZH	$t\bar{t}H$	$b\bar{b}H$
0	44.44 ± 0.15	46.38 ± 0.10	37.50 ± 0.30	40.21 ± 0.30	47.26 ± 0.85	46.59 ± 1.26
1	44.11 ± 0.16	45.97 ± 0.10	37.80 ± 0.30	40.39 ± 0.31	47.37 ± 0.83	46.39 ± 1.22
2	43.63 ± 0.19	46.08 ± 0.10	37.13 ± 0.30	39.54 ± 0.30	46.85 ± 0.81	46.04 ± 1.36
3	43.14 ± 0.21	45.62 ± 0.10	37.19 ± 0.30	39.09 ± 0.30	46.95 ± 0.85	42.89 ± 1.32
4	42.04 ± 0.17	45.25 ± 0.10	36.05 ± 0.30	38.97 ± 0.31	47.61 ± 0.87	47.78 ± 1.28
5	41.25 ± 0.19	44.52 ± 0.10	35.92 ± 0.30	38.32 ± 0.30	46.94 ± 0.85	41.89 ± 1.31
6	39.97 ± 0.15	43.86 ± 0.10	35.01 ± 0.29	37.42 ± 0.30	45.32 ± 0.82	41.67 ± 1.30
7	38.00 ± 0.15	43.11 ± 0.10	34.32 ± 0.29	37.05 ± 0.30	45.88 ± 0.82	40.12 ± 1.28
Correction factor [%]						
Bin	Production mode					
	ggF	VBF	WH	ZH	$t\bar{t}H$	$b\bar{b}H$
0	53.74 ± 0.42	57.65 ± 0.39	52.83 ± 0.97	51.74 ± 0.92	39.08 ± 1.96	50.79 ± 3.52
1	53.77 ± 0.42	57.25 ± 0.40	52.00 ± 0.96	52.10 ± 0.93	37.61 ± 1.92	54.35 ± 3.49
2	53.94 ± 0.43	57.44 ± 0.40	52.88 ± 0.98	52.04 ± 0.94	38.05 ± 1.84	52.87 ± 3.83
3	53.50 ± 0.43	56.90 ± 0.39	52.19 ± 0.96	51.93 ± 0.93	40.33 ± 2.02	50.43 ± 3.87
4	53.26 ± 0.43	56.70 ± 0.39	51.88 ± 0.96	52.15 ± 0.95	39.77 ± 2.02	52.14 ± 3.36
5	52.46 ± 0.43	57.14 ± 0.40	51.64 ± 0.96	52.47 ± 0.99	43.06 ± 2.12	59.62 ± 4.07
6	52.64 ± 0.44	56.16 ± 0.40	51.30 ± 0.98	52.46 ± 0.98	40.92 ± 2.01	51.83 ± 3.76
7	52.20 ± 0.45	56.04 ± 0.41	51.54 ± 0.99	50.00 ± 0.95	38.15 ± 1.94	49.85 ± 3.77

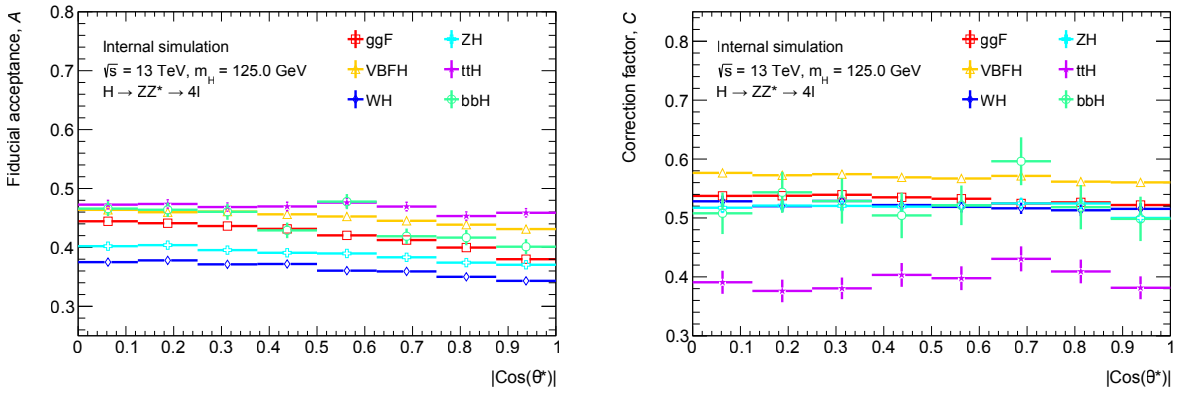

(a) Acceptance factor

(b) Correction factor

Figure 12.35 – Acceptance and correction factors per production mode, in bins of $|\cos(\theta^*)|$ [215]. Errors are statistical only.

Table 12.17 – Acceptance and correction factors per production mode, in bins of n_{jets} [215]. Errors are statistical only.

Acceptance factor [%]						
Bin	Production mode					
	ggF	VBF	WH	ZH	$t\bar{t}H$	$b\bar{b}H$
0	41.06 ± 0.08	39.68 ± 0.11	30.16 ± 0.20	35.54 ± 0.22	36.72 ± 5.55	43.38 ± 0.61
1	43.31 ± 0.10	44.34 ± 0.06	36.36 ± 0.18	38.31 ± 0.19	36.99 ± 1.94	45.72 ± 0.90
2	44.66 ± 0.18	47.20 ± 0.05	39.88 ± 0.21	40.90 ± 0.20	38.30 ± 0.98	44.25 ± 1.23
3	44.96 ± 0.27	44.21 ± 0.11	40.28 ± 0.27	41.16 ± 0.27	47.80 ± 0.31	47.56 ± 1.80
Correction factor [%]						
Bin	Production mode					
	ggF	VBF	WH	ZH	$t\bar{t}H$	$b\bar{b}H$
0	48.96 ± 0.19	47.16 ± 0.43	45.93 ± 0.69	48.40 ± 0.70	48.68 ± 17.70	51.43 ± 1.71
1	56.99 ± 0.29	51.92 ± 0.22	49.88 ± 0.57	49.46 ± 0.58	36.13 ± 5.37	53.47 ± 2.63
2	63.42 ± 0.52	57.72 ± 0.21	54.32 ± 0.66	53.62 ± 0.63	41.09 ± 2.79	56.00 ± 3.77
3	74.49 ± 0.99	82.40 ± 0.58	59.92 ± 0.92	57.51 ± 0.87	39.54 ± 0.73	58.73 ± 5.16

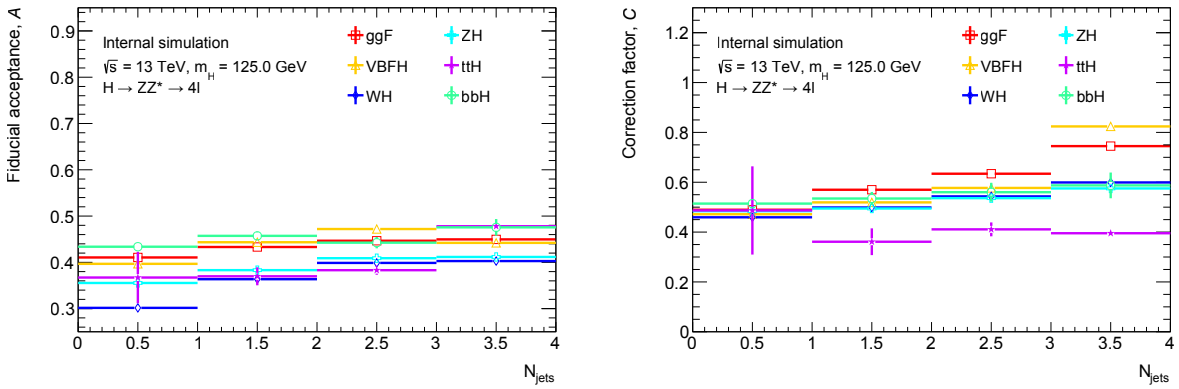

(a) Acceptance factor

(b) Correction factor

Figure 12.36 – Acceptance and correction factors per production mode, in bins of n_{jets} [215]. Errors are statistical only.

Table 12.18 – Acceptance and correction factors per production mode, in bins of $p_{\text{T}}^{\text{leading jet}}$ [215]. Errors are statistical only.

Acceptance factor [%]						
Bin	Production mode					
	ggF	VBF	WH	ZH	$t\bar{t}H$	$b\bar{b}H$
0	40.87 ± 0.16	40.85 ± 0.12	33.96 ± 0.31	35.91 ± 0.33	32.11 ± 3.91	43.49 ± 1.17
1	42.41 ± 0.16	42.11 ± 0.09	35.07 ± 0.25	36.82 ± 0.26	43.27 ± 1.66	45.27 ± 1.22
2	43.91 ± 0.23	43.89 ± 0.08	37.13 ± 0.26	38.40 ± 0.25	43.60 ± 0.90	46.42 ± 1.60
3	46.26 ± 0.18	46.60 ± 0.07	40.64 ± 0.25	41.61 ± 0.25	46.05 ± 0.52	48.98 ± 1.87
4	51.24 ± 0.23	51.46 ± 0.08	45.43 ± 0.32	46.60 ± 0.32	48.28 ± 0.43	53.36 ± 2.97
Correction factor [%]						
Bin	Production mode					
	ggF	VBF	WH	ZH	$t\bar{t}H$	$b\bar{b}H$
0	66.64 ± 0.55	54.12 ± 0.48	51.35 ± 1.06	51.35 ± 1.11	38.76 ± 10.79	55.15 ± 3.64
1	57.21 ± 0.49	53.15 ± 0.36	48.68 ± 0.80	47.36 ± 0.78	38.29 ± 3.81	53.74 ± 3.49
2	56.52 ± 0.54	56.36 ± 0.32	53.46 ± 0.83	51.65 ± 0.79	34.45 ± 2.12	56.85 ± 4.78
3	57.44 ± 0.53	58.64 ± 0.27	56.30 ± 0.80	55.70 ± 0.78	38.70 ± 1.21	53.83 ± 5.27
4	58.59 ± 0.66	62.56 ± 0.33	57.37 ± 0.99	57.25 ± 0.95	41.89 ± 1.03	53.96 ± 8.26

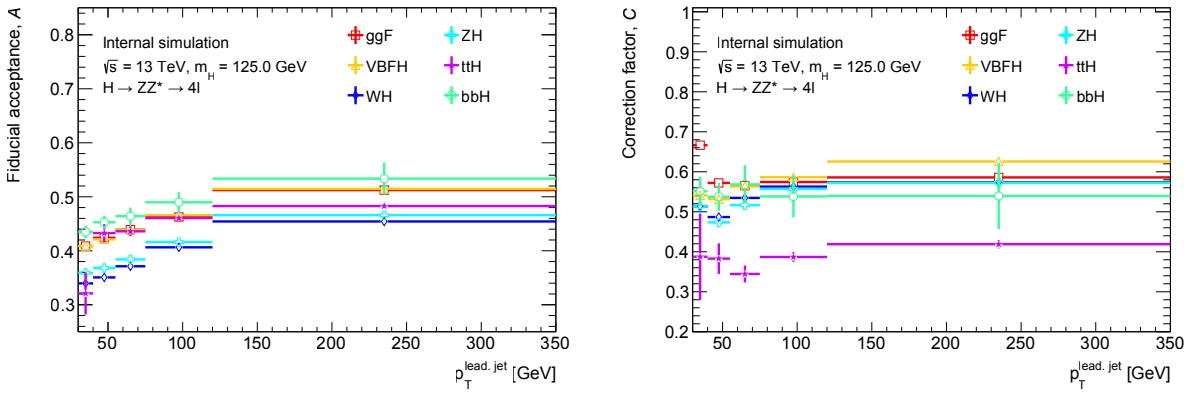

(a) Acceptance factor

(b) Correction factor

Figure 12.37 – Acceptance and correction factors per production mode, in bins of $p_{\mathrm{T}}^{\text{leading jet}}$ [215]. Errors are statistical only.

Table 12.19 – Acceptance and correction factors per production mode, in bins of m_{jj} [215]. Errors are statistical only.

Acceptance factor [%]						
Bin	Production mode					
	ggF	VBF	WH	ZH	$t\bar{t}H$	$b\bar{b}H$
0	44.72 ± 0.23	43.82 ± 0.17	40.33 ± 0.21	41.39 ± 0.21	45.96 ± 0.63	43.40 ± 1.74
1	44.75 ± 0.21	46.86 ± 0.05	39.53 ± 0.26	40.34 ± 0.26	47.30 ± 0.34	46.32 ± 1.24
Correction factor [%]						
Bin	Production mode					
	ggF	VBF	WH	ZH	$t\bar{t}H$	$b\bar{b}H$
0	68.29 ± 0.78	72.64 ± 0.81	56.23 ± 0.68	54.24 ± 0.64	38.16 ± 1.49	56.36 ± 5.47
1	64.78 ± 0.57	60.83 ± 0.21	56.53 ± 0.86	56.40 ± 0.85	40.09 ± 0.80	57.04 ± 3.65

Table 12.20 – Acceptance and correction factors per production mode, in bins of $|\Delta\eta_{jj}|$ [215]. Errors are statistical only.

Acceptance factor [%]						
Bin	Production mode					
	ggF	VBF	WH	ZH	$t\bar{t}H$	$b\bar{b}H$
0	44.88 ± 0.18	42.75 ± 0.12	40.38 ± 0.18	41.38 ± 0.18	46.99 ± 0.33	45.70 ± 1.24
1	44.53 ± 0.28	47.43 ± 0.05	37.96 ± 0.42	38.70 ± 0.42	47.06 ± 0.72	44.60 ± 1.72
Correction factor [%]						
Bin	Production mode					
	ggF	VBF	WH	ZH	$t\bar{t}H$	$b\bar{b}H$
0	63.76 ± 0.58	66.65 ± 0.55	54.91 ± 0.57	53.32 ± 0.54	39.47 ± 0.77	52.61 ± 3.54
1	69.59 ± 0.76	61.14 ± 0.22	65.06 ± 1.55	65.96 ± 1.56	40.45 ± 1.74	63.70 ± 5.60

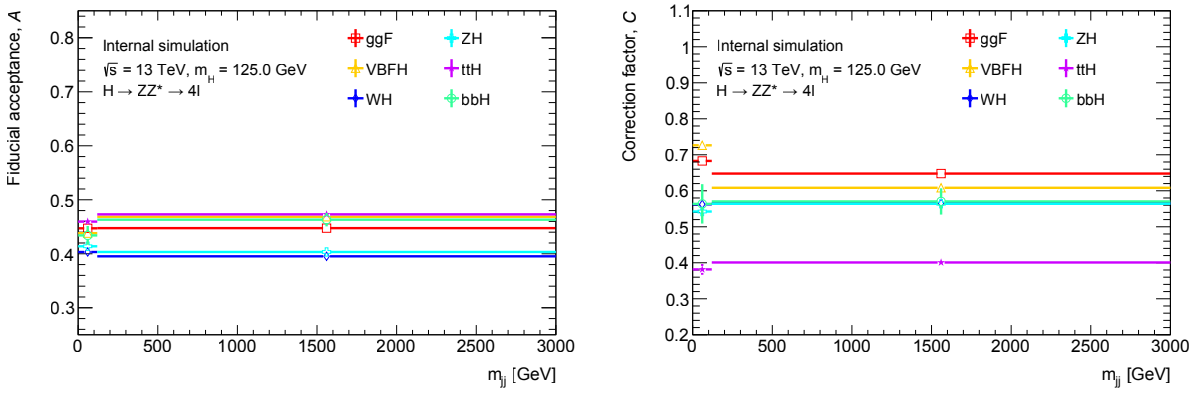

(a) Acceptance factor (b) Correction factor

Figure 12.38 – Acceptance and correction factors per production mode, in bins of m_{jj} [215]. Errors are statistical only.

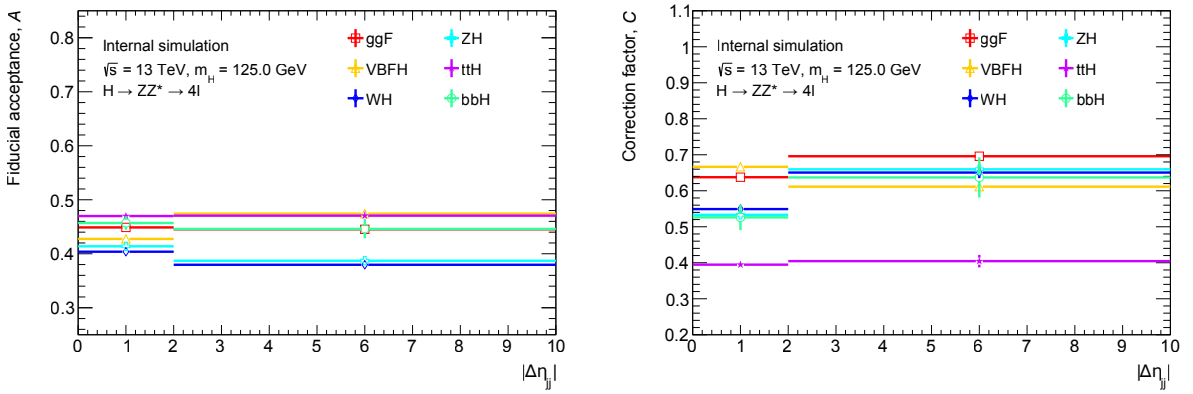

(a) Acceptance factor (b) Correction factor

Figure 12.39 – Acceptance and correction factors per production mode, in bins of $|\Delta\eta_{jj}|$ [215]. Errors are statistical only.

Table 12.21 – Acceptance and correction factors per production mode, in bins of $\Delta\phi_{jj}$ [215]. Errors are statistical only.

Acceptance factor [%]						
Bin	Production mode					
	ggF	VBF	WH	ZH	$t\bar{t}H$	$b\bar{b}H$
0	44.93 ± 0.20	46.77 ± 0.07	39.95 ± 0.23	40.94 ± 0.23	46.84 ± 0.43	43.97 ± 1.49
1	44.55 ± 0.23	46.56 ± 0.07	40.09 ± 0.23	41.05 ± 0.23	47.15 ± 0.41	46.42 ± 1.38
Correction factor [%]						
Bin	Production mode					
	ggF	VBF	WH	ZH	$t\bar{t}H$	$b\bar{b}H$
0	66.65 ± 0.67	62.10 ± 0.29	56.30 ± 0.76	55.32 ± 0.73	40.55 ± 1.03	56.14 ± 4.55
1	65.62 ± 0.64	61.85 ± 0.28	56.39 ± 0.75	54.77 ± 0.71	38.80 ± 0.97	57.51 ± 4.10

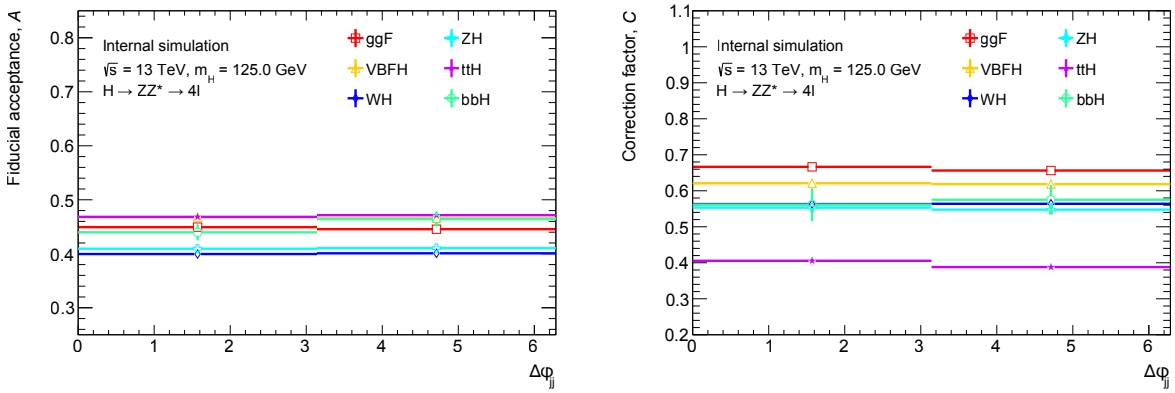

(a) Acceptance factor

(b) Correction factor

Figure 12.40 – Acceptance and correction factors per production mode, in bins of $\Delta\phi_{jj}$ [215]. Errors are statistical only.

Table 12.22 – Acceptance and correction factors per production mode, in bins of $n_{b\text{ jets}}$ [215]. Errors are statistical only.

Acceptance factor [%]						
Bin	Production mode					
	ggF	VBF	WH	ZH	$t\bar{t}H$	$b\bar{b}H$
0	42.02 ± 0.06	45.37 ± 0.04	36.34 ± 0.11	38.54 ± 0.12	50.95 ± 1.29	43.18 ± 0.54
1	46.34 ± 0.42	45.63 ± 0.25	39.04 ± 1.19	40.86 ± 0.29	46.53 ± 0.30	47.20 ± 0.85
Correction factor [%]						
Bin	Production mode					
	ggF	VBF	WH	ZH	$t\bar{t}H$	$b\bar{b}H$
0	53.24 ± 0.15	56.63 ± 0.14	50.83 ± 0.34	53.24 ± 0.37	171.75 ± 8.00	61.37 ± 1.71
1	51.72 ± 1.20	70.97 ± 1.15	190.65 ± 9.68	44.09 ± 0.78	31.66 ± 0.64	29.70 ± 1.72

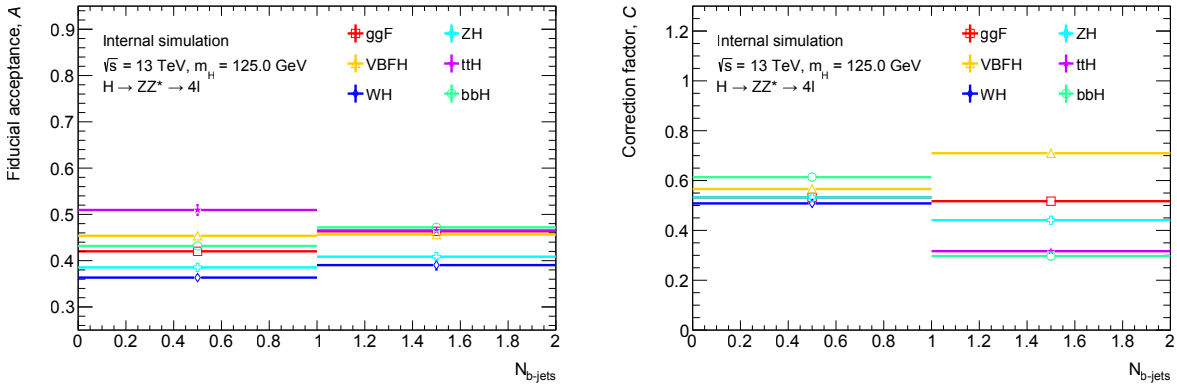

(a) Acceptance factor

(b) Correction factor

Figure 12.41 – Acceptance and correction factors per production mode, in bins of $n_{b\text{ jets}}$ [215]. Errors are statistical only.

12.5.6 Uncertainties

Uncertainties applied for differential measurements are the same as for inclusive cross sections, described in Sec. 12.4.3. They include uncertainties on the background shapes and modelling, uncertainties on acceptance and correction factors (Higgs mass, theory uncertainties, signal composition and experimental uncertainties), as well as theory and experimental uncertainties. Uncertainties are calculated for each bin of each differential variable for all the production modes combined and are treated as nuisance parameters in the fits.

12.5.7 Background and Asimov checks

Background checks are performed for each variable, in each bin, the same way as described in Sec. 12.4.2, using the $Z + \mu\mu$ and $Z + ee$ categories and the same- and opposite-sign control regions. Data and simulation distributions of $m_{4\ell}$ are compared for each bin in each control region to ensure the background yields (normalisation) and shapes are correct. Overall no strong discrepancies are found validating the background estimation.

Similarly to the inclusive case (see Sec. 12.4.4), pseudo data is generated to ensure the fitting procedure is not biased. These Asimov datasets are compared to MC to check the good accuracy of the pseudo data events. The fit is performed on generated data to check likelihood scans give symmetrical curves and that fitted values of cross sections in each bin of the differential variables are close to input predictions. Overall, results did not show any bias in the methodology and $-2\ln\Lambda$ appeared to follow a χ^2 law with one degree of freedom.

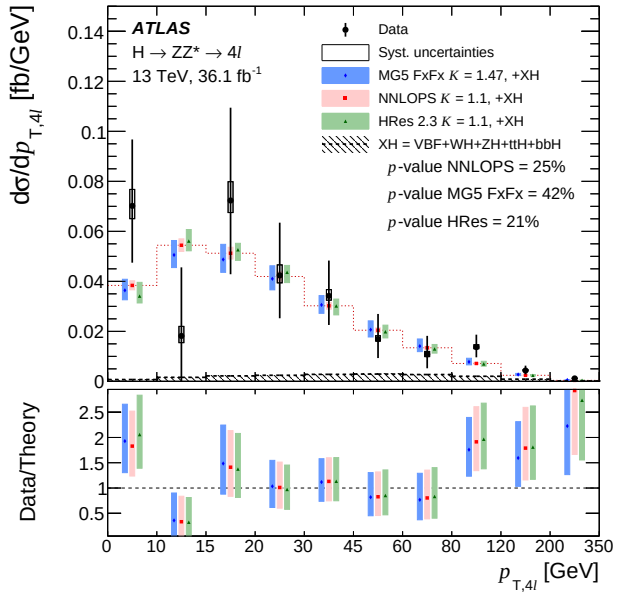

Figure 12.42 – Comparison of measured and expected differential fiducial cross section in bins of $p_{\mathrm{T}}^{4\ell}$ [215].

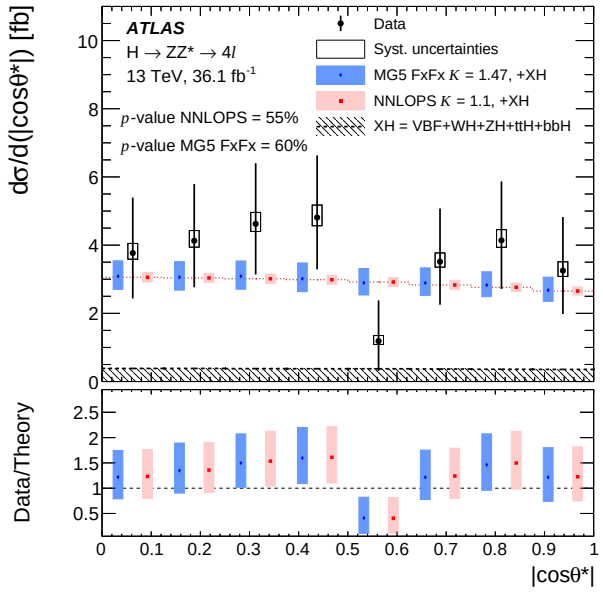

(a) $|\cos(\theta^*)|$

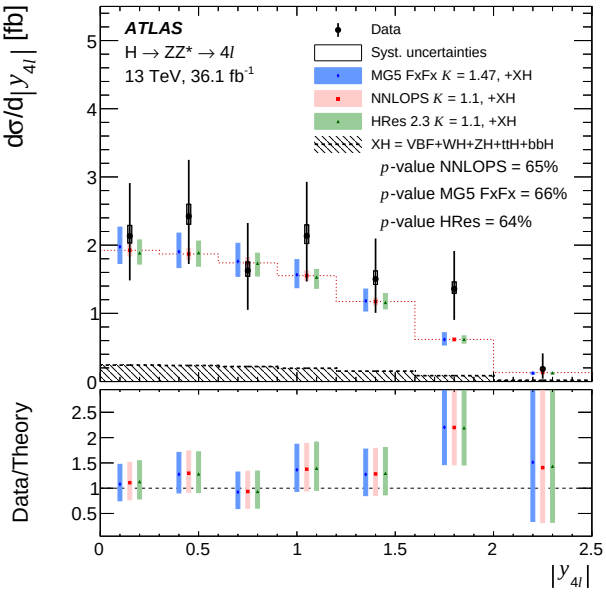

(b) $|y_{4\ell}|$

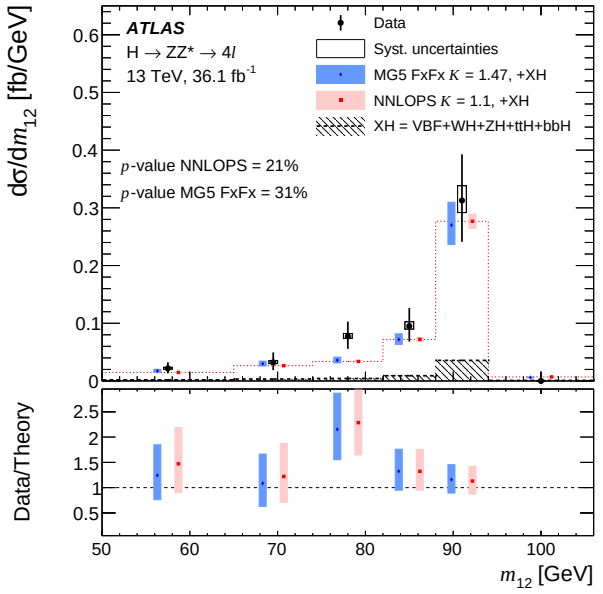

(c) m_{12}

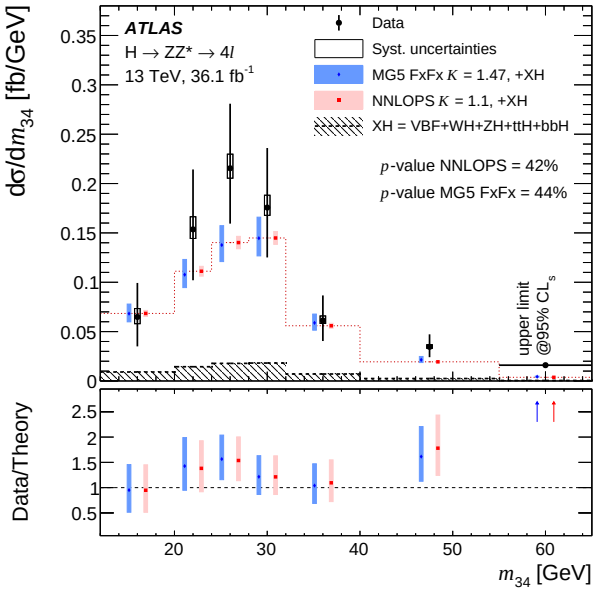

(d) m_{34}

Figure 12.43 – Comparison of measured and expected differential fiducial cross section in bins of the Higgs boson variables [215].

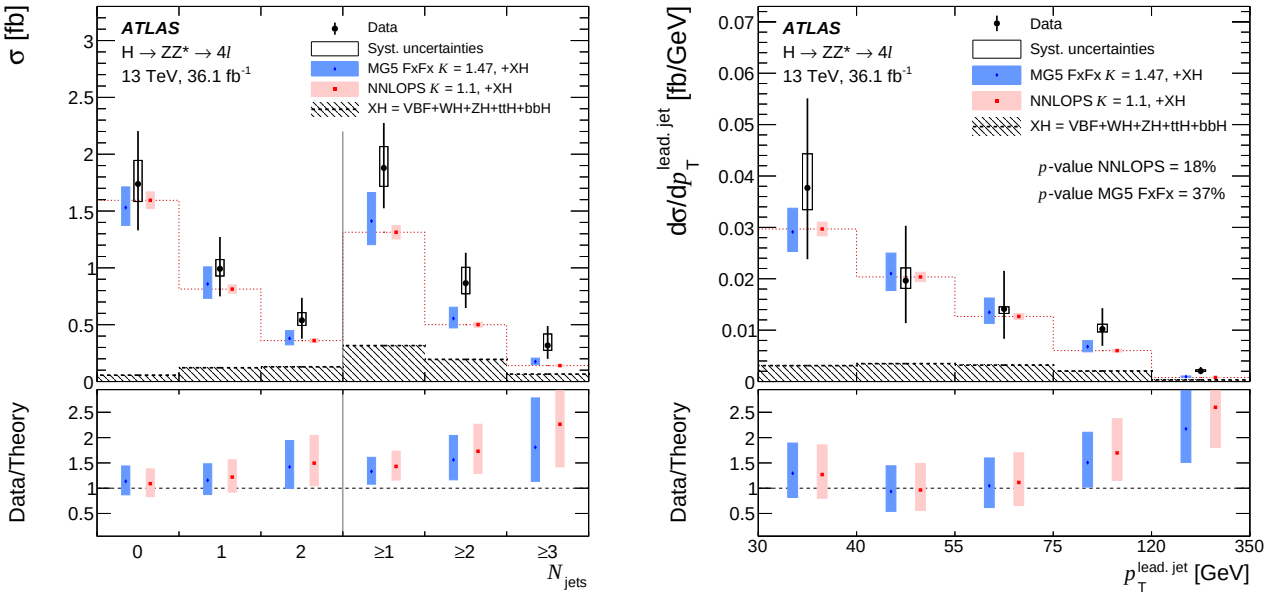

(a) n_{jets} (b) $p_{\text{T}}^{\text{leading jet}}$

Figure 12.44 – Comparison of measured and expected differential fiducial cross section in bins of n_{jets} and $p_{\text{T}}^{\text{leading jet}}$ [215].

12.5.8 Results using 36.1 fb^{-1}

For each variable, POIs are calculated using the fitting procedure in each bin. Results are presented for each variable:

- **Table of differential cross section per bin, comparing predictions and observations.** Results are presented in Tab. 12.23 for $p_{\text{T}}^{4\ell}$, 12.24 for $|y_{4\ell}|$, 12.25 for m_{12}, 12.26 for m_{34}, 12.27 for $|\cos(\theta^*)|$, 12.28 for n_{jets}, 12.29 for $p_{\text{T}}^{\text{leading jet}}$, 12.30 for m_{jj}, 12.31 for $|\Delta\eta_{jj}|$, 12.32 for $\Delta\phi_{jj}$ and 12.33 for $n_{b\text{ jets}}$. Overall no strong discrepancy with respect to the SM predictions are found.
- **Figures presenting the comparison between prediction and theory, and corresponding ratios.** Results are presented in Fig. 12.42 $p_{\text{T}}^{4\ell}$, 12.43 for the Higgs variables ($|y_{4\ell}|$, m_{12}, m_{34}, $|\cos(\theta^*)|$), and 12.44 for n_{jets} and $p_{\text{T}}^{\text{leading jet}}$, and 12.45 for the other jet variables (m_{jj}, $|\Delta\eta_{jj}|$, $\Delta\phi_{jj}$ and $n_{b\text{ jets}}$). Ratios between observation and predictions stay within unity, including the statistical and systematic uncertainties, showing no deviations from the SM.

Further to these results, likelihood scans in the vicinity of the observed cross-section value were plotted for each differential variable. The scans show quite symmetrical curves indicating a good behaviour for $-2\ln\Lambda$, except in the underflow and overflow bins which may be statistically dominated. The fits reach 0 indicating good significance of the results.

The value of the differential cross section in the second bin of $p_{\text{T}}^{4\ell}$ (Fig. 12.42) is attributed to a statistical fluctuation, which can also be observed in the data / MC comparison of the $p_{\text{T}}^{4\ell}$ distribution (see Fig. 11.15). This downward fluctuation is compensated by upward fluctuations in the close-by bins. Overall, the results are consistent with the SM predictions, taking into account the uncertainties.

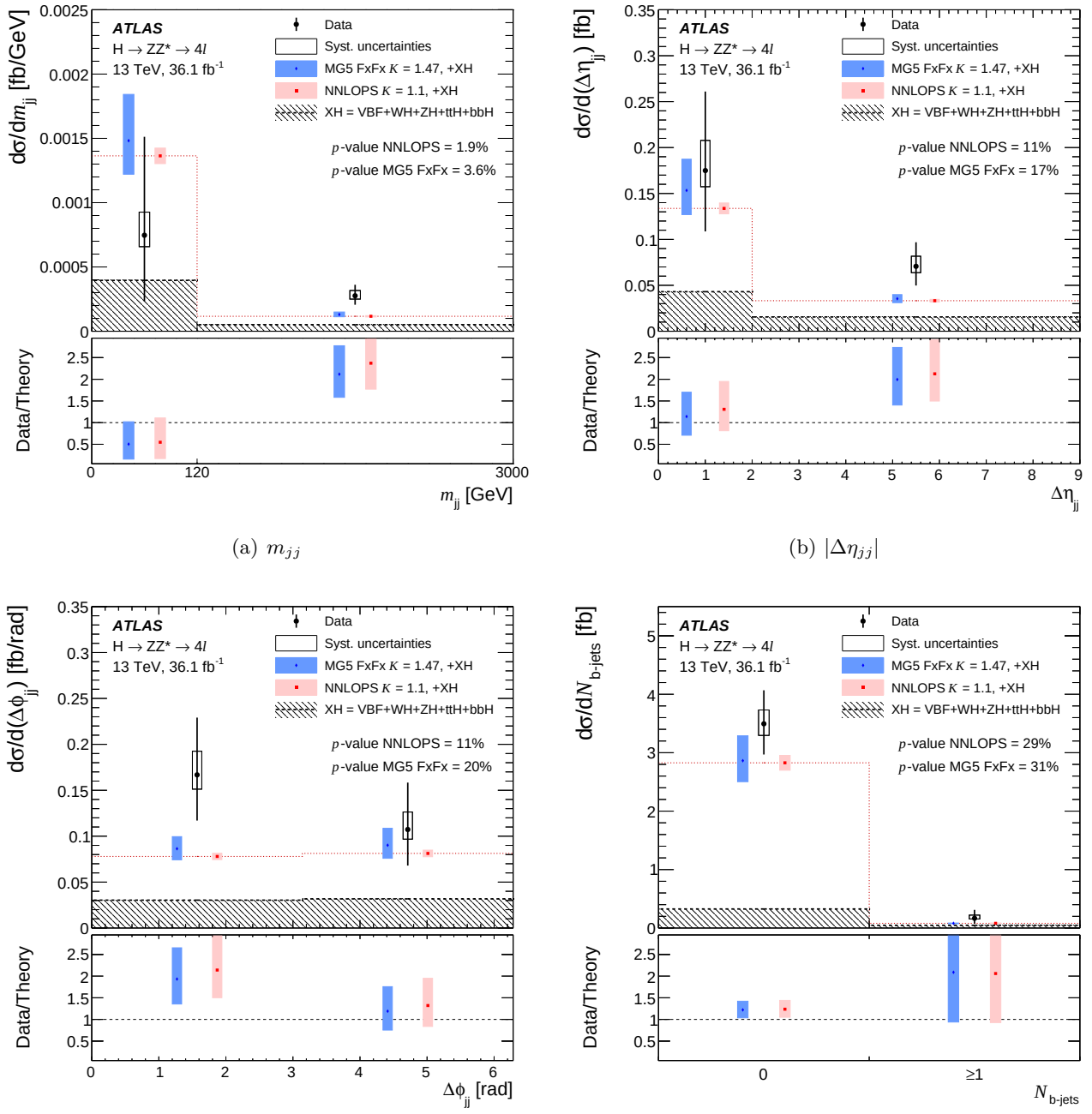

(a) m_{jj}

(b) $|\Delta\eta_{jj}|$

(c) $|\Delta\phi_{jj}|$

(d) $n_{b\ \mathrm{jets}}$

Figure 12.45 – Comparison of measured and expected differential fiducial cross section in bins of the jet variables [215].

Table 12.23 – Comparison of measured and expected differential fiducial cross section in bins of $p_{\mathrm{T}}^{4\ell}$ [215].

POI	σ_{inj} [fb]	σ_{fit} [fb]	Relative Error
$\sigma_{\text{bin 0}}$	0.0389	$0.07^{+0.03}_{-0.02}$	$^{+37\%}_{-31\%}$
$\sigma_{\text{bin 1}}$	0.0553	$0^{+0.4}_{-0.02}$	$^{+100\%}_{-100\%}$
$\sigma_{\text{bin 2}}$	0.052	$0.07^{+0.04}_{-0.03}$	$^{+51\%}_{-41\%}$
$\sigma_{\text{bin 3}}$	0.0426	$0.04^{+0.02}_{-0.02}$	$^{+49\%}_{-40\%}$
$\sigma_{\text{bin 4}}$	0.0306	$0.04^{+0.01}_{-0.01}$	$^{+40\%}_{-33\%}$
$\sigma_{\text{bin 5}}$	0.0207	$0.02^{+0.01}_{-0.008}$	$^{+58\%}_{-44\%}$
$\sigma_{\text{bin 6}}$	0.0135	$0.011^{+0.007}_{-0.006}$	$^{+65\%}_{-49\%}$
$\sigma_{\text{bin 7}}$	0.00719	$0.014^{+0.005}_{-0.004}$	$^{+36\%}_{-30\%}$
$\sigma_{\text{bin 8}}$	0.00243	$0.004^{+0.002}_{-0.002}$	$^{+44\%}_{-35\%}$
$\sigma_{\text{bin 9}}$	0.000319	$0.0009^{+0.0005}_{-0.0004}$	$^{+60\%}_{-43\%}$

Table 12.24 – Comparison of measured and expected differential fiducial cross section in bins of $|y_{4\ell}|$ [215].

POI	σ_{inj} [fb]	σ_{fit} [fb]	Relative Error
$\sigma_{\text{bin 0}}$	1.94	$2.2^{+0.8}_{-0.6}$	$^{+36\%}_{-30\%}$
$\sigma_{\text{bin 1}}$	1.89	$2.5^{+0.8}_{-0.7}$	$^{+33\%}_{-28\%}$
$\sigma_{\text{bin 2}}$	1.76	$1.7^{+0.7}_{-0.6}$	$^{+42\%}_{-35\%}$
$\sigma_{\text{bin 3}}$	1.57	$2.2^{+0.8}_{-0.7}$	$^{+36\%}_{-31\%}$
$\sigma_{\text{bin 4}}$	1.19	$1.5^{+0.6}_{-0.5}$	$^{+39\%}_{-33\%}$
$\sigma_{\text{bin 5}}$	0.628	$1.4^{+0.6}_{-0.5}$	$^{+40\%}_{-33\%}$
$\sigma_{\text{bin 6}}$	0.132	$0.2^{+0.5}_{-0.1}$	$^{+300\%}_{-100\%}$

Table 12.25 – Comparison of measured and expected differential fiducial cross section in bins of m_{12} [215].

POI	σ_{inj} [fb]	σ_{fit} [fb]	Relative Error
$\sigma_{\text{bin 0}}$	0.0149	$0.023^{+0.01}_{-0.008}$	$^{+47\%}_{-38\%}$
$\sigma_{\text{bin 1}}$	0.0268	$0.03^{+0.02}_{-0.01}$	$^{+52\%}_{-41\%}$
$\sigma_{\text{bin 2}}$	0.0342	$0.08^{+0.03}_{-0.02}$	$^{+33\%}_{-27\%}$
$\sigma_{\text{bin 3}}$	0.0728	$0.10^{+0.03}_{-0.03}$	$^{+32\%}_{-27\%}$
$\sigma_{\text{bin 4}}$	0.28	$0.32^{+0.08}_{-0.07}$	$^{+25\%}_{-23\%}$
$\sigma_{\text{bin 5}}$	0.00711	0^{+1}_{-1}	$^{+100\%}_{-100\%}$

Table 12.26 – Comparison of measured and expected differential fiducial cross section in bins of m_{34} [215].

POI	σ_{inj} [fb]	σ_{fit} [fb]	Relative Error
$\sigma_{\text{bin 0}}$	0.0692	$0.07^{+0.03}_{-0.03}$	$^{+49\%}_{-43\%}$
$\sigma_{\text{bin 1}}$	0.112	$0.16^{+0.06}_{-0.05}$	$^{+38\%}_{-33\%}$
$\sigma_{\text{bin 2}}$	0.142	$0.22^{+0.06}_{-0.06}$	$^{+30\%}_{-26\%}$
$\sigma_{\text{bin 3}}$	0.146	$0.18^{+0.06}_{-0.05}$	$^{+34\%}_{-28\%}$
$\sigma_{\text{bin 4}}$	0.0565	$0.06^{+0.03}_{-0.02}$	$^{+41\%}_{-34\%}$
$\sigma_{\text{bin 5}}$	0.0196	$0.04^{+0.01}_{-0.01}$	$^{+36\%}_{-30\%}$
$\sigma_{\text{bin 6}}$	0.00374	$0^{+0.07}_{-1}$	$^{+100\%}_{-100\%}$

Table 12.27 – Comparison of measured and expected differential fiducial cross section in bins of $|\cos(\theta^*)|$ [215].

POI	σ_{inj} [fb]	σ_{fit} [fb]	Relative Error
$\sigma_{\text{bin 0}}$	3.09	$3.9^{+1.6}_{-1.3}$	$^{+42\%}_{-34\%}$
$\sigma_{\text{bin 1}}$	3.07	$4.2^{+1.7}_{-1.4}$	$^{+39\%}_{-33\%}$
$\sigma_{\text{bin 2}}$	3.05	$4.7^{+1.8}_{-1.5}$	$^{+37\%}_{-31\%}$
$\sigma_{\text{bin 3}}$	3.02	$4.9^{+1.8}_{-1.5}$	$^{+37\%}_{-31\%}$
$\sigma_{\text{bin 4}}$	2.95	$1.2^{+1.2}_{-0.9}$	$^{+97\%}_{-72\%}$
$\sigma_{\text{bin 5}}$	2.87	$3.5^{+1.6}_{-1.3}$	$^{+44\%}_{-36\%}$
$\sigma_{\text{bin 6}}$	2.79	$4.2^{+1.7}_{-1.4}$	$^{+41\%}_{-34\%}$
$\sigma_{\text{bin 7}}$	2.68	$3.4^{+1.6}_{-1.3}$	$^{+47\%}_{-38\%}$

Table 12.28 – Comparison of measured and expected differential fiducial cross section in bins of n_{jets} [215].

POI	σ_{inj} [fb]	σ_{fit} [fb]	Relative Error
$\sigma_{\text{bin 0}}$	1.62	$1.79^{+0.47}_{-0.41}$	$^{+26\%}_{-23\%}$
$\sigma_{\text{bin 1}}$	0.82	$1.00^{+0.28}_{-0.24}$	$^{+28\%}_{-24\%}$
$\sigma_{\text{bin 2}}$	0.363	$0.53^{+0.20}_{-0.16}$	$^{+37\%}_{-30\%}$
$\sigma_{\text{bin 3}}$	0.141	$0.34^{+0.16}_{-0.12}$	$^{+46\%}_{-35\%}$

Table 12.29 – Comparison of measured and expected differential fiducial cross section in bins of $p_{\mathrm{T}}^{\text{leading jet}}$ [215].

POI	σ_{inj} [fb]	σ_{fit} [fb]	Relative Error
$\sigma_{\text{bin 0}}$	0.0301	$0.04^{+0.02}_{-0.01}$	$^{+46\%}_{-37\%}$
$\sigma_{\text{bin 1}}$	0.0206	$0.02^{+0.01}_{-0.008}$	$^{+54\%}_{-42\%}$
$\sigma_{\text{bin 2}}$	0.0128	$0.015^{+0.008}_{-0.006}$	$^{+52\%}_{-40\%}$
$\sigma_{\text{bin 3}}$	0.00632	$0.011^{+0.004}_{-0.003}$	$^{+40\%}_{-32\%}$
$\sigma_{\text{bin 4}}$	0.000713	$0.0018^{+0.0007}_{-0.0005}$	$^{+36\%}_{-29\%}$

Table 12.30 – Comparison of measured and expected differential fiducial cross section in bins of m_{jj} [215].

POI	σ_{inj} [fb]	σ_{fit} [fb]	Relative Error
$\sigma_{\text{bin 0}}$	0.00138	$0^{+0.04}_{-0}$	$^{+100\%}_{-67\%}$
$\sigma_{\text{bin 1}}$	0.000117	$2.8 \times 10^{-5}{}^{+8.3\times10^{-5}}_{-7.0\times10^{-5}}$	$^{+29\%}_{-25\%}$

Table 12.31 – Comparison of measured and expected differential fiducial cross section in bins of $|\Delta\eta_{jj}|$ [215].

POI	σ_{inj} [fb]	σ_{fit} [fb]	Relative Error
$\sigma_{\text{bin 0}}$	0.135	$0.18^{+0.08}_{-0.07}$	$^{+46\%}_{-36\%}$
$\sigma_{\text{bin 1}}$	0.0292	$0.06^{+0.02}_{-0.02}$	$^{+37\%}_{-30\%}$

Table 12.32 – Comparison of measured and expected differential fiducial cross section in bins of $\Delta\phi_{jj}$ [215].

POI	σ_{inj} [fb]	σ_{fit} [fb]	Relative Error
$\sigma_{\text{bin 0}}$	0.0785	$0.17^{+0.06}_{-0.05}$	$^{+37\%}_{-30\%}$
$\sigma_{\text{bin 1}}$	0.0818	$0.11^{+0.05}_{-0.04}$	$^{+46\%}_{-36\%}$

Table 12.33 – Comparison of measured and expected differential fiducial cross section in bins of $n_{b\text{ jets}}$ [215].

POI	σ_{inj} [fb]	σ_{fit} [fb]	Relative Error
$\sigma_{\text{bin 0}}$	2.85	$3.08^{+0.86}_{-0.83}$	$^{+28\%}_{-27\%}$
$\sigma_{\text{bin 1}}$	0.0629	$0.15^{+0.12}_{-0.08}$	$^{+80\%}_{-54\%}$

Table 12.34 – Binning chosen for the double-differential $p_{\mathrm{T}}^{4\ell}$ against n_{jets} variables [215].

Variable	Bin Edges	N_{bins}
$p_{\mathrm{T}}^{4\ell}$ ($n_{\mathrm{jets}} = 0$)	0, 15, 30, 120, 350 GeV	4
$p_{\mathrm{T}}^{4\ell}$ ($n_{\mathrm{jets}} = 1$)	0, 30, 60, 80, 120, 350 GeV	5
$p_{\mathrm{T}}^{4\ell}$ ($n_{\mathrm{jets}} \geq 2$)	0, 120, 350 GeV	2

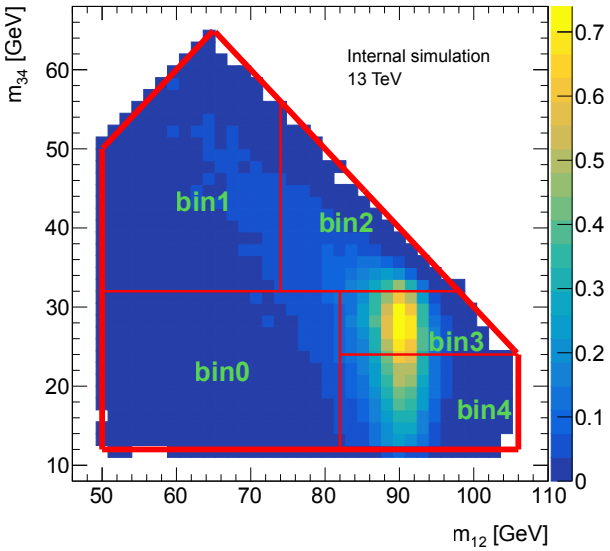

Variable	Bin Edges
0	$m_{12} < 82$ and $m_{34} < 32$
1	$m_{12} < 74$ and $m_{34} > 32$
2	$m_{12} > 74$ and $m_{34} > 32$
3	$m_{12} > 82$ and $24 < m_{34} < 32$
4	$m_{12} > 82$ and $m_{34} < 24$

Figure 12.46 – Binning chosen for the double-differential (m_{12}, m_{34}) variable [215].

12.6 Double-differential measurements

The data recorded during 2015 and 2016 enables the measurements of the Higgs-boson-to-four-lepton production cross sections in bins of two differential variables (double-differential measurements). Two kinds of double-differential variables are considered: the Higgs boson transverse momentum for various jet multiplicities, and the mass of the leading-pair as a function of the sub-leading mass.

Higgs boson transverse momentum measurements are split into three variables depending on the jet multiplicity $p_{\mathrm{T}}^{4\ell}$ ($n_{\mathrm{jets}} = 0$), $p_{\mathrm{T}}^{4\ell}$ ($n_{\mathrm{jets}} = 1$) and $p_{\mathrm{T}}^{4\ell}$ ($n_{\mathrm{jets}} \geq 2$), whereas the double-mass measurements are performed in five bins of (m_{12}, m_{34}), each bin being orthogonal to the others.

The definition of these variables enable one-dimensional measurements to be performed using the standard framework (described in Sec. 12.5), as the two-dimensional analysis can be simplified to one dimension applying additional cuts. The methodology is therefore the same as for the differential measurements: the categories are the variable bins and the POIs are those defined in Eq. 12.18. The bins of the variables are defined to minimise event migration and maximise significance.

The chosen binning for $p_{\mathrm{T}}^{4\ell}$ against n_{jets} is presented in Tab. 12.34. For the double-differential mass measurements, the bins presented in Fig. 12.46 were defined with the following constraints: the statistics in each bin should be large enough (at least 5 expected signal events) to ensure good sensitivity and low migration, but the bins should not overlap one to each other to allow a safe conversion to one-dimensional

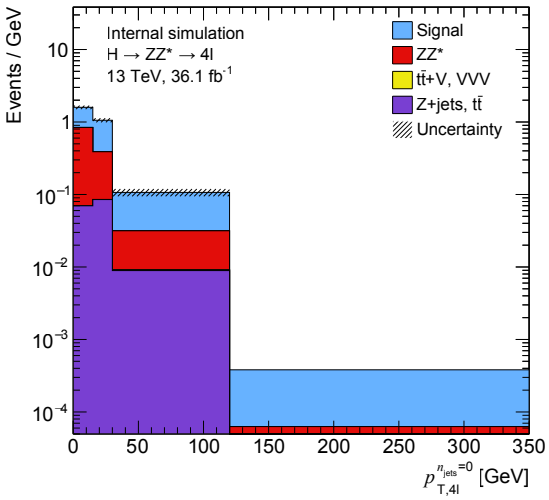

Bin	Signal	ZZ	$Z+\text{jets}\ /\ t\bar{t}$	$t\bar{t}V + VVV$	S/B	σ	Z_0
0	11	12	1	0.0009	0.9	2.3	2.8
1	10	4.6	1.3	0.003	1.7	2.5	3.4
2	6.8	2	0.8	0.03	2.4	2.2	3.1
3	0.07	0.005	0.007	0.003	5.1	0.25	0.41

Figure 12.47 – Expected signal and background yields, and significances for the $p_{\mathrm{T}}^{4\ell}$ ($n_{\mathrm{jets}} = 0$) differential variable [215].

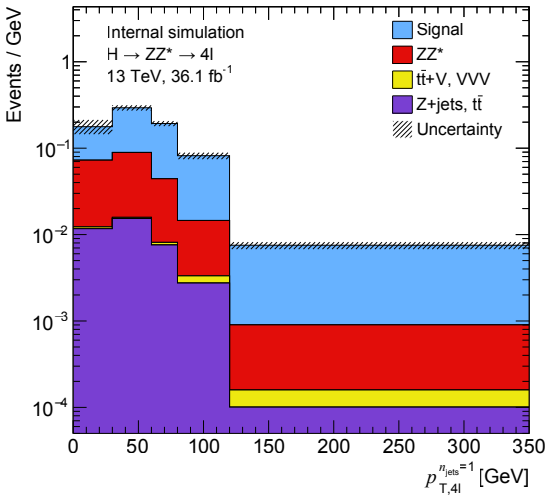

Bin	Signal	ZZ	$Z+\text{jets}\ /\ t\bar{t}$	$t\bar{t}V + VVV$	S/B	σ	Z_0
0	3.1	1.8	0.35	0.02	1.4	1.4	1.8
1	6.1	2.2	0.46	0.01	2.3	2.1	3
2	3	0.72	0.15	0.01	3.4	1.5	2.3
3	2.7	0.45	0.11	0.02	4.6	1.5	2.4
4	1.5	0.17	0.02	0.01	7.4	1.2	2.1

Figure 12.48 – Expected signal and background yields, and significances for the $p_{\mathrm{T}}^{4\ell}$ ($n_{\mathrm{jets}} = 1$) differential variable [215].

measurements. The bins should cover the entire fiducial phase space.

Following these definitions, expected signal and background yields, and significance are presented in Fig. 12.47, 12.48, 12.49, 12.50, for $p_{\mathrm{T}}^{4\ell}$ ($n_{\mathrm{jets}} = 0$), $p_{\mathrm{T}}^{4\ell}$ ($n_{\mathrm{jets}} = 1$), $p_{\mathrm{T}}^{4\ell}$ ($n_{\mathrm{jets}} \geq 2$) and (m_{12}, m_{34}), respectively. Overall, significances $\sigma > 2$ or $Z_0 > 2$ were targeted, except for the first and last bins.

12.6.1 Factors and uncertainties

Calculation of the acceptance and correction factors is performed the same way as described in Sec. 12.5.5, for each production mode (and all modes combined), per double-differential bin of the variables. Results are shown in Fig. 12.51 (Tab. 12.35), Fig. 12.52 (Tab. 12.36), Fig. 12.53 (Tab. 12.37), and Fig. 12.54

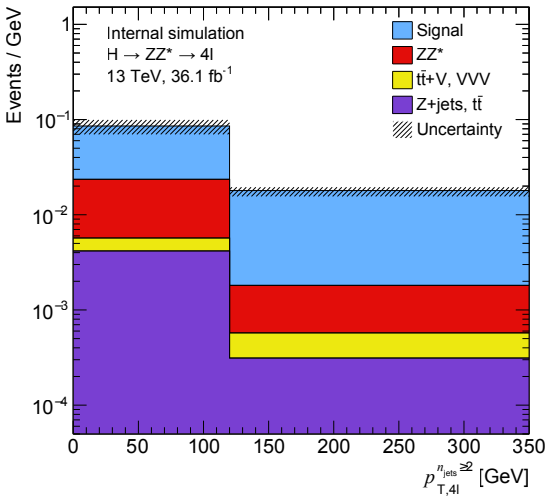

Bin	Signal	ZZ	$Z+\text{jets}\ /\ t\bar{t}$	$t\bar{t}V+VVV$	S/B	σ	Z_0
0	7.5	2.1	0.5	0.18	2.6	2.3	3.4
1	3.7	0.28	0.07	0.06	8.9	1.8	3.4

Figure 12.49 – Expected signal and background yields, and significances for the $p_{\mathrm{T}}^{4\ell}\,(n_{\mathrm{jets}} \geq 2)$ differential variable [215].

(Tab. 12.38), for $p_{\mathrm{T}}^{4\ell}\,(n_{\mathrm{jets}} = 0)$, $p_{\mathrm{T}}^{4\ell}\,(n_{\mathrm{jets}} = 1)$, $p_{\mathrm{T}}^{4\ell}\,(n_{\mathrm{jets}} \geq 2)$ and (m_{12}, m_{34}), respectively. Acceptance factors increase with $p_{\mathrm{T}}^{4\ell}$ for the same reasons as for the one-dimensional case, except that the bins have more inhomogeneous widths making the comparison difficult. This effect cancels out for $\mathcal{C}$ (for the $t\bar{t}H$ production mode, large uncertainties are observed for $p_{\mathrm{T}}^{4\ell}\,(n_{\mathrm{jets}} = 0)$ because the corresponding events contain several jets). For the double-differential mass bins, the evolution of the acceptance factors is similar for all production modes. As expected the bins 0 and 4 have lower acceptance, as they correspond to low m_{34} values: the dressed leptons are weakly boosted and are more likely not to pass the kinetic requirements. The opposite is observed for the bins 1 and 2 for which m_{34} is high. This effect cancels out again for the correction factors which have a flat distribution.

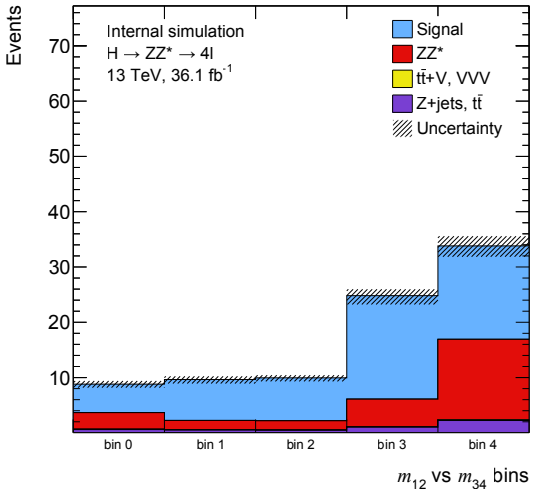

Bin	Signal	ZZ	$Z+\text{jets}\ /\ t\bar{t}$	$t\bar{t}V+VVV$	S/B	σ	Z_0
0	5.2	3	0.59	0.07	1.4	1.7	2.3
1	7.4	1.7	0.5	0.05	3.3	2.4	3.7
2	7.8	1.7	0.46	0.03	3.6	2.5	3.8
3	19	5	1	0.08	3.1	3.8	5.7
4	17	15	2.2	0.12	1	2.9	3.6

Figure 12.50 – Expected signal and background yields, and significances for the (m_{12}, m_{34}) differential variable [215].

Table 12.35 – Acceptance and correction factors per production mode, in bins of $p_{\mathrm{T}}^{4\ell}$ ($n_{\mathrm{jets}} = 0$) [215]. Errors are statistical only.

Acceptance factor [%]						
Bin	Production mode					
	ggF	VBF	WH	ZH	$t\bar{t}H$	$b\bar{b}H$
0	40.43 ± 0.13	38.08 ± 0.30	30.31 ± 0.77	34.11 ± 0.88	0.0 ± 100	40.49 ± 1.03
1	41.01 ± 0.15	38.77 ± 0.20	30.38 ± 0.50	33.40 ± 0.56	78.74 ± 22.15	45.05 ± 0.93
2	42.26 ± 0.14	40.60 ± 0.16	29.42 ± 0.25	34.44 ± 0.27	37.92 ± 6.95	44.64 ± 1.26
3	98.04 ± 5.71	68.35 ± 4.23	33.15 ± 0.58	43.25 ± 0.61	34.52 ± 10.58	16.13 ± 25.11
Correction factor [%]						
Bin	Production mode					
	ggF	VBF	WH	ZH	$t\bar{t}H$	$b\bar{b}H$
0	49.97 ± 0.32	45.49 ± 1.13	41.73 ± 2.38	43.41 ± 2.53	0.00 ± 100	54.64 ± 3.18
1	48.14 ± 0.32	46.32 ± 0.78	44.35 ± 1.69	43.36 ± 1.71	16.49 ± 24.21	49.74 ± 2.52
2	48.46 ± 0.39	47.53 ± 0.59	45.81 ± 0.87	48.83 ± 0.89	35.50 ± 20.58	50.01 ± 3.39
3	206 ± 49	312 ± 46	49.67 ± 2.06	52.66 ± 1.84	88.34 ± 47.40	600 ± 1200

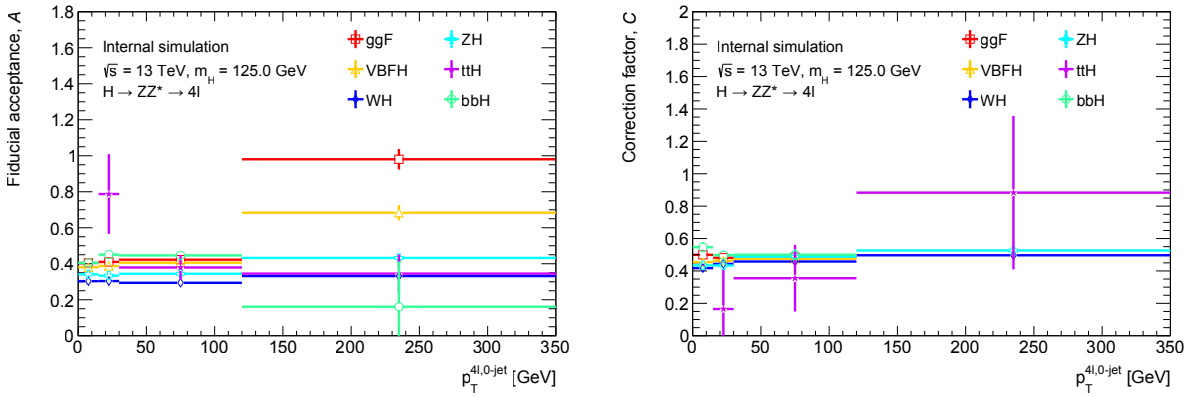

(a) Acceptance factor

(b) Correction factor

Figure 12.51 – Acceptance and correction factors per production mode, in bins of $p_{\mathrm{T}}^{4\ell}$ ($n_{\mathrm{jets}} = 0$) [215]. Errors are statistical only.

Correction factors above 1 are found for the $p_{\mathrm{T}}^{4\ell}$ variable at low jet multiplicities. This is due to the very few events which pass 100 GeV in the 0-jet bin or the 1-jet bin. Detector resolution effects in reconstruction affect the $\mathcal{C}$ factors greatly.

Uncertainties on the factors and background shape and yields are the same as for the standard differential measurements, described in Sec. 12.5.6.

12.6.2 Bin definition and methodology checks

The double-differential variable bin definition are further checked by calculating migration matrices a described in Sec. 12.5.3. Results are presented in Fig. 12.55. Migrations are very contained for the $p_{\mathrm{T}}^{4\ell}$

Table 12.36 – Acceptance and correction factors per production mode, in bins of $p_{\mathrm{T}}^{4\ell}$ ($n_{\mathrm{jets}} = 1$) [215]. Errors are statistical only.

Acceptance factor [%]						
Bin	Production mode					
	ggF	VBF	WH	ZH	$t\bar{t}H$	$b\bar{b}H$
0	36.85 ± 0.29	39.80 ± 0.20	33.04 ± 0.50	35.81 ± 0.53	42.63 ± 6.55	42.09 ± 1.78
1	42.28 ± 0.17	41.19 ± 0.10	34.03 ± 0.31	35.85 ± 0.33	40.77 ± 4.50	46.03 ± 1.25
2	44.23 ± 0.20	43.17 ± 0.12	36.30 ± 0.41	37.57 ± 0.42	38.04 ± 5.53	46.77 ± 2.39
3	46.19 ± 0.22	45.86 ± 0.12	37.99 ± 0.40	39.72 ± 0.41	30.26 ± 3.49	48.67 ± 3.45
4	51.72 ± 0.31	51.95 ± 0.15	42.22 ± 0.51	44.81 ± 0.52	37.68 ± 3.63	69.65 ± 6.89
Correction factor [%]						
Bin	Production mode					
	ggF	VBF	WH	ZH	$t\bar{t}H$	$b\bar{b}H$
0	106 ± 1	59.17 ± 0.86	51.83 ± 1.74	49.18 ± 1.70	35.89 ± 12.97	64.97 ± 6.22
1	52.84 ± 0.44	51.93 ± 0.41	47.73 ± 1.00	48.31 ± 1.05	27.16 ± 12.69	49.00 ± 3.48
2	47.55 ± 0.54	49.48 ± 0.47	47.49 ± 1.22	48.47 ± 1.29	33.50 ± 13.20	46.58 ± 6.06
3	49.55 ± 0.60	50.50 ± 0.42	49.21 ± 1.20	47.62 ± 1.18	27.36 ± 9.68	59.42 ± 10.19
4	53.43 ± 0.84	53.83 ± 0.52	56.57 ± 1.63	55.17 ± 1.52	51.48 ± 11.43	44.43 ± 12.84

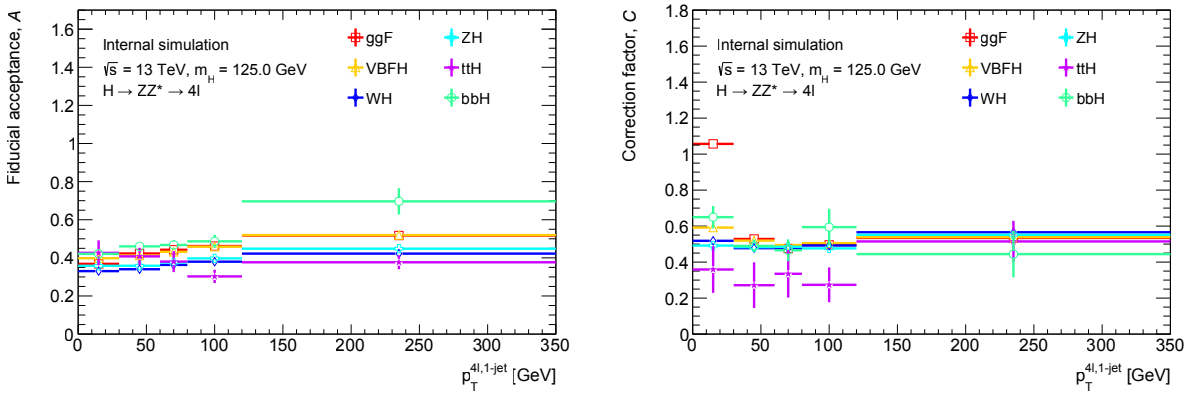

(a) Acceptance factor

(b) Correction factor

Figure 12.52 – Acceptance and correction factors per production mode, in bins of $p_{\mathrm{T}}^{4\ell}$ ($n_{\mathrm{jets}} = 1$) [215]. Errors are statistical only.

Table 12.37 – Acceptance and correction factors per production mode, in bins of $p_{\mathrm{T}}^{4\ell}$ ($n_{\mathrm{jets}} \geq 2$) [215]. Errors are statistical only.

Acceptance factor [%]						
Bin	Production mode					
	ggF	VBF	WH	ZH	$t\bar{t}H$	$b\bar{b}H$
0	42.31 ± 0.19	43.90 ± 0.06	36.83 ± 0.20	37.90 ± 0.20	45.11 ± 0.38	44.89 ± 1.05
1	50.47 ± 0.24	51.79 ± 0.08	45.90 ± 0.29	47.15 ± 0.29	50.34 ± 0.50	49.63 ± 3.65
Correction factor [%]						
Bin	Production mode					
	ggF	VBF	WH	ZH	$t\bar{t}H$	$b\bar{b}H$
0	68.86 ± 0.60	61.18 ± 0.25	54.84 ± 0.68	53.10 ± 0.63	36.44 ± 0.87	58.16 ± 3.23
1	60.64 ± 0.72	63.15 ± 0.33	58.29 ± 0.89	58.15 ± 0.88	44.02 ± 1.20	44.79 ± 9.13

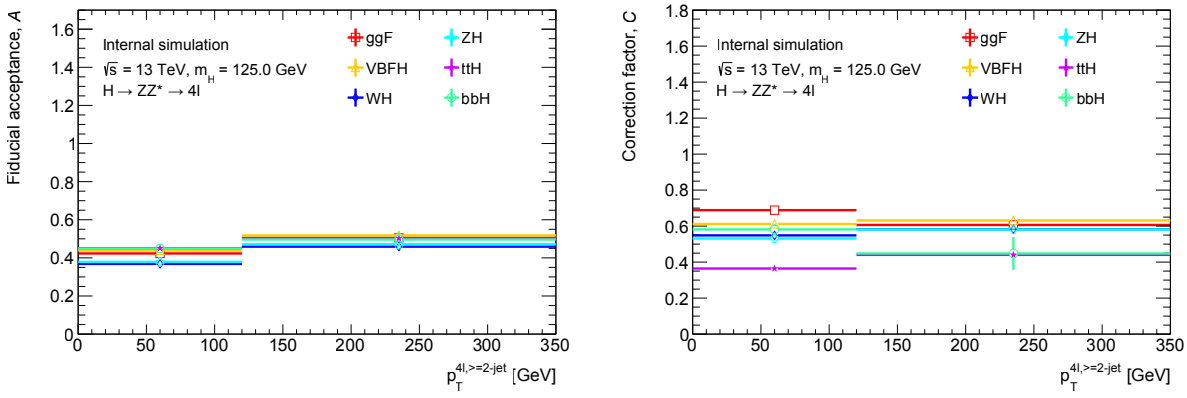

(a) Acceptance factor

(b) Correction factor

Figure 12.53 – Acceptance and correction factors per production mode, in bins of $p_{\mathrm{T}}^{4\ell}$ ($n_{\mathrm{jets}} \geq 2$) [215]. Errors are statistical only.

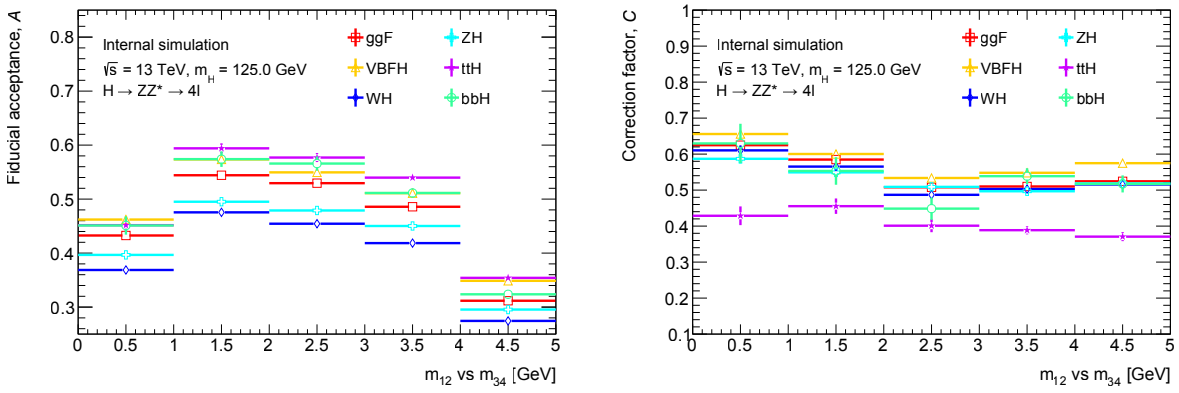

(a) Acceptance factor

(b) Correction factor

Figure 12.54 – Acceptance and correction factors per production mode, in bins of (m_{12}, m_{34}) [215]. Errors are statistical only.

Table 12.38 – Acceptance and correction factors per production mode, in bins of (m_{12}, m_{34}) [215]. Errors are statistical only.

Acceptance factor [%]						
Bin	Production mode					
	ggF	VBF	WH	ZH	$t\bar{t}H$	$b\bar{b}H$
0	43.26 ± 0.19	46.21 ± 0.13	36.87 ± 0.38	39.67 ± 0.39	45.17 ± 1.07	45.11 ± 1.70
1	54.42 ± 0.26	57.35 ± 0.12	47.55 ± 0.36	49.51 ± 0.37	59.40 ± 0.93	57.40 ± 1.44
2	52.95 ± 0.18	54.95 ± 0.10	45.44 ± 0.32	47.89 ± 0.33	57.70 ± 0.84	56.58 ± 1.33
3	48.58 ± 0.12	51.10 ± 0.07	41.85 ± 0.20	45.02 ± 0.20	53.98 ± 0.54	51.13 ± 0.84
4	31.17 ± 0.09	34.87 ± 0.05	27.44 ± 0.15	29.54 ± 0.16	35.41 ± 0.45	32.37 ± 0.67
Correction factor [%]						
Bin	Production mode					
	ggF	VBF	WH	ZH	$t\bar{t}H$	$b\bar{b}H$
0	62.47 ± 0.61	65.58 ± 0.54	61.04 ± 1.37	58.69 ± 1.28	42.87 ± 2.60	62.96 ± 5.46
1	58.48 ± 0.47	60.03 ± 0.42	56.53 ± 1.05	54.93 ± 1.01	45.54 ± 2.14	55.32 ± 3.83
2	50.78 ± 0.39	53.36 ± 0.36	48.69 ± 0.86	50.90 ± 0.89	40.11 ± 1.80	44.85 ± 3.10
3	51.00 ± 0.25	54.80 ± 0.24	50.29 ± 0.57	49.68 ± 0.56	38.86 ± 1.16	53.87 ± 2.20
4	52.44 ± 0.27	57.48 ± 0.25	51.56 ± 0.60	51.85 ± 0.59	37.07 ± 1.25	51.72 ± 2.37

variables, but the bins 2 and 3 of the double-mass measurements suffer from the peaked leading-mass distribution.

Background yields are also checked in the various control regions defined in Sec. 12.4.2, and tests on Asimov data following the standard procedure (see Sec. 12.4.4) are performed. Overall no unexpected behaviour is observed which would invalidate the methodology.

12.6.3 Results using 36.1 fb^{-1}

Distributions of the variables used for the double-differential measurements are presented in Fig. 11.15 (b, c, d) and 12.56, for $p_{\mathrm{T}}^{4\ell}$ ($n_{\mathrm{jets}} = 0$), $p_{\mathrm{T}}^{4\ell}$ ($n_{\mathrm{jets}} = 1$), $p_{\mathrm{T}}^{4\ell}$ ($n_{\mathrm{jets}} \geq 2$) and (m_{12}, m_{34}), respectively, for the inclusive events. Overall, there is no strong disagreement with the SM predictions.

Results of the fit are compared to the expectations in Tab. 12.39, Tab. 12.40, Tab. 12.41 and Tab. 12.42, for $p_{\mathrm{T}}^{4\ell}$ ($n_{\mathrm{jets}} = 0$), $p_{\mathrm{T}}^{4\ell}$ ($n_{\mathrm{jets}} = 1$), $p_{\mathrm{T}}^{4\ell}$ ($n_{\mathrm{jets}} \geq 2$) and (m_{12}, m_{34}), respectively. Same results are shown in Fig. 12.57. Taking into account the uncertainties, results are consistent with SM Higgs-boson production.

In order to check the quality of the fits, the likelihood scans in the vicinity of the fitted cross sections are checked, and $-2\ln\Lambda$ appears to follow a χ^2 law as expected as the curves are quite symmetrical.

12.7 Interpretations of the measurements

Following these measurements, additional studies were carried out, which are beyond the scope of this thesis. These studies aim at constraining the modified Higgs-boson interactions using the framework of pseudo variables [172, 173] (see Sec. 11.2.2 for the description of the MC sample used). Limits are set on the couplings ($\varepsilon_{\mathrm{L}}, \varepsilon_{\mathrm{R}}$ of SM values equal to 0) associated with the contact interaction of the Higgs

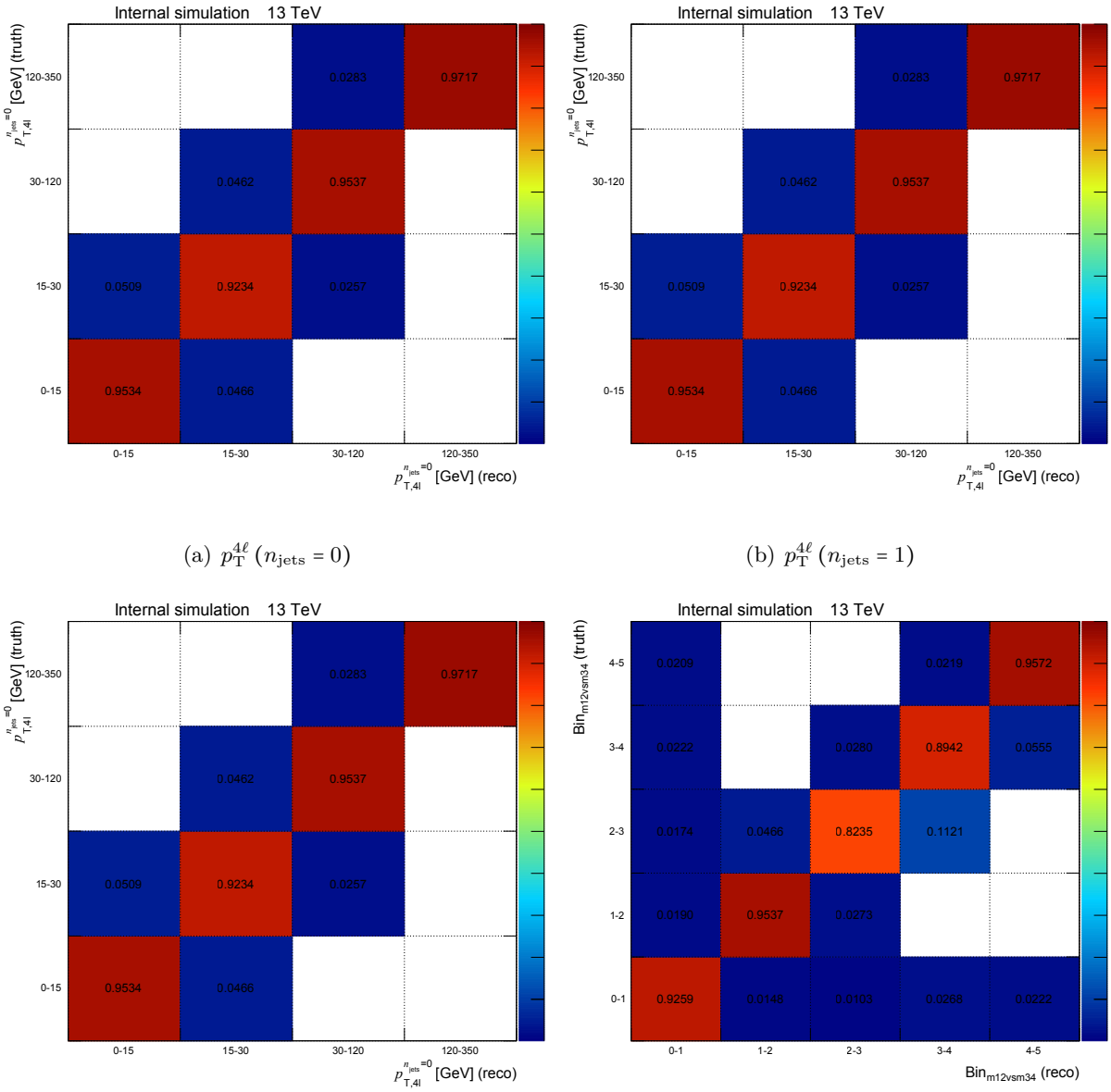

(a) $p_{\mathrm{T}}^{4\ell}$ ($n_{\mathrm{jets}} = 0$)

(b) $p_{\mathrm{T}}^{4\ell}$ ($n_{\mathrm{jets}} = 1$)

(c) $p_{\mathrm{T}}^{4\ell}$ ($n_{\mathrm{jets}} \geq 2$)

(d) (m_{12}, m_{34})

Figure 12.55 – Double-differential migration matrices [215].

Table 12.39 – Comparison of measured and expected differential fiducial cross section in bins of $p_{\mathrm{T}}^{4\ell}$ ($n_{\mathrm{jets}} = 0$) [215].

POI	σ_{inj} [fb]	σ_{fit} [fb]	Relative Error
σ_{bin0} [fb]	0.0423	$0.05^{+0.02}_{-0.02}$	$^{+42\%}_{-34\%}$
σ_{bin1} [fb]	0.039	$0.03^{+0.02}_{-0.01}$	$^{+52\%}_{-42\%}$
σ_{bin2} [fb]	0.00436	$0.007^{+0.003}_{-0.002}$	$^{+38\%}_{-30\%}$
σ_{bin3} [fb]	1.37×10^{-5}	$0^{+0.0002}_{-1}$	$^{+200\%}_{-100\%}$

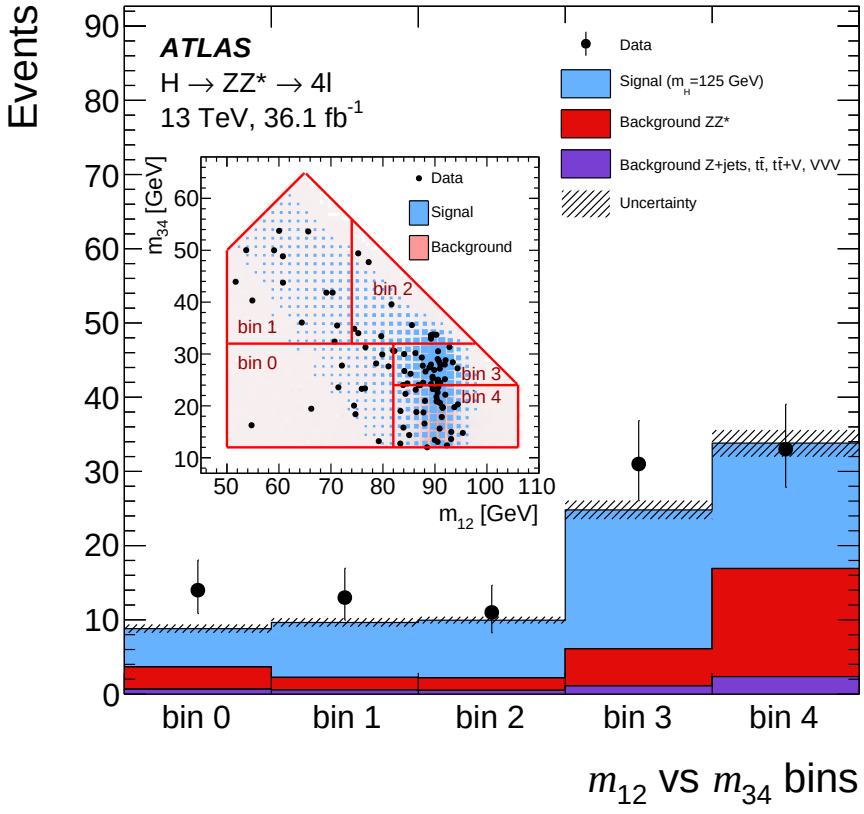

Figure 12.56 – Inclusive (m_{12}, m_{34}) distribution for the various bins [215].

Table 12.40 – Comparison of measured and expected differential fiducial cross section in bins of $p_{\mathrm{T}}^{4\ell}$ ($n_{\mathrm{jets}} = 1$) [215].

POI	σ_{inj} [fb]	σ_{fit} [fb]	Relative Error
σ_{bin0} [fb]	0.00296	$0.007^{+0.004}_{-0.003}$	$^{+52\%}_{-38\%}$
σ_{bin1} [fb]	0.0109	$0^{+0.01}_{-1}$	$^{+200\%}_{-100\%}$
σ_{bin2} [fb]	0.00867	$0.008^{+0.007}_{-0.005}$	$^{+81\%}_{-56\%}$
σ_{bin3} [fb]	0.00377	$0.008^{+0.004}_{-0.003}$	$^{+51\%}_{-38\%}$
σ_{bin4} [fb]	0.000283	$0.0005^{+0.0004}_{-0.0003}$	$^{+80\%}_{-54\%}$

Table 12.41 – Comparison of measured and expected differential fiducial cross section in bins of $p_{\mathrm{T}}^{4\ell}$ ($n_{\mathrm{jets}} \geq 2$) [215].

POI	σ_{inj} [fb]	σ_{fit} [fb]	Relative Error
σ_{bin0} [fb]	0.00271	$0.004^{+0.002}_{-0.001}$	$^{+41\%}_{-31\%}$
σ_{bin1} [fb]	0.000625	$0.0014^{+0.0006}_{-0.0004}$	$^{+41\%}_{-33\%}$

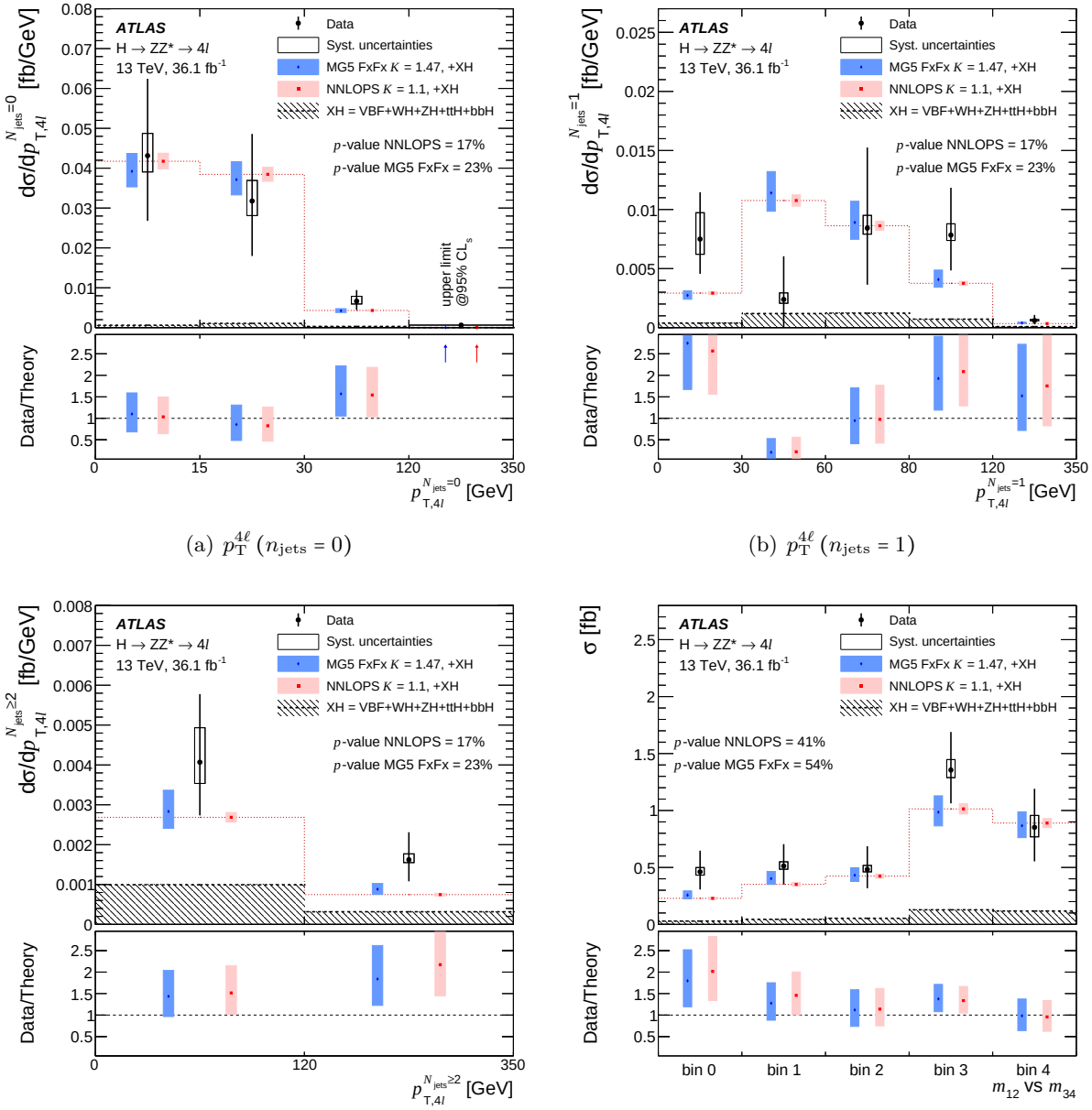

(a) $p_{\mathrm{T}}^{4\ell}$ ($n_{\mathrm{jets}} = 0$)

(b) $p_{\mathrm{T}}^{4\ell}$ ($n_{\mathrm{jets}} = 1$)

(c) $p_{\mathrm{T}}^{4\ell}$ ($n_{\mathrm{jets}} \geq 2$)

(d) $p_{\mathrm{T}}^{4\ell}$ (m_{12}, m_{34})

Figure 12.57 – Comparison of measured and expected double-differential fiducial cross sections [215].

Table 12.42 – Comparison of measured and expected differential fiducial cross section in bins of (m_{12}, m_{34}) [215].

POI	σ_{inj} [fb]	σ_{fit} [fb]	Relative Error
σ_{bin0} [fb]	0.231	$0.5^{+0.20}_{-0.17}$	$^{+42\%}_{-36\%}$
σ_{bin1} [fb]	0.355	$0.5^{+0.19}_{-0.16}$	$^{+37\%}_{-31\%}$
σ_{bin2} [fb]	0.428	$0.5^{+0.20}_{-0.17}$	$^{+41\%}_{-34\%}$
σ_{bin3} [fb]	1.03	$1.4^{+0.39}_{-0.36}$	$^{+28\%}_{-26\%}$
σ_{bin4} [fb]	0.899	$0.9^{+0.75}_{-0.74}$	$^{+84\%}_{-83\%}$

boson with the left-handed and right-handed leptons, under the assumption of lepton flavour universality. The coupling κ of the Higgs boson to the Z bosons is also varied from its SM value (1). All the other parameters of the framework are fixed their SM expectations (the other pseudo variables ε_{ZZ}, $\varepsilon_{Z\gamma}$ and $\varepsilon_{\gamma\gamma}$ are not included in the study).

Since all the contact terms and the coupling to the Z bosons have the same Lorentz structure as the other SM terms, the lepton angular distributions are not affected by any changes on these parameters. Only the dilepton invariant masses vary. The difference in χ^2 between observation and prediction for the measured double-differential cross sections in bins of (m_{12}, m_{34}) is therefore used to constrain the anomalous terms. Note that the measurements of the inclusive cross section would be sufficient to set a limit on the parameters of interest, but this limit would be elliptic and using the invariant masses allows the constraints to be further improved, especially in the positive ε_{R} and negative ε_{L} region.

The study enables two sets of limits (at 95% confidence level) to be derived: ε_{L} against ε_{R} and ε_{L} against κ. Following Ref. [173], $\varepsilon_{\text{R}} = 0.48 \times \varepsilon_{\text{L}}$ for the second set of limits. The p-values at 1σ and 2σ on the two-dimensional limits were checked using the generation of an Asimov dataset containing 500 SM-like events. Results are shown in Fig. 12.58. Expected and observed limits are shifted, but no significant deviations with respect to the SM are found.

12.8 Conclusion and potential improvements

Measurements of the inclusive and differential fiducial cross sections of Higgs-boson production in the $H \to ZZ^* \to 4\ell$ decay channel were presented in this chapter. These results are based on data extracted from $36.1\,\text{fb}^{-1}$ $\sqrt{s} = 13\,\text{TeV}$ proton–proton collisions recorded by the ATLAS detector at the LHC in 2015 and 2016. The inclusive fiducial cross section is measured to be $\sigma_{\text{Fid}} = 3.62^{+0.50}_{-0.50}(\text{stat})^{+0.25}_{-0.20}(\text{syst})\text{fb}$ in agreement with the SM prediction of $2.91 \pm 0.13\,\text{fb}$.

The inclusive fiducial cross section is also extrapolated to the total phase space. Several differential fiducial cross sections are measured for observables sensitive to the Higgs boson production and decay, including kinematic distributions of the jets produced together with the Higgs boson. Good agreement is found between the data and the predictions of the Standard Model. The extracted cross-section distributions are used to constrain anomalous Higgs boson interactions with Standard Model particles using the pseudo-observable framework.

Potential improvements of these results could be achieved in the coming years mainly from the reduced uncertainties due to increased statistics. Observations should be compared to the new predictions, especially the measurements of $p_{\text{T}}^{4\ell}$, the jet multiplicity and the transverse momentum of the leading jet, which

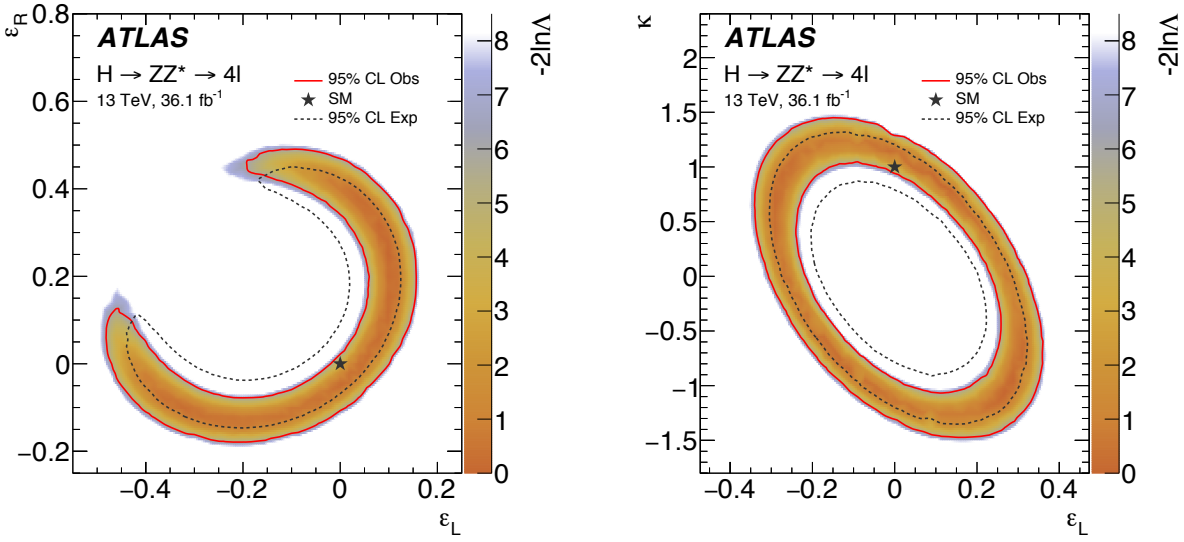

(a) ε_{R} against ε_{L}

(b) κ against ε_{L}

Figure 12.58 – Limits on contact-interaction decay to the left (ε_{L}) and right-handed (ε_{R}) leptons, and coupling to the Z bosons (κ) for the Higgs-to-four-lepton channel. The limits are presented for (a) ε_{R} against ε_{L} and (b) κ against ε_{L} ($\varepsilon_{\mathrm{R}} = 0.48 \times \varepsilon_{\mathrm{L}}$). The use of the double-differential cross-section measurements in bins of (m_{12}, m_{34}) improves the limits, especially in the region having $\varepsilon_{\mathrm{R}} > 0$ and $\varepsilon_{\mathrm{L}} < 0$. Expected and observed limits are shifted, but no significant deviations with respect to the SM are found [215].

are very sensitive to higher orders in QCD. The measurements should include more double-differential measurements (jet variables against each other) and differential measurements should be conducted per final state with more statistics. Especially the binning of the (m_{12}, m_{34}) distribution should be refined to precisely probe the phase space and improve the constraints on the anomalous couplings. The combination of the results with the $H \to \gamma\gamma$ is already on the way, and possible combination with CMS would be desirable. However, the frame of the measurements should be first adapted, especially the treatment of the systematic uncertainties. Finally, if statistics allow it, the measurements could be performed in various categories corresponding to the production modes.

Appendices

Appendix A

Additional information on the validation of the isolation scale factors

This appendix complements the information provided in Sec. 7.5.3.

Figures A.1, A.2, A.3, A.4, A.5 and A.6 show the validation plots against p_{T}^{μ} of the *LooseTrackOnly*, *Loose*, *Tight*, *GradientLoose*, *Gradient* and *FixedCutTightTrackOnly* isolation working points. The checks are carried out for all events, and for events falling in various η^{μ} bins.

Figures A.7, A.8, A.9, A.10, A.11 and A.12 present the validation plots against p_{T}^{μ} of the *LooseTrackOnly*, *Loose*, *Tight*, *GradientLoose*, *Gradient* and *FixedCutTightTrackOnly* isolation working points, for various $\Delta R_{\mu j}$ bins to check the additional $\Delta R_{\mu j}$ systematics.

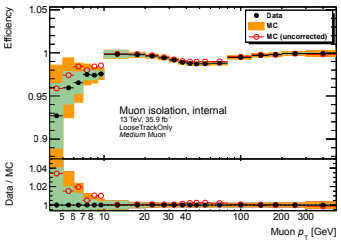

(a) Integrated over η

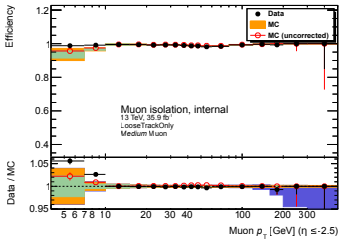

(b) $\eta < -2.5$

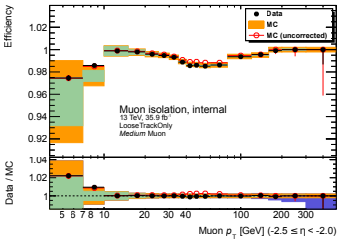

(c) $-2.5 < \eta < -2.0$

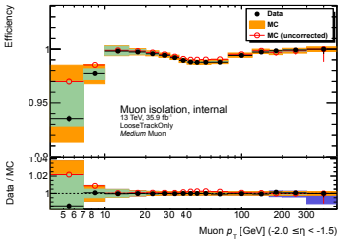

(d) $-2.0 < \eta < -1.5$

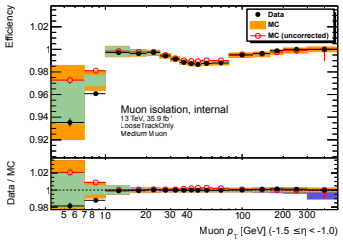

(e) $-1.5 < \eta < -1.0$

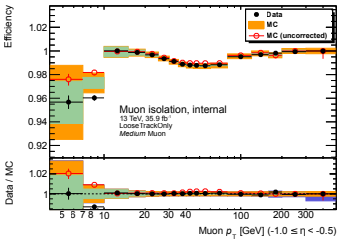

(f) $-1.0 < \eta < -0.5$

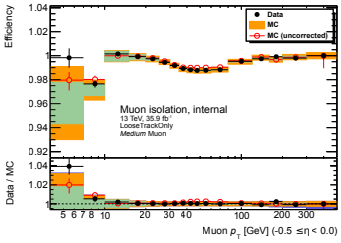

(g) $-0.5 < \eta < 0.0$

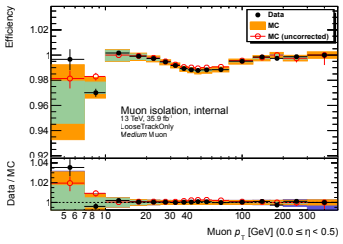

(h) $0.0 < \eta < 0.5$

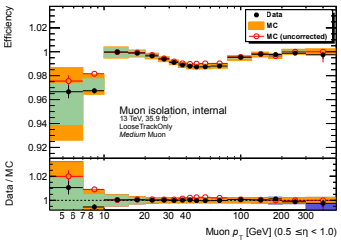

(i) $0.5 < \eta < 1.0$

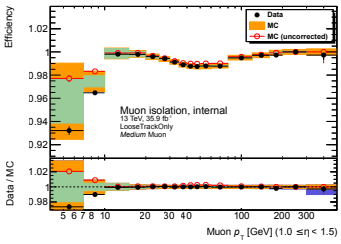

(j) $1.0 < \eta < 1.5$

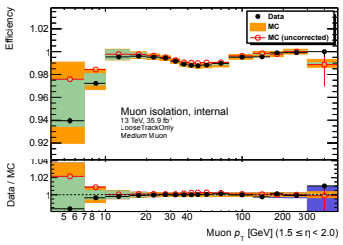

(k) $1.5 < \eta < 2.0$

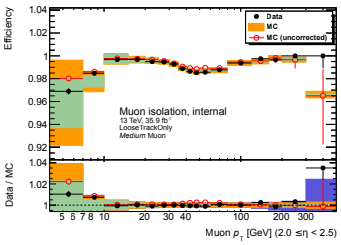

(l) $2.0 < \eta < 2.5$

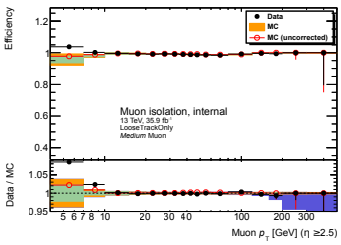

(m) $\eta > 2.5$

Figure A.1 – Validation plots of the *LooseTrackOnly* scale factors, integrated over η and in various η regions.

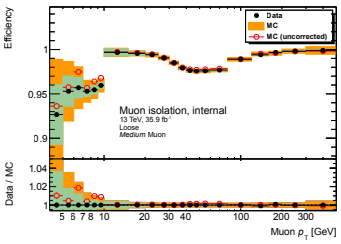

(a) Integrated over η

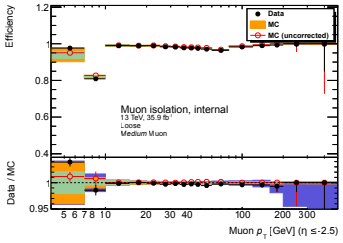

(b) $\eta < -2.5$

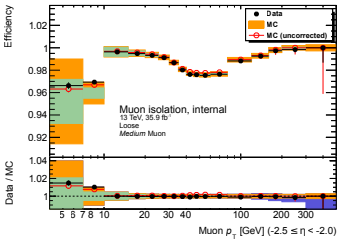

(c) $-2.5 < \eta < -2.0$

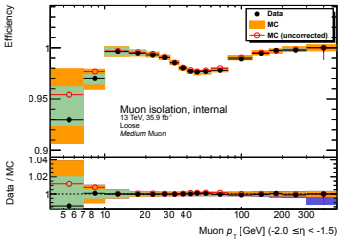

(d) $-2.0 < \eta < -1.5$

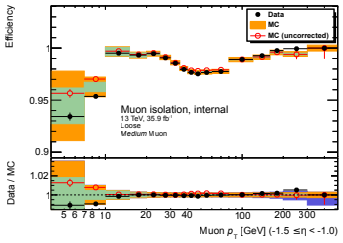

(e) $-1.5 < \eta < -1.0$

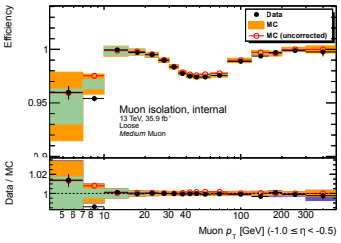

(f) $-1.0 < \eta < -0.5$

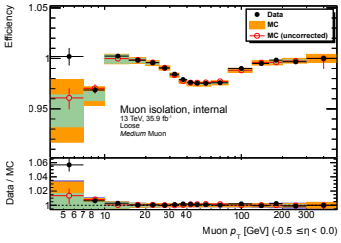

(g) $-0.5 < \eta < 0.0$

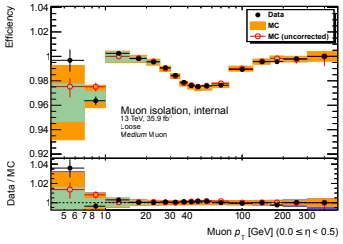

(h) $0.0 < \eta < 0.5$

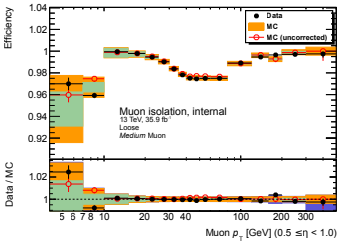

(i) $0.5 < \eta < 1.0$

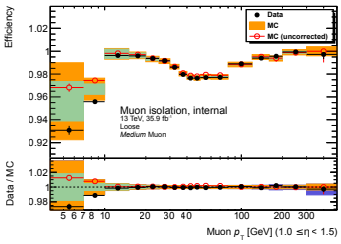

(j) $1.0 < \eta < 1.5$

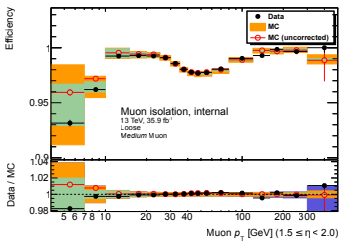

(k) $1.5 < \eta < 2.0$

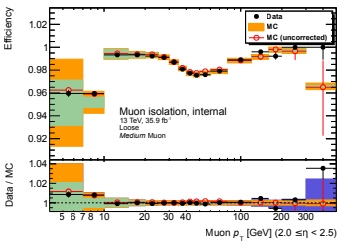

(l) $2.0 < \eta < 2.5$

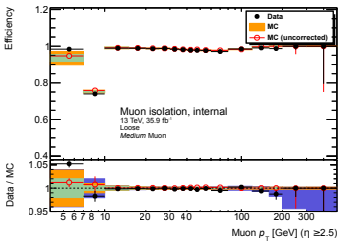

(m) $\eta > 2.5$

Figure A.2 – Validation plots of the *Loose* scale factors, integrated over η and in various η regions.

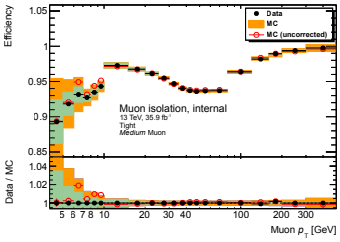

(a) Integrated over η

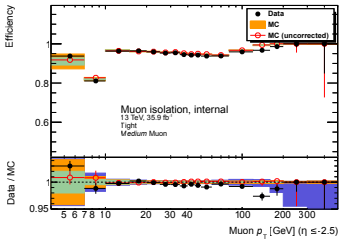

(b) $\eta < -2.5$

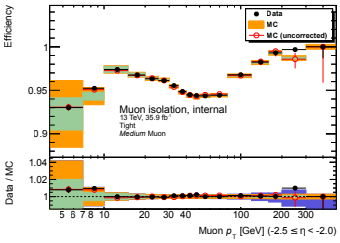

(c) $-2.5 < \eta < -2.0$

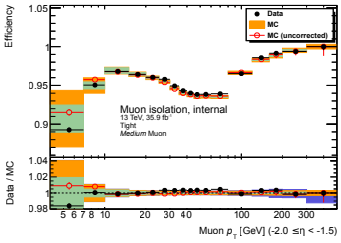

(d) $-2.0 < \eta < -1.5$

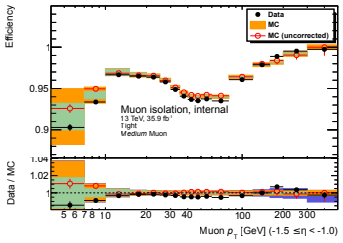

(e) $-1.5 < \eta < -1.0$

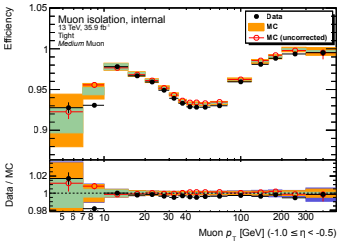

(f) $-1.0 < \eta < -0.5$

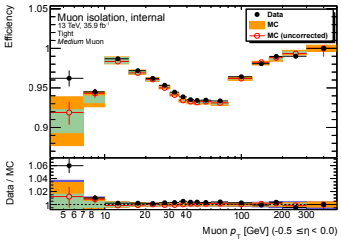

(g) $-0.5 < \eta < 0.0$

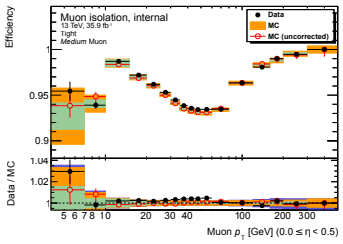

(h) $0.0 < \eta < 0.5$

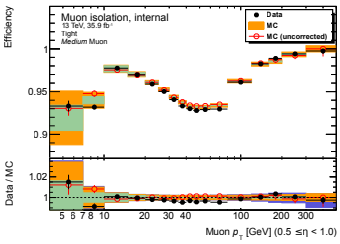

(i) $0.5 < \eta < 1.0$

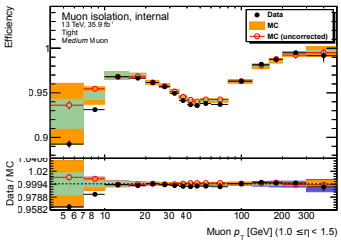

(j) $1.0 < \eta < 1.5$

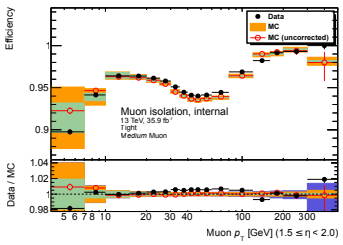

(k) $1.5 < \eta < 2.0$

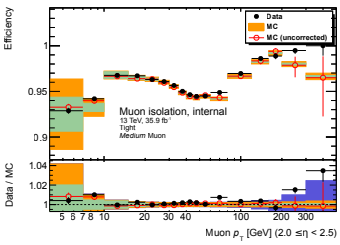

(l) $2.0 < \eta < 2.5$

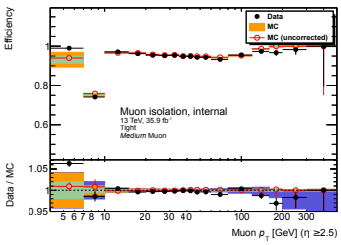

(m) $\eta > 2.5$

Figure A.3 – Validation plots of the *Tight* scale factors, integrated over η and in various η regions.

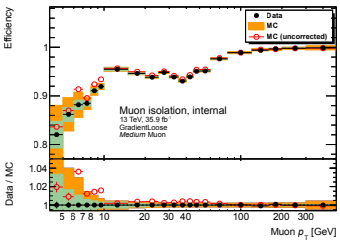

(a) Integrated over η

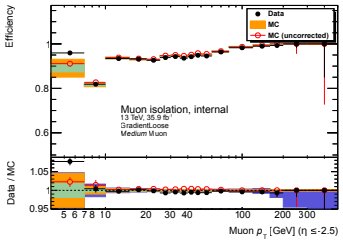

(b) $\eta < -2.5$

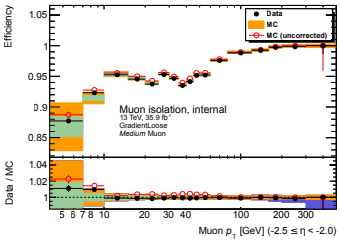

(c) $-2.5 < \eta < -2.0$

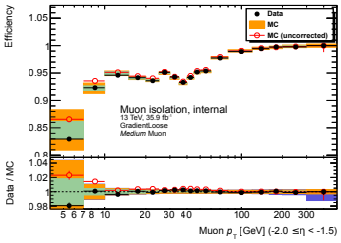

(d) $-2.0 < \eta < -1.5$

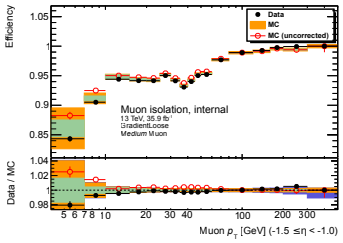

(e) $-1.5 < \eta < -1.0$

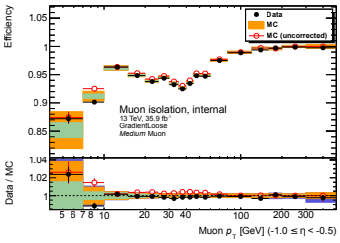

(f) $-1.0 < \eta < -0.5$

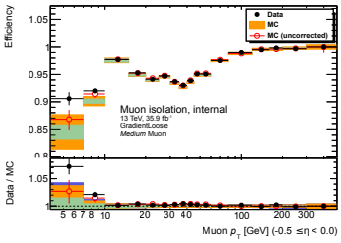

(g) $-0.5 < \eta < 0.0$

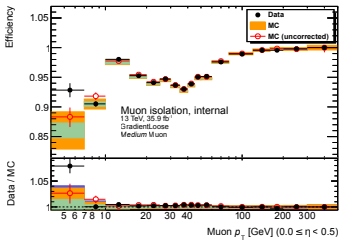

(h) $0.0 < \eta < 0.5$

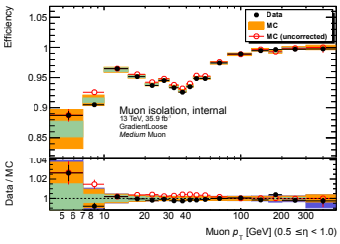

(i) $0.5 < \eta < 1.0$

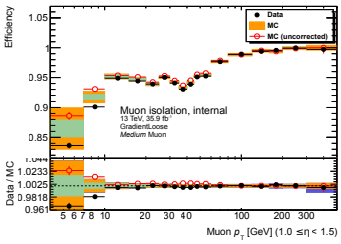

(j) $1.0 < \eta < 1.5$

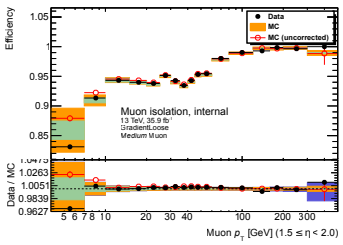

(k) $1.5 < \eta < 2.0$

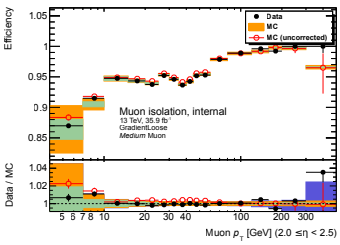

(l) $2.0 < \eta < 2.5$

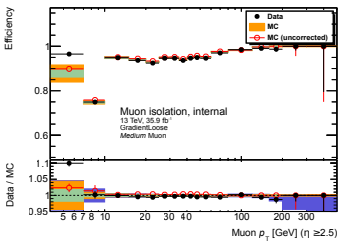

(m) $\eta > 2.5$

Figure A.4 – Validation plots of the *GradientLoose* scale factors, integrated over η and in various η regions.

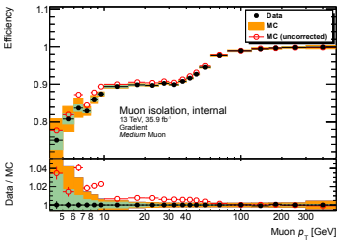

(a) Integrated over η

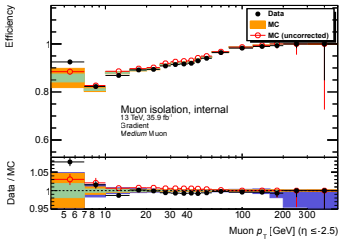

(b) $\eta < -2.5$

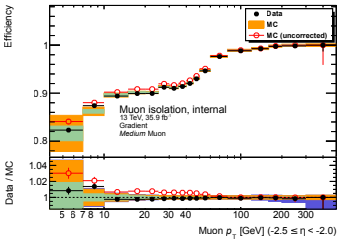

(c) $-2.5 < \eta < -2.0$

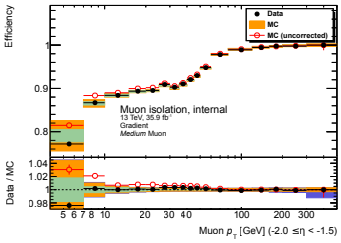

(d) $-2.0 < \eta < -1.5$

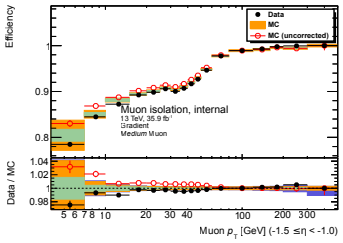

(e) $-1.5 < \eta < -1.0$

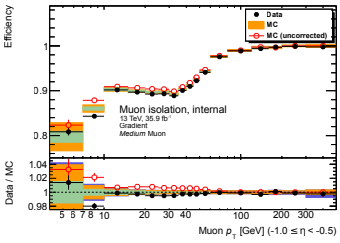

(f) $-1.0 < \eta < -0.5$

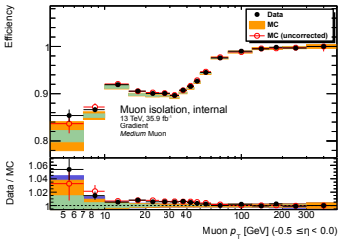

(g) $-0.5 < \eta < 0.0$

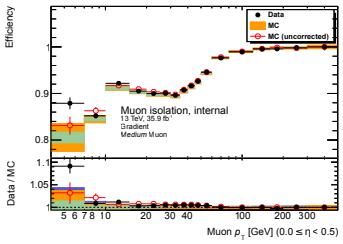

(h) $0.0 < \eta < 0.5$

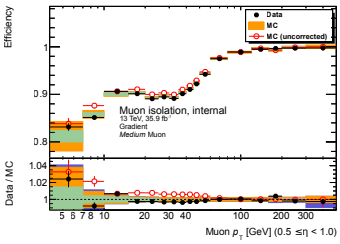

(i) $0.5 < \eta < 1.0$

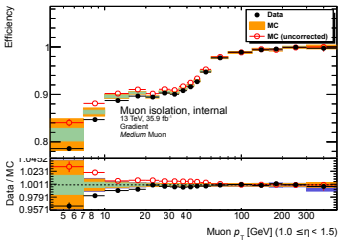

(j) $1.0 < \eta < 1.5$

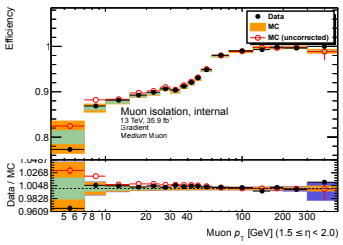

(k) $1.5 < \eta < 2.0$

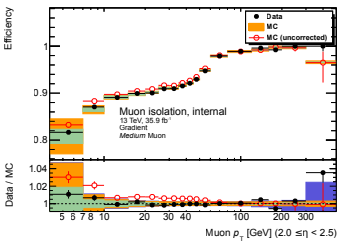

(l) $2.0 < \eta < 2.5$

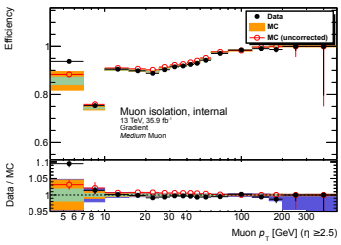

(m) $\eta > 2.5$

Figure A.5 – Validation plots of the *Gradient* scale factors, integrated over η and in various η regions.

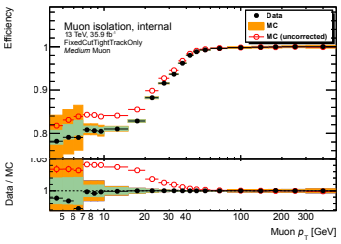

(a) Integrated over η

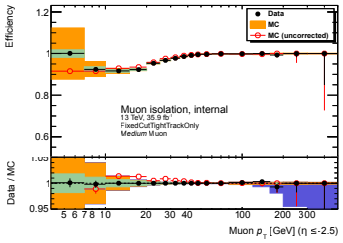

(b) $\eta < -2.5$

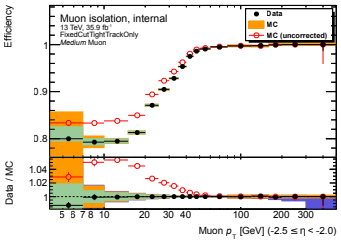

(c) $-2.5 < \eta < -2.0$

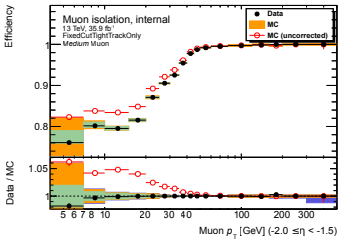

(d) $-2.0 < \eta < -1.5$

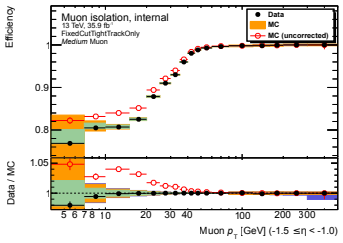

(e) $-1.5 < \eta < -1.0$

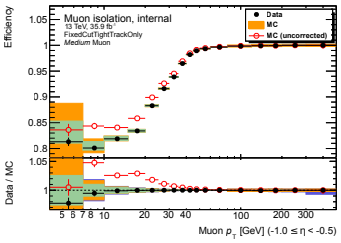

(f) $-1.0 < \eta < -0.5$

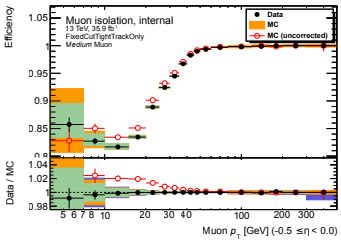

(g) $-0.5 < \eta < 0.0$

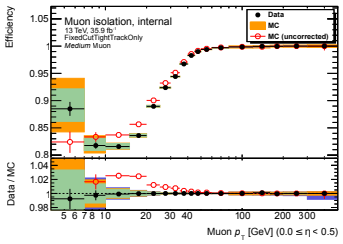

(h) $0.0 < \eta < 0.5$

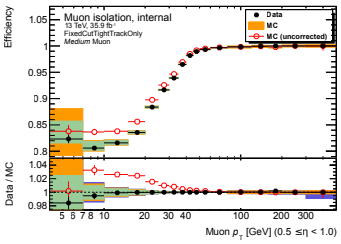

(i) $0.5 < \eta < 1.0$

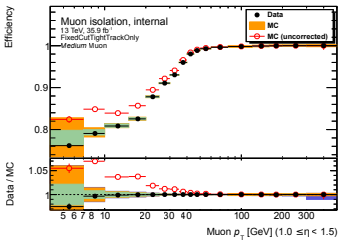

(j) $1.0 < \eta < 1.5$

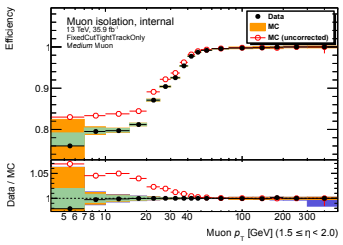

(k) $1.5 < \eta < 2.0$

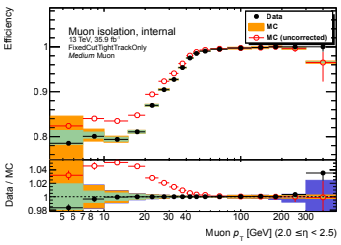

(l) $2.0 < \eta < 2.5$

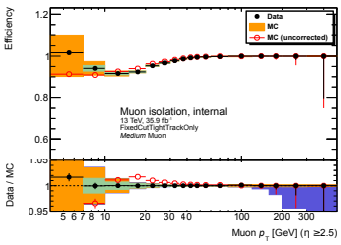

(m) $\eta > 2.5$

Figure A.6 – Validation plots of the *FixedCutTightTrackOnly* scale factors, integrated over η and in various η regions.

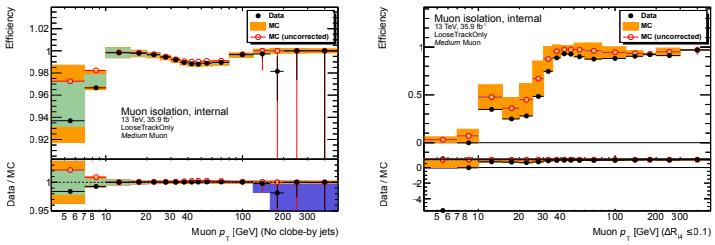

(a) No close-by jets

(b) $\Delta R_{\mu j} \leq 0.1$

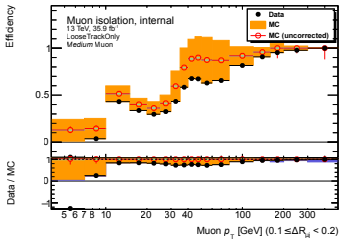

(c) $0.1 \leq \Delta R_{\mu j} < 0.2$

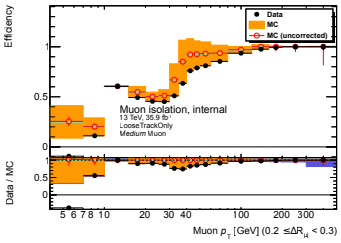

(d) $0.2 \leq \Delta R_{\mu j} < 0.3$

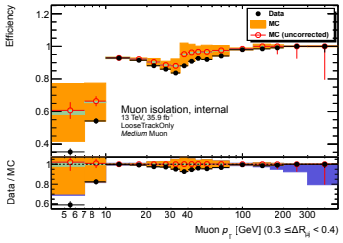

(e) $0.3 \leq \Delta R_{\mu j} < 0.4$

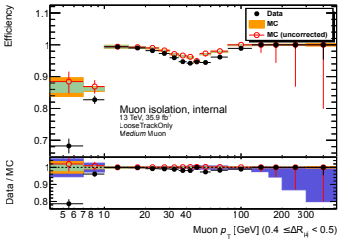

(f) $0.4 \leq \Delta R_{\mu j} < 0.5$

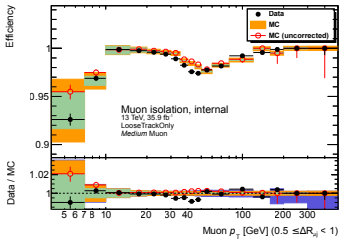

(g) $0.5 \leq \Delta R_{\mu j} < 1.0$

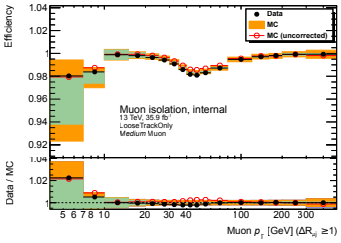

(h) $\Delta R_{\mu j} \geq 1.0$

Figure A.7 – Validation plots of the *LooseTrackOnly* scale factors, in various $\Delta R_{\mu j}$ regions.

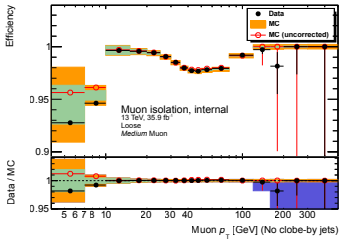

(a) No close-by jets

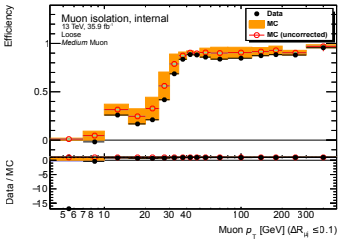

(b) $\Delta R_{\mu j} \leq 0.1$

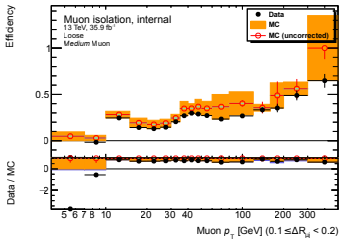

(c) $0.1 \leq \Delta R_{\mu j} < 0.2$

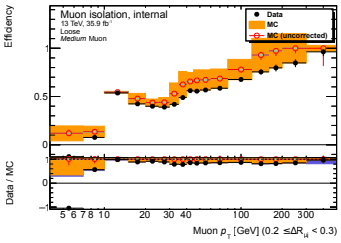

(d) $0.2 \leq \Delta R_{\mu j} < 0.3$

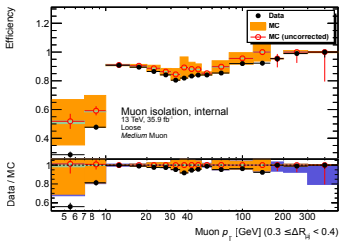

(e) $0.3 \leq \Delta R_{\mu j} < 0.4$

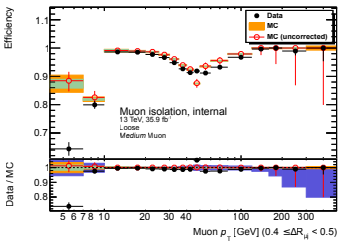

(f) $0.4 \leq \Delta R_{\mu j} < 0.5$

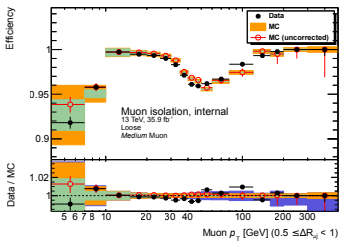

(g) $0.5 \leq \Delta R_{\mu j} < 1.0$

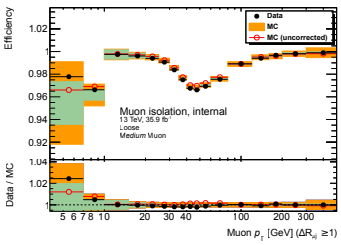

(h) $\Delta R_{\mu j} \geq 1.0$

Figure A.8 – Validation plots of the *Loose* scale factors, in various $\Delta R_{\mu j}$ regions.

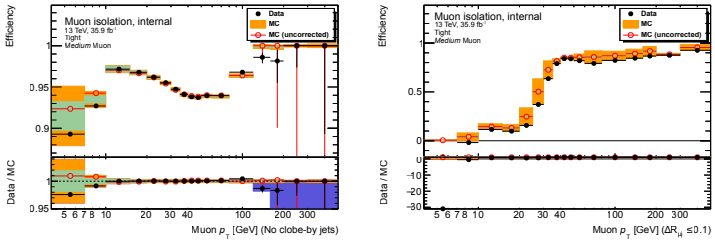

(a) No close-by jets

(b) $\Delta R_{\mu j} \leq 0.1$

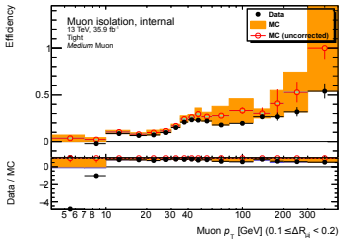

(c) $0.1 \leq \Delta R_{\mu j} < 0.2$

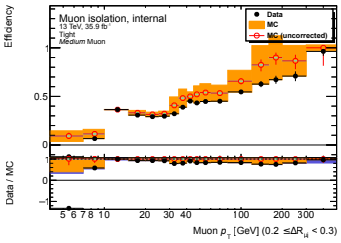

(d) $0.2 \leq \Delta R_{\mu j} < 0.3$

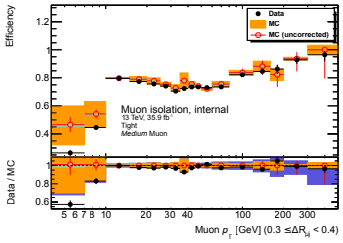

(e) $0.3 \leq \Delta R_{\mu j} < 0.4$

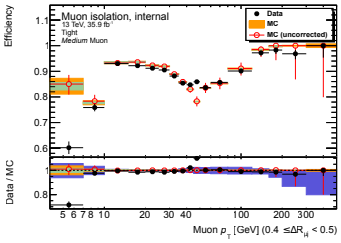

(f) $0.4 \leq \Delta R_{\mu j} < 0.5$

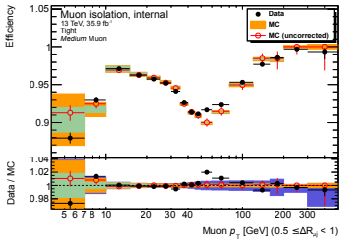

(g) $0.5 \leq \Delta R_{\mu j} < 1.0$

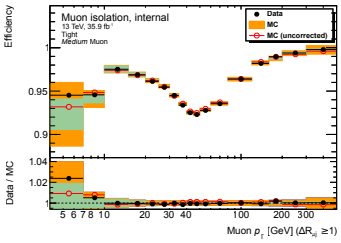

(h) $\Delta R_{\mu j} \geq 1.0$

Figure A.9 – Validation plots of the *Tight* scale factors, in various $\Delta R_{\mu j}$ regions.

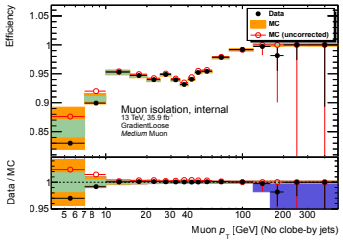

(a) No close-by jets

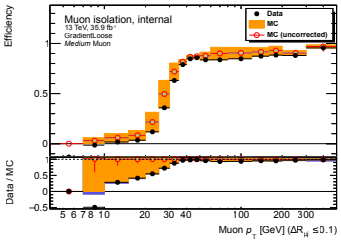

(b) $\Delta R_{\mu j} \leq 0.1$

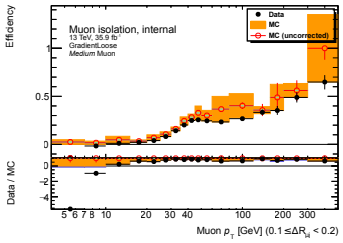

(c) $0.1 \leq \Delta R_{\mu j} < 0.2$

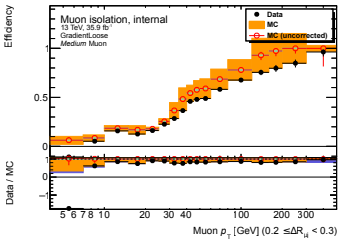

(d) $0.2 \leq \Delta R_{\mu j} < 0.3$

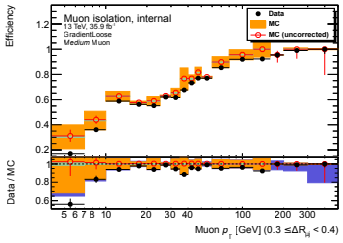

(e) $0.3 \leq \Delta R_{\mu j} < 0.4$

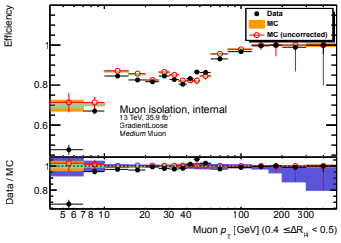

(f) $0.4 \leq \Delta R_{\mu j} < 0.5$

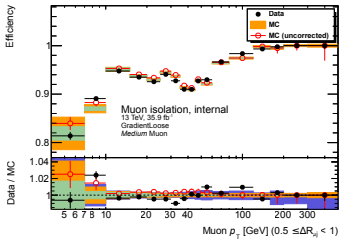

(g) $0.5 \leq \Delta R_{\mu j} < 1.0$

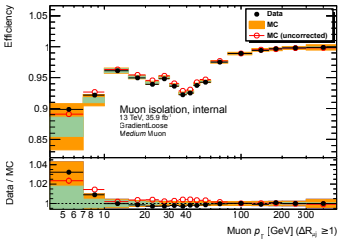

(h) $\Delta R_{\mu j} \geq 1.0$

Figure A.10 – Validation plots of the *GradientLoose* scale factors, in various $\Delta R_{\mu j}$ regions.

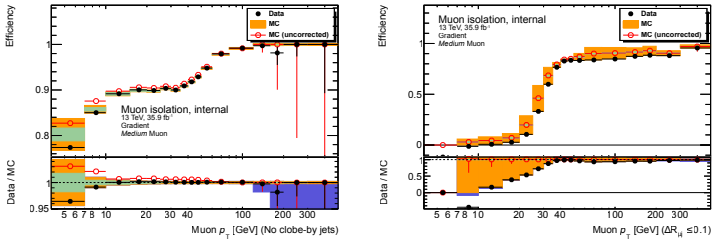

(a) No close-by jets

(b) $\Delta R_{\mu j} \leq 0.1$

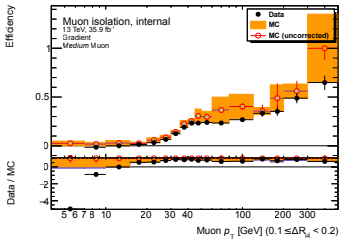

(c) $0.1 \leq \Delta R_{\mu j} < 0.2$

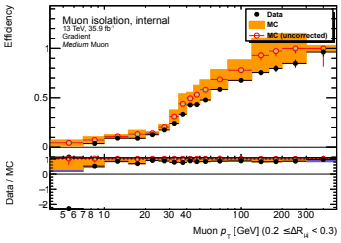

(d) $0.2 \leq \Delta R_{\mu j} < 0.3$

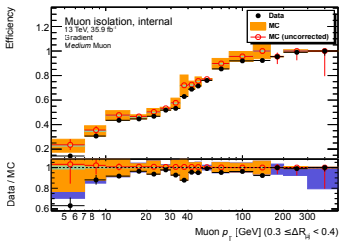

(e) $0.3 \leq \Delta R_{\mu j} < 0.4$

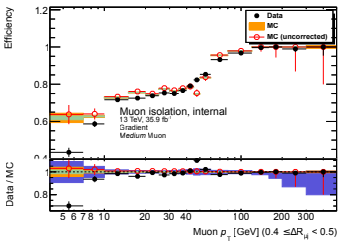

(f) $0.4 \leq \Delta R_{\mu j} < 0.5$

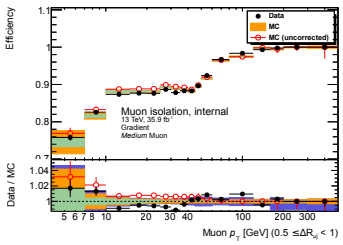

(g) $0.5 \leq \Delta R_{\mu j} < 1.0$

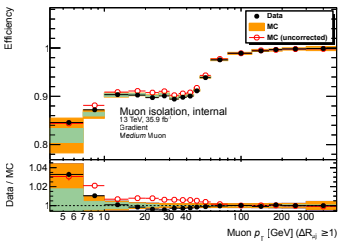

(h) $\Delta R_{\mu j} \geq 1.0$

Figure A.11 – Validation plots of the *Gradient* scale factors, in various $\Delta R_{\mu j}$ regions.

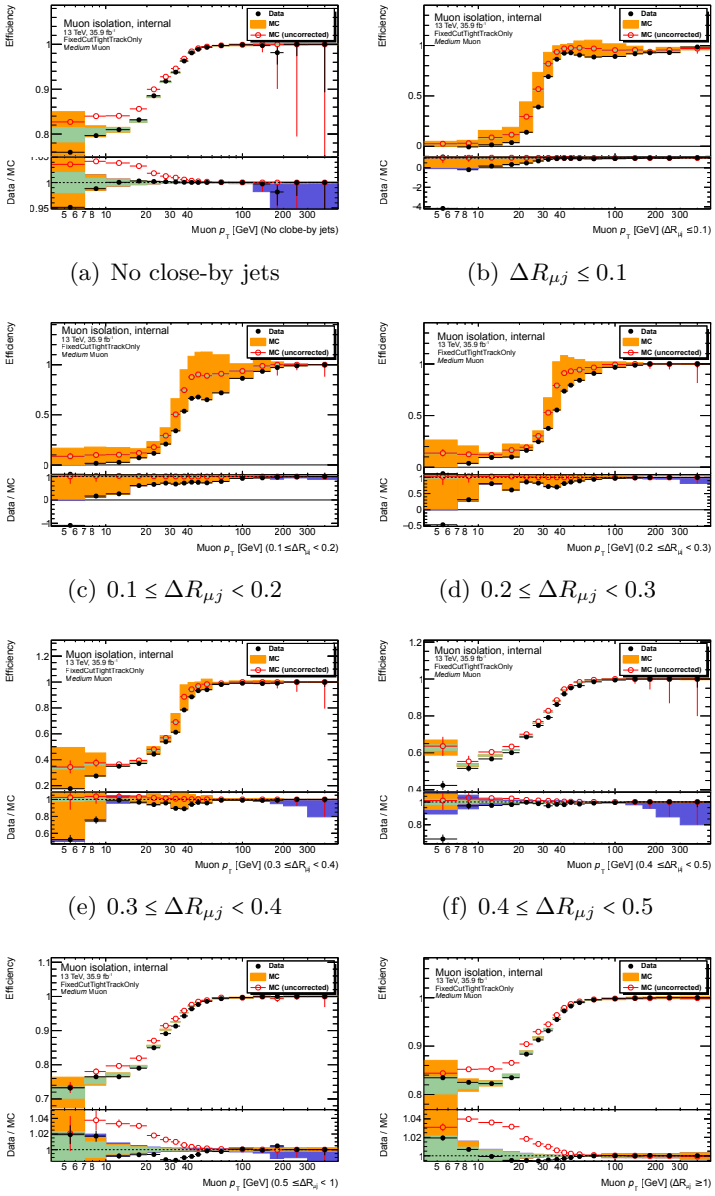

(a) No close-by jets

(b) $\Delta R_{\mu j} \leq 0.1$

(c) $0.1 \leq \Delta R_{\mu j} < 0.2$

(d) $0.2 \leq \Delta R_{\mu j} < 0.3$

(e) $0.3 \leq \Delta R_{\mu j} < 0.4$

(f) $0.4 \leq \Delta R_{\mu j} < 0.5$

(g) $0.5 \leq \Delta R_{\mu j} < 1.0$

(h) $\Delta R_{\mu j} \geq 1.0$

Figure A.12 – Validation plots of the *FixedCutTightTrackOnly* scale factors, in various $\Delta R_{\mu j}$ regions.

Appendix B

Models in case of missing topocluster information for isolation close-by correction

This appendix details the various models available in case topocluster information is missing for the close-by object correction of the isolation variables, described in Sec. 8.3.

The *basic* model. This model calculates a basic correction and is applied by default if the topocluster information is not available and if no models were specified. The core energy $E_{\mathrm{T}}^{\mathrm{topocore}}(\lambda)$ of the close-by objects is added to the correction if $\Delta R_{\lambda,\lambda'} \leq \frac{X}{100}$. Using this model would result in an over-estimation of the correction to apply.

The *minimal* model. This model calculates a minimal correction. The core energy of the close-by objects is added to the correction if $\Delta R_{\mathrm{core}} \leq \Delta R_{\lambda,\lambda'} \leq \frac{X}{100} - \Delta R_{\mathrm{core}}$. The lower limit ensures no topoclusters used to calculate $E_{\mathrm{T}}^{\mathrm{topocore}}(\lambda)$ and $E_{\mathrm{T}}^{\mathrm{topocore}}(\lambda')$ are shared, which would lead to double-counting. The upper limit ensures that no topoclusters outside the $\frac{X}{100}$ cone with respect to λ (but close enough to λ') are counted. Using this model would result in minimising the correction to be applied. However, double-counting could still happen if topoclusters are shared between close-by objects λ', whose $\Delta R_{\lambda,\lambda'}$ are within the limits, in the calculation of their core energies.

The *complex* model. This model calculates a correction which should be the closest to the reality. In this model, a fraction f of the core energy of the close-by objects λ' is added to the correction depending on $\Delta R_{\lambda,\lambda'}$. Again, it is assumed that the energy distribution of the topoclusters is homogeneous around the object whose isolation has to be corrected. This model is not as stringent as the *minimal* model, but suffers the same limits: there may be over-counting in case some topoclusters are shared among close-by objects. Noting $\Delta R_1 = \min\left(2\Delta R_{\mathrm{core}}, \frac{X}{100} - \Delta R_{\mathrm{core}}\right)$, $\Delta R_2 = \max\left(2\Delta R_{\mathrm{core}}, \frac{X}{100} - \Delta R_{\mathrm{core}}\right)$ and $\Delta R_3 = \frac{X}{100} + \Delta R_{\mathrm{core}}$, the fraction f of $E_{\mathrm{T}}^{\mathrm{topocore}}(\lambda')$ to be removed is given by:

- $\Delta R_{\mathrm{core}} \geq \frac{X}{100} \Rightarrow \forall \Delta R, f = 0.$
- $\Delta R_{\mathrm{core}} < \frac{X}{100} \Rightarrow$

$$\begin{cases} 0 \leq \Delta R \leq \Delta R_1 \Rightarrow f = \min\left(\frac{\Delta R}{\Delta R_{\mathrm{core}}}, 1\right). \\ \Delta R_1 \leq \Delta R \leq \Delta R_2 \Rightarrow f = \min\left(\frac{\Delta R_1}{\Delta R_{\mathrm{core}}}, 1\right). \\ \Delta R_2 \leq \Delta R \leq \Delta R_3 \Rightarrow f = \min\left(\frac{\Delta R_1}{\Delta R_{\mathrm{core}}}, 1\right) \times \frac{\Delta R_3 - \Delta R}{\Delta R_3 - \Delta R_1}. \\ \Delta R \geq \Delta R_3 \Rightarrow f = 0. \end{cases}$$

Note that the condition $\Delta R_{\text{core}} \geq \frac{X}{100} \Rightarrow \forall \Delta R, f = 0$ applies to all the models. Studies were performed comparing the corrections calculated using topocluster information and approximation of the various models. It was shown that the *complex* model was giving the most reliable results, but isolation was, as for all the models, over-corrected due to double-counting.

Appendix C

Trigger efficiencies in the Higgs-to-four-lepton channel

This appendix details the efficiencies of the lepton triggers used in the Higgs-to-four-lepton decay channel, for the data 2015 and 2016.

Table C.1 – Efficiencies of various triggers and their combinations, used in 2015, for 125 GeV ggF Higgs signals in the four decay channels [198].

trigger	$4e$	4μ	$2e2\mu$	$2\mu2e$
e24_lhmedium_L1EM18VH	0.97 ± 0.006		0.958 ± 0.006	0.29 ± 0.02
e60_lhmedium	0.23 ± 0.01		0.21 ± 0.01	0.024 ± 0.005
e120_lhloose	0.023 ± 0.005		0.020 ± 0.005	0.0006 ± 0.0006
mu20_iloose_L1MU15		0.966 ± 0.005	0.45 ± 0.02	0.936 ± 0.008
mu50		0.50 ± 0.01	0.043 ± 0.0067	0.50 ± 0.02
mu60_0eta105_msonly		0.17 ± 0.01	0.01 ± 0.004	0.17 ± 0.01
2e12_lhloose_L12EM10VH	0.983 ± 0.004		0.88 ± 0.01	0.38 ± 0.02
2mu10		0.960 ± 0.005	0.45 ± 0.02	0.68 ± 0.02
mu18_mu8noL1		0.977 ± 0.004	0.46 ± 0.02	0.878 ± 0.01
e17_lhloose_mu14			0.80 ± 0.01	0.53 ± 0.02
e7_medium_mu24			0.28 ± 0.01	0.84 ± 0.01
e24_medium_L1EM20VHI_mu8noL1			0.905 ± 0.009	0.24 ± 0.01
e17_lhloose_2e9_lhloose	0.927 ± 0.009			
3mu6		0.8568 ± 0.009		
3mu6_msonly		0.871 ± 0.009		
mu18_2mu4noL1		0.972 ± 0.004		
2e12_lhloose_mu10			0.83 ± 0.01	0.42 ± 0.02
e12_lhloose_2mu10			0.45 ± 0.02	0.63 ± 0.02
single-e triggers	0.974 ± 0.006			
di-e triggers	0.983 ± 0.004			
tri-e triggers	0.927 ± 0.009			
single-μ triggers		0.967 ± 0.005		
di-μ triggers		0.991 ± 0.003		
tri-μ triggers		0.980 ± 0.004		
single OR di-e triggers	0.994 ± 0.003			
single OR tri-e triggers	0.986 ± 0.004			
di OR tri-e triggers	0.986 ± 0.004			
single OR di-μ triggers		0.991 ± 0.003		
single OR tri-μ triggers		0.983 ± 0.003		
di OR tri-μ triggers		0.992 ± 0.002		
e triggers			0.979 ± 0.005	0.51 ± 0.02
μ triggers			0.694 ± 0.015	0.956 ± 0.007
$e\mu$ triggers			0.984 ± 0.004	0.955 ± 0.007
e OR μ triggers			0.998 ± 0.001	0.986 ± 0.004
e OR $e\mu$ triggers			0.994 ± 0.003	0.964 ± 0.006
μ OR $e\mu$ triggers			0.990 ± 0.003	0.980 ± 0.005
all combined	0.994 ± 0.003	0.992 ± 0.002	0.9996 ± 0.0003	0.990 ± 0.004

Table C.2 – Efficiencies of various triggers and their combinations, used in early 2016, for 125 GeV ggF Higgs signals in the four decay channels [198].

trigger	$4e$	4μ	$2e2\mu$	$2\mu2e$
single electron triggers:				
e24_lhtight_nod0_ivarloose	0.937±0.002		0.912±0.002	0.268±0.003
e60_lhmedium_nod0	0.227±0.003		0.207±0.002	0.0174±0.0008
e60_medium	0.216±0.003		0.197±0.002	0.0165±0.0008
e140_lhloose_nod0	0.0145±0.0008		0.0103±0.0006	0.0004±0.0001
e300_etcut	0.0000±0.0000		0.0000±0.0000	0.0000±0.0000
double electron triggers:				
2e15_lhvloose_nod0_L12EM13VH	0.966±0.001		0.857±0.002	0.181±0.002
triple electron triggers:				
e17_lhloose_nod0_2e9_lhloose_nod0	0.942±0.002			
single muon triggers:				
mu20_ivarloose_L1MU15		0.9597±0.0009	0.429±0.003	0.918±0.002
mu20_iloose_L1MU15		0.9587±0.0009	0.428±0.003	0.918±0.002
mu40		0.670±0.002	0.057±0.001	0.641±0.003
double muon triggers:				
2mu10		0.953±0.001	0.420±0.003	0.656±0.003
mu20_mu8noL1		0.9607±0.0009	0.339±0.003	0.855±0.002
triple muon triggers:				
3mu4		0.870±0.002		
mu6_2mu4		0.875±0.002		
mu20_2mu4noL1		0.957±0.001		
$e\mu$ triggers:				
e7_lhmedium_nod0_mu24			0.275±0.002	0.8673±0.002
e17_lhloose_nod0_mu14			0.766±0.002	0.5485±0.003
e24_lhmedium_nod0_L1EM20VHI_mu8noL1			0.939±0.001	0.292±0.003
e12_lhloose_nod0_2mu10			0.419±0.003	0.606±0.003
2e12_lhloose_nod0_mu10			0.804±0.002	0.416±0.003
all single-e triggers	0.941±0.002			
all di-e triggers	0.966±0.001			
all tri-e triggers	0.942±0.002			
all single-μ trigger		0.9614±0.0009		
all di-μ trigger		0.9840±0.0006		
all tri-μ trigger		0.9741±0.0008		
all single OR di-e triggers	0.9915±0.0006			
all single OR tri-e triggers	0.9905±0.0006			
all di OR tri-e triggers	0.9872±0.0007			
all single OR di-μ trigger		0.9844±0.0006		
all single OR tri-μ trigger		0.9775±0.0007		
all di OR tri-μ trigger		0.9855±0.0006		
all e triggers			0.964±0.001	0.340±0.003
all μ triggers			0.624±0.003	0.928±0.002
all $e\mu$ triggers			0.9848±0.0007	0.948±0.001
all e OR μ triggers			0.9892±0.0006	0.956±0.001
all e OR $e\mu$ triggers			0.9934±0.0004	0.951±0.001
all μ OR $e\mu$ triggers			0.9868±0.0006	0.966±0.001
all all combined	0.9951±0.0004	0.9859±0.0006	0.9952±0.0004	0.968±0.001

Table C.3 – Efficiencies of various triggers and their combinations, used in late 2016, for 125 GeV ggF Higgs signals in the four decay channels [198].

triggers:	$4e$	4μ	$2e2\mu$	$2\mu2e$
single electron triggers:				
e26_lhtight_nod0_ivarloose	0.919 ± 0.002		0.893 ± 0.002	0.222 ± 0.003
e60_lhmedium_nod0	0.226 ± 0.003		0.205 ± 0.002	0.0172 ± 0.0009
e60_medium	0.215 ± 0.003		0.197 ± 0.002	0.0163 ± 0.0009
e140_lhloose_nod0	0.0149 ± 0.0009		0.0101 ± 0.0006	0.0005 ± 0.0001
double electron triggers:				
2e17_lhvloose_nod0	0.935 ± 0.002		0.817 ± 0.002	0.122 ± 0.002
triple electron triggers:				
e17_lhloose_nod0_2e9_lhloose_nod0	0.943 ± 0.002		0.0026 ± 0.0003	0.0021 ± 0.0003
single muon triggers:				
mu26_ivarmedium		0.903 ± 0.002	0.218 ± 0.003	0.864 ± 0.002
mu26_imedium		0.894 ± 0.002	0.212 ± 0.002	0.844 ± 0.002
mu50		0.502 ± 0.003	0.0334 ± 0.001	0.478 ± 0.003
double muon triggers:				
2mu14		0.899 ± 0.002	0.197 ± 0.002	0.634 ± 0.003
mu22_mu8noL1		0.947 ± 0.001	0.271 ± 0.003	0.846 ± 0.002
triple muon triggers:				
mu20_2mu4noL1		0.957 ± 0.001	0.0119 ± 0.0006	0.028 ± 0.001
3mu4		0.871 ± 0.002	0.0094 ± 0.0006	0.0108 ± 0.0007
3mu6_msonly		0.837 ± 0.002	0.0048 ± 0.0004	0.0064 ± 0.0005
$e\mu$ triggers:				
e7_lhmedium_mu24	0.0006 ± 0.0002	0.0025 ± 0.0003	0.273 ± 0.003	0.869 ± 0.002
e12_lhloose_2mu10	0.0000 ± 0.0000	0.0022 ± 0.0002	0.417 ± 0.003	0.608 ± 0.003
2e12_lhloose_mu10	0.0032 ± 0.0004	0.0000 ± 0.0000	0.805 ± 0.002	0.422 ± 0.003
e12_lhloose_nod0_2mu10	0.0000 ± 0.0000	0.0023 ± 0.0003	0.417 ± 0.003	0.608 ± 0.003
2e12_lhloose_nod0_mu10	0.0032 ± 0.0004	0.0000 ± 0.0000	0.806 ± 0.002	0.423 ± 0.003
all single-e triggers	0.923 ± 0.002			
all di-e triggers	0.935 ± 0.002			
all tri-e triggers	0.943 ± 0.002			
all single-μ triggers		0.905 ± 0.002		
all di-μ triggers		0.9713 ± 0.0009		
all tri-μ triggers		0.9738 ± 0.0008		
all single OR di-e triggers	0.981 ± 0.001			
all single OR tri-e triggers	0.9890 ± 0.0007			
all di OR tri-e triggers	0.9834 ± 0.0009			
all single OR di-μ triggers		0.9716 ± 0.0009		
all single OR tri-μ triggers		0.9764 ± 0.0008		
all di OR tri-μ triggers		0.9805 ± 0.0007		
all e triggers	0.9933 ± 0.0006			
all μ triggers		0.9807 ± 0.0007		
all $e\mu$ triggers	0.0032 ± 0.0004	0.0040 ± 0.0003	0.872 ± 0.002	0.925 ± 0.002
all combined	0.9933 ± 0.0006	0.9808 ± 0.0007	0.9870 ± 0.0007	0.956 ± 0.001

Appendix D

Influence of alternative selections for the Higgs-to-four-lepton analysis

This appendix details the studies on possible improvements of the Higgs-to-four-lepton cut-flow, introduced in Sec. 11.4.4. These studies were carried out in order to test a new ordering of the selection criteria in order to improve signal sensitivities in the Higgs-to-four-lepton decay channel. The possibility of a late quadruplet selection as well as the application of isolation criteria at an earlier stage of the analysis cut flow were studied.

The MC samples used for the studies (signal and background) are listed in Tab. D.1. All these samples are normalised to the predicted cross sections.

In order to evaluate the improvement brought by the two tested changes, the event yields and significances are computed after the standard selection and are compared to the ones calculated either after the late quadruplet selection, or after applying early isolation cuts. Yields are calculated per channel decay (4μ, $4e$, $2\mu 2e$, $2e2\mu$ and all the previous channels combined), and the significance is defined as

$$Z = \frac{N_{\text{signal}}}{\sqrt{N_{\text{bkgs.}}}} = \frac{\sum_{i\in\{gg\text{F,VBF},ZH,WH,ttH\}} N^{i}_{\text{signal}}}{\sqrt{\sum_{j\in\{\text{red. bkgs.}\}} N^{j}_{\text{bkg.}} + \sum_{k\in\{\text{irr.bkgs.}\}} N^{k}_{\text{bkg.}}}}. \tag{D.1}$$

Using these quantities, ratios of event yields $r_N = \frac{N(\text{new selection})}{N(\text{standard selection})}$, as well as ratios of significance $r_Z = \frac{Z(\text{new selection})}{Z(\text{standard selection})}$ are derived. The second ratios indicate, if they are greater than 1, an improvement of the new selection over the current one.

Results obtained from the current selection are presented in Tab. D.2. They will be used as denominators of the ratios.

D.1 Influence of keeping all the quadruplets until the end of the selection

In the current selection procedure, the best quadruplets per decay channel (defined as the quadruplets having m_{12} the closest to the Z pole mass m_Z, and in case of equality, having m_{34} the closest to m_Z), are selected after the leading-p_{T} cuts and before the cuts on m_{12}. The first study assesses the impact of selecting the best quadruplet only at the end of the selection procedure (late selection), keeping all the quadruplets which pass the cuts.

Table D.1 – Signal, reducible and irreducible background samples used for the study of the late quadruplet selection and for the early isolation cut are presented. Signal samples include the ggF, VBF, ZH, WH, ttH samples for $m_H = 125\,\text{GeV}$, reducible background is made of $Z \to ee$ and $Z \to \mu\mu$ plus $t\bar{t}$ samples, and irreducible background is composed of $qq \to ZZ^*$ and $gg \to ZZ^*$ samples. All these samples are normalised to the predicted cross sections for the studies.

Signal samples	
ggF	mc15_13TeV.341505.PowhegPythia8EvtGen_CT10_AZNLOCTEQ6L1_ggH125_ZZ4lep_noTau
VBF	mc15_13TeV.341518.PowhegPythia8EvtGen_CT10_AZNLOCTEQ6L1_VBFH125_ZZ4lep_noTau
ZH	mc15_13TeV.341947.Pythia8EvtGen_A14NNPDF23LO_ZH125_ZZ4l
WH	mc15_13TeV.341964.Pythia8EvtGen_A14NNPDF23LO_WH125_ZZ4l
ttH	mc15_13TeV.342561.aMcAtNloHerwigppEvtGen_UEEE5_CTEQ6L1_CT10ME_JH125_4l
Reducible background	
$Z \to ee$	mc15_13TeV.344295.Sherpa_NNPDF30NNLO_Zee_4lMassFilter40GeV8GeV
$Z \to \mu\mu$	mc15_13TeV.344296.Sherpa_NNPDF30NNLO_Zmumu_4lMassFilter40GeV8GeV
$Z \to ee$	mc15_13TeV.344297.Sherpa_NNPDF30NNLO_Zee_3lPtFilter4GeV_4lMassVeto40GeV8GeV
$Z \to \mu\mu$	mc15_13TeV.344298.Sherpa_NNPDF30NNLO_Zmumu_3lPtFilter4GeV_4lMassVeto40GeV8GeV
$t\bar{t}$	mc15_13TeV.410000.PowhegPythiaEvtGen_P2012_Jbar_hdamp172p5_nonallhad
$t\bar{t}$	mc15_13TeV.410009.PowhegPythiaEvtGen_P2012_Jbar_hdamp172p5_dil
$t\bar{t}$	mc15_13TeV.344171.PowhegPythiaEvtGen_P2012_Jbar_hdamp172p5_4lMFilt_40_8
Irreducible background	
$qq \to ZZ^*$	mc15_13TeV.342556.PowhegPy8EG_CT10nloME_AZNLOCTEQ6L1_ZZllll_mll4_m4l_100_150
$qq \to ZZ^*$	mc15_13TeV.343232.PowhegPy8EG_CT10nloME_AZNLOCTEQ6L1_ZZllll_mll4_m4l_500_13000
$qq \to ZZ^*$	mc15_13TeV.361603.PowhegPy8EG_CT10nloME_AZNLOCTEQ6L1_ZZllll_mll4
$gg \to ZZ^*$	mc15_13TeV.343212.Powheggg2vvPythia8EvtGen_gg_ZZ_bkg_2e2mu_13TeV
$gg \to ZZ^*$	mc15_13TeV.343213.Powheggg2vvPythia8EvtGen_gg_ZZ_bkg_4l_noTau_13TeV

Table D.2 – Results of the standard selection. Yields are presented as sums over the MC samples, in three categories: signal, reducible and irreducible backgrounds. The results presented in this appendix (based on MC) may differ from the actual yields in the Higgs-to-four-lepton analysis, where the irreducible background contributions are modelled using data-driven techniques. The last row shows the significance.

Decay channels	4μ	$4e$	$2\mu 2e$	$2e2\mu$	Inclusive
Signal	0.56	0.30	0.30	0.39	1.55
Reducible bkgs.	0.02	0.02	0.03	0.02	0.08
Irreducible bkgs.	0.27	0.12	0.12	0.19	0.71
Significance Z	1.04	0.81	0.79	0.83	1.74

Table D.3 – Results of the late selection, where the best quadruplet is selected at the very end of the selection process. Yields are presented as sums over the samples introduced before, in three categories: signal, reducible and irreducible backgrounds. The last row shows the significance.

Decay channels	4μ	$4e$	$2\mu 2e$	$2e2\mu$	Inclusive
Signal	0.59	0.33	0.32	0.39	1.63
Reducible bkgs.	0.02	0.02	0.02	0.02	0.07
Irreducible bkgs.	0.35	0.16	0.13	0.20	0.84
Significance Z	0.98	0.77	0.82	0.86	1.71

Table D.4 – Comparison of the late and standard selections. The ratios r_N and r_Z are presented in three categories: signal, reducible and irreducible backgrounds. Overall, the significance worsens with the late selection and the signal yields are not improved at interesting scales.

Decay channels	4μ	$4e$	$2\mu 2e$	$2e2\mu$	Inclusive
r_N^{signal}	1.06	1.09	1.06	1.02	1.06
$r_N^{\text{red. bkgs.}}$	0.99	1.12	0.83	0.63	0.87
$r_N^{\text{irr. bkgs.}}$	1.29	1.32	1.08	1.03	1.19
r_Z	0.94	0.96	1.04	1.03	0.98

Table D.5 – Results of the early isolation selection, in which the isolation cuts are applied at an earlier stage of the selection process. Yields are presented as sums over the samples introduced before, in three categories: signal, reducible and irreducible backgrounds. The last row shows the significance.

Decay channels	4μ	$4e$	$2\mu 2e$	$2e2\mu$	Inclusive
Signal	0.56	0.30	0.30	0.39	1.54
Reducible bkgs.	0.01	0.02	0.02	0.02	0.06
Irreducible bkgs.	0.28	0.12	0.12	0.19	0.71
Significance Z	1.04	0.84	0.81	0.84	1.76

Table D.6 – Comparison of the early isolation and standard selections. The ratios r_N and r_Z are presented in three categories: signal, reducible and irreducible backgrounds. Overall, the significance improves slightly with the new selection, but the signal yields decrease.

Decay channels	4μ	$4e$	$2\mu 2e$	$2e2\mu$	Inclusive
r_N^{signal}	1.00	0.99	0.99	1.00	0.99
$r_N^{\text{red. bkgs.}}$	0.86	0.84	0.65	0.70	0.75
$r_N^{\text{irr. bkgs.}}$	1.00	1.00	1.00	1.00	1.00
r_Z	1.00	1.00	1.02	1.01	1.01

The results of the late selection are presented in Tab. D.3. An increase of event yields is generally expected as more quadruplets are offered the chance to be tested for the mass, d_0 and isolation cuts. The chances that at least one quadruplet passes these criteria is therefore increased. However, the increase affects both signal and background events, and the significance worsens slightly, as shown in Tab. D.4. The event yields decrease for some background channels, due to the negative weights of the MC samples, which result in more events selected reducing the overall yield.

This study confirms that the current selection is capable of reducing the background contamination and the observed increase of signal yields using the late selection is not significant enough. Although this increase is more noticeable for the $2\mu 2e$ and $2e2\mu$ channels, it is accompanied with an increase of the internal miss-pairing, where one lepton originally produced by the on-shell Z ends up in the sub-leading pair (and the opposite).

D.2 Influence of applying the isolation selection at an earlier stage

In the current selection, isolation cuts are applied after the criteria on the lepton opening angles and the J/ψ vetoes. These cuts are applied just prior to the d_0 significance cuts and the final selection of the best quadruplets. In this study, the opportunity of performing the isolation selection just after the formation of the quadruplets is considered. The early stage corresponds to a step in which several quadruplets per decay channel remain, just before the leading-p_{T} cuts. For this reason, the early isolation selection is performed on various quadruplets at the same time.

The results of this study are presented in Tab. D.5. The signal yields decrease with the new selection, but so do the reducible background yields. The irreducible backgrounds have increased yields, but these results based on MC may not reflect the actual yields in the Higgs-to-four-lepton analysis, where data-driven techniques are used to assess the reducible-background contributions. Ratios are shown in Tab. D.6. With the early isolation selection, significances are overall improved but the effect is at the per-mill level, and does not justify a change of selection, especially taking into account the decrease in signal yields.

Annexe E

Résumé de la thèse en français

Le domaine de la physique des particules a pour objectif de comprendre et de décrire comment les constituants élémentaires composant l'univers qui nous entoure interagissent entre eux. La théorie à ce jour la plus complète et la plus utilisée par les scientifiques est le Modèle Standard, qui fut développé au cours du siècle dernier et a réussi à prédire la plupart des résultats expérimentaux observés. Ses conjectures furent notamment confirmées par la découverte de particules manquantes. Afin de valider les prédictions du Modèle Standard, plusieurs expériences furent construites au CERN (Centre Européen pour la Recherche Nucléaire) près de Genève. Ces expériences consistent en des ensembles de détecteurs capables de recueillir et analyser les données issues des collions proton-proton produites par le LHC (Large Hadron Collider). Alors que durant le Run 1 (années 2011 et 2012), des énergies de centre de masse de $\sqrt{s} = 7,8\,\text{TeV}$ furent atteintes, permettant la découverte du boson de Higgs en 2012, le sujet de cette thèse porte sur l'analyse des premières données du Run 2 (années 2015 et 2016), collectées par le détecteur ATLAS (A Toroidal LHC ApparaTuS), qui correspondent à $36.1\,\text{fb}^{-1}$ à $\sqrt{s} = 13\,\text{TeV}$.

La thèse se concentre principalement sur l'étude de la désintégration du boson de Higgs en deux bosons Z qui se désintègrent en quatre leptons. Grâce à une excellente résolution du détecteur et une bonne reconstruction des leptons, la mesure de la masse des deux bosons Z se traduit par une estimation très précise de la masse du boson de Higgs tout en rejetant le bruit de fond de manière très efficace. La signifiance est dès lors très bonne et cette chaîne de décomposition, avec celle du boson de Higgs se désintégrant en deux photons, a permis la découverte de la particule en 2012. Grâce à l'augmentation de $\sqrt{s}$, la signifiance est améliorée au Run 2 permettant de poursuivre les recherches sur l'existence de phénomènes physiques au-delà du Modèle Standard. Au sein du groupe d'analyse, cette thèse détaille les premières mesures des sections efficaces de production du boson de Higgs en quatre leptons effectuées lors du début du Run 2. Ces mesures incluent la section efficace totale et fiducielle par état final du quadruplet de quatre leptons et en fonction de variables différentielles (cinématique du boson de Higgs dans l'état final et variables reliées aux jets de l'événement).

La deuxième partie de la thèse dévoile les études de l'isolation des muons. Ces études ont été faites en utilisant le même ensemble de données que pour l'analyse. L'étude de l'isolation des muons consiste à déterminer si la particule est produite en association avec une activité ambiante autour de sa trajectoire dans les détecteurs et quelle est la proportion d'énergie de cette activité vis-à-vis du moment ou de l'énergie transverses de la particule. Déterminer l'isolation d'un objet est un outil puissant pour discriminer le signal (événements composés d'objets bien isolés dans les détecteurs) du bruit de fond. Des coupures sont appliquées aux variables d'isolation pour définir des points de fonctionnement qui peuvent être utilisés par les groupes d'analyse.

Le Chap. 2 est consacré à la description du CERN et tout particulièrement du LHC, en insistant sur le

programme de physique de l'accélérateur de particules. Le Chap. 3 détaille les spécifications du détecteur ATLAS en donnant pour chaque sous-détecteur les technologies utilisées, la performance espérée après simulation, et la performance observée durant le Run 1 ou le début du Run 2. Le Chap. 5 présente les deux variables d'isolation introduites pour le Run 2 (isolation de trace ou calorimétrique, selon que le sous-détecteur utilisé soit le traceur ou les calorimètres). La discussion se poursuit dans le Chap. 6 avec la description des cartes de coupures mises en place pour la définition des points de fonctionnement de l'isolation des muons. Les résultats en utilisant les données collectées au Run 2 sont regroupés au Chap. 7 avec la comparaison données simulation et le calcul des efficacités du signal des points de fonctionnement. Les facteurs d'échelle résultants sont utilisés pour corriger les efficacités dans la simulation. Enfin, le Chap. 8 porte sur l'implémentation et la validation d'un outil permettant de corriger les variables d'isolation pour retirer les contributions des objets de signal proches. Concernant la partie analyse, le Chap. 10 propose une description succincte du Modèle Standard en insistant sur le mécanisme de Higgs et les modes de production et de décomposition du boson de Higgs au LHC. Le Chap. 11 présente la stratégie d'analyse dans l'état final à quatre leptons. Après avoir décrit les échantillons simulés utilisés pour l'analyse, le chapitre se poursuit par un résumé des coupures et des critères de sélection. Une attention particulière est portée à l'estimation et la modélisation du bruit de fond, ainsi que de la prise en compte des erreurs systématiques. Enfin, le Chap. 12 conclut avec le détail des mesures des sections efficaces de production du boson de Higgs. Ce chapitre inclut la définition de l'espace fiduciel, de la méthodologie pour l'ajustement des sections efficaces et enfin la présentation des résultats en utilisant $36.1\,\text{fb}^{-1}$ de données collectées au Run 2. Cette annexe résume succinctement le travail présenté dans cette thèse.

E.1 Étude de l'isolation des muons

Afin d'évaluer l'énergie entourant la trajectoire des muons dans le traceur et les calorimètres, deux variables d'isolation sont définies. Dans chacun des cas, un cone est construit dans le plan pseudo-rapidité, direction azimutale (η, ϕ) de la particule. Le cone est centré sur la trajectoire du muon et l'énergie collectée dans le cone de rayon $\Delta R_{\text{iso}} = \sqrt{(\Delta\eta)^2 + (\Delta\phi)^2}$ est additionnée. Cette énergie correspond à la somme des énergies mesurées dans les cellules des calorimètres pour l'isolation calorimétrique (variables topoetcone dénotées $E_{\text{T}}^{\text{topocone}}$) et la somme du moment transverse des traces pour l'isolation de trace (variables ptvarcone dénotées $p_{\text{T}}^{\text{varcone}}$). Afin de ne pas compter la contribution du muon dans les variables d'isolation, l'énergie de cœur est soustraite à ces dernières.

E.1.1 Définition des variables d'isolation pour le Run 2

Effet de l'empilement sur l'isolation calorimétrique

L'empilement correspond à l'enregistrement par les détecteurs de vertex additionnels (vertex secondaires) en plus de l'événement principal. Ces vertex secondaires ont pour effet de masquer l'information utile et peuvent provenir de deux sources. Dans le cas de l'empilement synchrone, les vertex secondaires surgissent de la même interaction proton-proton que le vertex primaire. Dans le cas de l'empilement asynchrone, les vertex secondaires sont produits par les interactions entre les protons de paquets consécutifs. Le nombre d'empilement est mesuré par la variable μ qui correspond au nombre moyen d'interactions proton-proton par paquet. Idéalement chaque paquet devrait ne produire qu'une seule interaction en cas d'absence d'empilement ($\mu = 1$), mais les conditions du Run 2 avec une augmentation significative de la luminosité et la réduction de l'écart entre deux paquets (séparation de 25 ns) mènent à des valeurs proches de $\mu \approx 25$.

L'empilement a deux conséquences sur l'énergie mesurée par les cellules calorimétriques. Tout d'abord le bruit enregistré par les calorimètres augmente ce qui conduit à plus de cellules ne contenant que

de l'énergie de bruit. Ce bruit est intrinsèque aux détecteurs mais devient plus critique lors de fort empilement. Ce phénomène cause une dégradation de la performance de l'isolation calorimétrique. Au Run 2, il fut dès lors décidé de regrouper les cellules en topo-ensembles dont les formes épousent au mieux les objets (jets, particules) de l'événement. Le choix judicieux des paramètres de l'algorithme de regroupement permet de réduire le nombre de cellules saturées en bruit pour ne sélectionner que l'énergie utile. Seuls les topo-ensembles entrant dans les cônes d'isolation sont sélectionnés et leur énergie (qui correspond à la somme des énergies des cellules les constituant) est ajoutée aux variables d'isolation.

Le second effet concerne l'augmentation de l'énergie ambiante mesurée dans les calorimètres due aux nombreux vertex secondaires. Ceci dégrade le pouvoir de rejet des variables d'isolation et ces dernières sont alors corrigées en soustrayant la contribution inhérente à l'empilement. Pour ce faire, la densité de jets laissant des dépôts d'énergie dans les calorimètres est mesurée par unité de surface dans le plan (η, ϕ). Cette densité est alors multipliée par l'aire du cone d'isolation et retranchée à la variable. Après correction, la dépendance à l'empilement est fortement réduite.

Calcul des variables

La taille du cone d'isolation $\Delta R_{\text{iso}} = \frac{X}{100}, X \in \{20, 30, 40\}$ dépend de la variable considérée. Pour la variable topoetcone, le cone est constant. La valeur $X = 20$ fournit le meilleur rejet du bruit de fond ($t\bar{t}$) à une efficacité de signal donnée ($Z \to \mu\mu$). Pour ptvarcone, le cone dépend du moment transverse du muon ($\Delta R_{\text{iso var}} = \min\left(\frac{X}{100}, \frac{10\,\text{GeV}}{p_{\text{T}}}\right)$), avec $X = 30$. Ce choix permet de ne pas pénaliser les événements stimulés pour lesquels les objets laissent des traces proches dans le traceur, et améliore de pouvoir de rejet vis-à-vis de la définition précédente durant le Run 1, qui utilisait un cone de taille constante. La valeur $X = 30$ est choisie pour correspondre aux variables d'isolation utilisées par les déclencheurs.

Dans chacun des cas, la contribution du muon à l'énergie est soustraite en calculant l'énergie de cœur. Cette énergie est évaluée différemment dans le traceur, où le moment du muon est soustrait, et dans les calorimètres, où un cone d'isolation au rayon réduit $\Delta R_{\text{core}} < \Delta R_{\text{iso}}$ est construit. Tous les topo-ensembles se trouvant dans ce petit cone voient leur énergie soustraite à la variable d'isolation. Ainsi, l'énergie restante correspond seulement aux contributions d'autres objets de l'événement et permet de mesurer efficacement l'isolation des muons, offrant une discrimination contre le bruit de fond. Le rayon ΔR_{core} fut spécialement optimisé et la valeur de $\Delta R_{\text{core}} = 0.05$ fut retenue car elle fournissait le meilleur rejet ($t\bar{t}$) à efficacité de signal donnée ($Z \to \mu\mu$).

Formules finales

En reprenant les différentes composantes des variables d'isolation, ces dernières peuvent se calculer via les deux équations suivantes, pour un muon μ :

$$p_{\text{T}}^{\text{varcone30}}(\mu) = p_{\text{T}}^{\text{varcone, iso30}}(\mu) - p_{\text{T}}^{\mu}, \tag{E.1}$$

$$E_{\text{T}}^{\text{topocone20}}(\mu) = E_{\text{T}}^{\text{topocone, iso20}}(\mu) - E_{\text{T}}^{\text{topocore}}(\mu) - E_{\text{T}}^{\text{corr20}}(\mu), \tag{E.2}$$

où les variables iso$X, X \in \{20, 30\}$ correspondent à l'énergie sélectionnée dans le grand cone d'isolation, alors que $E_{\text{T}}^{\text{topocore}}$ et p_{T}^{μ} correspondent aux énergies de cœur pour les variables topoetcone et ptvarcone. $E_{\text{T}}^{\text{corr20}}$ est la correction pour l'empilement.

E.1.2 Définition des points de fonctionnement

Afin de discriminer les événements entre signal et bruit de fond, des coupures sont appliquées aux deux variables d'isolation et seuls les événements ayant des variables inférieures à ces dernières sont sélectionnés. Les coupures sont regroupées dans des points de fonctionnement qui sont définis selon deux types. La première catégorie rassemble les points de fonctionnement qui visent des efficacités du signal dépendant du moment transverse du muon. La deuxième catégorie comprend les points de fonctionnement ayant des coupures fixes sur les variables d'isolation. Dans un effort d'harmonisation au Run 2, ces points de fonctionnement sont définis de manière centralisée pour satisfaire au mieux les besoins des groupes d'analyse en termes d'efficacité et de rejet de bruit de fond attendus. Seul un nombre limité de points de fonctionnement est supporté afin de réduire la charge de travail.

Pour déterminer les coupures à appliquer aux variables d'isolation, des cartes sont créées. Pour chaque région du moment transverse et de la pseudo-rapidité du muon, une valeur de coupure est enregistrée. Cette valeur correspond à une certaine efficacité déterminée sur un échantillon $Z \to \mu\mu$. Ainsi, pour chaque efficacité recherchée, la bonne valeur de coupure peut être récupérée en fonction de la cinématique du muon.

Dans une étude préliminaire effectuée sur des échantillons $Z \to \mu\mu$ et $t\bar{t}$, les cartes de coupures furent validées et les rejets de bruit de fond furent mesurés.

E.1.3 Performance de l'isolation au Run 2

La sélection des muons utilisés pour évaluer la performance de l'isolation dans les données repose sur la méthode du marqueur et de la sonde. Cette méthode utilise le processus de désintégration du boson Z en une paire de muons pour identifier des muons de bonne qualité. Ainsi, seuls les événements contenant deux muons compatibles avec une masse invariante proche de celle du boson Z sont sélectionnés. Dans cette paire, un muon, le marqueur, doit satisfaire des critères de sélection plus stricts afin de s'assurer de sa bonne identification et de sa bonne reconstruction. Il sert à marquer l'événement comme étant part du signal $Z \to \mu\mu$. Le second muon, la sonde, est utilisé pour effectuer les mesures. Afin d'éviter tout biais dans les résultats, les deux muons doivent être reconstruits en utilisant des sous-détecteurs (traceur et spectromètre à muons) distincts.

Comparaison des distributions

Afin de vérifier la bonne description des données par le générateur Monte Carlo (MC) $Z \to \mu\mu$, les distributions des variables d'isolation des sondes sont comparées. La contribution résiduelle du bruit de fond dans les données est soustraite afin de ne pas biaiser la comparaison.

Un désaccord apparait pour la variable ptvarcone30 : la simulation fournit des sondes plus isolées que les données. Ainsi, la distribution est plus peuplée en $p_{\mathrm{T}}^{\mathrm{varcone30}} = 0$ pour la simulation, alors que plus d'événements peuplent les hautes valeurs pour les données. Une étude approfondie de ce désaccord a permis de le lier à la mauvaise description de la densité de vertex par le générateur. Cette densité permet d'évaluer le nombre de vertex par unité de longueur dans la direction du faisceau incident de protons et apparait fortement corrélée avec l'empilement μ et le nombre de traces sélectionnées pour le calcul de $p_{\mathrm{T}}^{\mathrm{varcone30}}$, expliquant le désaccord. Après avoir appliqué des coupures et avoir pondéré les données et la simulation afin que la distribution de la densité soit la même, le désaccord disparait. Il n'est cependant pas envisageable d'effectuer une telle pondération car elle pénaliserait les analyses par de fortes incertitudes statistiques de la simulation. Le désaccord n'affecte les efficacités du signal des points de fonctionnement

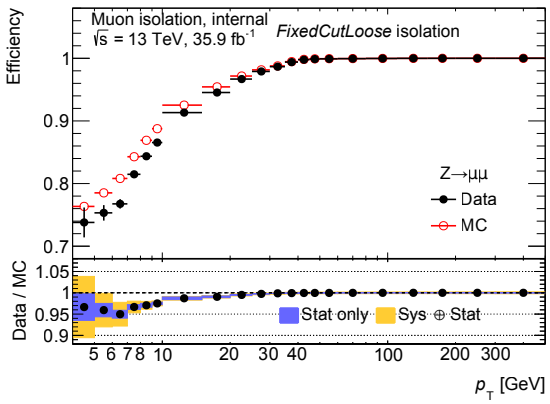

FIGURE E.1 – Efficacités (haut) et facteurs d'échelle (bas) du point de fonctionnement *FixedCutLoose*. Les données sont en noir et la simulation est en rouge. Les incertitudes statistiques seules (violet) et avec les systématiques (jaune) des facteurs d'échelle sont représentées par les plages de couleur.

que de manière limitée et les facteurs d'échelles introduits ci-après permettent de corriger les déviations. Il est à noter que certains critères de sélection des traces pour le calcul de la variable d'isolation minimisent le désaccord et une redéfinition de la variable pourrait améliorer l'accord.

Concernant la variable topoetcone20, l'accord est bon entre les données et la simulation après pondération de cette dernière afin que les distributions de la grandeur μ soient similaires entre données et simulation. Chacune des composantes entrant le calcul de la variable topoetcone20 est en bon accord. L'évolution de $E_{\mathrm{T}}^{\mathrm{topocone20}}$ avec μ montre une courbe plate, indiquant que la correction contre l'empilement est efficace.

Efficacités des points de fonctionnement

Afin de pleinement caractériser les points de fonctionnement de l'isolation des muons, les efficacités du signal dans les données et la simulation sont calculées. Elles sont définies comme le nombre de sondes passant les coupures sur le nombre total de sondes. En plus de la sélection des sondes suivant la méthode introduite ci-avant, les efficacités sont corrigées pour retirer les contributions des bruits de fond chromo-dynamiques et électro-faibles. Les deux composantes sont ajustées selon des patrons pris dans des générateurs dédiés et sont soustraites aux événements observés. Après correction, les efficacités peuvent être calculées pour chaque région de p_{T} du muon, pour chacun des points de fonctionnement (l'exemple du point de fonctionnement *FixedCutLoose* est présenté en Fig. E.1, les efficacités étant tracées dans le graphe du haut).

Afin de s'assurer que la simulation décrit les données au mieux, des facteurs d'échelle sont appliqués aux événements simulés. Ces facteurs sont calculés pour chaque région de p_{T} du muon, comme ratio des efficacités mesurées dans les données sur celles mesurées dans la simulation et sont présentés dans le graphe en bas de la Fig. E.1. En pondérant les échantillons par ces facteurs, les analyses bénéficient ainsi d'une meilleure description des événements dans les données. Les facteurs d'échelle sont assortis d'incertitudes statistiques et systématiques qui proviennent de la méthode de calcul. Les facteurs sont testés en vérifiant que la correction permet aux efficacités simulées d'être égales à celles mesurées dans les données, aux incertitudes près. La validation est correcte pour tous les points de fonctionnement sauf un, pour lequel les facteurs d'échelle sont calculées par région de (p_{T}, η) du muon.

E.1.4 Correction de l'isolation pour les objets proches

Les analyses pour lesquelles l'état final est composé d'objets signal proches peuvent être pénalisées par l'utilisation des variables d'isolation. En effet, les objets proches participent chacun à l'énergie ambiante de l'autre objet et augmentent artificiellement les valeurs des variables d'isolation, ce qui réduit leur pouvoir de rejet du bruit de fond. Afin de remédier à cela, un outil fut développé qui permet de soustraire les contributions des objets de signal proches, aux variables d'isolation. Ces dernières retrouvent donc leurs valeurs nominales et la discrimination peut se faire correctement. Cet outil fut validé et est maintenant largement utilisé par les différents groupes d'analyse.

E.2 Mesure de la section efficace de production du boson de Higgs en quatre leptons

Suivant la découverte du boson de Higgs en 2012, les données collectées par ATLAS et CMS au Run 1 à des énergies de centre de masse de $\sqrt{s} = 7$ et 8 TeV ont permis de mesurer la section efficace de production du boson, notamment dans les chaînes de décomposition $H \to \gamma\gamma$ et $H \to ZZ^* \to 4\ell, \ell \in \{e, \mu\}$.

Le travail décrit dans cette thèse présente la mesure de ces sections efficaces inclusives et différentielles en utilisant 36.1 fb^{-1} de données collectées par ATLAS au Run 2, en 2015 et 2016. À cette énergie de centre de masse record de $\sqrt{s} = 13$ TeV, la section efficace de production du signal augmente plus largement que celles des mécanismes de bruit de fond multipliant la signifiance dans le canal $H \to ZZ^* \to 4\ell$ par deux par rapport au Run 1. Ces nouvelles mesures explorent donc un plus large espace de phase que lors du Run 1, dans des conditions exceptionnelles. Elles permettent de confronter les observations avec les prédictions du Modèle Standard afin de déceler de possibles déviations indiquant la présence de nouvelle physique.

E.2.1 La chaîne de décomposition du boson de Higgs en quatre leptons

La chaîne de décomposition du boson de Higgs en deux bosons Z qui se décomposent en quatre leptons bénéficie de la bonne reconstruction des leptons composant l'état final (4μ, $4e$, $2\mu 2e$ et $2e2\mu$) ainsi que de la bonne résolution des masses invariantes. Ceci permet de maintenir un fort rejet du bruit de fond tout en conservant une bonne efficacité du signal. Grâce à sa haute signifiance, la chaîne de décomposition fut au premier plan dans la découverte du boson de Higgs en 2012 et dans la mesure de ses propriétés (mass, spin-parité et sections efficaces de production).

Dans ce canal, le bruit de fond principal est le continuum Z ($pp \to Z^{(*)}Z^{(*)} \to 4\ell$), irréductible car ayant les mêmes caractéristiques que le signal. D'autres contributions du bruit de fond proviennent des décompositions Z + jets et $t\bar{t}$ où le lepton complémentaire provient des désintégrations de quarks b ou c, de conversions de photons et de mauvaise identification des jets. Dans une moindre mesure, le bruit de fond des productions de deux ou trois bosons $Z/W^{\pm}$ sont prises en compte.

Pour l'étude, les échantillons simulés s'appuient sur les dernières prédictions du groupe de travail du Higgs du LHC. L'analyse sélectionne des états finaux composés de quatre leptons de bonne qualité et reconstruit les deux masses invariantes des bosons Z. Des coupures sont appliquées sur la cinématique des leptons, ainsi que sur les deux masses invariantes pour s'assurer qu'elles soient proches des résonances attendues. À partir de cette information, la mass invariante de tout l'état final ($m_{4\ell}$) est estimée et seuls les candidats satisfaisant $115 < m_{4\ell} < 130$ GeV sont sélectionnés. La paire ayant la masse invariante la plus proche de la masse pôle m_Z est appelée la paire principale, et la seconde paire est dénommée sous-principale. En notant d'abord la paire principale, les quatre états finaux possibles sont donc 4μ, $4e$, $2\mu 2e$ et $2e2\mu$ qui sont étudiés séparément.

TABLE E.1 – Nombre d'événements attendus et observés sous l'hypothèse du boson de Higgs de masse $m_H = 125\,\text{GeV}$ dans la fenêtre $115 < m_{4\ell} < 130\,\text{GeV}$, correspondant à $36.1\,\text{fb}^{-1}$ à $\sqrt{s} = 13\,\text{TeV}$.

État final	Signal	ZZ^*	$Z+\text{jets}$, $t\bar{t}$, WZ, ttV, VVV	Attendu	Observé
4μ	20.1 ± 1.6	9.8 ± 0.8	1.3 ± 0.3	31.2 ± 1.8	33
$4e$	10.6 ± 1.0	4.4 ± 0.4	1.3 ± 0.2	16.3 ± 1.1	16
$2e2\mu$	14.2 ± 1.1	7.1 ± 0.5	1.0 ± 0.2	22.3 ± 1.2	32
$2\mu 2e$	10.8 ± 1.0	4.6 ± 0.5	1.4 ± 0.3	16.8 ± 1.1	21
Total	56 ± 4	25.9 ± 2.0	5.0 ± 0.7	87 ± 5	102

La prise en compte du bruit de fond nécessite une attention tout particulière. Alors que le bruit de fond irréductible est bien modélisé par les générateurs, le bruit de fond réductible est estimé en utilisant des techniques basées sur l'exploitation des données dans des régions de contrôle. Ces régions sont définies pour être riches en une source de bruit de fond précise. Dans cette région, le nombre d'événements attendus (normalisation du Monte Carlo) et la forme des distributions $m_{4\ell}$ sont estimés. Ils sont ensuite extrapolés vers la région de signal en utilisant des facteurs de transfert définis comme ratios d'événements entre les deux régions. Grâce à cette méthode, les distributions du bruit de fond peuvent être ajustées dans la simulation et déterminées précisément dans la région de signal. Pour une meilleure estimation, l'étude est menée séparément pour les bruits de fond $Z + \mu\mu$ et $Z + ee$.

Les incertitudes sur la mesure du nombre d'événements sélectionnés proviennent de plusieurs sources. Tout d'abord les erreurs statistiques reflètent la connaissance approximative des rendements due à la taille limitée des échantillons et des données collectées. Se rajoutent à celles-ci les erreurs systématiques qui traduisent les biais de la méthode de mesure. Ces dernières incluent l'estimation de la normalisation et de la forme du bruit de fond, les erreurs théoriques sur le choix des échelles de factorisation et de renormalisation utilisées pour les Monte Carlo, et le choix des fonctions de densité des partons (PDF). Les dernières incertitudes concernent la reconstruction des leptons et jets, ainsi que la détermination des efficacités des coupures appliquées qui affectent la bonne description des données par la simulation.

L'ensemble de ces incertitudes est retranscrit sur le nombre d'événements observés par état final, pour le signal et le bruit de fond. Avec $36.1\,\text{fb}^{-1}$ de données, 31.3, 16.3, 22.3, 16.8 et 87 événements sont attendus pour les états finaux 4μ, $4e$, $2e2\mu$, $2\mu 2e$ et combinés, comme montré dans le Tab. E.1. Pour ces mêmes états finaux, 33, 16, 32, 21 et 102 événements sont observés. Les deux premiers états finaux ont la plus grande et plus basse efficacité de sélection à cause des coupures cinématiques plus sévères appliquées aux électrons vis-à-vis des muons. La comparaison entre observation et prédiction laisse apparaitre un excès de 1.3σ, surtout visible pour les états finaux $2e2\mu$ et $2\mu 2e$. Bien que les rendements soient compatibles avec les prédictions du Modèle Standard, ces excès furent vérifiés de manière approfondie. Cependant, aucun indice sur un éventuel biais de la méthode de mesure n'a été découvert. La comparaison des variables cinématiques du boson de Higgs, des deux bosons Z et des jets entre données et Monte Carlo ne montre pas de déviation significative.

E.2.2 Méthodologie des mesures et définition de l'espace de phase fiduciel

À partir des nombres d'événements observés, il est possible de calculer la section efficace totale du boson de Higgs se décomposant en quatre leptons. En utilisant ces valeurs ainsi que les formes des distributions de la masse invariante de l'état final à quatre leptons ($m_{4\ell}$) pour le signal et le bruit de fond, une

fonction de vraisemblance poissonnienne est construite. Cette dernière traduit la probabilité d'observer un nombre de candidats dans les données, sachant les nombres d'événements signal et bruit de fond attendus. Les incertitudes sont incluses comme paramètres de nuisance dans la vraisemblance. En exprimant le rendement d'événement signal en fonction de la section efficace de production, il est possible de déduire cette dernière en ajustant la distribution de $m_{4\ell}$ à l'aide d'un patron segmenté. Afin d'extrapoler les résultats de l'espace de phase accessible à l'analyse (espace de phase fiduciel qui prend en compte les coupures appliquées) à l'espace de phase total, des facteurs sont définis pour séparer les différents états finaux et modes de production.

Définition de l'espace de phase fiduciel

Pour retirer la dépendance au modèle qu'induit cette méthode de séparation, la section efficace fiducielle est définie correspondant à la production du boson de Higgs en quatre leptons dans l'espace de phase fiduciel seul. Cette section efficace est préférée à la section efficace totale car les résultats sont indépendants des générateurs choisis et les théoriciens peuvent facilement comparer leurs prédictions aux observations. Afin de réduire au maximum la dépendance au modèle, l'espace fiduciel est défini à l'aide d'un ensemble de coupures simples sur les leptons et jets directement produits par les générateurs, et vise à imiter au maximum l'espace de phase des événements reconstruits par les détecteurs. L'ensemble des coupures est communiqué aux théoriciens pour que ces derniers puissent facilement les reproduire dans leurs études.

Usage des leptons

Après la décomposition du boson Z ou $W^{\pm}$, les leptons dans l'état dit *né* émettent plusieurs photons (radiation de photon électro-faible), ce qui cause une diminution de leur impulsion jusqu'à leur état stable dit état *nu*. La perte d'énergie se fait au détriment de la résolution sur $m_{4\ell}$ dont le spectre bascule vers des valeurs plus faibles. Afin de récupérer une partie de cette énergie, les leptons nus sont regroupés avec les photons se trouvant à proximité de leur trajectoire d'après l'information fournie par les générateurs. Une fois l'énergie ajoutée, le lepton est dit *habillé* et le spectre $m_{4\ell}$ retrouve des valeurs plus proches de celles obtenues en utilisant les leptons nés. Afin d'imiter au mieux l'espace de phase reconstruit par les détecteurs, les leptons habillés sont utilisés pour l'espace de phase fiduciel. Lorsqu'il s'agit de l'espace de phase total, les leptons nés sont utilisés. Cette distinction permet de réduire le biais introduit par l'utilisation du générateur pour la définition de l'espace de phase fiduciel.

Facteurs d'acceptance et de correction

Pour l'extrapolation de l'espace de phase fiduciel à l'espace de phase total, les facteurs d'acceptance $\mathcal{A}$ sont définis comme le ratio d'événements entrant dans l'espace fiduciel (et satisfaisant les coupures, en utilisant les leptons habillés) sur le nombre total d'événements générés (sans coupures, en utilisant les leptons nés). Le calcul de ces facteurs est exclusivement mené sur les échantillons de signal simulés. Chaque mode de production est pris en compte, renormalisé par la section efficace attendue. Par définition, ces facteurs sont très dépendants au modèle choisi, et c'est pourquoi le calcul des sections efficaces totales dépend des générateurs choisis. Les facteurs sont calculés pour chaque état final, chaque mode de production et tous les événements combinés. Pour les mesures différentielles introduites ci-après, les facteurs sont de plus calculés par région des variables différentielles.

Afin de corriger les résultats obtenus pour prendre en compte les effets de résolution et de reconstruction des détecteurs, de seconds facteurs sont calculés. Ces facteurs de correction $\mathcal{C}$ s'expriment comme le ratio entre le nombre de candidats reconstruits passant les coupures (utilisation des variables et leptons

reconstruits par les détecteurs) sur le nombre de candidats sélectionnés dans l'espace de phase fiduciel (utilisation des leptons habillés). Le calcul de ces facteurs se fait également en utilisant les échantillons simulés. Si l'espace de phase fiduciel imite bien l'espace de phase reconstruit, ces facteurs sont indépendants des générateurs choisis. Les facteurs sont aussi calculés par état final, mode de production et région différentielle dans le cas de mesures différentielles. La bonne indépendance au modèle se vérifie par la non dépendance des facteurs vis-à-vis du mode de production, puisque ces derniers sont simulés en utilisant des générateurs différents. Exception est faite pour le mode $t\bar{t}H$, pour lequel l'isolation pénalise la sélection des événements reconstruits, cette dernière n'étant pas reproduite dans l'espace de phase fiduciel.

Ajustement et tests de la méthodologie

À partir de la vraisemblance introduite ci-avant et incluant les facteurs, rendements du signal et de bruit de fond avec leurs formes respectives, et intégrant les incertitudes systématiques, un profil de vraisemblance Λ est construit pour mesurer la section efficace de production totale σ_{Tot} ou fiducielle σ_{Fid}. Ce dernier s'exprime comme le ratio entre la vraisemblance maximisée pour une valeur de σ_{Tot} donnée (les paramètres s'ajustent en fonction), sur la vraisemblance maximisée indépendamment de σ_{Tot} (tous les paramètres incluant σ_{Tot} sont ajustés). Ce même profil est adapté dans le cas de σ_{Fid}. En minimisant le logarithme de ce profil, il est possible de déterminer les valeurs des sections efficaces de production.

Pour des nombres d'événements assez grands (loi des grands nombres), $-2\ln\Lambda$ suit une loi χ^2 avec un degré de liberté. Avec suffisamment de statistiques, il est donc possible d'estimer les intervalles de confiance à 68% et 95% des mesures des sections efficaces. Ces derniers se lisent sur les balayages du profil logarithmique aux alentours de la section efficace ajustée. Les valeurs de $\sigma_{\text{Tot / Fid}}$ pour lesquelles $-2\ln\Lambda < 1$ et 4 correspondent aux intervalles à 68% et 95%.

Afin de s'assurer que l'ajustement et la méthodologie n'introduisent pas de biais dans les mesures, la procédure est appliquée à des données générées en suivant directement les formes et normalisations des distributions de $m_{4\ell}$ attendues (pseudo-données). La génération de ces dernières ne demande pas autant de ressources que pour les MC et permet de vérifier que les résultats obtenus par la méthode sont proches des valeurs de sections efficaces injectées.

E.2.3 Mesures des sections efficaces inclusives

Pour la mesure des sections efficaces inclusives, une catégorie est définie par état final (quatre au total). L'ajustement des sections efficaces est fait pour chacune des catégories et pour toutes les catégories combinées. À partir de ces mesures, les points d'intérêts suivants sont définis : extraction de la section efficace fiducielle pour chaque état final et combinés (cinq points) et pour les états $4\mu + 4e$ et $2\mu 2e + 2e2\mu$ (deux points), ainsi que l'extraction de la section efficace total pour tous les états combinés (un point).

Les facteurs d'acceptance et de correction sont calculés pour chaque état final afin que leurs valeurs entrent dans l'ajustement. La normalisation et la forme des distributions du bruit de fond est vérifiée dans des régions de contrôle dédiées où la simulation est comparée aux données. Enfin, les incertitudes systématiques (sur le bruit de fond, sur la théorie et sur la reconstruction des événements) sont calculées comme décrit dans la section précédente. À celles-ci s'ajoutent les incertitudes qui affectent les deux facteurs : les choix des PDFs et des échelles de factorisation et de renormalisation, le choix de la masse du Higgs m_H = 125 GeV, la composition du signal (dans quelles proportions les différents modes de productions sont combinés) et le choix du générateur pour la production fusion gluon-gluon (cette dernière étant dominante). Les facteurs de corrections ont également une incertitude expérimentale qui affecte le calcul de leur numérateur.

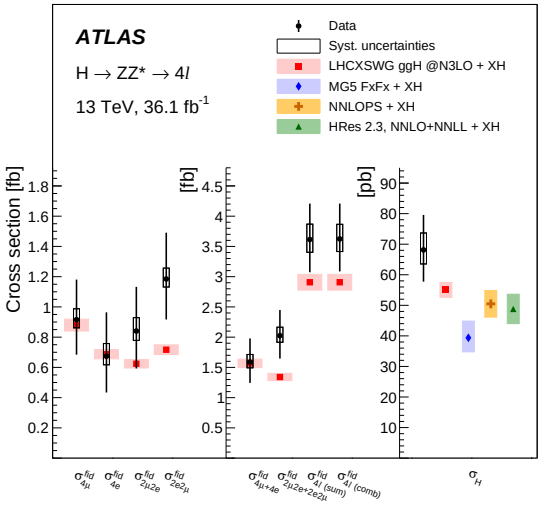

FIGURE E.2 – Sections efficaces inclusives attendues (rectangles colorés) et observées (rectangles noirs). Les incertitudes totales sont représentées par les barres d'erreur pour les données. Les incertitudes systématiques sont symbolisées par les rectangles noirs (données) et colorés (prédictions). De gauche à droite les sections efficaces fiducielles sont présentées par état final. σ_{sum} correspond à la somme des états finaux, alors que σ_{comb} est la section efficace ajustée de tous les événements combinés. Sur la droite, la section efficace total est indiquée, déduite des mesures fiducielles.

Ayant inclus ces incertitudes comme paramètres de nuisance, la procédure d'ajustement des sections efficaces est testée sur les pseudo-données. Ces tests ne laissent apparaitre aucun biais dans la méthodologie et donnent une estimation des intervalles de confiance attendus. Enfin, les sections efficaces sont déterminées pour chacun des points d'intérêt en utilisant les données correspondant à $36.1\,\text{fb}^{-1}$ collectés par ATLAS en 2015 et 2016 à $\sqrt{s} = 13\,\text{TeV}$. Pour ces mesures, les nombres présentés dans le Tab. E.1 sont utilisés comme entrées de l'ajustement. Les résultats sont regroupés dans la Fig. E.2

L'excès de candidats observés pour les états finaux $2\mu 2e$ et $2e2\mu$ résulte en des sections efficaces mesurées au-dessus de leur prédiction par le Modèle Standard. L'accord avec le modèle est estimé avec le calcul des valeurs-p qui désignent la probabilité, sachant l'hypothèse du Modèle Standard vraie, que les mesures prennent des valeurs en meilleur accord avec le modèle que celles observées. Une découverte est annoncée en physique des particules expérimentale si des valeurs-p inférieures à 5.7×10^{-7} sont obtenues. Les résultats présentés ici ne rejettent donc pas l'hypothèse du Modèle Standard.

E.2.4 Mesures des sections efficaces différentielles et interprétations

Grâce aux données collectées, il est possible de mesurer les sections efficaces de production par région de variables différentielles. Pour ces mesures, la méthodologie déployée dans le cas inclusif est utilisée, sauf que cette fois-ci les catégories correspondent aux régions et les mesures sont effectuées pour tous les états finaux combinés. Il y a donc une valeur de section efficace ajustée par région.

Les régions sont définies comme coupures sur les variables différentielles. Ces dernières incluent la cinématique du boson de Higgs dans l'état final à quatre leptons (moment transverse du boson de Higgs,

rapidité du boson de Higgs, le cosinus de l'angle polaire de la décomposition en deux bosons Z dans le référentiel au repos et les deux masses invariantes des paires de leptons), et les variables des jets de l'événement (multiplicité des jets, moment transverse du jet principal, mass invariante des deux jets principaux, écart en pseudo-rapidité et dans la direction azimutale entre les deux jets principaux, et multiplicité des jets marqués comme résultant de la décomposition de hadrons contenant des quarks bottom). Pour chacune des variables, les coupures sont définies à partir d'études sur la simulation. Il faut s'assurer d'une bonne signifiance du canal dans chaque région, d'une faible migration des événements entre les régions, et d'une bonne correspondance des régions entre espaces reconstruit, total et fiduciel. Ces régions sont en outre choisies en vue d'une future combinaison avec le canal $H \to \gamma\gamma$. En plus de ces variables, des mesures doublement différentielles sont effectuées. Les sections efficaces sont mesurées en fonction du moment transverse du boson de Higgs pour différentes multiplicités de jets, et dans des régions combinant des coupures sur les deux masses invariantes des bosons de Z.

De même que pour le cas inclusif, les facteurs d'acceptance et de correction sont calculés pour chaque région de chaque variable et il est vérifié que la dépendance au modèle reste faible. Les formes et normalisations des distributions du bruit de fond sont aussi vérifiées dans les régions de contrôle (pour chaque région différentielle) et la procédure est effectuée sur les pseudo-données pour chaque variable. À ces tests standards s'ajoutent le calcul des puretés et des matrices de migration à partir de la simulation. Les premières correspondent au nombre d'événements reconstruits entrant dans une région différentielle donnée dont l'événement fiduciel correspondant se trouve dans la même région fiducielle, divisé par le nombre d'événements reconstruits dans cette région. Ainsi plus la pureté est proche de un, plus la correction apportée par le facteur $\mathcal{C}$ sera efficace et moins la méthode sera dépendante du générateur. En effet, dans le cas optimal d'une pureté égale à l'unité, l'ensemble des événements fiduciel seront convertis en événements reconstruits sans perte ni sur-correction. De manière similaire, les matrices de migration sont des matrices dans lesquelles les rangs correspondent aux régions fiducielles et les colonnes aux régions reconstruites d'une même variable différentielle. Ainsi, chaque élément de la matrice contient le nombre d'événements entrant dans les régions fiducielles et reconstruites correspondantes. Une faible migration des événements entre les régions se traduit donc par des matrices presque diagonales, qui montrent que la définition des régions n'est pas dépendante du modèle. Pour ces mesures, les puretés (étroitement liées à la diagonale des matrices de migration) sont supérieures à 70% (40%) pour les variables de la cinématique du boson de Higgs (variables des jets). Ceci indique que la définition des régions différentielles est bonne.

L'application de la procédure aux données collectées au Run 2 pour chaque variable différentielle permet d'obtenir les sections efficaces différentielles. Ces dernières sont en bon accord avec les prédictions du Modèle Standard, aux erreurs statistiques et systématique près. Les mesures doublement différentielles en région des deux masses invariantes sont utilisées pour contraindre les interactions du boson de Higgs modifiées avec les leptons de chiralité gauche ε_{L} et droite ε_{R}, dans l'environnement des pseudo-variables. Ces mêmes mesures sont aussi utilisées pour contraindre le couplage κ du boson de Higgs avec les bosons Z. Alors que la mesure inclusive des sections efficaces permet déjà de contraindre ces paramètres de déviation au Modèle Standard, les mesures doublement différentielles améliorent les résultats : les limites dans le plan $(\varepsilon_{\mathrm{L}}, \varepsilon_{\mathrm{R}})$ et $(\varepsilon_{\mathrm{L}}, \kappa)$ permettent d'exclure la région $\varepsilon_{\mathrm{R}} > 0, \varepsilon_{\mathrm{L}} < 0$. L'ensemble des limites déduites reste en accord avec le Modèle Standard.

Bibliography

[1] L. Evans and P. Bryant. LHC machine. *Journal of Instrumentation*, 3:S08001, 2008.

[2] Group TeVI. Design report Tevatron 1 project. Technical Report FERMILAB-DESIGN-1984-01, Fermilab, 1984.

[3] J. Haffner. The CERN accelerator complex. General photo, 2013.

[4] The CERN Communication Group. LHC: the guide. Technical report, CERN, January 2008. English LHC guide.

[5] P. Grafström and W. Kozanecki. Luminosity determination at proton colliders. *Progress in Particle and Nuclear Physics*, 81:97 – 148, 2015.

[6] R. Bruce, R. W. Assmann, and S. Redaelli. Calculations of safe collimator settings and β^* at the CERN Large Hadron Collider. *Physical Review of Accelerators and Beams*, 18(6):061001, June 2015.

[7] M. Giovannozzi. Optics options for the 2015 LHC run. *arXiv*, 1410(7055), October 2014.

[8] The ATLAS Collaboration. Pile-up subtraction and suppression for jets in ATLAS. Technical report, CERN, August 2013.

[9] The ATLAS Collaboration. Luminosity public results. ATLAS public results.

[10] The MoEDAL Collaboration. Technical design report of the MoEDAL experiment. Technical Report CERN-LHCC-2009-006. MoEDAL-TDR-001, CERN, June 2009.

[11] The TOTEM Collaboration. The TOTEM experiment at the CERN Large Hadron Collider. *Journal of Instrumentation*, 3(08):S08007, 2008.

[12] The LHCf Collaboration. The LHCf detector at the CERN Large Hadron Collider. *Journal of Instrumentation*, 3(08):S08006, 2008.

[13] The ALICE Collaboration. The ALICE experiment at the CERN LHC. *Journal of Instrumentation*, 3(08):S08002, 2008.

[14] The ATLAS Collaboration. The ATLAS experiment at the CERN Large Hadron Collider. *Journal of Instrumentation*, 3(08):S08003, 2008.

[15] The CMS Collaboration. The CMS experiment at the CERN LHC. *Journal of Instrumentation*, 3(08):S08004, 2008.

[16] The LHCb Collaboration. The LHCb Detector at the LHC. *Journal of Instrumentation*, 3(08):S08005, 2008.

[17] F. Englert and R. Brout. Broken symmetry and the mass of gauge vector mesons. *Physical Review Letters*, 13(9):321–323, August 1964.

[18] P. W. Higgs. Broken symmetries and the masses of gauge bosons. *Physical Review Letters*, 13(16):508–509, October 1964.

[19] G. S. Guralnik, C. R. Hagen, and T. W. B. Kibble. Global conservation laws and massless particles. *Physical Review Letters*, 13(20):585–587, November 1964.

[20] The CMS Collaboration. Observation of a new boson at a mass of 125 GeV with the CMS experiment at the LHC. *Physics Letters B*, 716(1):30–61, 2012.

[21] The ATLAS Collaboration. Observation of a new particle in the search for the Standard Model Higgs boson with the ATLAS detector at the LHC. *Physics Letters B*, 716(1):1–29, 2012.

[22] R. Bruce *et al.* LHC Run 2: results and challenges . Technical Report CERN-ACC-2016-0103, CERN, Geneva, July 2016.

[23] E. S. Reich. Physicists plan to build a bigger LHC. *Nature*, 503(177), November 2013.

[24] C. Lester. Particle physics. Lectures of the Part III courses of the Department of Physics of the University of Cambridge, October 2013.

[25] J. Pequenao. Computer generated image of the whole ATLAS detector. Picture showing the entire ATLAS detector, 2008.

[26] J. Pequenao. Computer generated image of the ATLAS Inner Detector. Picture showing the ATLAS Inner Detector, March 2008.

[27] The ATLAS Collaboration. ATLAS Insertable B-Layer technical design report. Technical Report CERN-LHCC-2010-013. ATLAS-TDR-19, CERN, September 2010.

[28] The ATLAS Collaboration. Studies of the ATLAS Inner Detector material using $\sqrt{s}$ = 13 TeV pp collision data. Technical Report ATL-PHYS-PUB-2015-050, CERN, Geneva, November 2015.

[29] The ATLAS Collaboration. ATLAS Insertable B-Layer technical design report addendum. Technical Report CERN-LHCC-2012-009. ATLAS-TDR-19-ADD-1, CERN, May 2012. Addendum to CERN-LHCC-2010-013, ATLAS-TDR-019.

[30] The ATLAS TRT Collaboration. The ATLAS TRT Barrel Detector. *Journal of Instrumentation*, 3(02):P02014, 2008.

[31] The ATLAS TRT Collaboration. The ATLAS TRT end-cap detectors. *Journal of Instrumentation*, 3(10):P10003, 2008.

[32] The ATLAS TRT Collaboration. Basic ATLAS TRT performance studies of Run 1. Technical Report ATL-INDET-PUB-2014-001, CERN, Geneva, March 2014.

[33] The ATLAS Collaboration. Track reconstruction performance of the ATLAS Inner Detector at $\sqrt{s}$ = 13 TeV. Technical Report ATL-PHYS-PUB-2015-018, CERN, July 2015.

[34] The ATLAS Collaboration. Performance of the ATLAS detector using first collision data. *Journal of High Energy Physics*, 2010(9):1–66, 2010.

[35] The ATLAS Collaboration. Measurement of muon momentum resolution of the ATLAS detector. *European Physical Journal Web of Conferences*, 28:12039, June 2012.

[36] The ATLAS Collaboration. ATLAS liquid-argon calorimeter: technical design report. Technical report, CERN, 1996.

[37] J. Pequenao. Computer generated image of the ATLAS calorimeter. Overview of the ATLAS calorimeters, March 2008.

[38] The ATLAS Collaboration. Design, construction and installation of the ATLAS Hadronic Barrel Scintillator-Tile Calorimeter. Technical Report ATL-TILECAL-PUB-2008-001.ATL-COM-TILECAL-2007-019, CERN, November 2007.

[39] The ATLAS Collaboration. Electron and photon energy calibration with the ATLAS detector using data collected in 2015 at $\sqrt{s}$ = 13 TeV. Technical Report ATL-PHYS-PUB-2016-015, CERN, Geneva, August 2016.

[40] The ATLAS Collaboration. Muon reconstruction performance of the ATLAS detector in proton–proton collision data at $\sqrt{s}$ = 13 TeV. *The European Physical Journal C*, 76(5):1–30, 2016.

[41] Public Liquid-Argon Calorimeter plots on detector status.

[42] W. Lampl, S. Laplace, D. Lelas, P. Loch, H. Ma, S. Menke, S. Rajagopalan, D. Rousseau, S. Snyder, and G. Unal. Calorimeter clustering algorithms: description and performance. Technical Report ATL-LARG-PUB-2008-002, CERN, Geneva, April 2008.

[43] The ATLAS Collaboration. Electron efficiency measurements with the ATLAS detector using the 2015 LHC proton-proton collision data. Technical Report ATLAS-CONF-2016-024, CERN, Geneva, June 2016.

[44] The ATLAS Collaboration. ATLAS muon spectrometer: technical design report. Technical report, CERN, Geneva, 1997.

[45] E. Diehl. Calibration and Performance of the ATLAS Muon Spectrometer. *arXiv*, 2011.

[46] G. Artoni *et al.* Support Note for 2015 Muon Combined Performance Paper. Technical Report ATL-COM-PHYS-2015-1149, CERN, Geneva, September 2015. Support note for ATL-COM-PHYS-2015-1564.

[47] C. Grupen and B. Shwartz. *Particle detectors*, volume Cambridge Monographs on Particle Physics, Nuclear Physics and Cosmology. Cambridge University Press, 2011.

[48] C. Bini. Study of the performance of the ATLAS Muon Spectrometer. Technical Report ATL-MUON-SLIDE-2011-685, CERN, October 2011.

[49] P. Bagnaia *et al.* Calibration model for the MDT chambers of the ATLAS Muon Spectrometer. Technical Report ATL-MUON-PUB-2008-004. ATL-COM-MUON-2008-006, CERN, Geneva, February 2008.

[50] M. Iodice. Calibration and performance of the Precision Chambers of the ATLAS Muon Spectrometer. Technical Report ATL-MUON-PROC-2011-009, CERN, Geneva, November 2011.

[51] T. Argyropoulos *et al.* Cathode Strip Chambers in ATLAS: installation, commissioning and in situ performance. In *2008 IEEE Nuclear Science Symposium Conference Record*, pages 2819–2824, October 2008.

[52] G. Cattani. Performance of the ATLAS Resistive Plate Chambers. *Nuclear Instruments and Methods in Physics Research Section A: Accelerators, Spectrometers, Detectors and Associated Equipment*, 661, Supplement 1:S6 – S9, 2012. X. Workshop on Resistive Plate Chambers and Related Detectors (RPC 2010).

[53] The ATLAS NSW Collaboration. New Small Wheel technical design report. Technical Report CERN-LHCC-2013-006. ATLAS-TDR-020, CERN, June 2013.

[54] The ATLAS Collaboration. Muon alignment performance using the final 2015 muon alignment.

[55] T. Cornelissen, M. Elsing, S. Fleischmann, W. Liebig, E. Moyse, and A. Salzburger. Concepts, design and implementation of the ATLAS New Tracking (NEWT). Technical Report ATL-SOFT-PUB-2007-007. ATL-COM-SOFT-2007-002, CERN, Geneva, March 2007.

[56] The ATLAS Collaboration. Performance of the ATLAS Silicon Pattern Recognition Algorithm in data and simulation at $\sqrt{s} = 7\,\text{TeV}$. Technical Report ATLAS-CONF-2010-072, CERN, Geneva, July 2010.

[57] J. Illingworth and J. Kittler. A survey of the Hough transform. *Computer Vision, Graphics, and Image Processing*, 44(1):87 – 116, 1988.

[58] The ATLAS Collaboration. Performance of the ATLAS trigger system in 2015. Technical report, CERN, 2016.

[59] The ATLAS Collaboration. ATLAS computing: technical design report. Technical report, CERN, 2005.

[60] R. Brun *et al.* ROOT — An object oriented data analysis framework. *Nuclear Instruments and Methods in Physics Research Section A: Accelerators, Spectrometers, Detectors and Associated Equipment*, 389(1):81 – 86, 1997.

[61] The ATLAS Collaboration. ATLAS computing workbook.

[62] P. J. Laycock, N. Ozturk, M. Beckingham, R. Henderson, and L. Zhou. Derived physics data production in ATLAS: experience with Run 1 and looking ahead. *Journal of Physics: Conference Series*, 513(3):032052, 2014.

[63] The ATLAS Collaboration. Optimisation and performance measurements of ROOT-based data formats in the ATLAS experiment. *Journal of Physics: Conference Series*, 331(3):032032, 2011.

[64] A. Buckley, T. Eifert, M. Elsing, D. Gillberg, K. Koeneke, A. Krasznahorkay, and E. Moyse. Report of the xAOD design group. Technical Report ATL-COM-SOFT-2013-022, CERN, September 2013.

[65] The ATLAS Collaboration. The ATLAS simulation infrastructure. *The European Physical Journal C*, 70(3):823–874, 2010.

[66] C. Debenedetti. Concepts for fast large scale Monte Carlo production for the ATLAS experiment. Technical Report ATL-SOFT-SLIDE-2013-790, CERN, October 2013.

[67] J. Allison. Facilities and methods: Geant4 – a simulation toolkit. *Nuclear Physics News*, 17(2):20–24, 2007.

[68] https://twiki.cern.ch/twiki/bin/view/AtlasProtected/InDetTrackingPerformanceGuidelines, May 2016. The selection of tracks for the Loose working point.

[69] A. Lesage, D. Zhang, S. Laplace, J.-B. De Vivie De Regie, M. Zgubič, N. Kondrashova, R. Nikolaidou, J. Poveda, G. R. Lee, N. Proklova, Y.-T. Shen, Z. Wang, L. Zhang, J. Guo, and H. Yang. ATLAS electron, photon and muon isolation in Run 2. Technical Report ATL-COM-PHYS-2017-290, CERN, Geneva, March 2017.

[70] https://twiki.cern.ch/twiki/bin/viewauth/AtlasProtected/Run2IsolationHarmonisation, November 2014. The isolation variables for Run 2.

[71] https://twiki.cern.ch/twiki/bin/view/AtlasProtected/MuonIsolationPerformance, January 2016. The performance of the muon isolation.

[72] B. Lenzi. *Search for the Higgs boson decaying to four leptons in the ATLAS detector at LHC and studies of muon isolation and energy loss.* PhD thesis, Université Paris Sud XI, September 2010.

[73] S. Alioli, P. Nason, C. Oleari, and E. Re. NLO vector-boson production matched with shower in POWHEG. *Journal of High Energy Physics*, 07:060, 2008.

[74] T. Sjostrand, S. Mrenna, and P. Z. Skands. A Brief Introduction to PYTHIA 8.1. *Computer Physics Communications*, 178:852–867, 2008.

[75] The ATLAS Collaboration. Measurement of the Z/γ^* boson transverse momentum distribution in pp collisions at $\sqrt{s} = 7\,\text{TeV}$ with the ATLAS detector. *Journal of High Energy Physics*, 09:145, 2014.

[76] D. J. Lange. The EvtGen particle decay simulation package. *Nuclear Instruments and Methods in Physics Research Section A*, 462(1–2):152 – 155, 2001. BEAUTY2000, Proceedings of the 7th Int. Conf. on B-Physics at Hadron Machines.

[77] R. Frederix, E. Re, and P. Torrielli. Single-top t-channel hadron production in the four-flavour scheme with POWHEG and aMC@NLO. *Journal of High Energy Physics*, 09:130, 2012.

[78] T. Sjostrand, S. Mrenna, and P. Z. Skands. PYTHIA 6.4 physics and manual. *Journal of High Energy Physics*, 05:026, 2006.

[79] S. Laplace and J.-B. de Vivie. Calorimeter isolation and pile-up. Technical Report ATL-COM-PHYS-2012-467, CERN, Geneva, May 2012.

[80] https://twiki.cern.ch/twiki/bin/view/AtlasProtected/IsolationOptimization, September 2015. The optimisation of the isolation working points.

[81] https://twiki.cern.ch/twiki/bin/view/AtlasProtected/IsolationSelectionTool, September 2015. The IsolationSelectionTool.

[82] https://twiki.cern.ch/twiki/bin/view/Atlas/MuonSelectionTool, April 2015. Cuts on muon ID tracks.

[83] M. Cacciari, G. P. Salam, and G. Soyez. The Anti-k_t jet clustering algorithm. *Journal of High Energy Physics*, 04:063, 2008.

[84] The ATLAS Collaboration. Jet energy scale and its systematic uncertainty in proton-proton collisions at $\sqrt{s}$ = 7 TeV with ATLAS 2011 data. Technical Report ATLAS-CONF-2013-004, CERN, Geneva, January 2013.

[85] S. Alioli, P. Nason, C. Oleari, and E. Re. NLO Higgs boson production via gluon fusion matched with shower in POWHEG. *Journal of High Energy Physics*, 04:002, 2009.

[86] P. Nason and C. Oleari. NLO Higgs boson production via vector-boson fusion matched with shower in POWHEG. *Journal of High Energy Physics*, 02:037, 2010.

[87] https://twiki.cern.ch/twiki/bin/view/AtlasProtected/IsolationOverlapRemoval, August 2016. The isolation correction for close-by objects.

[88] The CMS Collaboration. Precise determination of the mass of the Higgs boson and studies of the compatibility of its couplings with the standard model. Technical Report CMS-PAS-HIG-14-009, CERN, Geneva, 2014.

[89] The ATLAS and the CMS Collaborations. Combined measurement of the Higgs boson mass in *pp* collisions at $\sqrt{s}$ = 7 and 8 TeV with the ATLAS and CMS experiments. *Physical Review Letters*, 114:191803, May 2015.

[90] The ATLAS Collaboration. Evidence for the spin-0 nature of the Higgs boson using ATLAS data. *Physics Letters B*, 726(1–3):120 – 144, 2013.

[91] The ATLAS Collaboration. Study of the spin and parity of the Higgs boson in diboson decays with the ATLAS detector. *The European Physical Journal C*, 75(10):476, 2015.

[92] The CMS Collaboration. Constraints on the spin-parity and anomalous HVV couplings of the Higgs boson in proton collisions at 7 and 8 TeV. *Physical Review D*, 92:012004, November 2014.

[93] the CMS Collaboration. Measurement of the properties of a Higgs boson in the four-lepton final state. *Physical Review D*, 89:092007, December 2013.

[94] The ATLAS and the CMS Collaborations. Measurements of the Higgs boson production and decay rates and constraints on its couplings from a combined ATLAS and CMS analysis of the LHC *pp* collision data at $\sqrt{s}$ = 7 and 8 TeV. *Journal of High Energy Physics*, 08:045, 2016.

[95] The ATLAS Collaboration. Fiducial and differential cross sections of Higgs boson production measured in the four-lepton decay channel in *pp* collisions at $\sqrt{s}$ = 8 TeV with the ATLAS detector. *Physics Letters B*, 738:234 – 253, 2014.

[96] The ATLAS Collaboration. Measurements of fiducial and differential cross sections for Higgs boson production in the diphoton decay channel at $\sqrt{s}$ = 8 TeV with ATLAS. *Journal of High Energy Physics*, 09:112, 2014.

[97] The ATLAS Collaboration. Measurements of the total and differential Higgs boson production cross sections combining the $H \to \gamma\gamma$ and $H \to ZZ^* \to 4\ell$ decay channels at $\sqrt{s}$ = 8 TeV with the ATLAS detector. *Physical Review Letters*, 115(9):091801, 2015.

[98] The ATLAS Collaboration. Measurement of fiducial differential cross sections of gluon-fusion production of Higgs bosons decaying to $WW^* \to e\nu\mu\nu$ with the ATLAS detector at $\sqrt{s}$ = 8 TeV. *Journal of High Energy Physics*, 08:104, 2016.

[99] The ATLAS Collaboration. Measurements of the Higgs boson production and decay rates and coupling strengths using *pp* collision data at $\sqrt{s}$ = 7 and 8 TeV in the ATLAS experiment. Technical Report ATLAS-CONF-2015-007, CERN, Geneva, March 2015.

[100] The CMS Collaboration. Measurement of differential and integrated fiducial cross sections for Higgs boson production in the four-lepton decay channel in *pp* collisions at $\sqrt{s}$ = 7 and 8 TeV. *Journal of High Energy Physics*, 04:005, 2016.

[101] The CMS Collaboration. Measurement of differential cross sections for Higgs boson production in the diphoton decay channel in *pp* collisions at $\sqrt{s}$ = 8 TeV. *European Physics Journal*, C76(1):13, 2016.

[102] S. L. Glashow. Partial-symmetries of weak interactions. *Nuclear Physics*, 22(4):579 – 588, 1961.

[103] S. Weinberg. A model of leptons. *Physical Review Letters*, 19:1264–1266, November 1967.

[104] A. Salam. Weak and electromagnetic interactions. *8th Nobel Symposium Lerum, Sweden, May 19-25, 1968*, C680519:367–377, 1968.

[105] G. 't Hooft and M. Veltman. Regularisation and renormalisation of gauge fields. *Nuclear Physics B*, 44(1):189 – 213, 1972.

[106] P. Paganini. Physique des particules avancée. Lectures of the Master HEP École Polytechnique, 2014.

[107] The Particle Data Group. Review of Particle Physics. *Chinese Physics C*, 40:100001, 2016.

[108] P. W. Anderson. Plasmons, gauge invariance, and mass. *Physical Review*, 130:439–442, April 1963.

[109] http://tex.stackexchange.com/questions/231706/special-effects-in-tikz-leads-to-unprintable-pdf.

[110] The MuLan Collaboration. Improved measurement of the positive-muon lifetime and determination of the Fermi constant. *Physical Review Letters*, 99:032001, July 2007.

[111] A. Djouadi. The anatomy of electroweak symmetry breaking. I: The Higgs boson in the standard model. *Physics Reports*, 457:1–216, 2008.

[112] The LEP Electroweak Working Group.

[113] The LEP Electroweak Working Group. Precision Electroweak Measurements and Constraints on the Standard Model. *arXiv*, 2010.

[114] T. Hambye and K. Riesselmann. Matching conditions and Higgs boson mass upper bounds reexamined. *Physical Review D*, 55:7255–7262, June 1997.

[115] J. T. Seeman. The Stanford Linear Collider. *Annual Review of Nuclear and Particle Science*, 41(1):389–428, 1991.

[116] CERN LEP. *LEP design report*. CERN, Geneva, 1984. Copies shelved as reports in LEP, PS and SPS libraries.

[117] The SLD Electroweak Group, the DELPHI Collaboration, the LEP Collaboration, the ALEPH Collaboration, the SLD Heavy Flavour Group, the OPAL Collaboration, the LEP Electroweak Working Group, and the L3 Collaboration. A Combination of preliminary electroweak measurements and constraints on the standard model. *arXiv*, 2004.

[118] The ALEPH Collaboration, the DELPHI Collaboration, the L3 Collaboration, the OPAL Collaboration, and the LEP Working Group for Higgs Boson Searches. Search for the Standard Model Higgs boson at LEP. *Physics Letters B*, 565:61 – 75, 2003.

[119] The CDF Collaboration and the D0 Collaboration. Higgs boson studies at the Tevatron. *Physical Review D*, 88:052014, September 2013.

[120] The CMS Collaboration. Study of the mass and spin-parity of the Higgs boson candidate via its decays to Z boson pairs. *Physical Review Letters*, 110:081803, February 2013.

[121] The CMS Collaboration. Precise determination of the mass of the Higgs boson and tests of compatibility of its couplings with the standard model predictions using proton collisions at 7 and 8 TeV. *The European Physical Journal C*, 75(5):212, 2015.

[122] The ATLAS Collaboration. Measurements of Higgs boson production and couplings in diboson final states with the ATLAS detector at the LHC. *Physics Letters B*, 726(1–3):88 – 119, 2013.

[123] LHC Higgs Cross Section Working Group, D. de Florian, C. Grojean, F. Maltoni, C. Mariotti, A. Nikitenko, M. Pieri, P. Savard, M. Schumacher, and R. Tanaka (Eds). Handbook of LHC Higgs cross sections: 4. Deciphering the nature of the Higgs sector. *arXiv*, 2016.

[124] M. Klasen, M. Pohl, and G. Sigl. Indirect and direct search for dark matter. *Progress in Particle and Nuclear Physics*, 85:1 – 32, 2015.

[125] The Supernova Cosmology Project. Measurements of Ω and Λ from 42 high-redshift supernovae. *The Astrophysical Journal*, 517(2):565, 1999.

[126] The Super-Kamiokande Collaboration. Evidence for oscillation of atmospheric neutrinos. *Physical Review Letters*, 81:1562–1567, August 1998.

[127] E. K. Akhmedov, G. C. Branco, and M. N. Rebelo. Seesaw mechanism and structure of neutrino mass matrix. *Physics Letters B*, 478(1–3):215 – 223, 2000.

[128] The ATLAS Collaboration. Measurements of Higgs boson production and couplings in the four-lepton channel in pp collisions at centre-of-mass energies of 7 and 8 TeV with the ATLAS detector. *Physical Review D*, 91:012006, January 2015.

[129] The ATLAS Collaboration. Search for an additional, heavy Higgs boson in the $H \to ZZ$ decay channel at $\sqrt{s} = 8$ TeV in pp collision data with the ATLAS detector. *European Physics Journal*, C76(1):45, 2016.

[130] LHC Higgs Cross Section Working Group, S. Dittmaier, C. Mariotti, G. Passarino, and R. Tanaka (Eds). Handbook of LHC Higgs cross sections: 1. Inclusive observables. Technical report, CERN, 2011.

[131] LHC Higgs Cross Section Working Group, S. Dittmaier, C. Mariotti, G. Passarino, and R. Tanaka (Eds). Handbook of LHC Higgs cross sections: 2. Differential distributions. Technical report, CERN, 2012.

[132] R. V. Harlander and W. B. Kilgore. Next-to-next-to-leading order Higgs production at hadron colliders. *Physical Review Letters*, 88:201801, 2002.

[133] C. Anastasiou and K. Melnikov. Higgs boson production at hadron colliders in NNLO QCD. *Nuclear Physics B*, B646:220–256, 2002.

[134] V. Ravindran, J. Smith, and W. L. van Neerven. NNLO corrections to the total cross-section for Higgs boson production in hadron hadron collisions. *Nuclear Physics B*, B665:325–366, 2003.

[135] C. Anastasiou *et al.* Higgs boson gluon–fusion production at threshold in N^3LO QCD. *Physical Letters*, B737:325–328, 2014.

[136] C. Anastasiou *et al.* Higgs boson gluon-gluon fusion production beyond threshold in N^3LO QCD. *Journal of High Energy Physics*, 03:091, 2015.

[137] C. Anastasiou *et al.* High precision determination of the gluon-gluon fusion Higgs boson cross-section at the LHC. *Journal of High Energy Physics*, 05:058, 2016.

[138] U. Aglietti, R. Bonciani, G. Degrassi, and A. Vicini. Two loop light fermion contribution to Higgs production and decays. *Physics Letters B*, B595:432–441, 2004.

[139] S. Actis, G. Passarino, C. Sturm, and S. Uccirati. NLO electroweak corrections to Higgs boson production at hadron colliders. *Physics Letters B*, B670:12–17, 2008.

[140] D. de Florian and M. Grazzini. Higgs production at the LHC: updated cross sections at $\sqrt{s} = 8$ TeV. *Physics Letters B*, B718:117–120, 2012.

[141] C. Anastasiou, S. Buehler, F. Herzog, and A. Lazopoulos. Inclusive Higgs boson cross-section for the LHC at 8 TeV. *Journal of High Energy Physics*, 04:004, 2012.

[142] J. Baglio and A. Djouadi. Higgs production at the LHC. *Journal of High Energy Physics*, 03:055, 2011.

[143] M. Ciccolini, A. Denner, and S. Dittmaier. Strong and electroweak corrections to the production of Higgs + 2 jets via weak interactions at the LHC. *Physical Review Letters*, 99:161803, 2007.

[144] M. Ciccolini, A. Denner, and S. Dittmaier. Electroweak and QCD corrections to Higgs production via vector-boson fusion at the LHC. *Physical Review D*, D77:013002, 2008.

[145] K. Arnold *et al.* VBFNLO: A parton level Monte Carlo for processes with electroweak bosons. *Computer Physics Communications*, 180:1661–1670, 2009.

[146] P. Bolzoni, F. Maltoni, S.-O. Moch, and M. Zaro. Higgs production via vector-boson fusion at NNLO in QCD. *Physical Review Letters*, 105:011801, 2010.

[147] O. Brein, A. Djouadi, and R. Harlander. NNLO QCD corrections to the Higgs-strahlung processes at hadron colliders. *Physics Letters B*, B579:149–156, 2004.

[148] M. L. Ciccolini, S. Dittmaier, and M. Kramer. Electroweak radiative corrections to associated WH and ZH production at hadron colliders. *Physical Review D*, D68:073003, 2003.

[149] W. Beenakker, S. Dittmaier, M. Krämer, B. Plümper, M. Spira, and P. M. Zerwas. Higgs radiation off top quarks at the Tevatron and the LHC. *Physical Review Letters*, 87:201805, October 2001.

[150] W. Beenakker, S. Dittmaier, M. Krämer, B. Plümper, M. Spira, and P. M. Zerwas. NLO QCD corrections to $t\bar{t}H$ production in hadron collisions. *Nuclear Physics B*, B653:151–203, 2003.

[151] S. Dawson, L. H. Orr, L. Reina, and D. Wackeroth. Next-to-leading order QCD corrections to $pp \to t\bar{t}H$ at the CERN Large Hadron Collider. *Physical Review D*, 67:071503, April 2003.

[152] S. Dawson, C. Jackson, L. H. Orr, L. Reina, and D. Wackeroth. Associated Higgs production with top quarks at the large hadron collider: NLO QCD corrections. *Physical Review D*, D68:034022, 2003.

[153] R. Harlander, M. Kramer, and M. Schumacher. Bottom-quark associated Higgs-boson production: reconciling the four- and five-flavour scheme approach. *arXiv*, 2011.

[154] A. Djouadi, J. Kalinowski, and M. Spira. HDECAY: A program for Higgs boson decays in the standard model and its supersymmetric extension. *Computer Physics Communications*, 108:56–74, 1998.

[155] A. Bredenstein, A. Denner, S. Dittmaier, and M. M. Weber. Precise predictions for the Higgs-boson decay $H \to WW/ZZ \to 4$ leptons. *Physical Review D*, D74:013004, 2006.

[156] A. Bredenstein, A. Denner, S. Dittmaier, and M. M. Weber. Radiative corrections to the semi-leptonic and hadronic Higgs-boson decays $H \to WW/ZZ \to 4$ fermions. *Journal of High Energy Physics*, 02:080, 2007.

[157] K. Hamilton, P. Nason, E. Re, and G. Zanderighi. NNLOPS simulation of Higgs boson production. *Journal of High Energy Physics*, 10:222, 2013.

[158] G. Luisoni, P. Nason, C. Oleari, and F. Tramontano. $HW^{\pm}/HZ + 0$ and 1 jet at NLO with the POWHEG BOX interfaced to GoSam and their merging within MiNLO. *Journal of High Energy Physics*, 10:083, 2013.

[159] J. Butterworth *et al.* PDF4LHC recommendations for LHC Run II. *Journal of Physics G*, G43:023001, 2016.

[160] K. Hamilton, P. Nason, and G. Zanderighi. MINLO: multi-scale improved NLO. *Journal of High Energy Physics*, 10:155, 2012.

[161] S. Catani and M. Grazzini. A NNLO subtraction formalism in hadron collisions and its application to Higgs boson production at the LHC. *Physical Letters*, 98:222002, 2007.

[162] M. Grazzini. NNLO predictions for the Higgs boson signal in the $H \to WW\ell\nu\ell\nu$ and $H \to ZZ \to 4\ell$ decay channels. *Journal of High Energy Physics*, 02:043, 2008.

[163] K. Hamilton, P. Nason, C. Oleari, and G. Zanderighi. Merging $H/W/Z + 0$ and 1 jet at NLO with no merging scale: a path to parton shower + NNLO matching. *Journal of High Energy Physics*, 05:082, 2013.

[164] J. Alwall, R. Frederix, S. Frixione, V. Hirschi, F. Maltoni, O. Mattelaer, H. S. Shao, T. Stelzer, P. Torrielli, and M. Zaro. The automated computation of tree-level and next-to-leading order differential cross sections, and their matching to parton shower simulations. *Journal of High Energy Physics*, 07:079, 2014.

[165] H.-L. Lai *et al.* New parton distributions for collider physics. *Physical Review D*, D82:074024, 2010.

[166] M. Bahr *et al.* Herwig++ physics and manual. *European Physics Journal*, C58:639–707, 2008.

[167] M. H. Seymour and A. Siódmok. Constraining MPI models using σ eff and recent Tevatron and LHC Underlying Event data. *Journal of High Energy Physics*, 2013(10):113, October 2013.

[168] R. Frederix and S. Frixione. Merging meets matching in MC@NLO. *Journal of High Energy Physics*, 12:061, 2012.

[169] D. de Florian, G. Ferrera, M. Grazzini, and D. Tommasini. Transverse-momentum re-summation: Higgs boson production at the Tevatron and the LHC. *Journal of High Energy Physics*, 11:064, 2011.

[170] D. de Florian, G. Ferrera, M. Grazzini, and D. Tommasini. Higgs boson production at the LHC: transverse momentum re-summation effects in the $H \to \gamma\gamma$, $H \to WW \to \ell\nu\ell\nu$ and $H \to ZZ \to 4\ell$ decay modes. *Journal of High Energy Physics*, 06:132, 2012.

[171] A. D. Martin, W. J. Stirling, R. S. Thorne, and G. Watt. Parton distributions for the LHC. *European Physics Journal*, C63:189–285, 2009.

[172] M. Gonzalez-Alonso, A. Greljo, G. Isidori, and D. Marzocca. Pseudo-observables in Higgs decays. *European Physics Journal*, C75:128, 2015.

[173] M. Gonzalez-Alonso, A. Greljo, G. Isidori, and D. Marzocca. Electroweak bounds on Higgs pseudo-observables and $H \to 4\ell$ decays. *European Physics Journal*, C75:341, 2015.

[174] A. Alloul, N. D. Christensen, C. Degrande, C. Duhr, and B. Fuks. FeynRules 2.0 - A complete toolbox for tree-level phenomenology. *Computer Physics Communications*, 185:2250–2300, 2014.

[175] The ATLAS Collaboration. ATLAS Run 1 Pythia8 tunes. Technical Report ATL-PHYS-PUB-2014-021, CERN, Geneva, November 2014.

[176] F. Cascioli *et al.* ZZ production at hadron colliders in NNLO QCD. *Physical Letters B*, B735:311–313, 2014.

[177] M. Grazzini, S. Kallweit, and D. Rathlev. ZZ production at the LHC: fiducial cross sections and distributions in NNLO QCD. *Physical Letters B*, B750:407–410, 2015.

[178] B. Biedermann, A. Denner, S. Dittmaier, L. Hofer, and B. Jäger. Electroweak corrections to $pp \to \mu^+\mu^-e^+e^-+X$ at the LHC: a Higgs background study. *Physical Review Letters*, 116(16):161803, 2016.

[179] T. Gleisberg, S. Höche, F. Krauss, M. Schönherr, S. Schumann, F. Siegert, and J. Winter. Event generation with SHERPA 1.1. *Journal of High Energy Physics*, 2009(02):007, 2009.

[180] F. Caola, K. Melnikov, R. Röntsch, and L. Tancredi. QCD corrections to ZZ production in gluon fusion at the LHC. *Physical Review D*, D92(9):094028, 2015.

[181] J. M. Campbell, R. K. Ellis, M. Czakon, and S. Kirchner. Two loop correction to interference in $gg \to ZZ$. *Journal of High Energy Physics*, 08:011, 2016.

[182] K. Melnikov and M. Dowling. Production of two Z-bosons in gluon fusion in the heavy top quark approximation. *Physical Letters B*, B744:43–47, 2015.

[183] C. S. Li, H. T. Li, D. Y. Shao, and J. Wang. Soft gluon re-summation in the signal-background interference process of $gg(\to H) \to ZZ$. *Journal of High Energy Physics*, 08:065, 2015.

[184] J. Alwall, M. Herquet, F. Maltoni, O. Mattelaer, and T. Stelzer. MadGraph 5: going beyond. *Journal of High Energy Physics*, 2011(6):128, 2011.

[185] P. Golonka and Z. Was. PHOTOS Monte Carlo: A precision tool for QED corrections in Z and W decays. *European Physics Journal*, C45:97–107, 2006.

[186] S. Jadach, Z. Was, R. Decker, and Johann H. Kuhn. The tau decay library TAUOLA: Version 2.4. *Computer Physics Communications*, 76:361–380, 1993.

[187] P. Golonka *et al.* The tauola-photos-F environment for the TAUOLA and PHOTOS packages, release II. *Computer Physics Communications*, 174(10):818 – 835, 2006.

[188] The ATLAS Collaboration. Electron efficiency measurements with the ATLAS detector using the 2012 LHC proton-proton collision data. Technical Report ATLAS-CONF-2014-032, CERN, Geneva, June 2014.

[189] The ATLAS Collaboration. Electron identification measurements in ATLAS using $\sqrt{s}$ = 13 TeV data with 50 ns bunch spacing. Technical Report ATL-PHYS-PUB-2015-041, CERN, Geneva, September 2015.

[190] The ATLAS Collaboration. Properties of jets and inputs to jet reconstruction and calibration with the ATLAS detector using proton-proton collisions at $\sqrt{s}$ = 13 TeV. Technical Report ATL-PHYS-PUB-2015-036, CERN, Geneva, Augst 2015.

[191] C. Sawyer, C. J. Young, C. Issever, and D. Lopez Mateos. Monte Carlo calibration and combination of in-situ measurements of jets in ATLAS. Technical Report ATL-COM-PHYS-2015-071, CERN, Geneva, January 2015.

[192] The ATLAS Collaboration. Jet calibration and systematic uncertainties for jets reconstructed in the ATLAS detector at $\sqrt{s} = 13\,\text{TeV}$. Technical Report ATL-PHYS-PUB-2015-015, CERN, Geneva, July 2015.

[193] The ATLAS Collaboration. Tagging and suppression of pileup jets with the ATLAS detector. Technical Report ATLAS-CONF-2014-018, CERN, Geneva, May 2014.

[194] The ATLAS Collaboration. Selection of jets produced in 13 TeV proton-proton collisions with the ATLAS detector. Technical Report ATLAS-COM-CONF-2015-024, CERN, Geneva, May 2015.

[195] The ATLAS Collaboration. Optimisation of the ATLAS b-tagging performance for the 2016 LHC run. Technical Report ATL-PHYS-PUB-2016-012, CERN, Geneva, June 2016.

[196] G. Piacquadio and C. Weiser. A new inclusive secondary vertex algorithm for b-jet tagging in ATLAS. *Journal of Physics: Conference Series*, 119(3):032032, 2008.

[197] A. Hocker *et al.* TMVA - Toolkit for Multivariate Data Analysis. *Proceedings, 11th International Workshop on Advanced computing and analysis techniques in physics research*, Advanced Computing and Analysis Techniques:040, April 2007.

[198] H. Abidi *et al.* Event selection and background estimation in the $H \to ZZ^* \to 4\ell$ channel at $\sqrt{s} = 13\,\text{TeV}$ - Moriond 2017 analysis. Technical Report ATL-COM-PHYS-2016-1599, CERN, Geneva, November 2016.

[199] T. Hryn'ova and K. Nagano. Trigger menu strategy for Run 2. Technical Report ATL-COM-DAQ-2014-054, CERN, Geneva, May 2014.

[200] H. Abidi *et al.* Common supporting note for the $H \to 4\ell$ channel: Event selection, background estimates, performance studies. Technical Report ATL-COM-PHYS-2015-1277, CERN, Geneva, October 2015.

[201] D. Adams *et al.* Recommendations of the physics objects and analysis harmonisation study groups 2014. Technical Report ATL-PHYS-INT-2014-018, CERN, Geneva, July 2014.

[202] V. Kostyukhin. VKalVrt - package for vertex reconstruction in ATLAS. Technical Report ATL-PHYS-2003-031, CERN, Geneva, August 2003.

[203] H. Abidi *et al.* Common supporting note for the $H \to 4\ell$ channel: MC samples, event selection, background estimates. Technical Report ATL-COM-PHYS-2016-413, CERN, Geneva, May 2016.

[204] H. Abidi *et al.* Event selection and background estimation for the measurement of the properties of the Higgs particle in the four-lepton decay channel with the ATLAS detector. Technical Report ATL-PHYS-INT-2014-032, CERN, Geneva, October 2014.

[205] The ATLAS Collaboration. Reconstruction of collinear final-state-radiation photons in Z decays to muons in $\sqrt{s} = 7\,\text{TeV}$ proton-proton collisions. Technical Report ATLAS-CONF-2012-143, CERN, Geneva, November 2012.

[206] H. Abidi *et al.* Mass and signal strength measurement of the Higgs particle in the four-lepton decay channel with the ATLAS detector. Technical Report ATL-COM-PHYS-2014-007, CERN, Geneva, January 2014.

[207] The ATLAS HSG2 group. Updated search for the Standard Model Higgs boson in the decay channel $H \to ZZ^{(*)} \to 4\ell$ with $4.8\,\text{fb}^{-1}$ of pp collision data at $\sqrt{s} = 7\,\text{TeV}$ with ATLAS. Technical Report ATL-COM-PHYS-2012-530, CERN, Geneva, May 2012.

[208] J. Meyer, S. Heim, R. Di Nardo, E. Mountricha, and A. Schaffer. Theoretical uncertainties and inputs occurring in $H \to ZZ$ analyses. Technical Report ATL-COM-PHYS-2015-1278, CERN, Geneva, October 2015.

[209] M. Pivk. sPlot: A Quick Introduction. *arXiv*, 2006.

[210] The ATLAS Collaboration. Measurement of differential production cross-sections for a Z boson in association with b-jets in 7 TeV proton-proton collisions with the ATLAS detector. *Journal of High Energy Physics*, 2014(10):141, 2014.

[211] H. Abidi *et al.* Supporting note for the search for additional heavy Higgs bosons in the 4ℓ final state. Technical Report ATL-COM-PHYS-2016-415, CERN, Geneva, May 2016.

[212] H. Abidi *et al.* Supporting note for the measurements of the cross sections of the Higgs boson in the $H \to 4\ell$ decay channel, categorised by production mode. Technical Report ATL-COM-PHYS-2016-414, CERN, Geneva, May 2016.

[213] K. S. Cranmer. Kernel estimation in high-energy physics. *Computer Physics Communications*, 136:198–207, 2001.

[214] J. Meyer and R. Di Nardo. Theoretical uncertainties occurring In $H \to ZZ$ analyses. Technical Report ATL-COM-PHYS-2016-1632, CERN, Geneva, Nov 2016.

[215] H. Abidi *et al.* Measurement of the fiducial, differential and total Higgs production cross sections in the $H \to ZZ^{(*)} \to 4\ell$ final state from proton–proton collisions at $\sqrt{s}$ = 13 TeV. Technical Report ATL-COM-PHYS-2016-1605, CERN, Geneva, November 2016.

[216] The ATLAS Collaboration. Study of the Higgs boson properties and search for high-mass scalar resonances in the $H \to ZZ^* \to 4\ell$ decay channel at $\sqrt{s}$ = 13 TeV with the ATLAS detector. Technical Report ATLAS-CONF-2016-079, CERN, Geneva, August 2016.

[217] M. Dobbs and J. B. Hansen. The HepMC C++ Monte Carlo event record for high energy physics. *Computer Physics Communications*, 134:41–46, 2001.

[218] A. Buckley *et al.* Proposal for truth particle observable definitions. Technical Report ATL-COM-PHYS-2014-439, CERN, Geneva, May 2014.

[219] The ATLAS Collaboration. Proposal for truth particle observable definitions in physics measurements. Technical Report ATL-PHYS-PUB-2015-013, CERN, Geneva, June 2015.

[220] Flavour tagging labelling.

[221] G. Cowan. A survey of unfolding methods for particle physics. Prepared for the Conference on Advanced Statistical Techniques in Particle Physics, Durham, England, 2002.

[222] W. Verkerke and D. P. Kirkby. The RooFit toolkit for data modelling. *European Physical Journal Web of Conferences*, C0303241:MOLT007, 2003.

[223] L. Moneta, K. Belasco, K. Cranmer, S. Kreiss, A. Lazzaro, D. Piparo, G. Schott, W. Verkerke, and M. Wolf. The RooStats project. *arXiv*, [physics.data-an](arXiv:1009.1003), September 2010.

[224] S. S. Wilks. The Large-sample distribution of the likelihood ratio for testing composite hypotheses. *The Annals of Mathematical Statistics*, 9(1):60–62, 03 1938.

[225] G. Cowan, K. Cranmer, E. Gross, and O. Vitells. Asymptotic formulae for likelihood-based tests of new physics. *European Physics Journal*, C71:1554, 2011.

[226] R. L. Wasserstein and N. A. Lazar. The ASA's statement on p-values: context, process, and purpose. *The American Statistician*, 70(2):129–133, 2016.

[227] G. Cowan. Discovery sensitivity for a counting experiment with background uncertainty, May 2012.

[228] G. Bozzi, S. Catani, D. de Florian, and M. Grazzini. Transverse-momentum re-summation and the spectrum of the Higgs boson at the LHC. *Nuclear Physics B*, 737(1–2):73 – 120, 2006.

[229] M. Grazzini and H. Sargsyan. Heavy-quark mass effects in Higgs boson production at the LHC. *Journal of High Energy Physics*, 09:129, 2013.

[230] D. Tommasini. QCD effects on Higgs boson production and decay at hadron colliders. LHCphenonet Annual Meeting, March 2012.

École Doctorale
PHENIICS
Doctoral School

Titre : Étude de la section efficace de production du boson de Higgs en quatre leptons et étude de l'isolation des muons avec l'expérience ATLAS au LHC

Mots clés : LHC, ATLAS, Higgs, Leptons, Isolation, Muons

Le sujet principal de la thèse est la mesure de la section efficace de production du boson de Higgs se décomposant en deux bosons Z dans l'état final à quatre leptons ($H \rightarrow ZZ^* \rightarrow 4l$, $l = e, \mu$), en utilisant 36.1 fb^{-1} de données collectées en 2015 et 2016 par l'expérience ATLAS au Grand Collisionneur de Hadrons (LHC) au CERN. La section efficace inclusive dans la chaîne de décomposition $H \rightarrow ZZ^* \rightarrow 4l$ est mesurée à 3.62 ± 0.53 (stat) ± 0.25 (syst) fb, en accord avec la prédiction du Modèle Standard, de 2.91 ± 0.13 fb. Plusieurs sections efficaces fiducielles différentielles sont mesurées en fonction d'observables sensibles aux modes de production et de décomposition du boson de Higgs, incluant les variables cinématiques des jets produits avec le boson de Higgs. Les données et les prédictions du Modèle Standard sont en bon accord. Les sections efficaces extraites sont aussi utilisées pour contraindre des interactions anormales du boson de Higgs avec des particules du Modèle Standard.
La deuxième partie de la thèse concerne l'isolation des muons. Les variables sont construites à partir des informations du tracker (isolation de trace) et des calorimètres (isolation calorimétrique). Elles mesurent l'activité ambiante autour de la trajectoire de la particule dans les détecteurs et constituent un outil puissant pour rejeter le bruit de fond. Avec les données collectées par ATLAS en 2015 et 2016, les distributions des variables sont comparées entre données et simulation. Des points de fonctionnement correspondant à des ensembles de coupures sur ces variables sont alors définis. En utilisant la décomposition du boson Z en deux muons, les efficacités du signal sont mesurées. Des facteurs d'échelle correspondant aux ratios entre données et simulation sont alors calculés. Le bon accord conduit à des facteurs d'échelle proches de l'unité.

Title: Study of the fiducial cross section of the Higgs boson decaying into four leptons and study of muon isolation in the ATLAS experiment at the LHC

Keywords: LHC, ATLAS, Higgs, Leptons, Isolation, Muons

The main subject of the thesis is the measurement of the production cross section of the Higgs boson decaying to two Z bosons in the four-lepton final state ($H \rightarrow ZZ^* \rightarrow 4l$, $l = e, \mu$), using 36.1 fb^{-1} of data recorded during 2015 and 2016 with the ATLAS experiment installed at the Large Hadron Collider (LHC) at CERN. The inclusive fiducial cross section in the $H \rightarrow ZZ^* \rightarrow 4l$ decay channel is measured to be 3.62 ± 0.53 (stat) ± 0.25 (syst) fb, in agreement with the Standard Model prediction of 2.91 ± 0.13 fb. Several differential fiducial cross sections are measured for observables sensitive to the Higgs-boson production and decay, including kinematic distributions of the jets produced together with the Higgs boson. Good agreement is found between the data and the predictions of the Standard Model. The extracted cross-section distributions are also used to constrain anomalous Higgs-boson interactions with Standard-Model particles.

The second part of the thesis is dedicated to the muon isolation. Isolation variables, based on information from the tracker (track-based isolation) and the calorimeters (calorimeter-based isolation) measure the ambient activity surrounding a particle in the detectors and are a powerful tool to reject background objects. Using 36.1 fb^{-1} of data recorded by ATLAS in 2015 and 2016, the variable distributions are compared with simulation. Working points are then defined as sets of cuts applied to the isolation variables. Using the Z boson decays to a pair of muons, the signal efficiency of the working points is calculated. Scale factors are then derived as ratio of efficiencies measured in data over simulation. The good agreement leads to scale factors close to one.

Université Paris-Saclay
Espace Technologique / Immeuble Discovery
Route de l'Orme aux Merisiers RD 128 / 91190 Saint-Aubin, France